Strategic Applications of Electrochemistry in Ammonia Oxidation and Alkyl Halide Reduction

Thesis by

Michael D. Zott

In Partial Fulfillment of the Requirements for

the Degree of

Doctor of Philosophy

CALIFORNIA INSTITUTE OF TECHNOLOGY

Pasadena, California

2023

(Defended February 28, 2023)

© 2023

Michael D. Zott
ORCID: 0000-0003-0535-0512

ACKNOWLEDGEMENTS

Although I do not come from an academic lineage, I want to first thank my parents for instilling in me an academic spirit. Growing up, I was always told that school was my first priority, and because of the sacrifices that my parents made, I was able to make this encouragement a reality. Despite the fact that my parents' understanding of the "schoolwork" that I now undertake is more limited than when they would help me with school assignments, they still remain fully committed to supporting me in my aspirations, even at the cost of me being far away from home. Likewise, my brother has been a staunch supporter of my academic aspirations despite this drawing me out of state. For this, I thank them, and I hope that one day these sacrifices will help me in finding a suitable job closer to home.

In the academic sphere, I have been blessed by a long list of teachers throughout my primary, secondary, and collegiate education. Each of these teachers has invigorated or inspired my learning in diverse ways, and there are too many to name individually. However, several of my scientific instructors bear mentioning. Having no particular talent or early interest in science, I credit a middle school teacher, Meeta Evers, for introducing science as a method, and often a fun one, for exploration rather than rote repetition. In high school, I enjoyed the unmatched teaching of Ed Bolton for two years. His dynamic, thorough, and (again) fun presentation of chemistry spurred my interest such that I entered college as a biochemistry major.

Before I even attended my first class, I had already found my first academic mentor in Prof. David Sherrill, my first research advisor. His dedication to the scientific community is such that he continually publishes popular theoretical chemistry course content on his website (vergil.chemistry.gatech.edu/). While teaching myself linear algebra during the summer prior to my first year, I encountered his course material online and was instantly hooked. My first day in Atlanta, I impetuously knocked on his door to meet the person that had published all the interesting material I had read online. (I later realized that this may not always be the most courteous way of connecting with someone, but this method is responsible for introducing me to a large number of incredible academic mentors throughout my undergraduate studies.) Prof. Sherrill kindly met with me and offered to introduce me to his research, and shortly thereafter I began my first foray into academic research. Although

I have drifted away from theoretical chemistry, I am grateful to Prof. Sherrill for his patience and enthusiasm in mentoring me as a young student and especially for paying for my attendance at a large number of conferences, including one at which he arranged for me to be an invited speaker.

The foreshadowing of my shift to experimental chemistry can be found in my enthusiasm for Prof. Gary Schuster's organic chemistry class that I enrolled in during my first semester at Georgia Tech. What I have always admired about organic chemists is their panache—and Prof. Schuster demonstrated this in abundance, a trait that helped initiate my interest in experimental chemistry. After doing rather poorly on the first exam, I showed up to his office hours and we chatted for a long time. I continued to stop by his office, but over time the purpose shifted from discussing organic chemistry specifically to chemistry and academia in general. Prof. Schuster truly introduced me into the academic world—its ways, its purposes, and its strategies—in a way that I would have remained wholly ignorant of without his guidance. Furthermore, he succeeded in disrupting my myopic vision of chemistry such that I became interested in myriad topics besides theoretical chemistry. By way of his advice, I eventually joined the group of Pete La Pierre in my final semester of undergraduate studies.

Prior to this shift, however, I first must mention Prof. E. Kent Barefield. As my instructor for both inorganic chemistry and an advanced synthesis lab, Prof. Barefield is the experimental chemistry analogue of Meeta Evers in that his lab course marked the first time I realized that lab work can be exciting rather than, again, rote repetition. We learned to develop our own synthetic protocols, a skill rarely taught in teaching laboratories, and we performed experiments that were on the frontier of scientific research. Of course, this also meant that some experiments failed. Adapting to failure is a crucial skill in scientific research, and I credit this class with first developing my capabilities to do so. Two aspects of inorganic chemistry caught my eye under the instruction of Prof. Barefield. First, inorganic chemistry often involves pretty colors and beautiful crystals. I will forever remember the beautiful green crystals of dibromobis(triphenylphosphine) nickel(II) that we prepared in his class, and this enthusiasm for crystals has served me well throughout my PhD. Second, inorganic chemistry is theoretically beautiful, a trait that helped bridge my interest in theoretical

chemistry with a growing enjoyment of experimental chemistry. The arguments of crystal field and molecular orbital theory continue to fascinate and inspire me, even as organic chemistry looms in my future.

In my last semester as an undergraduate, Prof. Pete La Pierre kindly introduced me to experimental chemistry in a research setting. Pete and his students, especially Dominic Russo (fellow undergraduate), provided unmatched training in synthetic inorganic chemistry that provided an excellent foundation for my PhD research. Considering how sparse my research progress was in Pete's group, I am especially grateful.

In addition to these professors, I fondly thank Prof. Joseph Sadighi, Prof. Charlie Liotta, Prof. JC Gumbart, Prof. Bill Baron, and many others for their contributions to broadening my perspective on chemistry and the academic world as a whole.

At Caltech, I was fortunate to be in the final class for which research rotations were optional, which allowed me to begin research with Prof. Jonas Peters in the summer and never look back. Jonas provides a superlative combination of training in scientific excellence and precision writing as well as access to the exact research essentials needed for success. Jonas also offered a range of sage advice, and I may have done well to have taken it to heart sooner rather than later. In particular, Jonas loved to tell me "a PhD is a marathon, not a sprint," to which I liked to respond that I used to be a sprinter. In fact, a PhD is a grueling slugfest, and 'running slower' at times may have helped me get to my destination sooner than 'sprinting.'

In the Peters Group, I overlapped with many excellent scientists, several of whom I highlight for the role they played in shaping my training:

Nina Gu—My first mentor, Nina helped me hit the ground running, and with her help I finally collected my first crystal structure.

Matt Chalkley—Both friend and colleague, Matt taught me a number of excellent lessons. The most important of all he imparted early: there is no credit for projects left unfinished. This mindset was crucial in helping me develop scientific discipline in the face of the fun prospect of starting a new project when the going gets tough.

Pablo Garrido-Barros—Pablo was an unmatched mentor in developing my appreciation for and capacity to perform electrochemical experiments. However, Pablo is also a great friend and first-rate cook, two traits that I value even more highly from our time together. I will always remember Pablo's diligence in working on our first paper together, including the late nights that often turned into early mornings.

Heejun Lee—A true synthetic mastermind, Heejun inspired me to tackle challenging synthetic problems. I will always be amazed by his encyclopedic knowledge of not only reaction conditions, but also yields and byproducts.

Meaghan Deegan—Meaghan helped shape my outlook on maintaining exceedingly high standards of scientific rigor, a lesson that we should all maintain as our foremost duty in the laboratory.

Christian Johansen—Christian's capacity for reading the scientific literature will always amaze me, and I thank him for his numerous, scrupulous corrections in my presentations and writings.

Marcus Drover—In what was often an intense scientific atmosphere, I thank Marcus for his general friendliness and encouragement to always be excited about science.

Joe Derosa—Although we did not get the chance to work on chemistry together, Joe was a constant friend in the group and a foremost companion in keeping me sane as I worked towards finishing my PhD.

Additionally, I thank my committee members: Prof. Ryan Hadt, Prof. Garnet Chan, Prof. Harry Gray, and Prof. Greg Fu. Their diverse research interests encouraged me to think outside of my, at times, narrow interests, and their insightful comments led to several large advancements in my research. In particular, a discussion with Ryan Hadt during my candidacy meeting provided the theoretical framework that inspired me to explore spin state as a handle for improving the iron complexes we have developed for ammonia oxidation.

Finally, I thank those who kept me going during my PhD. First and foremost, my love and soon to-be wife, Sara Dibrell. A gift from God and love at first sight, Sara accompanied me on more journeys than can be briefly mentioned. Working only one floor above me, it was a blessing to see you at work almost every day! Your confidence in, and loyalty to, me stabilized my life throughout the joys, and trials, of this PhD.

The other Mike of "The Mikes"—Michael Daugherty. A friend from day one, even after moving to Berkeley. Thank you for all the fun we had at Caltech and throughout California, especially your commitment to our annual Thanksgiving camping trips, even when they were cold and rainy.

Outside of Caltech, I enjoyed the constancy of my soccer team in playing almost every week: Jorge, Alfredo, Ben, Jamie, and more. They reminded me that there is a rhythm to life outside of graduate school, a lesson that is not always easy to remember.

Most importantly, I thank the triune God incarnated in Jesus Christ. No amount of scientific training could have prepared me for the challenges involved in completing my PhD. My faith in Christ and knowledge that my worth is independent of my works sustained me throughout many unexpected challenges that for long periods felt insurmountable. Relatedly, I thank my church community that provided encouragement and friendship here on Earth: Pat, Isaiah, Dan, Brian, Genti, Mark, Peter, Glenn, and many more. Your advice and patience throughout my many challenges has been invaluable.

ABSTRACT

This thesis describes the strategic application of electrochemistry in the development of catalytic systems for two challenging processes: alkyl halide reduction and ammonia oxidation. In the case of alkyl halide reduction, the ability to precisely tune electrochemical potential favored the use of electrochemistry as compared to chemical reagents. By contrast, for ammonia oxidation, electrochemistry was specifically targeted due to motivations in the eventual development of ammonia fuel cell technology. The first chapter introduces these and other advantages of electrochemistry, as well as details regarding the thermodynamic potentials and kinetic barriers associated with alkyl halide reduction or ammonia oxidation. The second chapter details our development of photoelectrochemical methodology to employ a strongly luminescent dicopper system for outer-sphere, single-electron transfer reduction of benzyl chlorides. The third chapter marks the beginning of our work in molecular iron-mediated ammonia oxidation catalysis, in which we develop our hypothesis that catalyst structures featuring *cis*-labile coordination sites should mediate ammonia oxidation. We disclose the first iron electrocatalyst ($[(TPA)Fe(MeCN)_2]^{2+}$) as well as a framework for the analysis of metrics such as overpotential, catalytic rate, and catalyst stability. The fourth chapter introduces a hypothesis for catalyst improvement—favoring low-spin electronic structures—and a model system for testing: ($[(BPM)Fe(MeCN)_2]^{2+}$). Using this second-generation catalyst, improved stability, enhanced activity, and lowered overpotential were observed. The fifth chapter explores the validity of the *cis*-labile and low-spin hypotheses via Hammett-type substituent studies on both the $[(TPA)Fe(MeCN)_2]^{2+}$ and the $[(BPM)Fe(MeCN)_2]^{2+}$ platforms. This study resulted in the development of a further enhanced molecular electrocatalyst for ammonia oxidation and revealed mechanistic information pertinent to the development of future catalytic systems.

PUBLISHED CONTENT AND CONTRIBUTIONS

Zott, M. D.; Canestraight, V. M.; Peters, J. C. Mechanism of a Luminescent Dicopper System That Facilitates Electrophotochemical Coupling of Benzyl Chlorides via a Strongly Reducing Excited State. *ACS Catal.* **2022**, *12*, 10781–10786. DOI: 10.1021/acscatal.2c03215.

M. D. Z. helped conceptualize the project and performed all experiments other than some luminescence and UV-vis titrations. M. D. Z. wrote the manuscript.

Zott, M. D.; Peters, J. C. Enhanced Ammonia Oxidation Catalysis by a Low-Spin Iron Complex Featuring *Cis* Coordination Sites. *J. Am. Chem. Soc.* **2021**, *143*, 7612–7616. DOI: 10.1021/jacs.1c02232

M. D. Z. conceptualized the project, performed the experiments, and wrote the manuscript.

Zott, M. D.;‡ Garrido-Barros, P.;‡ Peters, J. C. Electrocatalytic Ammonia Oxidation Mediated by a Polypyridyl Iron Catalyst. *ACS Catal.* **2019**, *9*, 10101–10108. DOI: 10.1021/acscatal.9b03499

M. D. Z. discovered the catalyst; solved and analyzed the crystal structures; performed and analyzed Mössbauer measurements; contributed to electrochemical and UV-vis studies; and contributed to the writing of the manuscript.

TABLE OF CONTENTS

Acknowledgements iii
Abstract viii
Published Content and Contributions ix
Table of Contents x
Abbreviations and Symbols xii

Chapter 1: Introduction 1
1.1 Opening Remarks 2
1.2 Electron Transfer Methods 3
1.3 Reaction Specific Considerations 7
1.3.1 Alkyl halide heduction 7
1.3.2 Ammonia oxidation 13
1.4 References 21

Chapter 2: Mechanism of a Luminescent Dicopper System That Facilitates Electrophotochemical Coupling of Benzyl Chlorides via a Strongly Reducing Excited State 25
2.1 Introduction 26
2.2 Results and Discussion 28
2.3 Conclusion 35
2.4 References 36

Chapter 3: Electrocatalytic Ammonia Oxidation Mediated by a Polypyridyl Iron Catalyst 40
3.1 Introduction 41
3.2 Results and Discussion 45
3.2.1 Electrocatalytic conversion of NH_3 to N_2 and H_2 45
3.2.2 Investigation of catalyst stability 46
3.2.3 Mechanistic insight into the first redox process (E_1) 51
3.2.4 Mechanistic insight into the catalytic process (E_2) 56
3.3 Conclusion 59
3.4 References 61

Chapter 4: Enhanced Ammonia Oxidation Catalysis by a Low-Spin Iron Complex Featuring *Cis* Coordination Sites 65
4.1 Introduction 66
4.2 Results and Discussion 68
4.3 Conclusion 76
4.4 References 77

Chapter 5: Improving Molecular Iron Ammonia Oxidation Electrocatalysts via Substituent Tuning 80
5.1 Introduction 81
5.2 Results and Discussion 83
5.3 Conclusion 90
5.4 References 91

Appendix A: Supplementary Information for Chapter 2 94

Appendix B: Supplementary Information for Chapter 3 144

Appendix C: Supplementary Information for Chapter 4 203

Appendix D: Supplementary Information for Chapter 5 311

ABBREVIATIONS AND SYMBOLS

A. Area

ANA. Ammonia Nucleophilic Attack

AO. Ammonia Oxidation

BDD. Boron Doped Diamond

BDFE. Bond Dissociation Free Energy

bpyPy$_2$Me *or* **BPM**. 6-(1,1-bis(pyridin-2-yl)ethyl)-2,2'-bipyridine

C. Charge

cm^{-1}. Wavenumbers

CPC. Controlled Potential Coulometry

CV. Cyclic Voltammetry (or Voltammogram)

°C. Degrees Celsius

δ. Isomer shift

Δ_{eq}. Quadrupole splitting

ΔG. Gibbs free energy

dap. 2,9-dianisyl-1,10-phenanthroline

DBU. 1,8-Diazabicyclo[5.4.0]undec-7-ene

DCA. Dicyanoanthracene

DFT. Density Functional Theory

DME. 1,2-dimethoxyethane

DPV. Differential Pulse Voltammetry (or Voltammogram)

E. Potential

$E_{1/2}$. Half-Wave Potential

$E°$. Standard Potential

$E°_{cat}$. Standard Potential for Catalysis

EC. Electrochemical-Chemical

E_{onset}. Onset Potential

E_p. Peak potential

$E_{p/2}$. Half-peak potential

Eq. Equation

equiv. Equivalent

ET. Electron Transfer

eV. Electron Volt

η. Overpotential

F. Faraday's constant

Fc. Ferrocene

FE. Faradaic Efficiency

GC. Gas Chromatography *or* Glassy Carbon

GJ. Gigajoules

h. Hours

I2N. Interaction of Two Nitrogens

K. Kelvin

k'_{obs}. Second order observed rate constant

kcal. Kilocalorie

L. Two-electron donor ligand

LFER. Linear Free Energy Relationship

LSV. Linear Sweep Voltammetry (or Voltammogram)

λ. Wavelength

M. Molar

Me. Methyl

mL. Milliliters

mm. Millimeters

MS. Mass Spectrometry

μB. Bohr magneton

nm. Nanometers

NpMI. *N*-arylmaleimide

ν. Frequency

R. Gas constant

RT. Room Temperature

s. Seconds

S. Electron Spin

SHE. Standard Hydrogen Electrode

SI. Supporting Information

SV. Stern-Volmer

T. Temperature

THF. Tetrahydrofuran

TOF. Turnover Frequency

TON. Turnover Number

TPA. Tris(2-pyridylmethyl)amine

τ_0. Fluorescence lifetime

UV-Vis. Ultraviolet-visible

V. Volt

XRD. X-ray Diffraction

C h a p t e r 1

Introduction

1.1 Opening Remarks

Electron transfer is a common mechanistic step in a wide range of chemical reactions.[1] This step is so prevalent that its appearance is seen in contexts as diverse as pharmaceutical synthesis,[2] qubit engineering,[3] biosensing,[4] sustainable fuels,[5,6] and many others. This is unsurprising given that, at least in our current conceptualization of physical reality, electrons are one of the primary subatomic particles, and their precise energies and arrangements in both atoms and molecules—the electronic structures—dictate chemical reactivity. Thus, by combining synthetic strategies to tune chemical structure with electrochemical methods that permit precise control over chemical potential, chemical reactions can be tuned in a well-controlled manner.[7,8,9,10] In this thesis, I develop reactions that follow this framework: carefully selected electrocatalyst structures are synergistically paired with an electrode at precisely tuned electrochemical potentials to address the specific challenges of enabling single-electron reduction of alkyl halides and multi-electron oxidation of ammonia (Scheme 1.1).

Scheme 1.1. Electron transfer in alkyl halide reduction and ammonia oxidation.

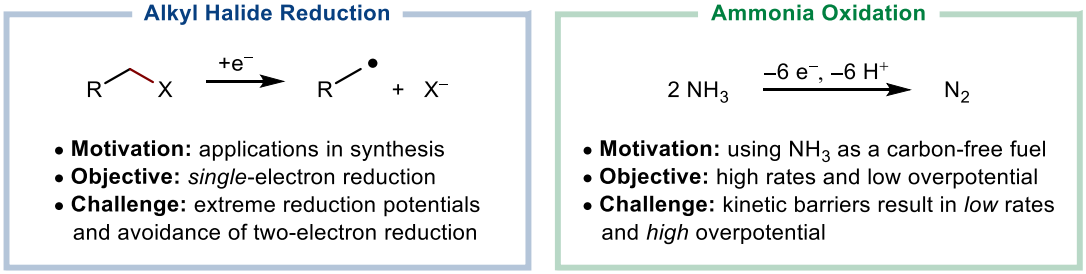

1.2 Electron Transfer Methods

To physically mediate electron transfer, numerous strategies exist, of which I highlight three prevalent in synthesis and sustainability chemistry: (1) chemical electron transfer, (2) photocatalysis, and (3) electrochemical bias.[2,11,12] Each strategy is distinct with respect to factors such as ease of tunability, electron transfer kinetics, and chemical compatibility, all of which can be influenced by characteristics such as the redox potential and the spatiotemporal availability of the electron transfer agent. We will first establish a framework for considering these principles using chemical reagents as an example, and then discuss the advantages and disadvantages of each strategy.

Chemical electron transfer reagents can be organic, inorganic, or organometallic in nature and typically promote either single- or multi-electron transfer in an irreversible fashion. Thus, they are commonly employed as stoichiometric reagents. As a simple example, an alkali metal such as lithium reacts via single-electron transfer with a proton, forming a lithium cation and a hydrogen atom (eventually released in the form of elemental hydrogen; Equation 1.1). To quantify the propensity of reagents to donate or receive electrons, their electrochemical potential can be analyzed versus a reference reaction, establishing a thermodynamic scale.[13] One such reference is the half-reaction describing reduction of protons to hydrogen, a component of Equation 1.1, which comprises the standard hydrogen electrode (SHE) that determines the potential reference of 0 V vs SHE. Since the reduction potential for Li^+/Li vs SHE is −3.1 V,[14] the reaction is highly favorable.

$$2\ Li + 2\ H^+ \longrightarrow 2\ Li^+ + H_2 \quad \text{(Equation 1.1)}$$

The thermodynamic driving force can be related to the reaction kinetics for electron transfer. For example, several models, such as Marcus theory, exist to quantify this relationship.[1] Kinetic factors that can be categorized as spatiotemporal strongly influence the experimentally observable reaction rates. For a heterogeneous reductant like lithium, the reaction rate is a function of surface area, with higher surface area resulting in higher reaction rate due to mass transfer effects. Furthermore, the reacting substrate (for Equation 1.1, H^+) must be brought within close proximity to the electron transfer agent. With soluble reaction components, this difficulty is obviated when the redox reagent is uniformly dispersed. Electron transfer is generally very fast, but temporal limitations can result in significantly reduced rates. For example, inner-sphere electron transfers that rely on complexation of the redox reagent and the substrate are regulated by the equilibrium between complexed and uncomplexed states.

An extensive discussion on advantages and disadvantages of chemical redox reagents, as well as details regarding their preparation and use, has been reviewed by Connelly and Geiger.[11] In brief, some advantages include superior applicability to large-scale reactions, compatibility with non-polar solvents, and, when soluble, extremely fast reaction rates. However, the greatest limitation of chemical redox reagents is their limited tunability, since any change in redox potential requires synthetic modifications. Such modifications may be challenging experimentally, and the resultant shifts in redox potential are discrete. While shifts can occasionally be brought about in a narrow capacity via solvent or electrolyte effects, more commonly, covalent modification via attachment of electron-donating or -withdrawing groups is required. Considering compatibility, chemical reagents can also be

problematic given that they are used in a stoichiometric fashion. Thus, for a reductant such as lithium or an oxidant such as a nitrosonium salt, the product species (lithium cation or nitric oxide) can interact chemically with other reaction components.

Electrochemical methods are the most developed alternatives to chemical reagents. Unlike chemical reagents that have discrete redox potentials, the electrochemical potential can be continuously tuned using a potentiostat. This allows for modifications to reaction driving force, small or large, to be readily interrogated. Furthermore, electrochemical cells can be engineered such that the byproducts of electron transfer do not come in contact with the reaction components of interest by utilizing a multi-compartment cell, since inert electrodes can serve solely as a conduit for electrons rather than as reagents themselves. This permits extensive engineering of the electrode surface to promote compatibility.[15] Since the potentiostat records both potential and current, a large number of electroanalytical methods exist for mechanistic investigations, and even extremely fast reactions can routinely be studied using voltametric methods. Some limitations of electrochemistry include the requirement of electrolyte, the typical reliance on polar solvents, and the difficulty of reaction setup.

Finally, photocatalysis is a growing strategy for effecting electron transfer in both redox-neutral and net-reductive or -oxidative transformations. Photocatalysis, like chemical redox strategies, relies on chemical compounds with unique redox properties and excited state lifetimes. The primary advantages of photocatalysis are the ability to access extreme redox potentials without jeopardizing compatibility, as well as the ease of favoring single-electron over multi-electron transfer. Since photon energies are high—blue light (440 nm) is

equivalent to 65 kcal/mol (2.8 eV)—substrates that would typically be challenging to selectively activate using chemical reagents become accessible. The preference for single-electron transfer arises from the fact that most photocatalyst structures are only photoactive in an oxidative or reductive capacity in a single oxidation state; upon gaining or losing an electron, their redox and photochemical properties become dramatically altered. This facilitates the generation of substrate-derived radical intermediates that are rapidly consumed in subsequent chemical steps. This prevents additional redox chemistry from occurring, since the photocatalyst must be turned over before an electron transfer of the same polarity occurs. One dual advantage/disadvantage is that in the quenched (i.e., post electron-transfer) state, the photocatalyst can again absorb energy via light and photosensitize a reaction of the opposite polarity. This establishes the basis for redox-neutral photocatalysis, an important and broad field, but can be detrimental to promoting purely reductive or oxidative transformations. Photocatalysts share the challenge of discrete redox potentials with chemical reagents but face the additional challenge that leveling effects are often observed when attempting to make a given photosensitizer more potent. That is, changing the ground state potential often compensatorily moves the excitation energy in the opposite direction, resulting in minimal perturbation of the net excited state redox potential. Additionally, the mass-transfer phenomena governing reaction rates with heterogeneous redox reagents find a parallel in photosensitizers in that photosensitizers are only active in the excited state, and excited state lifetimes are often short (less than several microseconds). While this can promote selectivity, it also challenges reaction scaleup and limits overall reaction rate.

1.3 Reaction-Specific Considerations

The specific reactions of interest, single-electron alkyl halide reduction and multi-electron ammonia oxidation (AO), feature distinct thermodynamic and kinetic challenges. Both reactions typically incur high overpotential (the amount of input energy required in excess of the thermodynamic minimum), but the origin of the overpotential is distinct. In this section, we discuss the fundamental reaction-specific challenges and considerations for alkyl halide reduction and ammonia oxidation.

1.3.1 Alkyl halide reduction

The research objective of single-electron alkyl halide reduction to produce alkyl radicals (Equation 1.2) is substantially motivated by synthetic utility as the resultant radicals can be employed in a wide variety of transformations.[16,17,18] As such, the primary constraints include chemoselectivity; amenability to primary, secondary, and tertiary alkyl halides; and compatibility with other reaction components (e.g., catalysts, other reagents, additives).

$$R–X + e^- \longrightarrow R\bullet + X^-$$ (Equation 1.2)

While large overpotential is a challenge inherent to the reaction class, it is limiting only insofar as it affects chemoselectivity, substrate applicability, and compatibility. Overpotential, and the requisite applied potential, vary dramatically depending on the precise structure of the alkyl halide.[19,20,21]

Factors that contribute to the effective reduction potential of alkyl halides include halide identity, conjugation, and substitution pattern (Scheme 1.2). In general, reduction is

easier (i.e., $E°$ is less negative) in the order I > Br > Cl > F. Thus, fluorides and chlorides are more challenging to reduce than are analogous bromides and iodides. When the halogen-bearing carbon is in conjugation with π-bonds, as in allylic or benzylic systems, or with electron-withdrawing groups, the reduction event also becomes easier. Finally, increased substitution at the halogen-bearing carbon makes reduction easier in the order tertiary > secondary > primary. Generally, the effect of these factors on $E°$ is in the range of 100–1000 mV, with halide identity being the most influential factor. Thus, the exact reaction outcome can be subject to many, potentially competing, factors.

Scheme 1.2. Effects of alkyl halide structure on reduction potential.

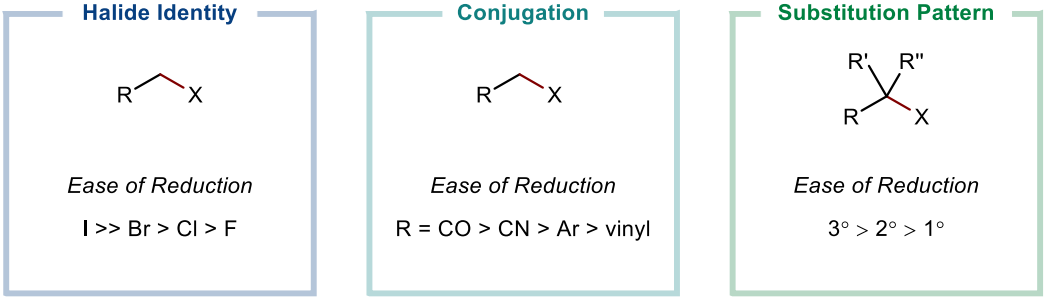

The reaction outcome of electron transfer to alkyl halides is further complicated by the presence of two closely spaced redox events: single electron reduction of the alkyl halide to the alkyl radical (E^{I}) and subsequent single electron reduction of the alkyl radical to an alkyl anion (E^{II}; Equation 1.3).[19,22] Net, these are single-electron and two-electron reduction processes, respectively. For easily reduced alkyl halides, such as alkyl iodides, precise control over the electrochemical potential can readily afford selective single-electron reduction for production of alkyl radicals since often $E^{I} > E^{II}$ (both values are negative). However, the more negative reduction potentials of some bromide and most chloride or

fluoride substrates is such that a potential inversion is observed, i.e., the reduction of the alkyl halide bond is more challenging than is the reduction of the resultant alkyl radical, $E^{I} < E^{II}$. Therefore, additional controls must be employed to favor single-electron transfer and mitigate two-electron reduction.

$$R\bullet + e^{-} \longrightarrow R^{-} \quad \text{(Equation 1.3)}$$

For alkyl halides susceptible to two-electron reduction, the primary means to control single- versus two-electron transfer is via the electron transfer method (see Sec 1.2). In direct electrolyses (i.e., without any electron transfer mediator), two-electron reduction to alkyl anions is almost always observed for bromide and chloride electrophiles that are not stabilized by conjugation due to the extremely negative potentials required for activation. Chemical reagents vary in their propensities to effect single- versus two-electron transfer. Simple, strongly reducing reagents such as alkali or alkaline metals or their adducts with polyaromatics (e.g., lithium napthalenide) generally promote two-electron reduction. Some specially designed reagents/catalysts that typically rely on inner-sphere Lewis-acid activation of the alkyl-halides can favor single-electron reduction by operating at lower reduction potentials, disfavoring reduction of the alkyl radical produced by the initial alkyl halide reduction.[23,24,25] However, the most developed method by which to produce alkyl radicals from alkyl halides is photochemistry. Photocatalysts by design favor single-electron transfer processes, and a variety of complex transformations exist wherein alkyl iodide and bromide substrates are transformed into reactive alkyl radical intermediates. Unfortunately, photocatalysts are typically insufficiently reducing to activate alkyl chloride or fluoride substrates that are not adjacent to conjugated systems or electron-withdrawing groups. Thus,

the most efficacious method for alkyl radical generation is typically unsuitable for one of the broadest and most economical/environmentally friendly class of alkyl halides, chloride electrophiles.

The dearth of photocatalytic methodologies for single-electron reduction of chloride electrophiles motivated our group and others to explore electrophotocatalysis.[26] Electrophotocatalysis takes advantage of the benefits of electrochemistry and photochemistry. For single-electron processes, a photochemical electron-transfer mediator can be paired with an electrode; the photocatalyst provides the means to favor single-electron processes, and the electrode provides a convenient means to precisely tune the electrochemical potential. While most photocatalysts rely on both reductive and oxidative quenching cycles to effect redox neutral transformations, the use of an electrode to turn the photocatalyst over, rather than an additional quenching cycle, permits net-reductive or net-oxidative transformations to be readily performed at extreme redox potentials (Scheme 1.3). Considering the hypothesis that chloride electrophiles were generally inert due to inadequate photocatalyst redox potentials, the advantages of electrophotocatalysis promised a solution to this chemical challenge.

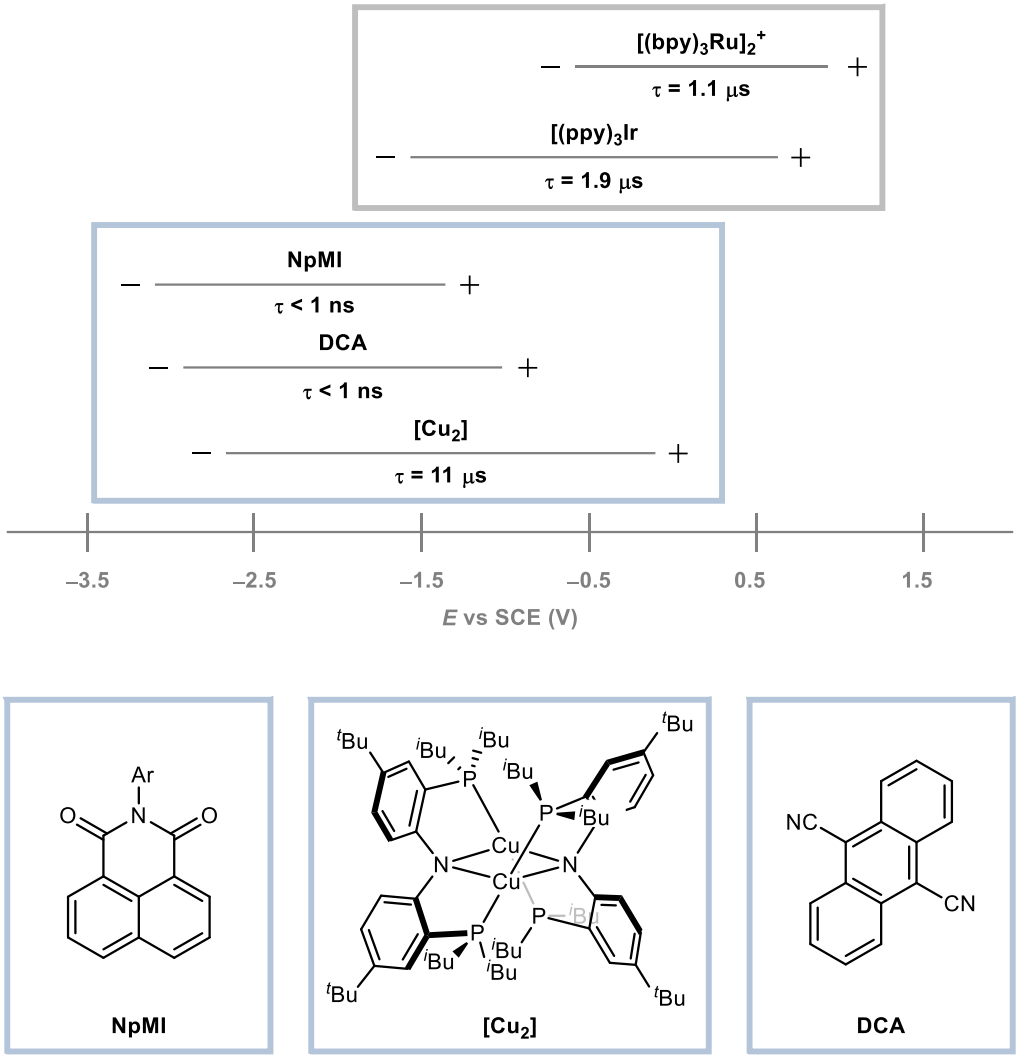

Scheme 1.3. Redox properties of various strongly reducing photocatalysts and their associated lifetimes. Redox neutral systems are highlighted in gray boxes, net-reductive or -oxidative systems are highlighted in blue boxes. Potentials of oxidative quenching (−) and reductive quenching (+) are marked with − and +, respectively.

Indeed, electrophotocatalytic activation of challenging to reduce chloride electrophiles was reported for the first time in 2020.[27,28] Concurrently, in independent publications from the Wickens group and collaboratively the Lin and Lambert groups, protocols to convert aryl chlorides into aryl radicals were disclosed (Scheme 1.4A). Aryl chlorides incur similar challenges as discussed for alkyl chlorides, such as extremely negative

reduction potentials and the potential for two-electron reduction. In both examples, organic photocatalysts (*N*-arylmaleimide, NpMI; dicyanoanthracene, DCA) were made more reducing by single-electron cathodic reduction followed by photoexcitation, reaching excited-state potentials in excess of −3.2 V vs SCE, albeit with short lifetimes on the scale of 1 ns or lower. While the precise mechanistic course of the reactions (namely, the identity of the photoreductant) has been brought under question by the Nocera group as a result of short photoexcited state lifetimes,[29] products characteristic of aryl radicals can be generated in synthetically useful quantities by reaction with common radical trapping agents. Subsequent work by the Barham group using NpMI revealed that similar protocols effect C–O cleavage in phosphinated alcohols, although *alkyl (benzylic) chlorides* were not reduced (Scheme 1.4B).[30] One potential factor responsible for the inertness of alkyl chlorides to NpMI is that aryl chlorides have lower free energies of activation for reduction than do alkyl chlorides as a result of a stepwise reduction pathway, and the associated kinetic penalty may prevent the use of photocatalysts with short lifetimes. Thus, we became interested in developing a protocol for alkyl chloride reduction via electrophotocatalysis, the details of which comprise Chapter 2.

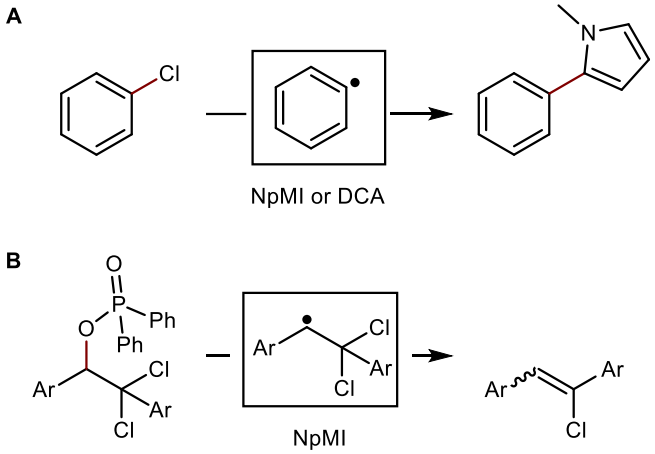

Scheme 1.4. Carbon radical generation via activation of challenging to reduce (A) aryl chloride and (B) alkyl phosphinate substrates under electrophotocatalysis.

1.3.2 Ammonia oxidation

Interest in ammonia oxidation, specifically the conversion of two equivalents of ammonia to dinitrogen, is burgeoning given recent appreciation for its capacity to serve as a method for carbon-free energy production.[31,32,33,34,35] The notably high volumetric energy density of ammonia (13.6 $GJ \cdot m^{-3}$) bests methanol, a comparable fuel that can also be readily produced in a carbon-neutral fashion, and it is more readily condensed and safer to transport than hydrogen.[36] Under a unified set of conditions, a complete technoeconomical analysis for hydrogen, methanol and ammonia produced using renewable energy found ammonia to feature the lowest source-to-tank cost (Scheme 1.5A).[37] While these beneficial attributes augur well for the future development of ammonia fuel technologies, high combustion temperatures for ammonia pose challenges to its immediate and widespread adoption.

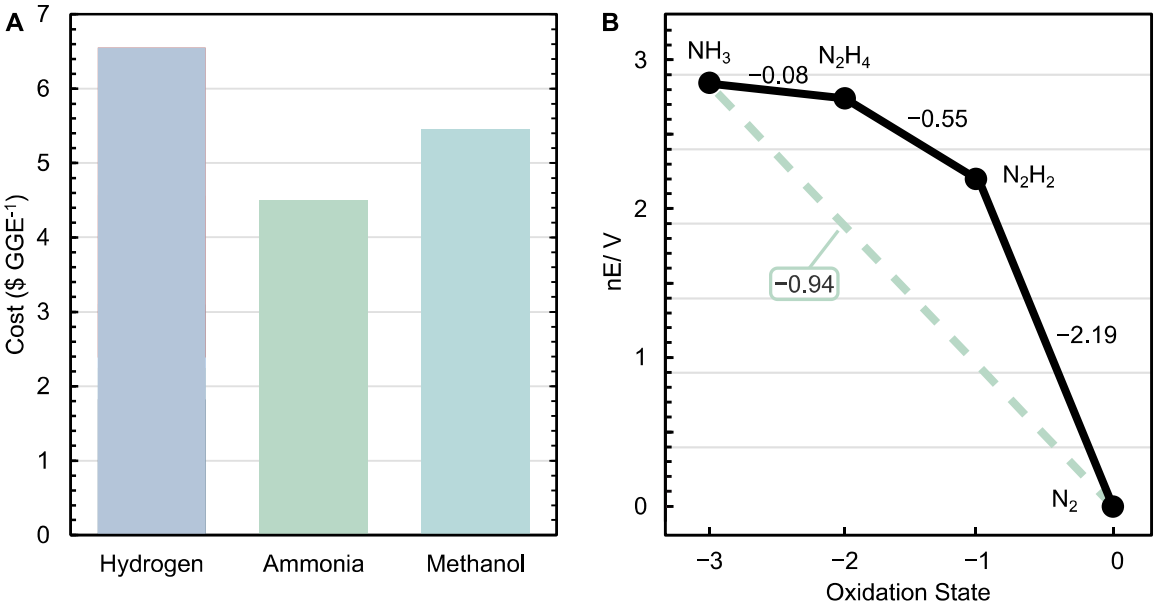

Scheme 1.5. Sustainable fuel economic and thermodynamic metrics. (A) Source-to-tank costs for various fuels generated under carbon-neutral conditions with renewable energy. (B) Frost-Latimer diagram illustrating ammonia oxidation thermodynamics in acetonitrile using ammonia as base (pK_a = 16.5) with Fc/Fc$^+$ as the reference potential.

A solution that promises to efficiently facilitate use of ammonia as fuel is electrochemical oxidation in a fuel cell. The theoretical potential for ammonia oxidation is very low, 0.09 V vs SHE (pH = 0) in aqueous conditions and −0.94 V vs Fc/Fc$^+$ in acetonitrile using ammonia as base (Scheme 1.5B).[38] Thus, when ammonia oxidation is paired with oxygen reduction, the maximum cell potential is comparable to a hydrogen fuel cell. Unfortunately, highly efficacious catalysts are required for ammonia oxidation since anodic oxidation on inert electrodes typically incurs an overpotential in excess of 1 V. The overpotential often observed for ammonia oxidation is unsurprising given the complexity of this six-electron, six-proton process. By analyzing the overall reaction in one- or two-electron steps, key contributors to the overpotential become apparent.

The first one-electron oxidation of ammonia can be considered in two cases wherein electron-transfer is coupled to, or independent of, electron transfer. Experimental thermodynamic data indicates a gas-phase bond-dissociation free energy value of 99.4 kcal/mol.[39] Thus, the N–H bonds in ammonia are extremely strong; as an example, this value exceeds the C–H bond-dissociation free energy of methane. Under non-aqueous (acetonitrile) electrochemical conditions, the mechanism of the first electron transfer from ammonia has been extensively investigated by Manthiram and coworkers.[40] Their analysis indicated that the first electron transfer occurs *without* coupled proton transfer, and this electron transfer is the rate-determining step in ammonia oxidation at inert electrodes such as glassy carbon. From DFT calculations, this step occurs at a potential of 1.77 V vs the computational hydrogen electrode, a theoretical electrode that is analogous to the experimental SHE. This potential is notably above the thermodynamic potential for the entire six-electron ammonia oxidation reaction.

The oxidation of ammonia by two- or four-electrons is more challenging to study experimentally in a direct fashion, but available thermodynamic data allows for the construction of a Frost-Latimer diagram (Scheme 1.5B).[38] Looking at the Frost-Latimer diagram, the slope of a line between any two chemical intermediates gives the thermodynamic potential vs Fc/Fc^+ for the given transformation. Thus, the line between NH_3 and N_2 has a slope of −0.94 V as previously discussed. Since most chemical processes proceed via one- or two-electron steps, it is interesting to consider the available two-electron pathways. The first available two-electron oxidation, the conversion of NH_3 to N_2H_4, has a potential of −0.08 V. Similar to the case of one-electron oxidation, this potential is

substantially above that of the overall six-electron process; therefore, it is expected that proceeding via this pathway would incur a substantial overpotential. For each subsequent two-electron transformation (N_2H_4 to N_2H_2 and N_2H_2 to N_2), oxidation becomes easier, which can be rationalized by the ability of the increasing N–N bond order to facilitate reactivity. If any of these N–N bond containing intermediates were generated, it is more easily oxidized than is ammonia. This motivates research into catalyst designs that lower the activation barrier for N–N formation.

The interplay of these thermodynamic factors can be integrated into an analysis of the available experimental data governing the mechanism of ammonia oxidation under catalytic conditions. Electrochemical ammonia oxidation underwent its first wave of intense interest in the 1960s, and the mechanistic hypotheses then established that persist to this day.[41,42,43,44] Namely, the reaction course is proposed to follow either the Oswin-Salomon[41] or the Gerischer-Mauerer[42] mechanisms (Scheme 1.6). The Oswin-Salomon mechanism proposes that N–N bond formation during electrocatalytic ammonia oxidation with platinum electrodes proceeds via the coupling of two metal nitrides. By contrast, the Gerischer-Mauerer mechanism proposes that N–N formation proceeds prior to removal of all hydrogen atoms from the ammonia-derived nitrogen. The Gerischer-Mauerer mechanism is now widely accepted to be correct, i.e., early N–N coupling of nitrogenous, ammonia-derived fragments that still contain hydrogen is most efficient. If ammonia-derived nitrides are produced, these are instead considered catalyst poisons.[45] Unfortunately, even heterogeneous catalysts using the most recent, carefully designed platinum alloys incur high overpotential despite decades of concerted research into improving overpotential.[46,47,48] Furthermore,

surface coverage by metal-nitrides still remains a substantial problem insofar as its contributes to catalyst poisoning that limits catalyst durability.

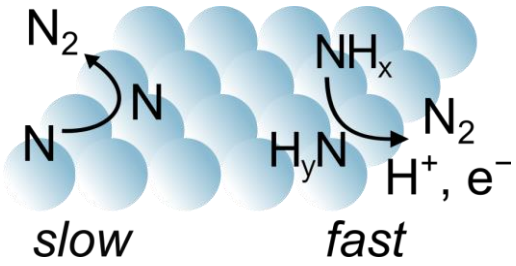

Scheme 1.6. Oswin-Salomon (slow) and Gerischer-Mauerer (fast) mechanisms of ammonia oxidation on platinum electrodes. The arrows represent N–N formation and, if necessary, further oxidation, to ultimately produce N_2.

The dearth of suitable catalysts and associated design principles thus motivates research into homogeneous complexes that catalyze ammonia oxidation. This would facilitate mechanistic studies, permitting validation of previous mechanisms—r the uncovering of new mechanisms. These fundamental discoveries would then inspire mechanistically directed development of more efficient heterogeneous catalysts. Furthermore, such molecular complexes could serve as active catalysts in their own right.

Given this context, at the onset of our research in 2018, it was striking that there were no reported transition metal systems that catalyzed ammonia oxidation over multiple cycles. In a stoichiometric fashion, Mayer demonstrated in 1981 that ruthenium polypyridyl complexes (Scheme 1.7A) can convert ammonia into nitrite and nitrate under oxidative electrochemical conditions.[49] Importantly, this work provided the first mechanistic insight into pathways that may be operative for ammonia oxidation in molecular systems: a disproportionation mechanism was proposed to furnish a high-valent Ru^{IV}=NH imido

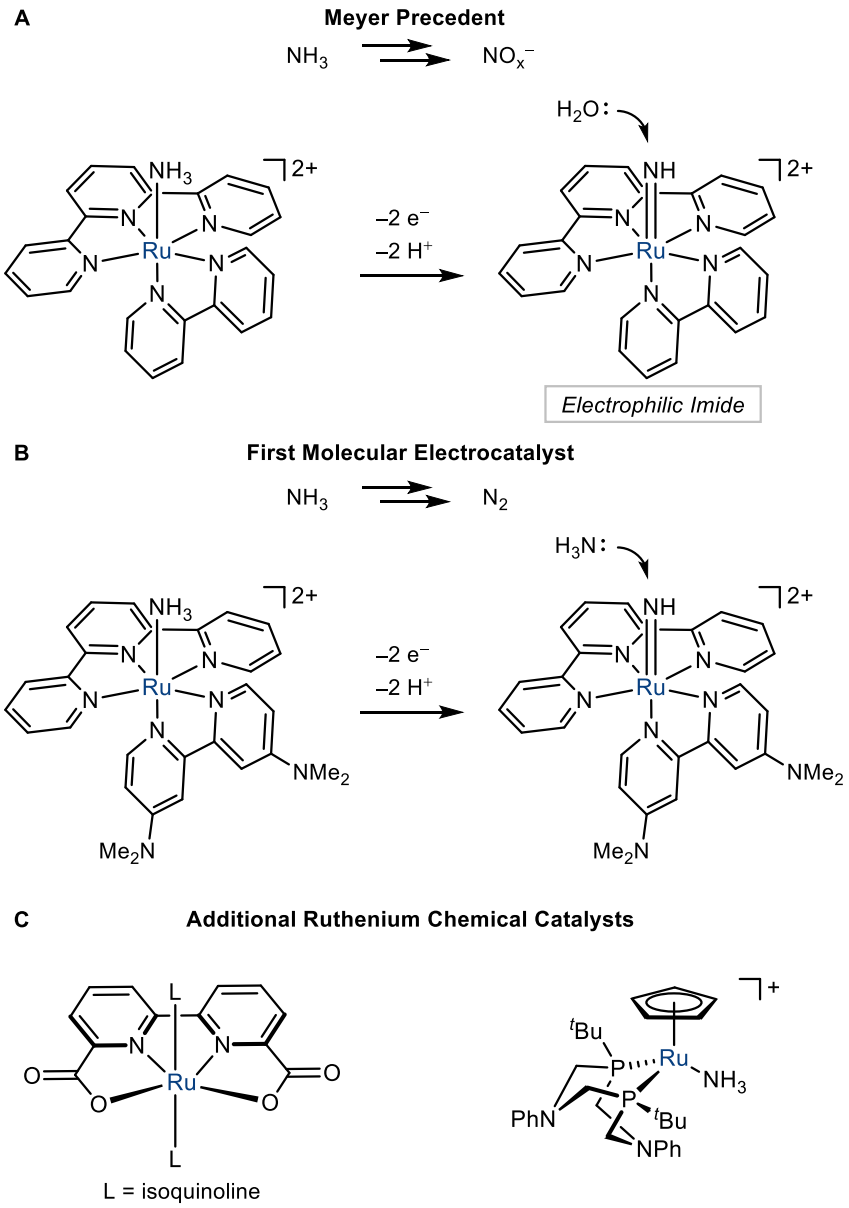

Scheme 1.7. Early precedent in molecular ammonia oxidation using ruthenium catalysts. (A) Generation of an electrophilic imide that captures a water nucleophile and (B) ammonia oxidation catalysts inspired thereof. (C) Additional ruthenium catalysts featuring alternative designs.

complex that exhibited electrophilic character at nitrogen. Thus, water could serve as a nucleophile to generate an N–O bond. In 2019, Smith and coworkers developed this chemistry into the first example of electrocatalytic ammonia oxidation mediated by a

molecular catalyst by working in anhydrous conditions, wherein N–N formation was proposed to follow an analogous mechanism (Scheme 1.7B).[50] Thus, at an applied potential of 0.2 V vs Fc/Fc^+, two equivalents of N_2 relative to ruthenium could be produced after 3 h. Within a short time period throughout 2019, two additional ruthenium catalysts (Scheme 1.7C) were reported using both electrochemical and chemical oxidation strategies, reaching a maximum of up to 14 equiv. N_2 under chemical catalysis (i.e., not electrocatalysis).[51,52,53]

Contemporaneous with the development of these early ammonia oxidation molecular catalysts, we were pursuing a catalyst design strategy that emulated the proposed mechanism for highly active ammonia oxidation heterogeneous catalysis: early coupling of NH_x and NH_y fragments (see Scheme 1.6). We became interested in a class of iron(II) water oxidation catalysts featuring neutral tetradentate ligands that enforce a coordination geometry marked by *cis* disposed, non-chelated coordination sites.[54] Using weakly coordinating triflate counterions in a high dielectric solvent such as acetonitrile, the triflate anions are completely displaced by acetonitrile.[55] Thus, we hypothesized that such a coordination sphere may be amenable to binding two ammonia-derived ligands *cis* to one another at an electrophilic metal, potentially allowing intramolecular N–N formation upon loss of protons following oxidation (Scheme 1.8). Since intermediates containing N–N bonds (e.g., hydrazine, diazene) are more readily oxidized than is ammonia, we considered it critical to intentionally design catalysts that feature properties capable of facilitating N–N coupling, the step that presumably would be rate- or potential-determining.

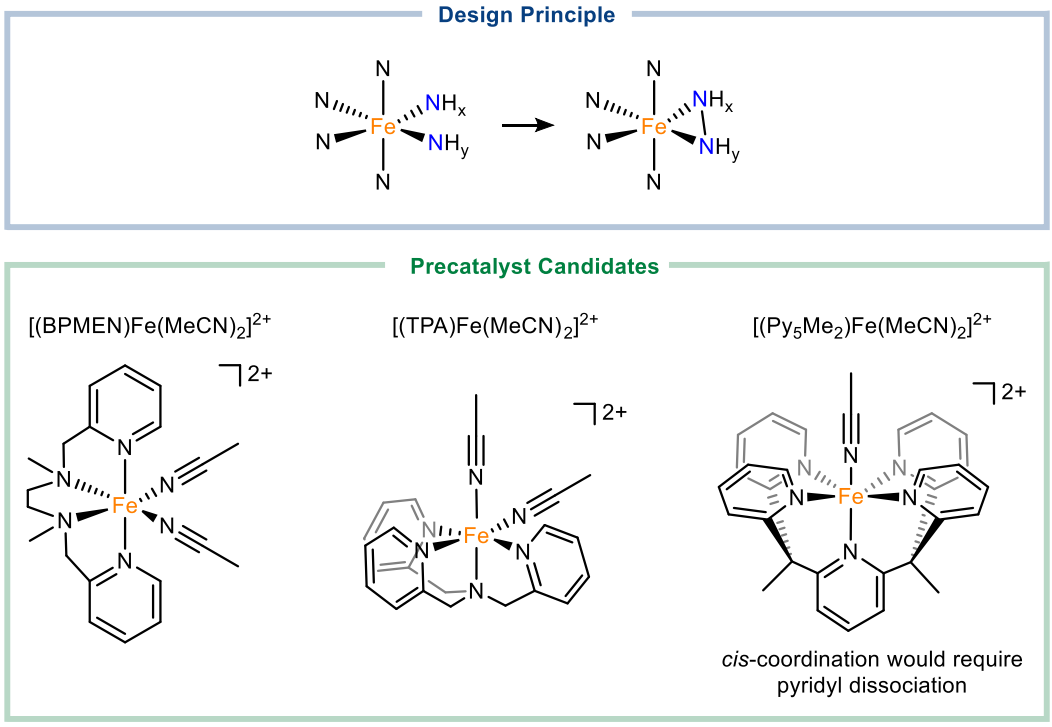

Scheme 1.8. Our motivation for investigating iron complexes featuring potential *cis* coordination sites for ammonia binding, and structures of our initial panel of proposed iron(II) ammonia-oxidation precatalysts.

Initially analyzing a panel of iron(II) complexes (Scheme 1.8), we found that $[(TPA)Fe(MeCN)_2]^{2+}$ exhibited the most promising activity for ammonia oxidation. The details of our studies into *cis*-ammonia coordination, electrocatalytic ammonia oxidation and mechanistic studies thereof are found in Chapter 3. Further development of $[(TPA)Fe(MeCN)_2]^{2+}$ inspired ammonia oxidation catalysts is the subject of Chapters 4 and 5.

1.4 References

[1] Marcus, R. A.; Sutin, N. Electron Transfers in Chemistry and Biology. *Biochim. Biophy. Acta – Rev. Bioenerg.* **1985**, *811*, 265–322.

[2] Verschueren, R. H.; De Borggraeve, W. M. Electrochemistry and Photoredox Catalysis: A Comparative Evaluation in Organic Synthesis. *Molecules* **2019**, *24*, 2122.

[3] Vandersypen, L. M. K.; Bluhm, H.; Clarke, J. S.; Dzurak, A. S.; Ishihara, R.; Morello, A.; Reilly, D. J.; Schreiber, L. R.; Veldhorst, M. Interfacing Spin Qubits in Quantum Dots and Donors—Hot, Dense, and Coherent. *npj Quantum Inf* **2017**, *3*, 1–10.

[4] Schachinger, F.; Chang, H.; Scheiblbrandner, S.; Ludwig, R. Amperometric Biosensors Based on Direct Electron Transfer Enzymes. *Molecules* **2021**, *26*, 4525.

[5] Nocera, D. G. Proton-Coupled Electron Transfer: The Engine of Energy Conversion and Storage. *J. Am. Chem. Soc.* **2022**, *144*, 1069–1081.

[6] Hammes-Schiffer, S. Theory of Proton-Coupled Electron Transfer in Energy Conversion Processes. *Acc. Chem. Res.* **2009**, *42*, 1881–1889.

[7] DuBois, D. L. Development of Molecular Electrocatalysts for Energy Storage. *Inorg. Chem.* **2014**, *53*, 3935–3960.

[8] Savéant, J.-M. Molecular Catalysis of Electrochemical Reactions. Mechanistic Aspects. *Chem. Rev.* **2008**, *108*, 2348–2378.

[9] Costentin, C.; Drouet, S.; Robert, M.; Savéant, J.-M. Turnover Numbers, Turnover Frequencies, and Overpotential in Molecular Catalysis of Electrochemical Reactions. Cyclic Voltammetry and Preparative-Scale Electrolysis. *J. Am. Chem. Soc.* **2012**, *134*, 11235–11242.

[10] Pegis, M. L.; Wise, C. F.; Koronkiewicz, B.; Mayer, J. M. Identifying and Breaking Scaling Relations in Molecular Catalysis of Electrochemical Reactions. *J. Am. Chem. Soc.* **2017**, *139*, 11000–11003.

[11] Connelly, N. G.; Geiger, W. E. Chemical Redox Agents for Organometallic Chemistry. *Chem. Rev.* **1996**, *96*, 877–910.

[12] Tay, N. E. S.; Lehnherr, D.; Rovis, T. Photons or Electrons? A Critical Comparison of Electrochemistry and Photoredox Catalysis for Organic Synthesis. *Chem. Rev.* **2022**, *122*, 2487–2649.

[13] Elgrishi, N.; Rountree, K. J.; McCarthy, B. D.; Rountree, E. S.; Eisenhart, T. T.; Dempsey, J. L. A Practical Beginner's Guide to Cyclic Voltammetry. *J. Chem. Educ.* **2018**, *95*, 197–206.

[14] Bard, A. J., Parsons, R. & Jordan, J. *Standard Potentials in Aqueous Solution* (1st ed.). (Dekker, New York, 1985).

[15] Heard, D. M.; Lennox, A. J. J. Electrode Materials in Modern Organic Electrochemistry. *Angewandte Chemie International Edition* **2020**, *59*, 18866–18884.

[16] Fu, G. C. Transition-Metal Catalysis of Nucleophilic Substitution Reactions: A Radical Alternative to S_N1 and S_N2 Processes. *ACS Cent. Sci*. **2017**, *3*, 692–700.

[17] Yan, M.; Lo, J. C.; Edwards, J. T.; Baran, P. S. Radicals: Reactive Intermediates with Translational Potential. *J. Am. Chem. Soc.* **2016**, *138*, 12692–12714.

[18] Mondal, S.; Dumur, F.; Gigmes, D.; Sibi, M. P.; Bertrand, M. P.; Nechab, M. Enantioselective Radical Reactions Using Chiral Catalysts. *Chem. Rev.* **2022**, *122*, 5842–5976.

[19] Andrieux, C. P.; Gallardo, I.; Saveant, J. M. Outer-Sphere Electron-Transfer Reduction of Alkyl Halides. A Source of Alkyl Radicals or of Carbanions? Reduction of Alkyl Radicals. *J. Am. Chem. Soc.* **1989**, *111*, 1620–1626.

[20] Zhang, N.; Samanta, S. R.; Rosen, B. M.; Percec, V. Single Electron Transfer in Radical Ion and Radical-Mediated Organic, Materials and Polymer Synthesis. *Chem. Rev.* **2014**, *114*, 5848–5958.

[21] Houmam, A. Electron Transfer Initiated Reactions: Bond Formation and Bond Dissociation. *Chem. Rev.* **2008**, *108*, 2180–2237.

[22] Isse, A. A.; Berzi, G.; Falciola, L.; Rossi, M.; Mussini, P. R.; Gennaro, A. Electrocatalysis and Electron Transfer Mechanisms in the Reduction of Organic Halides at Ag. *J Appl Electrochem* **2009**, *39*, 2217.

[23] Wu, X.; Hao, W.; Ye, K.-Y.; Jiang, B.; Pombar, G.; Song, Z.; Lin, S. Ti-Catalyzed Radical Alkylation of Secondary and Tertiary Alkyl Chlorides Using Michael Acceptors. *J. Am. Chem. Soc.* **2018**, *140*, 14836–14843.

[24] Okita, T.; Aida, K.; Tanaka, K.; Ota, E.; Yamaguchi, J. Chlorine Atom Transfer of Unactivated Alkyl Chlorides Enabled by Zirconocene and Photoredox Catalysis. *Precision Chemistry* **2023**. DOI: 10.1021/prechem.2c00002

[25] Claros, M.; Ungeheuer, F.; Franco, F.; Martin-Diaconescu, V.; Casitas, A.; Lloret-Fillol, J. Reductive Cyclization of Unactivated Alkyl Chlorides with Tethered Alkenes under Visible-Light Photoredox Catalysis. *Angewandte Chemie International Edition* **2019**, *58*, 4869–4874.

[26] Huang, H.; Steiniger, K. A.; Lambert, T. H. Electrophotocatalysis: Combining Light and Electricity to Catalyze Reactions. *J. Am. Chem. Soc.* **2022**, *144*, 12567–12583.

[27] Cowper, N. G. W.; Chernowsky, C. P.; Williams, O. P.; Wickens, Z. K. Potent Reductants via Electron-Primed Photoredox Catalysis: Unlocking Aryl Chlorides for Radical Coupling. *J. Am. Chem. Soc.* **2020**, *142*, 2093–2099.

[28] Kim, H.; Kim, H.; Lambert, T. H.; Lin, S. Reductive Electrophotocatalysis: Merging Electricity and Light To Achieve Extreme Reduction Potentials. *J. Am. Chem. Soc.* **2020**, *142*, 2087–2092.

[29] Rieth, A. J.; Gonzalez, M. I.; Kudisch, B.; Nava, M.; Nocera, D. G. How Radical Are "Radical" Photocatalysts? A Closed-Shell Meisenheimer Complex Is Identified as a Super-Reducing Photoreagent. *J. Am. Chem. Soc.* **2021**, *143*, 14352–14359.

[30] Tian, X.; Karl, T. A.; Reiter, S.; Yakubov, S.; de Vivie-Riedle, R.; König, B.; Barham, J. P. Electro-Mediated PhotoRedox Catalysis for Selective C(sp^3)–O Cleavages of Phosphinated Alcohols to Carbanions. *Angew. Chem. Int. Ed.* **2021**, *60*, 20817–20825.

[31] Service, R. F. Ammonia – a renewable fuel made from sun, air, and water – could power the globe without carbon. *Science* 2018, aau7489. DOI: 10.1126/science.aau7489.

[32] Schüth, F., Palkovits, R., Schlögl, R. & Su, D. S.. *Energy Environ. Sci.* **2012**, *5*, 6278–6289.

[33] Little, D. J., Smith III, M. R. & Hamann, T. W. Electrolysis of liquid ammonia for hydrogen generation. *Energy Environ. Sci.* **2015**, *8*, 2775–2781.

[34] Jeerh, G.; Zhang, M.; Tao, S. Recent Progress in Ammonia Fuel Cells and Their Potential Applications. *J. Mat. Chem. A* **2021**, *9*, 727–752.

[35] MacFarlane, D. R.; Cherepanov, P. V.; Choi, J.; Suryanto, B. H. R.; Hodgetts, R. Y.; Bakker, J. M.; Ferrero Vallana, F. M.; Simonov, A. N. A Roadmap to the Ammonia Economy. *Joule* **2020**, *4*, 1186–1205.

[36] Puértolas, B.; Comesaña-Hermo, M.; Besteiro, L. V.; Vázquez-González, M.; Correa-Duarte, M. A. Challenges and Opportunities for Renewable Ammonia Production via Plasmon-Assisted Photocatalysis. *Advanced Energy Materials* **2022**, *12*, 2103909.

[37] Zhao, Y. et al. An efficient direct ammonia fuel cell for affordable carbon-neutral transportation. *Joule* **2019**, *3*, 2472–2484.

[38] Lindley, B. M.; Appel, A. M.; Krogh-Jespersen, K.; Mayer, J. M.; Miller, A. J. M. Evaluating the Thermodynamics of Electrocatalytic N2 Reduction in Acetonitrile. *ACS Energy Lett.* **2016**, *1*, 698–704.

[39] Warren, J. J.; Tronic, T. A.; Mayer, J. M. Thermochemistry of Proton-Coupled Electron Transfer Reagents and Its Implications. *Chemical Reviews* **2010**, *110*, 6961–7001.

[40] Schiffer, Z. J.; Lazouski, N.; Corbin, N.; Manthiram, K. Nature of the First Electron Transfer in Electrochemical Ammonia Activation in a Nonaqueous Medium. *J. Phys. Chem. C* **2019**, *123*, 9713–9720.

[41] Oswin, H. G. & Salomon, M. The anodic oxidation of ammonia at platinum black electrodes in aqueous KOH electrolyte. *Can. J. Chem.* **1963**, *41*, 1686–1694.

[42] Gerischer, H.; Mauerer, A. Anodic oxidation of ammonia at platinum electrodes. *J. Electroanal. Chem.* **1970**, *25*, 421–433.

[43] Simons, E. L.; Cairns, E. J.; Surd, D. J. The Performance of Direct Ammonia Fuel Cells. *J. Electrochem. Soc.* **1969**, *116*, 556–561.

[44] McKee, D. W.; Scarpellino, A. J.; Danzig, I. F.; Pak, M. S. Improved Electrocatalysts for Ammonia Fuel Cell Anodes. *J. Electrochem. Soc.* **1969**, *116*, 562–568.

[45] Song, L.; Liang, Z.; Ma, Z.; Zhang, Y.; Chen, J.; Adzic, R. R.; Wang, J. X. Temperature-Dependent Kinetics and Reaction Mechanism of Ammonia Oxidation on Pt, Ir, and PtIr Alloy Catalysts. *J. Electrochem. Soc.* **2018**, *165* (15), J3095–J3100.

[46] Endo, K.; Nakamura, K.; Katayama, Y.; Miura, T. Pt-Me (Me = Ir, Ru, Ni) binary alloys as an ammonia oxidation anode. *Electrochim. Acta* **2004**, *49*, 2503– 2509

[47] Boggs, B.K.; Botte, G. G. Optimization of Pt–Ir on carbon fiber paper for the electro-oxidation of ammonia in alkaline media. *Electrochim. Acta* **2010**, *55*, 5287–5293.

[48] Kim, H.; Yang, W.; Lee, W. H.; Han, M. H.; Moon, J.; Jeon, C.; Kim, D.; Ji, S. G.; Chae, K. H.; Lee, K.-S.; Seo, J.; Oh, H.-S.; Kim, H.; Choi, C. H. Operando stability of Platinum electrocatalysts in ammonia oxidation reactions. *ACS Catal.* **2020**, *10*, 11674–11684.

[49] Thompson, M. S. & Meyer, T. J. Oxidation of coordinated ammonia to nitrate. *J. Am. Chem. Soc.* **1981**, *103*, 5577–5579.

[50] Habibzadeh, F., Miller, S. L., Hamann, T. W. & Smith, M. R. Homogeneous electrocatalytic oxidation of ammonia to N_2 under mild conditions. *Proc. Natl. Acad. Sci. U. S. A.* **2019**, *116*, 2849–2853.

[51] Bhattacharya, P.; Heiden, Z. M.; Chambers, G. M.; Johnson, S. I.; Bullock, R. M.; Mock, M. T. Catalytic Ammonia Oxidation to Dinitrogen by Hydrogen Atom Abstraction. *Angew. Chem. Int. Ed.* **2019,** *58*, 11618–11624.

[52] Nakajima, K.; Toda, H.; Sakata, K.; Nishibayashi, Y. Ruthenium-Catalysed Oxidative Conversion of Ammonia into Dinitrogen. *Nat. Chem.* **2019**, *11*, 702–709.

[53] Dunn, P. L.; Cook, B. J.; Johnson, S. I.; Appel, A. M.; Bullock, R. M. Oxidation of Ammonia with Molecular Complexes. *J. Am. Chem. Soc.* **2020**, *142* , 17845–17858.

[54] Fillol, J. L., Codolá, Z., Garcia-Bosch, I., Gómez, L., Pla, J. J. & Costas, M. Efficient water oxidation catalysts based on readily available iron coordination complexes. *Nat. Chem.* **2011**, *3*, 807–813.

[55] Diebold, A.; Hagen, K. S. Iron(II) Polyamine Chemistry: Variation of Spin State and Coordination Number in Solid State and Solution with Iron(II) Tris(2-Pyridylmethyl)Amine Complexes. *Inorg. Chem.* **1998**, *37*, 215–223.

C h a p t e r 2

Mechanism of a Luminescent Dicopper System That Facilitates Electrophotochemical Coupling of Benzyl Chlorides via a Strongly Reducing Excited State

Adapted from:

Zott, M. D.; Canestraight, V. M.; Peters, J. C.

ACS Catal. **2022**, *12*, 10781–10786.

DOI: 10.1021/acscatal.2c03215.

2.1 Introduction

Photochemistry, often in conjunction with transition-metal catalysis, is growing in prominence in modern synthetic methodology.[1,2,3,4] Photochemical activation of widely available electrophiles can afford versatile reactive intermediates, such as organic radicals,[5,6] which can be leveraged in a variety of transformations.[7,8,9,10] For instance, a recent focus of a number of labs, including our own, has been to partner photochemically generated radical intermediates (R•) with copper(II)-bound N-nucleophiles in catalytic, photoinduced N-alkylations (Scheme 2.1, eqns 1 and 2; $–N_{nuc}$ denotes an amide nucleophile).[9,11,12,13,14,15,16,17,18]

Production of R• from alkyl halides is integral to many modern organic transformations,[19,20,21] and hence there is considerable interest in expanding the types of alkyl halides compatible with R• generation under synthetically useful conditions.[22,23,24] Alkyl chlorides, with potentials below −2 V vs SCE, are desirable electrophiles but are challenging to reduce;[22,25] the limited examples of their outer-sphere photochemical activation typically feature harsh conditions.[26,27,28] Phosphine-supported copper-amide excited states[29,30,31,32,33] can be more reducing than those of typical ruthenium or iridium systems,[34] providing sufficient driving force for alkyl chloride reduction. To promote photoinduced R• generation via a copper species in a generalized fashion (e.g., avoiding the subsequent C–N coupling step as in Scheme 2.1, eqn 2), the copper byproduct of oxidative quenching must be recycled by a suitable reductant.

In 1987, Sauvage demonstrated an elegant solution to photocatalyst regeneration via the electrophotochemical reduction of 4-nitrobenzyl bromide with $[Cu(dap)_2]^+$ (E_{ox}^* ~

−1.4 V; τ_0 = 0.27 μs; dap = 2,9-dianisyl-1,10-phenanthroline).[35] Organic photosensitizers have more recently been used to reduce (pseudo)halides under extremely reducing electrophotoredox conditions ($E_{ox}^* < -3$ V).[36,37,38,39] The suggested lifetimes ($\tau_0 \sim 1$ ns) and nature of the photoreductant intermediates of these processes are still under investigation.[40]

In this study, we explore a dicopper diamond core system (hereafter [Cu_2]), previously developed by our lab[33] and featuring a combination of terminal phosphine and bridging amide ligands, as an attractive electrophotoredox catalyst (Scheme 2.1, bottom).

Scheme 2.1. Electrophotochemical Organohalide Reduction.

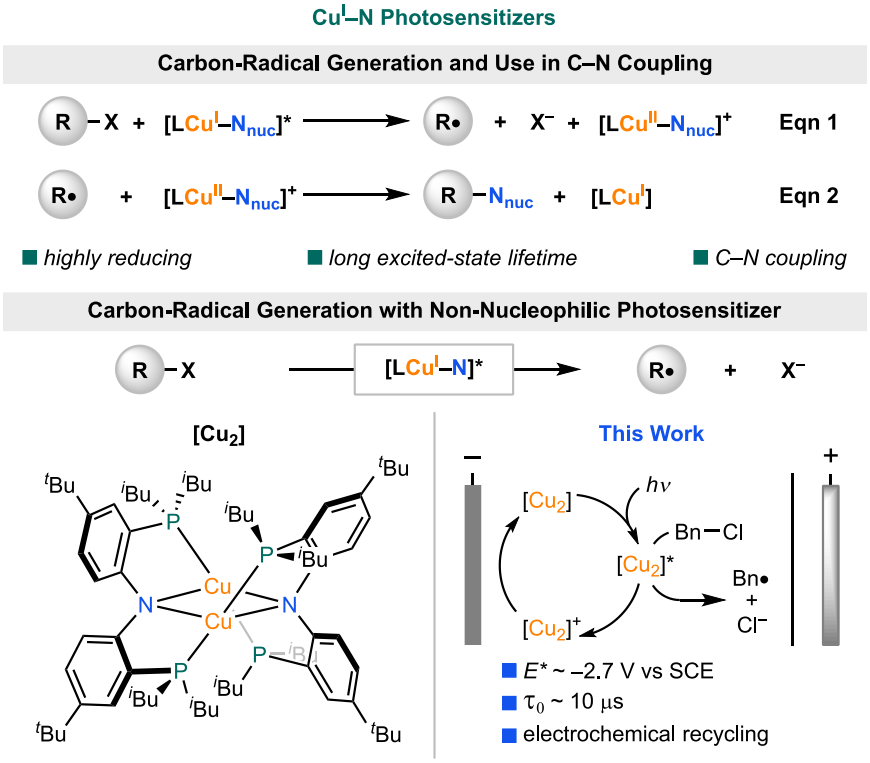

[Cu_2] is an especially strong excited-state reductant ($E_{ox}^* \sim -2.7$ V), with a long-lived excited state in solution at RT ($\tau_0 \sim 10$ μs). Charge delocalization by the $Cu_2(\mu\text{-}N)_2$ diamond core, as well as steric protection from ligand *iso*-butyl and *tert*-butyl groups, is expected to render the one-electron oxidized state $[Cu_2]^+$ non-nucleophilic. Furthermore, $[Cu_2]^+$ can be

electrochemically interconverted with $[Cu_2]$; $[Cu_2]^+$ has been isolated and characterized in the solid state.[41]

As a representative study of the excited state intermolecular photochemistry of Cu^I–amide systems, with an eye towards photoreductions using alkyl chlorides as R• precursors, we explore herein photochemically-driven, electrochemically-cycled, radical couplings using $[Cu_2]$ and benzyl chloride substates (E_p up to −2.5 V vs SCE). The dicopper system described here is mechanistically well-defined, and as we show, it is the $[Cu_2]^*$ excited state that serves as the outer-sphere photoreductant of benzyl chloride substrates; the ground-state oxidized byproduct, $[Cu_2]^+$, is electrochemically recycled to afford a catalytic, electrophotochemical C–C coupling process.

2.2 Results and Discussion

We began by investigating the reactivity of 4-methylbenzyl chloride (**1**) (E_p = −2.5 V vs SCE) as a model substrate. Benzyl chlorides are important substrates in modern synthesis and methodology[42,43,44] and also provide a convenient radical termination pathway via diffusion-limited dimerization, simplifying our mechanistic studies.[45] Exposing **1** to blue light irradiation (440 nm) in 1,2-dimethoxyethane (DME), no reaction is observed. However, when $[Cu_2]$ is added, bibenzyl product **1-D** is formed quantitatively (Figure 2.1A).

Benzyl chloride photoreduction was mechanistically interrogated via Stern-Volmer (SV) studies to establish outer-sphere electron transfer (ET) and to probe rates of ET. Time-resolved photoluminescence spectroscopy confirmed that electronically distinct benzyl chlorides **1**–**8** quench [Cu_2] in a dynamic (i.e., diffusional) process. The rates of quenching,

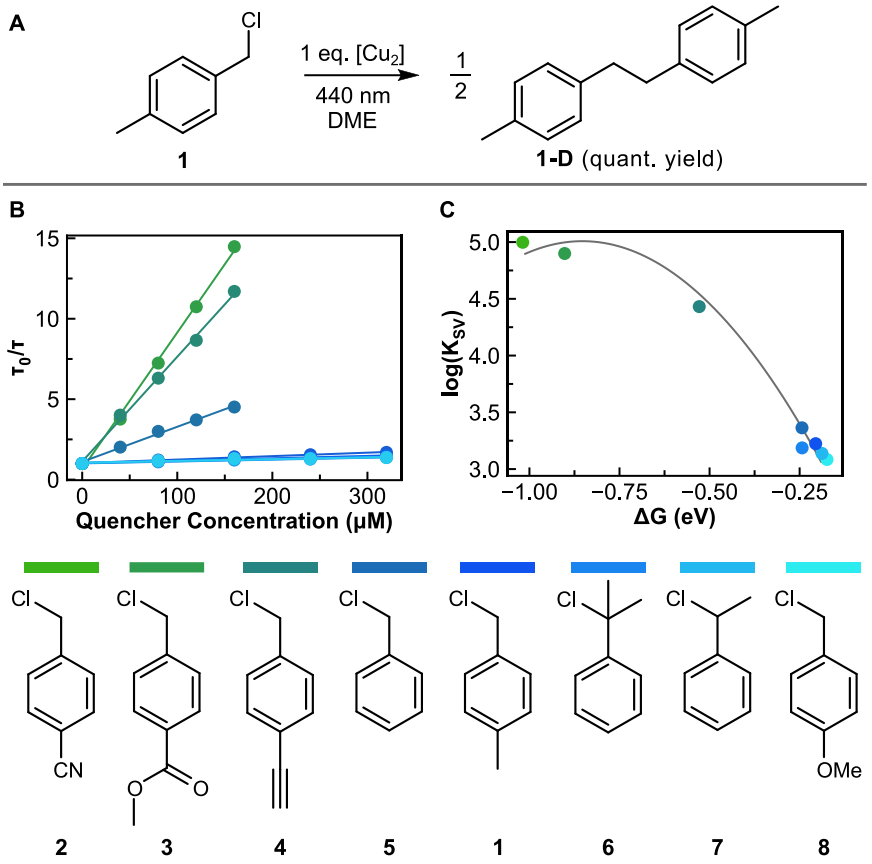

Figure 2.1. Photoreduction of benzyl chlorides. (A) Performed for 2 h with yield analyzed by ^{1}H NMR versus CH_2Br_2 internal standard. (B) Stern-Volmer quenching and (C) Marcus theory analysis in the presence of various benzyl chloride quenchers.

determined from linear SV plots (Figure 2.1B), were in the range of ~10^8 – 10^{10} $M^{-1} \cdot s^{-1}$ for K_{SV}/τ_0. These values indicate rapid quenching, reaching diffusion-limited values with electron poor **2**. Using benzyl chloride peak potentials obtained from cyclic voltammetry ($E_p = -1.7 - -2.5$ V; see SI), the quenching rates could be analyzed as a function of driving force, using $E_{ox}^* \sim -2.7$ V. Notably, a quadratic relationship between log(K_{SV}) and driving

force was observed, consistent with the behavior predicted by Marcus theory for outer-sphere electron transfer (Figure 2.1C).[46] Although such outer-sphere dynamic quenching is commonly assumed in photoredox mechanisms, this contrasts with the behavior of some organic electrophotoredox catalysts hypothesized to involve preassembly of the photocatalyst and substrate to compensate for short lifetimes.[38] These photophysical measurements thus indicate a rapid dynamic oxidative quenching step in which $[Cu_2]$ undergoes outer-sphere electron transfer to benzyl chloride electrophiles.

We expected oxidative quenching to produce the stable, red-brown, mono-oxidized species $[Cu_2]^+$ (Figure 2.2A).[41] 440 nm irradiation of $[Cu_2]$ and **1** in DME produces a pale-yellow solution, the UV-vis spectrum of which is mostly featureless (Figure 2.2B). Thus, the expected UV-vis features for $[Cu_2]^+$ at 520, 600, and 800 nm were not observed. Surprisingly, this suggests that the oxidative quenching reaction may involve either degradation following quenching or chemical steps at copper.

We hypothesized that the stability of $[Cu_2]^+$ could be compromised by chloride, a byproduct of benzyl chloride reductive C–Cl bond cleavage. Accordingly, addition of lithium chloride to a solution of $[Cu_2]^+$ in DME resulted in a loss of red-brown color over several hours, producing a yellow solution. Off-white crystals isolated from the reaction mixture were characterized by two ^{31}P NMR peaks (Figure 2.2C), and single-crystal XRD revealed the presence of two independent dimers, each comprised of two CuCl (chloro-cubane) or one CuCl (chloro-diamond) per H-PNP^{t}Bu ligand equivalent, i.e., $[(\text{H-PNP}^t\text{Bu})\text{Cu}_2(\mu\text{-Cl})_2]_2$ or $[(\text{H-PNP}^t\text{Bu})\text{Cu}(\mu\text{-Cl})]_2$, respectively. Independent synthesis of chloro-cubane and chloro-diamond (SI), produced white solids whose ^{31}P NMR resonances

reproduced those of the co-crystalline material (Figure 2.2C), and the characterization of chloro-diamond enabled its identification as a reaction product in the stoichiometric reaction described in Figure 2.1A (SI).

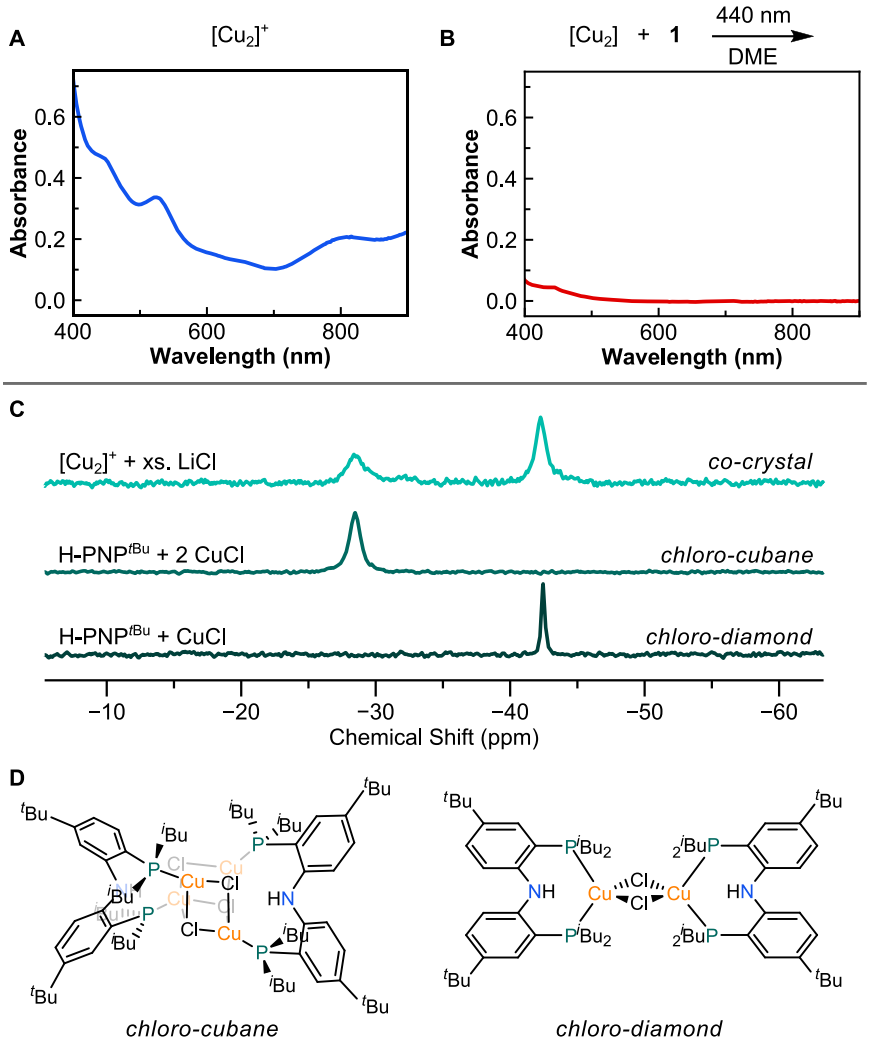

Figure 2.2. Influence of chloride on oxidized copper products. UV-vis spectra in DME of: (A) $[Cu_2]^+$ and (B) a mixture of $[Cu_2]$ and 4-methylbenzyl chloride irradiated (440 nm) for 5 minutes. (C) ^{31}P NMR spectra of chloride-bound copper products and (D) their structures.

We sought to detect and track the fate of $[Cu_2]^+$ in the presence of chloride via a UV-vis time course analysis, photolyzing $[Cu_2]$ and **1** under 440 nm irradiation (Figure 2.3A). Bands characteristic of $[Cu_2]^+$ grow in throughout 15–30 seconds, after which the 520 nm absorbance rapidly decreases. This accounts for our failure to observe the presence of $[Cu_2]^+$ in Figure 2.2B. Knowing that chloride in the form of lithium chloride slowly degrades $[Cu_2]^+$ over a period of several hours, we investigated whether lithium salts could sequester chloride via tight ion-pairing to mitigate degradation of $[Cu_2]^+$.[47]

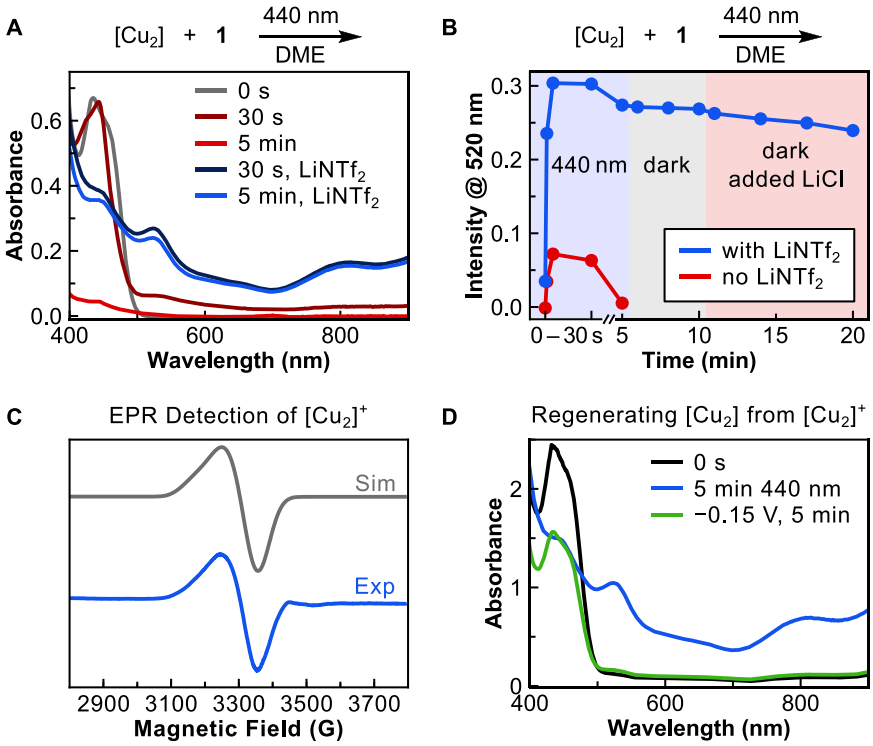

Figure 2.3. Stability and regeneration of $[Cu_2]^+$. Time course studies for a mixture of $[Cu_2]$ and **1** under 440 nm irradiation. (A) UV-vis spectra and (B) 520 nm absorbance vs time in the presence and absence of 0.2 M $LiNTf_2$. (C) 77 K EPR spectrum recorded after 15 s of irradiation in the presence of $LiNTf_2$. (D) UV-vis spectra pre- and post-irradiation, as well as following 5 minutes of −0.15 V applied potential in the dark.

When $[Cu_2]$ and **1** were irradiated in the presence of 0.2 M $LiNTf_2$, bands for $[Cu_2]^+$ became persistent, decreasing in intensity by only ~20% after 20 minutes (Figure 2.3B). This is consistent with kinetic measurements which indicate a rate of $\sim 3 \times 10^{-2}\ M^{-1} \cdot s^{-1}$

for the reaction between $[Cu_2]^+$ and tetrabutylammonium chloride in the presence of 0.2 M $LiNTf_2$; without $LiNTf_2$, the reaction is almost instantaneous (SI). Analysis of $[Cu_2]$ photolyzed in the presence of **1** and 0.2 M $LiNTf_2$ by EPR provided orthogonal support for assigning the product as $[Cu_2]^+$ (Figure 2.3C).[48] Thus, these analyses indicate $[Cu_2]^+$ to be the oxidative quenching product and corroborate its degradation by chloride.

Stabilizing $[Cu_2]^+$ enables the prospect of electrochemically regenerating $[Cu_2]$. $[Cu_2]^+$ was photochemically generated from $[Cu_2]$ and **1** in DME, with $LiNTf_2$ serving as both a chloride sequestrant and the electrolyte, then transferred into a two-compartment electrochemical cell. Applying $E_{app} = -0.15$ V for 5 minutes using a carbon cloth working electrode, cathodic of $E_{ox} = 0$ V for $[Cu_2]^{0/+}$, 0.76 e^- equivalents of current were passed (Figure 2.3D). One electron is required to fully reduce $[Cu_2]^+$ to its photoactive neutral state, thus up to 76% could be reduced. The UV-vis spectrum of this solution showed recovery of the 440 nm peak characteristic for $[Cu_2]$, albeit with ~60% of its original intensity, indicating successful, albeit incomplete, regeneration.[49] Electrochemical analysis of chloro-cubane and chloro-diamond indicated no electron transfer pathway for recovering $[Cu_2]$ at our operating potential, highlighting the importance of stabilizing $[Cu_2]^+$ and rationalizing the incomplete regeneration of $[Cu_2]$.

The described reactivity of the $[Cu_2]$ system constitutes the requirements for an electrophotoredox cycle (Scheme 2.1), so we turned to catalytic investigations under controlled potential conditions (Table 2.1). Indeed, $[Cu_2]$ is a competent electrophotoredox catalyst, generating **1-D** from **1** in 89% yield using 3 mol % $[Cu_2]$ (entry 1). Additional substrates **2**–**8** proceeded in 68–91% yield (entries 12–18). No reaction was observed in

the absence of either [Cu_2] or light (entries 2–3). In the absence of an applied potential, only the expected stoichiometric amount of **1-D** relative to [Cu_2] was produced (entry 4).

The intermediacy of benzyl radicals during catalysis is supported by several pieces of circumstantial evidence. Production of **1-D** in the presence of added water (entry 5), as

Table 2.1. Electrophotocatalytic Benzyl Chloride Reduction.[a]

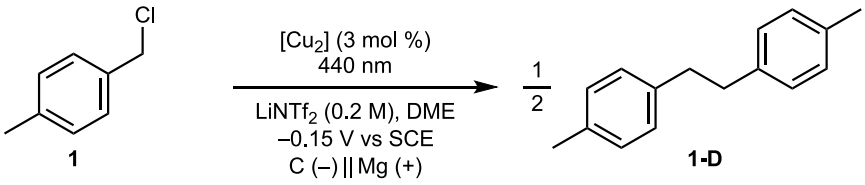

Entry	Variation	Yield[b]
1	none	90[c]
2	no [Cu_2]	0
3	no light	0
4	no applied potential	2
5	2 equiv. H_2O	62
6	5 mL air	4 {7}[d]
7	$LiClO_4$ instead of $LiNTf_2$	30
8	$TBAPF_6$ instead of $LiNTf_2$	10
9	$TBANTf_2$ instead of $LiNTf_2$	11
10	chloro-cubane instead of [Cu_2]	0
11	chloro-diamond instead of [Cu_2]	0
12	**2 → 2-D**	77[c]
13	**3 → 3-D**	77[c]
14	**4 → 4-D**	68[c]
15	**5 → 5-D**	81[c]
16	**6 → 6-D**	77[c]
17	**7 → 7-D**	91[c]
18	**8 → 8-D**	75[c]

[a]Performed for 1.5–3 h with 0.15 mmol benzyl chloride.
[b]Yields of known products determined by 1H NMR versus CH_2Br_2 internal standard.
[c]Average of two runs.
[d]Value for 4-methylbenzaldehyde in {braces}.

well as dimerization of tertiary and ester-substituted benzyl chlorides, are inconsistent with the intermediacy of benzyl anions. Although the reaction is highly sensitive to air due to quenching of $[Cu_2]^*$ (entry 6), 4-methylbenzaldehyde becomes the major product (7% yield). Benzaldehydes are known products of the reaction between benzyl radicals and oxygen.[35,50] Attempts to trap benzyl radicals with the radical trap TEMPO were unsuccessful as TEMPO quenches $[Cu_2]$.[51]

The catalytic reaction is very sensitive to factors that alter chloride binding to $[Cu_2]^+$. Li^+ from $LiNTf_2$ likely interacts with chloride through ion pairing as a Lewis acid; electrolytes expected to exhibit weaker ion pairing with chloride, such as tetrabutylammonium salts, performed notably worse (entries 7–9). The poorer performance of $LiClO_4$ (entry 7) is attributed to the fact that in DME ClO_4^- is more tightly associated to Li^+ than is NTf_2^-,[52] possibly limiting sequestration of Cl^-. Isolated chloro-cubane and chloro-diamond (Figure 2.2D) were catalytically inactive under the conditions (entries 10–11). Therefore, the detection of chloro-diamond by ^{31}P NMR at the end of the standard reaction (entry 1) suggests one pathway by which catalysis ceases.

2.3 Conclusion

To close, we have described the electrophotochemical reactivity of $[Cu_2]$ in the presence of benzyl chloride substrates. Our mechanistic studies enable assignment of facile electron-transfer from the excited state $[Cu_2]^*$ with substrate to liberate $[Cu_2]^+$, Cl^-, and a benzyl radical that undergoes homocoupling to produce bibenzyl. By tracking down off-path copper-cubane and -diamond chloride sinks, and devising a means of sequestering the chloride produced, we are able to demonstrate the electrophotocatalytic chemistry of

interest. Our study complements other recent reports employing organo-photocatalysts for R(Ar)–X electrophotochemical couplings where the nature of the photoreductants are still being studied.

2.4 References

[1] Skubi, K. L.; Blum, T. R.; Yoon, T. P. Dual Catalysis Strategies in Photochemical Synthesis. *Chem. Rev.* **2016**, *116*, 10035–10074.

[2] Genzink, M. J.; Kidd, J. B.; Swords, W. B.; Yoon, T. P. Chiral Photocatalyst Structures in Asymmetric Photochemical Synthesis. *Chem. Rev.* **2022**, *122*, 1654–1716.

[3] Chan, A. Y.; Perry, I. B.; Bissonnette, N. B.; Buksh, B. F.; Edwards, G. A.; Frye, L. I.; Garry, O. L.; Lavagnino, M. N.; Li, B. X.; Liang, Y.; Mao, E.; Millet, A.; Oakley, J. V.; Reed, N. L.; Sakai, H. A.; Seath, C. P.; MacMillan, D. W. C. Metallaphotoredox: The Merger of Photoredox and Transition Metal Catalysis. *Chem. Rev.* **2022**, *122*, 1485–1542.

[4] Romero, N. A.; Nicewicz, D. A. Organic Photoredox Catalysis. *Chem. Rev.* **2016**, *116*, 10075–10166.

[5] Studer, A.; Curran, D. P. Catalysis of Radical Reactions: A Radical Chemistry Perspective. *Angew. Chem. Int. Ed.* **2016**, *55*, 58–102.

[6] Plesniak, M. P.; Huang, H.-M.; Procter, D. J. Radical Cascade Reactions Triggered by Single Electron Transfer. *Nat. Rev. Chem.* **2017**, *1*, 1–16.

[7] Romero, K. J.; Galliher, M. S.; Pratt, D. A.; Stephenson, C. R. J. Radicals in Natural Product Synthesis. *Chem. Soc. Rev.* **2018**, *47*, 7851–7866.

[8] Narayanam, J. M. R.; Stephenson, C. R. J. Visible Light Photoredox Catalysis: Applications in Organic Synthesis. *Chem. Soc. Rev.*, **2011**, *40*, 102–113.

[9] Fu, G. C. Transition-Metal Catalysis of Nucleophilic Substitution Reactions: A Radical Alternative to S_N1 and S_N2 Processes. *ACS Cent. Sci*. **2017**, *3*, 692-700.

[10] Yan, M.; Lo, J. C.; Edwards, J. T.; Baran, P. S. Radicals: Reactive Intermediates with Translational Potential. *J. Am. Chem. Soc.* **2016**, *138*, 12692–12714.

[11] Creutz, S. E.; Lotito, K. J.; Fu, G. C.; Peters, J. C. Photoinduced Ullmann C–N Coupling: Demonstrating the Viability of a Radical Pathway. *Science* **2012**, *338*, 647–651

[12] Kainz, Q. M.; Matier, C. D.; Bartoszewicz, A.; Zultanski, S. L.; Peters, J. C.; Fu, G. C. Asymmetric Copper-Catalyzed C-N Cross-Couplings Induced by Visible Light. *Science* **2016**, *351*, 681–684.

[13] Ahn, J. M.; Ratani, T. S.; Hannoun, K. I.; Fu, G. C.; Peters, J. C. Photoinduced, Copper-Catalyzed Alkylation of Amines: A Mechanistic Study of the Cross-Coupling of Carbazole with Alkyl Bromides. *J. Am. Chem. Soc.* **2017**, *139*, 12716–12723.

[14] Chen, C.; Peters, J. C.; Fu., G. C. Photoinduced Copper-Catalysed Asymmetric Amidation via Ligand Cooperativity. *Nature*, **2021**, *596*, 250–256.

[15] Lee, H.; Ahn, J. M.; Oyala, P. H.; Citek, C.; Yin, H.; Fu, G. C.; Peters, J. C. Investigation of the C–N Bond-Forming Step in a Photoinduced, Copper-Catalyzed Enantioconvergent N–Alkylation: Characterization and Application of a Stabilized Organic Radical as a Mechanistic Probe. *J. Am. Chem. Soc.* **2022**, *144*, 4114–4123.

[16] Nakafuku, K. M.; Zhang, Z.; Wappes, E. A.; Stateman, L. M.; Chen, A. D.; Nagib, D. A. Enantioselective radical C–H amination for the synthesis of β-amino alcohols. *Nat. Chem.* **2020**, *12*, 697–704.

[17] Mao, R.; Frey, A.; Balon, J.; Hu, X. Decarboxylative C(sp^3)–N Cross-Coupling via Synergetic Photoredox and Copper Catalysis. *Nat. Catal.* **2018**, *1*, 120–126.

[18] Liang, Y.; Zhang, X.; MacMillan, D. W. C. Decarboxylative sp^3 C–N Coupling via Dual Copper and Photoredox Catalysis. *Nature* **2018**, *559*, 83–88.

[19] Demarteau, J.; Debuigne, A.; Detrembleur, C. Organocobalt Complexes as Sources of Carbon-Centered Radicals for Organic and Polymer Chemistries. *Chem. Rev.* **2019**, *119*, 6906–6955.

[20] Mondal, S.; Dumur, F.; Gigmes, D.; Sibi, M. P.; Bertrand, M. P.; Nechab, M. Enantioselective Radical Reactions Using Chiral Catalysts. *Chem. Rev.* **2022**, *122* (6), 5842–5976.

[21] Choi, J.; Fu, G. C. Transition Metal–Catalyzed Alkyl-Alkyl Bond Formation: Another Dimension in Cross-Coupling Chemistry. *Science* **2017**, *356*, eaaf7230.

[22] Sakai, H. A.; Liu, W.; Le, C. "Chip"; MacMillan, D. W. C. Cross-Electrophile Coupling of Unactivated Alkyl Chlorides. *J. Am. Chem. Soc.* **2020**, *142*, 11691–11697.

[23] Wu, X.; Hao, W.; Ye, K.-Y.; Jiang, B.; Pombar, G.; Song, Z.; Lin, S. Ti-Catalyzed Radical Alkylation of Secondary and Tertiary Alkyl Chlorides Using Michael Acceptors. *J. Am. Chem. Soc.* **2018**, *140*, 14836–14843.

[24] Claros, M.; Ungeheuer, F.; Franco, F.; Martin-Diaconescu, V.; Casitas, A.; Lloret-Fillol, J. Reductive Cyclization of Unactivated Alkyl Chlorides with Tethered Alkenes under Visible-Light Photoredox Catalysis. *Angew. Chem. Int. Ed.* **2019**, *58*, 4869–4874.

[25] Ratani, T. S.; Bachman, S.; Fu, G. C.; Peters, J. C. Photoinduced, Copper-Catalyzed Carbon–Carbon Bond Formation with Alkyl Electrophiles: Cyanation of Unactivated Secondary Alkyl Chlorides at Room Temperature. *J. Am. Chem. Soc.* **2015**, *137*, 13902–13907.

[26] Matsubara, R.; Yabuta, T.; Md Idros, U.; Hayashi, M.; Ema, F.; Kobori, Y.; Sakata, K. UVA- and Visible-Light-Mediated Generation of Carbon Radicals from Organochlorides Using Nonmetal Photocatalyst. *J. Org. Chem.* **2018**, *83*, 9381–9390.

[27] Glaser, F.; Larsen, C. B.; Kerzig, C.; Wenger, O. S. Aryl Dechlorination and Defluorination with an Organic Super-Photoreductant. *Photochem. Photobiol. Sci.* **2020,** *19*, 1035–1041.

[28] Giedyk, M.; Narobe, R.; Weiß, S.; Touraud, D.; Kunz, W.; König, B. Photocatalytic Activation of Alkyl Chlorides by Assembly-Promoted Single Electron Transfer in Microheterogeneous Solutions. *Nat Catal* **2020**, *3*, 40–47.

[29] Miller, A. J. M.; Dempsey, J. L.; Peters, J. C. Long-Lived and Efficient Emission from Mononuclear Amidophosphine Complexes of Copper. *Inorg. Chem.*, **2007**, *46*, 7244–7246.

[30] Lotito, K. J.; Peters, J. C. Efficient Luminescence from Easily Prepared Three-Coordinate Copper(I) Arylamidophosphines. *Chem. Commun.* **2010**, *46*, 3690–3692.

[31] Bergmann, L.; Friedrichs, J.; Mydlak, M.; Baumann, T.; Nieger, M.; Bräse, S. Outstanding Luminescence from Neutral Copper(I) Complexes with Pyridyl-Tetrazolate and Phosphine Ligands. *Chem. Commun.* **2013**, *49*, 6501–6503.

[32] Kim, Y.-E.; Kim, J.; Park, J. W.; Park, K.; Lee, Y. σ-Complexation as a Strategy for Designing Copper-Based Light Emitters. *Chem. Commun.* **2017**, *53*, 2858–2861.

[33] Harkins, S. B.; Peters, J. C. A Highly Emissive Cu_2N_2 Diamond Core Complex Supported by a $[PNP]^-$ Ligand. *J. Am. Chem. Soc.*, **2005**, *127*, 2030–2031.

[34] Wu, Y.; Kim, D.; Teets, T. S. Photophysical Properties and Redox Potentials of Photosensitizers for Organic Photoredox Transformations. *Synlett* **2021**, DOI: 10.1055/a-1390-9065.

[35] Kern, J.-M.; Sauvage, J.-P. Photoassisted C–C Coupling via Electron Transfer to Benzylic Halides by a Bis(Di-Imine) Copper(I) Complex. *J. Chem. Soc., Chem. Commun.* **1987**, 546–548.

[36] Cowper, N. G. W.; Chernowsky, C. P.; Williams, O. P.; Wickens, Z. K. Potent Reductants via Electron-Primed Photoredox Catalysis: Unlocking Aryl Chlorides for Radical Coupling. *J. Am. Chem. Soc.* **2020**, *142*, 2093–2099.

[37] Kim, H.; Kim, H.; Lambert, T. H.; Lin, S. Reductive Electrophotocatalysis: Merging Electricity and Light To Achieve Extreme Reduction Potentials. *J. Am. Chem. Soc.* **2020**, *142*, 2087–2092.

[38] Tian, X.; Karl, T. A.; Reiter, S.; Yakubov, S.; de Vivie-Riedle, R.; König, B.; Barham, J. P. Electro-Mediated PhotoRedox Catalysis for Selective $C(sp^3)$–O Cleavages of Phosphinated Alcohols to Carbanions. *Angew. Chem. Int. Ed.* **2021**, *60*, 20817–20825.

[39] Chernowsky, C. P.; Chmiel, A. F.; Wickens, Z. K. Electrochemical Activation of Diverse Conventional Photoredox Catalysts Induces Potent Photoreductant Activity. *Angew. Chem. Int. Ed.* **2021**, *60*, 21418–21425.

[40] Rieth, A. J.; Gonzalez, M. I.; Kudisch, B.; Nava, M.; Nocera, D. G. How Radical Are "Radical" Photocatalysts? A Closed-Shell Meisenheimer Complex Is Identified as a Super-Reducing Photoreagent. *J. Am. Chem. Soc.* **2021**, *143*, 14352–14359.

[41] Harkins, S. B.; Mankad, N. P.; Miller, A. J. M.; Szilagyi, R. K.; Peters, J. C. Probing the Electronic Structures of $[Cu_2(\mu\text{-}XR_2)]^{n+}$ Diamond Cores as a Function of the Bridging X Atom (X = N or P) and Charge (n = 0, 1, 2). *J. Am. Chem. Soc.*, **2008**, *130*, 3478–3485.

[42] Wang, Z.; Bachman, S.; Dudnik, A. S.; Fu, G. C. Nickel-Catalyzed Enantioconvergent Borylation of Racemic Secondary Benzylic Electrophiles. *Angew. Chem. Int. Ed.* **2018**, *57*, 14529–14532.

[43] Poremba, K. E.; Kadunce, N. T.; Suzuki, N.; Cherney, A. H.; Reisman, S. E. Nickel-Catalyzed Asymmetric Reductive Cross-Coupling To Access 1,1-Diarylalkanes. *J. Am. Chem. Soc.* **2017**, *139*, 5684–5687.

[44] Ju, L.; Lin, Q.; LiBretto, N. J.; Wagner, C. L.; Hu, C. T.; Miller, J. T.; Diao, T. Reactivity of (Bi-Oxazoline)Organonickel Complexes and Revision of a Catalytic Mechanism. *J. Am. Chem. Soc.* **2021**, *143*, 14458–14463.

[45] Tsentalovich, Y. P.; Fischer, H. Solvent Effect on the Decarbonylation of Acyl Radicals Studied by Laser Flash Photolysis. *J. Chem. Soc., Perkin Trans. 2* **1994**, 729–733.

[46] Marcus, R. A.; Sutin, N. Electron Transfers in Chemistry and Biology. *Biochimica et Biophysica Acta (BBA) - Reviews on Bioenergetics* **1985**, *811*, 265–322.

[47] Lovinger, G. J.; Aparece, M. D.; Morken, J. P. Pd-Catalyzed Conjunctive Cross-Coupling between Grignard-Derived Boron "Ate" Complexes and $C(sp^2)$ Halides or Triflates: NaOTf as a Grignard Activator and Halide Scavenger. *J. Am. Chem. Soc.* **2017**, *139*, 3153–3160.

[48] EPR parameters from this measurement were identical to those of isolated $[Cu_2]^+$.

[49] The remaining current is likely due to capacitive (charging) current; due to the low catalyst loading, the total current amounted to only 0.16 C.

[50] Salta, Z.; Kosmas, A. M.; Segovia, M. E.; Kieninger, M.; Tasinato, N.; Barone, V.; Ventura, O. N. Reinvestigation of the Deceptively Simple Reaction of Toluene with OH and the Fate of the Benzyl Radical: The "Hidden" Routes to Cresols and Benzaldehyde. *J. Phys. Chem. A* **2020**, *124*, 5917–5930.

[51] The reduction potential of TEMPO is −1 V vs SCE and therefore electron transfer is substantially exergonic. Reduction potential taken from: Ryan, M. C.; Whitmire, L. D.; McCann, S. D.; Stahl, S. S. Copper/TEMPO Redox Redux: Analysis of PCET Oxidation of TEMPOH by Copper(II) and the Reaction of TEMPO with Copper(I). *Inorg. Chem.* **2019**, *58*, 10194–10200.

[52] Brouillette, D.; Perron, G.; Desnoyers, J. E. Apparent Molar Volume, Heat Capacity, and Conductance of Lithium *Bis*(trifluoromethylsulfone)imide in Glymes and Other Aprotic Solvents. *J. Solution Chem.* **1998**, *27*, 151–182.

C h a p t e r 3

Electrocatalytic Ammonia Oxidation Mediated by a Polypyridyl Iron Catalyst

Adapted from:
Zott, M. D.;‡ Garrido-Barros, P.;‡ Peters, J. C.
ACS Catal. **2019**, *9*, 10101–10108.
DOI: 10.1021/acscatal.9b03499

.

3.1 Introduction

Ammonia is produced on a massive scale globally by industrial nitrogen fixation, primarily for use as fertilizer. New ammonia synthesis technologies may yet enable other vectors for ammonia use, for example as a transportation fuel. Accordingly, there are substantial efforts underway to explore whether electrocatalytic N_2-to-NH_3 (N_2RR) conversion, potentially coupled with renewable resources that generate electricity, could provide a new ammonia synthesis pathway (Equation 3.1) to be exploited in renewably formed fuel storage, transport, and on-site use.[1]

$$N_2 + 6\,H^+ + 6\,e^- \rightleftharpoons 2\,NH_3 \qquad \text{(Equation 3.1)}$$

Commensurate with these goals, there has been long-standing interest in exploring heterogeneous catalysts for selective ammonia oxidation (AO), the microscopic reverse of N_2-to-NH_3 conversion (Equation 3.1).[2] The realization of selective electrocatalysts for AO in principle could enable fuel cell applications for ammonia, akin to those currently being practiced or explored for hydrogen and methanol.[3]

Homogeneous (electro)catalysts for N_2RR and AO have much to offer in terms of fundamental mechanistic studies, and possibly longer-term practical applications if robust hybrid catalyst/electrode architectures can be realized. Indeed, the field of N_2RR catalysis mediated by molecular systems has witnessed a surge of activity in the past 10–15 years, in part motivated by a desire to explore hypotheses germane to the inorganic mechanism of biological nitrogen fixation.[4] This has been matched by significant progress in defining catalysts (e.g., featuring Mo or Fe) that operate with (comparatively) impressive turnovers

and selectivities, and in fundamental mechanistic understanding of how these transformations occur.[5] Interest in translating this progress to electrocatalytic N_2RR using synthetic coordination complexes is growing.[6]

By contrast, homogeneous approaches to ammonia oxidation have been slower to attract significant attention from the coordination chemistry community. This is surprising given that biological ammonia oxidation, mediated by both aerobic and anaerobic ammonia-oxidizing bacteria, involves steps thought to occur at iron, copper, or molybdenum active sites, and is essential to the global nitrogen cycle.[7] As a six-electron process with substantial kinetic barriers, this process presents fascinating challenges in energy conversion, electrochemistry, and coordination chemistry. Challenges associated with catalytically converting NH_3 to N_2 and proton/electron equivalents at a well-defined active site include the fact that NH_3 is a strong σ-donor ligand that features thermally robust N–H bonds ($BDFE_{N–H}$ = 99.4 kcal/mol).[8]

Despite the comparatively limited activity in this area, stoichiometric oxidation of ammonia is well precedented. For instance, in 1979 Buhr and Taube initiated the study of ammonia oxidation by molecular complexes when they reported both chemical and electrochemical oxidation of ammonia in aqueous solution by $[Os(NH_3)_5(CO)]^{2+}$ to form N_2 in the μ-N_2-bridged product $[(Os(NH_3)_4(CO))_2N_2]^{4+}$ (Chart 3.1, A).[9] Relatedly, Thompson and Meyer reported the stoichiometric electrochemical oxidation of ammonia to nitrite and nitrate by $[(trpy)(bpy)Ru(NH_3)]^{2+}$ (trpy = 2,2′:6′,2″-terpyridine, bpy = 2,2′-bipyridine) in aqueous solution (Chart 3.1, B),[10] and reported electrochemical (though not electrocatalytic) ammonia oxidation to N_2 by a similar ruthenium polypyridyl system,

$[(bpy)_2(NH_3)RuORu(NH_3)(bpy)_2]^{4+}$.[11] Collman and coworkers have studied chemical and electrochemical oxidation of ammonia at cofacial ruthenium porphyrins via hydrazine and diazene intermediates.[12] Most recently, Hamann, Smith, and coworkers demonstrated that modification of the Meyer system provides a bona fide electrocatalyst for ammonia oxidation to N_2, reporting the liberation of 2.1 eq N_2 at 0.2 V vs Fc/Fc^+ (0.03 V onset potential) under the conditions used (Chart 3.1, C).[13]

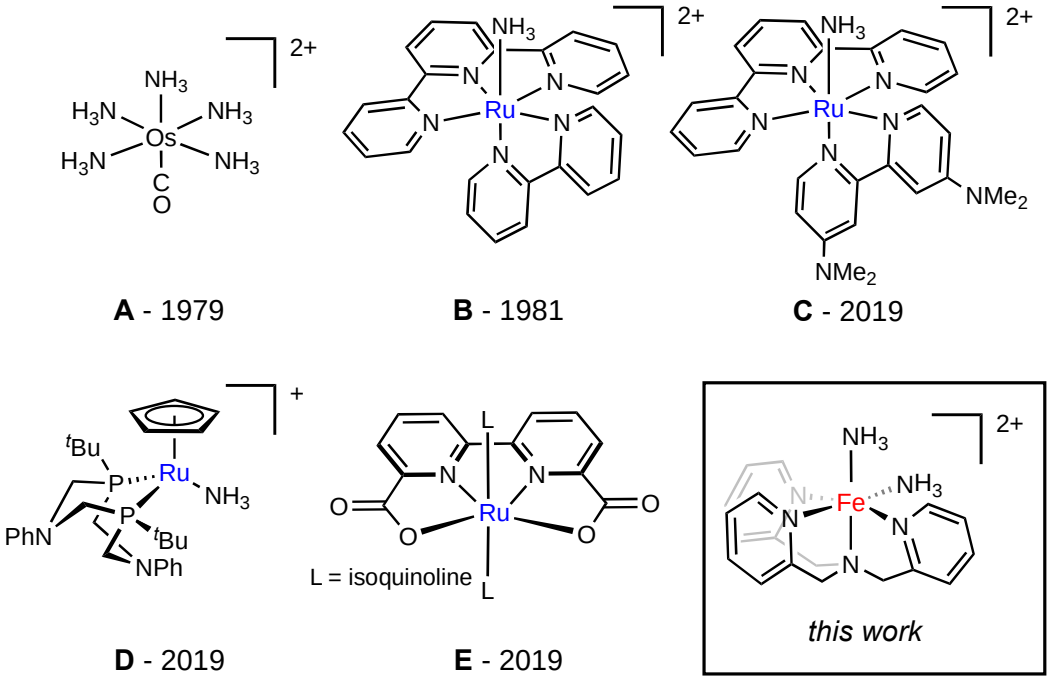

Chart 3.1. Molecular complexes that mediate AO.

There has also been growing interest in exploring molecular catalysts for ammonia oxidation that operate via net H-atom abstraction chemistry. In this context, a number of fascinating recent reports describe H-atom abstraction (HAA) reactions from coordinated NH_3, which can lead to $M(NH_2)$, M(NH), M(N), and in certain cases N_2 (via nitride coupling).[14] Catalytic ammonia oxidation via HAA has also been recently demonstrated using a ruthenium complex and 2,4,6-tri(*t*-butyl)phenoxyl radical by Mock and coworkers

(Chart 3.1, D).[15] Similarly, Nishibayashi and coworkers recently reported catalytic chemical oxidation of ammonia, again using a ruthenium system (Chart 3.1, E).[16]

Given the paucity of data available describing electrocatalytic ammonia oxidation, and the fact that biologically relevant first row metals such as iron have yet to be described for this process, we targeted the study of promising candidate iron (electro)catalysts as models well-suited to mechanistic interrogation. Noting that a number of polypyridyl iron complexes have been studied as potential water oxidation catalysts (WOC's),[17] we felt such systems might provide a prudent starting point.

In this context, we now describe that a previously reported iron complex featuring a tetradentate polypyridyl supporting ligand (TPA) and two cis-labile sites, $[(TPA)Fe(MeCN)_2]^{2+}$,[18] is highly active for electrocatalytic ammonia oxidation in acetonitrile under an applied bias. Important features of this system are that NH_3 can reversibly bind at the two labile sites, NH_3 itself is able to promote the proton-transfer steps needed for catalytic activity, and up to 16 eq of N_2 (per Fe) have been generated from NH_3 using this catalyst via controlled potential coulometry (CPC) experiments. At present, this is the highest TON to be verified for a molecular AO system. More importantly, the system is electrochemically well behaved and hence amenable to detailed study by a range of electrochemical experiments. Our data point to an observed rate constant, k_{obs}, for NH_3 oxidation of ~10^7 $M^{-1}\cdot s^{-1}$, with the catalytic process starting at an onset potential of ~0.7 V vs Fc/Fc^+, whose rate-determining step (RDS) is first order in $[(TPA)Fe(L)_2]^{2+}$ and NH_3. The available data also allow us to suggest $[(TPA)Fe^{III}(NH_2)(NH_3)]^{2+}$ and $[(TPA)Fe^{IV}(NH_2)(NH_3)]^{3+}$ species as early intermediates en route to N–N bond formation.

3.2 Results and Discussion

3.2.1 Electrocatalytic conversion of NH_3 to N_2 and H_2. The cyclic voltammogram of $[(TPA)Fe(MeCN)_2]OTf_2$ in acetonitrile using a boron-doped diamond (BDD) working electrode (see Figure 3.1A,B) has one reversible feature at 0.75 V vs Fc/Fc^+ corresponding to the Fe^{2+}/Fe^{3+} redox couple (Figure 3.1A). Two new redox features appeared (E_1 and E_2) in the presence of increasing amounts of added NH_3, and the reversible feature corresponding to $[(TPA)Fe(MeCN)_2]OTf_2$ disappeared. Moreover, the wave at E_2 continuously increased with increasing ammonia concentration. As a reference, when 100 equivalents of NH_3 were added to the $[(TPA)Fe(MeCN)_2]OTf_2$ solution in acetonitrile, E_1 and E_2 were centered at 0.4 V and 1.1 V, respectively, and E_2 featured dramatically increased current relative to that

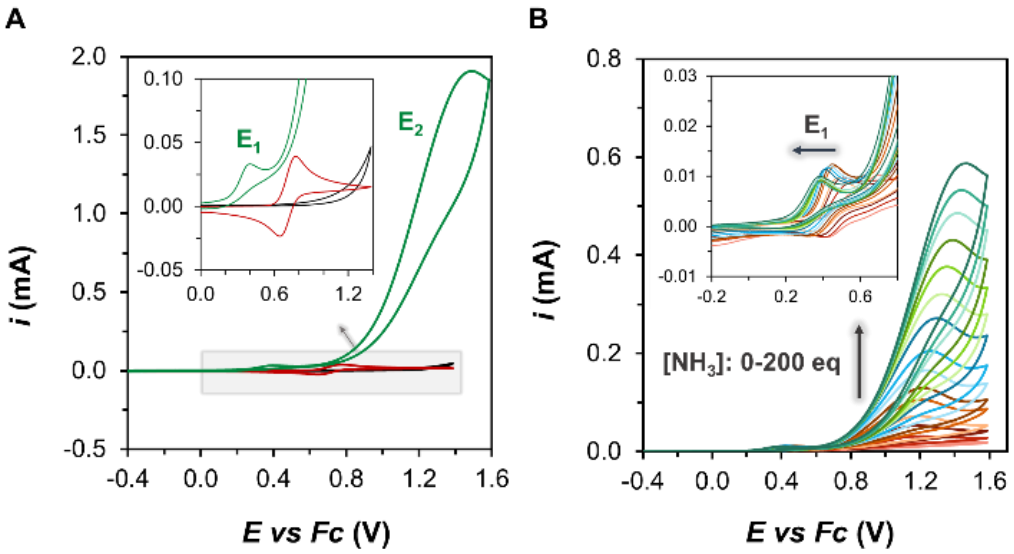

Figure 3.1. Electrochemical data. (A) Cyclic voltammograms in acetonitrile solutions of background AO on BDD in presence of 0.25 M NH_3 (black), 2.5 mM $[(TPA)Fe(MeCN)_2]OTf_2$ in the absence of NH_3 (red), and AO by $[(TPA)Fe(MeCN)_2]OTf_2$ with 0.25 M NH_3 (green). (B) Cyclic voltammograms in acetonitrile with 50 mM NH_4OTf and 0.5 mM $[(TPA)Fe(MeCN)_2]OTf_2$ with varying $[NH_3]$. The inset highlights the shift in E_1 with $[NH_3]$. CVs were recorded with a BDD disk electrode, a Pt counter electrode, and a custom Ag/AgOTf reference electrode corrected for the Fc/Fc^+ couple.

observed for the one-electron Fe^{2+}/Fe^{3+} redox couple. These observations are consistent with fast electrocatalytic ammonia oxidation at E_2.

To assess whether catalytic NH_3 oxidation occurs at the irreversible E_2 wave, CPC was performed using a BDD plate working electrode (1 cm^2) and a Pt counter electrode to facilitate H_2 evolution, and the headspace was analyzed via gas chromatography. CPC of a 0.5 mM $[(TPA)Fe(MeCN)_2]OTf_2$ acetonitrile solution with 65 mM NH_3 was performed at 1.1 V vs Fc/Fc^+. After 18 h, 33 C of charge had passed; headspace analysis indicated Faradaic efficiencies of 80% and 70% for the production of N_2 and H_2 (±10% error in gas quantification), respectively, correlating with the production of up to 16 equivalents of N_2.[19] This turnover number is the highest yet reported for a molecular NH_3 oxidation (electro)catalyst. The measured H_2:N_2 ratio was 2.6:1, in good agreement with the 3:1 ratio expected for NH_3. When isotopically enriched $^{15}NH_4OTf$ and $^{15}NH_3$ were employed, only $^{30}N_2$ was observed by GC-MS, confirming ammonia to be the source of detected N_2 (see SI for details).

Further CPC experiments in the absence of a (TPA)Fe source, at the same applied potential of 1.1 V vs Fc/Fc^+, suggest a critical role for (TPA)Fe-species in the catalysis. When CPC of a 65 mM NH_3 solution was performed, only 1.1 C of charge was passed, and only 0.5 eq N_2 were detected. Furthermore, when $[(TPA)Fe(MeCN)_2]OTf_2$ was replaced with $FeOTf_2$ as the precatalyst, only 1.9 C of charge were passed along with 1.0 eq N_2 being detected in the headspace.

3.2.2 Investigation of catalyst stability. Over multiple independent CPC experiments, the current after 18 h at an applied potential of 1.1 V vs Fc/Fc^+ had greatly attenuated. Such a

decrease in current typically suggests either catalyst decomposition or electrode passivation.[20] To study this phenomenon, X-ray photoelectron spectroscopy was performed on the BDD working electrode after CPC to try to identify potential degradation products. During CPC with 65 mM NH_3 and no added iron precatalyst, the current dropped to 10% of the initial current after only 3 h. XPS analysis of the BDD electrode revealed incorporation of nitrogen onto the electrode surface (see SI). This process passivates the electrode surface, as confirmed by measurements of the ferrocene/ferrocenium redox couple before and after CPC. This passivation is hence one process by which the catalysis can be arrested in the presence of NH_3 using BDD electrodes.

Although the chronoamperogram with $[(TPA)Fe(MeCN)_2]OTf_2$ as a precatalyst in the presence of NH_3 also showed a time-dependent decrease in current, a much longer time scale, ~15 h, was required to reach 10% of the initial current. Measurement of the working electrode after CPC again revealed incorporation of nitrogen, but now also iron, on the surface. The detection of iron on the electrode surface by XPS raises the possibility that a heterogeneous iron catalyst may be responsible for (or contribute to) the electrocatalytic AO discussed above. Indeed, it is difficult, if not impossible, to reliably discount a contributing role for heterogenous (electro)catalysis.[21] However, several lines of evidence lead us to suggest that a molecular, TPA-ligated iron catalyst dominates the aforementioned AO behavior. In the chronoamperogram for AO by the precatalyst $[(TPA)Fe(MeCN)_2]OTf_2$, no induction period was observed. Furthermore, a rinse test was performed with the BDD electrode following CPC using a fresh acetonitrile-ammonia solution. No catalytic current was passed in this case, ruling out a heterogeneous catalyst that is strongly attached to the electrode. Measurement of the catalyst solution after CPC with a clean BDD disk electrode

indicated a catalytic wave of similar intensity to that observed prior to CPC. To demonstrate the relative stability of the TPA-ligated Fe-species under catalytic conditions, 50 cycles of CV were performed, Figure 3.2A. Almost no reduction in catalytic current appeared between the first and last scan. While these experiments cannot reliably discount the possibility of a very rapidly formed, loosely bound and highly active heterogeneous catalyst forming under CPC experiments, we find such a scenario improbable.

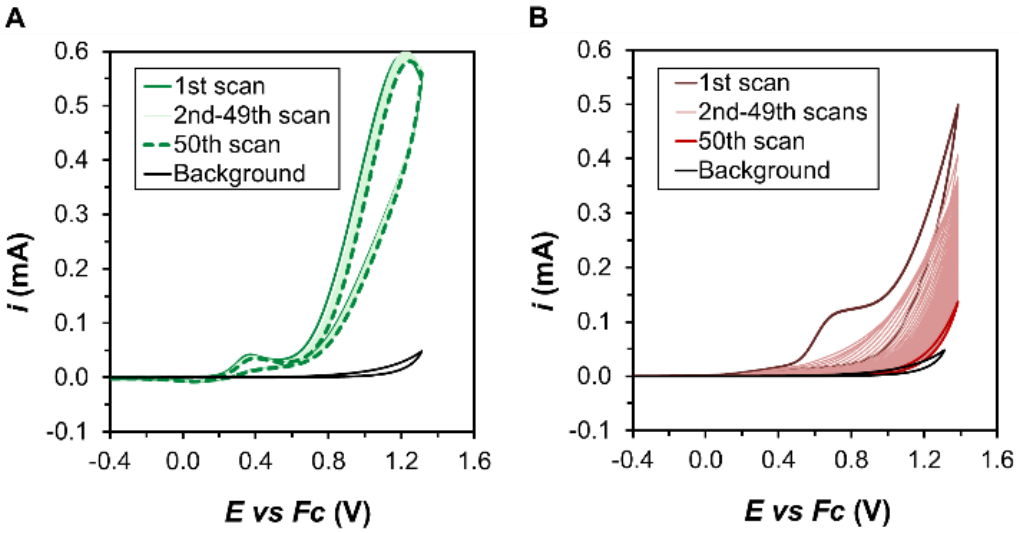

Figure 3.2. Cycling of (A) 2.5 mM $[(TPA)Fe(MeCN)_2]OTf_2$, or (B) 2.5 mM $FeOTf_2$, with a BDD disk electrode in an acetonitrile solution containing 50 mM NH_3 and 50 mM NH_4OTf. Pt wire was used as the counter electrode with a custom Ag/AgOTf reference electrode.

To probe this issue further, $[(TPA)Fe(MeCN)_2]OTf_2$ was replaced by $FeOTf_2$ as the precatalyst during CPC with ammonia. In this case, the current rapidly dropped to 10% of the initial current after only 1 h. After CPC, the XPS spectrum of the BDD electrode was almost identical to the spectrum obtained after CPC with $[(TPA)Fe(MeCN)_2]OTf_2$. 50 cycles of CV were also performed with $FeOTf_2$ in ammonia, Figure 3.2B. A continuous decrease in peak current, correlated with passivation of the electrode, was observed. In acetonitrile-ammonia solutions, we presume $FeOTf_2$ exists primarily as $[Fe(NH_3)_6]OTf_2$. The decrease

in current observed by CPC and CV, in addition to the iron observed on the electrode surface by XPS, establish the instability of $[Fe(NH_3)_6]OTf_2$ under the present conditions.

Given the instability of $[Fe(NH_3)_6]OTf_2$ under electrocatalytic conditions, we wondered if the source of the iron observed on the electrode surface post-CPC could be due to partial demetallation of TPA-ligated Fe species by NH_3, thereby forming $Fe(NH_3)_6^{2+}$, which can then degrade at the BDD electrode. The speciation of $[(TPA)Fe(L)_2]OTf_2$ with varying ammonia concentrations was therefore studied by UV-vis spectroscopy (Figure 3.3A,B). A plot of absorbance at 400 nm vs $[NH_3]$, Figure 3.3A, displays three distinct regions of different slopes. We assign these as regions of equilibria corresponding to the

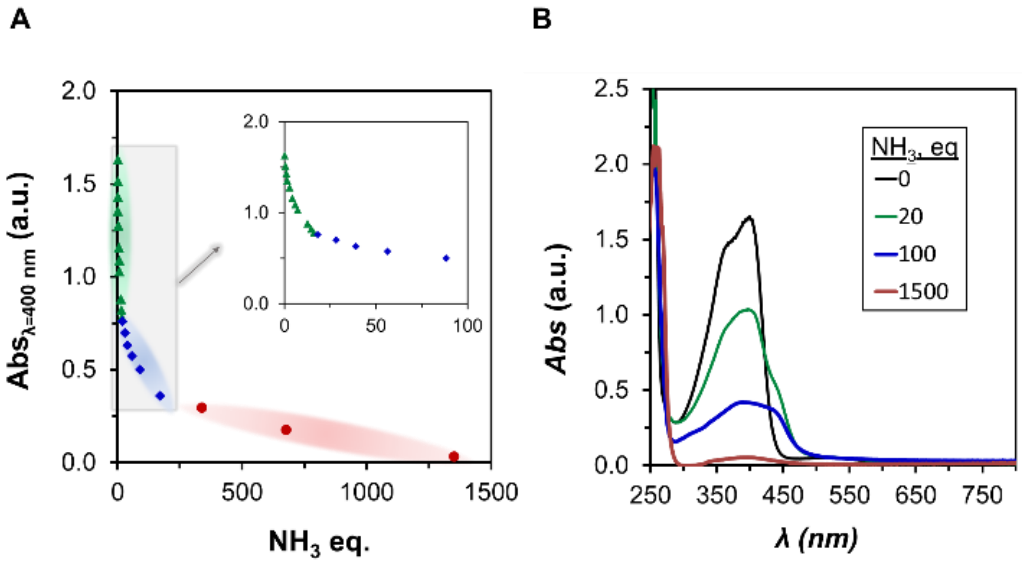

Figure 3.3. UV-vis monitoring of speciation. (A) Plot of absorbance at λ_{max} = 400 nm versus $[NH_3]$ demonstrating regions corresponding to mono-ammine, bis-ammine, and hexakis-ammine iron complexes. (B) UV-vis spectrum of 0.2 mM $[(TPA)Fe(MeCN)_2]OTf_2$ with 0, 20, 100, or 1500 eq NH_3 added in acetonitrile.

successive displacement by NH_3 of one MeCN (1–10 eq NH_3), a second MeCN (10–200 eq NH_3), and finally the additional displacement of TPA by NH_3 to form $Fe(NH_3)_6^{2+}$. In accord with these equilibria being reversible, the addition of free TPA to $FeOTf_2$ in MeCN with

excess NH_3, to reproduce the electrocatalytic conditions, produces the E_1 and E_2 redox features as well as the UV-vis spectrum associated with $[(TPA)Fe(NH_3)_2]^{2+}$; in the absence of $FeOTf_2$, an irreversible oxidation wave for free TPA is instead observed at ~ 1.0 V. Consistent with the viability of $[(TPA)Fe(NH_3)_2]OTf_2$, we were able to obtain its solid-state X-ray structure via crystals grown by diffusing NH_3 gas into a THF solution of dissolved $(TPA)FeOTf_2$. The solid-state structure of $[(TPA)Fe(NH_3)_2]OTf_2$ features four independent molecules in the asymmetric unit and interestingly, bond lengths that are consistent with the presence of *both* high- and low-spin iron centers (two of each type; see Figure 3.4 and SI).[22] Given that $[(TPA)Fe(NH_3)_2]OTf_2$ is structurally well-defined, as is $[(TPA)Fe(MeCN)_2]OTf_2$,[18] an intermediate structure, $[(TPA)Fe(NH_3)(MeCN)]OTf_2$, is highly plausible and we presume the primary species present in the 1–10 eq NH_3 region.

Although the aforementioned electrocatalytic conditions include 130 eq NH_3, a regime in which $[(TPA)Fe(NH_3)_2]OTf_2$ dominates, there is likely a small population of $[Fe(NH_3)_6]^{2+}$ and also free TPA under these conditions. The source of iron on the electrode presumably results as $[Fe(NH_3)_6]^{2+}$ is continuously degraded, shifting the equilibrium toward further demetallation. Fortunately, degradation is slow, as evidenced by CV cycling experiments, the chronoamperogram as well as CVs and UV-vis acquired before and after CPC, (see SI).

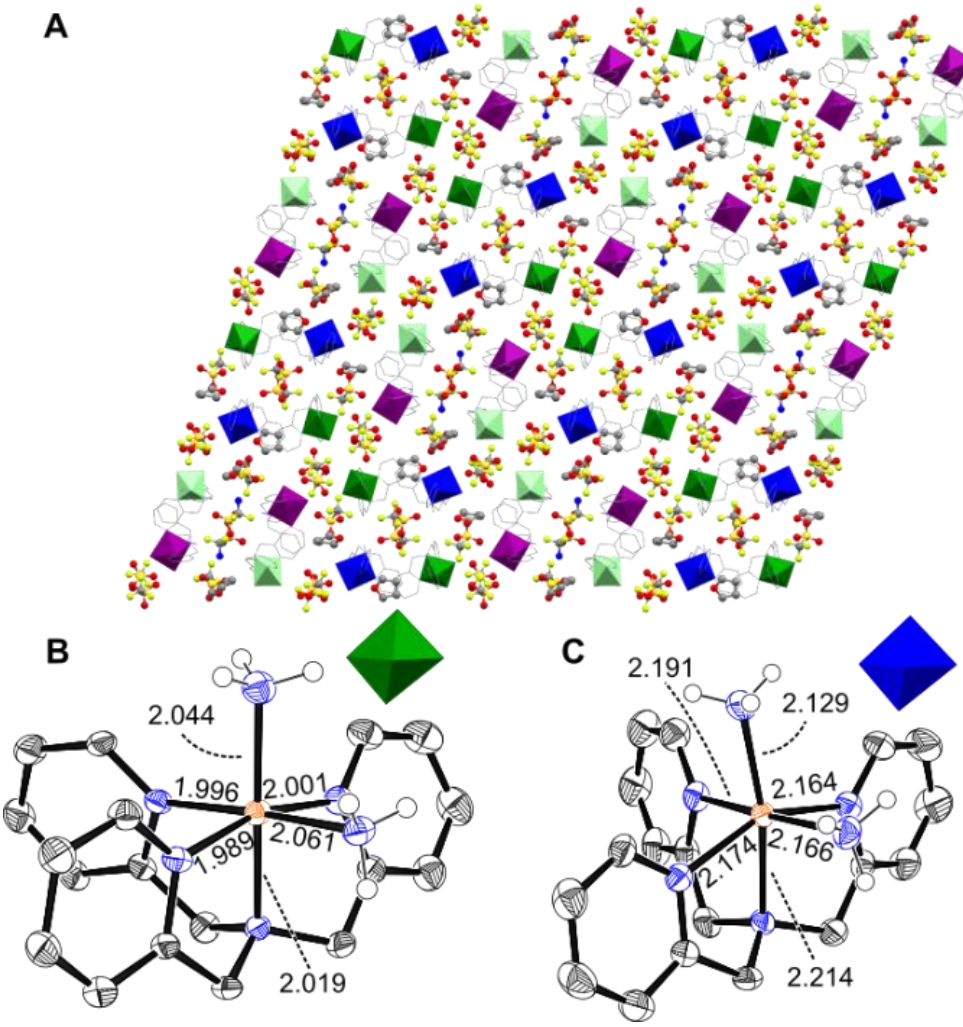

Figure 3.4. Solid-state crystal structure of $[(TPA)Fe(NH_3)_2]OTf_2$ at 100 K. (A) View down the b-axis with 4 unit cells shown. Green/light green octahedra represent low spin Fe(II) sites, while blue/purple octahedra represent high spin Fe(II) sites. Representative low spin (B) and high spin (C) sites are shown, with bond lengths labeled in Å. Thermal ellipsoids are shown at 50% probability. Triflate counterions, hydrogen, and co-solvent are omitted for clarity.

3.2.3 Mechanistic insight into the first redox process (E_1). The sequential addition of NH_3 to $[(TPA)Fe(L)_2]^{2+}$ increased the catalytic current at E_2 (E_{cat}), Figure 3.1B. Another change observed in the cyclic voltammogram of $[(TPA)Fe(L)_2]^{2+}$ in MeCN with increasing amounts of ammonia is a shift in the potential of the first redox process, E_1, toward more cathodic values. This observation indicates that the electron transfer step (E) in the oxidation is

coupled to a chemical step (C) involving NH_3 as a reactant. This EC mechanism is further supported by an increasing irreversibility at E_1 concomitant with the appearance of a new reduction peak $E_{1'}$ at −0.4 V (Figure 3.5A), arising from the formation of a new species as $[NH_3]$ is increased.

Scheme 3.1. Equilibria relevant to substitution of acetonitrile and TPA by ammonia in acetonitrile solution for $[(TPA)Fe(L)_2]^{2+}$.

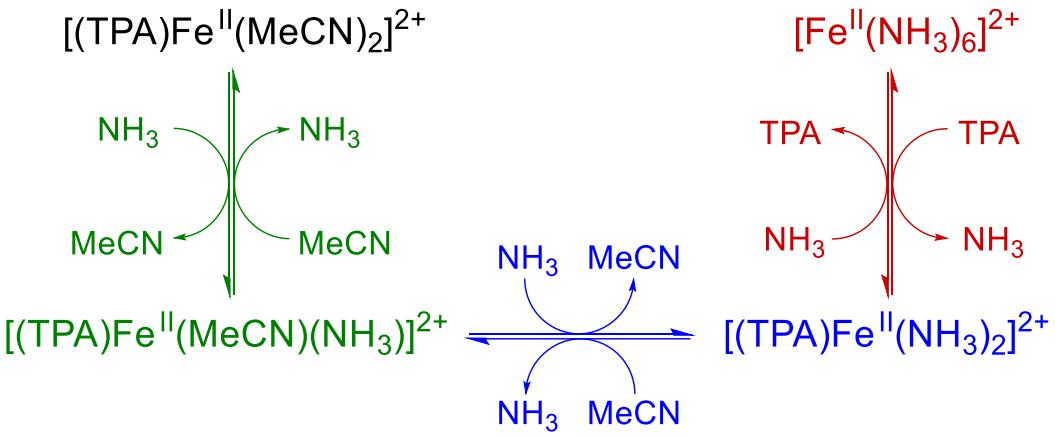

Interestingly, only one oxidation peak was observed at lower ammonia concentrations. This can be rationalized via a fast equilibrium between $[(TPA)Fe(MeCN)(NH_3)]^{2+}$ and $[(TPA)Fe(NH_3)_2]^{2+}$ as described in Scheme 3.1. The bis-ammine complex is expected to have a more cathodically shifted oxidation potential (NH_3 being a stronger donor than MeCN). Thus, as the population of $[(TPA)Fe(NH_3)_2]^{2+}$ is oxidized to Fe(III) near the electrode, the equilibrium shifts, driving coordination of a second NH_3 eq to $[(TPA)Fe(MeCN)(NH_3)]^{2+}$; the latter species should still be primarily in the Fe(II) oxidation state as it is expected to have a redox potential ~150 mV more positive than the $[(TPA)Fe(NH_3)_2]^{2+}$.[23] Rapid solvent equilibration is expected for high spin iron(II), on the order of ~10^4–10^6 s^{-1}.[24]

The voltammetric response of an EC mechanism is governed by the pseudo-first order equilibrium constant of the chemical step (K), as well as the competition between the pseudo-first order rate constant of the chemical step (k') and diffusion.[25,26] Under our present conditions, the first redox event E_1 shows quasi-reversible character typical for the KE regime in the kinetic zone diagram, where the redox potential is governed by the following equation:

$$E_{ox} = E^0_{ox} - \frac{RT}{F} ln\left(\frac{k'_{1f}}{k'_{1b}}\right) \qquad \text{(Equation 3.2)}$$

F is the Faraday constant, R is the gas constant, T is the temperature, E_{ox} is the oxidation potential, E^0_{ox} is the standard oxidation potential, and k'_{1f} and k'_{1b} are, respectively, the pseudo first order rate constants for the forward and backward chemical reaction. Using Equation 3.2, the change in peak potential with the natural logarithm of ammonia concentration reveals a linear dependence with a negative slope of −0.030, in good agreement with the theoretical value of −0.026 (Figure 3.5B). Due to its character as a Brønsted base, one plausible explanation for the role of NH_3 in the chemical step following oxidation is the abstraction of a proton from one of the NH_3 ligands coordinated to Fe(III). Such a mechanism would produce NH_4^+ as a product, together with the oxidized iron complex $[(TPA)Fe^{III}(NH_3)(NH_2)]^{2+}$. Accordingly, the E_1 potential with varying concentrations of NH_4^+ at a fixed concentration of NH_3 (Figure 3.5C) shows a linear relationship, with an observed slope of +0.024. This finding is in agreement with the predicted value of +0.026.

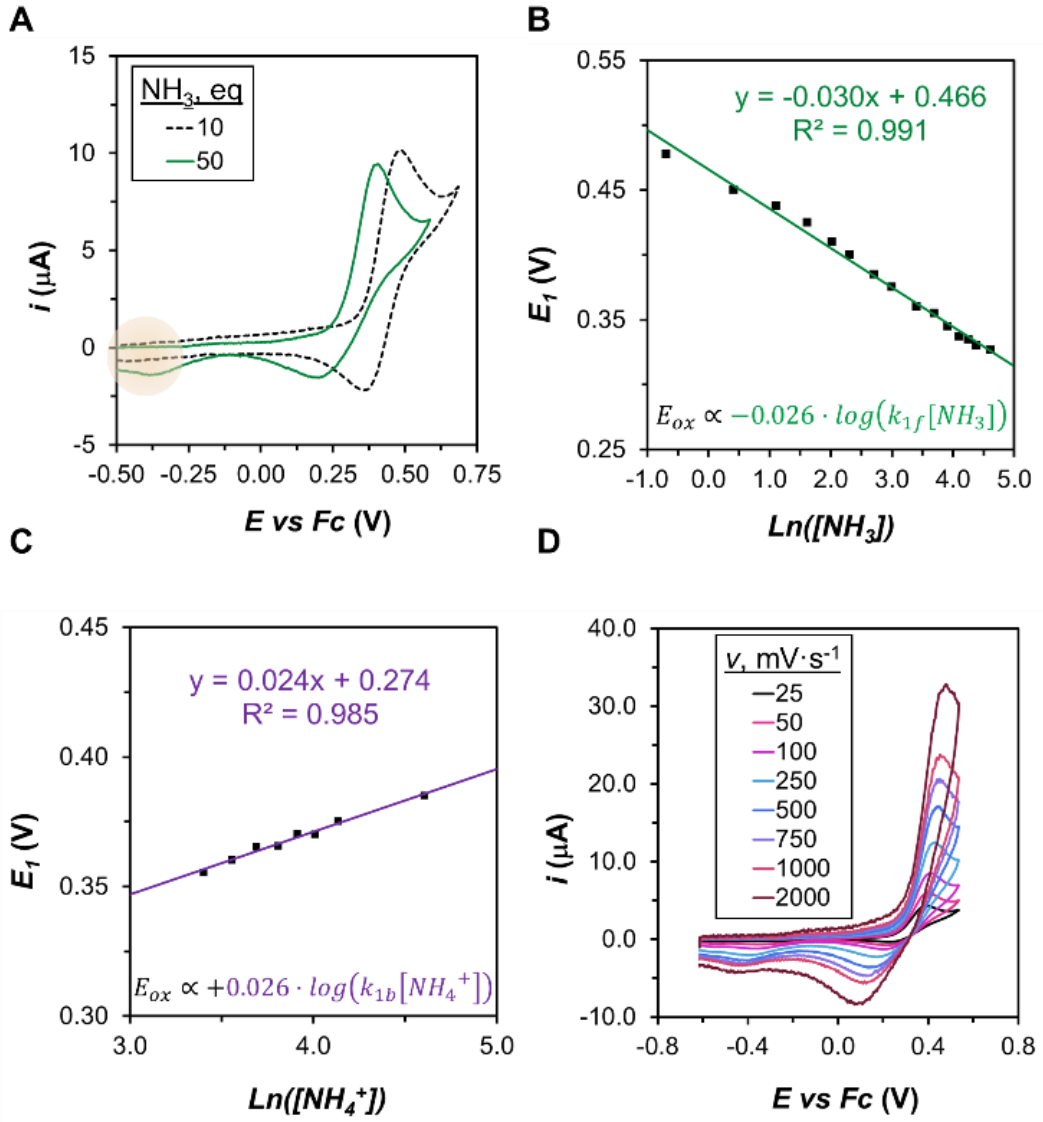

Figure 3.5. Evidence supporting an EC mechanism. (A) CV of an acetonitrile solution containing 0.5 mM $[(TPA)Fe(MeCN)_2]^{2+}$, 50 mM NH_4OTf, and 10 (black dashed trace) or 50 (solid green trace) eq NH_3. (B) Plot of the potential for the first redox event E_1 versus the natural logarithm of $[NH_3]$. (C) Plot of the potential for the first redox event E_1 versus the natural logarithm of $[NH_4^+]$. (D) CV of an acetonitrile solution containing 0.5 mM of $[(TPA)Fe(MeCN)_2]^{2+}$, 50 mM NH_4OTf, and 50 mM NH_3 at different scan rates. CVs recorded with a BDD disk electrode, a Pt counter electrode, and a custom Ag/AgOTf reference electrode.

Hence, the proposed EC mechanism is consistent with the electrochemical behavior at E_1 as reactant, NH_3, and product, NH_4^+, concentrations are varied.

Using the above logic, we assign the reduction peak $E_{1'}$, appearing at −0.4 V in Figure 3.5A, to the one-electron reduction of $[(TPA)Fe^{III}(NH_3)(NH_2)]^{2+}$. Upon its reduction, no return oxidation peak could be detected in the following anodic scan near −0.4 V, indicating fast protonation to regenerate $[(TPA)Fe^{II}(NH_3)_2]^{2+}$. This is consistent with the basic character that might be expected for an octahedral Fe–NH_2 species.[27] Therefore, this first E_1 redox event involves a square mechanism, with a preliminary E_1C_1 oxidation reaction (blue equations in Scheme 3.2) coupled to a second E_2C_2 reduction reaction (red equations in Scheme 3.2).

Scheme 3.2. Proposed square mechanism for the first redox event, E_1, at 0.4 V. The presence of the TPA ligand is implied for the species shown.

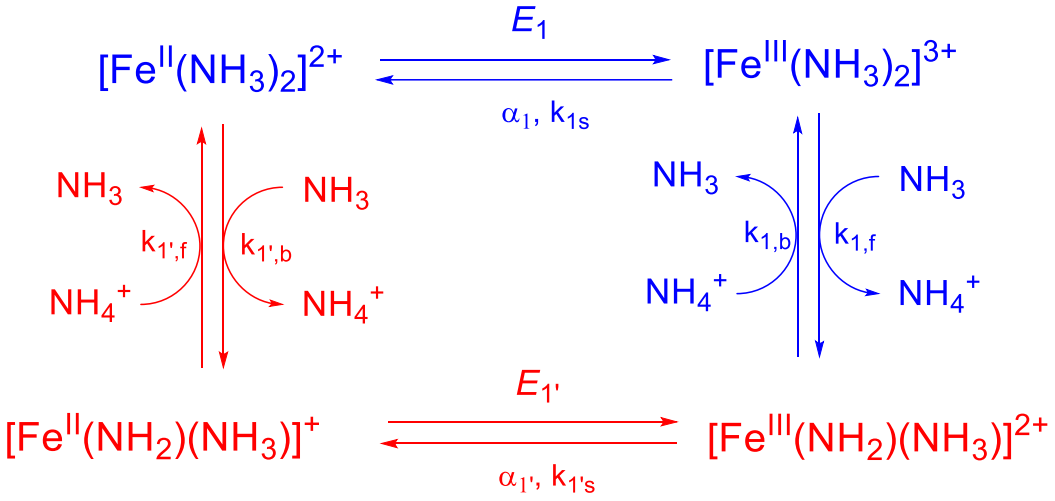

We have further confirmed this mechanism by performing cyclic voltammetry at different scan rates, as depicted in Figure 3.5D. At low scan rates, where C_1 reaches equilibrium, two reductive peaks could be detected with similar intensities, corresponding to $[(TPA)Fe^{III}(NH_3)_2]^{3+}$ and $[(TPA)Fe^{III}(NH_3)(NH_2)]^{2+}$. However, when the scan rate was increased, the reduction peak at around 0.2 V showed greater intensity as compared to the

peak at −0.4 V. This is a consequence of the relatively slow forward reaction, C_1, as compared to the fast scan rate, such that C_1 does not reach equilibrium, and hence $[(TPA)Fe^{III}(NH_3)_2]^{2+}$ is the main species reduced at the electrode.

Analysis of the peak currents at E_1 obtained from CVs at different scan rates reveals a linear relationship with $v^{1/2}$, following the predicted behavior from the Randles-Sevcik equation for an electrochemically reversible electron transfer process of a freely diffusing molecule in solution.[28] Further analysis of the current corresponding to the oxidative peak with increasing concentrations of $[(TPA)Fe(L)_2]^{2+}$ again reveals the linear dependence expected for a one electron oxidation. This data, in combination with the well-behaved shift in E_1 potential with both NH_3 and NH_4^+ concentration, collectively support a primary process at E_1 to form a reactive Fe^{III}–NH_2 species.

3.2.4 Mechanistic insight into the catalytic process (E_2). We performed a similar analysis of the E_2 (E_{cat}) event where fast catalysis is observed. While a detailed analysis for this six-electron/six-proton process can in principle be performed,[29] in practice such an analysis quickly becomes intractable. A common mechanistic approximation is therefore to consider the simplest case scenario, where electron transfer from the catalyst to the electrode is

Scheme 3.3. A simplified catalytic mechanism for ammonia oxidation at $E_2 \approx 1.1$ V. P and Q represent the inferred intermediates $[(TPA)Fe^{III}(NH_3)(NH_2)]^{2+}$ and its one-electron oxidized species $[Fe^{IV}(NH_3)(NH_2)]^{3+}$, respectively. The latter intermediate would then react with ammonia in a process that ultimately releases N_2. $E_{P/Q}$ is the potential for the P/Q redox couple, and k_{obs} is the apparent second-order rate constant of the catalytic chemical step.

$$P \underset{}{\overset{E_{P/Q}}{\rightleftharpoons}} Q + e^-$$

$$Q + NH_3 \xrightarrow{k_{obs}} P + N_2 + 6H^+$$

followed by a rate determining homogeneous catalytic reaction with the substrate, EC_{cat}, as shown in Scheme 3.3.[25,30]

A related strategy has been previously applied to electrocatalytic redox processes for CO_2 reduction[31] and water oxidation,[32] and provides essential information regarding the mechanism and the overall kinetics for the catalytic process. Such an approach is justified here because the potential of the first EC step (E_1) is cathodically well separated from E_2. Furthermore, oxidation following an N–N bond formation step is expected to occur at less oxidizing potentials. In support of this notion, we found that a CV of $[(TPA)Fe(L)_2]^{2+}$ in acetonitrile with added hydrazine displayed a catalytic oxidation around 0.4 V. Our primary assumption is thus that electrocatalytic NH_3 oxidation to N_2 is triggered via a single electron transfer step that occurs at a substantially more oxidizing potential than all other steps. If correct, simplification to an EC mechanism is reasonable, and it then becomes possible to obtain a kinetic constant (k_{obs}) that reflects the overall rate of the catalytic reaction, after scaling for the number of electrons transferred (n).[33]

To calculate k_{obs}, we performed a foot of the wave analysis (FOWA).[31] Due to non-Nernstian behavior in the ET step (see Supporting Information for further details), the Butler-Volmer law, which includes a charge transfer coefficient (α) and the rate constant for interfacial electron transfer (k_s), was utilized:[34]

$$FIT\left(E_{cat}^{0}-E\right)=\frac{\frac{i}{i_p}}{1-0.446\frac{i}{i_p}\frac{\sqrt{D_{cat}}}{k_s}\sqrt{\frac{F}{R\cdot T}v}\exp\left[\alpha\frac{F}{R\cdot T}\left(E_{cat}^{0}-E\right)\right]}=\frac{n\cdot 2.24\cdot\sqrt{\frac{R\cdot T}{F\cdot v}\cdot k'_{obs}}}{1+\exp\left[\frac{F}{R\cdot T}\left(E_{cat}^{0}-E\right)\right]} \qquad \text{(Equation 3.3)}$$

Plotting the FIT equation versus $1/(1+\exp[F/(RT)(E_{cat}-E)]$ gives the value for pseudo first-order constant $k'_{obs}=k_{obs}\cdot[NH_3]$ (see SI). To use these equations, α and k_s were determined from the precatalytic wave by analyzing the peak potential at different scan rates (see SI).[25] We found an α value of 0.66, close to the typical value when use of the Butler-Volmer equation is necessary,[25] and a diffusion coefficient D_{cat}: $9.5\cdot10^{-10}$ ($m^2\cdot s^{-1}$), which is typical for molecular complexes in solution (see Supporting Information).[35] With these values, we could obtain the kinetic constant for the electron transfer k_s of around 111 $m\cdot s^{-1}$. These data enable a FOWA according to Equation 3.3, which provides a second order apparent rate constant, k_{obs}, of $3.7\cdot10^7$ $M^{-1}\cdot s^{-1}$ on average for different concentrations of catalyst (Figure 3.6A; see SI for details). Hence, this iron catalyst for AO is able to operate at a remarkably fast rate under a large applied bias of 1.1 V.

In addition to providing kinetic information, this method of analysis also offers important mechanistic information about the catalytic process, because the validity of these equations is intrinsically related to the validity of the assumed mechanism. Our assumed mechanism includes a rate-determining step which is first order both in catalyst and in NH_3. Accordingly, the calculated pseudo-first order rate constant, k'_{obs}, should be constant with respect to the $[(TPA)Fe(L)_2]^{2+}$ concentration (because k'_{obs} is normalized by its molarity), and should respond linearly to the NH_3 concentration. We have confirmed both relationships by analysis at different concentrations of $[(TPA)Fe(L)_2]^{2+}$ and $[NH_3]$ (Figure 3.6A,B).

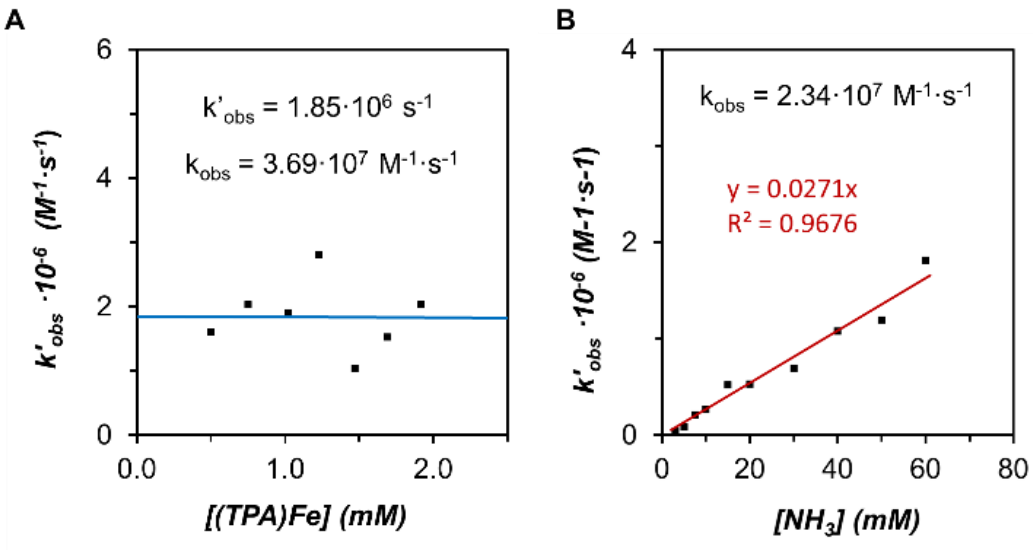

Figure 3.6. Rate law data. (A) Dependence of the calculated k'_{obs} on the concentration of $[(TPA)Fe(MeCN)_2]^{2+}$ precatalyst. (B) Dependence of the calculated k'_{obs} on the concentration of NH_3. In both cases, k'_{obs} has been calculated using FOWA as described in the SI.

3.3 Conclusion

With interest growing in the study of molecular (electro)catalysts for AO, a fascinating multi-electron redox reaction that represents the microscopic reverse of N_2-to-NH_3 conversion, electrochemically well-defined model systems are needed. In this context we have described in detail the capacity of a polypyridyl iron catalyst, $[(TPA)Fe(MeCN)_2]OTf_2$, to perform AO at extremely fast rates (~10^7 $M^{-1}{\cdot}s^{-1}$ via FOWA) under the application of a 1.1 V applied bias. We have also used CPC to confirm that N_2 is selectively formed via this AO reaction, confirming as many as 16 eq of N_2 (32 eq NH_3 being consumed) per Fe. While TONs do not necessarily reflect overall efficiency of a catalyst, the value we measure is higher than other values reported to date. Mechanistic data extracted from a range of electrochemical studies suggest that an Fe^{III}–NH_2 species is generated at the first E_1 process (0.4 V vs Fc/Fc^+) via net H-atom removal from intermediate $[(TPA)Fe(NH_3)_2]^{2+}$.

The first wave, E_1 at ~0.4 V vs Fc/Fc^+, has been determined to correspond to a subsequent electron and proton transfer (EC) from a newly characterized $[(TPA)Fe(NH_3)_2]^{2+}$ species to generate a reactive terminal amide $[(TPA)Fe^{III}(NH_2)(NH_3)]^{2+}$ intermediate. This intermediate then undergoes a subsequent EC step at E_2 around 1.1 V, and this is the feature associated with catalytic AO. We speculate that at this potential Fe(III) is oxidized to Fe(IV), possibly via an $[(TPA)Fe^{IV}(NH_3)(NH_2)]^{3+}$ intermediate. Future studies will focus on the direct spectroscopic detection of these (or other) candidate intermediates. Regardless, we intuit that N–N bond forming steps occur subsequent to the generation of $[(TPA)Fe^{IV}(NH_3)(NH_2)]^{3+}$ or some similar species. We cannot yet determine from the available data whether or not such steps are intramolecular (e.g., via N–N coupling from adjacent Fe–NH_x ligands) or intermolecular (e.g., via nucleophilic attack of NH_3 on Fe–NH_x). We are, however, able to say from FOWA that the overall catalytic reaction is first order in both $[(TPA)Fe(L)_2]^{2+}$ and NH_3.

The catalysis is ultimately arrested due to passivation of the BDD working electrode surface, likely via a combination of incorporation of nitrogen and iron, which can be detected via analysis of the electrode post CPC. It may be that exploring less labile polydentate ligands, such as those possessing a negative charge, will attenuate the lability of TPA that is operative in this system and ultimately leads to catalyst degradation. Such approaches may also afford a catalyst that operates at less oxidizing potentials, though this may in turn attenuate the overall catalytic rate.

3.4 References

[1] (a) Service, R. F. Ammonia—A Renewable Fuel Made from Sun, Air, and Water—Could Power the Globe without Carbon. *Science* **2018**, aau8489 DOI:10.1126/science.aau7489. (b) Wan, Y.; Xu, J.; Lv, R. Heterogeneous Electrocatalysts Design for Nitrogen Reduction Reaction Under Ambient Conditions. *Mater. Today* **2019**, *27*, 69–90. (c) Martin, A. J.; Shinagawa, T.; Perez–Ramirez, J. Electrocatalytic Reduction of Nitrogen: From Haber-Bosch to Ammonia Artificial Leaf. *Chem* **2019**, *5*, 263–283. (d) Cui, X.; Tang, C.; Zhang, Q. A Review of Electrocatalytic Reduction of Dinitrogen to Ammonia Under Ambient Conditions. *Adv. Energy Mater.* **2018**, *8*, 1800369. (e) Valera-Medina, A.; Xiao, H.; Owen-Jones, M.; David, W. I. F.; Bowen, P. J. Ammonia for Power. *Prog. Energy Combust. Sci.* **2018**, *69*, 63–102. (f) Adli, N. M.; Zhang, H.; Mukherjee, S.; Wu, G. Ammonia Oxidation Electrocatalysis for Hydrogen Generation and Fuel Cells. *J. Electrochem. Soc.* **2018**, *165*, J3130–J3147.

[2] (a) Cairns, E. J.; Simons, E. L.; Tevebaugh, A. D. Ammonia–Oxygen Fuel Cell. *Nature* **1968**, *217*, 780–781. (b) Lan, R.; Tao, S. Ammonia as a Suitable Fuel for Fuel Cells. *Front. in Energy Res.* **2014**, *2*, 00035. (c) Zhong, C.; Hu, W. B.; Cheng, Y. F. Recent Advances in Electrocatalysts for Electro-Oxidation of Ammonia. *J. Mater. Chem. A*, **2013**, *1*, 3216–3238. (d) Gang, L.; van Grondelle, J.; Anderson, B. G.; van Santen, R. A. Selective Low Temperature NH_3 Oxidation to N_2 on Copper-Based Catalysts. *J. Catal.* **1999**, *186*, 100–109. (e) Cui, X.; Chen, L.; Wang, Y.; Chen, H.; Zhao, W.; Li, Y.; Shi, J. Fabrication of Hierarchically Porous RuO_2–CuOAl–ZrO_2 Composite as Highly Efficient Catalyst for Ammonia-Selective Catalytic Oxidation. *ACS Catal.* **2014**, *4*, 2195–2206. (f) Song, S.; Jiang, S. Selective Catalytic Oxidation of Ammonia to Nitrogen over CuO/CNTs: The Promoting Effect of the Defects of CNTs on the Catalytic Activity and Selectivity. *Appl. Catal. B* **2012**, *117–118*, 346–350. (g) Katsounaros, I.; Chen, T.; Gewirth, A. A.; Markovic, N. M.; Koper, M. T. M. Evidence for Decoupled Electron and Proton Transfer in the Electrochemical Oxidation of Ammonia on Pt(100). *J. Phys. Chem. Lett.* **2016**, *7*, 387–392.

[3] (a) Staffell, I.; Scamman, D.; Abad, A. V.; Balcombe, P.; Dodds, P. E.; Ekins, P.; Shah, N.; Ward, K. R. The Role of Hydrogen and Fuel Cells in the Global Energy System. *Energy Environ. Sci.* **2019**, *12*, 463–491. (b) Joghee, P.; Malik, J.; Pylypenko, S.; O'Hayre, R. A Review on Direct Methanol Fuel Cells – In the Perspective of Energy and Sustainability. *MRS Energy & Sustainability*, **2015**, *2*, E3.

[4] (a) Stucke, N.; Flöser, B. M.; Wyrich, T.; Tuczek, F. Nitrogen Fixation Catalyzed by Transition Metal Complexes: Recent Developments. *Eur. J. Inorg. Chem*. **2018**, 1337–1355. (b) Nishibayashi, Y. Development of Catalytic Nitrogen Fixation Using Transition Metal–Dinitrogen Complexes Under Mild Reaction Conditions. *Dalton Trans.* **2018**, *47*, 11290–11297.

[5] (a) Yandulov, D. V.; Schrock, R. R. Catalytic Reduction of Dinitrogen to Ammonia at a Single Molybdenum Center. *Science*, **2003**, *301*, 76–78. (b) Anderson, J. S.; Rittle, J.; Peters, J. C. Catalytic Conversion of Nitrogen to Ammonia by an Iron Model Complex. *Nature*, **2013**, *501*, 84–87. (c) Arashiba, K.; Miyake, Y.; Nishibayashi, Y. A Molybdenum Complex Bearing PNP-type Pincer Ligands Leads to the Catalytic Reduction of Dinitrogen into Ammonia. *Nat. Chem.* **2011**, *3*, 120–125. (d) Chalkley, M. J.; Castillo, T. J. Del; Matson, B. D.; Peters, J. C. Fe-Mediated Nitrogen Fixation with a Metallocene Mediator: Exploring pK_a Effects and Demonstrating Electrocatalysis. *J. Am. Chem. Soc.* **2018**, *140*, 6122–6129. (e) Ashida, Y.; Arashiba, K.; Nakajima, K.; Nishibayashi, Y. Molybdenum-catalyzed Ammonia Production with Samarium Diiodide and Alcohols or Water. *Nature* **2019**, *568*, 536–540.

[6] Minteer, S. D.; Christopher, P.; Linic, S. Recent Developments in Nitrogen Reduction Catalysts: A Virtual Issue. *ACS Energy Lett.* **2019**, *4*, 1163–166.

[7] (a) Lancaster, K. M.; Caranto, J. D.; Majer, S. H.; Smith, M. A. Alternative Bioenergy: Updates to and Challenges in Nitrification Metalloenzymology. *Joule*, **2018**, *3*, 421–441. (b) Kartal, B.; Keltjens, J. T. Anammox Biochemistry: a Tale of Heme c Proteins. *Trends Biochem. Sci.* **2016**, 41, 998–1011.

[8] Warren, J. J.; Tronic, T. A.; Mayer, J. M. Thermochemistry of Proton-Coupled Electron Transfer Reagents and its Implications. *Chem. Rev.* **2010**, *110*, 6961–7001.

[9] Buhr, J. D.; Taube, H. Oxidation of $[Os(NH_3)_5CO]^{2+}$ to $[(Os(NH_3)_4CO)_2N_2]^{4+}$. *Inorg. Chem.* **1979**, *18*, 2208–2212.

[10] Thompson, M. S.; Meyer, T. J. Oxidation of Coordinated Ammonia to Nitrate. *J. Am. Chem. Soc.* **1981**, *103*, 5577–5579.

[11] (a) Ishitani, O.; White, P. S.; Meyer, T.J. Formation of Dinitrogen by Oxidation of $[(bpy)_2(NH_3)RuORu(NH_3)(bpy)_2]^{4+}$. *Inorg. Chem.* **1996**, *35*, 2167–2168. (b) Ishitani, O.; Ando, E.; Meyer, T. J. Dinitrogen Formation by Oxidative Intramolecular N—N Coupling in cis,cis-$[(bpy)_2(NH_3)RuORu(NH_3)(bpy)_2]^{4+}$. *Inorg. Chem.* **2003**, *42*, 1707–1710.

[12] Collman, J. P.; Hutchison, J. E.; Ennis, M. S.; Lopez, M. A.; Guilard, R. Reduced Nitrogen Hydride Complexes of a Cofacial Metallodiporphyrin and Their Oxidative Interconversion. An Analysis of Ammonia Oxidation and Prospects for a Dinitrogen Electroreduction Catalyst Based on Cofacial Metallodiporphyrins. *J. Am. Chem. Soc.* **1992,** *114*, 8074–8080.

[13] Habibzadeh, F.; Miller, S. L.; Hamann, T. W.; Smith, M. R. Homogeneous Electrocatalytic Oxidation of Ammonia to N_2 Under Mild Conditions. *Proc. Natl. Acad. Sci. U.S.A.* **2019**, *116*, 2849–2853.

[14] (a) Man, W.; Tang, T.; Wong, T.; Lau, T.; Peng, S.; Wong, W. Highly Electrophilic (Salen)ruthenium(VI) Nitrido Complexes. *J. Am. Chem. Soc.* **2004**, *126*, 478–479. (b) Scheibel, M. G.; Wu, Y.; Stückl, A. C.; Krause, L.; Carl, E.; Stalke, D.; de Bruin, B.; Schneider, S. Synthesis and Reactivity of a Transient, Terminal Nitrido Complex of Rhodium. *J. Am. Chem. Soc.* **2013,** *135*, 17719–17722. (c) Scheibel, M. G.; Abbenseth, J.; Kinauer, M.; Heinemann, F. W.; Würtele, C.; de Bruin, B.; Schneider, S. Homolytic N−H Activation of Ammonia: Hydrogen Transfer of Parent Iridium Ammine, Amide, Imide, and Nitride Species. *Inorg. Chem.* **2015**, *54*, 9290–9302. (d) Abbenseth, J.; Finger, M.; Würtele, C.; Kasanmascheff, M.; Schneider, S. Coupling of Terminal Iridium Nitrido Complexes. *Inorg. Chem. Front.* **2016**, *3*, 469–477. (e) Clarke, R. M.; Storr, T. Tuning Electronic Structure To Control Manganese Nitride Activation. *J. Am. Chem. Soc.* **2016**, *138*, 15299–15302. (f) Bezdek, M. J.; Guo, S.; Chirik, P. J. Coordination-Induced Weakening of Ammonia, Water, and Hydrazine X–H Bonds in a Molybdenum Complex. *Science*, **2016**, *354*, 730–733. (g) Bhattacharya, P.; Heiden, Z. M.; Wiedner, E. S.; Raugei, S.; Piro, N. A.; Kassel, W. S.; Bullock, R. M.; Mock, M. T. Ammonia Oxidation by Abstraction of Three Hydrogen Atoms from a Mo−NH_3 Complex. *J. Am. Chem. Soc.* **2017**, *139*, 2916–2919. (h) Keener, M.; Peterson, M.; Hernández Sánchez, R.; Oswald, V. F.; Wu, G.; Ménard, G. Towards Catalytic Ammonia Oxidation to Dinitrogen: A Synthetic Cycle by Using a Simple Manganese Complex. *Chem. Eur. J.* **2017**, *23*, 11479–11484.

[15] Bhattacharya, P.; Heiden, Z. M.; Chambers, G. M.; Johnson, S. I.; Bullock, R. M.; Mock, M. T. Catalytic Ammonia Oxidation to Dinitrogen by Hydrogen Atom Abstraction. *Angew. Chem. Int. Ed.* **2019**, *58*, 11618–11624.

[16] Nakajima, K.; Toda, H.; Sakata, K.; Nishibayashi, Y. Ruthenium-Catalysed Oxidative Conversion of Ammonia into Dinitrogen. *Nat. Chem.* **2019**, *11*, 702–709.

[17] For select examples see: (a) Fillol, J. L.; Codolà, Z.; Garcia-Bosch, I.; Gómez, L.; Pla, J. J.; Costas, M. Efficient Water Oxidation Catalysts Based on Readily Available Iron Coordination Complexes. *Nat. Chem.* **2011**, *3*, 807–813. (b) Zhang, B.; Li, F.;Yu, F.; Cui, H.; Zhou, X.; Li, H.; Wang, Y.; Sun, L. Homogeneous Oxidation of Water by Iron

Complexes with Macrocyclic Ligands. *Chem. Asian J.* **2014**, *9*, 1515–1518. (c) To, W.-P.; Chow, T. W.-S.; Tse, C.-W.; Guan, X.; Huang, J.-S.; Che, C.-M. Water Oxidation Catalysed by Iron Complex of N,N′-dimethyl-2,11-diaza[3,3](2,6)pyridinophane. Spectroscopy of Iron–Oxo Intermediates and Density Functional Theory Calculations. *Chem. Sci.* **2015**, *6*, 5891–5903. (d) Das, B.; Orthaber, A.; Ott, S.; Thapper, A. Iron Pentapyridyl Complexes as Molecular Water Oxidation Catalysts: Strong Influence of a Chloride Ligand and pH in Altering the Mechanism. *ChemSusChem* **2016**, *9*, 1178–1186. (e) Coggins, M. K.; Zhang, M.-T.; Vannucci, A. K.; Dares, C. J.; Meyer, T. J. Electrocatalytic Water Oxidation by a Monomeric Amidate-Ligated Fe(III)-Aqua Complex. *J. Am. Chem. Soc.* **2014**, *136*, 5531–5534. (f) Wickramasinghe, L. D.; Zhou, R.; Zong, R.; Vo, P.; Gagnon, K.J.; Thummel, R. P. Iron Complexes of Square Planar Tetradentate Polypyridyl-Type Ligands as Catalysts for Water Oxidation. *J. Am. Chem. Soc.* **2015**, *137*, 13260−13263.

[18] Diebold, A.; Hagen, K. S. Iron(II) Polyamine Chemistry: Variation of Spin State and Coordination Number in Solid State and Solution with Iron(II) Tris(2-pyridylmethyl)amine Complexes. *Inorg. Chem.* **1998**, *37*, 215–223.

[19] Charge passed and Faradaic efficiencies are averaged over six experiments. Turn over numbers are averaged over two experiments with 2.5 mmol $[(TPA)Fe(MeCN)_2]OTf_2$, the optimum condition studied. Reported values for N_2 are all corrected for background nitrogen, determined by integrating the oxygen peak in the gas chromatograms. For N_2 produced by 2.5 mmol $[(TPA)Fe(L)_2]^{2+}$, 1.0 equivalent of background N_2 produced by the electrode has been subtracted.

[20] Lee, K. J.; McCarthy, B. D.; Dempsey, J. L. On Decomposition, Degradation, and Voltammetric Deviation: The Electrochemist's Field Guide to Identifying Precatalyst Transformation. *Chem. Soc. Rev.* **2019**, *48*, 2927–2945.

[21] Folkman, S. J.; Soriano-Lopez, J.; Galán-Mascarós, J.; Finke, R. J. Electrochemically Driven Water-Oxidation Catalysis Beginning with Six Exemplary Cobalt Polyoxometalates: Is It Molecular, Homogeneous Catalysis or Electrode-Bound, Heterogeneous CoO_x Catalysis? *J. Am. Chem. Soc.;* **2018,** *140*, 12040–12055.

[22] Solid-State structures simultaneously featuring metal centers in different spin states are uncommon but not unprecedented. See, for example: (a) Sheu, C.; Pillet, S.; Lin, Y.; Chen, S.; Hsu, I.; Lecomte, C.; Wang, Y. Magnetostructural Relationship in the Spin-Crossover Complex t-$\{Fe(abpt)_2[N(CN)_2]_2\}$: Polymorphism and Disorder Phenomenon. *Inorg. Chem.* **2008**, *47*, 10866–10874. (b) Sheu, C.; Chen, S.; Wang, S.; Lee, G.; Liu, Y.; Wang, Y. The Commensurate Modulated Structure of the Metastable State in Spin Crossover Complex $[Fe(abpt)_2(NCS)_2]$. *Chem. Commun.* **2009**, 7512–7514.

[23] The bis-ammine has a redox potential 300 mV lower than the bis-acetonitrile complex, therefore replacement of each MeCN by NH_3 can be estimated to shift the potential by 150 mV assuming a linear relationship.

[24] Funahashi, S.; Jordan, R. B. Solvent-Exchange Kinetics in Iron(II) Solutions of N,N-Dimethylformamide and Dimethyl Sulfoxide Studied by Nuclear Magnetic Resonance Line Broadening. *Inorg. Chem.* **1977**, *16*, 1301–1306.

[25] Costentin, C.; Savéant, J. M. *Elements of Molecular and Biomolecular Electrochemistry: An Electrochemical Approach to Electron Transfer Chemistry*, 2nd ed.; John Wiley & Sons, Hoboken, NJ, 2006.

[26] Savéant, J-M.; Vianello, E. Potential-Sweep Voltammetry: General Theory of Chemical Polarization. *Electrochim. Acta,* **1967**, *12*, 629–646.

[27] Fox, D. J.; Bergman, R. G. Synthesis of a First-Row Transition Metal Parent Amido Complex and Carbon Monoxide Insertion into the Amide N-H Bond. *J. Am. Chem. Soc.* **2003,** *125*, 8984–8985.

[28] Bard, A. J.; Faulkner, L. R. *Electrochemical Methods: Fundamentals and Applications*, 2nd ed.; John Wiley & Sons, Hoboken, NJ, 2001.

[29] Costentin, C.; Savéant, J.-M. Multielectron, Multistep Molecular Catalysis of Electrochemical Reactions: Benchmarking of Homogeneous Catalysts. *ChemElectroChem*, **2014,** *1*, 1226–1236.

[30] Andrieux, C. P.; Blocman, C.; Dumas-Bouchiat, J. M.; M'Halla, F.; Savéant, J. M. Homogeneous Redox Catalysis of Electrochemical Reactions: Part V. Cyclic Voltammetry. *J. Electroanal. Chem.* **1980**, *113*, 19–40

[31] Costentin, C.; Drouet, S.; Robert, M.; Savéant, J.-M. Turnover Numbers, Turnover Frequencies, and Overpotential in Molecular Catalysis of Electrochemical Reactions. Cyclic Voltammetry and Preparative-Scale Electrolysis. *J. Am. Chem. Soc.* **2012**, *134*, 11235–11242.

[32] Matheu, R.; Neudeck, S.; Meyer, F.; Sala, X.; Lllobet, A. Foot of the Wave Analysis for Mechanistic Elucidation and Benchmarking Applications in Molecular Water Oxidation Catalysis. *ChemSusChem*. **2016**, *9*, 3361–3369.

[33] Wang, V. C.-C.; Johnson, B. A. Interpreting the Electrocatalytic Voltammetry of Homogeneous Catalysts by the Foot of the Wave Analysis and Its Wider Implications. *ACS Catal.* **2019**, *9*, 7109–7123.

[34] Costentin, C.; Drouet, S.; Robert, M.; Savéant, J.-M. A Local Proton Source Enhances CO_2 Electroreduction to CO by a Molecular Fe Catalyst. *Science*, **2012**, *338*, 90–94.

[35] Baur, J. E.; Diffusion Coefficients. In *Handbook of Electrochemistry*. Zoski, C. G.; Elsevier, 2007, 829–848.

C h a p t e r 4

Enhanced Ammonia Oxidation Catalysis by a Low-Spin Iron Complex Featuring *Cis* Coordination Sites

Adapted from:
Zott, M. D.; Peters, J. C.
J. Am. Chem. Soc. **2021**, *143*, 7612–7616.
DOI: 10.1021/jacs.1c02232

.

4.1 Introduction

Ammonia is produced at industrial scale for use in fertilizer and chemical synthesis,[1,2] but could become a promising carbon-free fuel if its selective and efficient catalytic oxidation to nitrogen can be achieved. Catalysts sufficiently active and stable for fuel cell applications are still needed.[2,3,4] Platinum-based materials, perhaps the current best current candidates,[5,6,7] suffer from low current densities due to side reactions that can result at moderate applied bias.

Molecular systems offer several advantages with respect to fundamental studies that address both activity and selectivity in AO.[8] The first molecular AO catalysts were reported in 2019.[9,10,11,12,13] Thus far, ruthenium catalysts have shown the highest turnover number[14] (TON; ~120 for $[(TMP)Ru(NH_3)_2]^{2+}$ using phenoxyl HAA reagents),[13] and the lowest demonstrated onset potential for electrocatalysis (E_{onset} = 0.04 V vs Fc/Fc^+ for $[(bpydma)(tpy)Ru(NH_3)]^{2+}$; TON = 2).[9] We reported a distinct example of a first-row metal electrocatalyst, $[(TPA)Fe(NH_3)_2]OTf_2$, with a TON of 16 and a comparatively very fast rate (10^7 $M^{-1}\cdot s^{-1}$), but requiring a substantial E_{onset} bias of 0.7 V (all potentials are reported vs Fc/Fc^+).[12]

To improve on the AO activity of $[(TPA)Fe(NH_3)_2]OTf_2$, we targeted an iron system that would display enhanced catalyst stability while showing higher activity at a lower applied bias. Catalyst degradation with $[(TPA)Fe(NH_3)_2]OTf_2$ appears to initiate from substitution of the TPA ligand, an equilibrium process under the catalytic conditions that is likely favored by the presence of a large excess of NH_3. The extent of TPA displacement

from [(TPA)Fe(NH$_3$)$_2$]OTf$_2$ is likely increased by the complex's dominant high-spin population (S = 2) at RT, which results in more labile M–L bonds.

For the present system, given that the initial iron species in bulk solution during catalysis is [(TPA)Fe(NH$_3$)$_2$]OTf$_2$, we explored whether modifying the auxiliary ligand (L$_{aux}$) in such a fashion so as to support a low-spin (L$_{aux}$)Fe(II)–NH$_3$ adduct might limit substitution by NH$_3$ and hence enhance overall stability, while maintaining high catalyst activity. We decided to replace the weak-field tertiary amine donor of TPA, along with one of its pyridyl arms, with a bipyridine ligand (Scheme 4.1); bipyridine has similar σ-donating properties to pyridine but enhanced π-accepting properties.[15,16,17] We also sought to maintain the *cis*-labile sites present in [(TPA)Fe(NH$_3$)$_2$]OTf$_2$,[18,19,20,21] which may facilitate intramolecular N–N bond formation. A rigid ligand containing each of these characteristics, bpyPy$_2$Me (Scheme 4.1), has been reported,[22] as has its iron(II) complex, [(bpyPy$_2$Me)Fe(MeCN)$_2$]OTf$_2$. The latter has been studied in the context of alkane oxidation.[21]

Scheme 4.1. Targeting enhanced Fe-mediated AO via an alternative auxiliary ligand strategy.

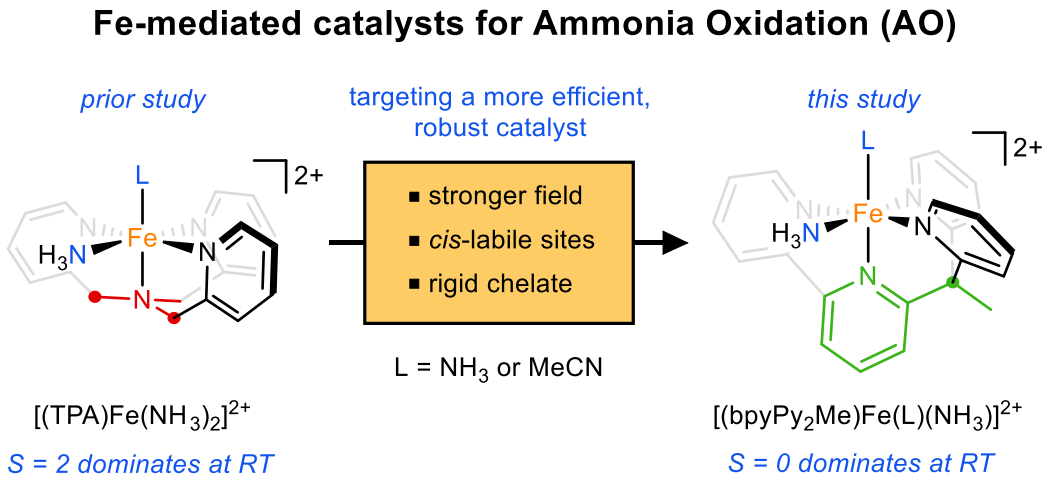

4.2 Results and Discussion

We first compared the electronic structure of both [(TPA)Fe(MeCN)$_2$]OTf$_2$ and [(bpyPy$_2$Me)Fe(MeCN)$_2$]OTf$_2$ in the presence of NH_3 in solution by the Evans method, using trimethoxybenzene as an inert reference signal. At room temperature in the absence of NH_3, both systems display NMR spectra with resonances in the typical diamagnetic window, and bulk magnetic moments of 0.7–0.8μ_B (see SI), indicating a dominant low-spin population. In the presence of 75 equivalents NH_3 (~0.8 M at NMR concentrations), however, the solution prepared with [(TPA)Fe(MeCN)$_2$]OTf$_2$ gives rise to a spin-only magnetic moment of 5.2μ_B, indicative of a fully populated S = 2 state. By contrast, under identical conditions, a solution prepared with [(bpyPy$_2$Me)Fe(MeCN)$_2$]OTf$_2$ produces a bulk magnetic moment of 1.2μ_B. Assuming a mixture of S = 0 and S = 2 species at spin-only values, this moment corresponds to a 94:6 mixture in favor of the low-spin derivative in the presence of NH_3.

To assess the stability of [(bpyPy$_2$Me)Fe(MeCN)$_2$]OTf$_2$ to substitution by NH_3 in MeCN, we monitored its speciation by UV-vis spectroscopy while titrating in NH_3. A monotonic decrease in the absorbance for [(bpyPy$_2$Me)Fe(L)$_2$]OTf$_2$ (L = MeCN, NH_3), as well as a loss of isosbestic behavior, becomes discernable in the presence of > 600 equivalents NH_3 (see SI). By contrast, [(TPA)Fe(MeCN)$_2$]OTf$_2$ begins showing demetallation with > 200 equivalents NH_3.[12]

We next assessed catalytic AO by [(bpyPy$_2$Me)Fe(MeCN)$_2$]OTf$_2$ via cyclic voltammetry (CV) and controlled potential coulometry (CPC) using boron-doped diamond (BDD) working electrodes. CV of [(bpyPy$_2$Me)Fe(MeCN)$_2$]OTf$_2$ with added NH_3 as

substrate shows a precatalytic one-electron feature E_1 at 0.24 V and an irreversible multi-electron E_2 wave at 0.79 V (Figure 4.1; see SI for DPV data), which replace the reversible one-electron wave observed in the absence of NH_3 ($E_{1/2}$ = 0.82 V); this behavior mirrors that of $[(TPA)Fe(NH_3)_2]OTf_2$.[12] The catalytic onset potential of 0.45 V for $[(bpyPy_2Me)Fe(MeCN)_2]OTf_2$ is ~250 mV cathodic of that for $[(TPA)Fe(MeCN)_2]OTf_2$, and the catalytic current is ~fourfold higher. By contrast, applying less potential bias most typically results in a concomitant decrease in catalytic current.[23,24]

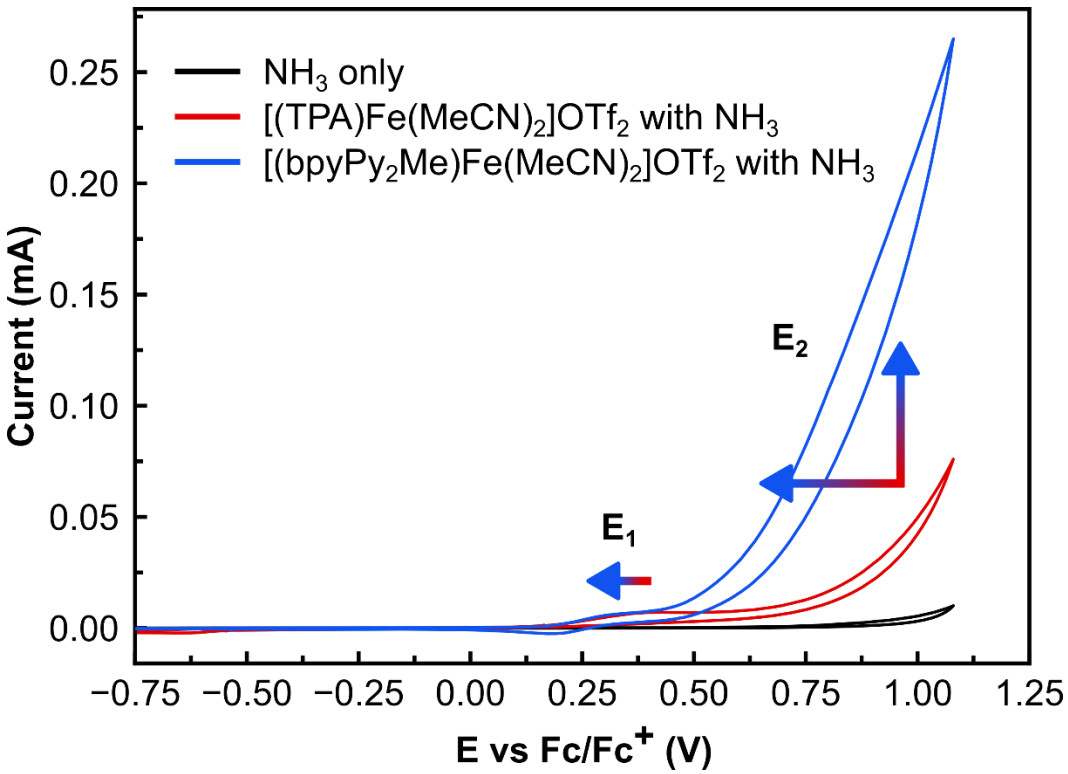

Figure 4.1. CV of MeCN solutions containing 0.2 M NH_3 (400 equivalents), 0.05 M NH_4OTf, and 0.5 mM $[(TPA)Fe(MeCN)_2]OTf_2$ or $[(bpyPy_2Me)Fe(MeCN)_2]OTf_2$ with BDD working, Pt counter, and 5 mM Ag/AgOTf reference electrodes.

CPC confirms that $[(bpyPy_2Me)Fe(MeCN)_2]OTf_2$ is a highly active AO catalyst. With a 0.05 mM $[(bpyPy_2Me)Fe(MeCN)_2]OTf_2$ solution containing 400 equivalents NH_3 in MeCN with NH_4OTf supporting electrolyte (0.05 M), holding the bias at 0.85 V produces

N_2 with a high faradaic efficiency (FE) of 87%. After 24 h, a TON of 93 (average of 4 runs; STD = 8) was measured. Furthermore, active catalyst remains after 24 h; a reload experiment was performed in which the BDD electrode was cleaned and the NH_3 concentration was reset to its original value; after an additional 24 h, another 56 equivalents N_2 were detected (average of 2 runs), resulting in a net TON of 149. With respect to TON, this value is a marked improvement on both the previously reported Ru AO electrocatalyst (TON of 2) and $[(TPA)Fe(MeCN)_2]OTf_2$ (TON of 16).[9,12] CPC with $^{15}NH_3$ (^{15}N = 99%) produces >90% $^{30}N_2$ by GC-MS, indicating NH_3 as the source of nitrogen in the liberated N_2. Post-catalysis, a thoroughly rinsed electrode showed no catalytic activity, under the same conditions but without added $[(bpyPy_2Me)Fe(MeCN)_2]OTf_2$.[25]

To probe mechanistic issues for the $[(bpyPy_2Me)Fe(MeCN)_2]OTf_2$ system, we further investigated the E_1 process. By CV, as the concentration of NH_3 is increased, the E_1 potential shifts cathodically. This is characteristic of an EC mechanism (single electron transfer followed by a chemical step).[26,27] For an EC mechanism in the observed kinetic regime (KE), the peak potential of such a process obeys Eq. 1 (Scheme 4.2). Two plausible stoichiometries are provided, involving either one or two molecules of NH_3 in the forward reaction (Scheme 4.2a and 4.2b, respectively). Plotting E_1 versus either $[NH_3]$ or $[NH_4^+]$ (Scheme 4.2c and 4.2d, respectively), the respective slopes support stoichiometries of two NH_3 in the forward reaction and one NH_4^+ in the backward reaction, matching Scheme 4.2b. Taking the iron species to be $[(bpyPy_2Me)Fe(MeCN)(NH_3)]OTf_2$, we thus propose that the product of this EC reaction is $[(bpyPy_2Me)Fe(NH_2)(NH_3)]OTf_2$, formed via substitution and net hydrogen atom abstraction. This behavior parallels $[(TPA)Fe(NH_3)_2]OTf_2$, which follows Scheme 4.2a at a nearly identical potential.[12]

Scheme 4.2. Evidence supporting an EC mechanism at the E_1 potential. Possible stoichiometries of the E_1 potential are shown in (a) and (b). Plots of E_1 potential versus the natural logarithm of (c) NH_3 or (d) NH_4^+ concentration for $[(bpyPy_2Me)Fe(MeCN)_2]OTf_2$.

$$E_{ox} = E^\circ_{ox} - \frac{RT}{nF} \ln \frac{k_{1f}[NH_3]^m}{k_{1b}[NH_4^+]}$$

$$= E^\circ_{ox} - m \times 0.026 \ln(k_{1f}[NH_3]) + 0.026 \ln(k_{1b}[NH_4^+]) \quad \textbf{(1)}$$

$$Fe^{II}\text{–}NH_3 + NH_3 \underset{k_{1b}}{\overset{k_{1f}}{\rightleftharpoons}} Fe^{III}\text{–}NH_2 + NH_4^+ + e^- \quad \textbf{(a)}$$

$$\begin{matrix} MeCN \\ | \\ Fe^{II}\text{–}NH_3 \end{matrix} + 2\ NH_3 \underset{k_{1b}}{\overset{k_{1f}}{\rightleftharpoons}} \begin{matrix} NH_2 \\ | \\ Fe^{III}\text{–}NH_3 \end{matrix} + NH_4^+ + MeCN + e^- \quad \textbf{(b)}$$

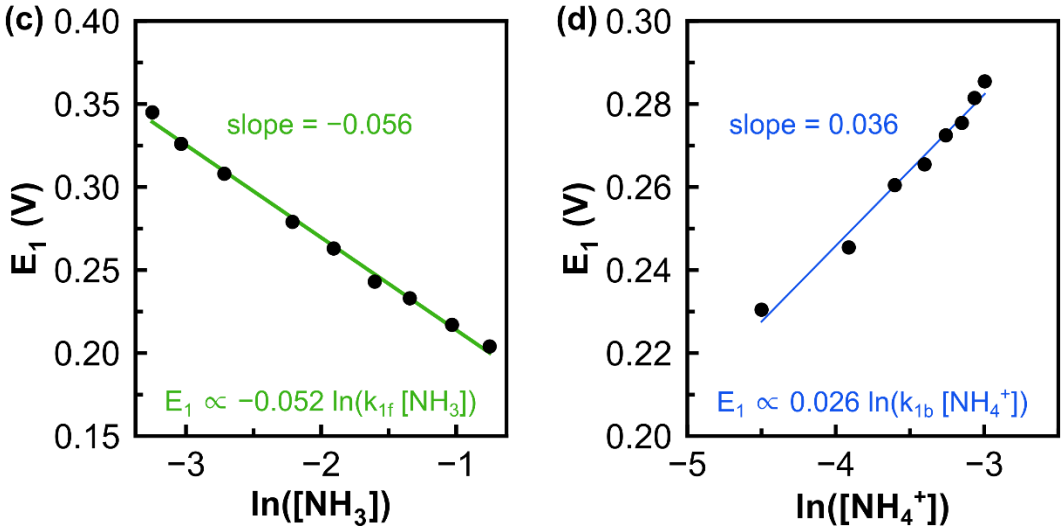

The iron speciation deduced from the above electrochemical data, favoring $[(bpyPy_2Me)Fe(MeCN)(NH_3)]OTf_2$ prior to E_1, is notionally consistent with a solid-state XRD study of a crystal grown from an ammoniacal MeCN solution (Figure 4.2). The short

Fe–N_{bpy} bond length *trans* to MeCN of 1.89 Å also underscores tight binding of the bpyPy_2Me ligand.

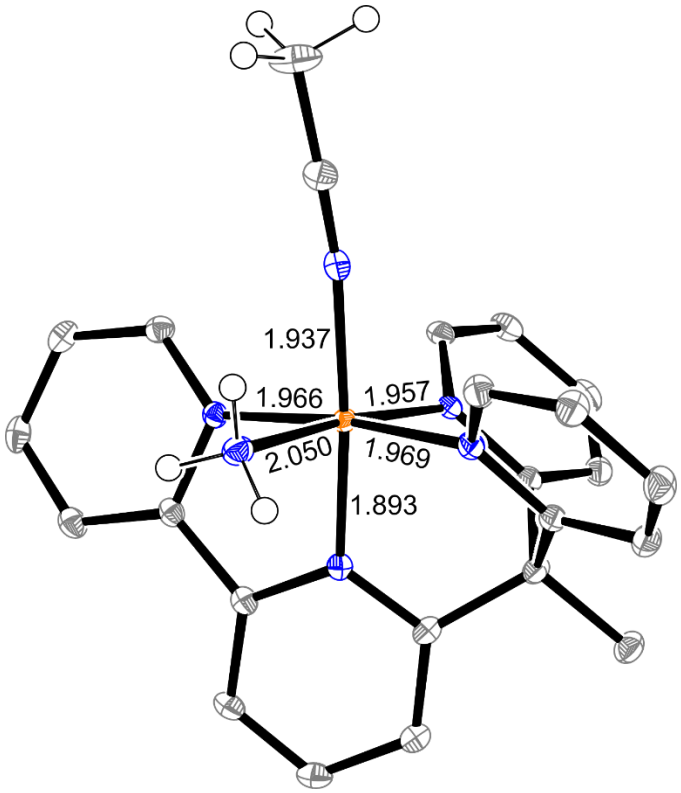

Figure 4.2. Solid-state crystal structure of [(bpyPy_2Me)Fe(MeCN)(NH_3)]OTf_2 at 100 K, with select bond lengths labeled in angstroms. Thermal ellipsoids are shown at 50% probability. Triflate counterions and L_{aux} hydrogen atoms are omitted for clarity.

To understand the character of the turnover-limiting E_2 step, we studied the rate dependence on [Fe] and [NH_3] concentrations. [(bpyPy_2Me)Fe(MeCN)(NH_3)]OTf_2 demonstrates first-order behavior for both [Fe] and [NH_3] (SI). The concentration ranges studied ([Fe] = 0.05–2 mM, [NH_3] = 0–0.5 M) span the conditions employed for both CV and CPC experiments. Using the foot-of-the-wave analysis with a standard EC_{cat} scheme to simplify the multi-electron, multi-proton wave, [28,29] the first-order dependence on iron was recapitulated; however, while a clear dependence on [NH_3] is evident from the FOWA,

ascertaining the quantitative dependence on [NH_3] is hindered by uncertainty in $E°_{cat}$ at high NH_3 concentrations. Still, we are able to compare the intrinsic AO reaction rates for $[(TPA)Fe(NH_3)_2]^{2+}$ and $[(bpyPy_2Me)Fe(MeCN)(NH_3)]^{2+}$. We previously reported a second-order rate constant (k'_{obs}) of $3.7 \times 10^7\ M^{-1} \cdot s^{-1}$ for $[(TPA)Fe(NH_3)_2]^{2+}$;[12] for the present catalyst $[(bpyPy_2Me)Fe(MeCN)(NH_3)]^{2+}$, the average k'_{obs} is $1.8 \times 10^9\ M^{-1} \cdot s^{-1}$. Thus, $[(bpyPy_2Me)Fe(MeCN)(NH_3)]^{2+}$ is ca. 1.5 orders of magnitude faster than $[(TPA)Fe(NH_3)_2]^{2+}$.

The aforementioned electrochemical data are limited in mechanistic utility with respect to the various steps that follow E_2, governing the pathway for N–N bond formation. Literature precedent for N–N formation in systems applied to AO, whether mono- or bimolecular in nature with respect to the metal complex, suggests two broad scenarios for consideration: (1) interaction of two nitrogen ligands (I2N), as via nitride,[8,11,30,31,32] imide, or amide[33,34] coupling, or (2) ammonia nucleophilic attack (ANA) on an electrophilic nitrido or imido ligand.[9,10] To begin to explore these issues for the present iron system, we have undertaken a theoretical study (Schemes 4.3, 4.4), using density functional theory due to the size of the present system, and the TPSS functional owing to its minimal bias for Fe^{2+} versus Fe^{3+} states.[35,36]

As an initial point of calibration, our chosen method reliably predicts the low-spin ground state of $[(bpyPy_2Me)Fe(MeCN)(NH_3)]^{2+}$ and also its E_1 potential (0.24 V calcd; see SI), which is analogous to that experimentally observed at 0.2 M NH_3. The latter result is encouraging as it involves both a change in oxidation state and a chemical step (to produce $[(bpyPy_2Me)Fe(NH_2)(NH_3)]^{2+}$, in accordance with our electrochemical data).

Scheme 4.3. Possible E_2 steps and calculated E (V) values. DFT-predicted ground spin-state values are shown.

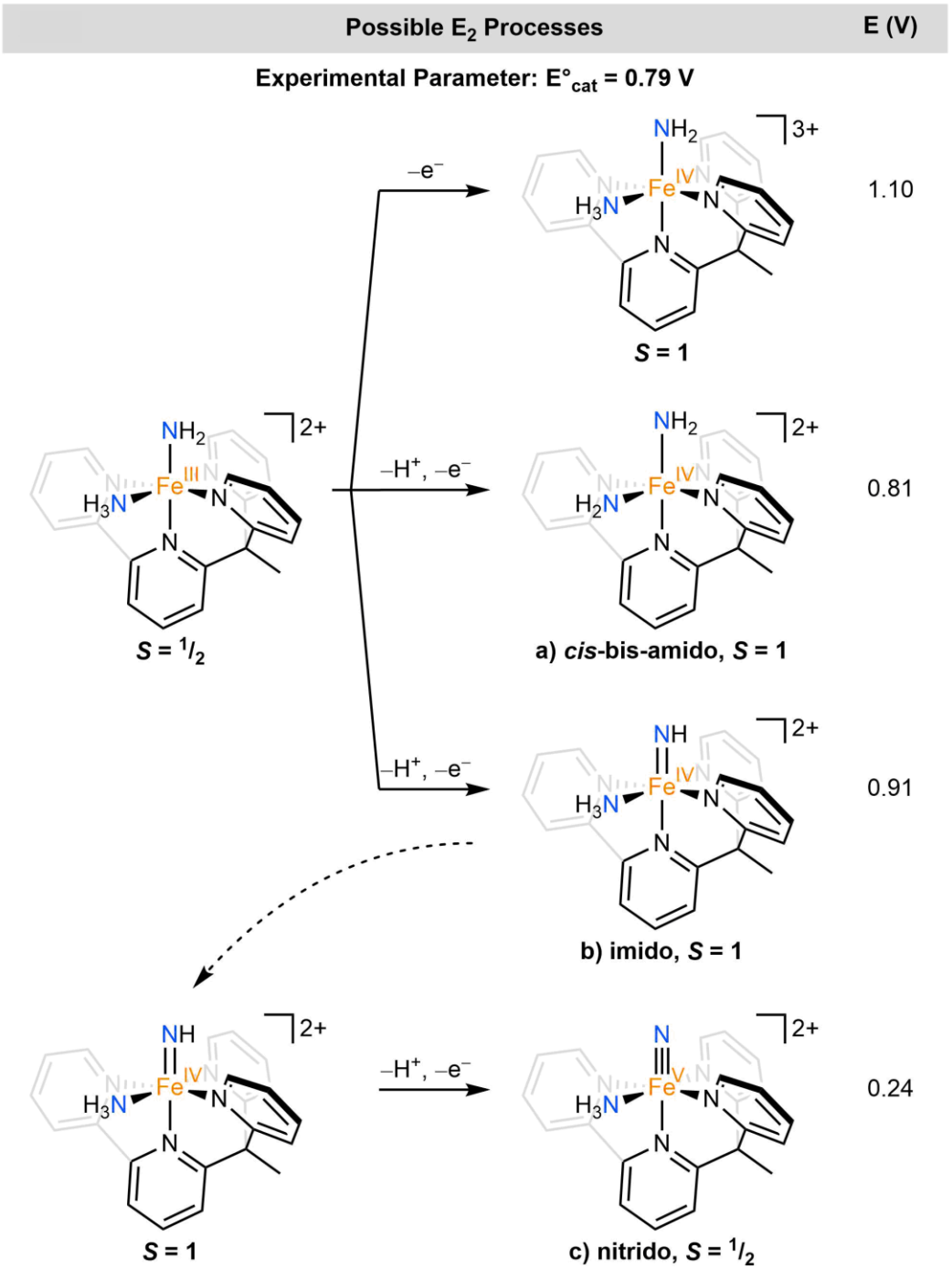

From the E_1 product, $[(bpyPy_2Me)Fe(NH_2)(NH_3)]^{2+}$, one can consider a subsequent 1-electron oxidation step that determines the E_2 potential (0.79 V by DPV). Calculations suggest oxidation to $[(bpyPy_2Me)Fe(NH_2)(NH_3)]^{3+}$ requires a potential of 1.10 V, well above 0.79 V. However, a proton-coupled oxidation step to instead generate a *cis*-bis-amido complex, $[(bpyPy_2Me)Fe(NH_2)(NH_2)]^{2+}$, occurs at 0.81 V (Scheme 4.3, (a)). Alternatively, a proton-coupled oxidation to generate the imido complex $[(bpyPy_2Me)Fe(NH)(NH_3)_2]^{2+}$ occurs at 0.91 V (Scheme 4.3, (b)), from which a subsequent proton-coupled oxidation to produce the nitride species $[(bpyPy_2Me)Fe(N)(NH_3)]^{2+}$ can occur at much lower potential (0.24 V, Scheme 4.3, (c)). On thermodynamic grounds, both scenarios remain plausible in working towards a mechanistic model.

We have also probed subsequent N–N bond formation steps. For example, we investigated both reductive elimination (I2N) from the *cis*-bis-amido and ANA from the imido/nitrido species; the first scenario highlights a *cis*-labile catalyst design, as in $[(bpyPy_2Me)Fe(MeCN)_2]OTf_2$. From $[(bpyPy_2Me)Fe(NH_2)(NH_2)]^{2+}$, N–N reductive elimination to form the η^2-hydrazine adduct $[(bpyPy_2Me)Fe(\eta^2\text{-}N_2H_4)]^{2+}$ (Scheme 4.4, (d)) is exergonic by 6.3 kcal/mol. Alternatively, ANA at either the imido or nitrido (Scheme 4.4, (e) and (f)) is exergonic by 16.0 or 28.7 kcal/mol, respectively, affording another plausible path towards N–N bond formation. Other pathways, such as those including bimolecular N–N coupling (e.g., from NH_2, NH, or N intermediates), may also be plausible (see SI for additional details).

Scheme 4.4. Possible N–N coupling reactions; ΔG (kcal/mol). DFT-predicted ground spin-state values are shown.

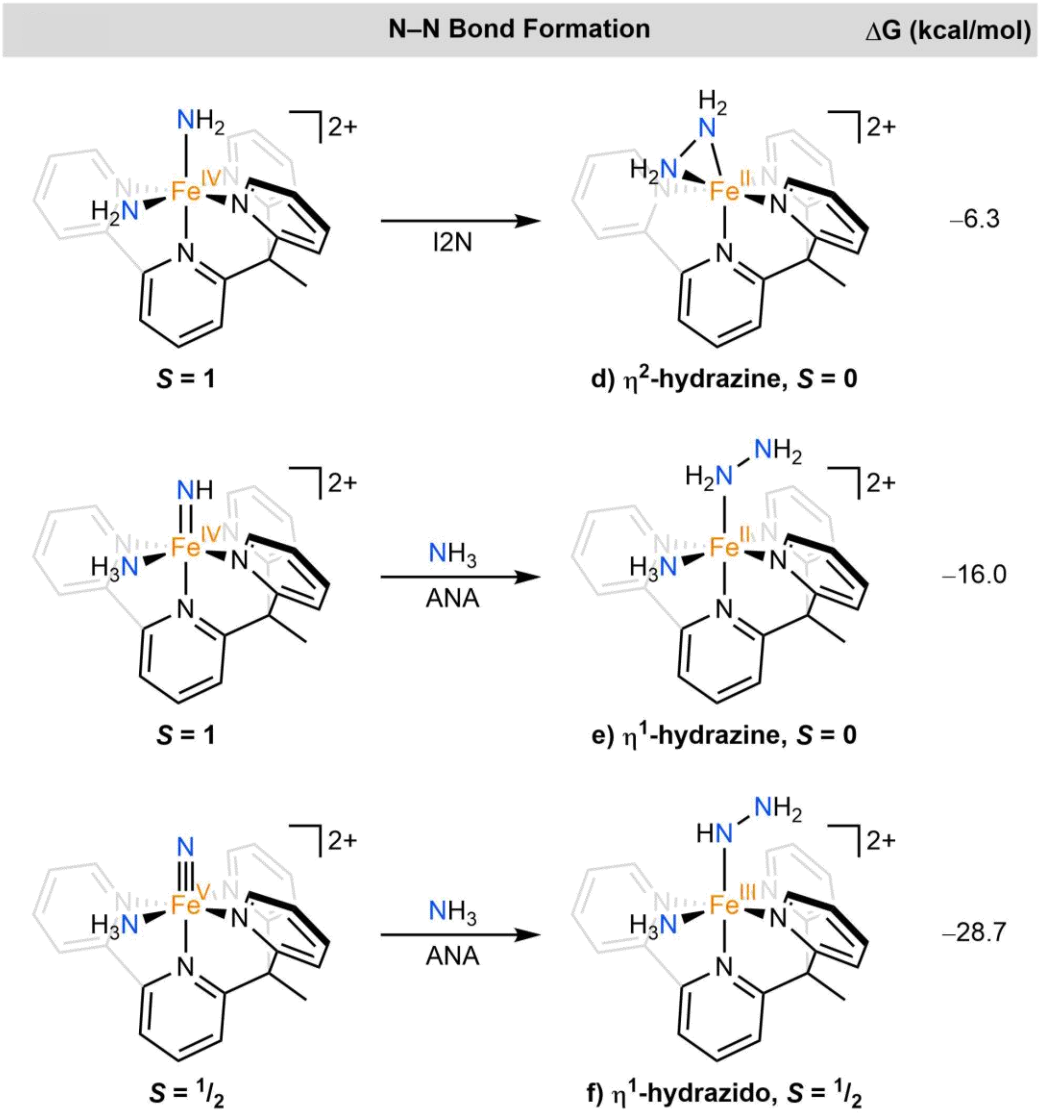

4.3 Conclusion

In conclusion, $[(bpyPy_2Me)Fe(MeCN)(NH_3)]OTf_2$ is an effective AO catalyst, yielding a net TON of 149 after 48 h, which is the highest TON value reported to date for a molecular catalyst. Compared to its related iron congener, $[(TPA)Fe(NH_3)_2]OTf_2$, $[(bpyPy_2Me)Fe(MeCN)(NH_3)]OTf_2$ is substantially more stable and operates at a higher rate

at significantly lower overpotential. While a number of mechanistic insights have been discussed, including a net H-atom abstraction at E_1 to furnish $[(bpyPy_2Me)Fe(NH_2)(NH_3)]^{2+}$ prior to the onset of catalysis at E_2, future efforts are needed to probe mechanistic aspects of the N–N bond-forming step(s), guided by the thermodynamic considerations from the experiments and theory discussed herein.

4.4 References

[1] Valera-Medina, A.; Xiao, H.; Owen-Jones, M.; David, W. I. F.; Bowen, P. J. Ammonia for Power. *Prog. Energ. Combust.* **2018,** *69*, 63–102.

[2] Zhao, Y.; Setzler, B. P.; Wang, J.; Nash, J.; Wang, T.; Xu, B.; Yan, Y. An Efficient Direct Ammonia Fuel Cell for Affordable Carbon-Neutral Transportation. *Joule* **2019,** *3*, 2472–2484.

[3] For a review on early work see: Nowak, E. J. Catalytic Oxidation of Ammonia on Platinum. *Chem. Eng. Sci*. **1966**, *21*, 19–27.

[4] Adli, N. M.; Zhang, H.; Mukherjee, S.; Wu, G. Review—Ammonia Oxidation Electrocatalysis for Hydrogen Generation and Fuel Cells. *J. Electrochem. Soc.* **2018**, *165*, J3130–J3147.

[5] de Vooys, A. C. A.; Koper, M. T. M.; van Santen, R. A.; van Veen, J. A. R. The Role of Adsorbates in the Electrochemical Oxidation of Ammonia on Noble and Transition Metal Electrodes. *J. Electroanal. Chem.* **2001**, *506*, 127–137.

[6] Li, Z.-F.; Wang, Y.; Botte, G. G. Revisiting the Electrochemical Oxidation of Ammonia on Carbon-Supported Metal Nanoparticle Catalysts. *Electrochim. Acta* **2017**, *228*, 351–360.

[7] Song, L.; Liang, Z.; Ma, Z.; Zhang, Y.; Chen, J.; Adzic, R. R.; Wang, J. X. Temperature-Dependent Kinetics and Reaction Mechanism of Ammonia Oxidation on Pt, Ir, and PtIr Alloy Catalysts. *J. Electrochem. Soc.* **2018**, *165*, J3095–J3100.

[8] Dunn, P. L.; Cook, B. J.; Johnson, S. I.; Appel, A. M.; Bullock, R. M. Oxidation of Ammonia with Molecular Complexes. *J. Am. Chem. Soc.* **2020**, *142*, 17845–17858

[9] Habibzadeh, F.; Miller, S. L.; Hamann, T. W.; Smith, M. R. Homogeneous Electrocatalytic Oxidation of Ammonia to N_2 Under Mild Conditions. *Proc. Natl. Acad. Sci. U.S.A.* **2019**, *116*, 2849–2853.

[10] Bhattacharya, P.; Heiden, Z. M.; Chambers, G. M.; Johnson, S. I.; Bullock, R. M.; Mock, M. T. Catalytic Ammonia Oxidation to Dinitrogen by Hydrogen Atom Abstraction. *Angew. Chem. Int. Ed.* **2019,** *58*, 11618–11624.

[11] Nakajima, K.; Toda, H.; Sakata, K.; Nishibayashi, Y. Ruthenium-Catalysed Oxidative Conversion of Ammonia into Dinitrogen. *Nat. Chem.* **2019**, *11*, 702–709.

[12] Zott, M. D.; Garrido-Barros, P.; Peters, J. C. Electrocatalytic Ammonia Oxidation Mediated by a Polypyridyl Iron Catalyst. *ACS Catal.* **2019,** *9*, 10101–10108.

[13] Dunn, P. L.; Johnson, S. I.; Kaminsky, W.; Bullock, R. M. Diversion of Catalytic C–N Bond Formation to Catalytic Oxidation of NH_3 through Modification of the Hydrogen Atom Abstractor. *J. Am. Chem. Soc.* **2020,** *142*, 3361–3365.

[14] As a convention, we define one turnover as the production of one equivalent of N_2 per catalyst equivalent.

[15] Lindoy, L. F.; Livingstone, S. E. Complexes of Iron(II), Cobalt(II) and Nickel(II) with α-Diimines and Related Bidentate Ligands. *Coord. Chem. Rev.* **1967**, *2*, 173–193.

[16] Phan, H.; Hrudka, J. J.; Igimbayeva, D.; Lawson Daku, L. M.; Shatruk, M. A Simple Approach for Predicting the Spin State of Homoleptic Fe(II) Tris-Diimine Complexes. *J. Am. Chem. Soc.* **2017**, *139*, 6437–6447.

[17] Ashley, D. C.; Jakubikova, E. Tuning the Redox Potentials and Ligand Field Strength of Fe(II) Polypyridines: The Dual π-Donor and π-Acceptor Character of Bipyridine. *Inorg. Chem.* **2018**, *57*, 9907–9917.

[18] Chen, K.; Que, L. Stereospecific Alkane Hydroxylation by Non-Heme Iron Catalysts: Mechanistic Evidence for an Fe^{V}=O Active Species. *J. Am. Chem. Soc.* **2001**, *123*, 6327–6337.

[19] Que, L., Jr.; Tolman, W. B. Biologically Inspired Oxidation Catalysis. *Nature* **2008**, *455*, 333–340.

[20] Fillol, J. L.; Codolá, Z.; Garcia-Bosch, I.; Gómez, L.; Pla, J. J.; Costas, M. Efficient Water Oxidation Catalysts Based on Readily Available Iron Coordination Complexes. *Nat. Chem.* **2011**, *3*, 807−813.

[21] Chen, L.; Su, X.-J.; Jurss, J. W. Selective Alkane C–H Bond Oxidation Catalyzed by a Non-Heme Iron Complex Featuring a Robust Tetradentate Ligand. *Organometallics* **2018**, *37*, 4535–4539.

[22] Khnayzer, R. S.; Thoi, V. S.; Nippe, M.; King, A. E.; Jurss, J. W.; El Roz, K. A.; Long, J. R.; Chang, C. J.; Castellano, F. N. Towards a Comprehensive Understanding of Visible-Light Photogeneration of Hydrogen from Water Using Cobalt(II) Polypyridyl Catalysts. *Energy Environ. Sci.* **2014**, *7*, 1477–1488.

[23] Pegis, M. L.; Wise, C. F.; Koronkiewicz, B.; Mayer, J. M. Identifying and Breaking Scaling Relations in Molecular Catalysis of Electrochemical Reactions. *J. Am. Chem. Soc.* **2017**, *139*, 11000–11003.

[24] Azcarate, I.; Costentin, C.; Robert, M.; Savéant, J.-M. Through-Space Charge Interaction Substituent Effects in Molecular Catalysis Leading to the Design of the Most Efficient Catalyst of CO_2-to-CO Electrochemical Conversion. *J. Am. Chem. Soc.* **2016**, *138*, 16639–16644.

[25] As previously reported,[12] $FeOTf_2$ itself is rapidly deposited on the electrode and produces minimal N_2; a reload experiment shows no activity. At the low applied bias used in this work, N_2 levels are too low to be quantified in the absence of iron sources.

[26] Costentin, C.; Savéant, J.-M. *Elements of Molecular and Biomolecular Electrochemistry: An Electrochemical Approach to Electron Transfer Chemistry*, 2nd ed.; John Wiley & Sons: Hoboken, NJ, 2006.

[27] Savéant, J.-M.; Vianello, E. Potential-Sweep Voltammetry: General Theory of Chemical Polarization. *Electrochim. Acta* **1967**, *12*, 629−646.

[28] Costentin, C.; Drouet, S.; Robert, M.; Savéant, J.-M. Turnover Numbers, Turnover Frequencies, and Overpotential in Molecular Catalysis of Electrochemical Reactions. Cyclic Voltammetry and Preparative-Scale Electrolysis. *J. Am. Chem. Soc.* **2012**, *134*, 11235−11242.

[29] Wang, V. C.-C.; Johnson, B. A. Interpreting the Electrocatalytic Voltammetry of Homogeneous Catalysts by the Foot of the Wave Analysis and Its Wider Implications. *ACS Catal.* **2019**, *9*, 7109−7123.

[30] Buhr, J. D.; Taube, H. Oxidation of $[Os(NH_3)_5CO]^{2+}$ to $[(Os(NH_3)_4CO)_2N_2]^{4+}$. *Inorg. Chem.* **1979**, *18*, 2208−2212.

[31] Abbenseth, J.; Finger, M.; Würtele, C.; Kasanmascheff, M.; Schneider, S. Coupling of Terminal Iridium Nitrido Complexes. *Inorg. Chem. Front.* **2016**, *3*, 469–477.

[32] Keener, M.; Peterson, M.; Hernandez Sanchez, R.; Oswald, V. F.; Wu, G.; Menard, G. Towards Catalytic Ammonia Oxidation to Dinitrogen: A Synthetic Cycle by Using a Simple Manganese Complex. *Chem. - Eur. J.* **2017**, *23*, 11479−11484.

[33] Collman, J. P.; Hutchison, J. E.; Ennis, M. S.; Lopez, M. A.; Guilard, R. Reduced Nitrogen Hydride Complexes of a Cofacial Metallodiporphyrin and Their Oxidative Interconversion. An Analysis of Ammonia Oxidation and Prospects for a Dinitrogen Electroreduction Catalyst Based on Cofacial Metallodiporphyrins. *J. Am. Chem. Soc.* **1992**, *114*, 8074−8080.

[34] Gu, N. X.; Oyala, P. H.; Peters, J. C. Hydrazine Formation via Coupling of a Nickel(III)–NH_2 Radical. *Angew. Chem. Int. Ed.* **2021**, *60*, 4009–4013.

[35] Siig, O.; Kepp, K. Iron(II) and Iron(III) Spin Crossover: Toward an Optimal Density Functional. *J. Phys. Chem. A* **2018**, *122*, 4208–4217.

[36] See SI for full details. Calculations considered all possible spin multiplicities and plausible isomers.

Chapter 5

Improving Molecular Iron Ammonia Oxidation Electrocatalysts via Substituent Tuning

.

5.1 Introduction

Ammonia oxidation (AO), and its mediation by transition metal catalysts, are burgeoning research topics across industry and academia.[1,2,3,4] Simple catalysts such as platinum and other precious metals degrade due to metal-nitride formation,[5,6] thus there is a pressing need for new catalysts that are both highly active and robust.[7,8] This motivation has inspired research into molecular AO catalysis, with the first reports appearing in 2019.[9,10,11,12] To date, a wide variety of catalyst structures have been reported, featuring ruthenium, iron, manganese, nickel, and copper catalysts with a wide variety of ligands.[13,14,15,16,17,18,19,20] Strategies such as achieving "low and level" N–H bond strengths, promoting early N–N formation to hydrazine, or enabling intermolecular nitride homocoupling all require distinct catalyst designs. As of yet, molecular AO does not feature a prevailing strategy for catalyst improvement.

Our lab has been interested in dicationic polypyridyl iron complexes $[(L_{aux})Fe(N')_2]^{2+}$ (L_{aux} = tetradentate ligand; N' = MeCN or NH_3) containing *cis*-coordination sites that bind ammonia-derived ligands (Scheme 5.1). First-generation $[(TPA)Fe(MeCN)_2]^{2+}$ featured high catalytic rates, but it was subject to degradation proceeding via displacement of the TPA ligand by excess ammonia (Eq. 1), limiting the demonstrated turnover number (TON)[21] to 16.[12] Considering the high-spin (S = 2) state of $[(TPA)Fe(NH_3)_2]^{2+}$, the primary species present during electrocatalysis, we hypothesized that degradation could be mitigated by favoring a low-spin electronic structure; indeed, use of stronger field **b**py**P**y2**M**e (BPM) led to a low-spin (S = 0) state for $[(BPM)Fe(MeCN)(NH_3)]^{2+}$ and an increased TON of 149 was demonstrated.[14]

$$[(L_{aux})Fe(NH_3)_2]^{2+} + 4\ NH_3 \rightleftharpoons L_{aux} + [Fe(NH_3)_6]^{2+} \qquad \text{(Eq. 5.1)}$$

Scheme 5.1. Molecular AO Catalysts Under Study Herein.[a]

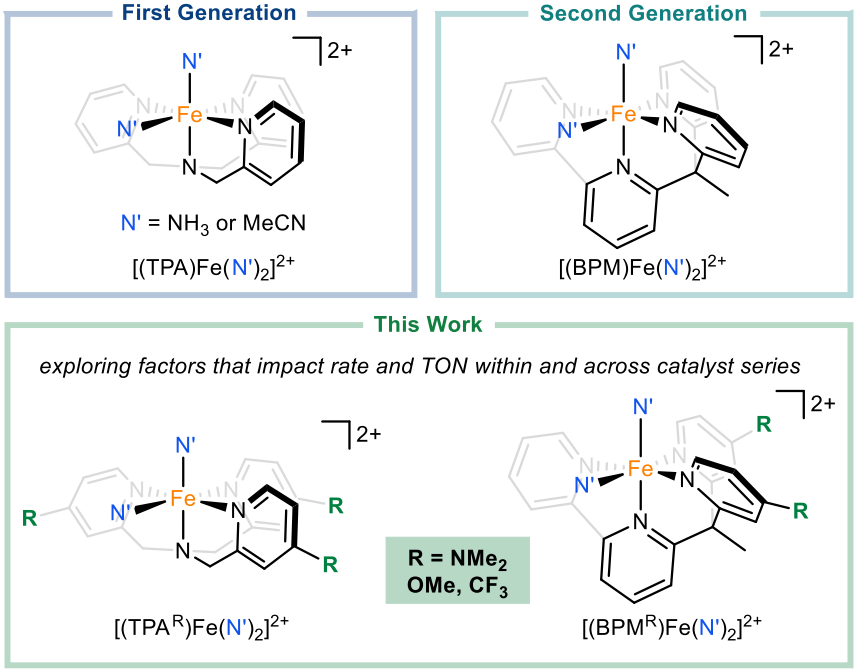

[a]Parent protio (reported) and 4-pyridyl substituted (new) complexes.

Second-generation $[(BPM)Fe(MeCN)(NH_3)]^{2+}$ also featured enhanced intrinsic catalytic rate and lowered overpotential. To rationalize this improved performance,[22,23,24,25] we consider (a) the standard potentials ($E°$) of $[(L_{aux})Fe(MeCN)_2]^{2+}$ and (b) the stability of $[(L_{aux})Fe(N')_2]^{2+}$ to demetallation. Following standard linear free energy relationships (LFER), more oxidizing complexes typically catalyze oxidative processes more rapidly, and $E°$ is greater for L_{aux} = BPM than for TPA.[26,27,28,29] In addition, demetallation of

$[(L_{aux})Fe(N')_2]^{2+}$ is reduced for L_{aux} = BPM compared to TPA, potentially increasing the concentration of active, ligated L_{aux}–Fe catalyst. In this work, we investigate these hypotheses with the goal of understanding general design principles for AO and ultimately developing an improved electrocatalyst.

5.2 Results and Discussion

To enable systematic investigation of the effect of $E°$ on catalysis, we prepared a series of 4-pyridyl-substituted auxiliary ligands and the corresponding $[(TPA^R)Fe(MeCN)_2]^{2+}$ and $[(BPM^R)Fe(MeCN)_2]^{2+}$ complexes (R = NMe_2, OMe, H, CF_3). Substitution in the 4-pyridyl position manipulates electronic structure via resonance and inductive effects without impacting the steric environment of the inner-coordination sphere. The TPA^{CF3} and substituted BPM^R ligands had not been previously synthesized. Synthetic routes analogous to the parent protio ligands furnished the trifluoromethyl derivatives but were unsuccessful for BPM^{OMe} and BPM^{NMe2}, for which we report new protocols (see SI for details).

The electronic structures of the iron complexes were quantitatively analyzed by cyclic voltametric measurement of $Fe^{2+/3+}$ redox couples (Figure 5.1). Both $[(TPA^R)Fe(MeCN)_2]^{2+}$ and $[(BPM^R)Fe(MeCN)_2]^{2+}$ exhibited reversible redox events for R = NMe_2, OMe, and H; for R = CF_3, ostensibly irreversible waves were observed. Given that the peak currents for R = CF_3 derivatives minimally change with scan number, and that reverse current is observed at more cathodic potentials (see SI), irreversibility most likely arises from a reversible change in inner-coordination sphere upon oxidation (e.g., by triflate coordination). The standard potentials were estimated using the half-wave potential ($E_{1/2}$),

except for R = CF_3, for which the half-peak potential ($E_{p/2}$) was used instead. Since half-wave and half-peak potentials for all complexes are within ±0.03 V, this approximation appears reasonable. For both $[(TPA^R)Fe(MeCN)_2]^{2+}$ and $[(BPM^R)Fe(MeCN)_2]^{2+}$, linear relationships between $E°$ and Hammett σ_p (para) values[30] were observed (see SI). The wide range of $E°$, 880 mV for TPA^R and 510 mV for BPM^R, reflects substantial variation in redox character due to 4-pyridyl substituents.

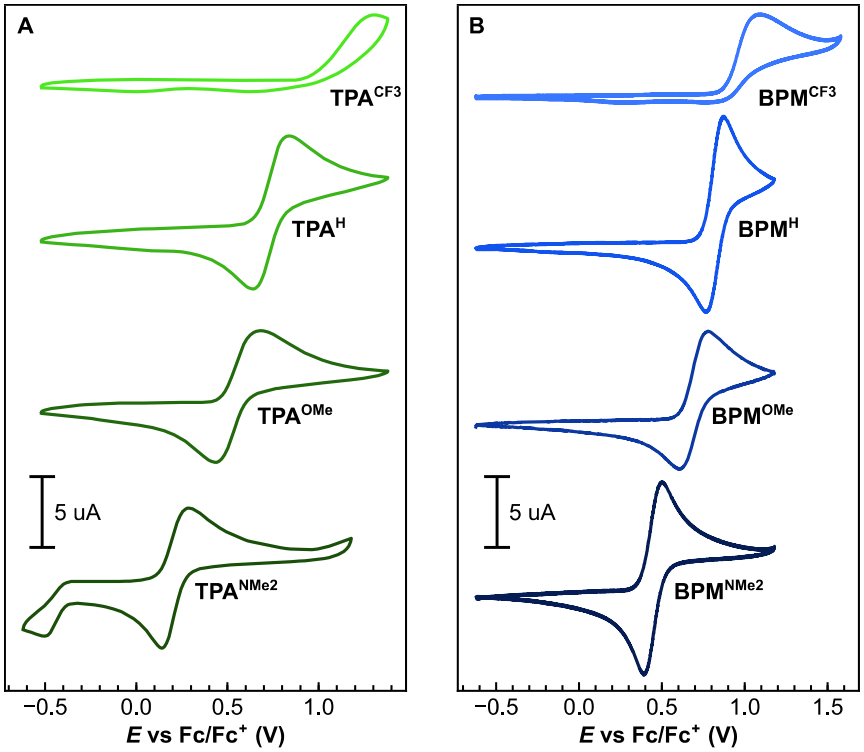

Figure 5.1. Cyclic voltammograms of (A) $[(TPA^R)Fe(MeCN)_2]^{2+}$ and (B) $[(BPM^R)Fe(MeCN)_2]^{2+}$ in acetonitrile using 0.1 M tetrabutylammonium hexafluorophosphate as supporting electrolyte at 100 mV/s with BDD WE.

To probe AO performance as a function of $E°$, we obtained cyclic voltammograms (CVs) in the presence of NH_3 (Figure 5.2A). Both $[(TPA^R)Fe(N')_2]^{2+}$ and $[(BPM^R)Fe(N')_2]^{2+}$ (N' = NH_3 or MeCN) exhibit two features in their voltammetry, E_1 and E_2, in the presence of NH_3. The lower-potential E_1 feature has been demonstrated via previous mechanistic studies

to involve net loss of a hydrogen atom from a coordinated ammine ligand (Eq. 5.2).[12,14] At the E_2 feature, these catalysts fully convert NH_3 to N_2 (Eq. 5.3).

$$E_1: \quad Fe^{II}–NH_3 + NH_3 \rightarrow Fe^{III}–NH_2 + NH_4^+ + e^- \qquad \text{(Eq. 5.2)}$$

$$E_2: \quad Fe^{III}–NH_2 + NH_3 \rightarrow Fe^{II} + N_2 + 5\ H^+ + 5\ e^- \qquad \text{(Eq. 5.3)}$$

The precatalytic wave potential (E_1) was determined using differential pulse voltammetry and analyzed as a function of $E°$ (Figure 5.2B; see SI for details). For both $[(TPA^R)Fe(N')_2]^{2+}$ and $[(BPM^R)Fe(N')_2]^{2+}$, linear correlations between E_1 and $E°$ were observed, and these correlations feature nearly identical slopes. Thus, 4-pyridyl substitution appears to exert similar influence on both catalyst series at E_1, indicating that an alteration in the first hydrogen-atom transfer in AO is not responsible for the improved performance of $[(BPM^R)Fe(N')_2]^{2+}$.

The effective turnover frequency (TOF) for the E_2 catalytic wave was similarly analyzed as a function of $E°$ (Figure 5.2C).[31] For $[(TPA^R)Fe(N')_2]^{2+}$, the datapoints are colinear. The small slope of this linear regression indicates that while $E°$ may affect AO performance within this ligand series, it does so to a very modest degree. Notably, the datapoint for $[(BPM^H)Fe(N')_2]^{2+}$ (boxed) is a clear outlier, i.e., its TOF is substantially greater than what would be predicted based upon its $E°$ value if the $[(TPA^R)Fe(N')_2]^{2+}$ regression were used. This behavior is consistent for each BPM^R complex, regardless of $E°$. However, the $[(BPM^R)Fe(N')_2]^{2+}$ series does not display an obvious correlation between TOF and $E°$, and the dataset does not indicate whether this results from an outlier versus a real trend.

However, we can disfavor the hypothesis that higher activity with $[(BPM^{H})Fe(N')_2]^{2+}$ relative to $[(TPA^{H})Fe(N')_2]^{2+}$ results primarily from greater $E°$.

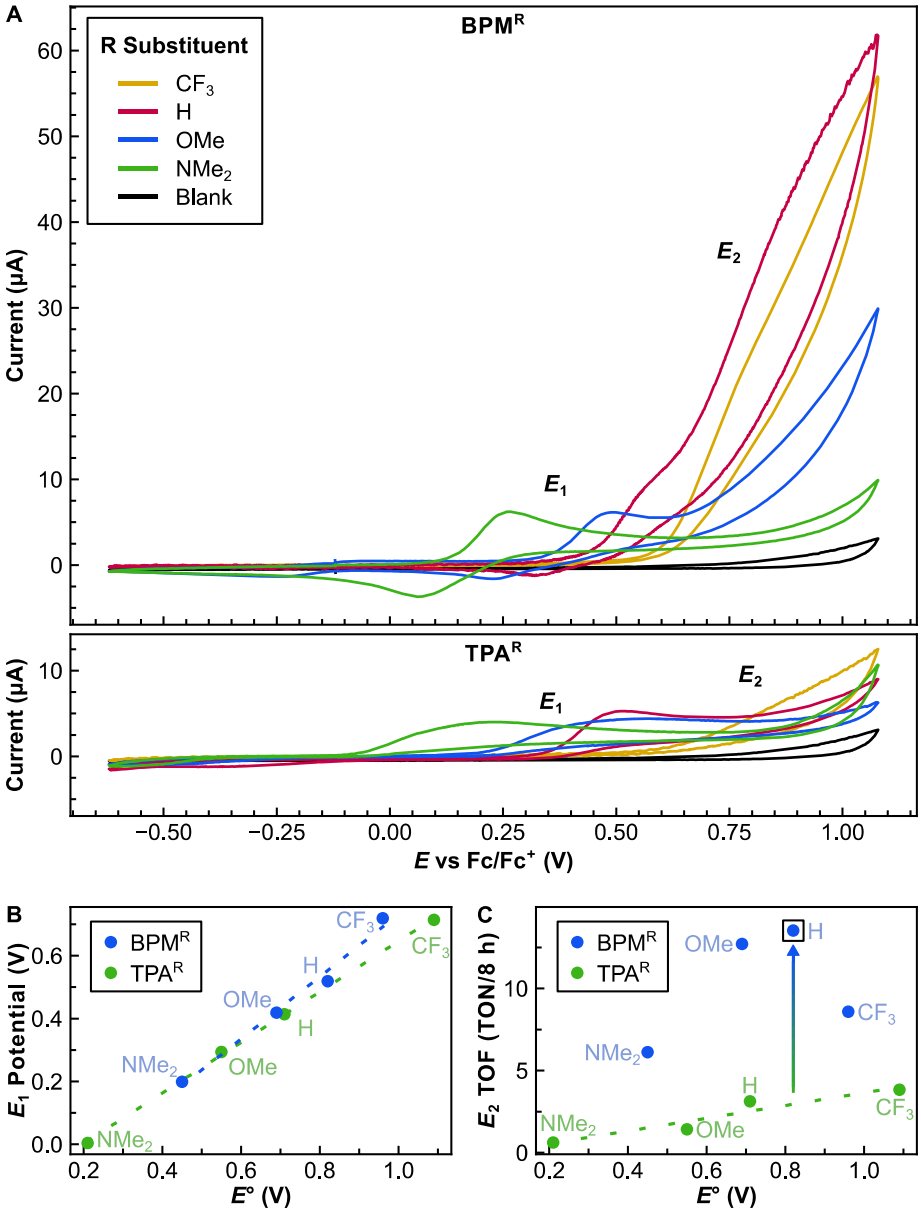

Figure 5.2. Electrochemical data. (A) Cyclic voltammograms, (B) E_1 potentials, and (C) catalytic activity at E_2 for $[(TPA^{R})Fe(N')_2]^{2+}$ and $[(BPM^{R})Fe(N')_2]^{2+}$ in acetonitrile with 50 equiv. NH_3 using 0.05 M ammonium triflate as supporting electrolyte with BDD WE.

We next studied the L_{aux} demetallation behavior of $[(L_{aux})Fe(N')_2]^{2+}$. To investigate ammonia coordination and potential displacement of L_{aux}, we titrated NH_3 into acetonitrile solutions of $[(L_{aux})Fe(MeCN)_2]^{2+}$ and monitored speciation by UV-vis spectroscopy. Following previous work, we analyzed the onset of demetallation, a metric we assign upon loss of isosbestic behavior (Figure 5.3A). The unsubstituted $[(TPA^{H})Fe(N')_2]^{2+}$ and $[(BPM^{H})Fe(N')_2]^{2+}$ AO catalysts begin to demetallate with 200 and 600 equiv. NH_3, respectively (Figure 5.3B).[12,14] The electron-withdrawing CF_3-substitutuent on both ligand scaffolds engenders substantially enhanced demetallation. By contrast, NMe_2 and OMe substituents increased the coordinating ability of the respective TPA^{R} and BPM^{R} ligands. These electron-donating groups uniformly push the measurable demetallation onset to >>2000 equivalents of NH_3. Interestingly, for L_{aux} = TPA^{NMe2} and TPA^{OMe}, stability to demetallation in the presence of ammonia is maintained despite each complex featuring of a high-spin (S = 2; see SI for details) ground state. Thus, electron-donating groups greatly reduce demetallation of catalytically relevant L_{aux}–Fe species.

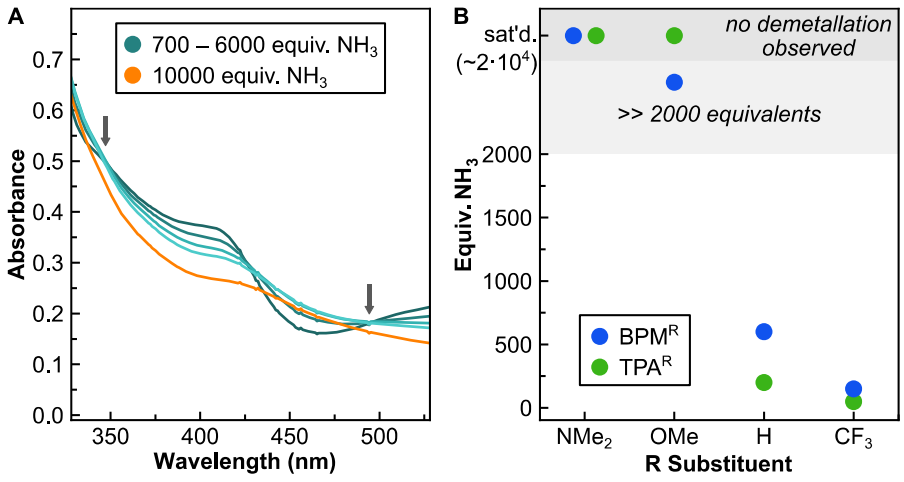

Figure 5.3. Qualitatively analyzed onset of demetallation as identified by loss of isosbestic behavior for $[(L_{aux})Fe(N')_2]^{2+}$ subjected to varying equiv. NH_3 in MeCN. (A) Example raw data for $[(BPM^{OMe})Fe(N')_2]^{2+}$ with isosbestic points marked by arrows and (B) compiled data.

By analyzing the catalysis data (Figure 5.2C) and the demetallation data (Figure 5.3) together, it is possible to rule out the hypothesis that enhanced catalysis owes to greater equilibrium catalyst concentration for $[(BPM^{H})Fe(N')_2]^{2+}$. It is important to note that our previously reported intrinsic catalytic rates ($\sim 10^7$ $M^{-1}\cdot s^{-1}$ and $\sim 10^8$ $M^{-1}\cdot s^{-1}$ for $L_{aux} = TPA^{H}$ and BPM^{H}, respectively), as well as the effective TOF data reported in Figure 2C, were obtained under ammonia concentration regimes well below the onset of demetallation. This should mitigate the influence of demetallation, if present, on catalytic rate. Three comparisons all corroborate that such a hypothesis is invalid. First, $[(TPA^{NMe2})Fe(N')_2]^{2+}$ and $[(TPA^{OMe})Fe(N')_2]^{2+}$ are both *more resistant* to demetallation but *less active* than $[(TPA^{H})Fe(N')_2]^{2+}$ or $[(TPA^{CF3})Fe(N')_2]^{2+}$. This is more readily explained as arising from the intuitive LFER between TOF and $E°$ which predicts that more oxidizing complexes operate at higher rates for oxidative processes. Second, $[(BPM^{CF3})Fe(N')_2]^{2+}$ is *less resistant* to demetallation than are $[(TPA^{R})Fe(N')_2]^{2+}$ for R = {NMe_2, OMe, or H}, but it features the *highest TOF* of these four complexes. This too could be explained by a TOF vs $E°$ LFER. However, the third comparison also invalidates any hypothesis concerning $E°$. Although $[(BPM^{NMe2})Fe(N')_2]^{2+}$ and $[(TPA^{OMe})Fe(N')_2]^{2+}$ feature *similar stability* to demetallation, and $[(TPA^{OMe})Fe(N')_2]^{2+}$ is more oxidizing than $[(BPM^{NMe2})Fe(N')_2]^{2+}$, $[(BPM^{NMe2})Fe(N')_2]^{2+}$ features a *higher TOF*. Therefore, some remaining, yet unidentified factor strongly influences catalysis.

While the aforementioned data indicate that the catalytic rate enhancement conferred by the BPM^{R} ligand scaffolds is not directly due to altered $E°$ or increased stability, increased stability is likely beneficial for achieving improved catalysis on a preparative scale, as reflected by TON. Thus, we were interested in demonstrating the practical value of these

mechanistic studies by way of improving net TON. We selected $[(BPM^{OMe})Fe(N')_2]^{2+}$ for further analysis since its TOF is minimally reduced as compared to $[(BPM^{H})Fe(N')_2]^{2+}$ (Figure 5.2C) but its stability to demetallation is substantially increased (Figure 5.3). Controlled potential coulometry data for $[(BPM^{OMe})Fe(N')_2]^{2+}$ is shown in Figure 5.4. Using the same potential as previously investigated with $[(BPM^{H})Fe(N')_2]^{2+}$ (0.85 V) allows for direct comparison. At this potential, no background electrode-mediated AO is observed.[14] In the presence of 2000 equiv. NH_3, catalytic AO proceeded for at least 48 hours, after which time 381 equiv. N_2 were measured with a quantitative faradaic efficiency (FE; within ± 5%) of 100 ± 5%. Furthermore, some catalytic activity remained after 48 hours, with a reload experiment producing 52 additional equiv. N_2. Post-catalysis, no activity is observed in a rinse test of the electrode. As $[(BPM^{H})Fe(N')_2]^{2+}$ previously demarcated the highest TON of 149 in molecular AO, this three-fold increase marks a considerable improvement. In addition to increased net activity, the higher NH_3 concentration lowered the onset potential to 0.29 V as compared to 0.45 V for $[(BPM^{H})Fe(N')_2]^{2+}$.

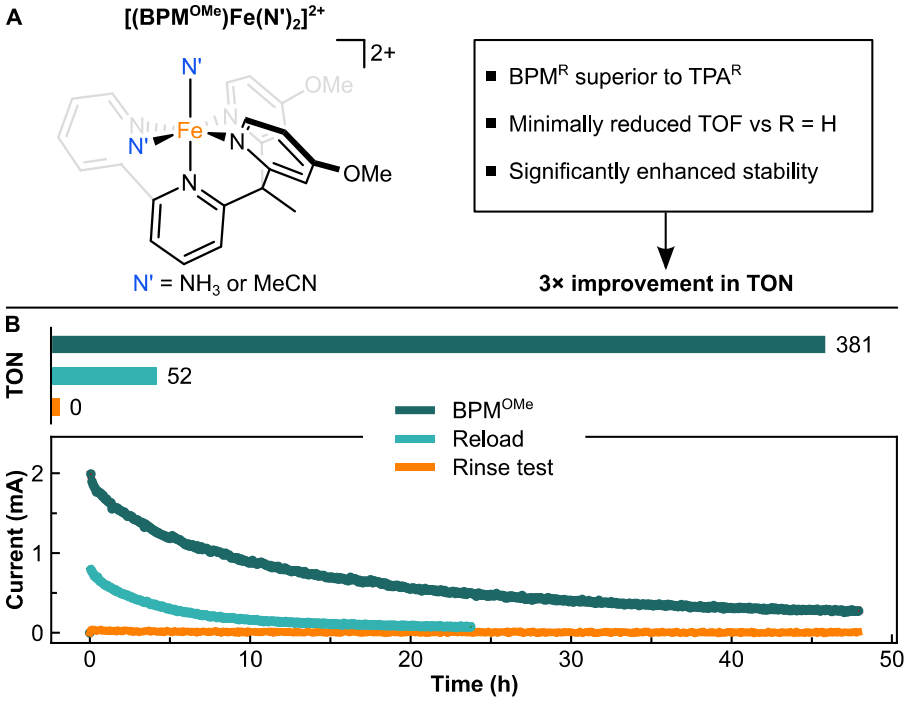

Figure 5.4. Catalyst characteristics. (A) Design elements and (B) performance of $[(BPM^{OMe})Fe(N')_2]^{2+}$. Coulometry experiments were performed with 0.05 mM [Fe] in acetonitrile with 2000 equiv. NH_3 using 0.05 M ammonium triflate as supporting electrolyte with BDD WE.

5.3 Conclusion

In conclusion, by systematically investigating $[(TPA^{R})Fe(N')_2]^{2+}$ and $[(BPM^{R})Fe(N')_2]^{2+}$ complexes, we have conclusively demonstrated that BPM^{R} ligands imbue superior performance for AO. Based on our studies of catalytic rate as a function of $E°$, we disfavor the hypothesis that enhanced catalysis in the case of R = H is solely a result of the BPM^{R} ligand producing a more oxidizing iron complex. Furthermore, we have validated the role of a low-spin electronic structure in mitigating demetallation but invalidated reduced demetallation as a rationale for the enhanced catalytic rate of $[(BPM^{H})Fe(N')_2]^{2+}$. Nevertheless, demetallation mitigation via electron-donating substituents, as in $[(BPM^{OMe})Fe(N')_2]^{2+}$, enabled the development of a third-generation AO catalyst featuring

improved net performance as characterized by the highest TON to date. While the precise origin of enhanced catalytic rate for BPM^R ligands remains elusive, we expect that these results related to the interplay of substituent effects on activity, stability, and spin state will aid in the development of new first-row metal AO catalysts with still greater performance, as demonstrated here for $[(BPM^{OMe})Fe(N')_2]^{2+}$.

5.4 References

[1] Mandra, J. O. Yara Clean Ammonia to use Amogy's ammonia-to-power system in shipping projects. *Offshore Energy*, Novemberr 10, 2022. https://www.offshore-energy.biz/yara-clean-ammonia-to-use-amogys-ammonia-to-power-system-in-shipping-projects/.

[2] Chen, J. G.; Crooks, R. M.; Seefeldt, L. C.; Bren, K. L.; Bullock, R. M.; Darensbourg, M. Y.; Holland, P. L.; Hoffman, B.; Janik, M. J.; Jones, A. K.; Kanatzidis, M. G.; King, P.; Lancaster, K. M.; Lymar, S. V.; Pfromm, P.; Schneider, W. F.; Schrock, R. R. Beyond Fossil Fuel–Driven Nitrogen Transformations. *Science* **2018**, *360* (6391), eaar6611.

[3] MacFarlane, D. R.; Cherepanov, P. V.; Choi, J.; Suryanto, B. H. R.; Hodgetts, R. Y.; Bakker, J. M.; Ferrero Vallana, F. M.; Simonov, A. N. A Roadmap to the Ammonia Economy. *Joule* **2020**, *4* 1186–1205.

[4] Dunn, P. L.; Cook, B. J.; Johnson, S. I.; Appel, A. M.; Bullock, R. M. Oxidation of Ammonia with Molecular Complexes. *J. Am. Chem. Soc.* **2020**, *142*, 17845–17858.

[5] de Vooys, A. C. A.; Koper, M. T. M.; van Santen, R. A.; van Veen, J. A. R. The Role of Adsorbates in the Electrochemical Oxidation of Ammonia on Noble and Transition Metal Electrodes. *J. Electroanal. Chem.* **2001**, *506*, 127–137.

[6] Song, L.; Liang, Z.; Ma, Z.; Zhang, Y.; Chen, J.; Adzic, R. R.; Wang, J. X. Temperature-Dependent Kinetics and Reaction Mechanism of Ammonia Oxidation on Pt, Ir, and PtIr Alloy Catalysts. *J. Electrochem. Soc.* **2018**, *165*, J3095–J3100.

[7] Kim, H.; Hong, S.; Kim, H.; Jun, Y.; Kim, S. Y.; Ahn, S. H. Recent Progress in Pt-Based Electrocatalysts for Ammonia Oxidation Reaction. *Appl. Mat. Today* **2022**, *29*, 101640.

[8] Zhao, Y.; Setzler, B. P.; Wang, J.; Nash, J.; Wang, T.; Xu, B.; Yan, Y. An Efficient Direct Ammonia Fuel Cell for Affordable Carbon-Neutral Transportation. *Joule* **2019,** *3*, 2472–2484.

[9] Habibzadeh, F.; Miller, S. L.; Hamann, T. W.; Smith, M. R. Homogeneous Electrocatalytic Oxidation of Ammonia to N_2 Under Mild Conditions. *Proc. Natl. Acad. Sci. U.S.A.* **2019**, *116*, 2849–2853.

[10] Bhattacharya, P.; Heiden, Z. M.; Chambers, G. M.; Johnson, S. I.; Bullock, R. M.; Mock, M. T. Catalytic Ammonia Oxidation to Dinitrogen by Hydrogen Atom Abstraction. *Angew. Chem. Int. Ed.* **2019,** *58*, 11618–11624.

[11] Nakajima, K.; Toda, H.; Sakata, K.; Nishibayashi, Y. Ruthenium-Catalysed Oxidative Conversion of Ammonia into Dinitrogen. *Nat. Chem.* **2019**, *11*, 702–709.

[12] Zott, M. D.; Garrido-Barros, P.; Peters, J. C. Electrocatalytic Ammonia Oxidation Mediated by a Polypyridyl Iron Catalyst. *ACS Catal.* **2019,** *9*, 10101–10108.

[13] Dunn, P. L.; Johnson, S. I.; Kaminsky, W.; Bullock, R. M. Diversion of Catalytic C–N Bond Formation to Catalytic Oxidation of NH_3 through Modification of the Hydrogen Atom Abstractor. *J. Am. Chem. Soc.* **2020,** *142*, 3361–3365.

[14] Zott, M. D.; Peters, J. C. Enhanced Ammonia Oxidation Catalysis by a Low-Spin Iron Complex Featuring Cis Coordination Sites. *J. Am. Chem. Soc.* **2021**, *143*, 7612–7616.

[15] Trenerry, M. J.; Wallen, C. M.; Brown, T. R.; Park, S. V.; Berry, J. F. Spontaneous N_2 Formation by a Diruthenium Complex Enables Electrocatalytic and Aerobic Oxidation of Ammonia. *Nat. Chem.* **2021**, *13*, 1221–1227.

[16] Holub, J.; Vereshchuk, N.; Sánchez-Baygual, F.-J.; Gil-Sepulcre, M.; Benet-Buchholz, J.; Llobet, A. Synthesis, Structure, and Ammonia Oxidation Catalytic Activity of Ru-NH_3 Complexes Containing Multidentate Polypyridyl Ligands. *Inorg. Chem.* **2021**, *60*, 13929–13940.

[17] Toda, H.; Kuroki, K.; Kanega, R.; Kuriyama, S.; Nakajima, K.; Himeda, Y.; Sakata, K.; Nishibayashi, Y. Manganese-Catalyzed Ammonia Oxidation into Dinitrogen under Chemical or Electrochemical Conditions. *ChemPlusChem* **2021**, *86*, 1511–1516.

[18] Li, Y.; Chen, J.-Y.; Miao, Q.; Yu, X.; Feng, L.; Liao, R.-Z.; Ye, S.; Tung, C.-H.; Wang, W. A Parent Iron Amido Complex in Catalysis of Ammonia Oxidation. *J. Am. Chem. Soc.* **2022**, *144*, 4365–4375.

[19] Beiler, A. M.; Denisiuk, A.; Holub, J.; Sánchez-Baygual, F.-J.; Gil-Sepulcre, M.; Ertem, M. Z.; Moonshiram, D.; Piccioni, A.; Llobet, A. Heterogeneous Electrochemical Ammonia Oxidation with a Ru-Bda Oligomer Anchored on Graphitic Electrodes via CH–π Interactions. *ACS Energy Lett.* **2023**, *8*, 172–178.

[20] Ahmed, M. E.; Raghibi Boroujeni, M.; Ghosh, P.; Greene, C.; Kundu, S.; Bertke, J. A.; Warren, T. H. Electrocatalytic Ammonia Oxidation by a Low-Coordinate Copper Complex. *J. Am. Chem. Soc.* **2022**, *144*, 21136–21145.

[21] E_{onset} is the onset potential for catalysis, and TON is the turnover number, defined as the number of equivalents of N_2 produced per catalyst equivalent.

[22] Klug, C. M.; Cardenas, A. J. P.; Bullock, R. M.; O'Hagan, M.; Wiedner, E. S. Reversing the Tradeoff between Rate and Overpotential in Molecular Electrocatalysts for H_2 Production. *ACS Catal.* **2018**, *8*, 3286–3296.

[23] Pegis, M. L.; Wise, C. F.; Koronkiewicz, B.; Mayer, J. M. Identifying and Breaking Scaling Relations in Molecular Catalysis of Electrochemical Reactions. *J. Am. Chem. Soc.* **2017**, *139*, 11000–11003.

[24] Azcarate, I.; Costentin, C.; Robert, M.; Savéant, J.-M. Through-Space Charge Interaction Substituent Effects in Molecular Catalysis Leading to the Design of the Most Efficient Catalyst of CO_2-to-CO Electrochemical Conversion. *J. Am. Chem. Soc.* **2016**, *138*, 16639–16644.

[25] Nie, W.; Tarnopol, D. E.; McCrory, C. C. L. Enhancing a Molecular Electrocatalyst's Activity for CO_2 Reduction by Simultaneously Modulating Three Substituent Effects. *J. Am. Chem. Soc.* **2021**, *143*, 3764–3778.

[26] DuBois, D. L. Development of Molecular Electrocatalysts for Energy Storage. *Inorg. Chem.* **2014**, *53*, 3935–3960.

[27] Solomon, E. I.; Stahl, S. S. Introduction: Oxygen Reduction and Activation in Catalysis. *Chem. Rev.* **2018**, *118*, 2299–2301.

[28] Martin, D. J.; Wise, C. F.; Pegis, M. L.; Mayer, J. M. Developing Scaling Relationships for Molecular Electrocatalysis through Studies of Fe-Porphyrin-Catalyzed O_2 Reduction. *Acc. Chem. Res.* **2020**, *53*, 1056–1065.

[29] Costentin, C.; Drouet, S.; Robert, M.; Savéant, J.-M. Turnover Numbers, Turnover Frequencies, and Overpotential in Molecular Catalysis of Electrochemical Reactions. Cyclic Voltammetry and Preparative-Scale Electrolysis. *J. Am. Chem. Soc.* **2012**, *134*, 11235–11242.

[30] Hansch, Corwin.; Leo, A.; Taft, R. W. A Survey of Hammett Substituent Constants and Resonance and Field Parameters. *Chem. Rev.* **1991**, *91*, 165–195.

[31] Because of the absence of diffusion limited plateau currents, we have chosen to assess the catalytic performance at E_2 coulometrically via constant-potential experiments at E = 0.85 V vs Fc/Fc^+, as opposed to voltammetrically. While more laborious, this method proved especially important in this instance due to the presence of lower faradaic efficiencies with the derivatives bearing electron-donating groups. See the SI for additional discussion.

Appendix A

Supplementary Information for Chapter 2

Adapted from:

Zott, M. D.; Canestraight, V. M.; Peters, J. C.
ACS Catal. **2022**, *12*, 10781–10786.
DOI: 10.1021/acscatal.2c03215.

.

A.1 General procedures

General Considerations: All manipulations were carried out using standard Schlenk or glovebox techniques under an N_2 or Ar atmosphere. Unless otherwise noted, solvents were deoxygenated and dried by thoroughly sparging with N_2 gas followed by passage through an activated alumina column in a solvent purification system (SG Water, USA LLC). All solvents were stored over activated 3 or 4 Å molecular sieves prior to use. Electrolytes were dried by heating (>100 °C) under vacuum (<1 torr) for at least 12 hours. All reagents were purchased from commercial vendors and used without further purification unless otherwise stated. [Cu_2] (also known as [(PNP$^{t\text{Bu}}$)Cu]$_2$) and its constituent protonated ligand (H-PNP$^{t\text{Bu}}$) were prepared as previously described.[1] ^{1}H NMR chemical shifts are reported in ppm relative to tetramethylsilane, using residual solvent resonances as internal standards.

Electrochemistry: Voltammetry experiments were carried out with a Biologic VSP or CH Instruments 600B potentiostat using a one-compartment three-electrode cell, and coulometry experiments were carried out with a Biologic VSP potentiostat using a two-compartment three-electrode cell. For voltammetry, a glassy carbon (GC) working electrode (3 mm diameter), a Pt wire counter electrode, and a Ag/AgOTf reference electrode (5 mM AgOTf and 0.2 M $LiNTf_2$ in DME) were employed. For CPC, the same reference electrode was used, but a carbon cloth (geometric area: 5 cm^2) and a Mg coil were used respectively as working and counter electrode. All redox potentials in the present work are reported versus SCE. Redox potentials were calibrated against Fc/Fc$^+$ and converted to SCE using $E_{SCE} = E_{Fc/Fc^+} + 0.51$ V (Equation A1).[2]

CVs were collected at 100 $mV \cdot s^{-1}$ unless specified otherwise. $E_{1/2}$ values for the reversible waves were obtained from the half potential between the oxidative and reductive peaks. Irreversible waves have potentials reported as their peak potential (E_p).

NMR: NMR spectroscopy was performed using Varian and Bruker 400 or 600 MHz NMR spectrometers equipped with broadband auto-tune probes. ^{1}H NMR chemical shifts are reported in ppm relative to tetramethylsilane, using residual solvent resonances as internal standards.

UV-Vis: Spectra were collected using a Cary 60 instrument with Cary WinUV software. Spectra were background corrected.

Mass Spectrometry: Mass spectra were obtained in direct infusion mode with electrospray ionization on a Thermo Fisher LTQ Linear Ion Trap Mass Spectrometer. Ions were measured in the range 150–2000 m/z, and product ions were isolated and further analyzed by collision-induced dissociation to further corroborate identification.

X-ray Crystallography: XRD studies were carried out at the Beckman Institute Crystallography Facility on a Bruker D8 Venture diffractometer (Cu Kα radiation). Structures were solved using direct methods with SHELXS or SHELXT and refined against F^2 on all data by full-matrix least squares with SHELXL.[3] All of the solutions were performed in the Olex2 program.[4] The crystals were mounted on a glass fiber under Paratone N oil.

Luminescence: Steady-state and time-resolved luminescence measurements were carried out in the Beckman Institute Laser Resource Center at Caltech and performed under an Ar

atmosphere at room temperature. Samples were prepared in 1 cm path length quartz cuvettes in a dark, argon-filled glovebox. Prior to measurement, all samples were protected from light by wrapping in aluminum foil.

Steady-state emission spectra were recorded on a modified Jobin Yvon Spex Fluorolog-3. A xenon arc lamp was used for sample excitation, with wavelength selection performed by a monochromator. Luminescence was collected at 90° to the excitation direction and directed by a bifurcated optical fiber bundle to two Ocean Optics QEPro CCD spectrometers spanning 300 to 930 nm. Spectra were corrected for instrument response.

For time-resolved measurements, laser excitation was provided by 8 ns pulses from a Q-switched Nd:YAG laser (Spectra-Physics Quanta-Ray PRO-Series) operating at 10 Hz. The first harmonic was used to provide laser pulses at 355 nm. Probe wavelengths were selected for detection by a double monochromator (Instruments SA DH-10) with 1 mm slits. All instruments and electronics in these systems were controlled by software written in LabVIEW (National Instruments). Luminescence decay traces were fit to a single exponential (after an appropriate time delay to remove scattered excitation light).

For each Stern-Volmer series, 5 cuvettes were prepared with 20 μM [Cu_2] and quencher (40-320 μM) in DME in a dark argon glovebox. The cuvettes were sealed with a threaded Teflon valve and covered in aluminum foil to prevent ambient light exposure. Fluorescence lifetime measurements were carried out with excitation wavelength of λ_{ex} = 355 nm and a recording wavelength of λ_{em} = 510 nm at 25 °C. A long pass filter λ>500 was used to diminish scattered excitation light. The emission decay was averaged over 50 laser

pulses and was fit to a monoexponential function. The lifetime was determined to occur when the intensity was 1/e its initial value, or I_0/e.

Chromatography: All chromatography experiments were performed using standard silica gel unless otherwise indicated. For column chromatography, F60, 40 – 63 μm, 60 Å silica from SiliCycle (R10030B) was used. For thin layer chromatography, aluminum-backed 60 Å silica gel coated with a 254 nm fluorescent indicator was used (MilliporeSigma, EM1.05554.0001).

A.2 Luminescence data for [Cu_2]

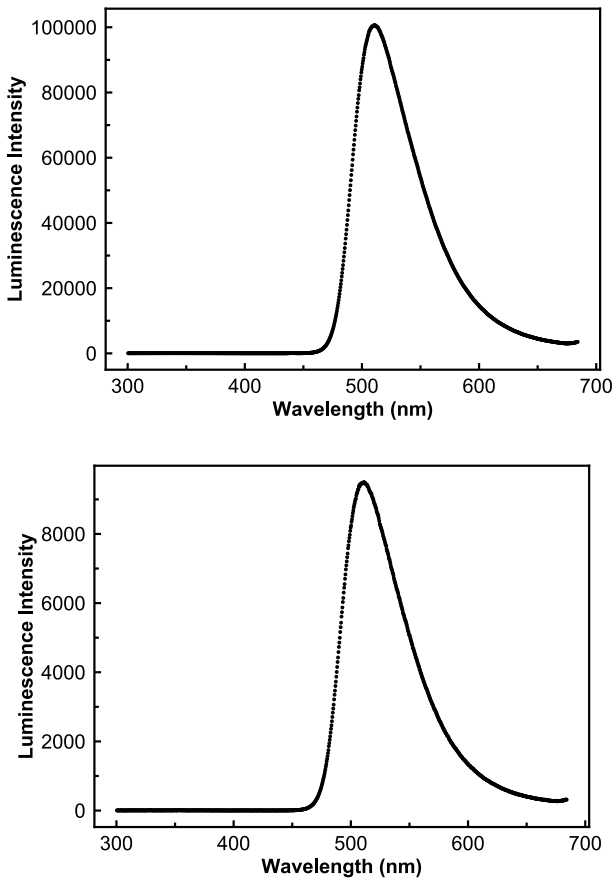

Figure A1. Emission spectra for 160 μM [Cu_2] in DME with excitation at 440 nm (left) or 355 nm (right).

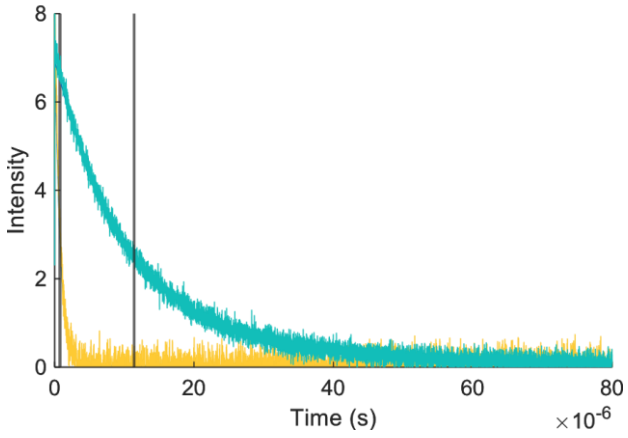

Figure A2. Example time-resolved luminescence decays for 20 µM [Cu_2] in DME with excitation at 355 nm. The teal trace has no additives; the yellow trace is in the presence of a quencher, 160 µM 4-cyanobenzyl chloride. Gray vertical lines are plotted at the timepoint at which the luminescence intensity is reduced to 1/*e* of the initial value, representing the lifetime (τ).

A.3 Stern-Volmer plots and Marcus theory analysis

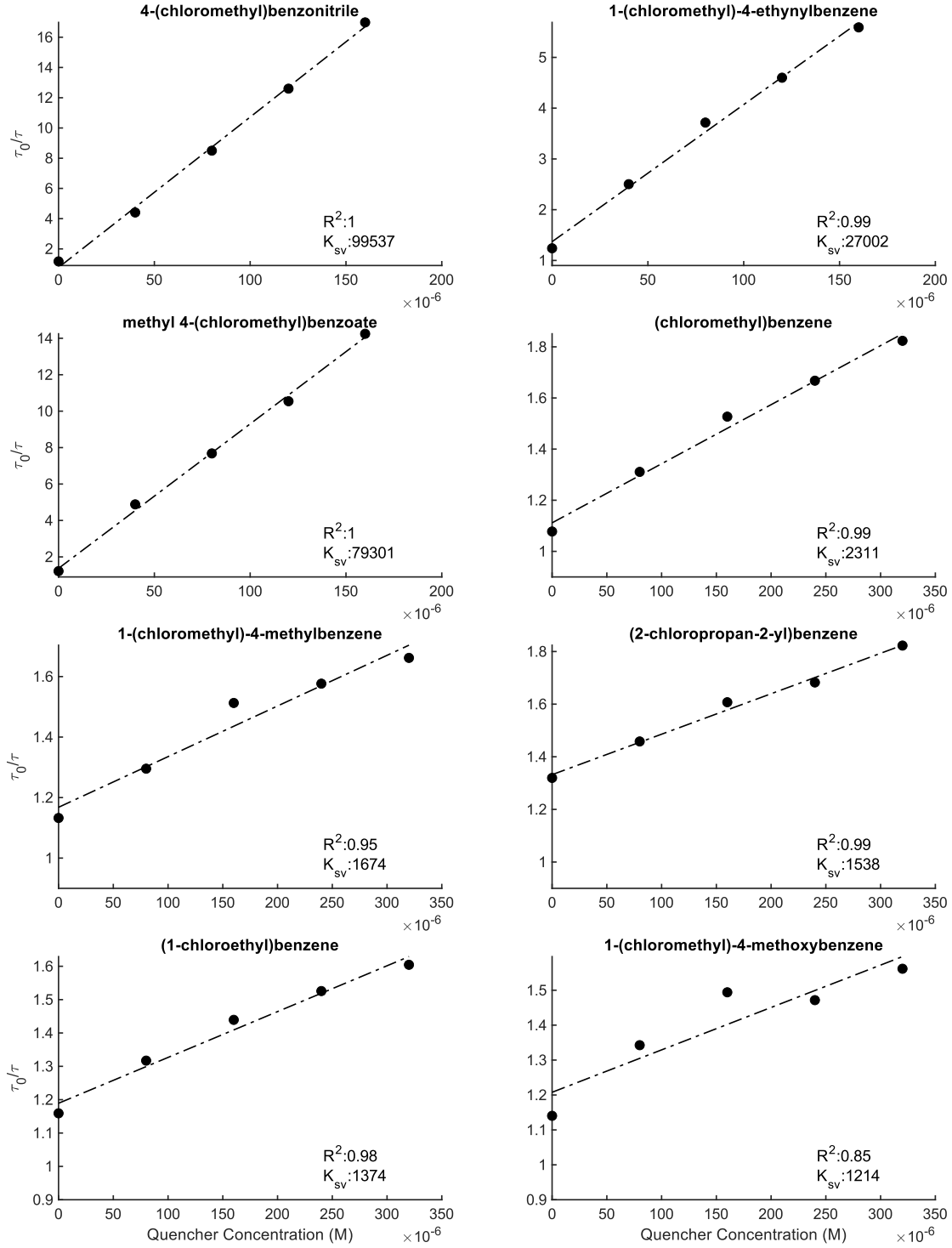

Figure A3. Stern-Volmer plots of 20 μM [Cu_2] in DME in the presence of various benzyl chloride quenchers at 25 °C. This data is presented in the main text as one plot with all eight SV plots overlaid.

Based on these quenching rates and the driving force as estimated using various redox potential data for the benzyl chloride quenchers, an analysis following Marcus theory was performed. Using non-linear regression (Levenberg–Marquardt) and the simplified Marcus equation (Equation A2) for transfer between neutral molecules,[5] relating k_{obs} and ΔG (defined as K_{SV}/τ_0 and $E_{quencher}-E_{ox}^{*}$, respectively), the reorganization energy (λ) was obtained and compared using $E_{quencher}$ values from: peak potentials (E_p), half-peak potentials ($E_{p/2}$), and potentials from differential pulse voltammetry (DPV).

$$\ln(k_{obs}) = -\left[\frac{\lambda}{4RT}\left(1+\frac{\Delta G}{\lambda}\right)^2\right] + \text{Const.} \qquad \text{(Equation A2)}$$

The data using peak potentials is presented in the main text, but all data sets yield qualitatively identical results. All fits are presented below. These various $E_{quencher}$ values result in different reorganization energies in the range: λ = 18.8–37.1 kcal/mol, which are low to modest in magnitude. Using E_p data to model driving force better reproduces the low driving force regime, whereas using DPV data better reproduces the high driving force regime. The deviations at high driving force for the E_p data set could result from nearing the diffusion limit, a challenge first discussed by Rehm and Weller, whereupon the inverted region is not observed in certain photoinduced charge transfer reactions.[6]

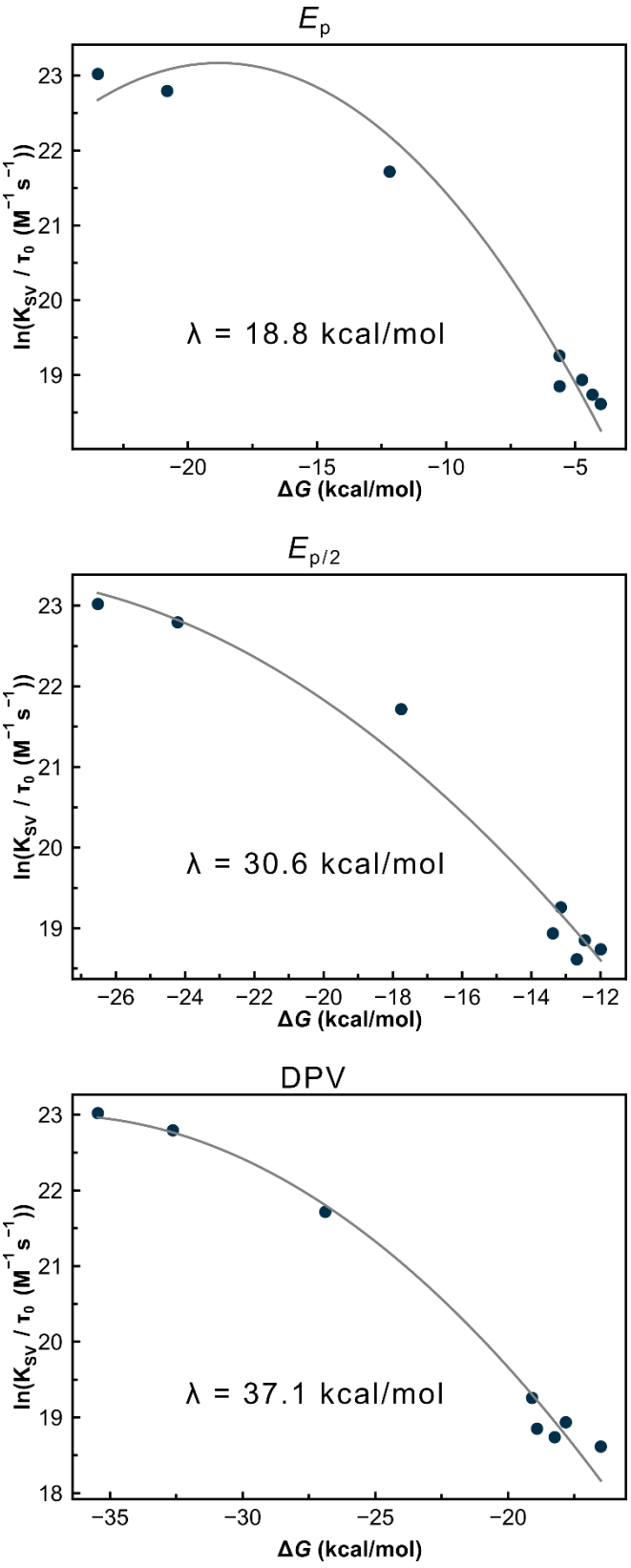

Figure A4. Rate-driving force relationships modelled using Marcus theory at T = 25 °C.

A.4 Cyclic voltammograms of benzyl chloride quenchers

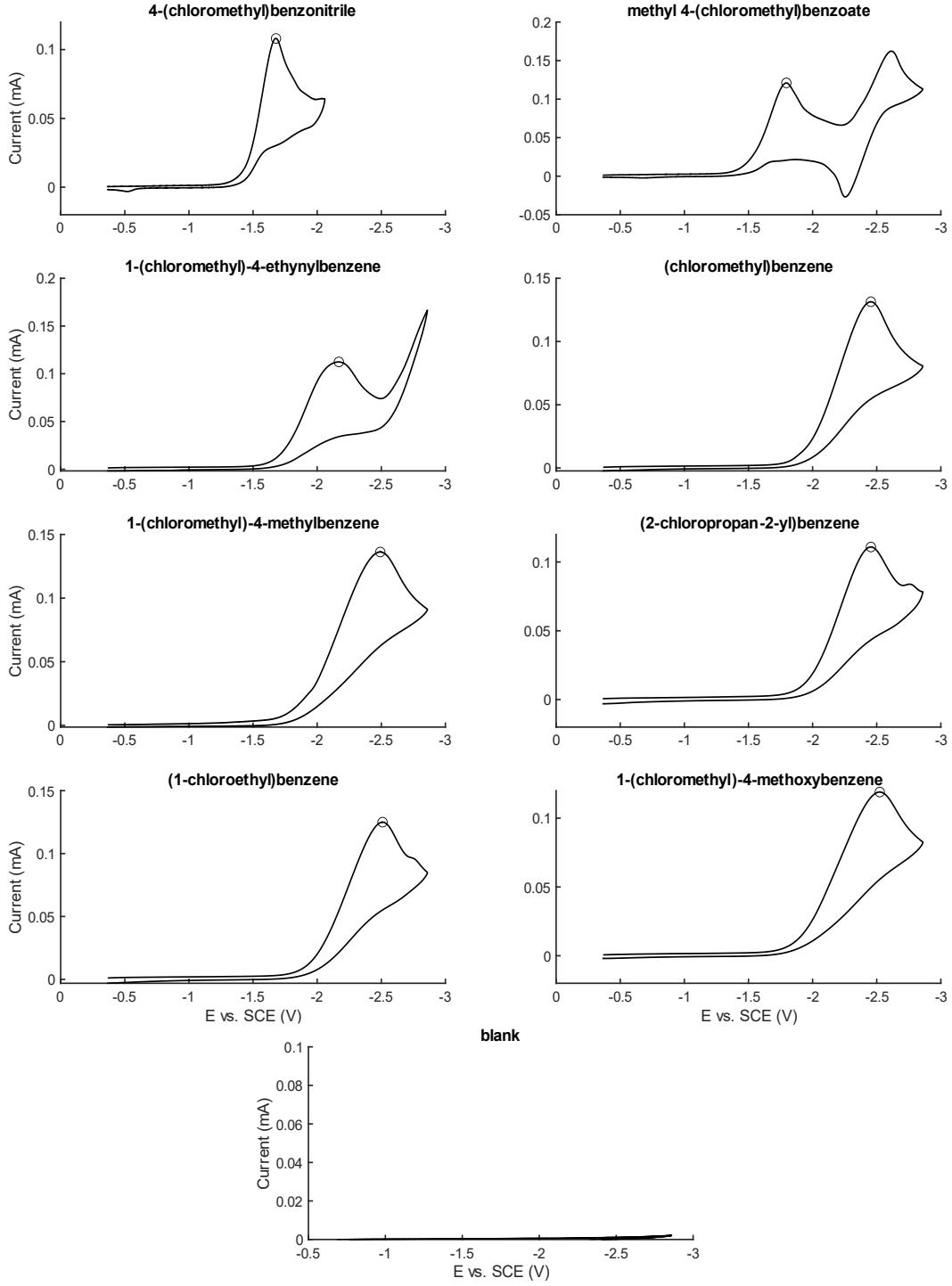

Figure A5. Cyclic voltammograms of various benzyl chlorides**.** Recorded in DME with 5 mM benzyl chloride and 0.2 M $TBAPF_6$. Glassy carbon working electrode, Ag/AgOTf reference electrode, and Pt counter electrode. Scan rate: 100 mV/s.

Note that these cyclic voltammograms were recorded in DME with $TBAPF_6$ supporting electrolyte instead of $LiNTf_2$, the optimum electrolyte for controlled potential coulometry. Unfortunately, the solvent window with 0.2 M $LiNTf_2$ was too narrow and thus the benzyl chloride reduction waves were masked.

A.5 UV-vis time-course data

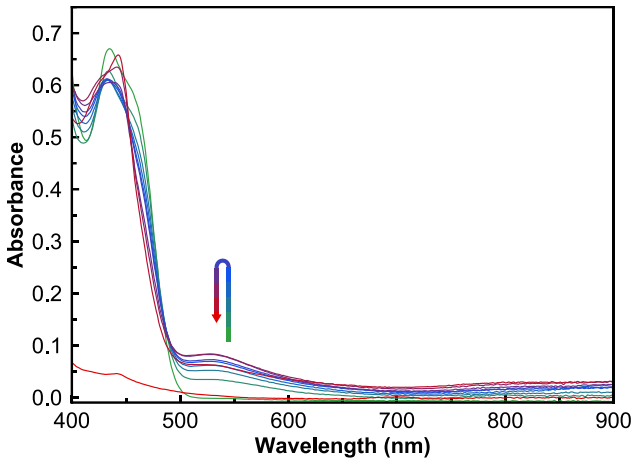

Figure A6. UV-vis spectra of 160 µM [Cu_2] in DME taken after 440 nm irradiation for 0, 1, 2, 3, 4, 5, 10, 15, 30, and 300 cumulative seconds. The colors change from greens (0–3 s) to blues (4–10 s) to reds (15–300 s). A subset of this data is presented in the main text.

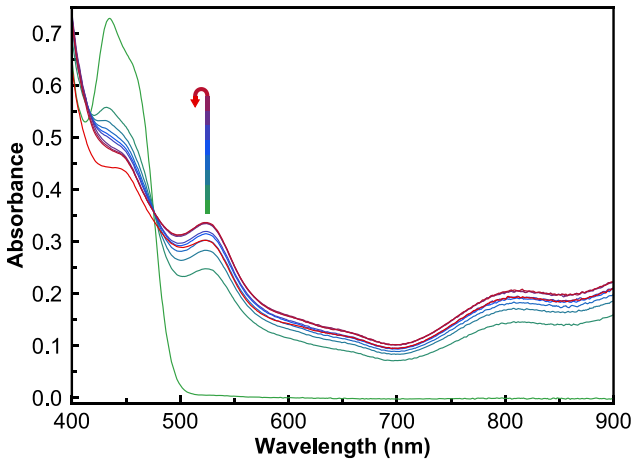

Figure A7. UV-vis spectra of 160 µM [Cu_2] in DME with 0.2 M $LiNTf_2$ taken after 440 nm irradiation for 0, 1, 2, 3, 4, 5, 10, 15, 30, and 300 cumulative seconds. The colors change from greens (0–3 s) to blues (4–10 s) to reds (15–300 s). A subset of this data is presented in the main text.

A.6 Synthesis and characterization of chloro-cubane and chloro-diamond

Chloro-cubane, $[(H\text{-}PNP^{tBu})Cu_2Cl_2]_2$

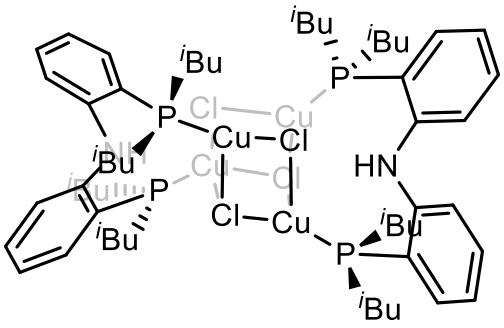

In a glovebox, H-PNP^{tBu} (50 mg, 1 eq) and copper(I) chloride (17.4 mg, 2 eq) were combined in tetrahydrofuran (1 mL) and stirred for 1 day. The solution remained colorless. The solution was concentrated and triturated with pentane prior to being dissolved in pentane:tetrahydrofuran (2 mL, 9:1) and filtered through a glass microfilter. After concentration, the product was afforded as a white solid (Yield: 65.0 mg, 99%).

^{1}H NMR (C_6D_6, 400 MHz): δ (ppm) = 7.93 (s, 1H), 7.55 (d, J = 8.3 Hz, 2H), 7.14 – 7.08 (m, 4H), 2.83 – 1.68 (m, 12H), 1.33–0.72 (m, 42H).

^{31}P NMR (C_6D_6, 162 MHz): δ (ppm) = −28.5 (s).

MS (FD, *m/z*): $[M]^+$ calculated: 1530.44911, found: 1530.44884.

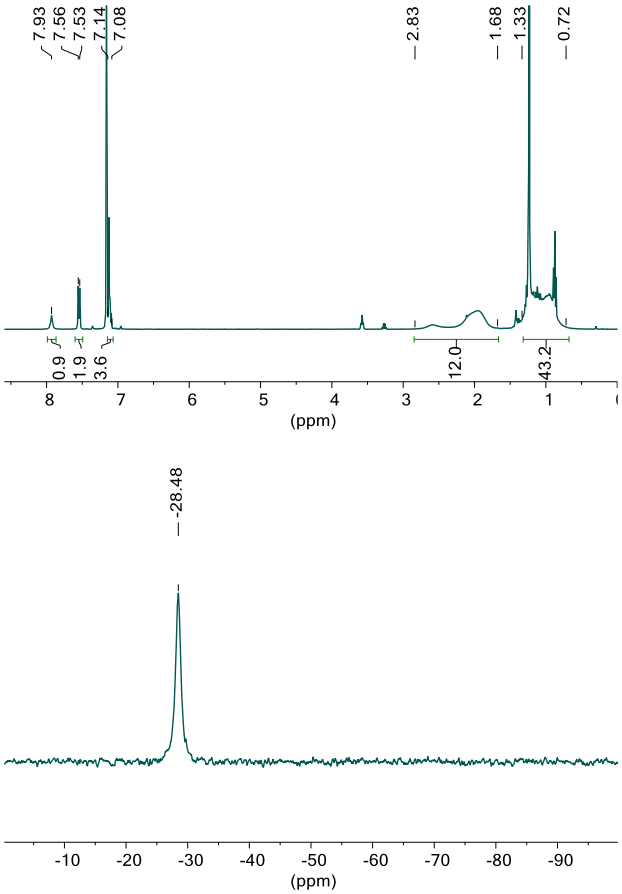

Figure A8. ^{1}H (left) and ^{31}P (right) NMR spectra for chloro-cubane in C_6D_6. The broadness of the peaks may be attributed to fluxionality in solution.

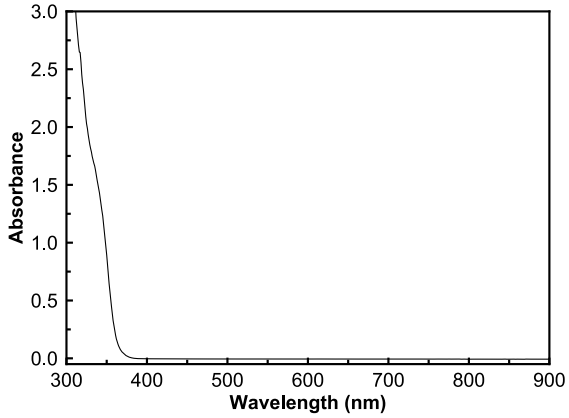

Figure A9. UV-vis absorption spectrum for 130 µM chloro-cubane in DME.

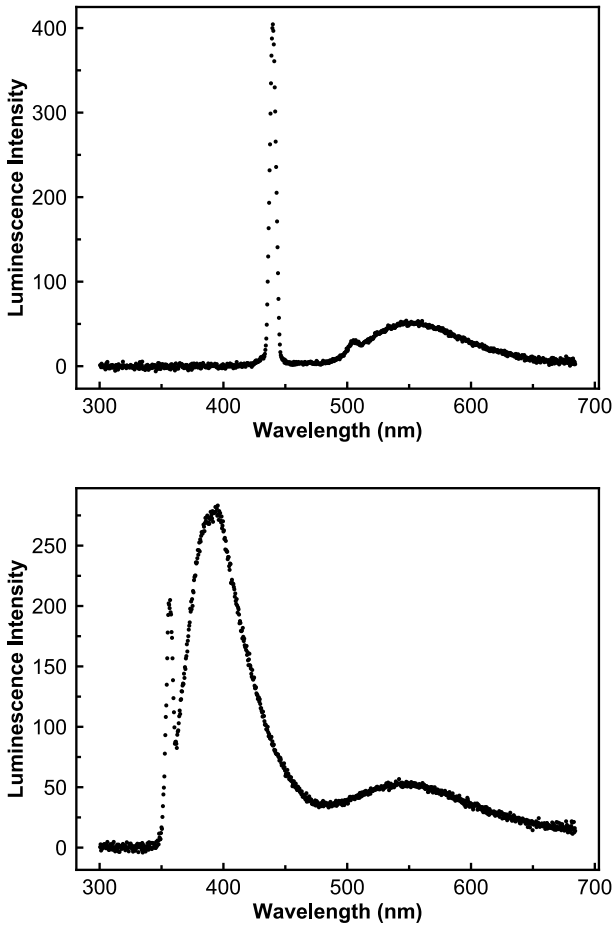

Figure A10. Emission spectra for 130 μM chloro-cubane in DME with excitation at 440 nm (left) or 355 nm (right).

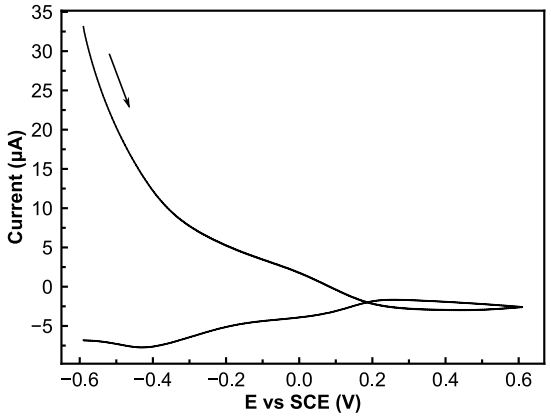

Figure A11. Cyclic voltammogram for ~1 mM chloro-cubane in DME with 0.2 M LiNTf2 supporting electrolyte, GC working, Pt counter, and Ag/AgOTf reference electrodes. Scan rate: 100 mV/s.

Chloro-diamond, [(H-PNP^{tBu})CuCl]$_2$

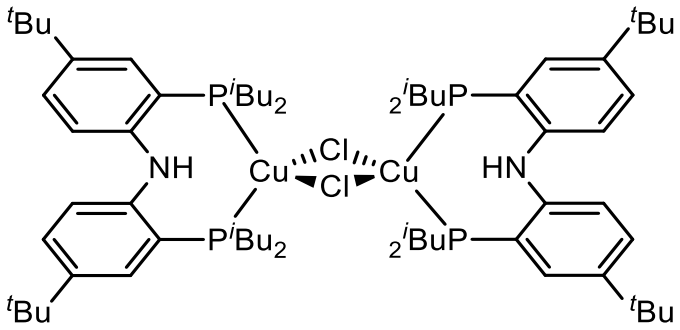

In a glovebox, H-PNP^{tBu} (50 mg, 1 eq) and copper(I) chloride (8.7 mg, 1 eq) were combined in tetrahydrofuran (1 mL) and stirred for 1 day. The solution remained colorless. The solution was concentrated and triturated with pentane prior to being dissolved in pentane:tetrahydrofuran (2 mL, 9:1) and filtered through a glass microfilter. After concentration, the product was afforded as a white solid (Yield: 56.1 mg, 96%).

^{1}H NMR (C_6D_6, 400 MHz): δ (ppm) = 10.96 (t, *J* = 11.1 Hz, 1H), 7.47 (q, *J* = 3.3 Hz, 2H), 7.42 (dt, *J* = 8.7, 2.6 Hz, 2H), 7.21 (dd, *J* = 8.6, 2.3 Hz, 2H), 2.06 (m, 8H), 1.80 – 1.64 (m, 4H), 1.11 (d, *J* = 6.3 Hz, 12H), 0.84 (d, *J* = 6.5 Hz, 12H).

^{31}P NMR (C_6D_6, 162 MHz): δ (ppm) = −42.5 (s).

MS (FD, *m/z*): $[M]^+$ calculated: 1334.65221, found: 1334.65070.

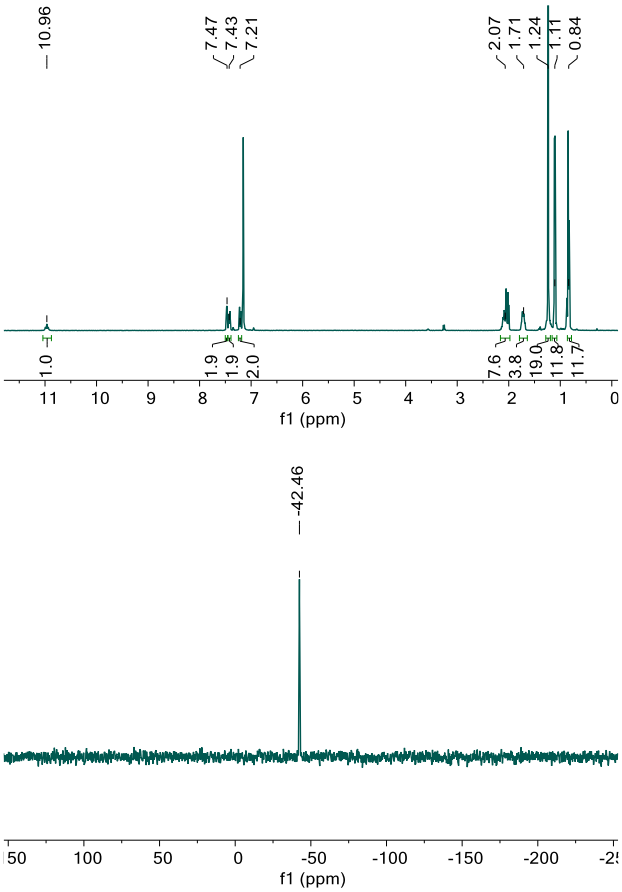

Figure A12. ^{1}H (left) and ^{31}P (right) NMR spectra for chloro-diamond in C_6D_6.

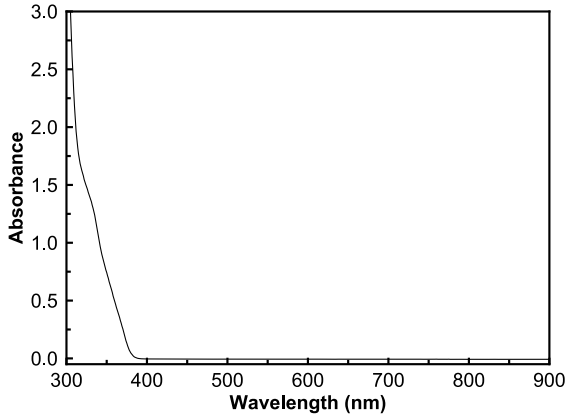

Figure A13. UV-vis absorption spectrum for 120 μM chloro-diamond in DME.

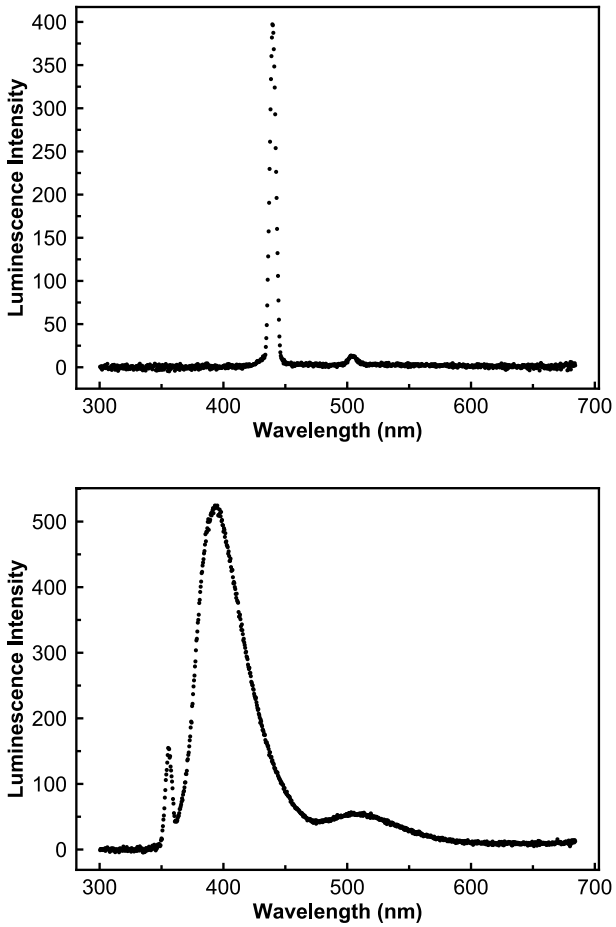

Figure A14. Emission spectra for 120 μM chloro-diamond in DME with excitation at 440 nm (left) or 355 nm (right).

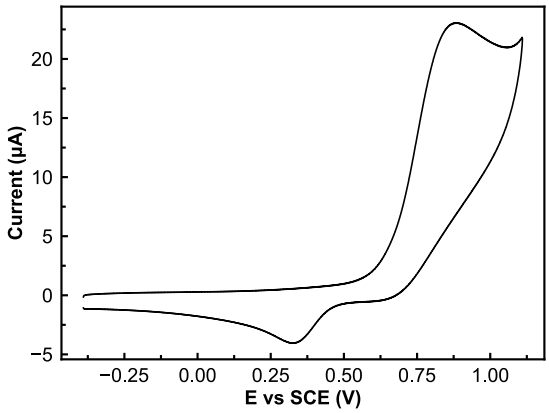

Figure A15. Cyclic voltammogram for ~1 mM chloro-diamond in DME with 0.2 M LiNTf2 supporting electrolyte, GC working, Pt counter, and Ag/AgOTf reference electrodes. Scan rate: 100 mV/s.

A.7 X-ray crystallography of chloro-cubane and chloro-diamond

The structures for chloro-cubane and chloro-diamond (see Figure 2 of maintext) were obtained in a single crystal containing each independent molecule. Due to the limited quality of the data obtained we do not provide detailed discussion of bond metrics. Still, the structures obtained corroborate their assignments and are of value to the discussion in the maintext.

Chloro-cubane and chloro-diamond crystallize together in the monoclinic space group $P2_1/c$ with one molecule each in the asymmetric unit. The structure was strongly disordered (see refinement details below). The program PLATON[7] revealed the presence of large voids which were not able to be refined, and the program SQUEEZE[8] was used to remove the contribution of the disordered electron density inside this void from the structure factors.

Whole molecule disorder was modeled for chloro-cubane. All non-hydrogen atoms were refined anisotropically. All hydrogen atoms were included into the model at geometrically calculated positions and refined using a riding model. Although hydrogen atoms bound to the diphenylamine nitrogens were not located in the difference map, their presence was experimentally corroborated by high-res mass spec and ^{1}H NMR. The isotropic displacement parameters of all hydrogen atoms were fixed to 1.2 times the *U* value of the atoms they are linked to (1.5 times for methyl groups). All disordered atoms were refined with the help of similarity restraints on the 1,2- and 1,3-distances. All atoms were refined with the help of similarity restraints on the displacement parameters as well as rigid bond restraints for anisotropic displacement parameters.

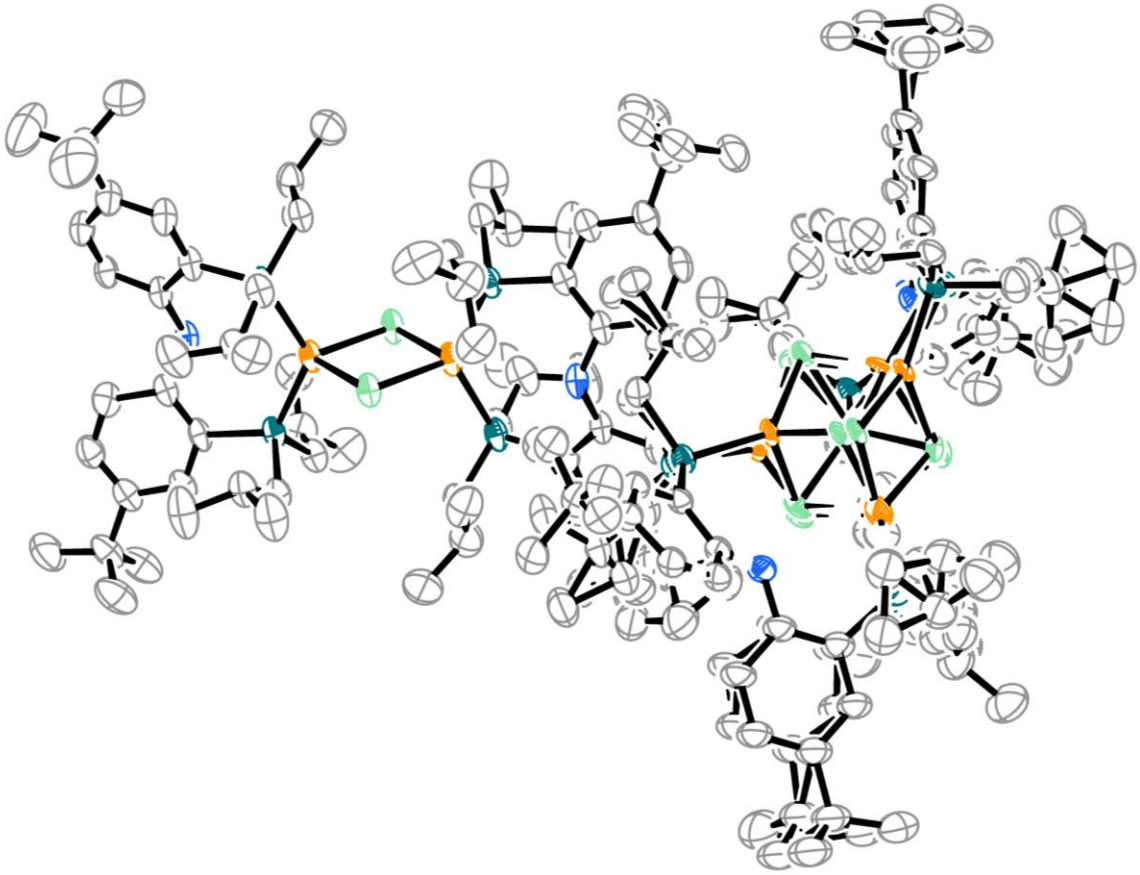

Figure A16. Solid-state structure of cocrystallized chloro-cubane and chloro-diamond with thermal ellipsoids shown at 50%. Hydrogen-atoms are not shown for clarity. The whole molecule disorder model for chloro-cubane is shown.

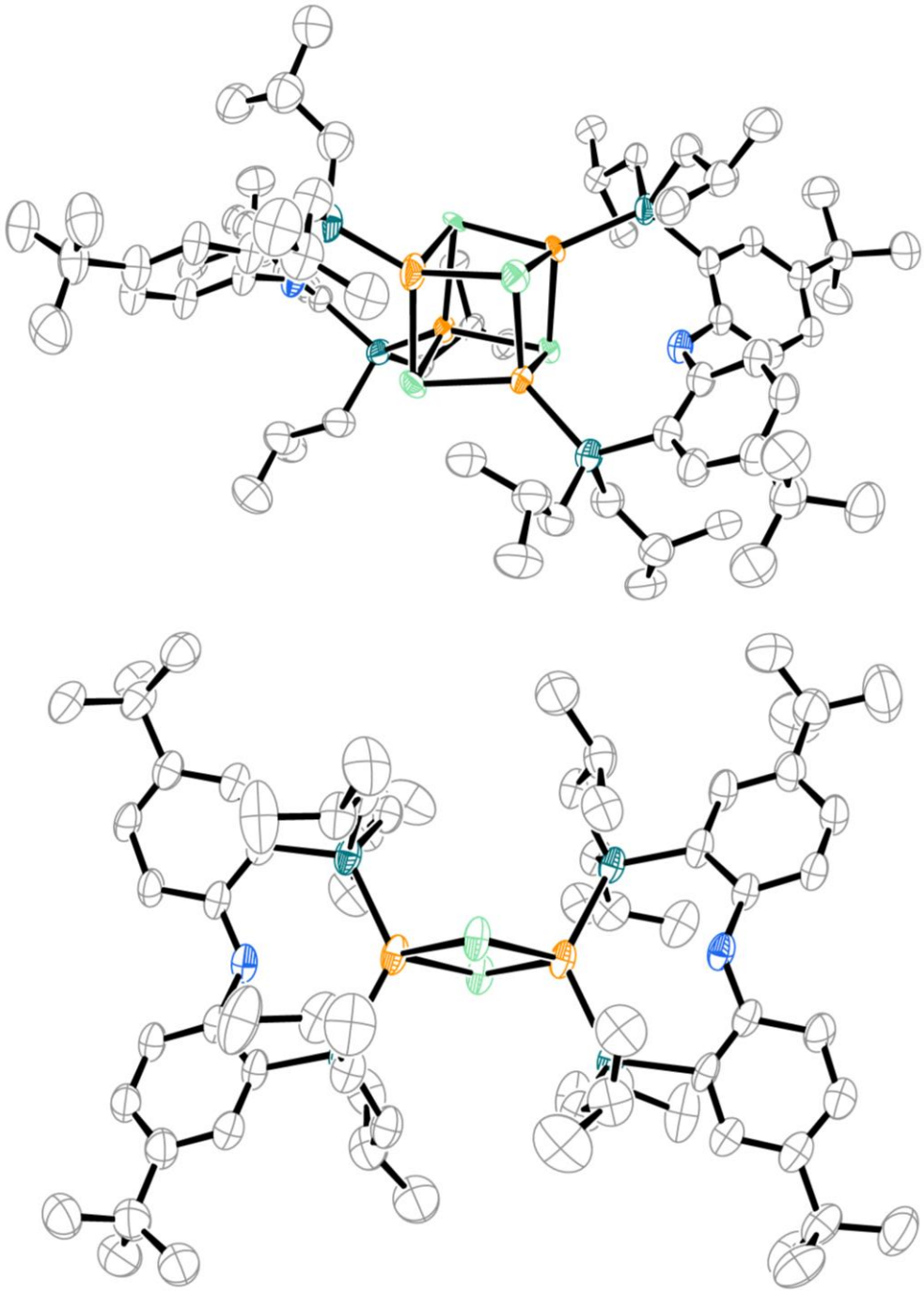

Figure A17. Solid-state structures of chloro-cubane (top) and chloro-diamond (bottom) extracted from the cocrystalline structure with thermal ellipsoids shown at 50%. Hydrogen-atoms are not shown for clarity. Only one of the two disordered sites is shown for chloro-cubane for clarity.

A.8 NMR and luminescence data of irradiated reaction mixtures

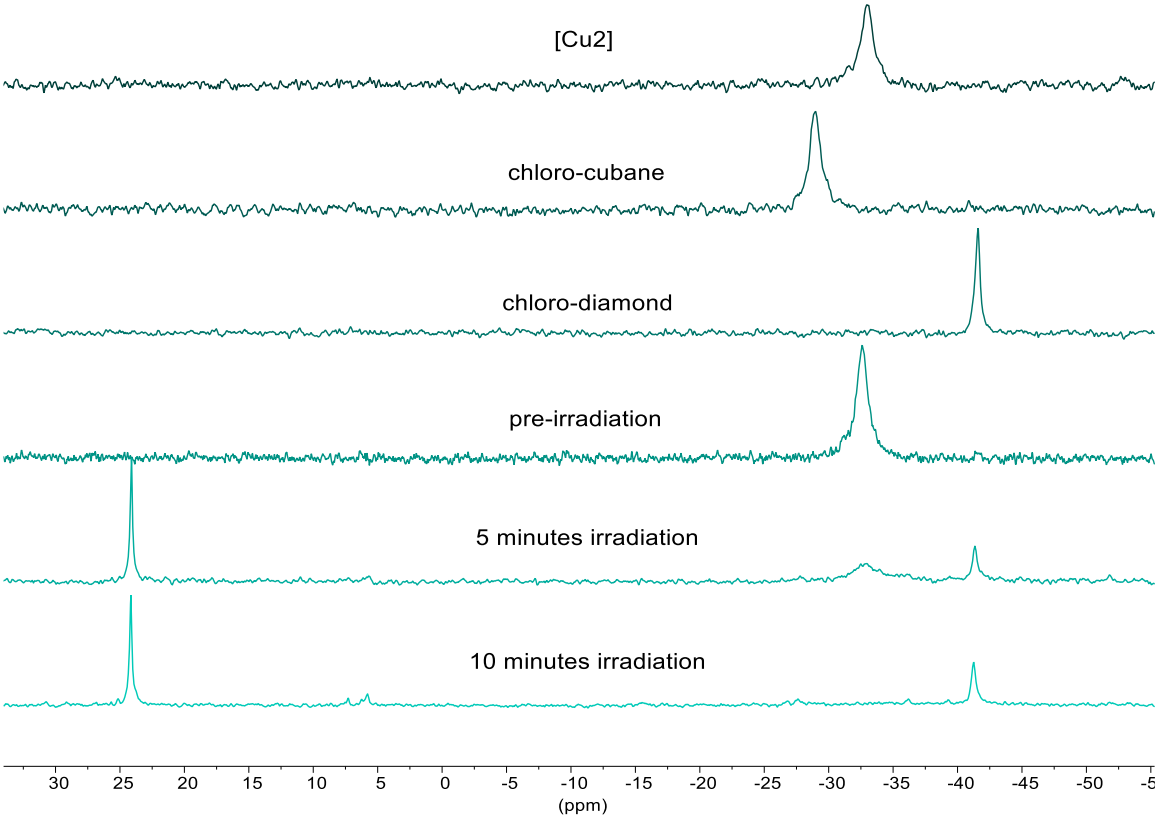

Figure A18. ^{31}P NMR spectra recorded in DME. The top three spectra are for isolated [Cu_2], chloro-cubane, and chloro-diamond. The bottom three spectra correspond to an NMR experiment containing [Cu_2] in the presence of 30 equivalents of 4-methylbenzyl chloride. Pre-irradiation, only starting material is observed. After 5 minutes of 440 nm irradiation, an unknown peak at 24.5 ppm, starting material, and chloro-diamond are observed. After 10 minutes, the unknown 24.5 ppm peak and chloro-diamond are the major phosphorus containing diamagnetic products.

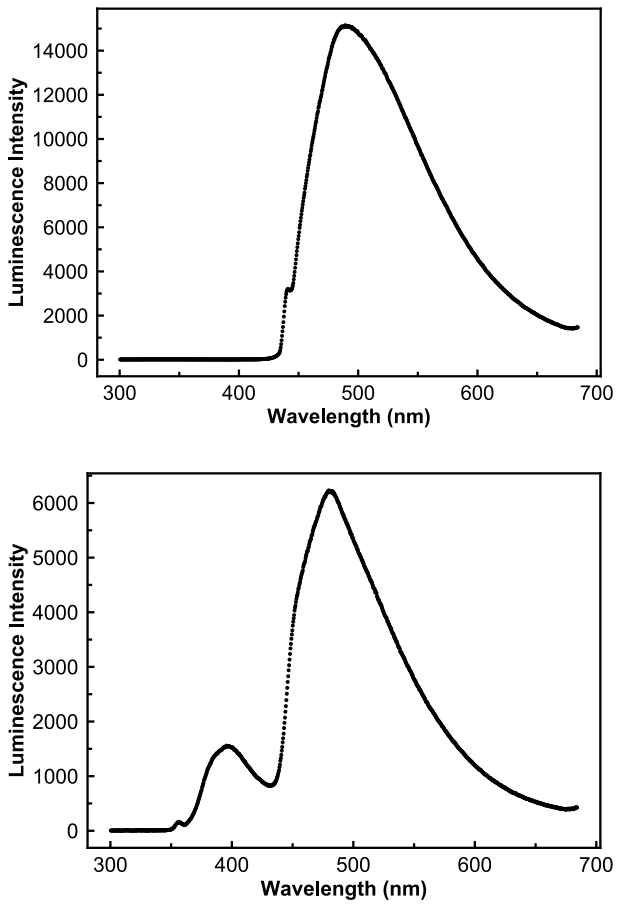

Figure A19. Emission spectra for a solution of 160 μM [Cu_2] in DME with 30 equivalents 4-methylbenzyl chloride after 440 nm irradiation for 5 minutes. Excitation was performed at 440 nm (left) or 355 nm (right).

A.9 Kinetics data for interaction of chloride and $[Cu_2]^+$

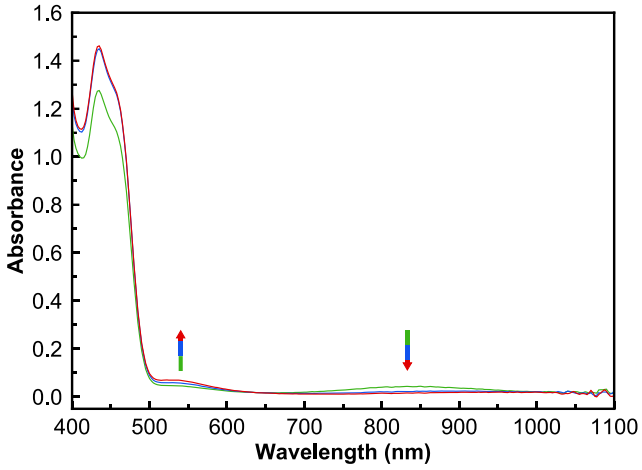

Figure A20. UV-vis traces for a mixture of $[Cu_2]^+$ (560 µM) and tetrabutylammonium chloride (5.6 mM, 10 eq) in DME at 30 s (green), 60 s (blue), and 90 s (red) at room temperature. Loss of $[Cu_2]^+$ absorbances is almost instantaneous upon mixing; thus, under these conditions, kinetics measurements were not possible due to the rapid rate of the reaction. Note that no change is observed over at least 1 hour for UV-vis spectra of $[Cu_2]^+$ in DME in the absence of tetrabutylammonium chloride.

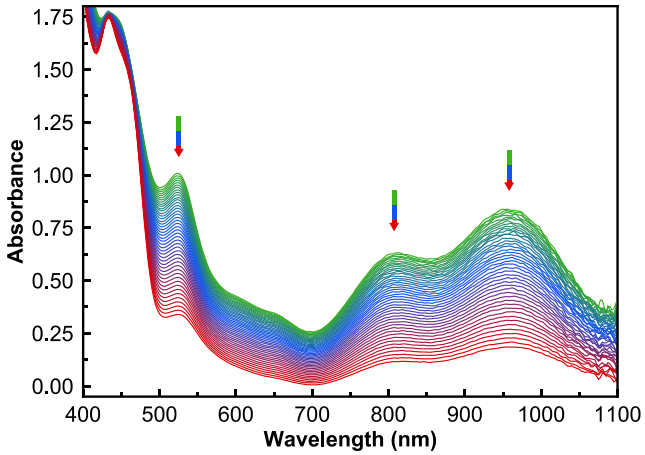

Figure A21. UV-vis traces for a mixture of $[Cu_2]^+$ (560 µM) and tetrabutylammonium chloride (5.6 mM, 10 eq) in DME with 0.2 M $LiNTf_2$ at 30 s intervals (green to blue to red) at room temperature.

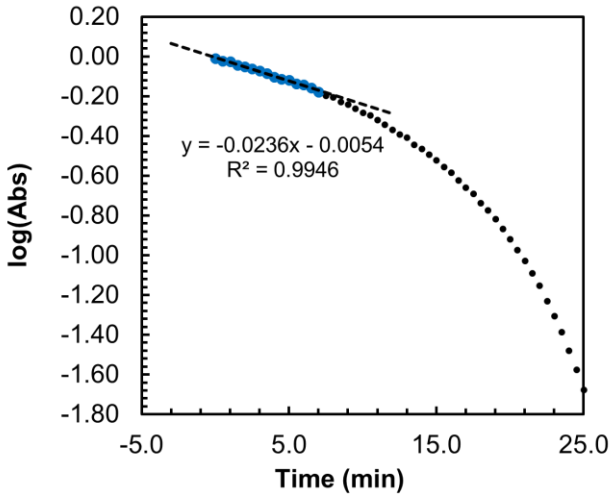

Figure A22. Kinetic trace monitoring absorbance at 958 nm versus time for a mixture of $[Cu_2]^+$ (560 µM) and tetrabutylammonium chloride (5.6 mM, 10 eq) in DME with 0.2 M $LiNTf_2$ at room temperature. The linear initial rate (highlighted as blue points) observed in the plot of log(Abs) versus time is characteristic of a first-order process.

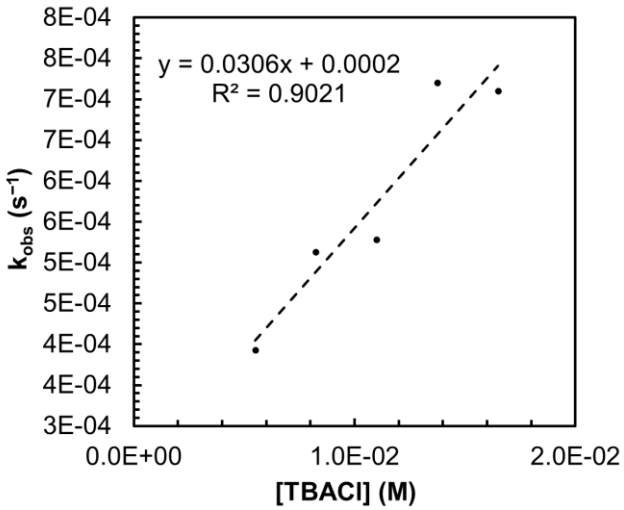

Figure A23. Analysis of the reaction rate for $[Cu_2]^+$ (560 µM) and tetrabutylammonium chloride (TBACl; 10–30 eq) in DME with 0.2 M $LiNTf_2$ at room temperature. A linear relationship between k_{obs} and TBACl concentration is observed.

A.10 Controlled potential coulometry procedures

General Procedure: In a glovebox, 4 mL of 1,2-dimethoxyethane solution containing lithium bis(trifluoromethane)sulfonimide electrolyte (0.2 M) is added to each side of an oven-dried two compartment (H-type) cell equipped with a fine porosity glass frit. The anode side is equipped with a coiled magnesium ribbon (3 mm x 0.2 mm x 5 cm) counter electrode. Prior to use, the magnesium electrode is rinsed with dilute (~1 M) HCl, water, and acetone. The 1,2-dimethoxyethane solution from the cathode side is used to transfer the benzyl chloride electrophile (0.15 mmol) and [Cu_2] photoredox catalyst (2.8 mg, 1.5 mol %) into the cathode compartment. The cathode compartment is fitted with a carbon cloth working electrode and Ag/AgOTf reference electrode.

The cell is removed from the glovebox, a nitrogen line is fitted, a fan is directed toward the cell, and the electrodes are connected to a potentiostat. The cell is polarized to a constant potential of −0.15 V vs SCE and a 440 nm Kessil lamp (Kessil PR160, intensity 50) placed 3 inches from the cathode compartment is turned on.

After ~1 h, a second portion of [Cu_2] photoredox catalyst (2.8 mg, 1.5 mol %) is transferred via syringe to the cell using an additional 0.2 mL of 1,2-dimethoxyethane solution containing lithium bis(trifluoromethane)sulfonimide electrolyte (0.2 M). This was found to increase yields by ~10% as compared to adding all of the catalyst in the beginning.

When the current decreases to ~5% of the initial current (1.5–3 hours), the lamp is turned off and the cell is disconnected from the potentiostat. The working and reference electrodes are removed from the cell and rinsed into the cell with 1,2-dimethoxyethane. The

solution from the cathode compartment is removed and concentrated on a rotary evaporator. Once concentrated, drying under high vacuum (<1 torr) is critical to reduce the 1,2-dimethoxyethane content as 1,2-dimethoxyethane can coordinate lithium bis(trifluoromethane)sulfonimide and facilitate its passage through chromatography media. This residue is dissolved in ethanol-free chloroform and eluted through a plug of neutral alumina to remove the lithium bis(trifluoromethane)sulfonimide electrolyte. Dichloromethane better solubilizes lithium bis(trifluoromethane)sulfonimide and should not be used. The eluant is concentrated and transferred to an NMR tube using $CDCl_3$. Dibromomethane (5 µL) is added as an internal standard, and a one-pulse ^1H qNMR spectrum is acquired.

Graphical Procedure:

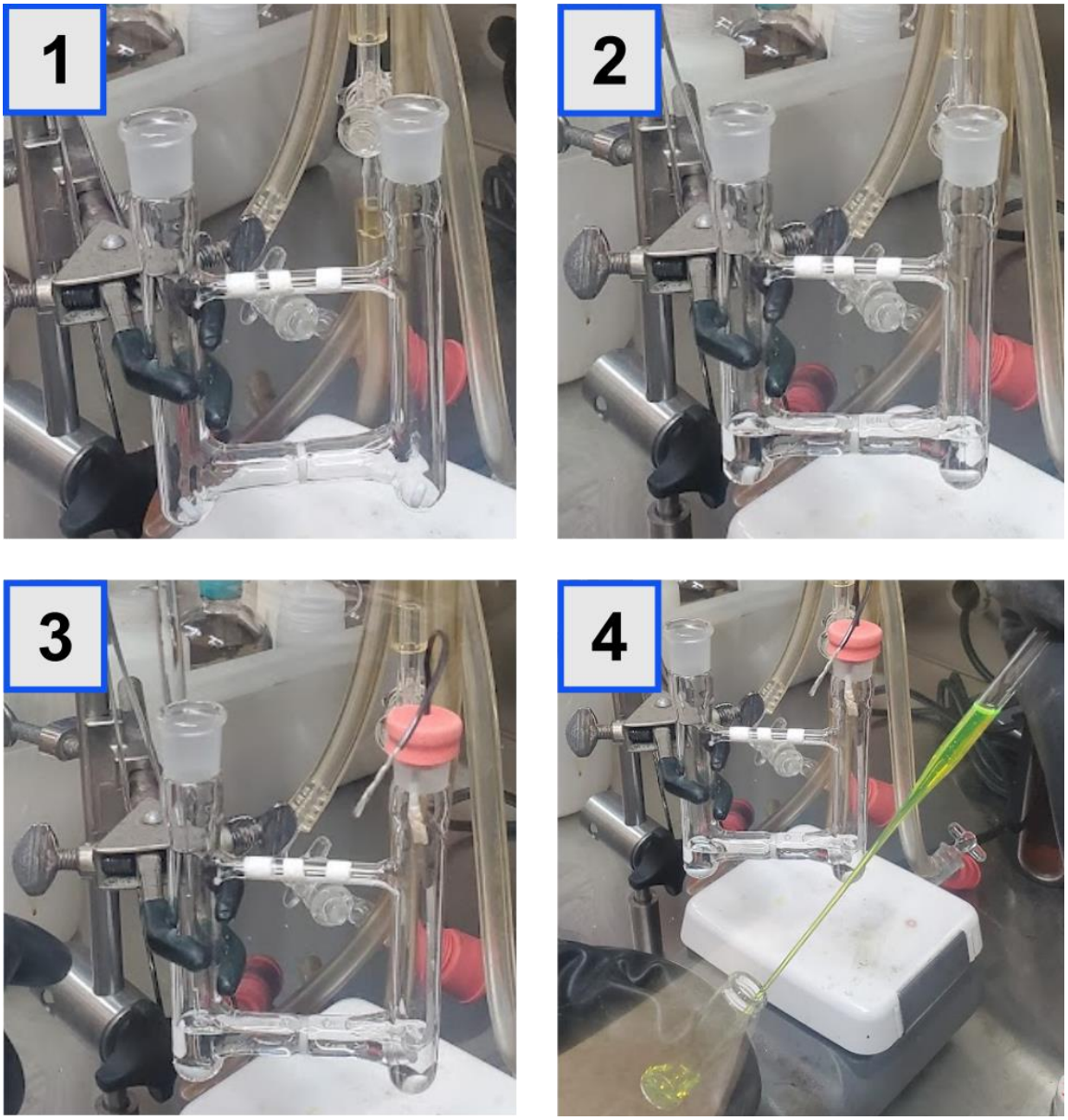

1. Place empty, oven-dried two compartment cell in glovebox.
2. Fill each compartment with 4 mL of 0.2 M $LiNTf_2$ in 1,2-dimethoxyethane (DME).
3. Fit counter electrode compartment with magnesium coil electrode.
4. Dissolve [Cu_2] in working electrode compartment using the DME electrolyte solution.

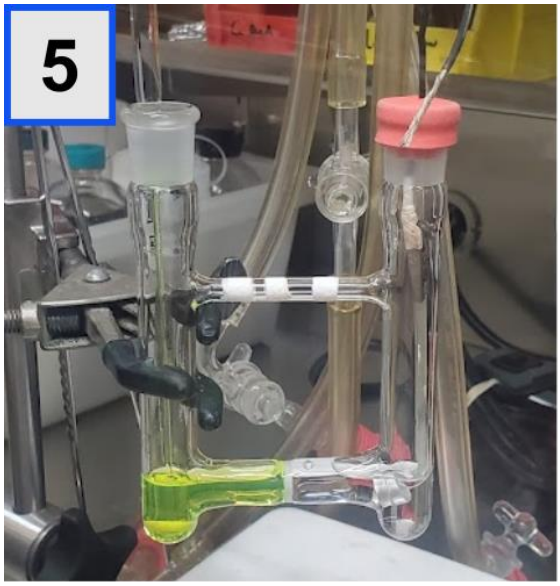

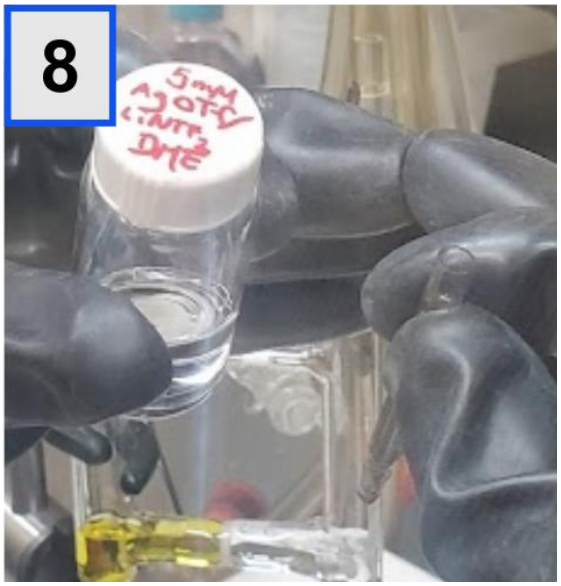

5. Transfer [Cu_2] solution into working electrode compartment.
   At this stage, the rest of the steps are performed with the lights off (lights left on here for clarity).

6. Dissolve benzyl chloride electrophile using working electrode compartment solution.

7. Transfer electrophile solution into working electrode compartment.

8. Fill reference electrode shell with 5 mM Ag^+ solution.

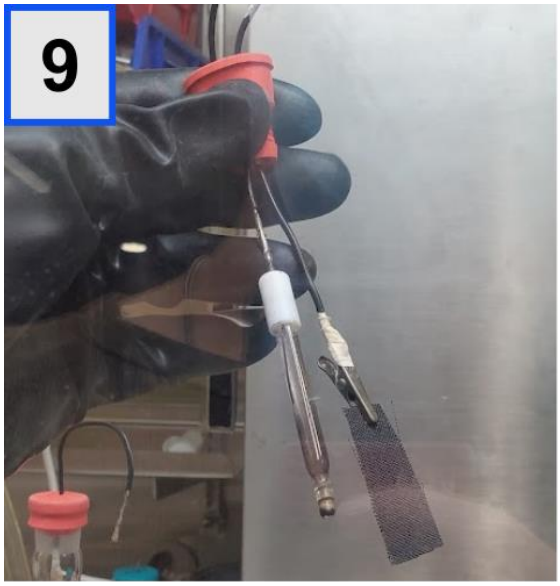

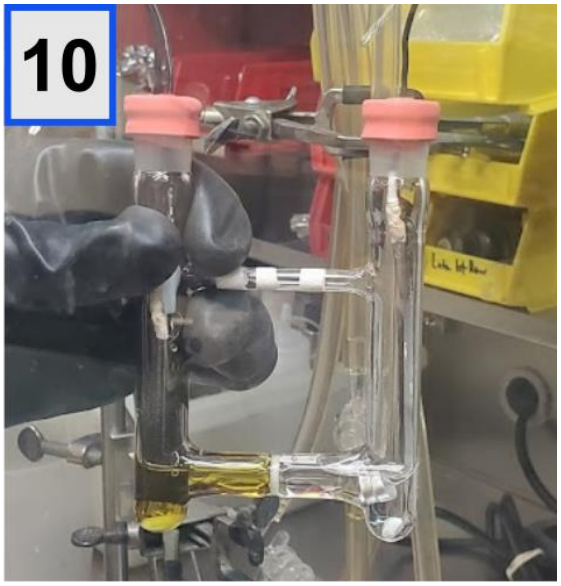

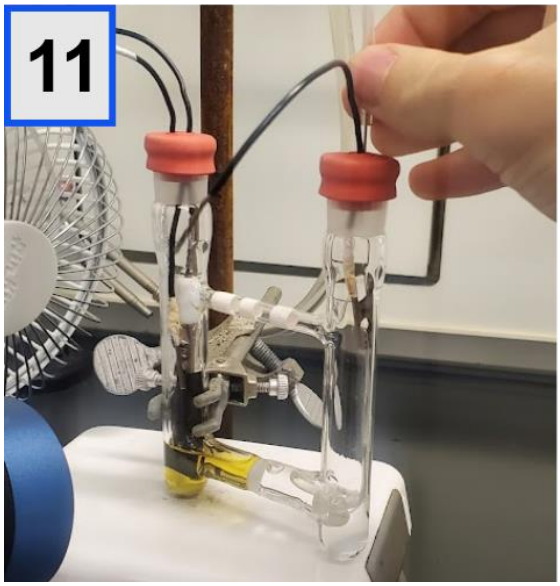

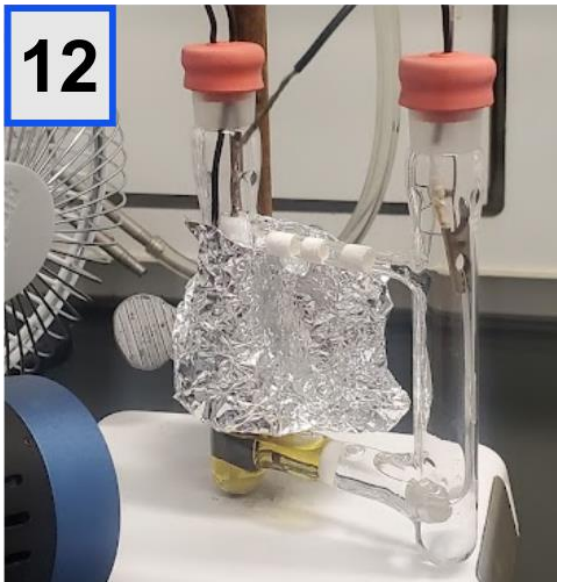

9. Fit reference electrode shell to wire cap; carbon cloth working electrode shown on right hand side.
10. Fit working and reference electrodes into working electrode compartment.
11. Remove cell from glovebox and insert nitrogen inlet through septum.
12. Protect upper part of reference electrode with aluminum foil (Ag^+ is light sensitive).

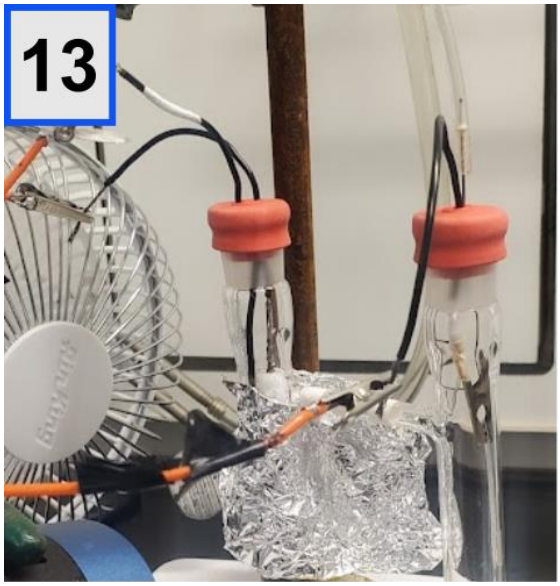

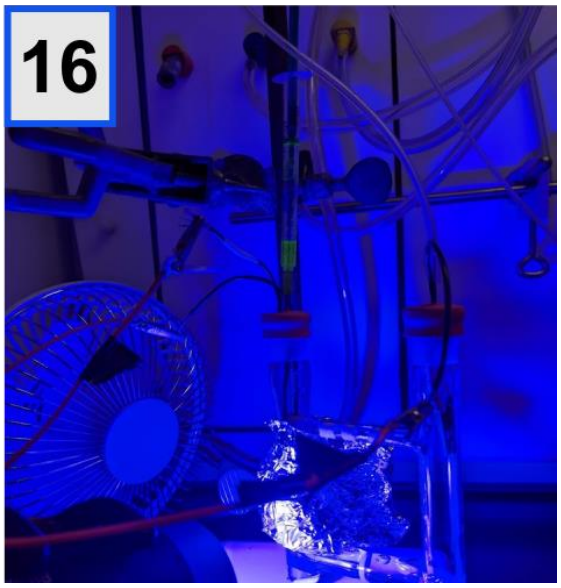

13. Attach electrode leads to working, reference, and counter electrode wires.
14. Apply a potential of −0.15 V vs SCE and irradiate reaction (440 nm).
15. After ~1 hour (when current has decreased ~75%), in a glovebox, dissolve the second catalyst portion in ~0.3 mL of 0.2 M $LiNTf_2$ in DME and transfer it to a syringe.
16. Remove the syringe from the glovebox and add the catalyst solution to the working electrode compartment.

A.11 Controlled potential coulometry traces

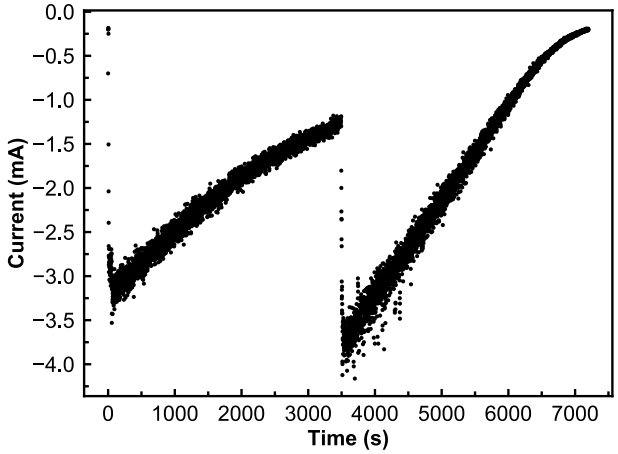

Figure A24. Current trace for a representative catalytic controlled potential coulometry experiment. Notice the increase in current in the first 5 seconds; the light is turned on after 5 seconds. At ~3600 seconds, the second portion of [Cu_2] is added, and an increase in current is observed.

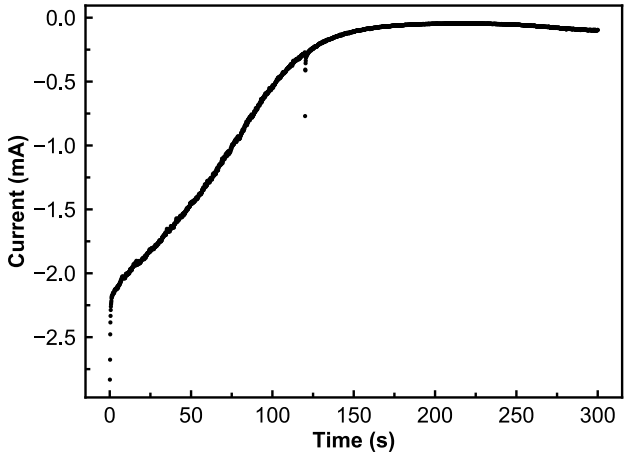

Figure A25. Current trace for the catalyst regeneration experiment described in the main text. After irradiating (440 nm) a solution of [Cu_2] and 4-methylbenzyl chloride in DME containing 0.2 M $LiNTf_2$ for 5 minutes, the solution was reduced at a carbon cloth electrode at −0.15 V vs SCE. The charge passed corresponds to 0.8 e^- per [Cu_2] equivalent.

A.12 Open circuit potential during irradiation

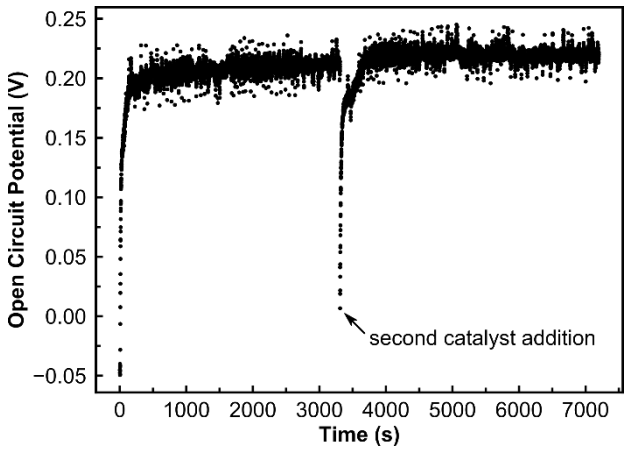

Figure A26. Open circuit potential (OCP) measurement for the control experiment in which no potential was applied in the presence of both catalyst and light (Scheme 5, Entry 4). Notice that the effective reaction rate can be intuited from the rapid decrease in OCP over the period of ~150 s at time = 0 s and time ~ 3200 s, corresponding to the beginning of the reaction and the addition of a second [Cu_2] catalyst portion, respectively.

A.13 Speciation after controlled potential coulometry

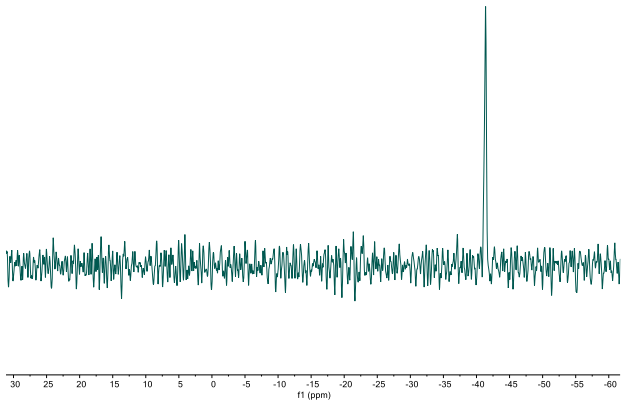

Figure A27. ^{31}P NMR spectrum of a crude reaction mixture post controlled potential coulometry. The reaction mixture was transferred from the two-compartment electrochemical cell into an NMR tube using inert-atmosphere syringe techniques. The chemical shift is that of chloro-diamond.

A.14 qNMR yields and isolated NMR spectra for catalytic experiments

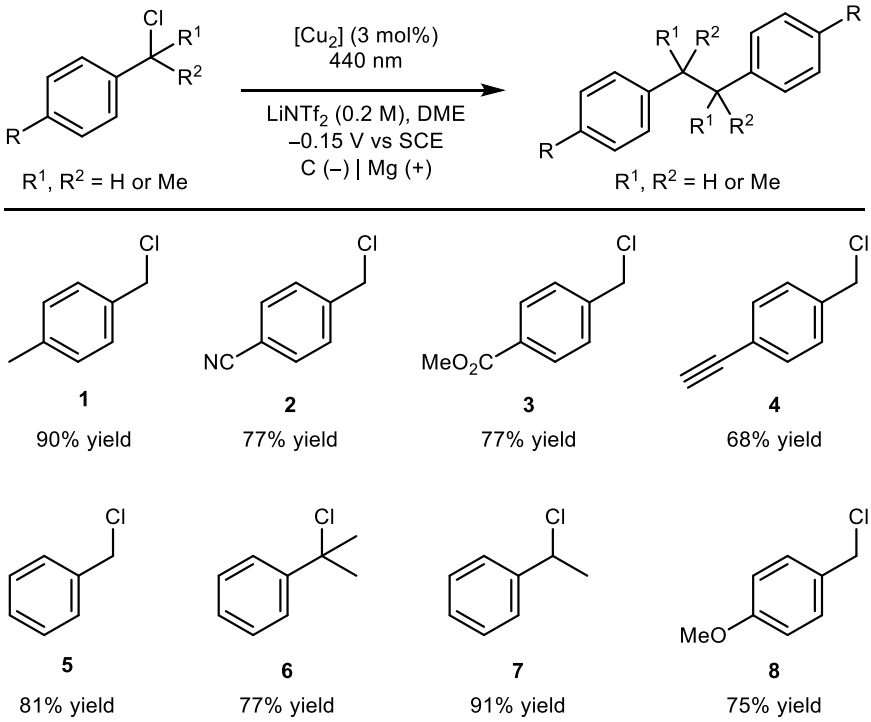

Figure A28. Electro-photocatalytic reduction of substituted benzyl chlorides featuring various substituents. NMR yields for the average of two runs are reported.

References for reported NMR characterization data

Substrates	Ref
1, 2, 5, 7	9
3, 8	10
6	11
4	12

1-D (1,2-di-*p*-tolylethane)

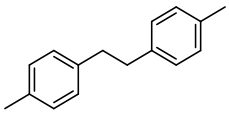

The general procedure from A.10 was used, employing 4-methylbenzyl chloride (21.1 mg, 0.15 mmol) as the electrophile. The reaction was worked up after 2 hours (89% NMR yield, 90% FE) and purified via column chromatography using ethyl acetate:hexane (0:1 to 1:100) as eluant to afford the product as a white solid (14.4 mg, 91%). TLC plates were visualized with ceric ammonium molybdate (blue spot; hexane, R_f = 0.4). Spectroscopic data was consistent with reported data.[9]

^{1}H NMR (qNMR left, isolated right):

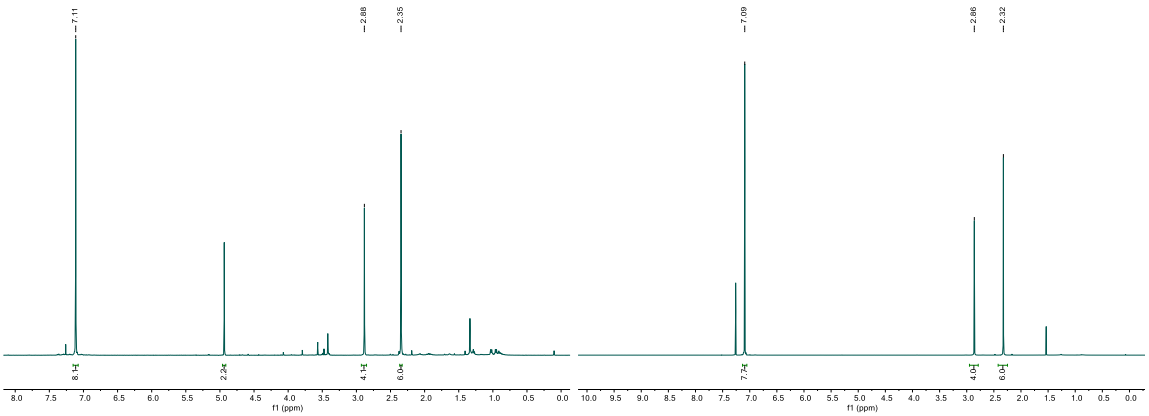

^{13}C{^{1}H} NMR:

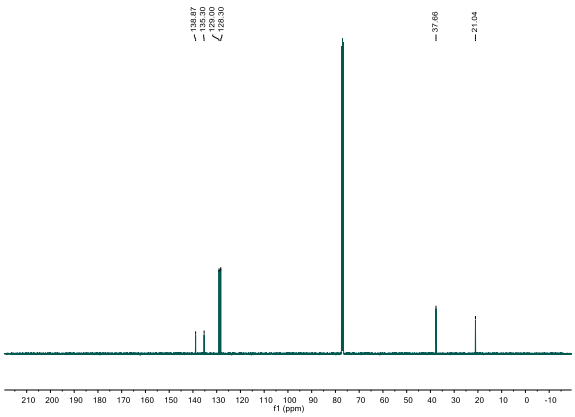

2-D (4,4'-(ethane-1,2-diyl)dibenzonitrile)

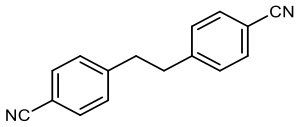

The general procedure from A.10 was used, employing 4-cyanobenzyl chloride (22.7 mg, 0.15 mmol) as the electrophile. The reaction was worked up after 1.5 hours (74% NMR yield, 78% FE) and purified via column chromatography using dichloromethane as eluant to afford the product as a white solid (12.7 mg, 74%). TLC plates were visualized by UV (dichloromethane, R_f = 0.4). Spectroscopic data was consistent with reported data.[9]

^{1}H NMR (qNMR left, isolated right):

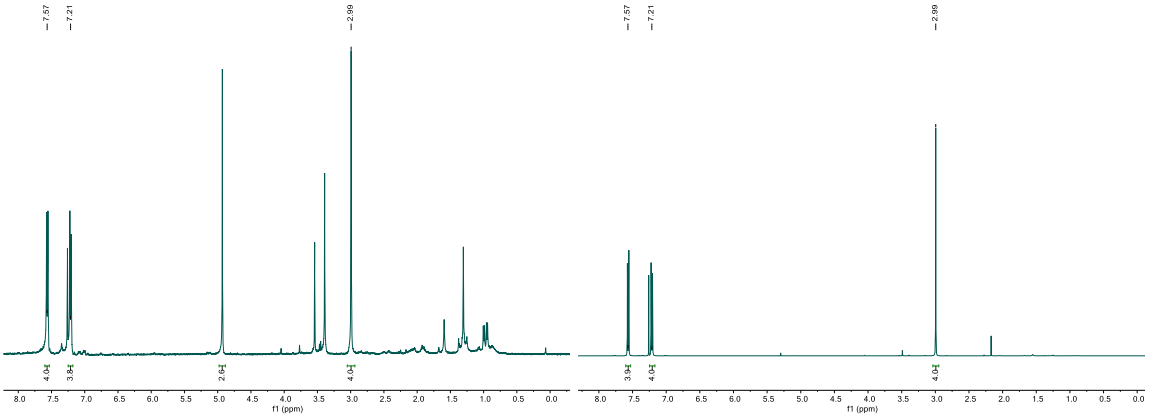

^{13}C{^{1}H} NMR:

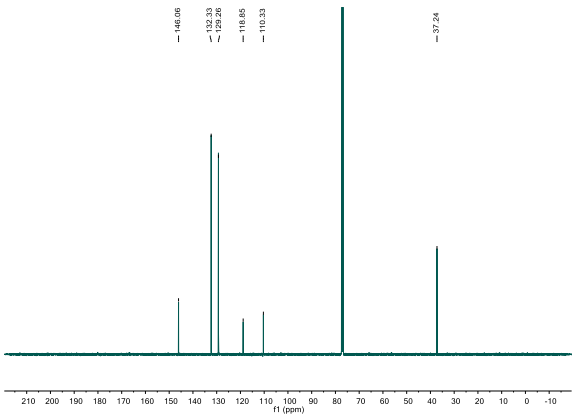

3-D (dimethyl 4,4'-(ethane-1,2-diyl)dibenzoate)

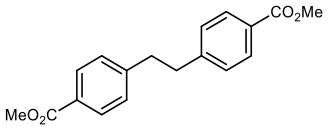

The general procedure from A.10 was used, employing methyl 4-(chloromethyl)benzoate (27.7 mg, 0.15 mmol) as the electrophile. The reaction was worked up after 2.5 hours (76% NMR yield, 78% FE) and purified via column chromatography using ethyl acetate:hexane (1:9 to 1:4) as eluant to afford the product as a white solid (16.5 mg, 74%). TLC plates were visualized by UV (ethyl acetate:hexane (1:9), R_f = 0.2). Spectroscopic data was consistent with reported data.[10]

^{1}H NMR (qNMR left, isolated right):

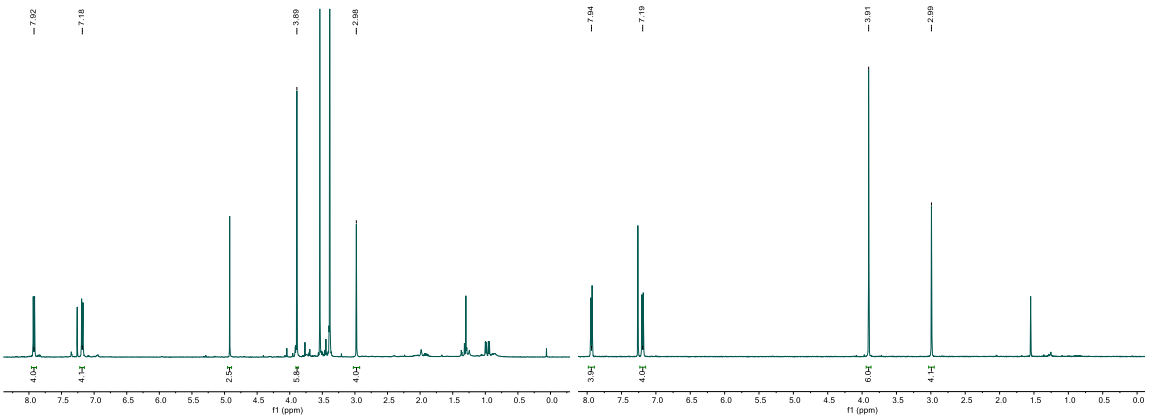

^{13}C{^{1}H} NMR:

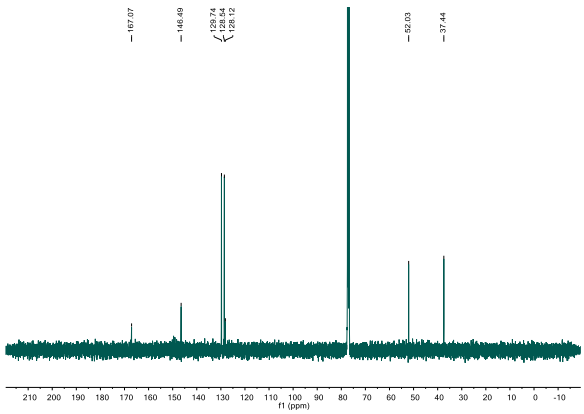

4-D (1,2-bis(4-ethynylphenyl)ethane)

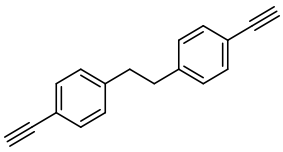

The general procedure from A.10 was used, employing 1-(chloromethyl)-4-ethynylbenzene (22.6 mg, 0.15 mmol) as the electrophile. The reaction was worked up after 1.5 hours (73% NMR yield, 77% FE) and purified via column chromatography using ethyl acetate:hexane (2:98) as eluant to afford the product as a white solid (12.6 mg, 73%). TLC plates were visualized by UV (ethyl acetate:hexane (2:98), R_f = 0.4). Spectroscopic data was consistent with reported data.[12]

^{1}H NMR (qNMR left, isolated right):

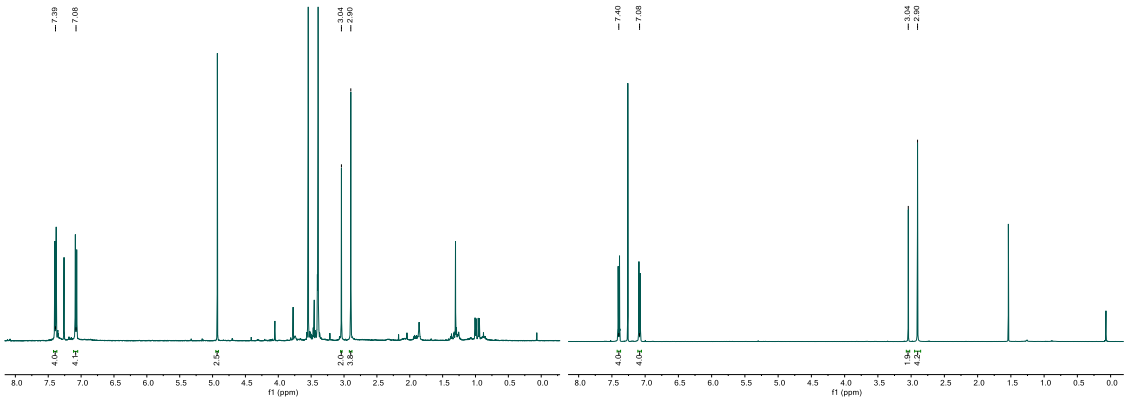

^{13}C{^{1}H} NMR:

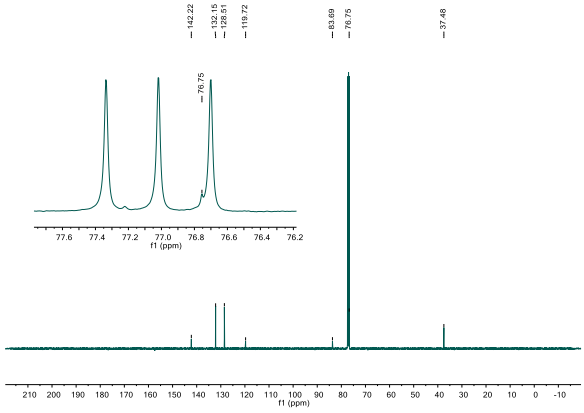

5-D (1,2-diphenylethane)

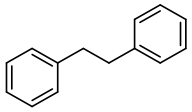

The general procedure from A.10 was used, employing benzyl chloride (19.0 mg, 0.15 mmol) as the electrophile. The reaction was worked up after 2 hours (82% NMR yield, 84% FE) and purified via column chromatography using ethyl acetate:hexane (0:1 to 1:100) as eluant to afford the product as a white solid (11.0 mg, 80%). TLC plates were visualized with ceric ammonium molybdate (blue spot; hexane, R_f = 0.4). Spectroscopic data was consistent with reported data.[9]

^{1}H NMR (qNMR left, isolated right):

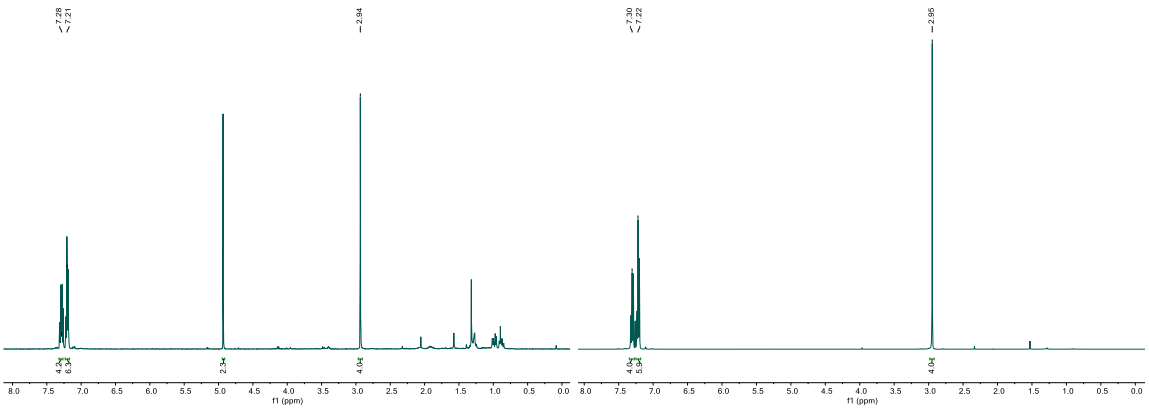

^{13}C{^{1}H} NMR:

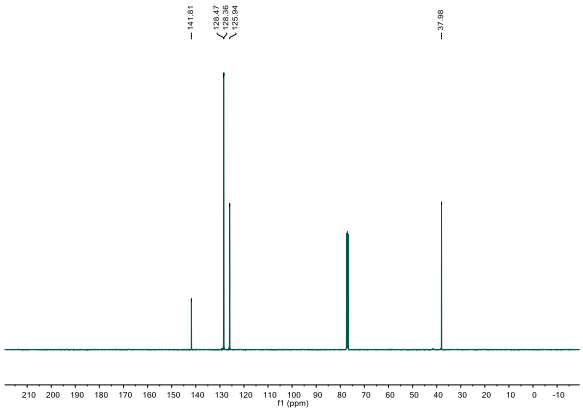

6-D (2,3-dimethyl-2,3-diphenylbutane)

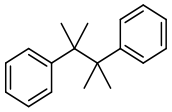

The general procedure from A.10 was used, employing (1-chloro-1-methylethyl)benzene (23.2 mg, 0.15 mmol) as the electrophile. The reaction was worked up after 1.5 hours (79% NMR yield, 99% FE) and purified via column chromatography using hexane as eluant to afford the product as a white solid (15.5 mg, 87%). TLC plates were visualized with ceric ammonium molybdate (blue spot; hexane, R_f = 0.4). Spectroscopic data was consistent with reported data.[13]

^{1}H NMR (qNMR left, isolated right):

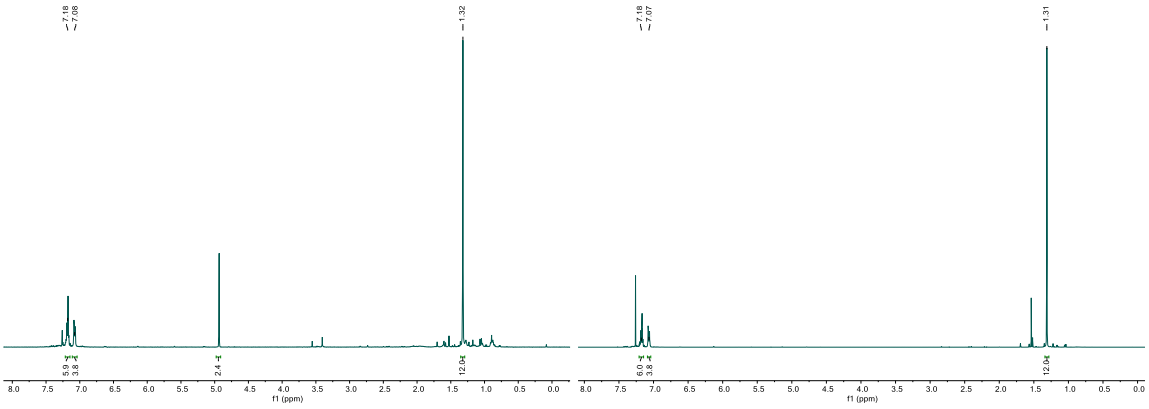

^{13}C{^{1}H} NMR:

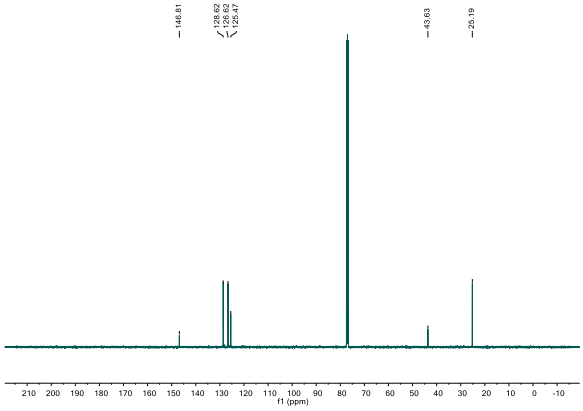

7-D (2,3-diphenylbutane)

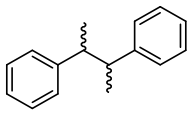

The general procedure from A.10 was used, employing (1-chloroethyl)benzene (21.1 mg, 0.15 mmol) as the electrophile. The reaction was worked up after 2 hours (92% NMR yield, 96% FE) and purified via column chromatography using hexane as eluant to afford the product as a white solid (12.2 mg, 77%). The product was isolated as an approximately equimolar mixture of diastereomers. TLC plates were visualized with ceric ammonium molybdate (blue spot; hexane, R_f = 0.4). Spectroscopic data was consistent with reported data.[9]

^{1}H NMR (qNMR left, isolated right):

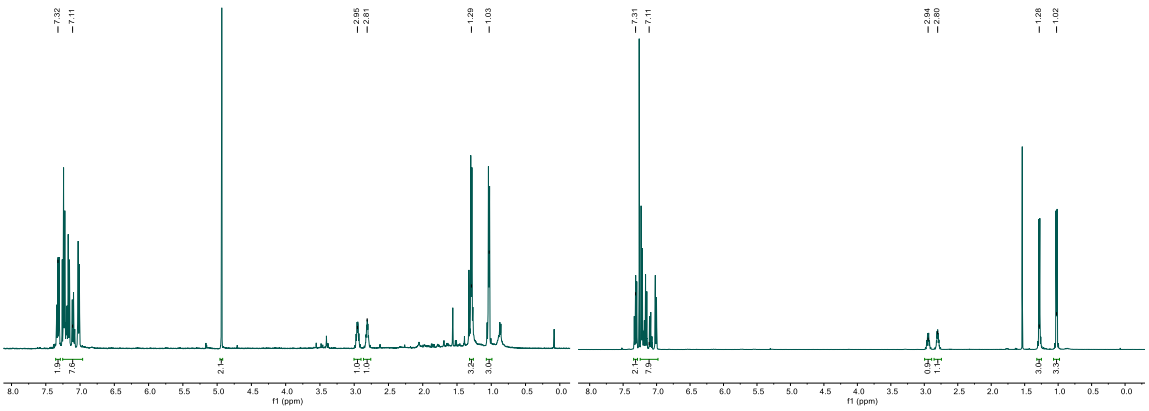

^{13}C{^{1}H} NMR:

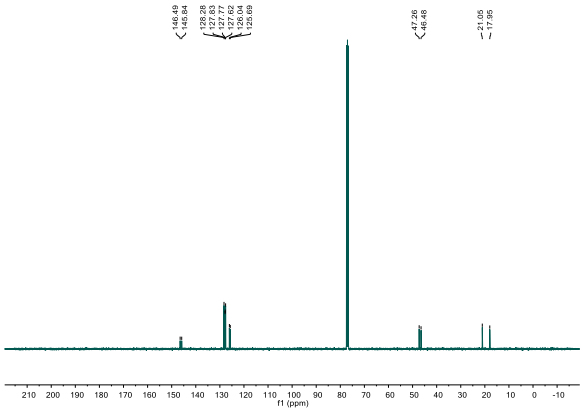

8-D (1,2-bis(4-methoxyphenyl)ethane)

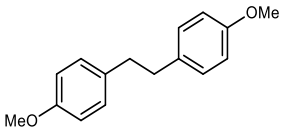

The general procedure from A.10 was used, employing 4-methoxybenzyl chloride (23.5 mg, 0.15 mmol) as the electrophile. The reaction was worked up after 2.5 hours (79% NMR yield, 93% FE) and purified via column chromatography using ethyl acetate:hexane (1:20) as eluant to afford the product as a white solid (14.3 mg, 79%). TLC plates were visualized with ceric ammonium molybdate (blue spot; ethyl acetate:hexane (1:20)), $R_f = 0.3$). Spectroscopic data was consistent with reported data.[10]

^{1}H NMR (qNMR left, isolated right):

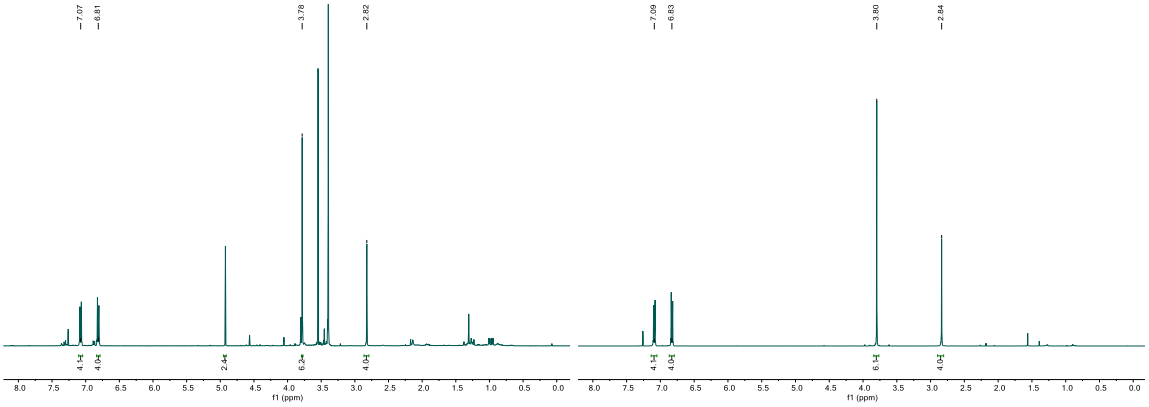

^{13}C{^{1}H} NMR:

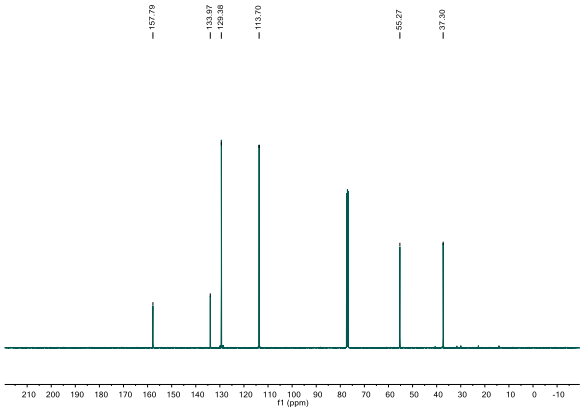

A.15 Synthesis and characterization of known electrophiles

1-(chloromethyl)-4-ethynylbenzene

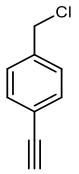

This compound was made by following a literature procedure,[14] and its spectroscopic data is consistent with reported data.[15]

^{1}H NMR:

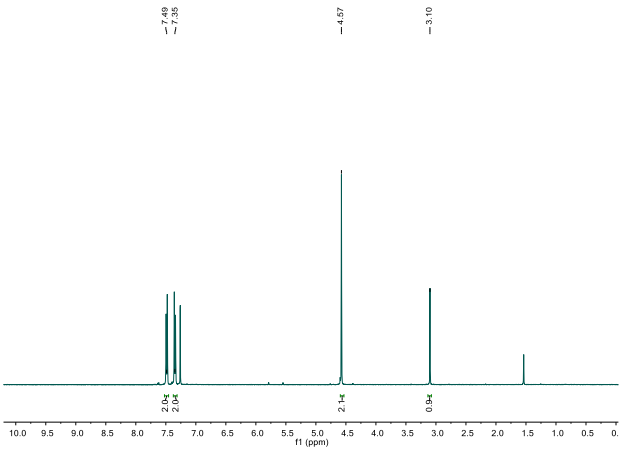

^{13}C{^{1}H} NMR:

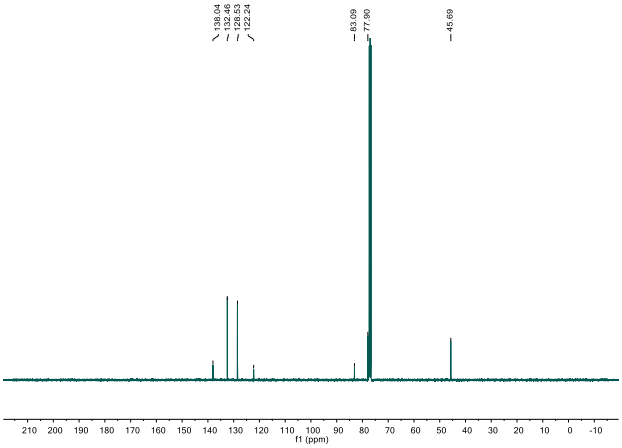

2-chloro-2-phenylpropane

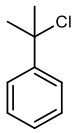

This compound was made by following a literature procedure, and its spectroscopic data is consistent with reported data.[16]

^{1}H NMR:

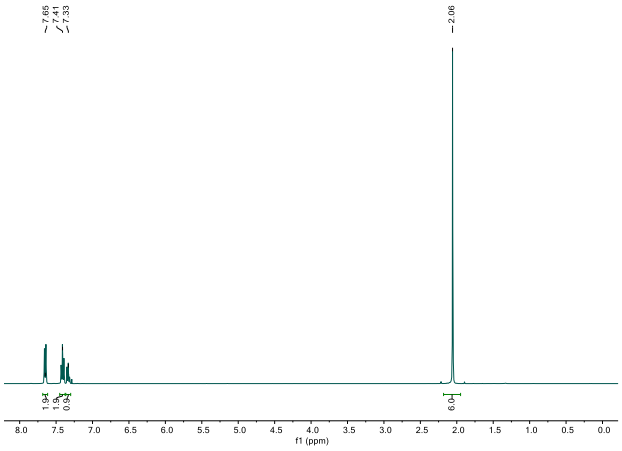

^{13}C{^{1}H} NMR:

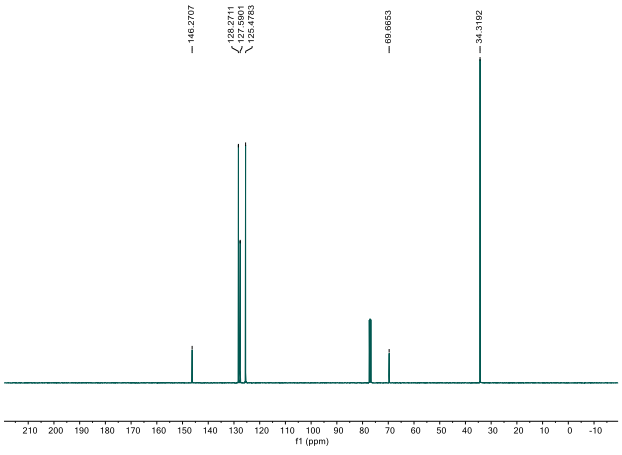

A.16 References

[1] Harkins, S. B.; Mankad, N. P.; Miller, A. J. M.; Szilagyi, R. K.; Peters, J. C. Probing the Electronic Structures of $[Cu_2(\mu\text{-}XR_2)]^{n+}$ Diamond Cores as a Function of the Bridging X Atom (X = N or P) and Charge (*n* = 0, 1, 2). *J. Am. Chem. Soc.* **2008**, *130*, 3478–3485.

[2] Connelly, N. G.; Geiger, W. E. Chemical Redox Agents for Organometallic Chemistry. *Chem. Rev.* **1996**, *96*, 877-910.

[3] Sheldrick, G. SHELXT - Integrated Space-Group and Crystal-Structure Determination. *Acta Crystallogr., Sect. C: Struct.* **2015**, *71*, 3–8.

[4] Dolomanov, O. V.; Bourhis, L. J.; Gildea, R. J.; Howard, J. A. K.; Puschmann, H. OLEX2: a Complete Structure Solution, Refinement and Analysis Program. *J. Appl. Crystallogr.* **2009**, *42*, 339–341.

[5] Eberson, L. *Electron-Transfer Reactions in Organic Chemistry*; Springer-Verlag: Berlin, 1987; p 32.

[6] Rehm, D.; Weller, A. Kinetics of Fluorescence Quenching by Electron and H-Atom Transfer. *Israel J. Chem.* **1970**, *8*, 259–271.

[7] Spek, A. L. Structure Validation in Chemical Crystallography. *Acta Cryst.* **2009**, *D65*, 148–155.

[8] Van der Sluis, P.; Spek, A. L. BYPASS: An Effective Method for the Refinement of Crystal Structures Containing Disordered Solvent Regions. *Acta Cryst.* **1990**, *A46*, 194–201.

[9] Sato, K.; Inoue, Y.; Mori, T.; Sakaue, A.; Tarui, A.; Omote, M.; Kumadaki, I.; Ando, A. Csp^3–Csp^3 Homocoupling Reaction of Benzyl Halides Catalyzed by Rhodium. *Org. Lett.* **2014**, *16*, 3756–3759.

[10] Cao, D.; Li, C.-C.; Zeng, H.; Peng, Y.; Li, C.-J. $C(sp^3)$−$C(sp^3)$ Bond Formation via Nickel-Catalyzed Deoxygenative Homo-Coupling of Aldehydes/Ketones Mediated by Hydrazine. *Nat. Commun.* **2021**, *12*, 3729.

[11] Z.-J. Wang, J.-J. Lv, R.-N. Yi, M. Xiao, J.-J. Feng, Z.-W. Liang, A.-J. Wang, X. Xu. Nondirecting Group sp^3 C−H Activation for Synthesis of Bibenzyls via Homo-coupling as Catalyzed by Reduced Graphene Oxide Supported PtPd@Pt Porous Nanospheres. *Adv. Synth. Catal.* **2018**, *360*, 932–941.

[12] Galán, E.; Perrin, M. L.; Lutz, M.; van der Zant, H. S. J.; Grozema, F. C.; Eelkema, R. Synthesis of 1,2-Biphenylethane Based Single-Molecule Diodes. Org. Biomol. Chem., **2016**, **14**, 2439–2443.

[13] Z.-J. Wang, J.-J. Lv, R.-N. Yi, M. Xiao, J.-J. Feng, Z.-W. Liang, A.-J. Wang, X. Xu. Nondirecting Group sp^3 C−H Activation for Synthesis of Bibenzyls via Homo-coupling as Catalyzed by Reduced Graphene Oxide Supported PtPd@Pt Porous Nanospheres. *Adv. Synth. Catal.* **2018**, *360*, 932–941.

[14] Landgrebe, J. A.; Rynbrandt, R. H. Synthesis and Solvolysis of o-, m-, and p-Ethynylbenzyl Chloride and Closely Related Structures. The Electronic Nature of the Acetylene Group. *J. Org. Chem.* **1966**, *31*, 2585–2593.

[15] Pedersen, P. J.; Henriksen, J.; Gotfredsen, C. H.; Clausen, M. H. Regio- and Stereoselective Hydrosilylation of Immobilized Terminal Alkynes. *Tetrahedron Lett.* **2008**, *49*, 6220–6223.

[16] Ajvazi, N.; Stavber, S. Direct Halogenation of Alcohols with Halosilanes Under Catalyst- and Organic Solvent-Free Reaction Conditions. *Tetrahedron Lett.* **2016**, *57*, 2430–2433.

Appendix B

Supplementary Information for Chapter 3

Adapted from:
Zott, M. D.;‡ Garrido-Barros, P.;‡ Peters, J. C.
ACS Catal. **2019**, *9*, 10101–10108.
DOI: 10.1021/acscatal.9b03499

.

B.1 General Procedures

General Considerations: All manipulations were carried out using standard Schlenk or glovebox techniques under an N_2 or Ar atmosphere. Unless otherwise noted, solvents were deoxygenated and dried by thoroughly sparging with N_2 gas followed by passage through an activated alumina column in the solvent purification system by SG Water, USA LLC. For electrochemical measurements under an Ar atmosphere, solvents were further degassed and then left under Ar. All solvents were stored over activated 4 Å molecular sieves prior to use. Anhydrous ammonia gas was dried by passage through a calcium oxide drying tube. All reagents were purchased from commercial vendors and used without further purification unless otherwise stated. Tris(2-pyridylmethyl)amine (TPA)[1] and tris(2-pyridylmethylamine) iron(II) triflate bis acetonitrile[2] were synthesized according to literature procedures. $^{15}NH_4OTf$ was prepared from $^{15}NH_4Cl$ (Cambridge Isotope Laboratories) by anion exchange with silver triflate followed by repeated recrystallization from acetonitrile. ^1H NMR chemical shifts are reported in ppm relative to tetramethylsilane, using residual solvent resonances as internal standards.

Electrochemistry: Cyclic Voltammetry (CV), Linear Sweep Voltammetry (LSV), Differential Pulse Voltammetry (DPV) and Controlled Potential Coulometry (CPC) experiments were carried out with a Biologic VSP-300 potentiostat using a one-compartment three-electrode cell. For CV, LSV and DPV, a Boron Doped Diamond (BDD) disk electrode (3 mm diameter) was used as the working electrode, Pt wire as the counter electrode, and a Ag/AgOTf reference electrode was employed using an acetonitrile solution containing 5 mM AgOTf and 0.1 M $TBAPF_6$. For CPE, the same reference electrode was used, but a BDD

plate (geometric area: 1 cm^2) and a Pt mesh were used respectively as working and counter electrode. All redox potentials in the present work are reported versus the Fc/Fc^+ couple, measured before each experiment to be +0.115 V versus our Ag/AgOTf reference electrode.

CVs and LSVs were collected at 100 $mV \cdot s^{-1}$ unless specified otherwise. DPVs were obtained with the following parameters: amplitude = 50 mV, step height = 4 mV, pulse width = 0.05 s, pulse period = 0.5 s and sampling width = 0.0167 s. $E_{1/2}$ values for the reversible waves were obtained from the half potential between the oxidative and reductive peaks. All measurements were performed applying IR compensation, compensating 85% of the resistance measured at one high frequency value (100 kHz).

Gas Chromatography: Gas chromatography was performed in the Environmental Analysis Center using HP 5890 Series II instruments. Gas quantification was performed using a molecular sieve column attached to a thermal conductivity detector. Argon was the carrier gas. Standard curves were generated by direct injection of hydrogen or nitrogen gas. Quantification of background nitrogen was determined using the background oxygen signal. Isotopic measurements were performed with a separate HP 5890 Series II equipped with a GasPro column using helium as the carrier gas.

NMR: NMR spectroscopy was performed using a Varian 400 MHz NMR spectrometer equipped with a broadband auto-tune probe. ^1H NMR chemical shifts are reported in ppm relative to tetramethylsilane, using residual solvent resonances as internal standards.

Mössbauer: Spectra were recorded on a spectrometer from SEE Co. operating in the constant acceleration mode in a transmission geometry. Spectra were recorded with the

temperature of the sample maintained at 80 K or 100 K. The sample was kept in an SVT-400 Dewar from Janis. The quoted isomer shifts are relative to the centroid of the spectrum of a metallic foil of α-Fe at room temperature. Data analysis was performed using the program WMOSS (www.wmoss.org) and quadrupole doublets were fit to Lorentzian lineshapes.

UV-vis: Spectra were collected using a Cary 60 instrument with Cary WinUV software.

IR: Spectra were obtained using a Bruker Alpha Platinum ATR spectrometer with OPUS software in a glovebox under an N_2 atmosphere.

X-Ray Crystallography: XRD studies were carried out at the Beckman Institute Crystallography Facility on a Bruker D8 Venture diffractometer (Cu Kα radiation). Structures were solved using direct methods with SHELXS or SHELXT and refined against F^2 on all data by full-matrix least squares with SHELXL.[3] All of the solutions were performed in the Olex2 program.[4] The crystals were mounted on a glass fiber under Paratone N oil.

B2. Catalytic controlled potential coulometry experiments

Procedures for controlled potential coulometry

Preparation of the BDD electrode: A 2 cm^2 boron-doped diamond (BDD) plate electrode (Element Six Technologies, Santa Clara, CA) was connected to standard electrical wire using conductive silver epoxy. The silver epoxy was then covered in Loctite 9460 (Hysol) epoxy to protect the electrical connection from contact with chemical reagents. After covering with epoxy, the total exposed surface geometric area decreased to around 1 cm^2.

BDD has a surface that exists in various states of reduction (H-terminated) and oxidation (O-terminated).[5] In order to remove attached nitrogen and iron generated during controlled potential coulometry experiments and to ensure a reliable electrode surface prior to CPC measurements, the BDD plate electrode was oxidatively treated prior to use. First, the electrode was soaked in concentrated nitric acid for 5 minutes. Then, a potential of 3.0 V vs Ag/AgCl was applied to the BDD electrode in a 0.5 M H_2SO_4 solution for 10 minutes. The electrode was then thoroughly rinsed with water prior to use.

Preparation of the platinum counter electrode: In order to ensure a highly active Pt surface for HER prior to CPC experiments, the Pt mesh counter electrode was soaked in concentrated hydrochloric acid for at least 5 minutes prior to usage.

Preparation of the custom Ag/AgOTf reference electrode: To ensure reliable potential measurements, the custom Ag/AgOTf reference electrode was prepared prior to each CPC experiment and then a CV of ferrocene was measured. In a glass tube fitted with a Vycor porous glass frit attached by Teflon heatshrink tubing, an acetonitrile solution containing 5

mM AgOTf and 0.1 M $TBAPF_6$ was added. A silver wire was placed inside and the electrode was sealed.

Preparation of ammonia solutions. For experiments with natural abundance ammonia, saturated 2 M solutions[6] in acetonitrile were prepared by bubbling anhydrous ammonia through acetonitrile in a Schlenk tube under an argon atmosphere. For experiments with labeled $^{15}NH3$, ammonia was liberated from $^{15}NH_4OTf$ by addition of 1.1 equivalents of 1,8-Diazabicyclo[5.4.0]undec-7-ene (DBU) to ammonium triflate dissolved in acetonitrile in a Schlenk tube inside of an argon glovebox. This solution was then vacuum transferred to a separate clean Schlenk tube.

CPC: Inside an argon glovebox, a gas-tight electrochemical cell equipped with a 24/40 cap containing three tungsten rods for electrical contacts and a 14/20 joint carefully sealed with a Suba-Seal septum was prepared. A BDD plate electrode (A = 1 cm^2), high surface area platinum mesh electrode, and custom Ag/AgOTf reference electrode were connected to the 24/40 cap. All chemical reagents were then rapidly added to the cell to prevent evaporation of ammonia and then the cell was sealed with the 24/40 cap. Prior to each CPC, a ZIR and CV were taken. Then, manual IR compensation using 85% of the uncompensated resistance determined by the ZIR measurement was applied and the CPC was started. At the end of the CPC experiment, another CV was taken to assess any difference in current pre- and post-CPC. The cell was then removed from the glovebox for analysis by gas chromatography. For headspace analysis, 100 μL of the headspace was injected into a GC-TCD for quantification using a lockable Hamilton syringe with a 26S gauge needle. For GC-MS, only 50 μL of the headspace was injected.

For each experiment, a 10 mL solution containing 0.5 mM [(TPA)Fe(MeCN)$_2$]OTf$_2$ (3.6 mg), 65 mM NH_3 (0.33 mL of 2.0 M solution), and 50 mM NH_4OTf (83.6 mg) was prepared in acetonitrile. For experiments with 2.5 μmol [Fe], 5.0 mL of this solution was added to the electrochemical cell. Otherwise, the entire 10 mL portion was added.

Table B1: Results of catalytic CPC experiments.

Entry	Fe Source	Eq. N_2	μmol [Fe]	Charge (C)	FE N_2 (%)	FE H_2 (%)
1	(TPA)Fe	18.1	2.5	37.1	70	62
2	(TPA)Fe	16.4	2.5	29.7	79	66
3	(TPA)Fe	9.4	5	30.8	87	70
4	(TPA)Fe	10.6	5	40.6	75	72
5*	(TPA)Fe	9.6	5	29.8	93	74
6*	(TPA)Fe	7.5	5	28.6	75	69

* Experiment performed with $^{15}NH_3$ and $^{15}NH_4$OTf

Table B2: Results of control CPC experiments. For control experiments, the electrochemical cell was filled with the entire 10 mL acetonitrile solution of 65 mM NH_3 and 50 mM NH_4OTf.

Entry	Fe Source	Eq. N_2	μmol [Fe]	Charge (C)
1	None	0.5[†]	0	1.05
2	$FeOTf_2$	1.0	5	1.89

[†] For the NH_3 only control experiment, one equivalent is set equal to the number of moles of iron in the corresponding catalytic experiment, i.e., 5 mmol.

B3. Chronoamperograms for catalytic and control experiments

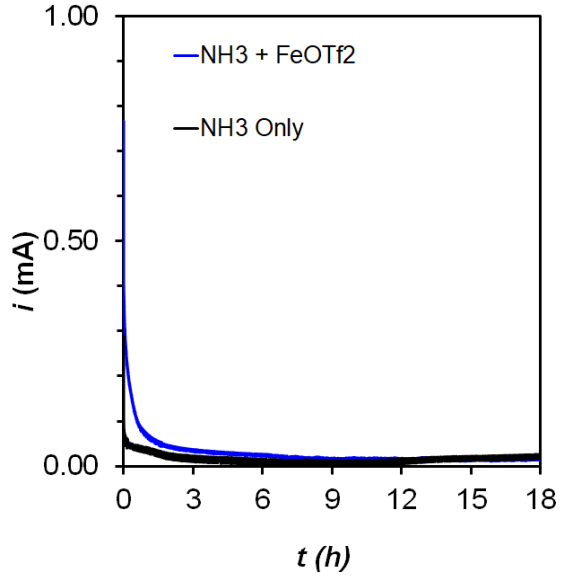

Figure B1: Chronoamperograms corresponding to 18 h CPC background measurements with 50 mM NH_4OTf supporting electrolyte with (black) only 65 mM NH_3 and (blue) 65 mM NH_3 with 0.5 mM $FeOTf_2$.

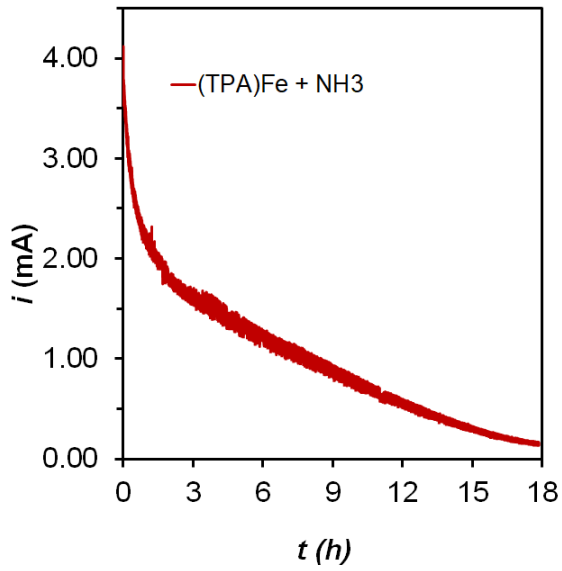

Figure B2: Chronoamperogram corresponding to 18 h CPC catalytic experiment with 0.5 mM $[(TPA)Fe(MeCN)_2]OTf_2$, 65 mM NH_3, and 50 mM NH_4OTf supporting electrolyte.

B4. Cyclic voltammograms with BDD plate/disk electrode pre- and post-CPC

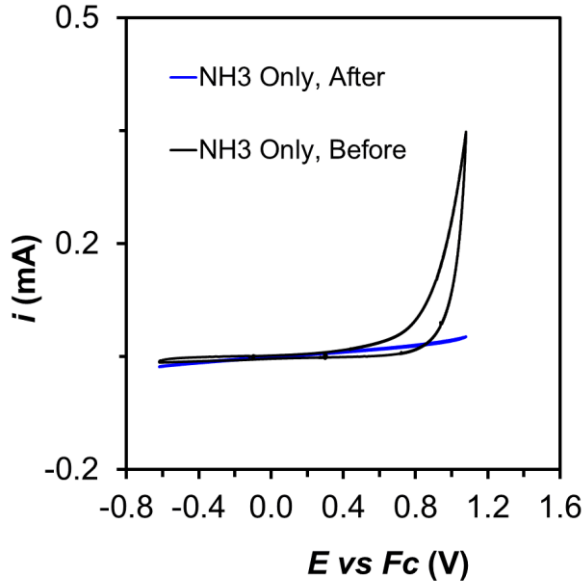

Figure B3: CVs of 65 mM NH_3 solution with 50 mM NH_4OTf supporting electrolyte before (black trace) and after (blue trace) 18 hours of controlled potential coulometry at 1.1 V vs Fc/Fc^+. The decrease in current is due to passivation of the electrode surface.

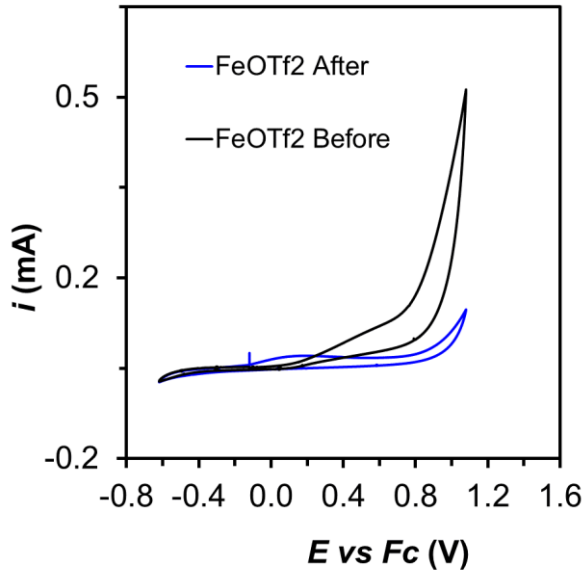

Figure B4: CVs of 0.5 mM $FeOTf_2$ solution with 65 mM NH_3 and 50 mM NH_4OTf supporting electrolyte before (black trace) and after (blue trace) 18 hours of controlled potential coulometry at 1.1 V vs Fc/Fc^+. The decrease in current is due to passivation of the electrode surface.

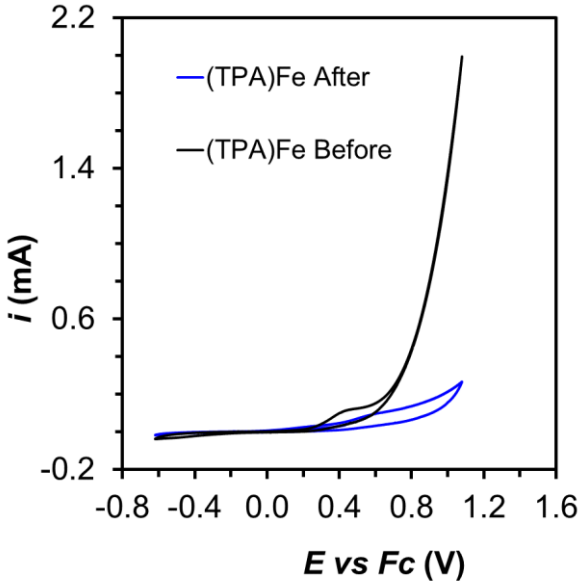

Figure B5: CVs of 0.5 mM [(TPA)Fe(MeCN)$_2$]OTf$_2$ solution with 65 mM NH_3 and 50 mM NH_4OTf supporting electrolyte before (black trace) and after (blue trace) 18 hours of controlled potential coulometry at 1.1 V vs Fc/Fc^+. The decrease in current is due to passivation of the electrode surface.

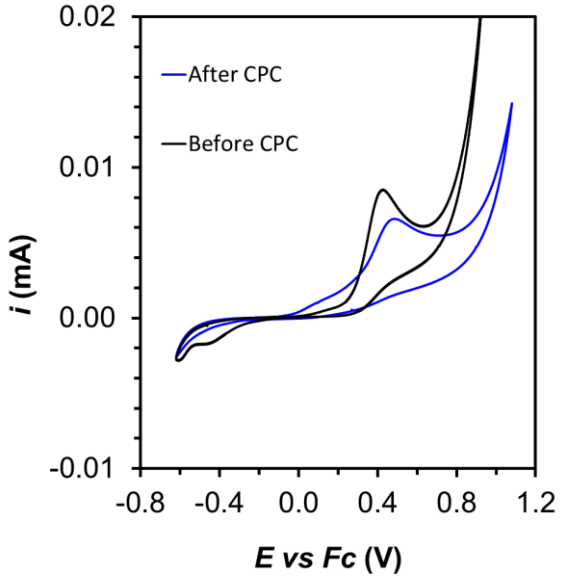

Figure B6: Cyclic voltammograms of 0.5 mM [(TPA)Fe(MeCN)$_2$]OTf$_2$ solution with BDD disk electrode before and after 18 h CPC experiment.

B5. UV-Vis spectra of catalytic mixture pre- and post-CPC

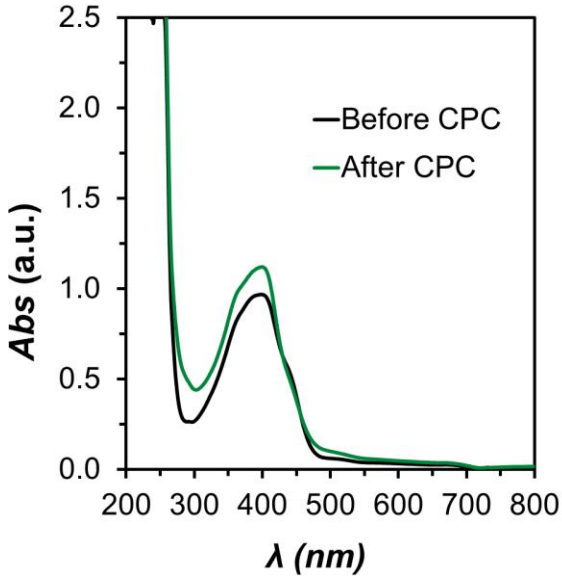

Figure B7: UV-Vis spectrum of 0.2 mM $[(TPA)Fe(MeCN)_2]OTf_2$ solution diluted from 0.5 mM $[(TPA)Fe(MeCN)_2]OTf_2$ solution before and after 18 h CPC experiment.

Figures B6 and B7 provide evidence that after 18 h of CPC, the $[(TPA)Fe(MeCN)_2]OTf_2$ solution from catalytic experiments still contains active $[(TPA)Fe(L)_2]^{2+}$. Exact quantification of catalyst present before and after catalysis is difficult due to the speciation of $[(TPA)Fe(L)_2]OTf_2$ with varying ammonia concentrations. As the ammonia concentration decreases, the absorbance at 400 nm increases in this concentration range, further complicating analysis.

B6. GC-MS and GC-TCD traces

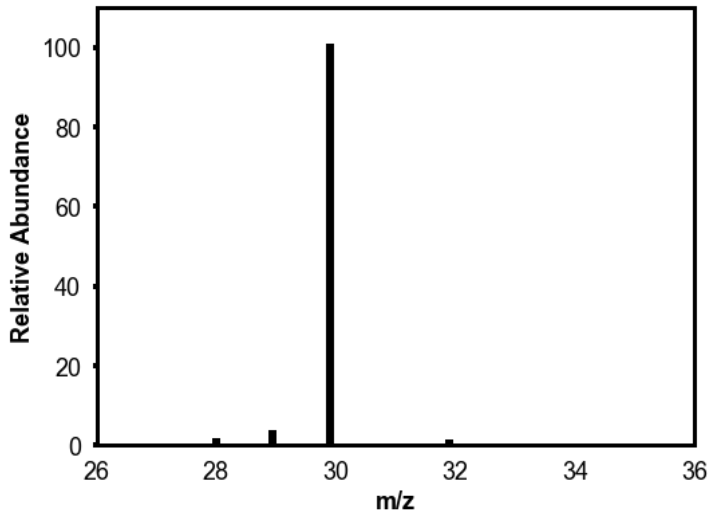

Figure B8: GC-MS data for representative catalytic experiment with 5 μmol [(TPA)Fe(MeCN)$_2$]OTf$_2$ performed with $^{15}NH_3$ and $^{15}NH_4OTf$.

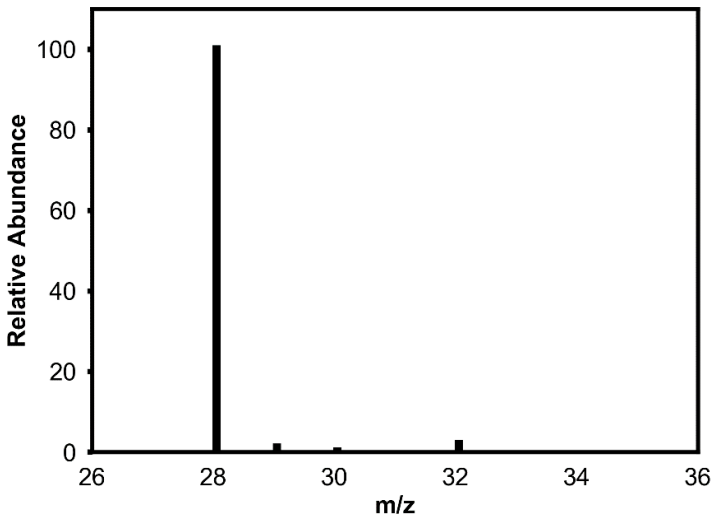

Figure B9: GC-MS data for representative catalytic experiment with 5 μmol [(TPA)Fe(MeCN)$_2$]OTf$_2$ performed with natural abundance NH_3 and NH_4OTf.

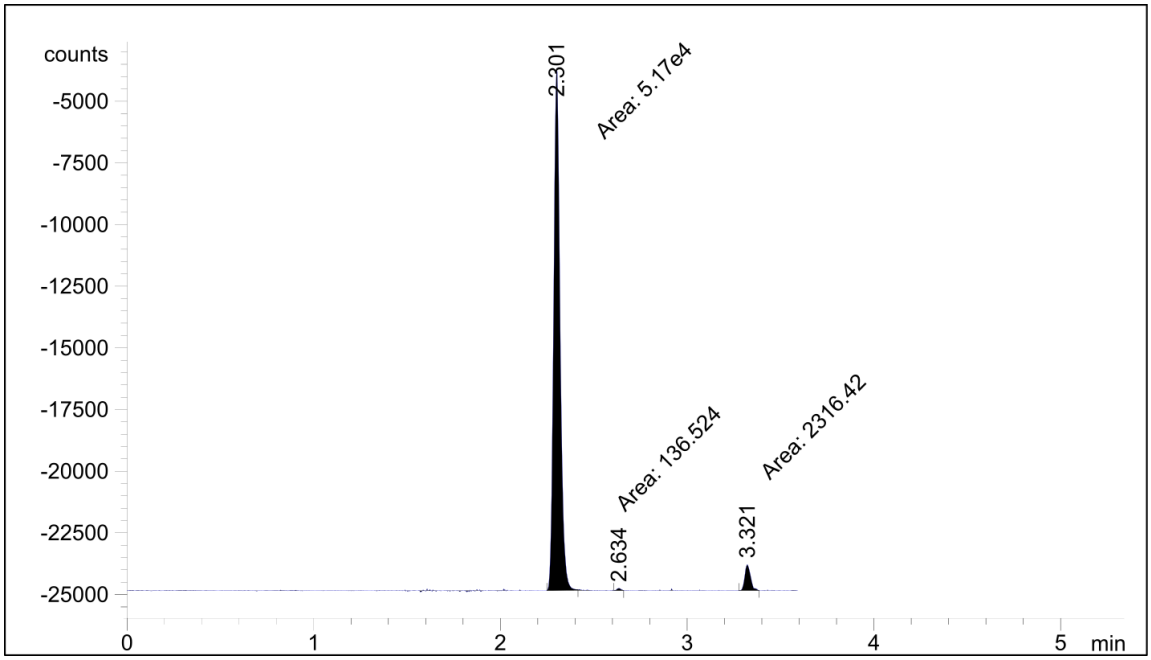

Figure B10: Representative GC-TCD trace showing H_2 (RT = 2.3 min), O_2 (RT = 2.6 min), and N_2 (RT = 3.3 min).

B7. Standard curves for quantification of N_2 and H_2

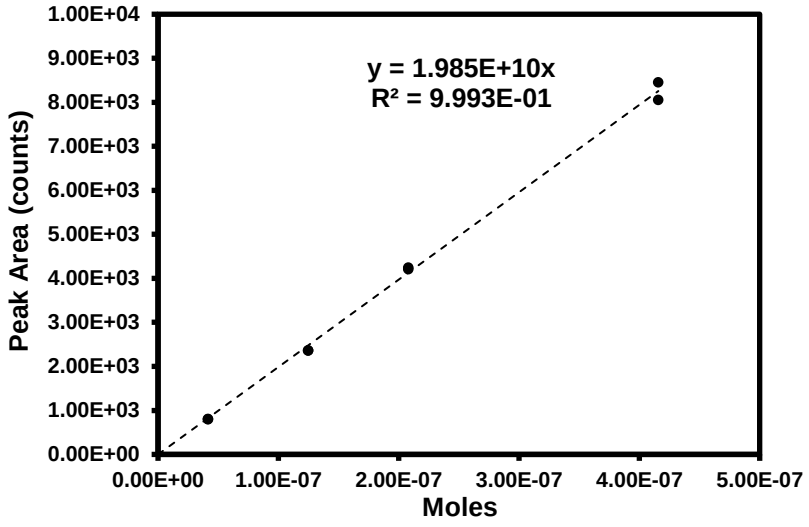

Figure B11: Standard curve for quantification of N_2 generated by direct injection of N_2 gas from a Suba-Seal rubber septum capped Schlenk tube.

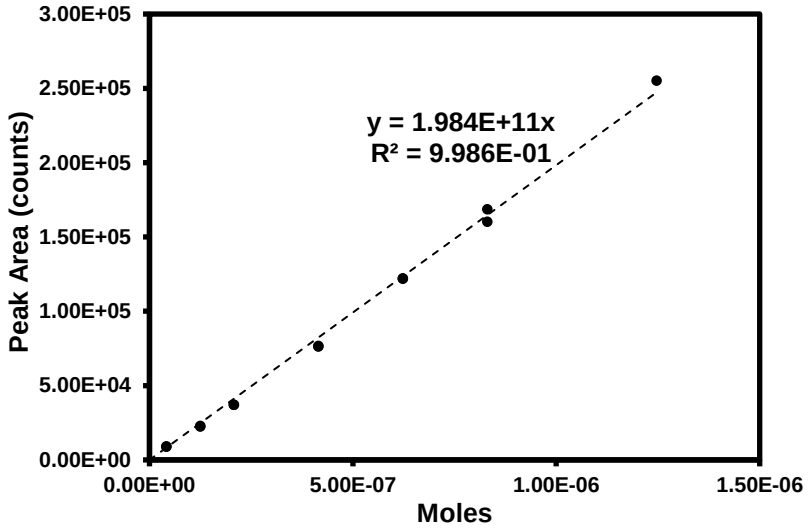

Figure B12: Standard curve for quantification of H_2 generated by direct injection of H_2 gas from a Suba-Seal rubber septum capped Schlenk tube.

B8. CV cycling experiments and rinse tests

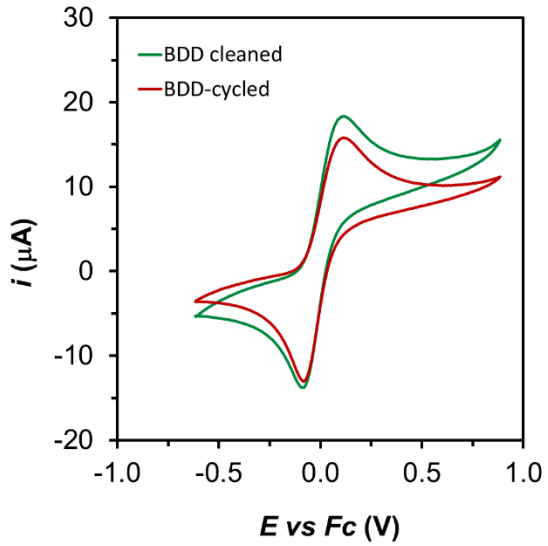

Figure B13: Cyclic voltammograms of acetonitrile solution containing 1 mM Fc using the rinsed BDD disk electrode before and after 50 CV cycles in acetonitrile solution with 2.5 mM $[(TPA)Fe(MeCN)_2]OTf_2$, 0.05 M NH_3 and 0.05 M NH_4OTf. The scan rate was set to 0.1 $V \cdot s^{-1}$, Pt was used as the counter electrode, with a custom Ag/AgOTf reference electrode.

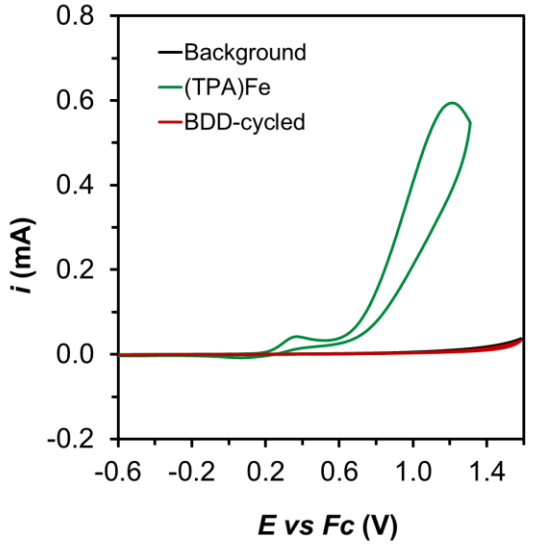

Figure B14: Cyclic voltammograms of acetonitrile solution containing 0.05 M NH_3 and 0.05 M NH_4OTf using a clean BDD electrode (black trace) or the rinsed BDD disk electrode after 50 CV cycles with $[(TPA)Fe(MeCN)_2]OTf_2$ (red trace), showing that no active material was deposited. The green trace depicts the CV of 2.5 mM $[(TPA)Fe(MeCN)_2]OTf_2$ under the same conditions.

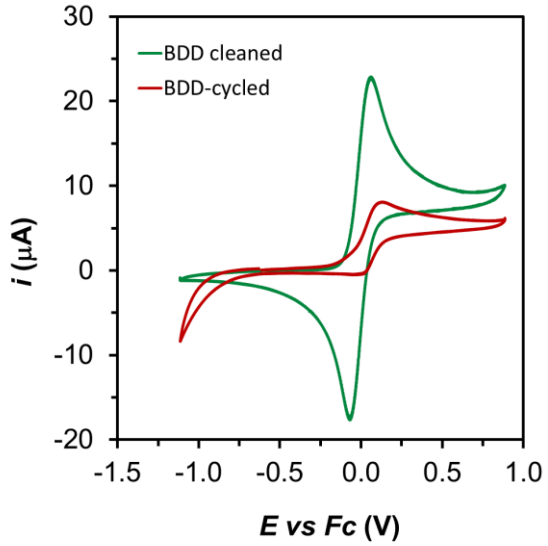

Figure B15: Cyclic voltammograms of acetonitrile solution containing 1 mM Fc using the rinsed BDD disk electrode before and after 50 CV cycles in acetonitrile solution with 2.5 mM $FeOTf_2$, 0.05 M NH_3 and 0.05 M NH_4OTf. The scan rate was set to 0.1 $V \cdot s^{-1}$, Pt was used as the counter electrode, with a custom Ag/AgOTf reference electrode.

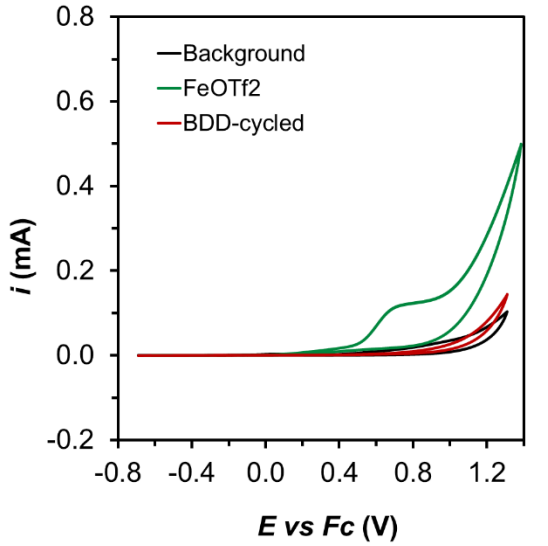

Figure B16: Cyclic voltammograms of acetonitrile solution containing 0.05 M NH_3 and 0.05 M NH_4OTf using a clean BDD electrode (black trace) or the rinsed BDD disk electrode after 50 CV cycles with $FeOTf_2$ (red trace), showing that no active material was deposited. The green trace depicts the CV of a 2.5 mM $FeOTf_2$ under the same conditions.

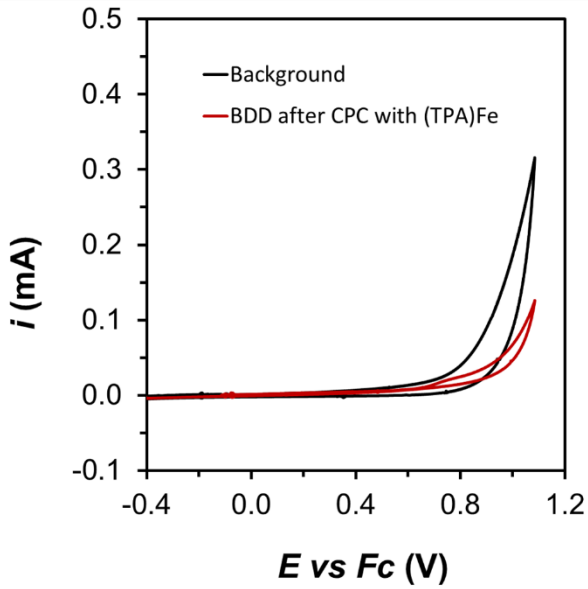

Figure B17: Cyclic voltammograms of acetonitrile solution containing 0.05 M NH_3 and 0.05 M NH_4OTf using a clean BDD electrode (black trace) and the rinsed BDD disk electrode after CPC for 18 hours using 0.5 mM $[(TPA)Fe(MeCN)_2]OTf_2$ as catalyst (red trace). Results show that no active material was deposited, but significant passivation is observed.

B9. XPS spectra of BDD plate electrode

Procedures for XPS: For XPS measurements, the BDD plate electrode was dipped into fresh acetonitrile twice to remove any soluble components. Then, the electrode was left in a 60^{o} C vacuum oven overnight to decrease off-gassing in the sample chamber. XPS measurements are corrected for surface charging by setting the binding energy of the carbon 1s peak to be 285 eV. This correction was always less than 1 eV. A full scan from 0-1000 eV was acquired, and then scans at the binding energies typical for carbon (274-294 eV), boron (176-196 eV), nitrogen (389-409 eV), oxygen (522-542 eV), and iron (690-730 eV) were measured.

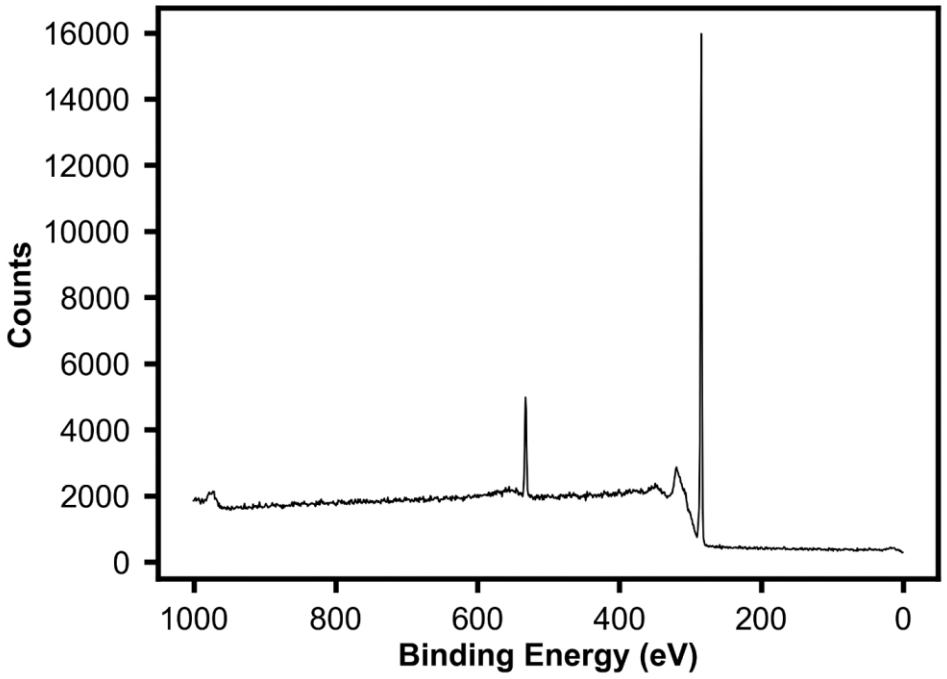

Figure B18: XPS spectrum of BDD plate electrode before AO conditions. Binding energy is corrected for surface charging by setting C1s to be 285 eV.

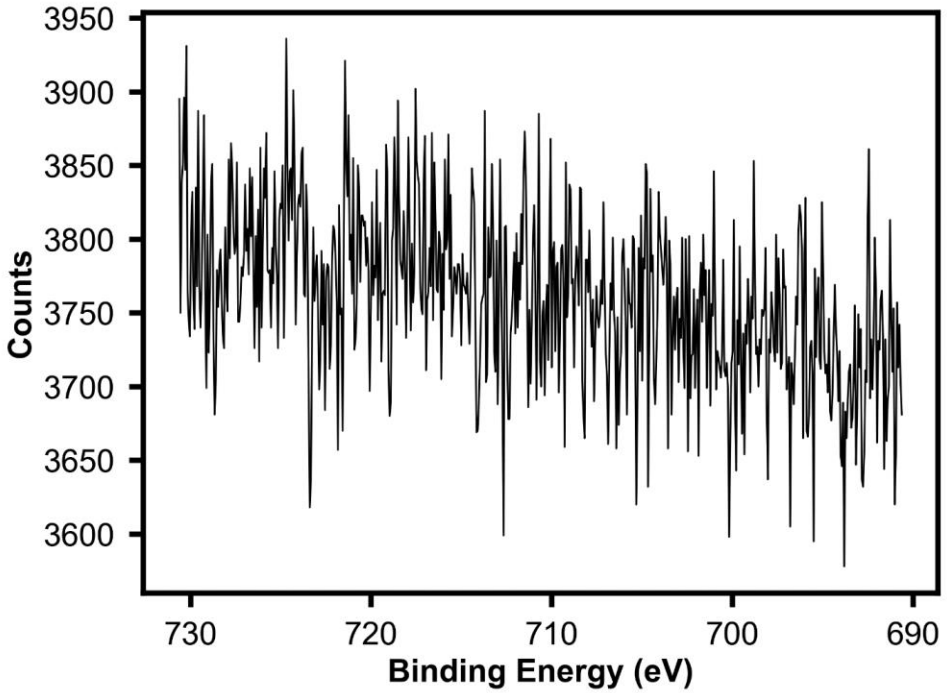

Figure B19: XPS spectrum of BDD plate electrode before AO conditions centered on the region characteristic for Fe 2p. Binding energy is corrected for surface charging by setting C1s to be 285 eV.

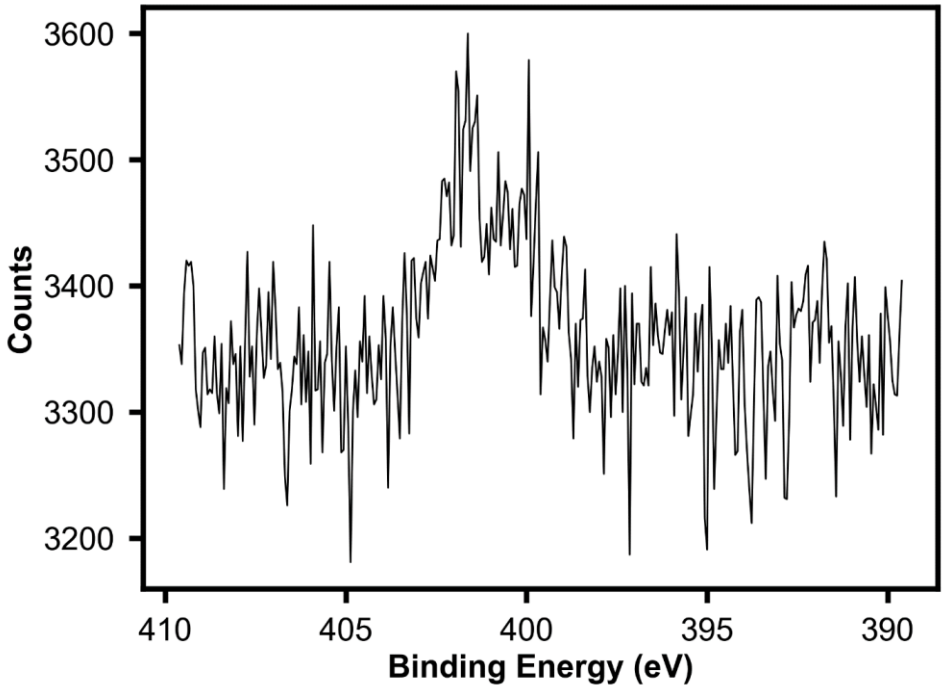

Figure B20: XPS spectrum of BDD plate electrode before AO conditions centered on the region characteristic for N 1s. Binding energy is corrected for surface charging by setting C1s to be 285 eV.

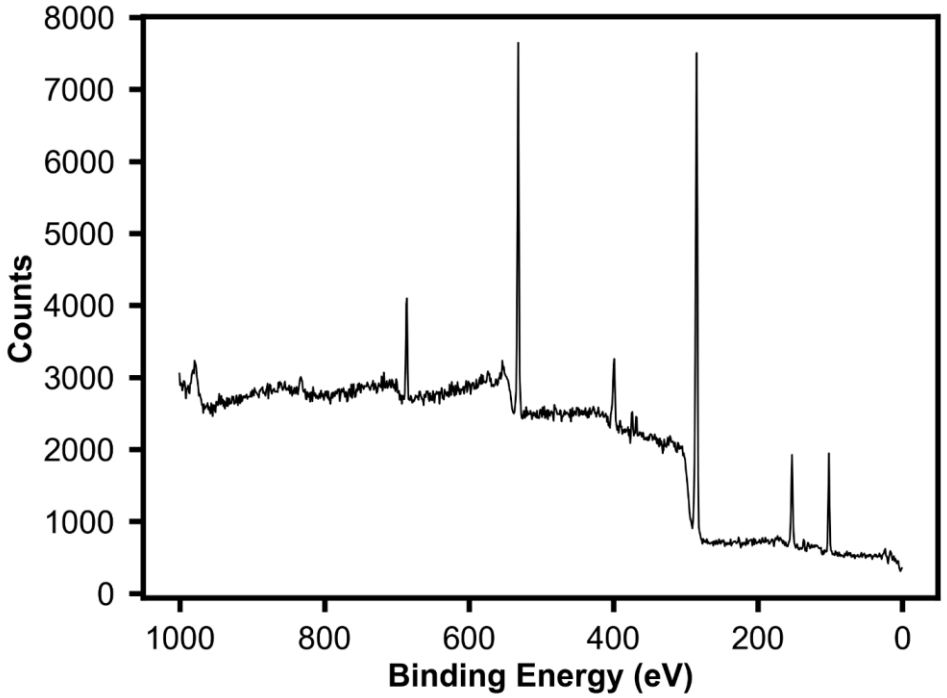

Figure B21: XPS spectrum of BDD plate electrode after 18 h CPC with 65 mM NH_3 solution. Binding energy is corrected for surface charging by setting C1s to be 285 eV.

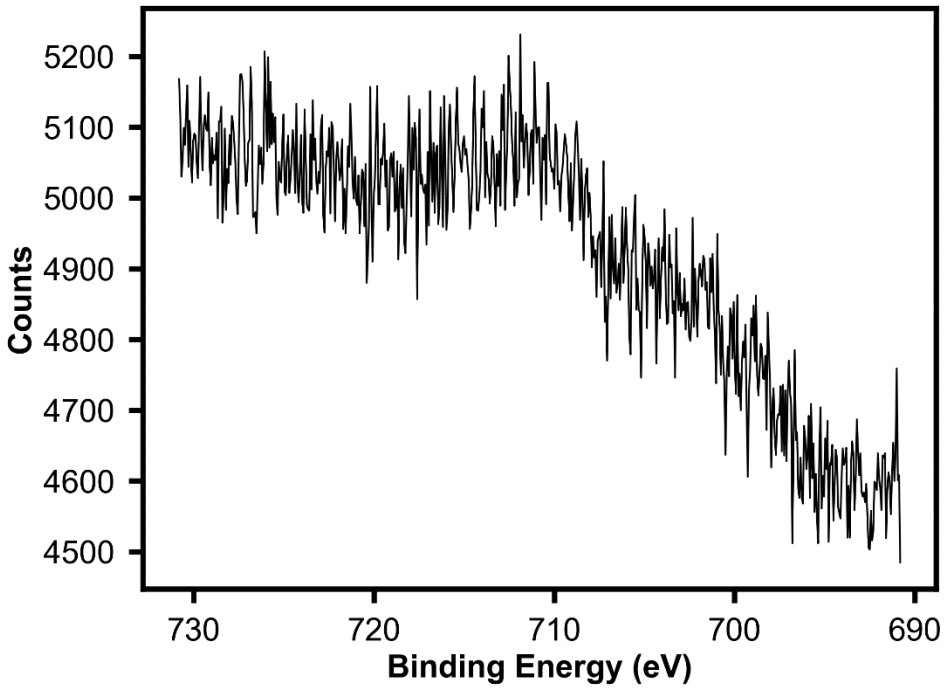

Figure B22: XPS spectrum of BDD plate electrode after 18 h CPC with 65 mM NH_3 solution centered on the region characteristic for Fe 2p. Binding energy is corrected for surface charging by setting C1s to be 285 eV.

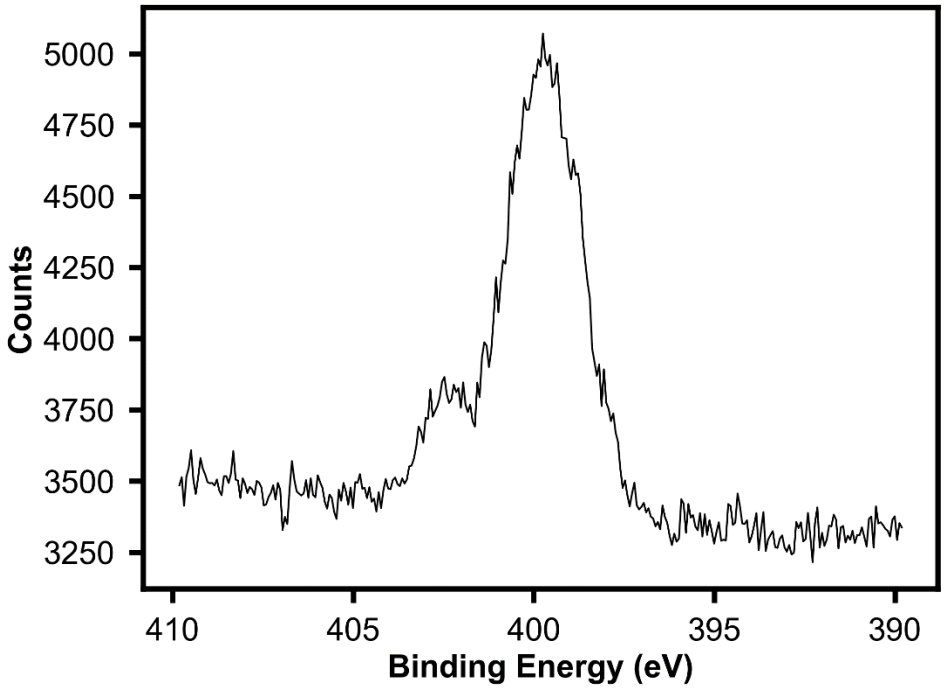

Figure B23: XPS spectrum of BDD plate electrode after 18 h CPC with 65 mM NH_3 solution centered on the region characteristic for N 1s. Binding energy is corrected for surface charging by setting C1s to be 285 eV.

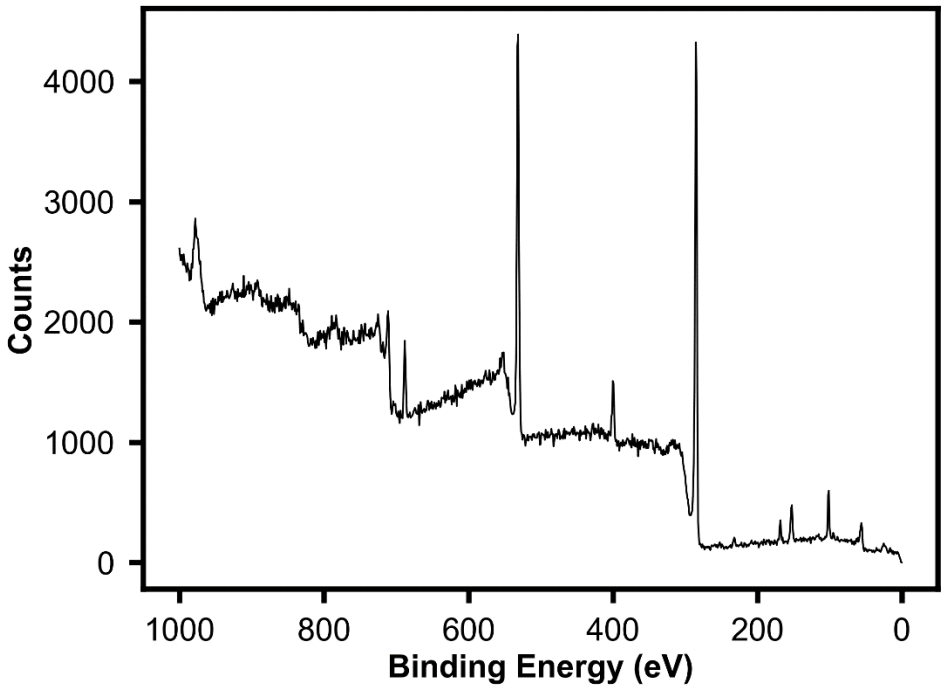

Figure B24: XPS spectrum of BDD plate electrode after 18 h CPC with 0.5 mM $[(TPA)Fe(MeCN)_2]OTf_2$ and 65 mM NH_3 solution. Binding energy is corrected for surface charging by setting C1s to be 285 eV.

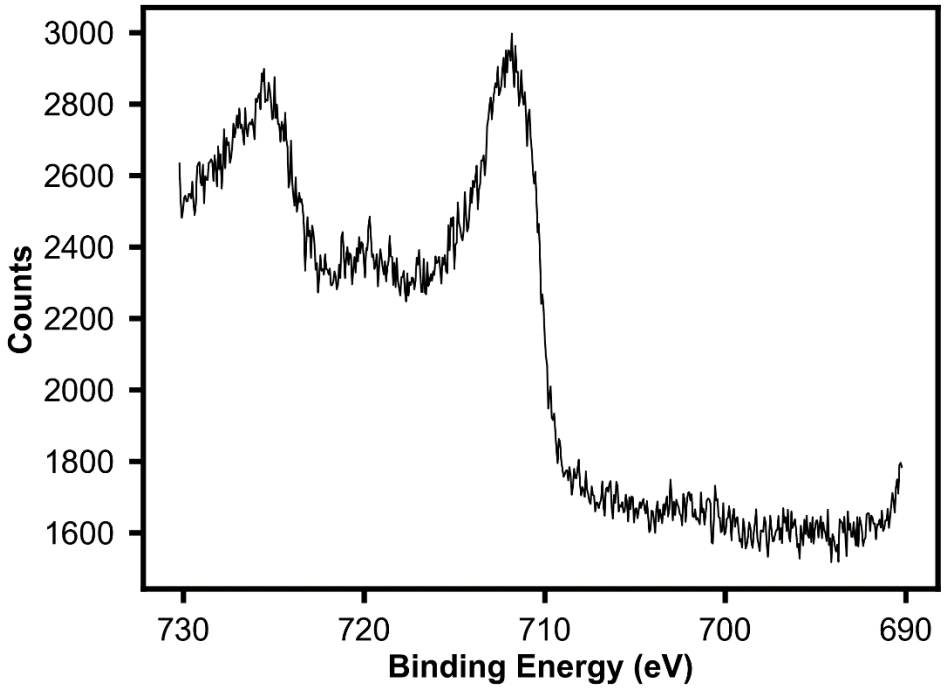

Figure B25: XPS spectrum of BDD plate electrode after 18 h CPC with 0.5 mM $[(TPA)Fe(MeCN)_2]OTf_2$ and 65 mM NH_3 solution centered on the region characteristic for Fe 2p. Binding energy is corrected for surface charging by setting C1s to be 285 eV.

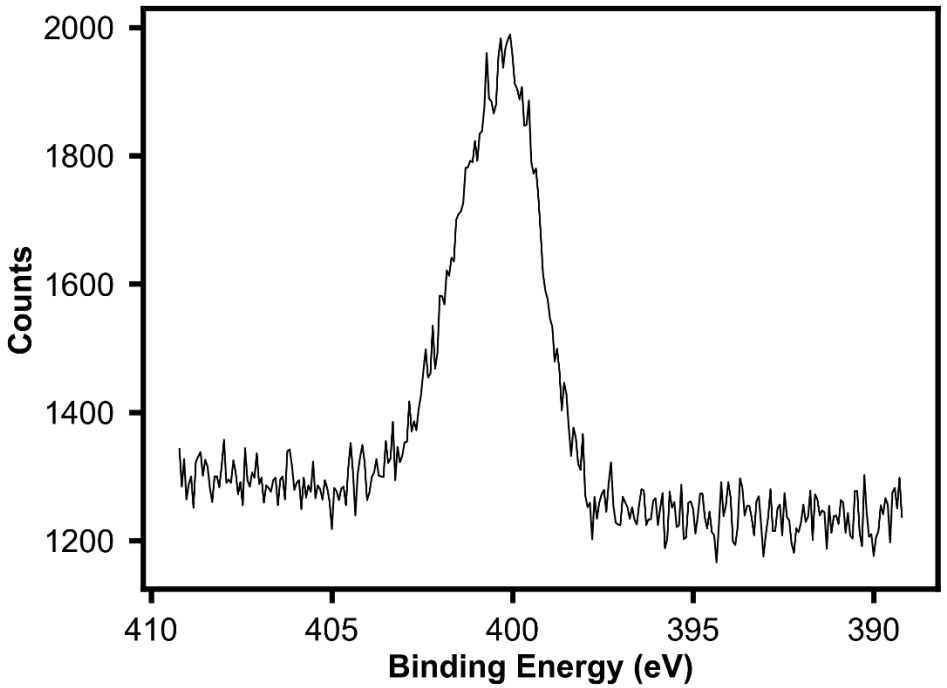

Figure B26: XPS spectrum of BDD plate electrode after 18 h CPC with 0.5 mM $[(TPA)Fe(MeCN)_2]OTf_2$ and 65 mM NH_3 solution centered on the region characteristic for N 1s. Binding energy is corrected for surface charging by setting C1s to be 285 eV.

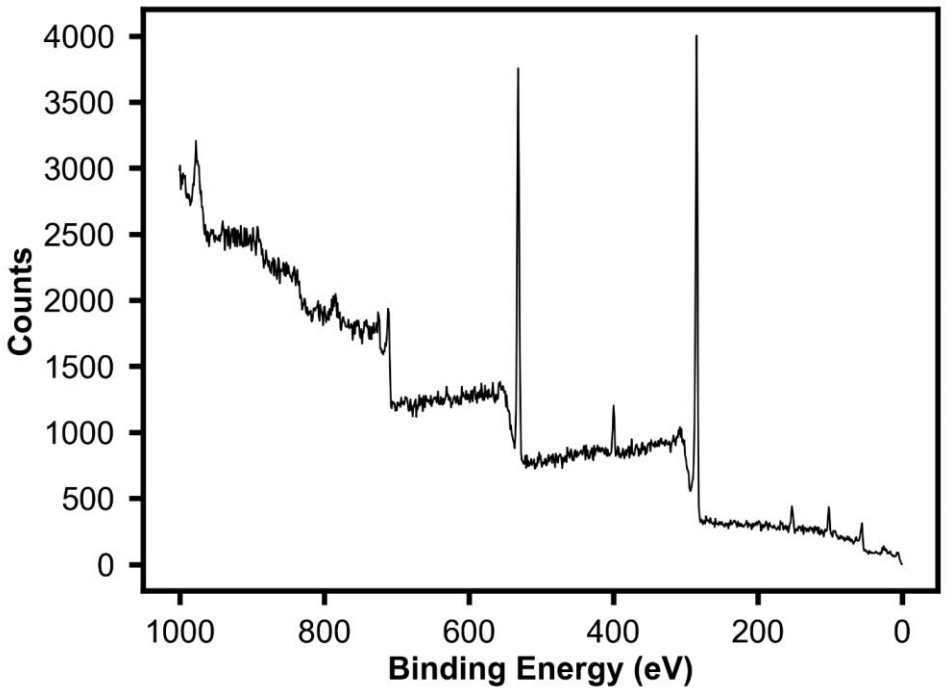

Figure B27: XPS spectrum of BDD plate electrode after 18 h CPC with 0.5 mM $FeOTf_2$ and 65 mM NH_3 solution. Binding energy is corrected for surface charging by setting C1s to be 285 eV.

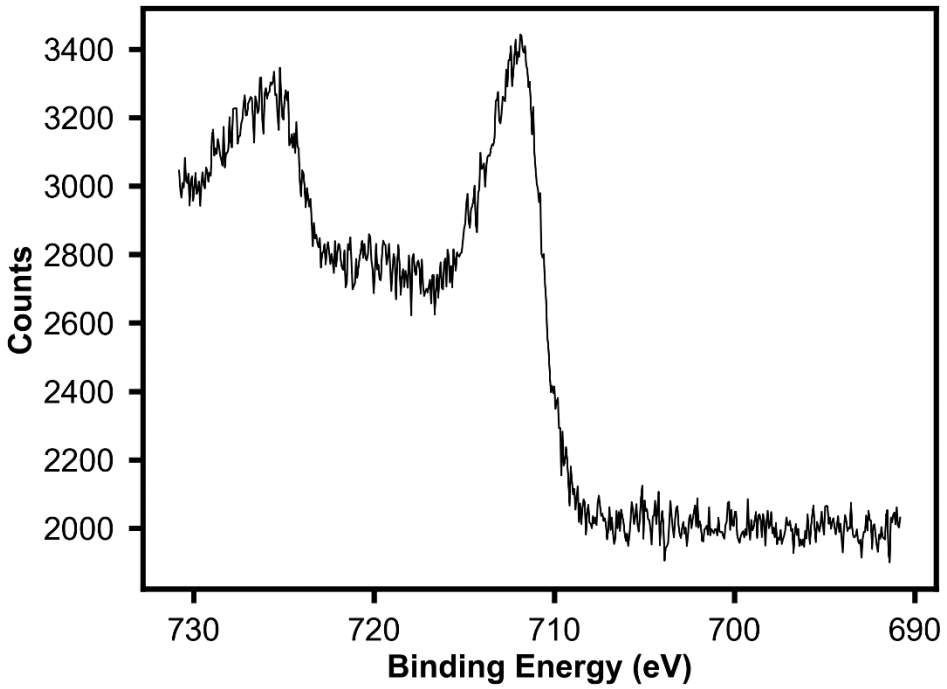

Figure B28: XPS spectrum of BDD plate electrode after 18 h CPC with 0.5 mM $FeOTf_2$ and 65 mM NH_3 solution centered on the region characteristic for Fe 2p. Binding energy is corrected for surface charging by setting C1s to be 285 eV.

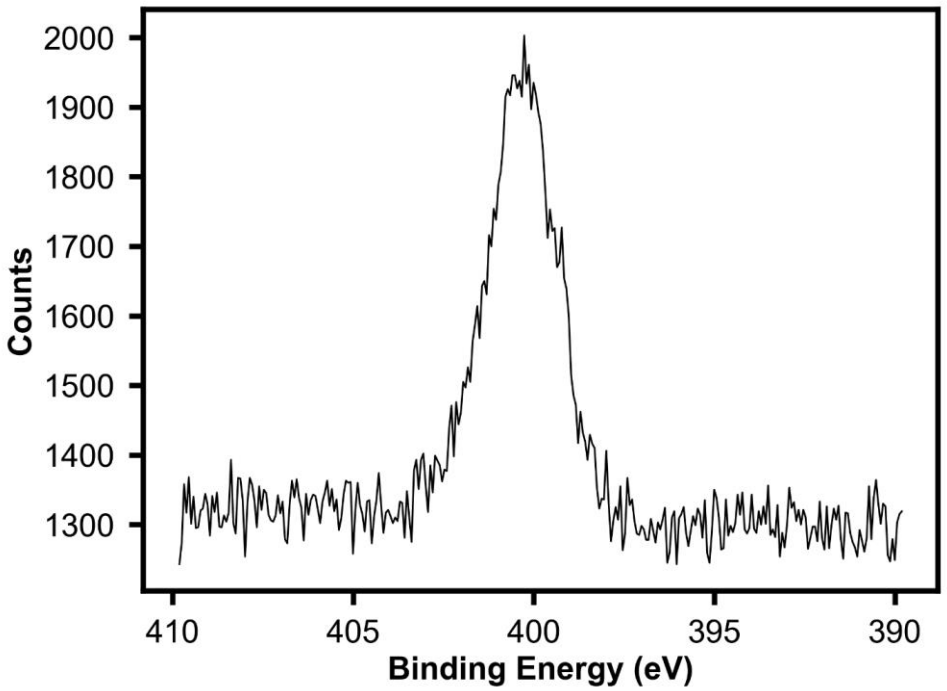

Figure B29: XPS spectrum of BDD plate electrode after 18 h CPC with 0.5 mM $FeOTf_2$ and 65 mM NH_3 solution centered on the region characteristic for N 1s. Binding energy is corrected for surface charging by setting C1s to be 285 eV.

B10. Synthesis and solid-state structure of [(TPA)Fe(NH_3)$_2$]OTf_2

The title compound was prepared by slow diffusion of ammonia gas from a saturated ammonia- THF solution into an acetonitrile free solution of (TPA)FeOTf_2 in THF at room temperature. Over the course of 12-24 hours, the clear yellow solution gradually turned orange and orange needles precipitated. These orange needles were confirmed by SC-XRD to be [(TPA)Fe(NH_3)$_2$]OTf_2. Upon cooling the needles to 100 K under the cold stream, they changed color from orange to red, evidence of spin-crossover behavior. The color change was reversible.

[(TPA)Fe(NH_3)$_2$]OTf_2 crystallizes in the space group P 2_1/n with four independent cations in the asymmetric unit. At 100 K, two of the iron sites are low spin based on their bond distances (and corresponding solid-state Mössbauer analysis) and the other two sites are high spin. The cations in the crystal structure suffer from disorder at only one of the four iron sites. Unsurprisingly, the triflates are also disordered. Hydrogen atoms were not refined but were placed using a riding model.

To model the disorder at the one disordered iron site, SADI, SIMU, and RIGU restraints were used to model a separate iron unit with head-to-tail like disorder. Positional and rotational disorder of the triflate anions was also modeled with the help of SADI, SIMU, and RIGU restraints. Remaining unmodeled electron density is primarily located near the triflate anions and THF solvent molecules.

Further details are provided in the CIF file that has been electronically uploaded as additional Supporting Information.

Table B3: Crystal data and structure refinement for $[(TPA)Fe(NH_3)_2]OTf_2$.

Temperature/K	99.99
Crystal system	monoclinic
Space group	$P2_1/n$
a/Å	31.690(8)
b/Å	12.063(5)
c/Å	34.405(5)
α/°	90
β/°	109.475(13)
γ/°	90
Volume/Å^3	12399(6)
Z	16
ρ_{calc}g/cm^3	1.573
μ/mm^{-1}	5.952
F(000)	6033.0
Crystal size/mm^3	0.287 × 0.281 × 0.144
Radiation	CuKα (λ = 1.54178)
2Θ range for data collection/°	4.642 to 159.956
Index ranges	$-40 \leq h \leq 38$, $-14 \leq k \leq 15$, $-42 \leq l \leq 43$
Reflections collected	316748
Independent reflections	26746 [R_{int} = 0.0838, R_{sigma} = 0.0384]
Data/restraints/parameters	26746/2397/1991
Goodness-of-fit on F^2	1.097
Final R indexes [I>=2σ (I)]	R_1 = 0.0739, wR_2 = 0.1587
Final R indexes [all data]	R_1 = 0.0812, wR_2 = 0.1623
Largest diff. peak/hole / e Å^{-3}	1.83/-0.89

B11. UV-vis spectroscopy of $[(TPA)Fe(L)_2]^{2+}$ species

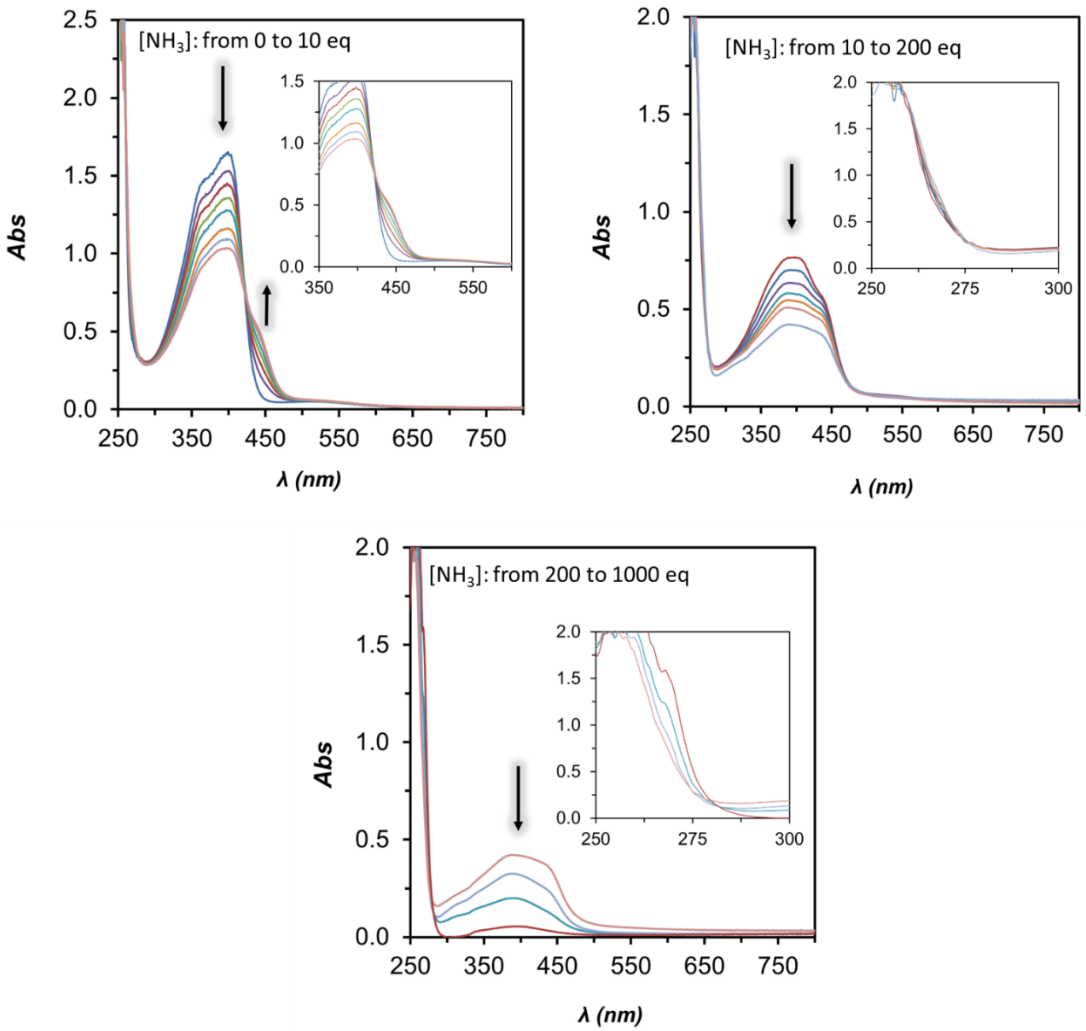

Figure B30: UV-vis spectra of 0.2 mM $[(TPA)Fe(MeCN)_2]OTf_2$ in MeCN with increasing concentrations of NH_3.

B12. ^{1}H NMR spectroscopy of $[(TPA)Fe(L)_2]^{2+}$ species

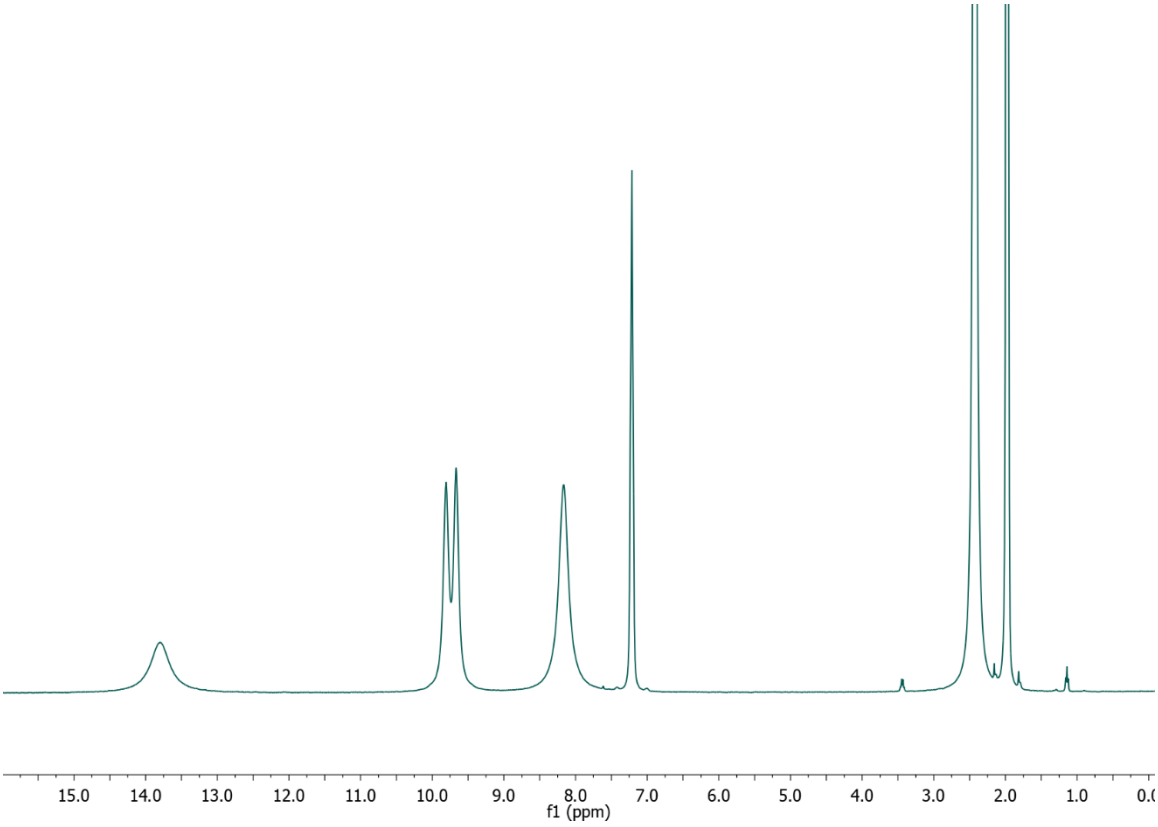

Figure B31: ^{1}H NMR (400 MHz) spectrum of $[(TPA)Fe(MeCN)_2]OTf_2$ in CD_3CN.

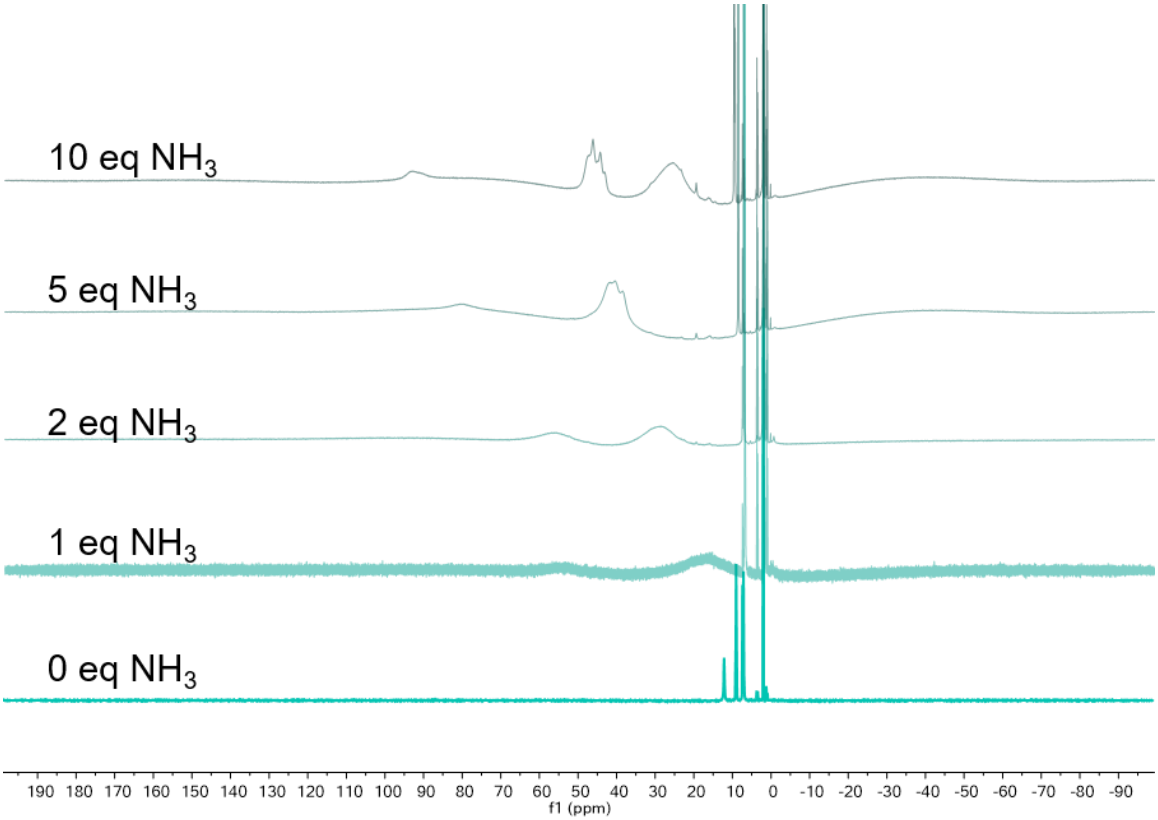

Figure B32: ^{1}H NMR (400 MHz) spectrum of $[(TPA)Fe(MeCN)_2]OTf_2$ in CD_3CN with 0, 1, 2, 5, and 10 equivalents of NH_3 added via calibrated bulb to a J. Young NMR tube.

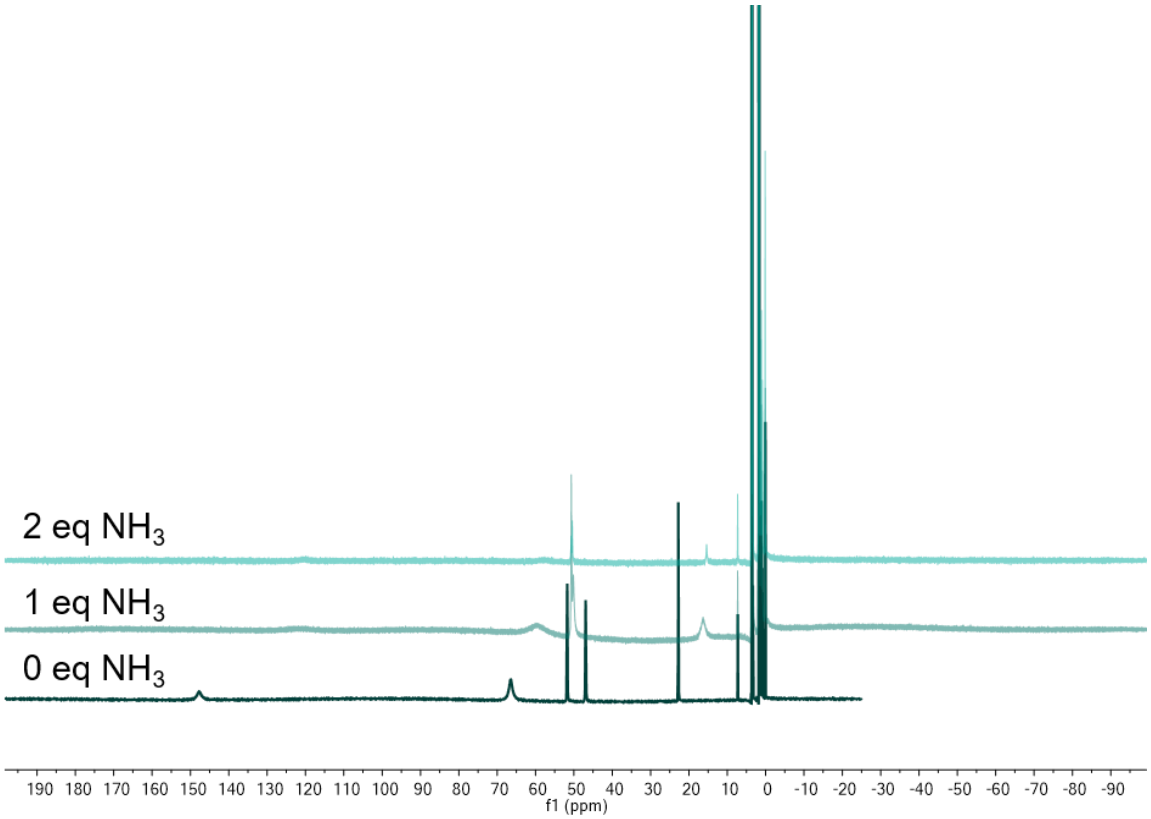

Figure B33: ^{1}H NMR (400 MHz) spectrum of (TPA)Fe(OTf)$_2$ in d8-THF with 0, 1, and 2 equivalents of NH_3 added via calibrated bulb to a J. Young NMR tube. The loss in intensity upon addition of ammonia is due to precipitation.

B13. Mössbauer spectroscopy of $[(TPA)Fe(L)_2]^{2+}$ species

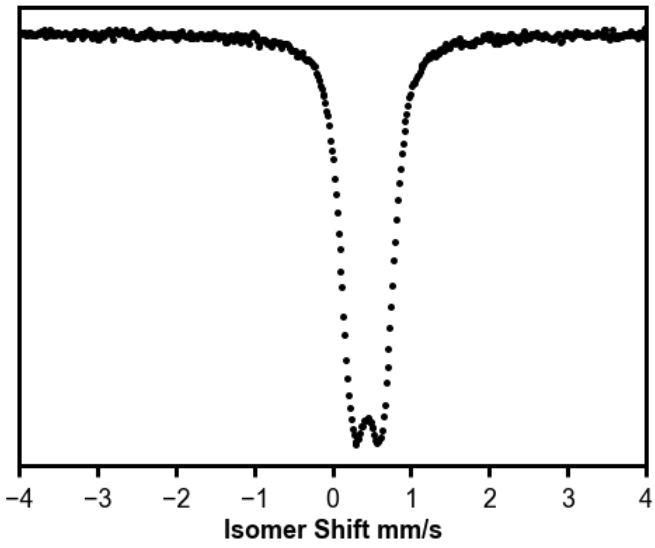

Figure B34: Mössbauer spectrum of $[(TPA)Fe(MeCN)_2]OTf_2$ recorded at 80 K. The isomer shift δ (mm/s) is 0.44, and the absolute value of the quadrupole splitting |ΔEQ| (mm/s) is 0.34.

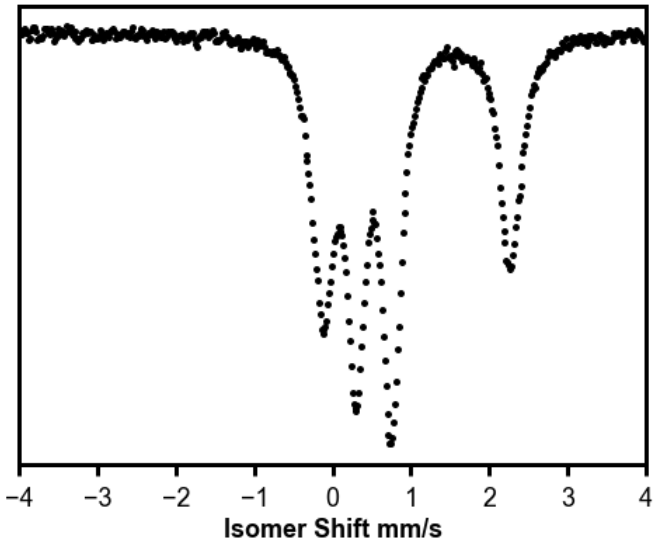

Figure B35: Mössbauer spectrum of crystalline $[(TPA)Fe(NH_3)_2]OTf_2$ recorded at 100 K.

The Mössbauer spectrum at 100 K, the temperature that diffraction data was collected at, can be fit by two quadrupole doublets. One doublet has isomer shift 1.06 mm/s and quadrupole splitting 2.38 mm/s, and the second has isomer shift 0.52 mm/s and quadrupole splitting 0.47 mm/s. Asymmetry in the quadrupole doublets is observed; this is likely due to the anisotropic orientation of the needle-like crystalline sample in the Mössbauer cup. The relative peak areas of these quadrupole doublets are 0.45:0.55, respectively. These quadrupole doublets are in agreement with the presence of both high spin and low spin Fe(II) in similar abundance; this is in agreement with the observed ratio of high spin and low spin Fe(II) in the solid state structure.

B14. ATR-IR spectrum of [(TPA)Fe(NH$_3$)$_2$]OTf$_2$

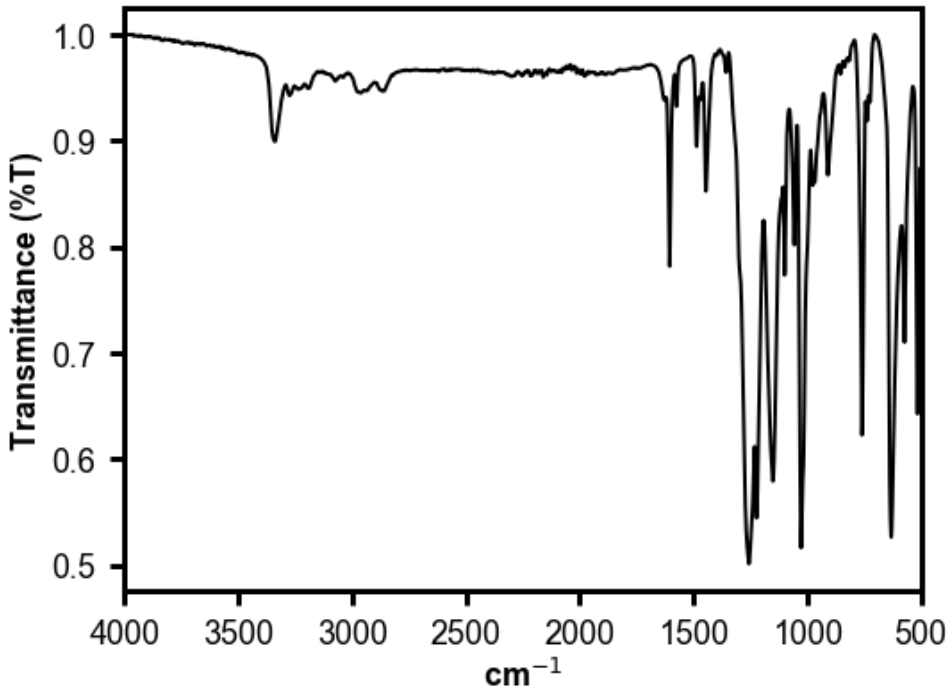

Figure B36: ATR-IR spectrum of a solid sample of crystalline [(TPA)Fe(NH$_3$)$_2$]OTf$_2$.

B15. UV-Vis spectrum of $[Fe(NH_3)_6]OTf_2$

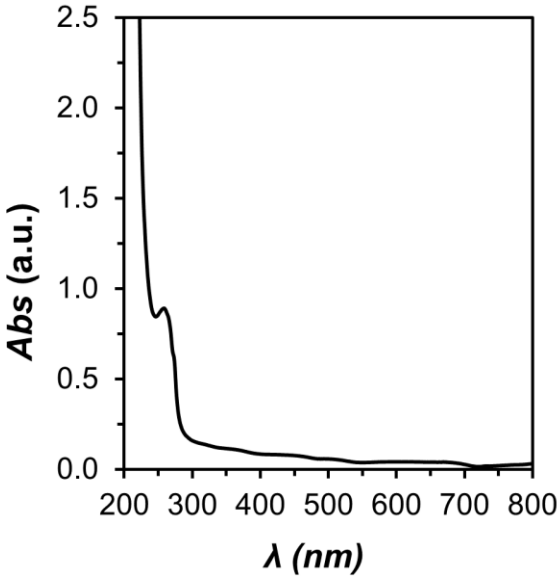

Figure B37: UV-Vis spectrum of 0.4 mM $[Fe(NH_3)_6]OTf_2$ formed by dissolving $FeOTf_2$ in a 2 M NH_3 solution.

B16. Electrochemistry of the first redox process (E_1)

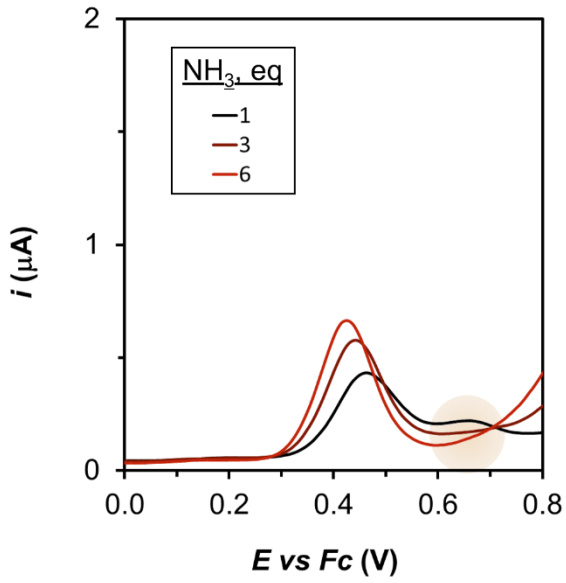

Figure B38: Differential pulse voltammograms in acetonitrile with 0.5 mM $[(TPA)Fe(MeCN)_2]OTf_2$ and 0.05 M NH_4OTf at low ammonia concentrations reflecting the equilibrium character in the substitution of MeCN by NH_3 in the coordination sphere of $[(TPA)Fe]^{2+}$, since the feature at 0.65 V corresponds to remaining $[(TPA)Fe(MeCN)_2]^{2+}$.

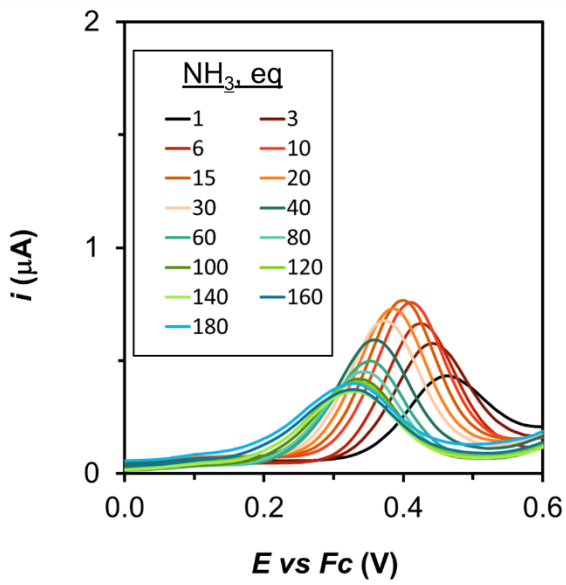

Figure B39: Differential pulse voltammograms in acetonitrile with 0.5 mM [(TPA)Fe(MeCN)$_2$]OTf$_2$ and 0.05 M NH_4OTf with varying ammonia concentrations.

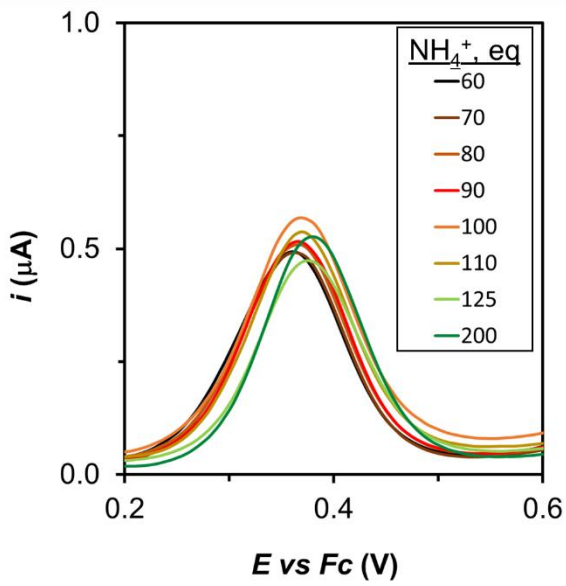

Figure B40: Differential pulse voltammograms in acetonitrile with 0.5 mM [(TPA)Fe(MeCN)$_2$]OTf$_2$, 0.025 M NH_3, and varying NH_4OTf concentration.

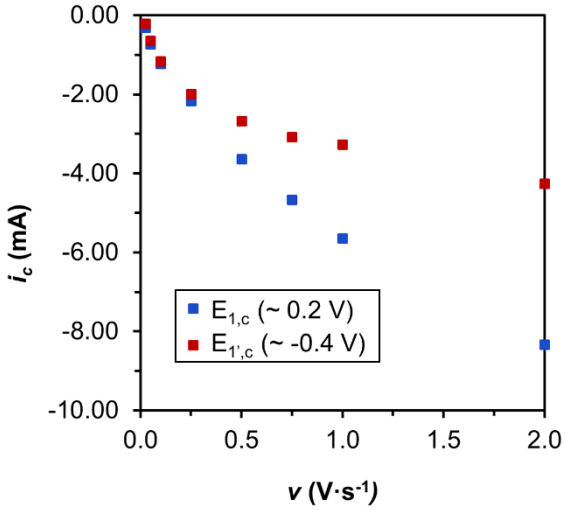

Figure B41: Intensity of the cathodic peaks at the potential $E_{1,c}$ and $E_{1',c}$ depending on the scan rate. At low scan rates, both peaks show similar intensities corresponding to similar concentrations of species $[(TPA)Fe^{III}(NH_3)_2]^{3+}$ and $[(TPA)Fe^{III}(NH_3)(NH_2)]^{2+}$. As the scan rate increases, the intensity of the $[(TPA)Fe^{III}(NH_3)_2]^{3+}$ reductive peak at around 0.2 V decreases faster than the one corresponding to $[(TPA)Fe^{III}(NH_3)(NH_2)]^{2+}$, indicating higher concentrations of the former due to the scan rate being faster than the deprotonation equilibrium. Both intensity values were measured with respect to the anodic baseline due to difficulties in establishing the baseline from the cathodic scan arising from the proximity of both redox events E_1 and E_2.

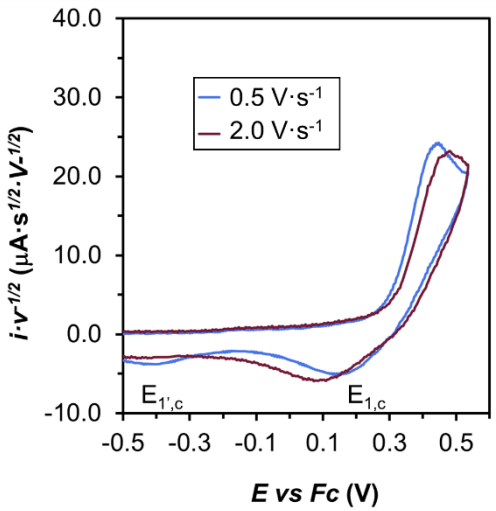

Figure B42: CV of an acetonitrile solution containing 0.5 mM (TPA)Fe(MeCN)$_2$]OTf$_2$, 0.05 M NH_4OTf, and 0.05 M NH_3 performed at two scan rates to show the different ratio of the intensities at $E_{1,c}$ and $E_{1',c}$.

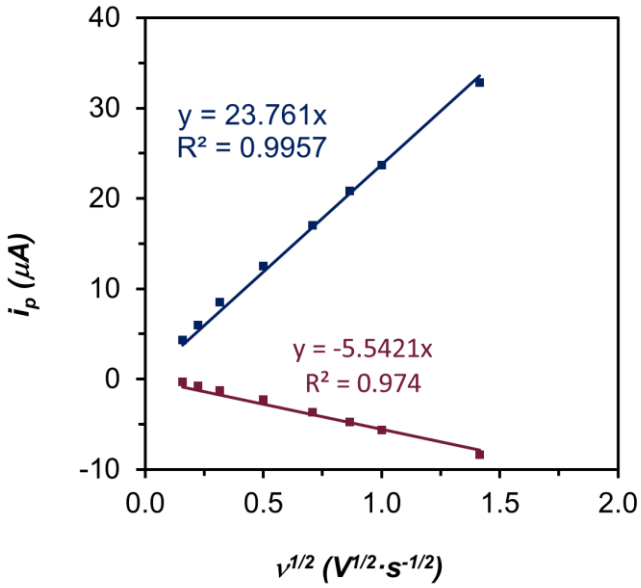

Figure B43: Plot of the intensity of the anodic (blue) and cathodic (red) scans in the precatalytic wave centered at E_1 versus the square root of the scan rate according to the Randles-Sevcik equation. Both intensity values were measured with respect to the anodic baseline due to difficulties in establishing the baseline from the cathodic scan arising from

the proximity of both redox events E_1 and E_2. This fact, together with the equilibrium between $[(TPA)Fe^{III}(NH_3)_2]^{3+}$ and $[(TPA)Fe^{III}(NH_3)(NH_2)]^{2+}$, accounts for the difference in the cathodic and anodic intensities.

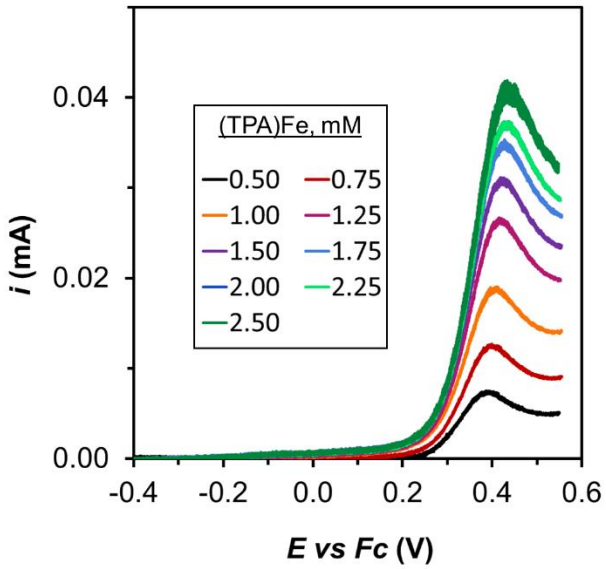

Figure B44: Linear sweep voltammograms recorded at 100 $mV \cdot s^{-1}$ in a MeCN solution containing, 0.05 M NH_3, 0.05 M NH_4OTf, and different concentrations of $[(TPA)Fe(MeCN)_2]OTf_2$.

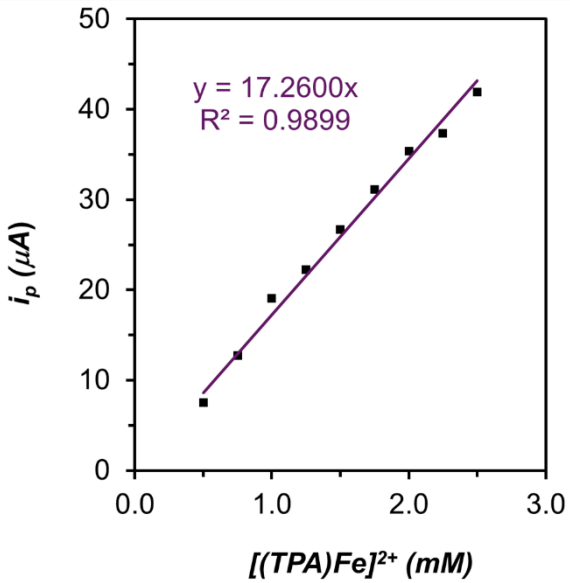

Figure B45: Plot of the intensity of the precatalytic wave E_1 at different $[(TPA)Fe(MeCN)_2]OTf_2$ concentrations.

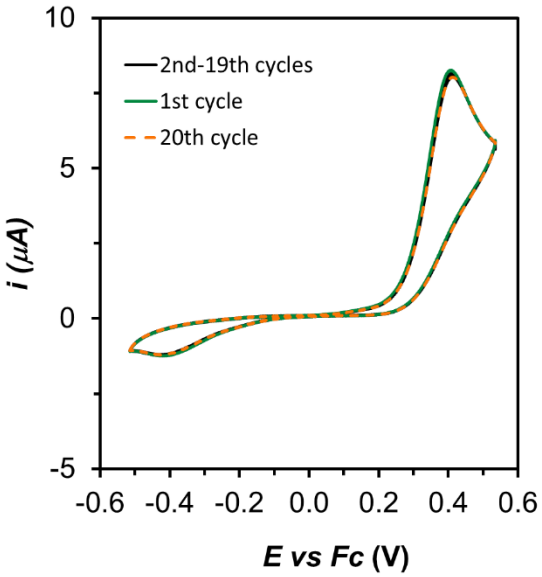

Figure B46: Successive cyclic voltammograms in an acetonitrile solution containing 0.5 mM $[(TPA)Fe(MeCN)_2]OTf_2$, 0.05 M NH_3, and 0.05 M NH_4OTf, showing the high stability of the first redox event.

B17. Electrochemistry of the catalytic process (E_2) based on Nernstian behavior

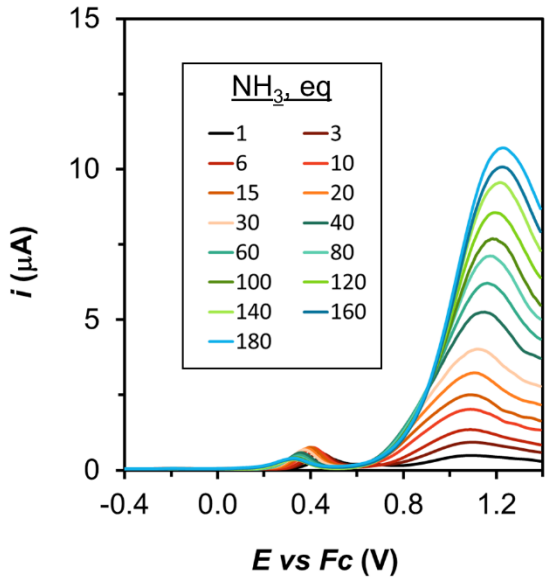

Figure B47: Differential pulse voltammograms in acetonitrile of 0.5 mM [(TPA)Fe(MeCN)$_2$]OTf$_2$, 0.05 M NH_4OTf, and varying ammonia concentrations.

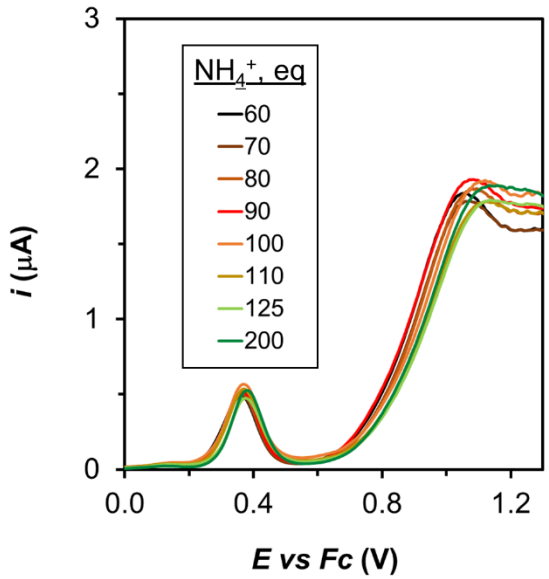

Figure B48: Differential pulse voltammograms in acetonitrile of 0.5 mM [(TPA)Fe(MeCN)$_2$]OTf$_2$, 0.025 M NH_3, and varying NH_4OTf concentration.

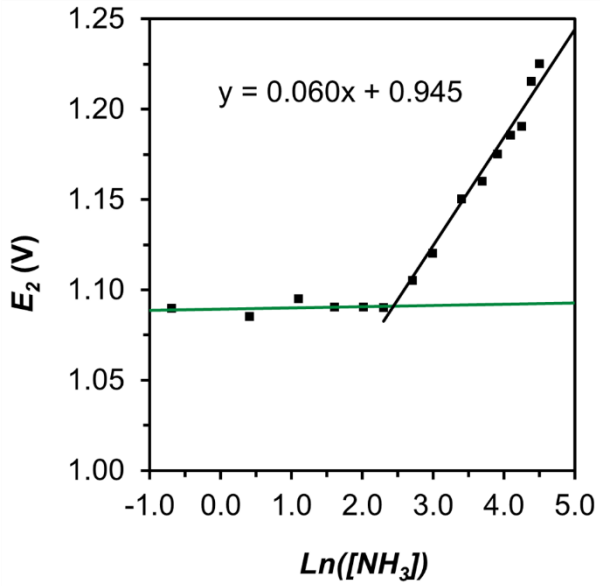

Figure B49: Plot of the potential for the first redox event E_2 versus the natural logarithm of the ammonia concentration. E_2 values were estimated from DPV experiments. At low ammonia concentrations the constant value of E_2 is consistent with an EC_{cat} mechanism.[7] The increase in E_2 at higher concentrations of ammonia suggests a non-Nernstian behavior arising from a chemical step faster than electron transfer.[8]

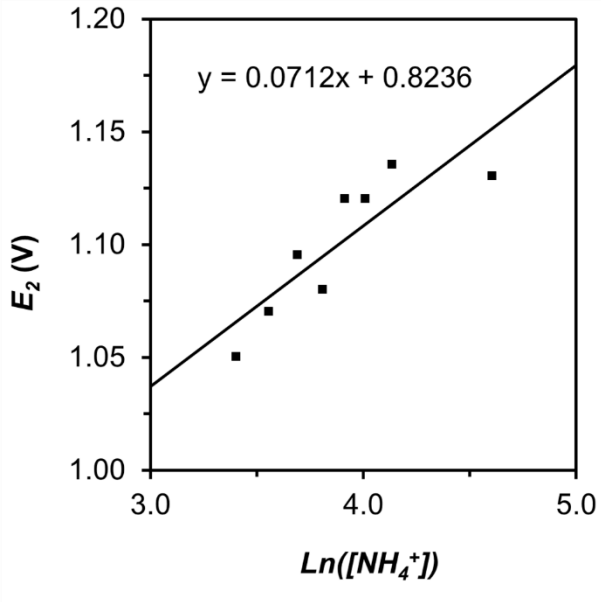

Figure B50: Plot of the potential for the first redox event E_2 versus the natural logarithm of the NH_4OTf concentration. E_2 values were estimated from DPV experiments. The increase in E_2 at higher concentrations of ammonia suggests a non-Nernstian behavior arising from a chemical step faster than electron transfer.

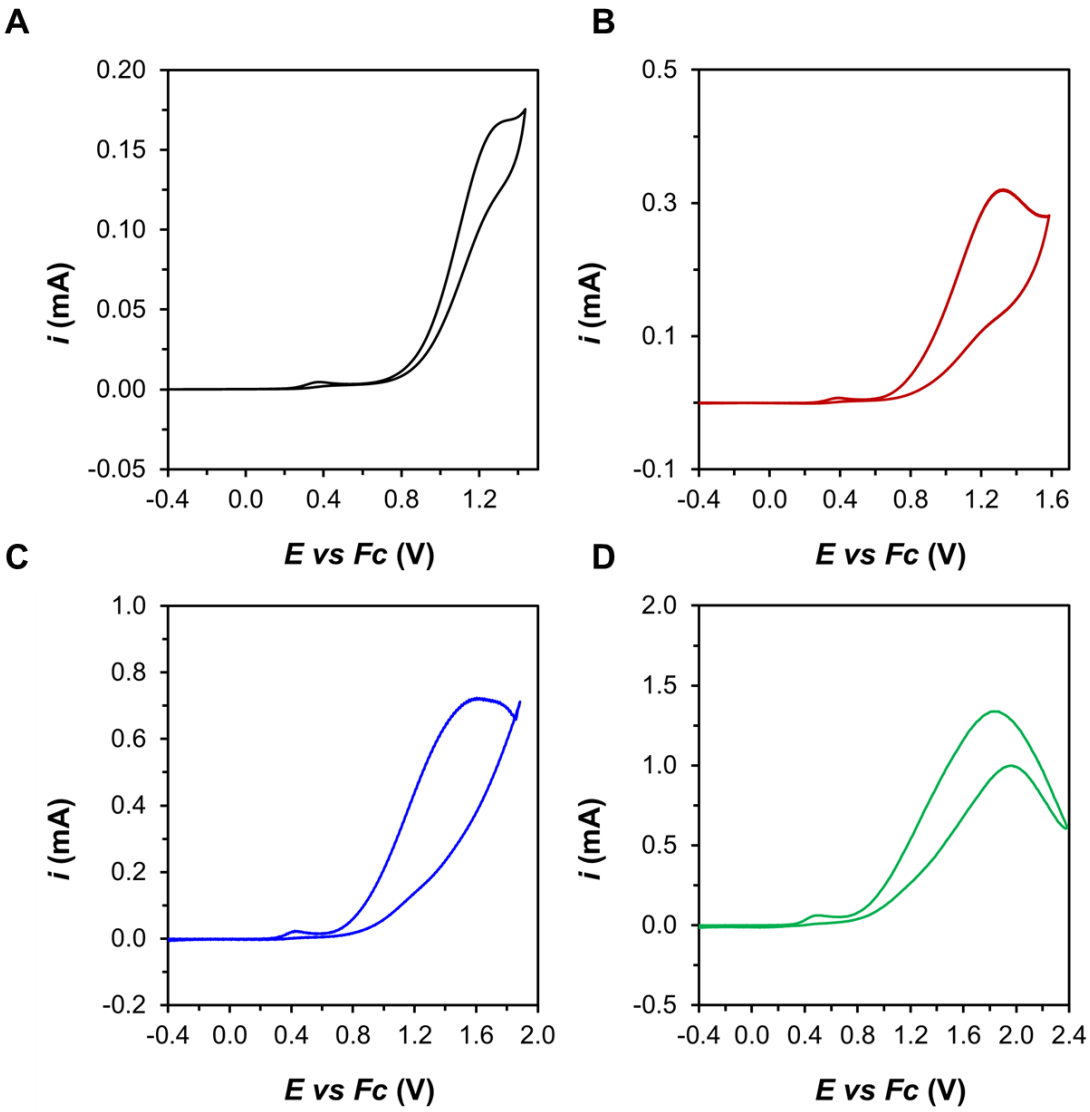

Figure B51: Background corrected CV recorded at (A) 0.01 $V \cdot s^{-1}$, (B) 0.1 $V \cdot s^{-1}$, (C) 1 $V \cdot s^{-1}$, and (D) 10 $V \cdot s^{-1}$ in a MeCN solution containing 0.5 mM $[(TPA)Fe(MeCN)_2]OTf_2$, 0.05 M NH_3, and 0.05 M NH_4OTf. Results show the deviation from ideal S-shape response in the whole range of studied scan rates.

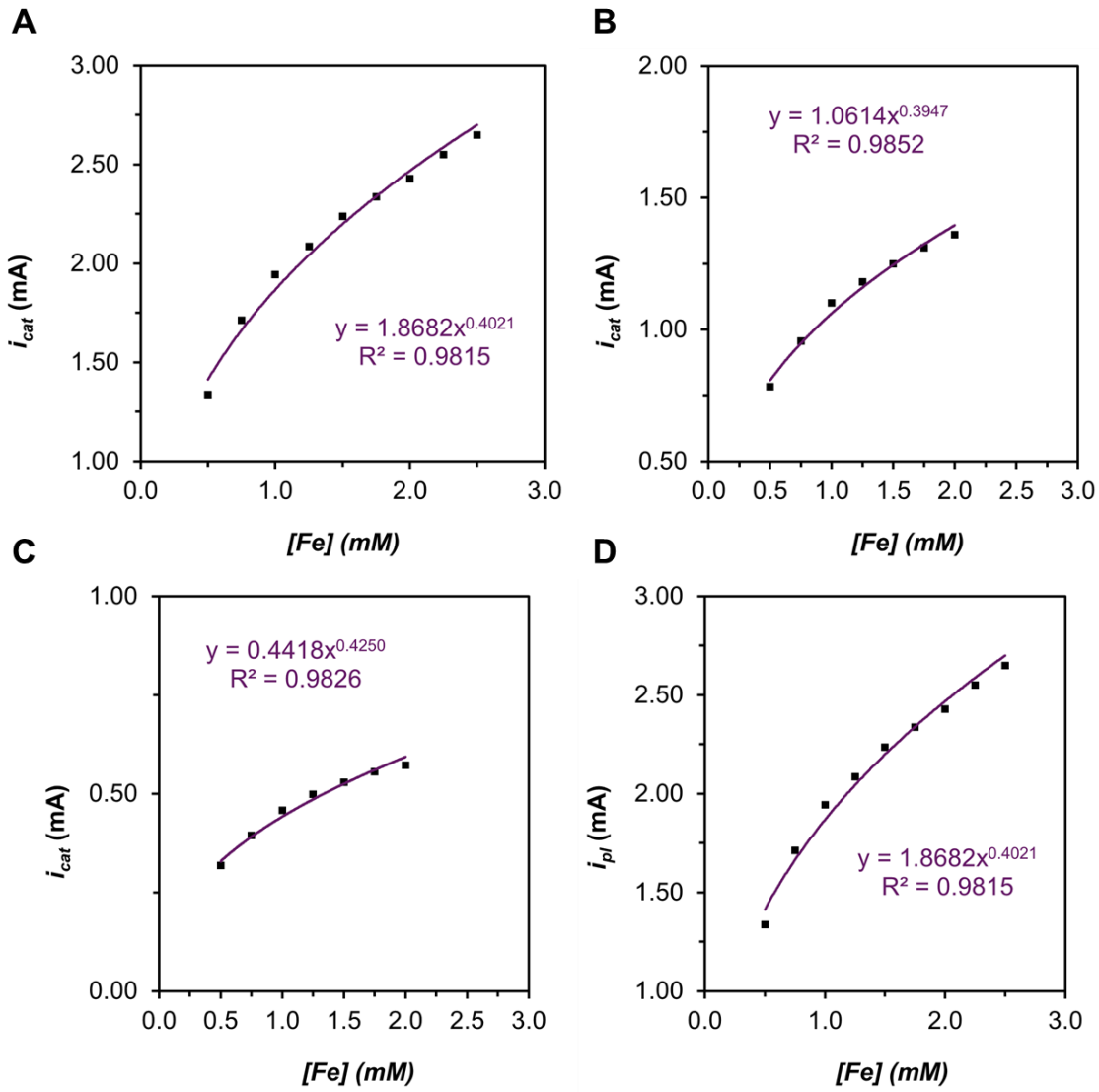

Figure B52: Plot of the intensity of the catalytic wave (i_{cat}) in CVs obtained at (A) 10 $V \cdot s^{-1}$, (B) 1 $V \cdot s^{-1}$, (C) 0.1 $V \cdot s^{-1}$, and (D) 0.01 $V \cdot s^{-1}$ at different $[(TPA)Fe(MeCN)_2]OTf_2$ concentrations. In all cases, the apparent order of reaction in $[(TPA)Fe(MeCN)_2]OTf_2$ is lower than 1 and does not seem to change with the scan rate. This behavior is consistent with the electron transfer to the electrode being the rate determining step of the catalytic process resulting in non-Nernstian behavior.

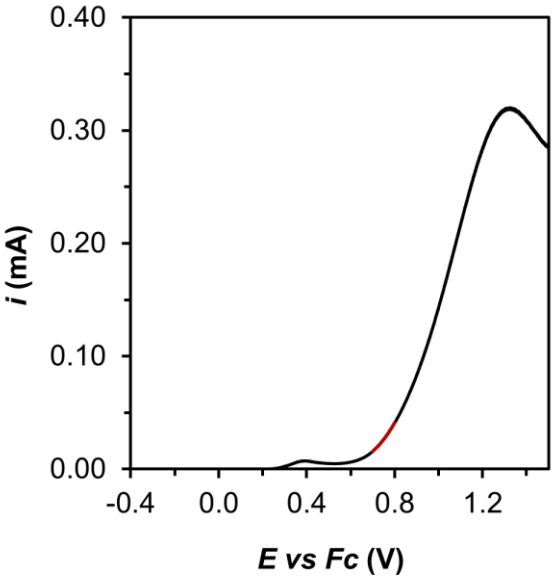

Figure B53: Background corrected linear sweep voltammetry (LSV) recorded at 100 $mV \cdot s^{-1}$ in a MeCN solution containing 0.5 mM $[(TPA)Fe(MeCN)_2]OTf_2$, 0.05 M NH_3, and 0.05 M NH_4OTf. Red trace shows the data range employed for performing the FOWA.

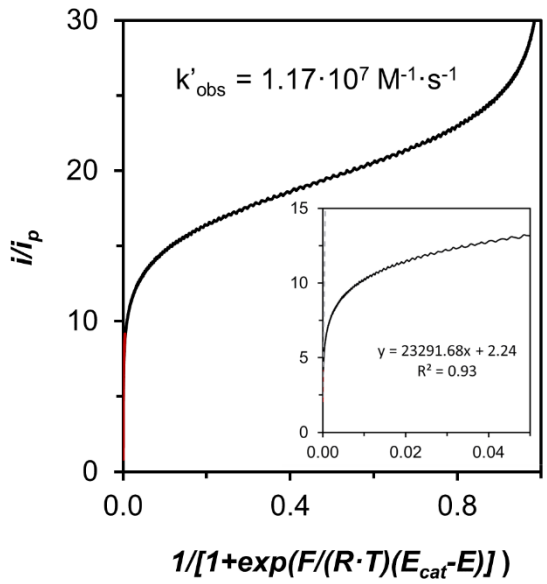

Figure B54: FOWA for a EC_{cat} mechanism[9] calculated from the previous linear sweep voltammetry (Figure B53) recorded at 100 $mV \cdot s^{-1}$ in a MeCN solution containing 0.5 mM $[(TPA)Fe(MeCN)_2]OTf_2$, 0.05 M NH_3, and 0.05 M NH_4OTf. The convex form obtained in the curve is consistent with a non-Nernstian behavior as previously reported.[8] E_{cat} was determined as the potential for the half-wave catalytic current.

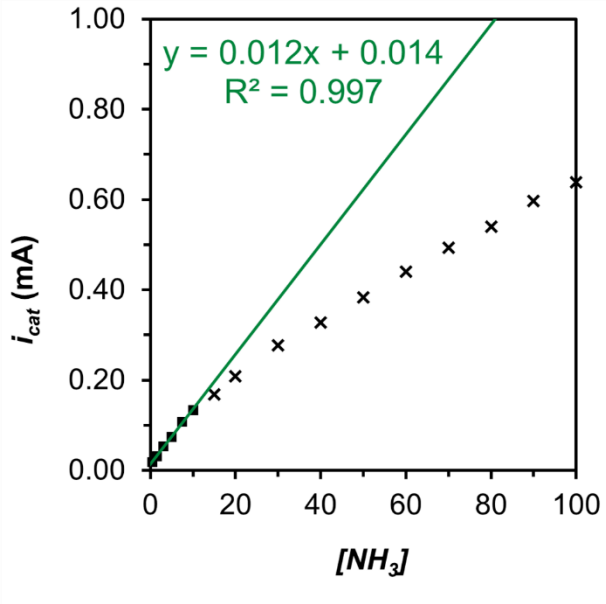

Figure B55: Plot of the intensity of the catalytic wave (i_{cat}) from CV obtained at 100 $mV \cdot s^{-1}$ at different NH_3 concentrations using 0.5 mM $[(TPA)Fe(MeCN)_2]OTf_2$ and 0.05 M NH_4OTf. For the low ammonia concentration, the catalytic current follows a linear trend suggesting first order in NH_3. At higher ammonia concentration, the fast catalysis obtained deviates from Nernstian behavior as previously evidenced and the apparent order of reaction is lower than 1.

B18. Discussion of the non-Nernstian behavior in catalytic process (E_2)

The equations governing the electrochemical behavior of an EC_{cat} mechanism depend again on the regime of the voltammetry response in the kinetic zone diagram for catalytic processes. The easiest mathematical treatment is obtained with the S-shape response when the intensity of the catalytic wave purely depends on the kinetics of the process rather than the diffusion of substrate to the electrode.[7] Unfortunately, no pure S-shape has been found in the whole range of analyzed scan rates as previously shown. In fact, analysis of the dependence of the catalytic current i_{cat} on the catalyst concentration revealed a non-linear relationship with an apparent order of reaction close to 0.5 for all of the different scan rate values. This is in contrast with the linear response expected for a pseudo-first order reaction according to the following equation:

$$i_{pl} = 6FSC_{cat}^{0}\sqrt{D_{cat}}\sqrt{k_e C_{NH_3}^{0}} \qquad \text{(Equation B1)}$$

Influence of a fast deactivation process as responsible for the apparent order of reaction lower than 1 can be ruled out in the CV time scale based on the reproducibility of the CV upon 50 cycles. The deactivation process found during CPC experiments leading to Fe deposition on the electrode operates at a much longer timescale so that it is unlikely to affect the order of reaction obtained by CV. Moreover, in the EC_{cat} mechanism, the potential for the half wave of the catalytic process ($E_{cat/2}$) should be constant and independent of the concentration of substrate (NH_3). However, we have found a linear dependence between the $E_{cat/2}$ and the ln[NH_3], which features a positive slope of 0.06. Only at very low concentrations of NH_3, the potential is constant as expected. Proper treatment of the obtained

diffusion controlled waves by the foot of the wave analysis (FOWA) leads to a convex curvature in the FOWA plot which, together with the observed increase in the $E_{cat/2}$ with increasing [NH_3], is typical from a non-Nernstian behavior in the electron transfer step.[8] In such cases, other theories such as the Butler-Volmer law or Marcus-Husch model have to be applied to model the electron transfer between the catalyst and the electrode.[10] This fact might be explained by a catalytic process with a large kinetic rate so that the kinetic of the electron transfer starts to have an influence in the overall response. The influence of the electron transfer rate might also account for the apparent 0.5 order of reaction, as only a fraction of the catalyst is oxidized to the active species. In such cases, equations have been derived using the Butler-Volmer law that includes the charge transfer coefficient (α) and the rate constant for interfacial electron transfer (k_s).

B19. Electrochemistry of the catalytic process (E_2) based on Butler-Volmer law

Determination of α, k_s and D_{cat} can be achieved based on the following equations describing the CV response of an electron transfer following the Butler-Volmer law:

$$i_p = 0.496FSC_{cat}^0\sqrt{D_{cat}}\sqrt{\frac{\alpha F v}{RT}} \qquad \text{(Equation B2)}$$

$$E_{p,c} = E^0 + 0.78\frac{RT}{\alpha F} - \frac{RT}{\alpha F}\ln\left(k_s\sqrt{\frac{RT}{\alpha F v D_{cat}}}\right) \qquad \text{(Equation B3)}$$

Due to the extremely fast catalytic character of the wave at E_2 and the impossibility of obtaining reversible behavior at that potential, we have used the precatalytic wave E_1 as a reference to obtain those values as the species involved in both processes are expected to have similar properties.

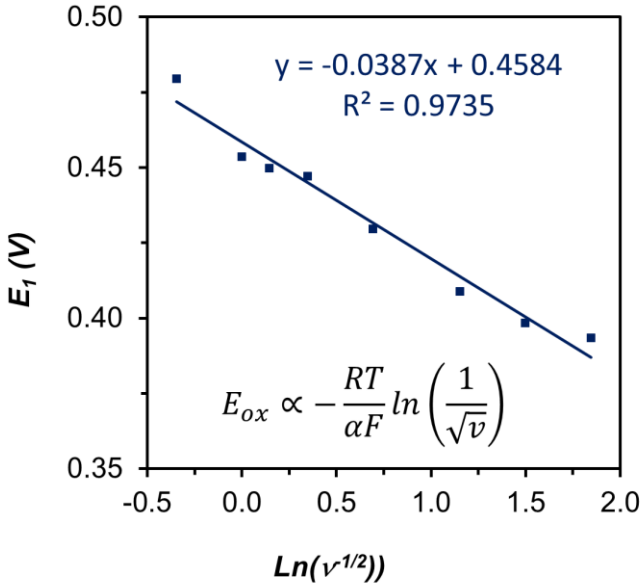

Figure B56: Plot of the E_1 potential of the anodic peak in the precatalytic wave versus Ln($1/v^{-1/2}$) following the equation for the potential using the Butler-Volmer law. The slope of that plot allows a value of 0.66 for α to be obtained.

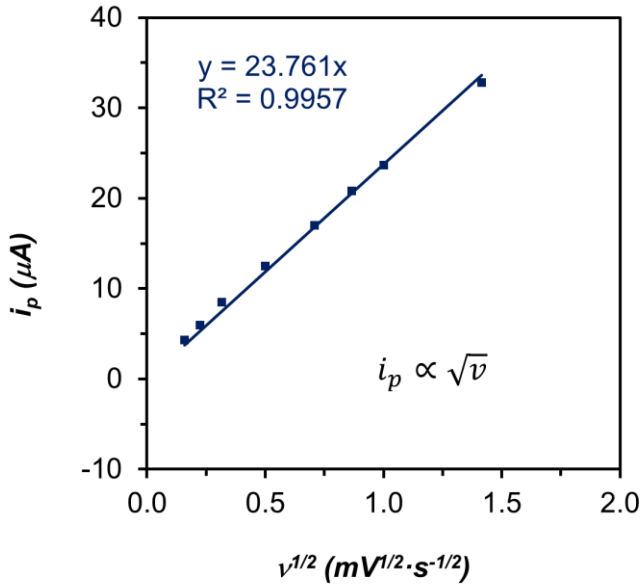

Figure B57: Plot of the intensity of the anodic scans in the precatalytic wave centered at E_1 versus the square root of the scan rate.

D_{cat} has been determined from the slope in previous plot of the intensity of the peak at E_1 versus the square root of the scan rate, resulting in a value of $9.5 \cdot 10^{-10}$ $m^2 \cdot s^{-1}$. Then, using α, D_{cat} and the equation for the previous anodic peak potential with an E^0 of 0.3 V determined from $E_{1/2} = (E_{1,a}+E_{1,c})/2$, the calculated value of k_s is 111 $m \cdot s^{-1}$.

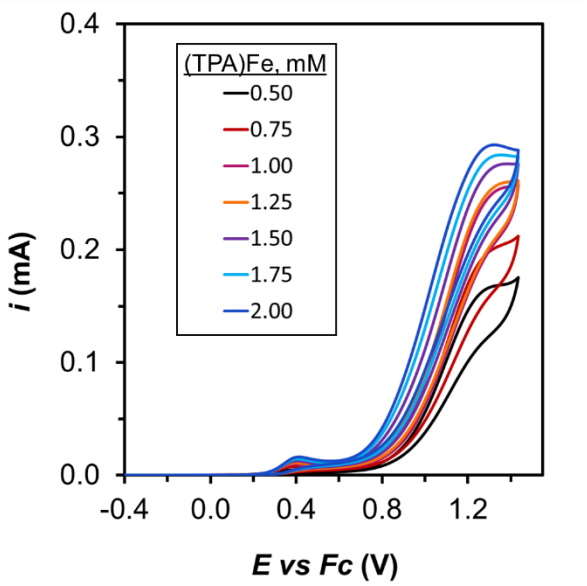

Figure B58: Cyclic voltammograms recorded at 10 $mV \cdot s^{-1}$ in a MeCN solution containing, 0.05 M NH_3, 0.05 M NH_4OTf, and different concentrations of $[(TPA)Fe(MeCN)_2]OTf_2$.

Procedure for the Foot-of-the-wave analysis performed in each condition:

Foot-of-the-wave analysis was performed by using the equations deducted for EC_{cat} obeying the Butler –Volmer law[11], following the next equation:

$$FIT\left(E^0_{P/Q} - E\right) = \frac{\frac{i}{i_p}}{1 - 0.446\frac{i}{i_p}\frac{\sqrt{D_{cat}}}{k_s}\sqrt{\frac{F}{R \cdot T}v}\exp\left[\alpha\frac{F}{R \cdot T}\left(E^0_{cat} - E\right)\right]}$$

$$= \frac{n \cdot 2.24 \cdot \sqrt{\frac{R \cdot T}{F \cdot v} \cdot k'_{obs}}}{1 + \exp\left[\frac{F}{R \cdot T}\left(E^0_{cat} - E\right)\right]} \qquad \text{(Equation B4)}$$

F is the Faraday constant, R is the gas constant, T is the temperature. The parameters α, k_s and D_{cat} have been previously obtained using the precatalytic wave as model for the electron transfer. In this case, n = 6 due to the 6 electrons involved in the catalytic ammonia oxidation to molecular nitrogen. The intensity of the one-electron wave (i_p) has been estimated from the one-electron oxidation precatalytic wave at E_1 for each condition. E^0_{cat} has been determined as the potential of the half-wave for the catalytic process. For each condition, involving concentration of catalyst, concentration of NH_3 and scan rate (v), the FOWA has been performed in similar regions of the potential range in order to allow a fair comparison upon changing the conditions. This region has been selected as the foot of the wave region where the plot of FIT versus 1/(1+exp[F/(RT)(E_{cat}-E)]) behaves linearly (R^2 > 0.85). Then, from the slope of that plot, the apparent pseudo-first order rate constant k'_{obs} can be obtained and thus the value of the apparent second-order rate constant k_{obs}. A representative example of this methodology is shown below for one specific condition.

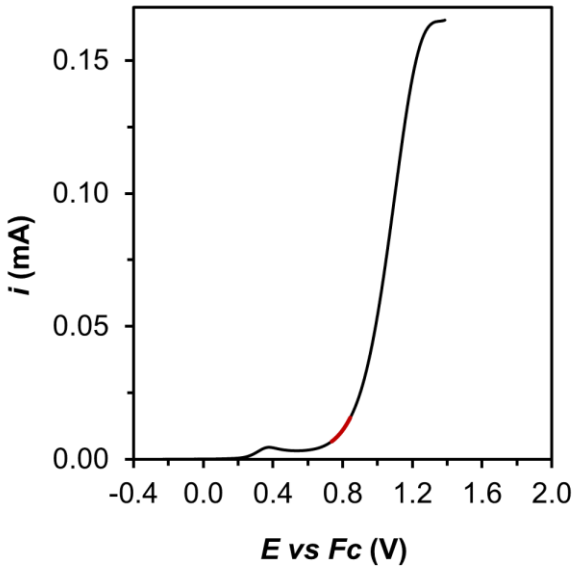

Figure B59: Background corrected linear sweep voltammetry (LSV) recorded at 10 $mV \cdot s^{-1}$ in a MeCN solution containing 0.5 mM $[(TPA)Fe(MeCN)_2]OTf_2$, 0.05 M NH_3, and 0.05 M NH_4OTf. Red trace shows the data range employed for performing the FOWA.

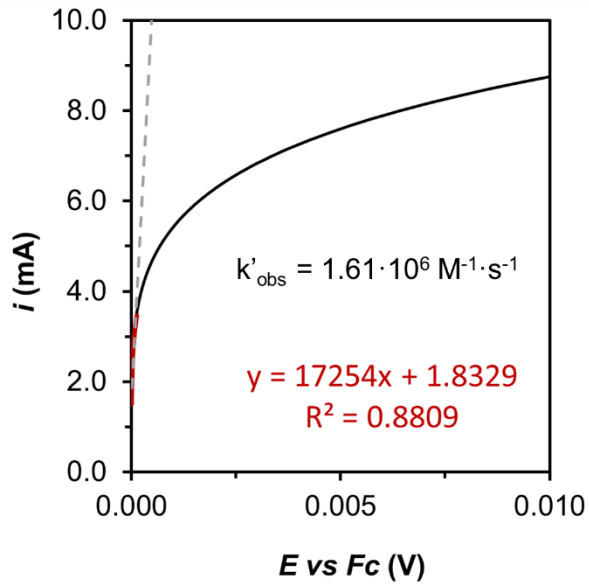

Figure B60: FOWA for an EC_{cat} mechanism obeying the Butler–Volmer law calculated from previous linear sweep voltammetry recorded at 10 $mV \cdot s^{-1}$ in a MeCN solution containing 0.5 mM $[(TPA)Fe(MeCN)_2]OTf_2$, 0.05 M NH_3, and 0.05 M NH_4OTf.

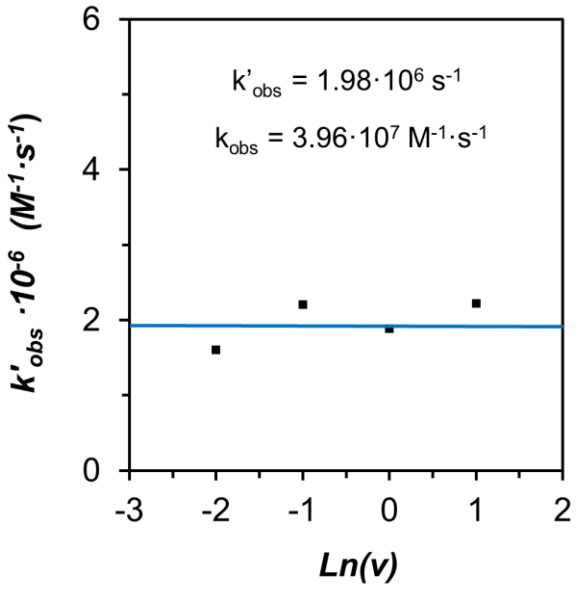

Figure B61: Plot of the k'$_{obs}$ calculated by FOWA from LSV using 0.5 mM [(TPA)Fe(MeCN)$_2$]OTf$_2$, 0.05 M NH_3, and 0.05 M NH_4OTf at different scan rates versus the natural logarithm of the scan rate. The observed independence leading to an average value of $1.98 \cdot 10^6$ s^{-1} is consistent with the assumed mechanism.

B20. Reversible binding of TPA to $FeOTf_2$

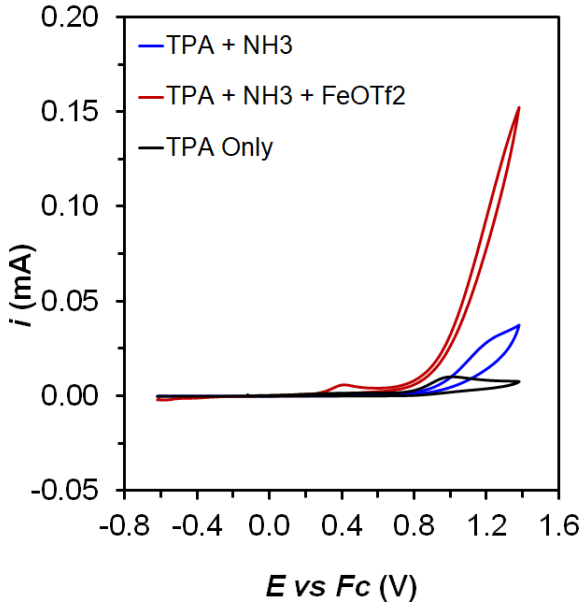

Figure B62: Cyclic voltammograms in acetonitrile with 50 mM NH_4OTf and (black) free TPA, (red) free TPA and 65 mM NH_3, and (blue) free TPA, 65 mM NH_3, and 0.5 mM $FeOTf_2$ added sequentially to demonstrate the ability of $FeOTf_2$ to rebind TPA after demetallation.

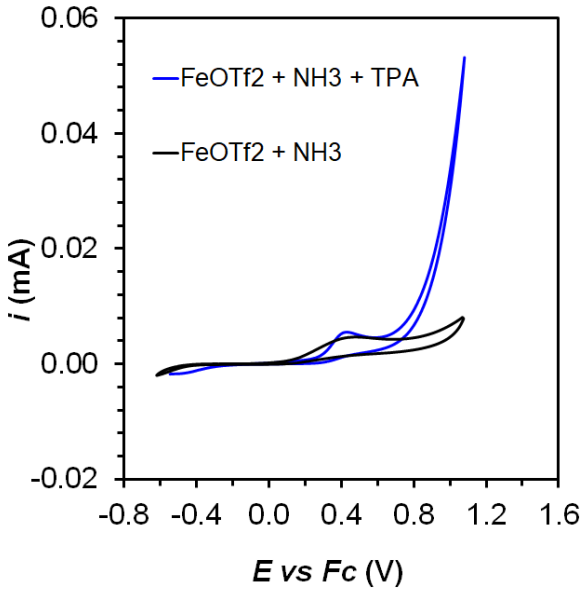

Figure B63: Cyclic voltammograms in acetonitrile with 0.5 mM $FeOTf_2$, 50 mM NH_3, and 50 mM NH_4OTf in the absence of added TPA (black) and in the presence of TPA (blue). Free TPA was added to the iron(II) triflate solution to show that it can rebind after demetallation and coordination of ammonia.

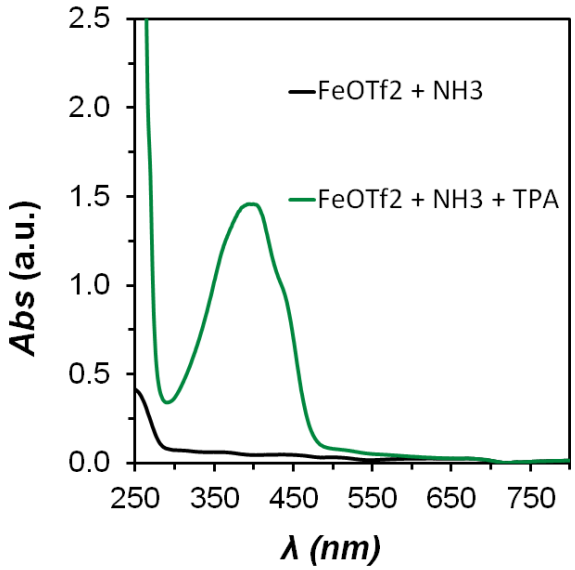

Figure B64: UV-Vis spectra in acetonitrile with 0.5 mM $FeOTf_2$, 50 mM NH_3, and 50 mM NH_4OTf in the absence of added TPA (black) and in the presence of TPA (blue). Free TPA was added to the iron(II) triflate solution to show that it can rebind after demetallation and coordination of ammonia.

B21. Electrochemistry of (TPA)Fe in presence of hydrazine

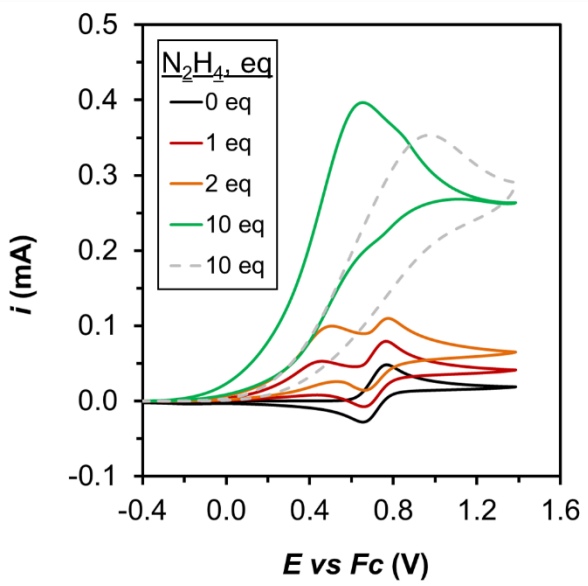

Figure B65. CV experiments of an acetonitrile solution containing 2.5 mM of $[(TPA)Fe(MeCN)_2]^{2+}$ with increasing concentrations of N_2H_4. The grey dashed line shows the background current using 10 equivalents of hydrazine in the absence of (TPA)Fe complex. BDD was used as the working electrode, and the scan rate was set to 100 $mV \cdot s^{-1}$.

B22. References

[1] Canary, J. W.; Wang, Y.; Roy, R. Tris[(2-pyridyl)methyl]amine (TPA) and (+)-bis[(2-pyridyl)methyl]-1-(2-pyridyl)-ethylamine (α-METPA). *Inorg. Synth.* **1998**, *32*, 70–75.

[2] Diebold, A.; Hagen, K. S. Iron(II) Polyamine Chemistry: Variation of Spin State and Coordination Number in Solid State and Solution with Iron(II) Tris(2-pyridylmethyl)amine Complexes. *Inorg. Chem.* **1998**, *37*, 215–223.

[3] Sheldrick, G. SHELXT - Integrated Space-Group and Crystal-Structure Determination. *Acta Crystallogr., Sect. C: Struct.* **2015**, *71*, 3–8.

[4] Dolomanov, O. V.; Bourhis, L. J.; Gildea, R. J.; Howard, J. A. K.; Puschmann, H. OLEX2: a Complete Structure Solution, Refinement and Analysis Program. *J. Appl. Crystallogr.* **2009**, *42*, 339–341.

[5] Macpherson, J. V. A Practical Guide to Using Boron Doped Diamond in Electrochemical Research. *Phys. Chem. Chem. Phys.* **2015**, *17*, 2935–2949.

[6] Lindley, B. M.; Appel, A. M.; Krogh-Jespersen, K.; Mayer, J. M.; Miller, A. J. M. Evaluating the Thermodynamics of Electrocatalytic N_2 Reduction in Acetonitrile. *ACS Energy Lett.* **2016,** *1*, 698–704.

[7] Costentin, C.; Savéant, J. M. Elements of Molecular and Biomolecular Electrochemistry: An Electrochemical Approach to Electron Transfer Chemistry, John Wiley & Sons, Hoboken, 2006.

[8] Wang, V. C.-C.; Johnson, B. A. Interpreting the Electrocatalytic Voltammetry of Homogeneous Catalysts by the Foot of the Wave Analysis and Its Wider Implications. *ACS Catal.* **2019**, *9*, 7109–7123.

[9] Costentin, C.; Drouet, S.; Robert, M.; Savéant, J.-M. Turnover Numbers, Turnover Frequencies, and Overpotential in Molecular Catalysis of Electrochemical Reactions. Cyclic Voltammetry and Preparative-Scale Electrolysis. *J. Am. Chem. Soc.* **2012**, *134*, 11235–11242.

[10] Costentin, C.; Robert, M.; Savéant, J.-M. Catalysis of the Electrochemical Reduction of Carbon Dioxide. *Chem. Soc. Rev.* **2013**, *42*, 2423–2436.

[11] Costentin, C.; Drouet, S.; Robert, M.; Savéant, J.-M. A Local Proton Source Enhances CO_2 Electroreduction to CO by a Molecular Fe Catalyst. *Science* **2012**, *338*, 90–94.

Appendix C

Supplementary Information for Chapter 4

Adapted from:
Zott, M. D.; Peters, J. C.
J. Am. Chem. Soc. **2021**, *143*, 7612–7616.
DOI: 10.1021/jacs.1c02232

.

C.1 General procedures

General Considerations: All manipulations were carried out using standard Schlenk or glovebox techniques under an N_2 or Ar atmosphere. Unless otherwise noted, solvents were deoxygenated and dried by thoroughly sparging with N_2 gas followed by passage through an activated alumina column in a solvent purification system (SG Water, USA LLC). For electrochemical measurements under an Ar atmosphere, solvents were further degassed and then left under Ar. All solvents were stored over activated 3 or 4 Å molecular sieves prior to use. Anhydrous ammonia gas was dried by passage through a calcium oxide drying tube. All reagents were purchased from commercial vendors and used without further purification unless otherwise stated. Tris(2-pyridylmethyl)amine (TPA),[1] tris(2-pyridylmethylamine) iron(II) triflate bis-acetonitrile ($[(TPA)Fe(MeCN)_2]OTf_2$),[2] 6-(1,1-di(pyridin-2-yl)ethyl)-2,2'-bipyridine ($bpyPy_2Me$),[3] and 6-(1,1-di(pyridin-2-yl)ethyl)-2,2'-bipyridine iron(II) triflate bis-acetonitrile ($[(bpyPy_2Me)Fe(MeCN)_2]OTf_2$)[4] $^{15}NH_4OTf$ was prepared from $^{15}NH_4Cl$ (Cambridge Isotope Laboratories) by anion exchange with silver triflate or metathesis with triflic acid, followed by repeated recrystallization from boiling acetonitrile. ^1H NMR chemical shifts are reported in ppm relative to tetramethylsilane, using residual solvent resonances as internal standards.

Electrochemistry: Voltammetry experiments were carried out with a Biologic VSP-300 or CH Instruments 600B potentiostat using a one-compartment three-electrode cell, and coulometry experiments were carried out with a Biologic VSP-300 potentiostat using a one-compartment three-electrode cell with a septum capped 14/20 joint for headspace analysis. For voltammetry, a boron-doped diamond (BDD) working electrode (3 mm diameter), a Pt

wire counter electrode, and a Ag/AgOTf reference electrode (5 mM AgOTf and 0.1 M $TBAPF_6$ in MeCN) were employed. For CPC, the same reference electrode was used, but a BDD plate (geometric area: 4 cm^2) and a Pt mesh were used respectively as working and counter electrode. All redox potentials in the present work are reported versus the Fc/Fc^+ couple, measured before each experiment to be approximately +0.12 V versus our Ag/AgOTf reference electrode.

CVs were collected at 100 $mV \cdot s^{-1}$ unless specified otherwise. $E_{1/2}$ values for the reversible waves were obtained from the half potential between the oxidative and reductive peaks. CV measurements were performed applying IR compensation, compensating 85% of the resistance measured at one high frequency value (100 kHz). Potential values for waves that are not fully reversible were obtained as the apparent standard potential from differential pulse voltammetry measurements

Gas Chromatography: Gas chromatography was performed in the Environmental Analysis Center using HP 5890 Series II instruments. Gas quantification was performed using a molecular sieve column attached to a thermal conductivity detector. Argon was the carrier gas. Standard curves were generated by direct injection of hydrogen or nitrogen gas. Quantification of background nitrogen was determined using the background oxygen signal. Isotopic measurements were performed with a separate HP 5890 Series II equipped with a GasPro column using helium as the carrier gas.

NMR: NMR spectroscopy was performed using Varian and Bruker 400 MHz NMR spectrometers equipped with broadband auto-tune probes. ^1H NMR chemical shifts are

reported in ppm relative to tetramethylsilane, using residual solvent resonances as internal standards.

UV-vis: Spectra were collected using a Cary 60 instrument with Cary WinUV software.

X-ray Crystallography: XRD studies were carried out at the Beckman Institute Crystallography Facility on a Bruker D8 Venture diffractometer (Cu Kα radiation). Structures were solved using direct methods with SHELXS or SHELXT and refined against F^2 on all data by full-matrix least squares with SHELXL.[5] All of the solutions were performed in the Olex2 program.[6] The crystals were mounted on a glass fiber under Paratone N oil.

X-ray Photoelectron Spectroscopy: XPS measurements were carried out in the Caltech Molecular Materials Resource Center using a Surface Science Instruments M-Probe ESCA spectrometer with the sample held at ultra-high vacuum (< 2 x 10^{-9} Torr), using the Al K α line at 1486.6 eV as a monochromatic X-ray source. XPS measurements were checked for surface charging effects, and the diamond carbon (sp3) 1s peak was verified to be within ±0.3 eV of 285 eV. A full scan from 0–1000 eV was acquired, and then scans at the binding energies typical for carbon (274-294 eV), boron (176-196 eV), nitrogen (389-409 eV), oxygen (522-542 eV), and iron (690-730 eV) were measured. For measurements of the BDD plate electrode after catalysis, the electrode was rinsed with acetonitrile and air dried prior to data collection.

C.2 NMR spectra for electronic structure elucidation

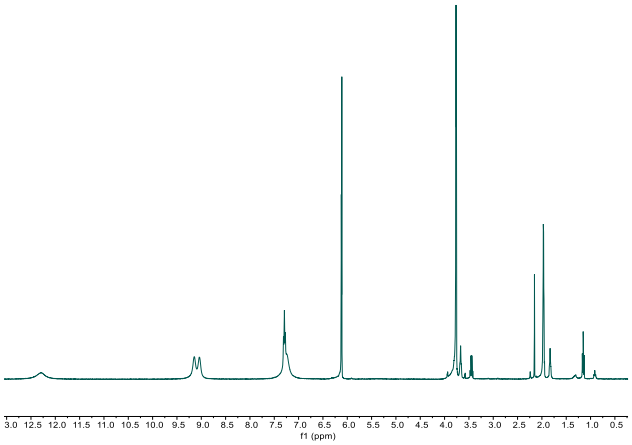

Figure C1. ^{1}H NMR spectrum of [(TPA)Fe(MeCN)$_2$]OTf$_2$ in CD_3CN at 25 °C. Spectrum also shows 1,3,5-trimethoxybenzene used for Evan's method.

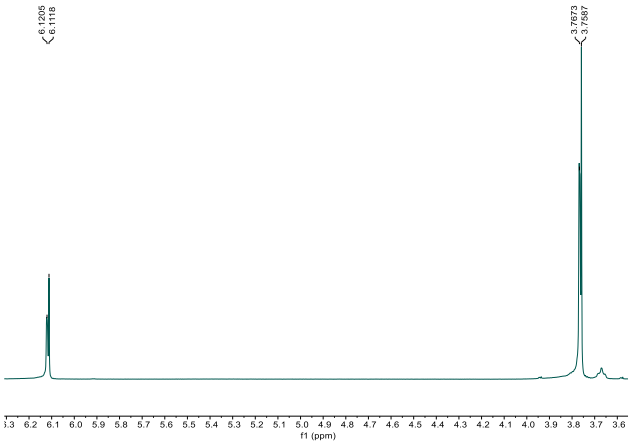

Figure C2. 1,3,5-trimethoxybenzene signals used for Evan's method for [(TPA)Fe(MeCN)$_2$]OTf$_2$ in CD_3CN at 25 °C. [Fe] = 0.011 M, $\Delta f = 3.46$ Hz, f = 400.15 MHz, $\mu = 0.68\mu_B$.

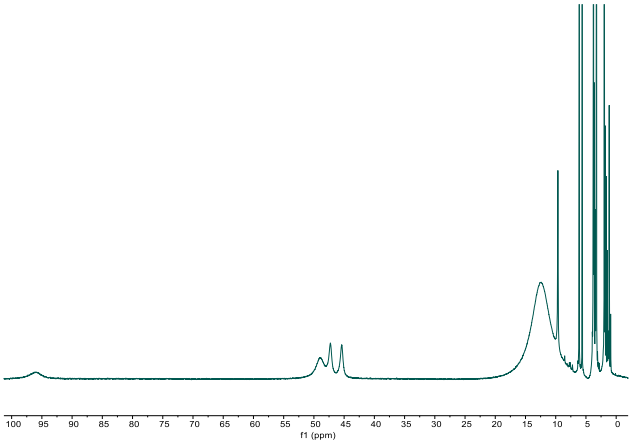

Figure C3. ^{1}H NMR spectrum of $[(TPA)Fe(L)_2]OTf_2$ (L = MeCN, NH_3) formed by mixing $[(TPA)Fe(MeCN)_2]OTf_2$ with 75 equivalents of NH_3 in CD_3CN at 25 °C. Spectrum also shows 1,3,5-trimethoxybenzene used for Evan's method.

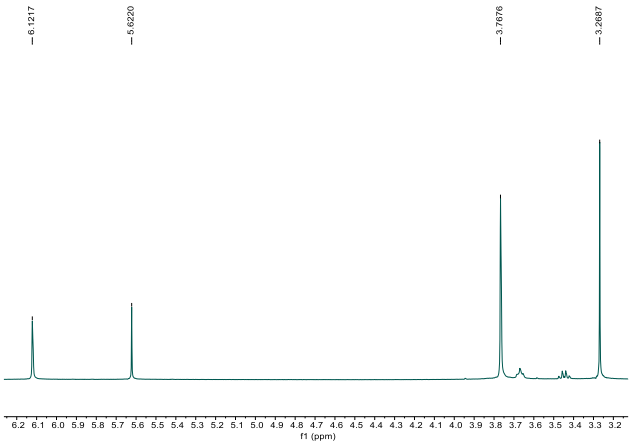

Figure C4. 1,3,5-trimethoxybenzene signals used for Evan's method for $[(TPA)Fe(L)_2]OTf_2$ (L = MeCN, NH_3), formed by mixing $[(TPA)Fe(MeCN)_2]OTf_2$ with 75 equivalents of NH_3 in CD_3CN at 25 °C. [Fe] = 0.011 M, Δf = 200 Hz, f = 400.15 MHz, $\mu = 5.2\mu_B$.

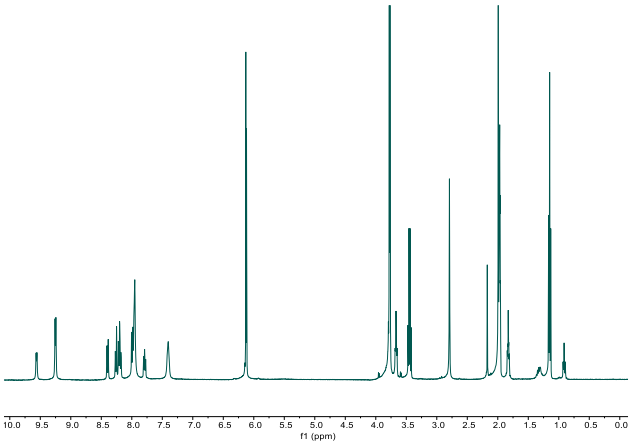

Figure C5. ^{1}H NMR spectrum of [(bpyPy$_2$Me)Fe(MeCN)$_2$]OTf$_2$ in CD$_3$CN at 25 °C. Spectrum also shows 1,3,5-trimethoxybenzene used for Evan's method.

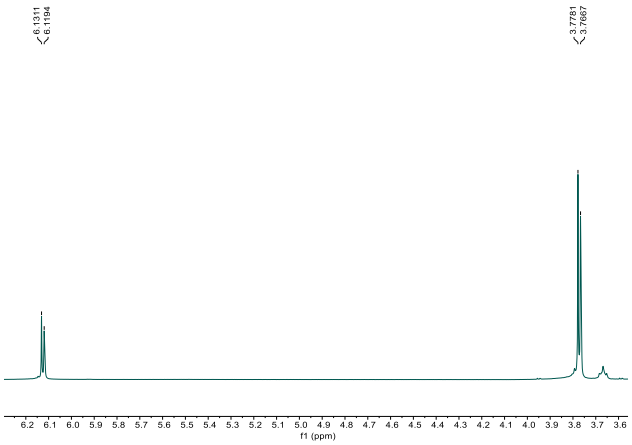

Figure C6. 1,3,5-trimethoxybenzene signals used for Evan's method for [(bpyPy$_2$Me)Fe(MeCN)$_2$]OTf$_2$ in CD$_3$CN at 25 °C. [Fe] = 0.011 M, $\Delta f = 4.62$ Hz, $f = 400.15$ MHz, $\mu = 0.79\mu_B$.

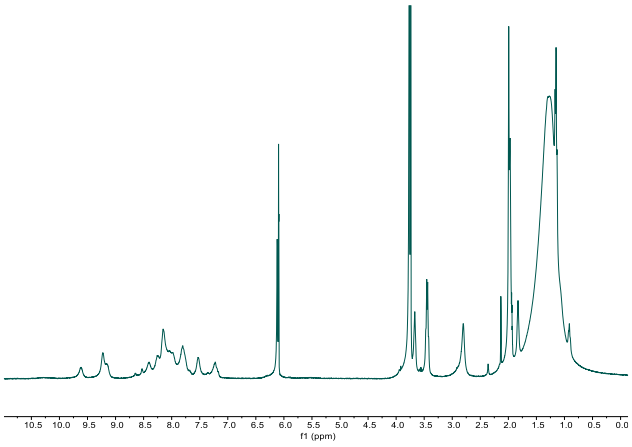

Figure C7. ^{1}H NMR spectrum of [(bpyPy$_2$Me)Fe(L)$_2$]OTf$_2$ (L = MeCN, NH$_3$) formed by mixing [(bpyPy$_2$Me)Fe(MeCN)$_2$]OTf$_2$ with 75 equivalents of NH$_3$ in CD$_3$CN at 25 °C. Spectrum also shows 1,3,5-trimethoxybenzene used for Evan's method.

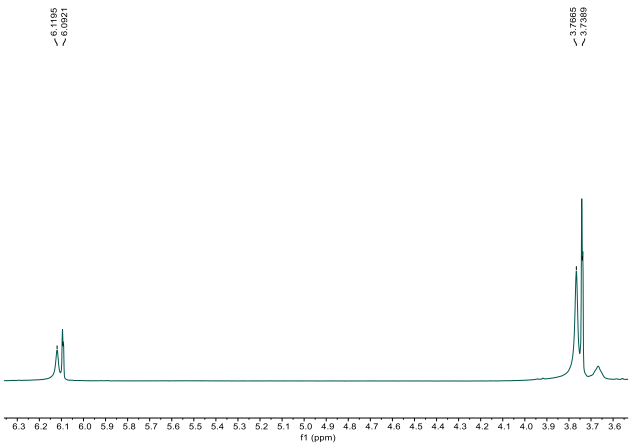

Figure C8. 1,3,5-trimethoxybenzene signals used for Evan's method for [(bpyPy$_2$Me)Fe(L)$_2$]OTf$_2$ (L = MeCN, NH$_3$), formed by mixing [(bpyPy$_2$Me)Fe(MeCN)$_2$]OTf$_2$ with 75 equivalents of NH$_3$ in CD$_3$CN at 25 °C. [Fe] = 0.011 M, Δf = 11.0 Hz, f = 400.15 MHz, μ = 1.2μ_B.

C.3 UV-vis spectra

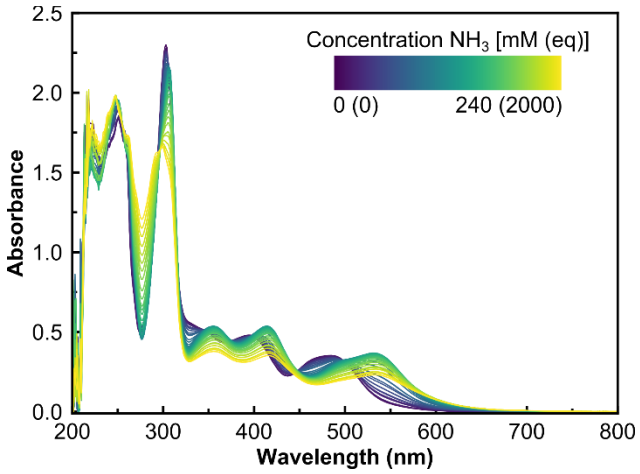

Figure C9. UV-vis spectra of acetonitrile solutions containing 0.12 mM [(bpyPy$_2$Me)Fe(MeCN)$_2$]OTf$_2$ and varying equivalents NH_3 in a 1 cm cuvette.

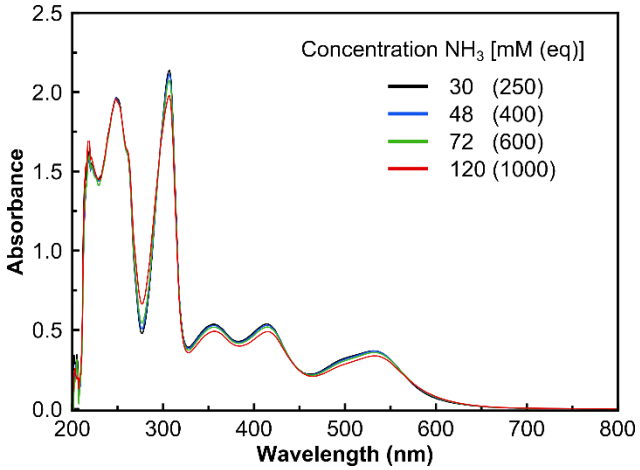

Figure C10. UV-vis spectra of acetonitrile solutions containing 0.12 mM [(bpyPy$_2$Me)Fe(MeCN)$_2$]OTf$_2$ with 250 (black), 400 (blue), 600 (green), or 1000 (red) equivalents NH_3 in a 1 cm cuvette. This shows the onset of demetallation around 600 equivalents NH_3.

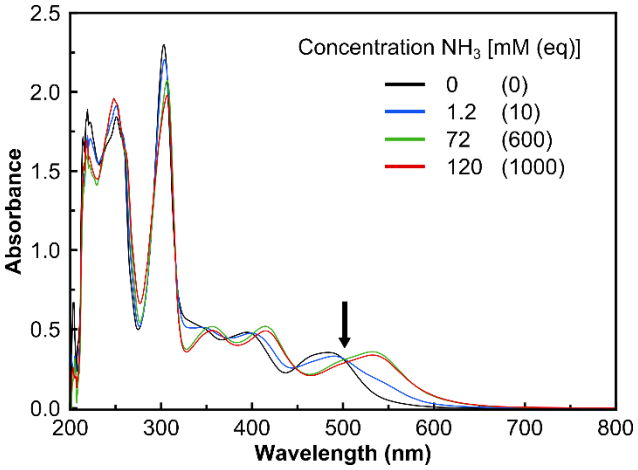

Figure C11. UV-vis spectra of acetonitrile solutions containing 0.12 mM $[(bpyPy_2Me)Fe(MeCN)_2]OTf_2$ with 0 (black), 10 (blue), 600 (green), or 1000 (red) equivalents NH_3 in a 1 cm cuvette. An arrow highlights an isosbestic point ~500 nm which is maintained for 0, 10, and 600 equivalents but has begun to show deviations assigned to demetallation at 1000 equivalents.

C.4 Catalytic controlled potential coulometry experiments

Procedures for controlled potential coulometry:

Preparation of the BDD electrode: A 10 cm^2 boron-doped diamond (BDD) plate electrode (IKA) was physically attached to standard electrical wire coated with chemical-resistant insulation, and the connection was covered with Teflon tape. The surface area of the electrode submerged in solution was around 4 cm^2.

BDD has a surface that exists in various states of reduction (H-terminated) and oxidation (O-terminated).[7] In order to remove attached nitrogen and iron generated during controlled potential coulometry experiments and to ensure a reliable electrode surface prior to CPC measurements, the BDD plate electrode was oxidatively treated prior to use. First, the electrode was soaked in concentrated nitric acid for 5 minutes. Then, a potential of 3.0 V vs Ag/AgCl was applied to the BDD electrode in a 0.5 M H_2SO_4 solution for 10 minutes. The electrode was then thoroughly rinsed with water prior to use.

Preparation of the platinum counter electrode: In order to ensure a highly active Pt surface for hydrogen evolution prior to CPC experiments, the Pt mesh counter electrode was soaked in concentrated hydrochloric acid for at least 5 minutes prior to usage.

Preparation of the custom Ag/AgOTf reference electrode: To ensure reliable potential measurements, the custom Ag/AgOTf reference electrode was prepared prior to each CPC experiment and then a CV of ferrocene was measured. In a glass tube fitted with a Vycor porous glass frit attached by Teflon heatshrink tubing, an acetonitrile solution containing 5

mM AgOTf and 0.1 M $TBAPF_6$ was added. A silver wire was placed inside and the electrode was sealed.

Preparation of ammonia solutions. For experiments with natural abundance ammonia, saturated 2 M solutions[8] in acetonitrile were prepared by bubbling anhydrous ammonia through acetonitrile in a Schlenk tube under an argon/ammonia atmosphere. For experiments with labeled $^{15}NH_3$, ammonia was liberated from $^{15}NH_4OTf$ by addition of 1.1 equivalents of 1,8-diazabicyclo[5.4.0]undec-7-ene (DBU) to ^{15}N labeled ammonium triflate dissolved in acetonitrile in a Schlenk tube inside of an argon glovebox. This solution was then vacuum transferred to a separate, clean Schlenk tube.

CPC: Inside an argon glovebox, a gas-tight electrochemical cell equipped with a 24/40 cap containing three tungsten rods for electrical contacts and a valved 14/20 joint carefully sealed with a Suba-Seal septum was prepared. A BDD plate electrode (A = 4 cm^2), high surface area platinum mesh electrode, and custom Ag/AgOTf reference electrode were connected to the 24/40 cap. All chemical reagents were then rapidly added to the cell to prevent evaporation of ammonia, and then, the cell was sealed with the 24/40 cap. Prior to each CPC experiment, a ZIR and CV were taken. No IR compensation was applied for CPC measurements. The CPC experiment was then conducted for 24 h. The cell was then removed from the glovebox for analysis by gas chromatography. For headspace analysis, 100 μL of the headspace was injected into a GC-TCD for quantification using a lockable Hamilton syringe with a 26S gauge needle. For GC-MS, only 50 μL of the headspace was injected.

For each experiment, a 10 mL solution containing 0.05 mM [Fe], 20 mM NH_3 (1.0 mL of 0.2 M solution), and 50 mM NH_4OTf (84 mg) was prepared in acetonitrile.

Reload experiments: After a completed CPC experiment, the valved 14/20 joint on the electrochemical cell was sealed, the septum was removed, and a 14/20 joint-to-tubing adapter was connected. This joint was connected to a double-manifold Schlenk line and put under an argon atmosphere. Under a positive counter-flow of argon, the 24/40 electrode cap was removed and replaced with a ground-glass stopper. The cell was then carefully evaporated to dryness under vacuum and brought into an argon glovebox. To this cell containing ammonium triflate electrolyte and used catalyst was added 9 mL acetonitrile and 1.0 mL of a 0.2 M NH_3 solution to reset the ammonia concentration to the initial value. Then, the CPC experiment was performed following our standard procedures.

Table B1. Results of catalytic CPC experiments performed at 0.85 V vs Fc/Fc^+ for 24 h with 0.05 mM [Fe] and 20 mM NH_3 (400 equivalents). For entries where reload experiments were conducted, the entries are listed as x.1 and x.2 for the initial and subsequent reload experiment, respectively. LOQ indicates that the amount of gas produced was below the limit of quantification.

Entry	Fe Source	Eq. N_2	Charge (C)	FE N_2 (%)	FE H_2 (%)
1.1	$[(bpyPy_2Me)Fe(MeCN)_2]OTf_2$	89	29.9	86	77
2.1	$[(bpyPy_2Me)Fe(MeCN)_2]OTf_2$	83	26.5	91	80
3	$[(bpyPy_2Me)Fe(MeCN)_2]OTf_2$	97	31.1	91	93
4*	$[(bpyPy_2Me)Fe(MeCN)_2]OTf_2$	102	36.5	81	84
Avg. 1.1–4	$[(bpyPy_2Me)Fe(MeCN)_2]OTf_2$	93	–	87	84
1.2	$[(bpyPy_2Me)Fe(MeCN)_2]OTf_2$	55	21.1	77	78
2.2	$[(bpyPy_2Me)Fe(MeCN)_2]OTf_2$	57	19.7	84	67
Avg. Reload	$[(bpyPy_2Me)Fe(MeCN)_2]OTf_2$	56	–	81	73
3	None (NH_3 only)	LOQ	0.86	LOQ	73
4.1	$FeOTf_2 \cdot 2$ MeCN	7.7	8.2	27	74
5	$FeOTf_2 \cdot 2$ MeCN	7.1	7.5	28	33
Avg. 4.1–5	$FeOTf_2 \cdot 2$ MeCN	7.4	–	28	54
4.2	$FeOTf_2 \cdot 2$ MeCN	LOQ	1.2	LOQ	65

* Experiment performed with $^{15}NH_3$ and $^{15}NH_4OTf$

NMR spectra showing active catalyst after CPC:

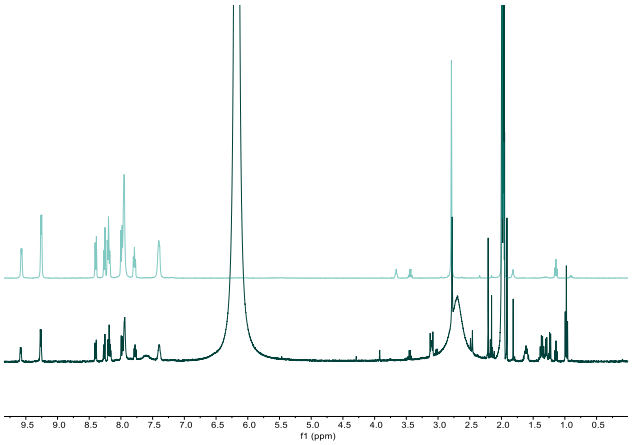

Figure C12. ^{1}H NMR spectra of [(bpyPy$_2$Me)Fe(MeCN)$_2$]OTf$_2$ precatalyst (top) and a sample extracted after a CPC experiment (bottom) in CD_3CN. The bottom spectrum shows that active catalyst remains after CPC experiments, as corroborated by reload experiments.

C.5 Electrode rinse test after CPC

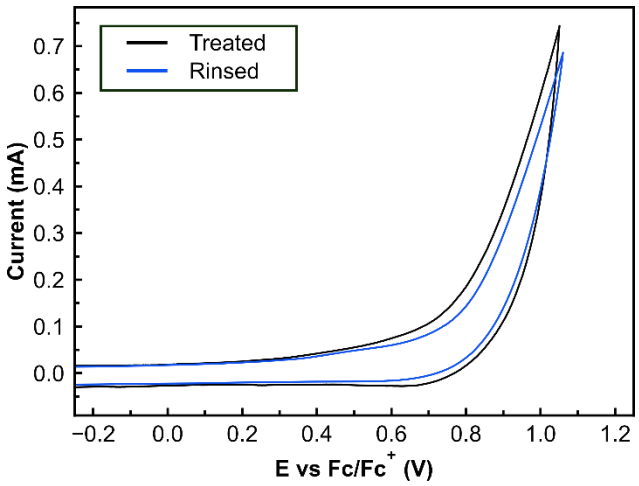

Figure C13. CVs of treated BDD plate electrode and the same electrode after CPC and rinsing with MeCN, recorded in MeCN with 0.05 M NH_4OTf and 20 mM NH_3; Pt counter and Ag/AgOTf reference electrodes. The rinsed electrode corresponds to the electrode after a 2 hour CPC experiment containing the new $[(bpyPy_2Me)Fe(MeCN)_2]OTf_2$ electrocatalyst under the optimized conditions detailed in Table C1. These measurements do not support the possibility of deposition of catalytically active material onto the electrode. This is in agreement with our previous investigation of the electrode after CPC with $[(TPA)Fe(MeCN)_2]OTf_2$.[9]

C.6 GC-MS data for $^{15}NH_3$ experiment

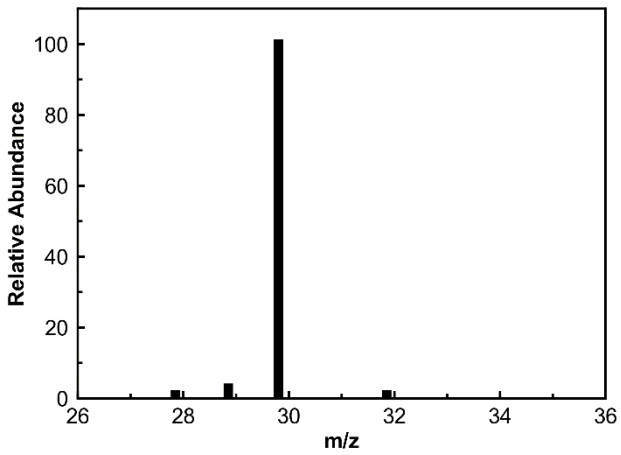

Figure C14. GC mass spectrum of headspace after CPC experiment using $^{15}NH_3$, showing $^{30}N_2$ as the major product.

C.7 XPS spectra of BDD plate electrode

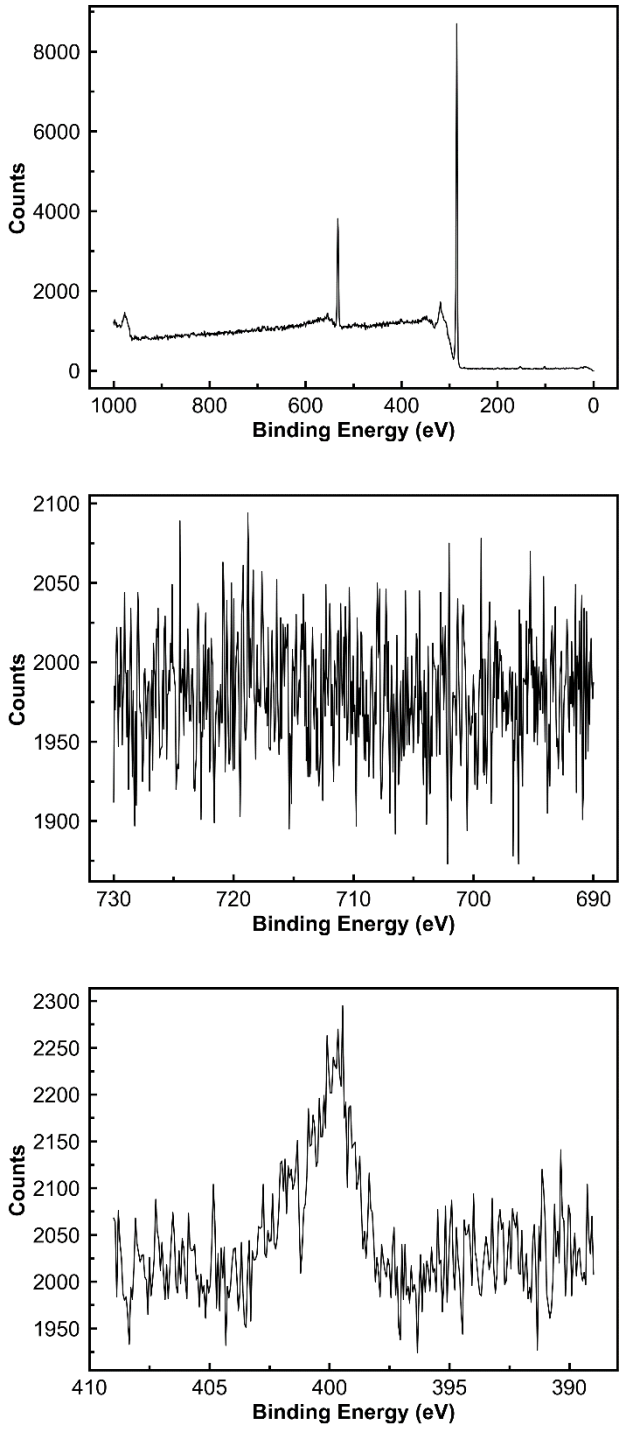

Figure C15. Full XPS spectrum of clean, treated BDD plate electrode and higher resolution spectra centered on the regions characteristic for Fe 2p and N 1s.

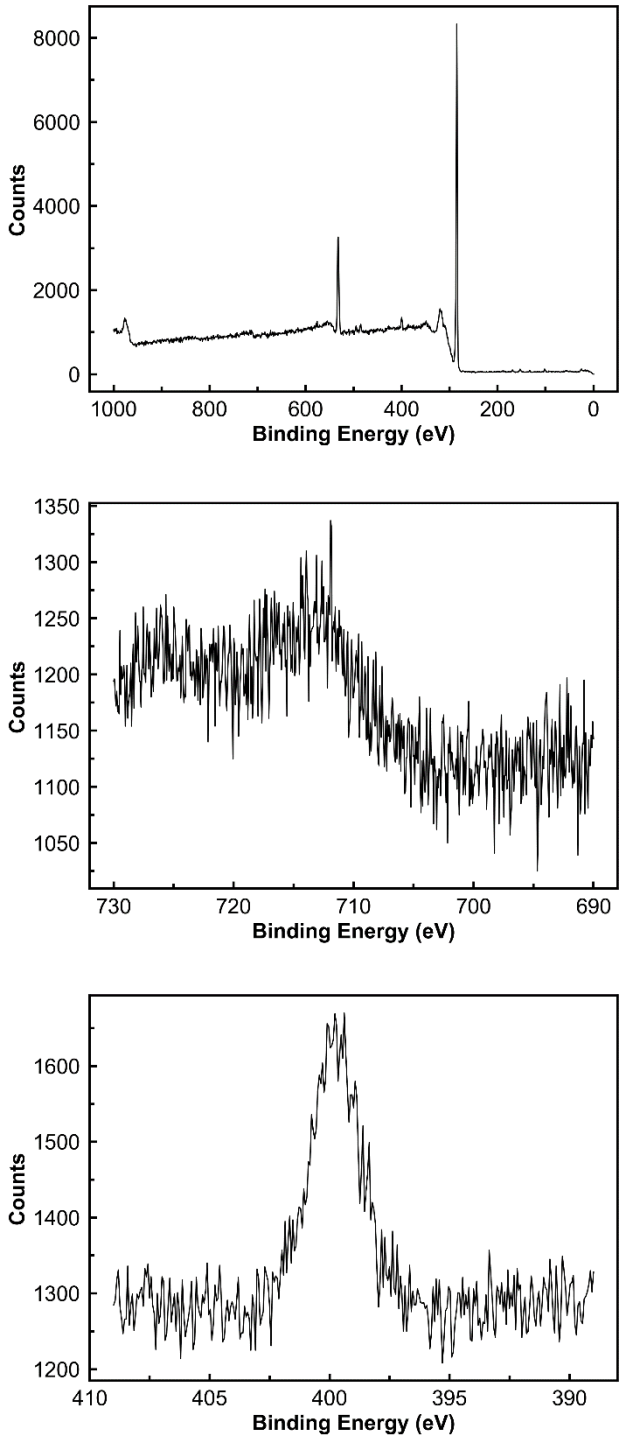

Figure C16. Full XPS spectrum of rinsed BDD plate electrode after 24 h CPC with 0.05 mM $[(bpyPy_2Me)Fe(MeCN)_2]OTf_2$ and 20 mM NH_3 solution and higher resolution spectra centered on the regions characteristic for Fe 2p and N 1s.

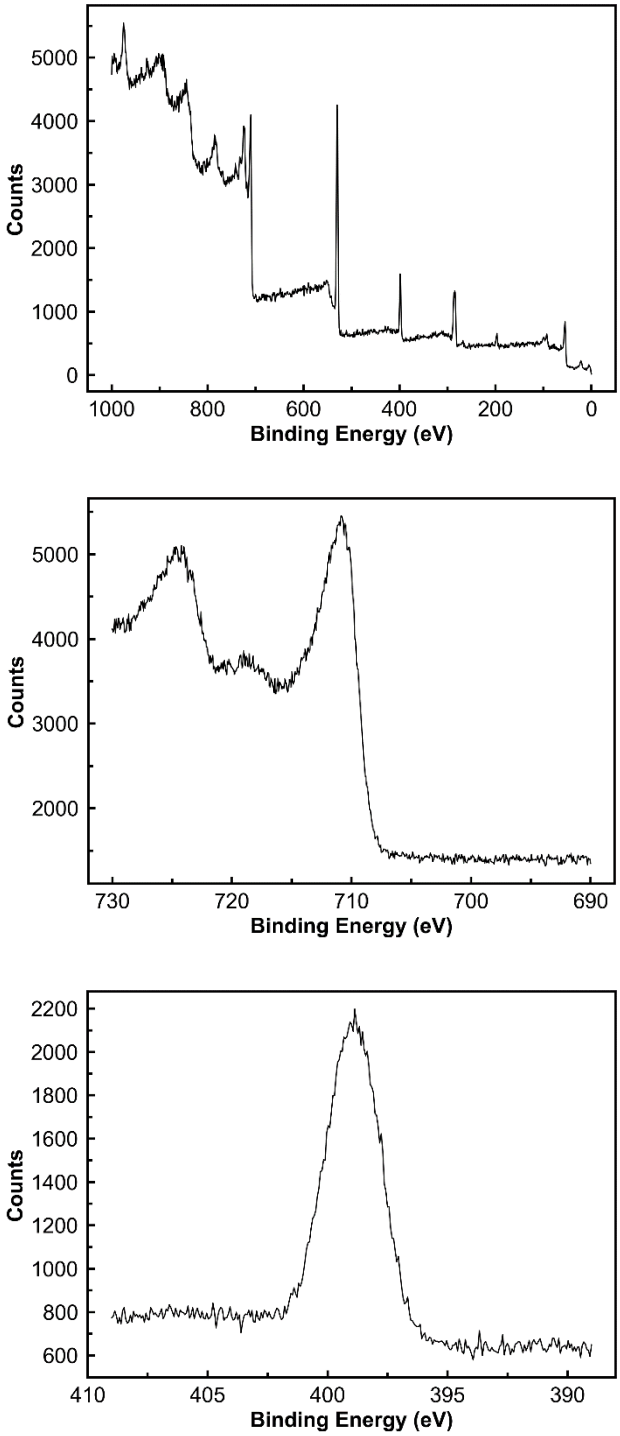

Figure C17. Full XPS spectrum of rinsed BDD plate electrode after 24 h CPC with 0.05 mM $FeOTf_2 \cdot 2$ MeCN and 20 mM NH_3 solution and higher resolution spectra centered on the regions characteristic for Fe 2p and N 1s.

C.8 DPV data for E_1 analysis

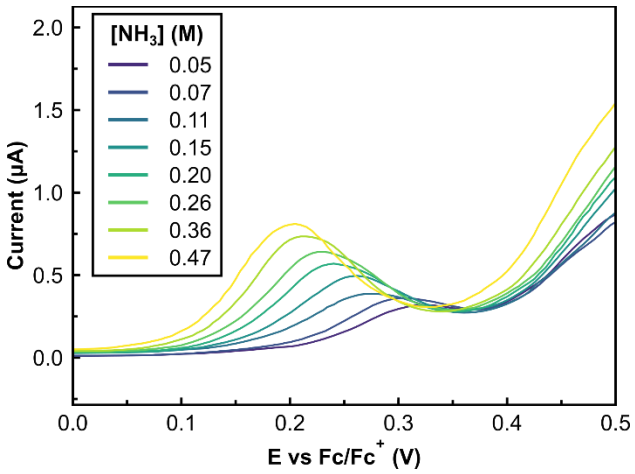

Figure C18. DPVs of 0.5 mM $[(bpyPy_2Me)Fe(MeCN)_2]OTf_2$ with varying NH_3 concentration in order to study the EC process at E_1. Recorded in MeCN with 0.05 M NH_4OTf using BDD working, Pt counter, and Ag/AgOTf reference electrodes.

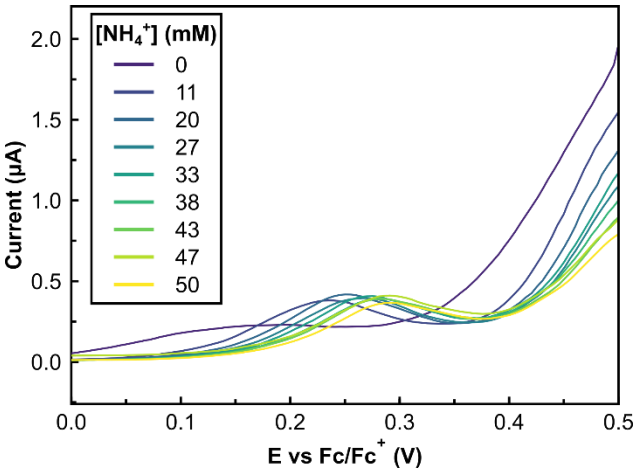

Figure C19. DPVs of 0.5 mM $[(bpyPy_2Me)Fe(MeCN)_2]OTf_2$ with varying NH_4^+ concentration in order to study the EC process at E_1. Recorded in MeCN with 0.2 M NH_3 and 0.1 M $TBAPF_6$ using BDD working, Pt counter, and Ag/AgOTf reference electrodes.

C.9 Further analysis of speciation related to E_1

In addition to the electrochemical and crystallographic data presented in the main text, we provide additional support for the assignment of the E_1 process here. We first further address the speciation at Fe(II), prior to E_1. The predominance of $[(bpyPy_2Me)Fe(MeCN)(NH_3)]OTf_2$ prior to E_1 in MeCN containing NH_3 is corroborated by SC-XRD (Fig. C20). From MeCN/NH_3 mixtures, $[(bpyPy_2Me)Fe(MeCN)(NH_3)]OTf_2$ can be isolated; alternatively, only $[(bpyPy_2Me)Fe(NH_3)_2]OTf_2$ has been crystallized in DCM/NH_3 mixtures containing 2 equivalents MeCN from the $[(bpyPy_2Me)Fe(MeCN)_2]OTf_2$ starting material. Isolation of the bis-ammine in DCM is compatible with DFT calculations which indicate a slight (3 kcal/mol) thermodynamic preference versus the mono-ammine; however, in MeCN solvent the large excess of MeCN relative to NH_3 likely favors the mono-acetonitrile adduct. Thus, $[(bpyPy_2Me)Fe(MeCN)(NH_3)]OTf_2$ is likely the primary iron species in bulk solution under our catalytic conditions.

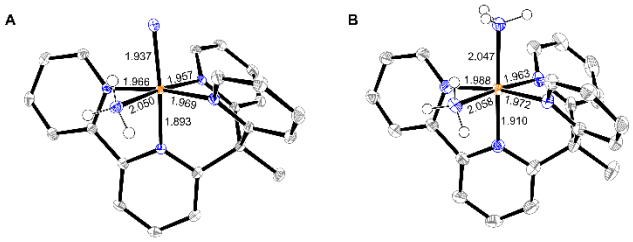

Figure C20. Solid-state crystal structure of **(A)** $[(bpyPy_2Me)Fe(MeCN)(NH_3)]OTf_2$ and **(B)** $[(bpyPy_2Me)Fe(NH_3)_2]OTf_2$ at 100 K, with select bond lengths labeled in angstroms. Thermal ellipsoids are shown at 50% probability. Triflate counterions and L_{aux} hydrogen atoms are omitted for clarity. The acetonitrile in **(A)** is truncated at nitrogen.

As mentioned in the main text, we have assigned the E_1 process to the proton-coupled oxidation of $[(bpyPy_2Me)Fe(MeCN)(NH_3)]^{2+}$ to $[(bpyPy_2Me)Fe(NH_2)(NH_3)]^{2+}$. This conclusion is in excellent agreement with our DFT results (Fig. C21) which show identical experimental and predicted potentials. However, two other likely pathways from $[(bpyPy_2Me)Fe(MeCN)(NH_3)]^{2+}$ are proton-coupled oxidation without additional ammonia substitution (Scheme 4.2a in main text) or oxidation without proton transfer. Based on our DFT results, oxidation without proton transfer is the next lowest energy process, generating $[(bpyPy_2Me)Fe(MeCN)(NH_3)]^{3+}$. The computed oxidation potential is 0.61 V, and we label this process E_1*.

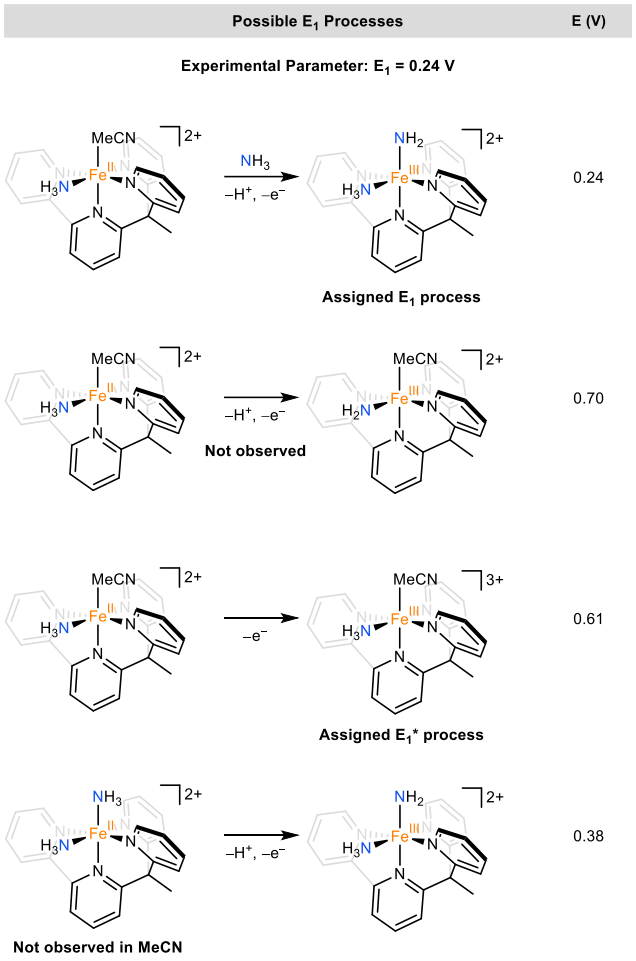

Figure C21. Possible E_1 processes and their calculated E (V) values.

When $[(bpyPy_2Me)Fe(MeCN)(NH_3)]^{2+}$ is investigated by CV at high scan rates under certain concentration regimes, an additional feature appears in the cyclic voltammogram as a shoulder in the catalytic E_2 wave at about 0.55 V (Fig. C22). This shoulder is minor at 200 mV/s but becomes clear at higher scan rates, e.g., 10000 mV/s. By DPV, this shoulder is more easily identified (Fig. C23). Given that the E_1 process, a proton-coupled oxidation associated with an additional ammonia substitution, could be slow due to

the second order dependence on NH_3, it is unsurprising that this second feature can be observed. Interestingly, this shoulder does not move with varying NH_3 concentration as would be expected if it were also coupled to proton transfer. Furthermore, an increase in current at E1* (Fig. C21, 2000 mV/s) results in an increase in return current at E_1, indicating that they are linked via a square mechanism, i.e., E_1 and E_1* generate the same product upon reduction. All of these data points agree with our assignment of E_1* as oxidation without proton transfer to generate $[(bpyPy_2Me)Fe(MeCN)(NH_3)]^{3+}$.

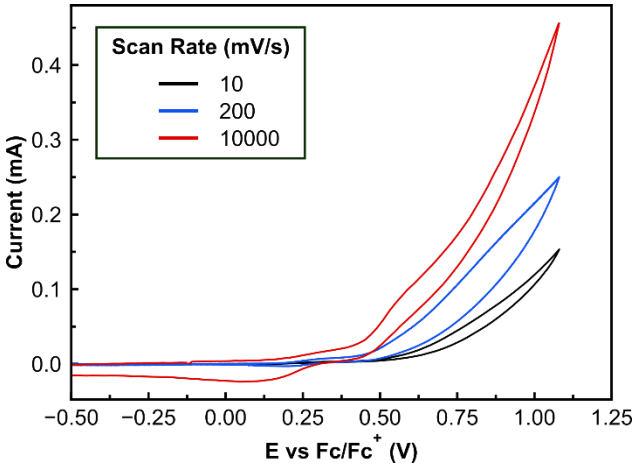

Figure C22. CVs of 0.5 mM $[(bpyPy_2Me)Fe(MeCN)_2]OTf_2$ with 0.2 M NH_3 at varying scan rates. Recorded in MeCN with 0.05 M NH_4OTf using BDD working, Pt counter, and Ag/AgOTf reference electrodes. The shoulder that appears at ~0.55 V is discussed above.

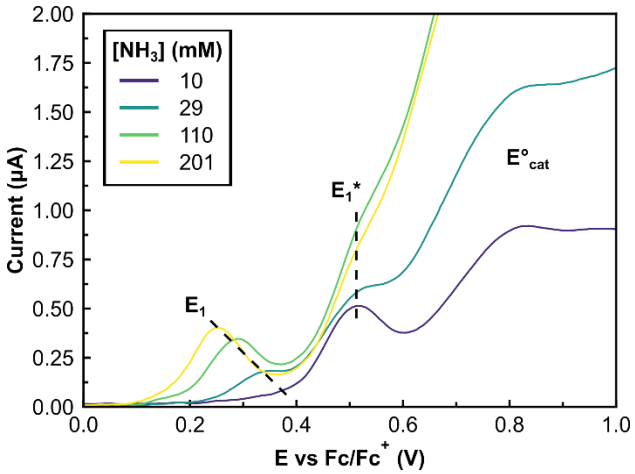

Figure C23. DPVs of 0.5 mM $[(bpyPy_2Me)Fe(MeCN)_2]OTf_2$ with varying NH_3 concentration in order to study the EC process at E_1. Recorded in MeCN with 0.05 M NH_4OTf using BDD working, Pt counter, and Ag/AgOTf reference electrodes. Labels highlight the E_1* and $E°_{cat}$ processes discussed above.

C.10 Catalytic rate versus iron and NH_3 concentrations (E_2)

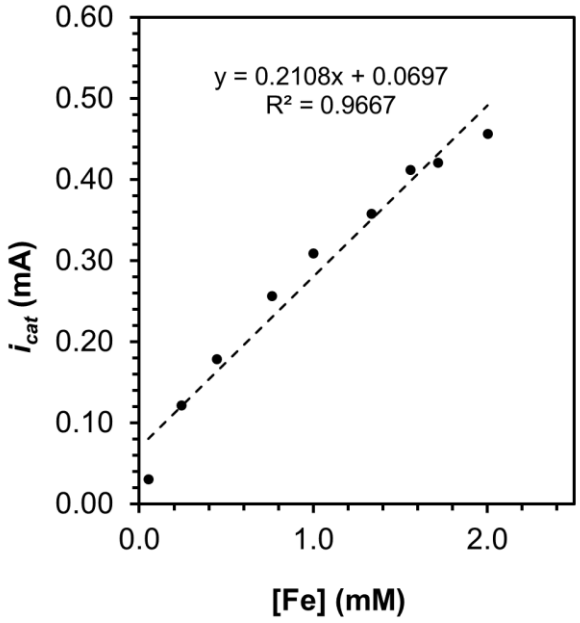

Figure C24. Rate dependence as measured by catalytic current at 1.08 V with varying concentrations of $[(bpyPy_2Me)Fe(MeCN)_2]OTf_2$ in MeCN with 0.05 M NH_4OTf and 0.2 M NH_3 with BDD working, Pt counter, and Ag/AgOTf reference electrodes.

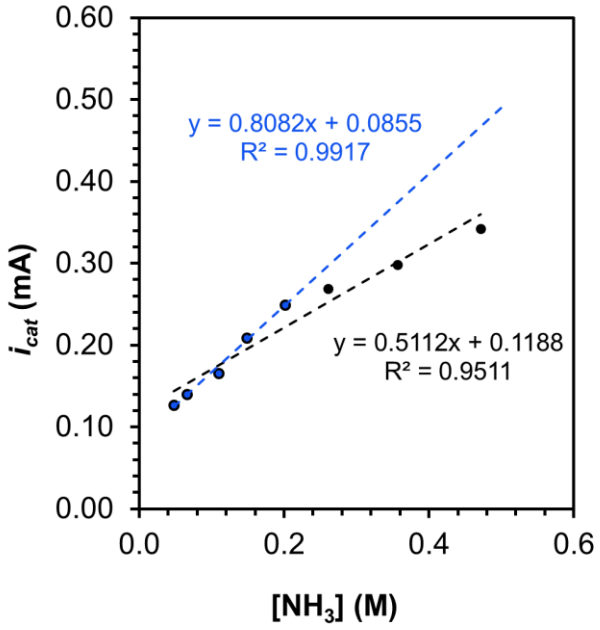

Figure C25. Rate dependence as measured by catalytic current at 1.08 V with varying concentrations of NH_3 and 0.5 mM $[(bpyPy_2Me)Fe(MeCN)_2]OTf_2$ in MeCN with 0.05 M NH_4OTf with BDD working, Pt counter, and Ag/AgOTf reference electrodes. The linear regression lines indicate a first-order dependence on $[NH_3]$. The low $[NH_3]$ regime is perfectly linear (R^2 = 0.99), but at higher concentrations the higher rate likely results in substrate depletion manifested by the mild concave behavior for the overall fit (R^2 = 0.95).

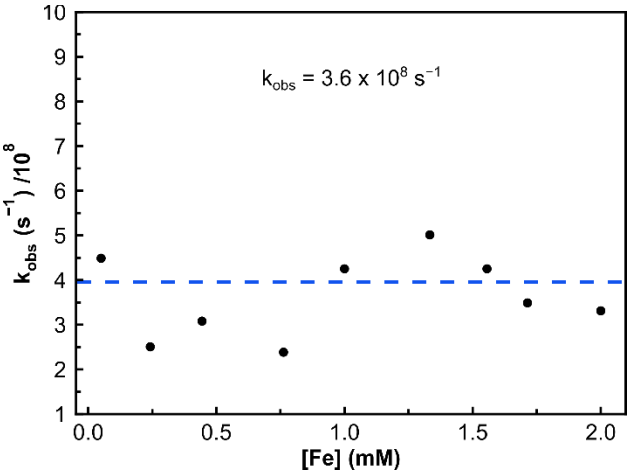

Figure C26. FOWA calculated k_{obs} for AO using varying concentrations of $[(bpyPy_2Me)Fe(MeCN)_2]OTf_2$ in MeCN with 0.05 M NH_4OTf and 0.2 M NH_3 with BDD working, Pt counter, and Ag/AgOTf reference electrodes. A first-order dependence on [Fe] is incorporated into k_{obs}, thus the zero-order dependence of k_{obs} on [Fe] in this plot indicates an overall first-order dependence on [Fe].

C.11 Procedure for FOWA

Foot of the wave analysis was performed by using the equations deducted for EC_{cat}:

$$\frac{i}{i_p} = \frac{n \cdot 2.24 \cdot \sqrt{\frac{R \cdot T}{F \cdot \nu} \cdot k_{obs}}}{1 + \exp\left[\frac{F}{R \cdot T}(E°_{cat} - E)\right]}$$

F is Faraday's constant, R is the gas constant, and T is the temperature. In this case, n = 6 due to the 6 electrons involved in ammonia oxidation to dinitrogen. The intensity of the one-electron wave (i_p) has been estimated from the one-electron oxidation precatalytic wave at E_1 for each condition. $E°_{cat}$ was determined via differential pulse voltammetry. For each condition, the FOWA was performed in similar regions of the potential range in order to ensure a fair comparison. This region was selected as the foot-of-the-wave region where the plot of i/i_p versus $1/(1+\exp[F/(RT)(E°_{cat}–E)])$ behaves linearly ($R^2 > 0.85$). Then, from the slope of that plot, the apparent pseudo-first order rate constant k_{obs} can be obtained and thus the value of the apparent second-order rate constant k'_{obs}. A representative example of this methodology is shown below for one condition.

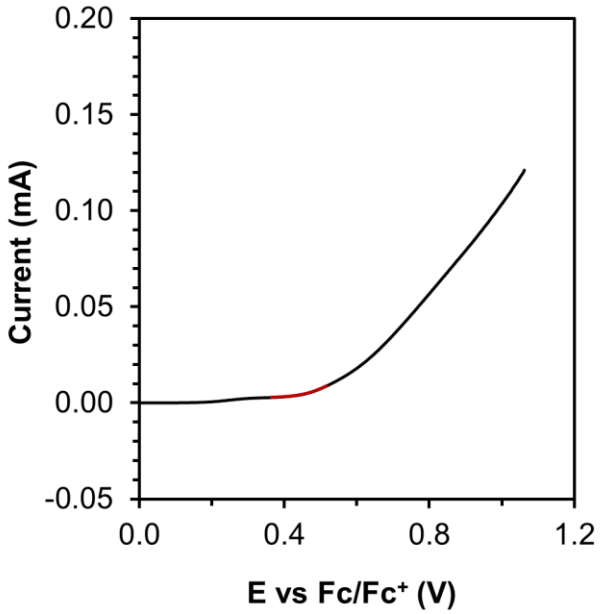

Figure C27. Linear sweep voltammogram with red trace showing the data range employed for performing the FOWA.

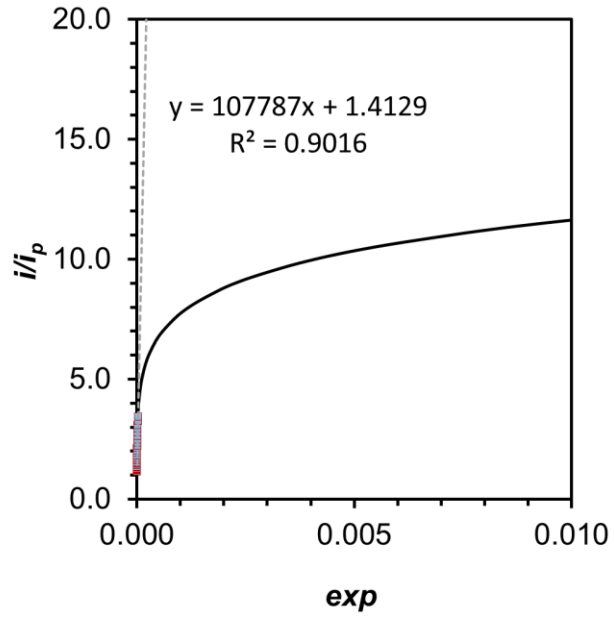

Figure C28. FOWA for an EC_{cat} mechanism calculated from the above linear sweep voltammogram showing strong concavity. The highlighted section and dotted line show the data employed for FOWA.

C.12 Further reactivity considered at E_2

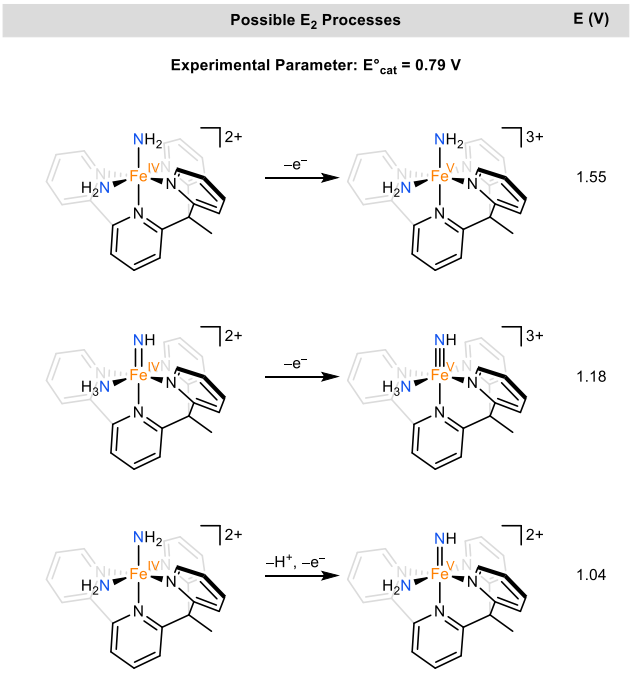

Figure C29. Further E_2 processes considered and their calculated E (V) values. All estimated E values are above the experimental $E°_{cat}$ value. This data supports the hypothesis that N–N bond formation occurs after formation of the species presented in the main text, prior to further removal of protons and electrons.

C.13 Computational methodology

All computations were performed using the ORCA software package, version 4.0 or above.[10] The DFT functional used was TPSS with the def2-SVP basis set for all atoms except iron, for which an augmented def2-TZVP basis set was used. An acetonitrile solvation model (conductor-like polarizable continuum model, CPCM) was used as implemented in ORCA. The RI-J approximation was used to speed up Coulomb integrals (as default). The convergence criteria employed were “tightscf” and “veryslowconv” as defined by ORCA. The Gibbs free energy at 298.15 K was computed in ORCA using harmonic vibrational frequencies computed numerically via “NumFreq”.

Sample input header:

```
! RI TPSS def2-SVP def2/J Opt NumFreq PAL8 tightscf veryslowconv
! CPCM(acetonitrile)
%basis
newgto Fe "def2-TZVP" end
end
```

To determine thermochemical values, oxidations are referenced to ferrocene/ferrocenium (Fc/Fc^+), and reactions involving net hydrogen atom transfer are computed using TEMPO as a reference value (BDFE = 66.5 kcal/mol) and the acetonitrile C_G value of 54.9 kcal/mol.[11]

For oxidations:

$Ox^- + Fc \rightarrow Ox + Fc^+ \quad \Delta G_{ox}$

E (V) = ΔG_{ox} / F, where F (Faraday's constant) is in units of Hartree. 1 Hartree = 27.211 eV.

For reactions involving net hydrogen atom transfer:

Reactants + TEMPO $\rightarrow$ Products + TEMPOH $\quad \Delta G_{BDFE}$

E (V) = [ΔG_{BDFE} – 54.9 + 66.5 – 1.37 pK_a] / 23.06, where ΔG_{BDFE} is in units of kcal/mol (1 Hartree = 627.51 kcal/mol). The pK_a is derived from that of NH_3, 16.5 in MeCN,[8] and adjusted by the Henderson–Hasselbalch equation to match the standard experimental CV conditions of 0.2 M NH_3 and 0.05 M NH_4^+, resulting in pK_a = 17.1.

C.14 DFT spin-state ordering

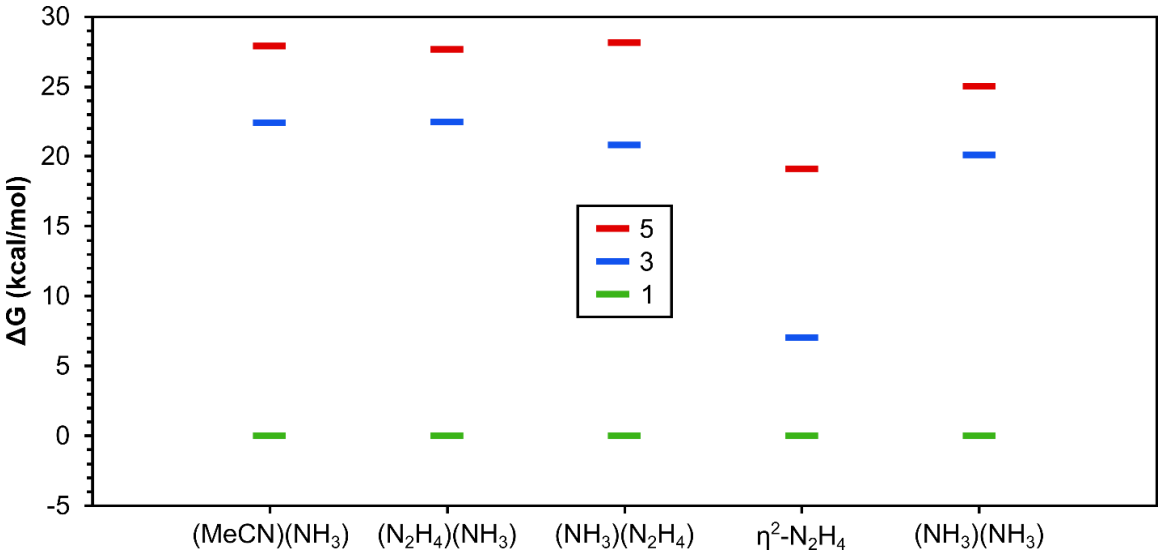

Figure C30. Relative energies for multiplicities of $[(bpyPy_2Me)Fe(L_{ax})(L_{eq})]^{n+}$ complexes with formal oxidation states of +2. L_{ax} and L_{eq} represent ligands axial/*trans* to bipyridine and equatorial/*trans* to pyridine, respectively, in accordance with the orientation defined in the main-text. The lowest energy multiplicity is defined as 0.

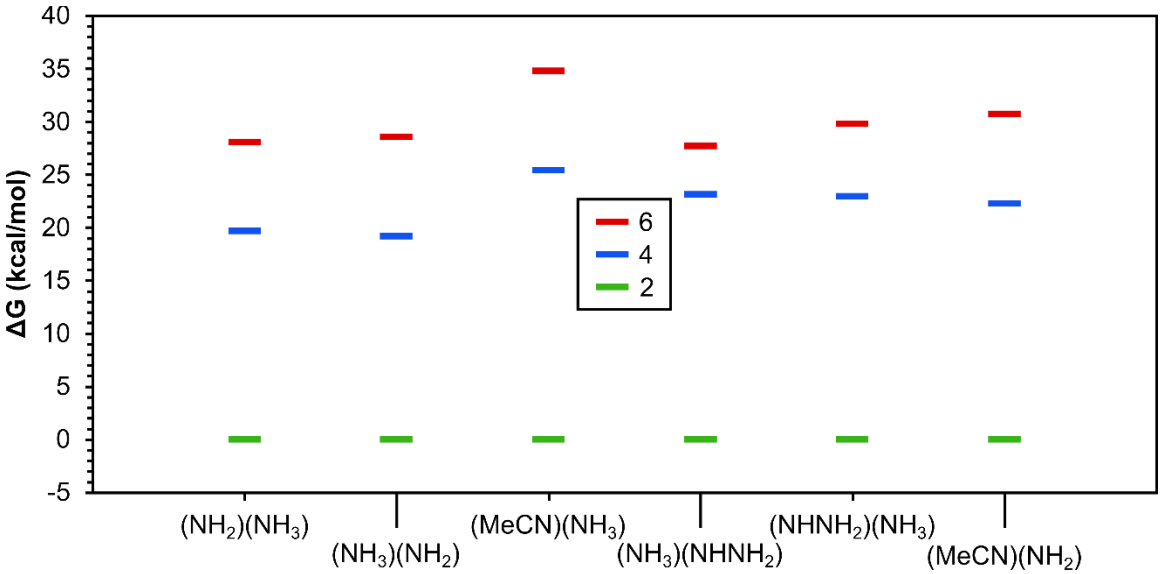

Figure C31. Relative energies for multiplicities of $[(bpyPy_2Me)Fe(L_{ax})(L_{eq})]^{n+}$ complexes with formal oxidation states of +3. L_{ax} and L_{eq} represent ligands axial/*trans* to bipyridine and equatorial/*trans* to pyridine, respectively, in accordance with the orientation defined in the main-text. The lowest energy multiplicity is defined as 0.

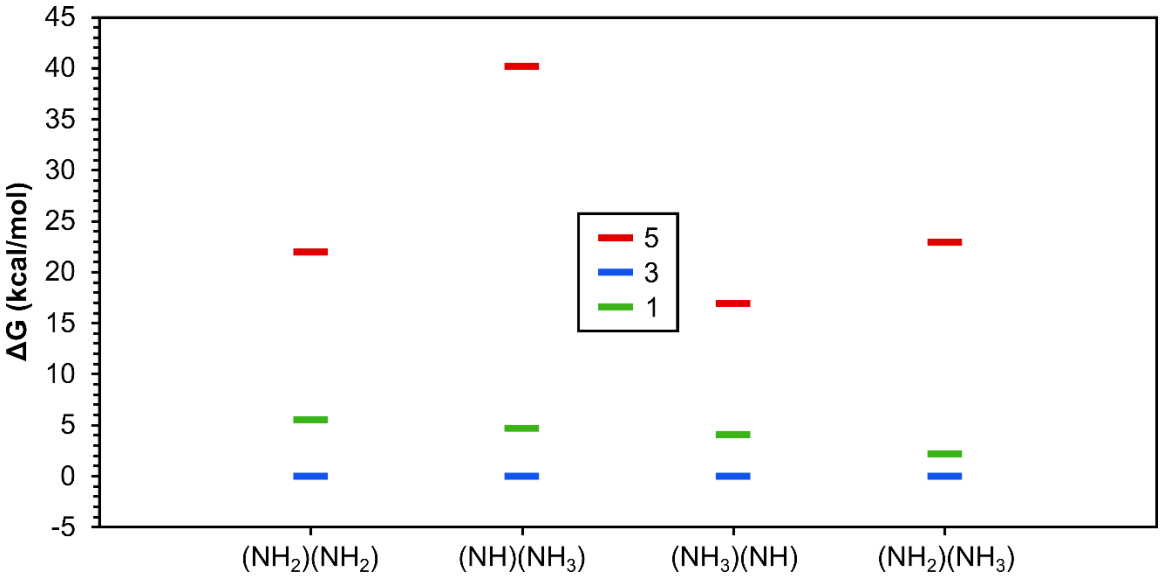

Figure C32. Relative energies for multiplicities of $[(bpyPy_2Me)Fe(L_{ax})(L_{eq})]^{n+}$ complexes with formal oxidation states of +4. L_{ax} and L_{eq} represent ligands axial/*trans* to bipyridine and equatorial/*trans* to pyridine, respectively, in accordance with the orientation defined in the main-text. The lowest energy multiplicity is defined as 0.

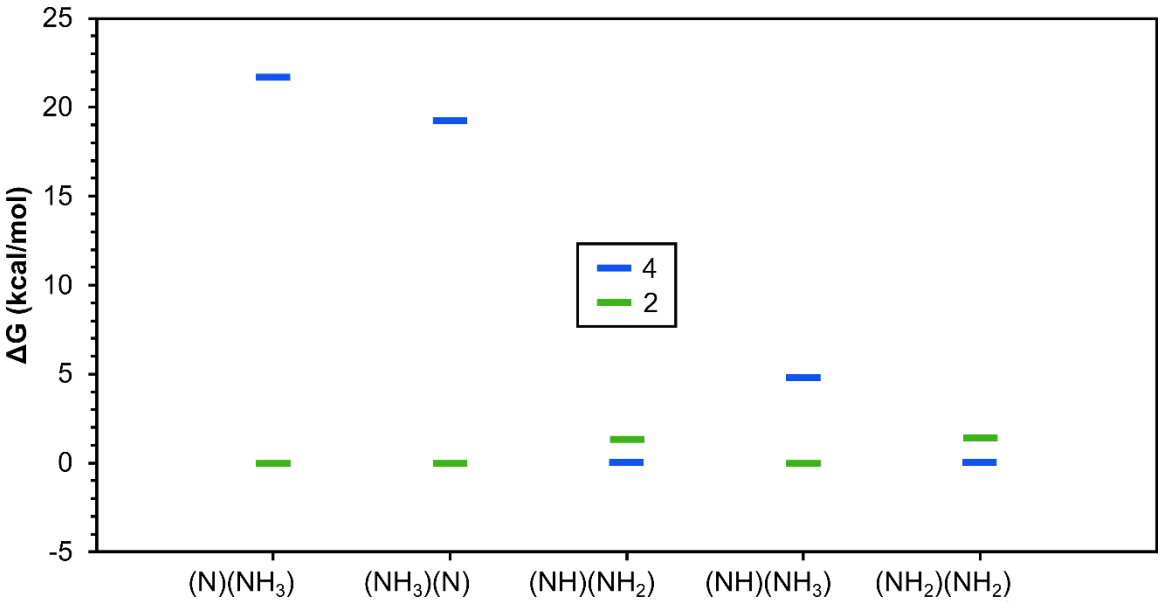

Figure C33. Relative energies for multiplicities of $[(bpyPy_2Me)Fe(L_{ax})(L_{eq})]^{n+}$ complexes with formal oxidation states of +5. L_{ax} and L_{eq} represent ligands axial/*trans* to bipyridine and equatorial/*trans* to pyridine, respectively, in accordance with the orientation defined in the main-text. The lowest energy multiplicity is defined as 0.

C.15 DFT tabulated energies

Table C2. Gibbs free energy, oxidation state (O.S.), charge, and multiplicity for each compound studied in this work. The naming convention for $[(bpyPy_2Me)Fe(L_{ax})(L_{eq})]^{n+}$, where L_{ax} and L_{eq} represent ligands axial/*trans* to bipyridine and equatorial/*trans* to pyridine, respectively, in accordance with the orientation defined in the main-text, is $Fe(L_{ax})(L_{eq})$.

Compound	O.S.	Charge	Multiplicity	Gibbs Free Energy (E_h)
$Fe(MeCN)(NH_3)$	2	2	1	−2520.170506
$Fe(MeCN)(NH_3)$	2	2	3	−2520.134781
$Fe(MeCN)(NH_3)$	2	2	5	−2520.126099
$Fe(N_2H_4)(NH_3)$	2	2	1	−2499.275282
$Fe(N_2H_4)(NH_3)$	2	2	3	−2499.239539
$Fe(N_2H_4)(NH_3)$	2	2	5	−2499.231216
$Fe(NH_3)(N_2H_4)$	2	2	1	−2499.280876
$Fe(NH_3)(N_2H_4)$	2	2	3	−2499.247766
$Fe(NH_3)(N_2H_4)$	2	2	5	−2499.236084
$Fe(\eta^2\text{-}N_2H_4)$	2	2	1	−2442.758364
$Fe(\eta^1\text{-}N_2H_4)$*	2	2	3	−2442.747149
$Fe(\eta^1\text{-}N_2H_4)$*	2	2	5	−2442.727913
$Fe(NH_3)_2$	2	2	1	−2444.013227
$Fe(NH_3)_2$	2	2	3	−2443.981207
$Fe(NH_3)_2$	2	2	5	−2443.973412
$Fe(NH_2)(NH_3)$	3	2	2	−2443.388803
$Fe(NH_2)(NH_3)$	3	2	4	−2443.357443
$Fe(NH_2)(NH_3)$	3	2	6	−2443.34405
$Fe(NH_3)(NH_2)$	3	2	2	−2443.383476
$Fe(NH_3)(NH_2)$	3	2	4	−2443.352874
$Fe(NH_3)(NH_2)$	3	2	6	−2443.337927
$Fe(MeCN)(NH_3)$	3	3	2	−2519.973567
$Fe(MeCN)(NH_3)$	3	3	4	−2519.933032
$Fe(MeCN)(NH_3)$	3	3	6	−2519.918134
$Fe(NH_3)(NHNH_2)$	3	2	2	−2498.67244
$Fe(NH_3)(NHNH_2)$	3	2	4	−2498.635561
$Fe(NH_3)(NHNH_2)$	3	2	6	−2498.628327
$Fe(NHNH_2)(NH_3)$	3	2	2	−2498.676109
$Fe(NHNH_2)(NH_3)$	3	2	4	−2498.639554
$Fe(NHNH_2)(NH_3)$	3	2	6	−2498.628596
$Fe(MeCN)(NH_2)$	3	2	2	−2519.534136
$Fe(MeCN)(NH_2)$	3	2	4	−2519.498649
$Fe(MeCN)(NH_2)$	3	2	6	−2519.48518
$Fe(NH_2)(NH_2)$	4	2	3	−2442.748256
$Fe(NH_2)(NH_2)$	4	2	1	−2442.739497

Compound	O.S.	Charge	Multiplicity	Gibbs Free Energy (E_h)
$Fe(NH_2)(NH_2)$	4	2	5	−2442.713299
$Fe(NH)(NH_3)$	4	2	3	−2442.74475
$Fe(NH)(NH_3)$	4	2	1	−2442.737322
$Fe(NH)(NH_3)$	4	2	5	−2442.680746
$Fe(NH_3)(NH)$	4	2	3	−2442.734741
$Fe(NH_3)(NH)$	4	2	1	−2442.72829
$Fe(NH_3)(NH)$	4	2	5	−2442.707865
$Fe(NH_2)(NH_3)$	4	3	3	−2443.173804
$Fe(NH_2)(NH_3)$	4	3	1	−2443.170371
$Fe(NH_2)(NH_3)$	4	3	5	−2443.137346
$Fe(N)(NH_3)$	5	2	2	−2442.125412
$Fe(N)(NH_3)$	5	2	4	−2442.090902
$Fe(NH_3)(N)$	5	2	2	−2442.11944
$Fe(NH_3)(N)$	5	2	4	−2442.088784
$Fe(NH)(NH_2)$	5	2	4	−2442.099408
$Fe(NH)(NH_2)$	5	2	2	−2442.097272
$Fe(NH)(NH_3)$	5	3	2	−2442.526792
$Fe(NH)(NH_3)$	5	3	4	−2442.519145
$Fe(NH_2)(NH_2)$	5	3	4	−2442.516784
$Fe(NH_2)(NH_2)$	5	3	2	−2442.514531
MeCN	–	0	1	−132.6671601
NH_3	–	0	1	−56.50501517
N_2H_4	–	0	1	−111.7692421
Ferrocene	2	0	1	−1650.613945
Ferrocenium	3	1	2	−1650.439308
TEMPO	–	0	2	−483.24406649
TEMPOH	–	0	1	−483.83585272

* For $Fe(N_2H_4)$, calculations with multiplicities of 3 or 5 resulted in optimized geometries containing η^1-N_2H_4 moieities; η^2-N_2H_4 coordination was only observed for the lowest energy singlet state.

C.16 DFT structures

Cartesian coordinates in angstrom units are provided. The naming convention is $[(bpyPy_2Me)Fe(L_{ax})(L_{eq})]^{n+}$, where L_{ax} and L_{eq} represent ligands axial/*trans* to bipyridine and equatorial/*trans* to pyridine, respectively, in accordance with the orientation defined in the main-text.

$[(bpyPy_2Me)Fe(MeCN)(NH_3)]^{2+}$, multiplicity = 1
C -2.5812420000 2.1854410000 -0.9943090000
C -3.0217660000 0.8802290000 -0.7505960000
C -2.0629920000 -0.1136280000 -0.5108580000
N -0.7289330000 0.1718060000 -0.5950930000
C -0.2977210000 1.4502580000 -0.6623920000
C -1.2134820000 2.4865760000 -0.8951380000
C -3.5780150000 -2.0225160000 0.2320770000
C -2.3105100000 -1.4688140000 -0.0023780000
C -3.6734330000 -3.2780260000 0.8408120000
C -2.4942460000 -3.9450220000 1.2012940000
C -1.2610950000 -3.3495070000 0.9214680000
N -1.1564730000 -2.1402770000 0.3264780000
C 1.1970940000 1.6469490000 -0.3363680000
C 1.5351780000 3.1453320000 -0.2748940000
C 2.0661280000 0.9212210000 -1.3777610000
C 1.4461390000 0.9552330000 1.0342530000
N 1.1544700000 -0.3733690000 1.1334160000
C 1.3453510000 -1.0144660000 2.3113780000
C 1.8462000000 -0.3726350000 3.4428090000
C 2.1614110000 0.9876660000 3.3544860000
C 1.9557160000 1.6528890000 2.1400560000
C 3.0282510000 1.5819880000 -2.1571800000
C 3.8083240000 0.8578870000 -3.0658040000
C 3.6113300000 -0.5236210000 -3.1683230000
C 2.6406570000 -1.1208780000 -2.3661030000
N 1.8728370000 -0.4188090000 -1.4921070000
H -3.3027470000 2.9809780000 -1.2012290000
H -4.6524710000 -3.7255750000 1.0338840000
H -2.5173130000 -4.9241040000 1.6862270000
H -0.3246170000 -3.8545620000 1.1679380000
H 0.9171690000 3.6524760000 0.4812650000
H 2.5936540000 3.2996290000 -0.0173040000

H 1.3459720000 3.6226960000 -1.2486520000
H 1.0817780000 -2.0748540000 2.3319930000
H 1.9826380000 -0.9378570000 4.3688070000
H 2.5602980000 1.5301510000 4.2168980000
H 2.1956700000 2.7136940000 2.0594060000
H 3.1720610000 2.6584090000 -2.0561060000
H 4.5587950000 1.3686600000 -3.6767970000
H 4.1975990000 -1.1415180000 -3.8541250000
H 2.4634050000 -2.1979560000 -2.4119290000
Fe 0.4571770000 -1.3049970000 -0.4451370000
H -0.8754380000 3.5195090000 -0.9871880000
N 1.5623420000 -2.8147330000 -0.1573420000
N -0.2218100000 -2.1161660000 -2.1835550000
H -1.2230990000 -1.9408650000 -2.3488320000
H -0.1113430000 -3.1381050000 -2.2216850000
H 0.2538100000 -1.7453880000 -3.0160680000
H -4.4765270000 -1.4701800000 -0.0537390000
H -4.0881310000 0.6442440000 -0.7153050000
C 2.2675500000 -3.7299440000 0.0181330000
C 3.1447560000 -4.8685140000 0.2448010000
H 3.1314360000 -5.1387990000 1.3141690000
H 4.1753420000 -4.6094880000 -0.0521240000
H 2.7994910000 -5.7290660000 -0.3521540000

[(bpyPy$_2$Me)Fe(MeCN)(NH$_3$)]$^{2+}$, multiplicity = 3
C -2.5824880000 2.1460730000 -0.9169440000
C -3.0324110000 0.8471120000 -0.6690650000
C -2.0863310000 -0.1507490000 -0.4025140000
N -0.7419370000 0.1224020000 -0.4351310000
C -0.2987770000 1.3998360000 -0.5541770000
C -1.2130030000 2.4311930000 -0.8206540000
C -3.6840890000 -2.0375660000 0.2040690000
C -2.3912740000 -1.5215580000 0.0178920000
C -3.8329320000 -3.3374540000 0.6962860000
C -2.6873640000 -4.0923620000 0.9901690000
C -1.4298680000 -3.5283890000 0.7635690000
N -1.2784660000 -2.2736220000 0.2866340000
C 1.2048740000 1.6561840000 -0.2965590000
C 1.4938760000 3.1680460000 -0.3206260000
C 2.0742640000 0.9209440000 -1.3429870000
C 1.5452160000 1.0604650000 1.1006020000
N 1.3213110000 -0.2634900000 1.2705060000
C 1.5973720000 -0.8505890000 2.4549890000
C 2.1115330000 -0.1391160000 3.5401800000
C 2.3527340000 1.2299800000 3.3791580000
C 2.0692190000 1.8356970000 2.1481130000

C 3.0576920000 1.5814380000 -2.0991920000
C 3.8362550000 0.8555720000 -3.0083490000
C 3.6196040000 -0.5201190000 -3.1430230000
C 2.6286700000 -1.1116540000 -2.3596260000
N 1.8740470000 -0.4100370000 -1.4838040000
H -3.2933810000 2.9449010000 -1.1459380000
H -4.8316850000 -3.7555380000 0.8521190000
H -2.7595320000 -5.1099590000 1.3819800000
H -0.5130760000 -4.0895170000 0.9598960000
H 0.8790410000 3.6941750000 0.4246930000
H 2.5513980000 3.3657480000 -0.0912070000
H 1.2743590000 3.5913770000 -1.3128660000
H 1.3942420000 -1.9244530000 2.5259210000
H 2.3179800000 -0.6534600000 4.4828190000
H 2.7596440000 1.8274590000 4.2008150000
H 2.2604540000 2.9013370000 2.0160400000
H 3.2236110000 2.6527970000 -1.9828400000
H 4.6031200000 1.3648320000 -3.6003170000
H 4.2019380000 -1.1309680000 -3.8384200000
H 2.4203800000 -2.1822780000 -2.4291840000
Fe 0.4314340000 -1.3768780000 -0.3002340000
H -0.8670940000 3.4568510000 -0.9488960000
N 1.5536280000 -2.8964380000 -0.0980340000
N -0.2953420000 -2.1685180000 -2.3912990000
H -1.3200360000 -2.2127780000 -2.4611410000
H 0.0300950000 -3.1215040000 -2.5954550000
H 0.0048990000 -1.5914940000 -3.1861440000
H -4.5597620000 -1.4262630000 -0.0263830000
H -4.0992050000 0.6115320000 -0.6679220000
C 2.2564570000 -3.8127910000 0.0770920000
C 3.1340060000 -4.9499100000 0.2983210000
H 3.1015970000 -5.2351960000 1.3633560000
H 4.1678670000 -4.6795440000 0.0247890000
H 2.8018600000 -5.8020760000 -0.3176030000

[(bpyPy$_2$Me)Fe(MeCN)(NH$_3$)]$^{2+}$, multiplicity = 5
C -2.5913420000 2.1732430000 -0.9514330000
C -3.0444050000 0.8798530000 -0.6775890000
C -2.0961820000 -0.1107950000 -0.3766080000
N -0.7665160000 0.1721160000 -0.3849780000
C -0.3203310000 1.4345020000 -0.5466250000
C -1.2233960000 2.4662420000 -0.8555790000
C -3.7585250000 -1.9490980000 0.2003710000
C -2.4386660000 -1.4910890000 0.0435500000
C -3.9810450000 -3.2470860000 0.6720410000
C -2.8822570000 -4.0624810000 0.9766090000

C -1.5965210000 -3.5496450000 0.7807710000
N -1.3776460000 -2.2993740000 0.3275740000
C 1.1949840000 1.6837070000 -0.2930150000
C 1.4682350000 3.2004550000 -0.2816540000
C 2.0595490000 0.9972930000 -1.3824250000
C 1.5627530000 1.0638920000 1.0897630000
N 1.4487890000 -0.2801680000 1.2376680000
C 1.7644720000 -0.8621850000 2.4147980000
C 2.2057320000 -0.1338270000 3.5208370000
C 2.3253150000 1.2532990000 3.3879390000
C 2.0032010000 1.8553060000 2.1642040000
C 2.9624920000 1.7169350000 -2.1857690000
C 3.7566890000 1.0369030000 -3.1174860000
C 3.6419020000 -0.3531080000 -3.2296610000
C 2.7187840000 -1.0021370000 -2.4083180000
N 1.9448120000 -0.3440370000 -1.5182120000
H -3.3029320000 2.9640690000 -1.2059870000
H -5.0029410000 -3.6156390000 0.8024300000
H -3.0117400000 -5.0808990000 1.3517550000
H -0.7077980000 -4.1552780000 0.9847850000
H 0.8445620000 3.7036890000 0.4721460000
H 2.5239650000 3.4062520000 -0.0501460000
H 1.2406700000 3.6447870000 -1.2624190000
H 1.6563810000 -1.9517240000 2.4612080000
H 2.4508390000 -0.6479160000 4.4542570000
H 2.6698910000 1.8691410000 4.2244400000
H 2.1017700000 2.9363690000 2.0601310000
H 3.0589270000 2.7988620000 -2.0894260000
H 4.4622250000 1.5939950000 -3.7421260000
H 4.2487460000 -0.9281170000 -3.9346370000
H 2.5855770000 -2.0881270000 -2.4546760000
Fe 0.5269130000 -1.4856610000 -0.3052620000
H -0.8803890000 3.4885080000 -1.0158050000
N 1.7136470000 -3.1823430000 -0.0153630000
N -0.1855920000 -2.2733400000 -2.2998310000
H -1.2044920000 -2.2068480000 -2.4235270000
H 0.0396140000 -3.2663820000 -2.4431900000
H 0.2133460000 -1.7778280000 -3.1063020000
H -4.6034930000 -1.2982370000 -0.0356300000
H -4.1128770000 0.6528260000 -0.6889350000
C 2.3960080000 -4.1115610000 0.1642010000
C 3.2508080000 -5.2641530000 0.3855240000
H 3.2304940000 -5.5401030000 1.4528750000
H 4.2831960000 -5.0132540000 0.0890140000
H 2.8904250000 -6.1101210000 -0.2228040000

[(bpyPy$_2$Me)Fe(N$_2$H$_4$)(NH$_3$)]$^{2+}$, multiplicity = 1
C -2.5311680000 2.2158950000 -0.9662520000
C -2.9964880000 0.9156060000 -0.7445590000
C -2.0568180000 -0.1008550000 -0.5200790000
N -0.7172990000 0.1572450000 -0.6052750000
C -0.2621780000 1.4298830000 -0.6511140000
C -1.1570080000 2.4881510000 -0.8622560000
C -3.6124250000 -1.9680340000 0.2236470000
C -2.3292670000 -1.4520730000 -0.0146090000
C -3.7493290000 -3.2107110000 0.8487580000
C -2.5904050000 -3.9021860000 1.2272430000
C -1.3423420000 -3.3434040000 0.9400920000
N -1.1897470000 -2.1520470000 0.3187460000
C 1.2417600000 1.5864010000 -0.3402380000
C 1.6144190000 3.0755470000 -0.2551220000
C 2.0647750000 0.8648050000 -1.4188950000
C 1.4870000000 0.8669310000 1.0147370000
N 1.1608740000 -0.4567800000 1.0937370000
C 1.2998900000 -1.1044610000 2.2780470000
C 1.8022620000 -0.4884520000 3.4225820000
C 2.1719100000 0.8595230000 3.3464670000
C 2.0036860000 1.5381890000 2.1339000000
C 3.0100580000 1.5268920000 -2.2175570000
C 3.7276760000 0.8215280000 -3.1895080000
C 3.4796980000 -0.5473370000 -3.3398880000
C 2.5307550000 -1.1467500000 -2.5149760000
N 1.8280490000 -0.4678390000 -1.5668570000
H -3.2372110000 3.0288160000 -1.1585290000
H -4.7417710000 -3.6270020000 1.0440400000
H -2.6392350000 -4.8697740000 1.7336750000
H -0.4348620000 -3.8845640000 1.2220750000
H 1.0171780000 3.5806620000 0.5192210000
H 2.6796750000 3.2025520000 -0.0099370000
H 1.4208390000 3.5757220000 -1.2163830000
H 0.9839610000 -2.1515960000 2.2975900000
H 1.8954770000 -1.0624030000 4.3483430000
H 2.5770010000 1.3827870000 4.2177290000
H 2.2740620000 2.5925370000 2.0655540000
H 3.1871020000 2.5948060000 -2.0852810000
H 4.4639720000 1.3350080000 -3.8147860000
H 4.0075670000 -1.1541090000 -4.0804360000
H 2.3184580000 -2.2146420000 -2.6166500000
Fe 0.4407880000 -1.3387660000 -0.4885150000
H -0.7989910000 3.5161960000 -0.9350340000
N 1.6166560000 -2.9986050000 -0.2531350000
H 1.6297220000 -3.5603360000 -1.1168580000

H 1.1999820000 -3.6570130000 0.4184420000
N -0.3047020000 -2.1396150000 -2.2083820000
H -1.2775510000 -1.8419740000 -2.3691680000
H -0.3382760000 -3.1685140000 -2.2324920000
H 0.1944130000 -1.8579710000 -3.0626450000
N 3.0270290000 -2.9312410000 0.1535600000
H -4.4933830000 -1.3916630000 -0.0698180000
H -4.0675550000 0.7013380000 -0.7121780000
H 3.4802590000 -2.3051930000 -0.5251420000
H 3.0343470000 -2.3935700000 1.0304540000

[(bpyPy$_2$Me)Fe(N$_2$H$_4$)(NH$_3$)]$^{2+}$, multiplicity = 3
C -2.5298590000 2.1912600000 -0.8523600000
C -3.0066840000 0.8996760000 -0.6233860000
C -2.0804990000 -0.1251500000 -0.3830640000
N -0.7313200000 0.1161450000 -0.4232790000
C -0.2609060000 1.3867640000 -0.5298410000
C -1.1516710000 2.4433370000 -0.7668370000
C -3.7169530000 -1.9825640000 0.1806700000
C -2.4096030000 -1.4949390000 0.0099410000
C -3.9075850000 -3.2891690000 0.6342430000
C -2.7813080000 -4.0818560000 0.9068790000
C -1.5111300000 -3.5437220000 0.7002060000
N -1.3100070000 -2.2800030000 0.2596710000
C 1.2529720000 1.5980190000 -0.2919360000
C 1.5843070000 3.1019130000 -0.3112410000
C 2.0768780000 0.8503860000 -1.3648030000
C 1.5822070000 0.9889940000 1.1015650000
N 1.3151760000 -0.3287420000 1.2743010000
C 1.5342050000 -0.9037510000 2.4792610000
C 2.0492270000 -0.2002430000 3.5681830000
C 2.3509610000 1.1558080000 3.3959850000
C 2.1125180000 1.7551340000 2.1530840000
C 3.0581160000 1.4954050000 -2.1383650000
C 3.7682310000 0.7742820000 -3.1041670000
C 3.4822400000 -0.5839420000 -3.2849330000
C 2.5017780000 -1.1605060000 -2.4794220000
N 1.8210270000 -0.4682200000 -1.5364310000
H -3.2247980000 3.0100320000 -1.0592430000
H -4.9180210000 -3.6837010000 0.7750890000
H -2.8779020000 -5.1093960000 1.2673330000
H -0.6239960000 -4.1544980000 0.8886290000
H 0.9924130000 3.6396810000 0.4446030000
H 2.6493890000 3.2704840000 -0.0938880000
H 1.3635340000 3.5360210000 -1.2981850000
H 1.2789250000 -1.9653280000 2.5714870000

H 2.2067290000 -0.7102090000 4.5223700000
H 2.7636330000 1.7477050000 4.2187010000
H 2.3400020000 2.8126590000 2.0144640000
H 3.2706650000 2.5551490000 -1.9964210000
H 4.5301870000 1.2735620000 -3.7105320000
H 3.9995820000 -1.1896530000 -4.0336810000
H 2.2312840000 -2.2139390000 -2.5994560000
Fe 0.4200680000 -1.4117840000 -0.3108980000
H -0.7841690000 3.4634630000 -0.8807960000
N 1.5711780000 -3.0641470000 -0.0564850000
H 1.4148000000 -3.7334140000 -0.8234460000
H 1.2399040000 -3.5850740000 0.7690220000
N -0.3680710000 -2.2503840000 -2.4324230000
H -1.3960100000 -2.2373610000 -2.4274440000
H -0.1244980000 -3.2081770000 -2.7174640000
H -0.1022850000 -1.6560710000 -3.2277480000
N 3.0250010000 -3.0124930000 0.1298570000
H -4.5734120000 -1.3393790000 -0.0354300000
H -4.0789250000 0.6905920000 -0.6169730000
H 3.4145540000 -2.6910410000 -0.7649480000
H 3.1922950000 -2.2297610000 0.7754710000

[(bpyPy$_2$Me)Fe(N$_2$H$_4$)(NH$_3$)]$^{2+}$, multiplicity = 5
C -2.5482370000 2.2118170000 -0.8660130000
C -3.0251570000 0.9251060000 -0.6068490000
C -2.0937800000 -0.0966560000 -0.3591690000
N -0.7586960000 0.1513340000 -0.4039240000
C -0.2862710000 1.4083310000 -0.5442900000
C -1.1712460000 2.4688220000 -0.8020160000
C -3.7921790000 -1.9055510000 0.1736860000
C -2.4601980000 -1.4741410000 0.0394540000
C -4.0529030000 -3.2068280000 0.6129930000
C -2.9731820000 -4.0499850000 0.9104200000
C -1.6755960000 -3.5578620000 0.7444540000
N -1.4126800000 -2.3038770000 0.3204060000
C 1.2370490000 1.6227490000 -0.3098900000
C 1.5418620000 3.1338850000 -0.2862040000
C 2.0760530000 0.9349000000 -1.4148400000
C 1.5931300000 0.9836710000 1.0674650000
N 1.4073100000 -0.3533940000 1.2212580000
C 1.6627960000 -0.9269670000 2.4190380000
C 2.1343450000 -0.2135900000 3.5210270000
C 2.3473130000 1.1607380000 3.3712620000
C 2.0703260000 1.7614040000 2.1371760000
C 3.0057340000 1.6427730000 -2.1978210000
C 3.7547200000 0.9676740000 -3.1688450000

C 3.5619880000 -0.4064470000 -3.3480620000
C 2.6164840000 -1.0428180000 -2.5442010000
N 1.8973070000 -0.3934700000 -1.6018200000
H -3.2468460000 3.0258520000 -1.0807420000
H -5.0841530000 -3.5552030000 0.7228620000
H -3.1250900000 -5.0739900000 1.2623210000
H -0.8140980000 -4.1973030000 0.9602440000
H 0.9369610000 3.6414820000 0.4801210000
H 2.6036240000 3.3161940000 -0.0637840000
H 1.3141980000 3.5911340000 -1.2606860000
H 1.4742620000 -2.0026150000 2.4962500000
H 2.3259980000 -0.7301550000 4.4653740000
H 2.7203890000 1.7664250000 4.2028610000
H 2.2276420000 2.8337620000 2.0203790000
H 3.1531670000 2.7138750000 -2.0595630000
H 4.4787800000 1.5166420000 -3.7789390000
H 4.1206670000 -0.9770260000 -4.0947370000
H 2.4141170000 -2.1127150000 -2.6601430000
Fe 0.5180970000 -1.5432720000 -0.3760180000
H -0.8077010000 3.4867210000 -0.9444220000
N 1.6235250000 -3.3676580000 0.1303610000
H 1.4332610000 -4.1268230000 -0.5379230000
H 1.3588850000 -3.7869510000 1.0330130000
N -0.2361700000 -2.3391660000 -2.3441890000
H -1.2551340000 -2.4759060000 -2.3357210000
H 0.1462760000 -3.2416450000 -2.6558170000
H -0.0626590000 -1.6893870000 -3.1218820000
N 3.0897250000 -3.2460880000 0.1873860000
H -4.6181890000 -1.2297160000 -0.0592890000
H -4.0988540000 0.7264980000 -0.5854740000
H 3.4028070000 -3.1885520000 -0.7894640000
H 3.2746050000 -2.3081820000 0.5684080000

[(bpyPy$_2$Me)Fe(NH$_3$)(N$_2$H$_4$)]$^{2+}$, multiplicity = 1
C -2.5696540000 2.2279200000 -0.9630660000
C -3.0387160000 0.9305160000 -0.7306690000
C -2.1017520000 -0.0874850000 -0.5034830000
N -0.7603950000 0.1663290000 -0.5928590000
C -0.3006750000 1.4382070000 -0.6474420000
C -1.1939210000 2.4963110000 -0.8653060000
C -3.6556790000 -1.9607600000 0.2383530000
C -2.3743910000 -1.4379400000 0.0025820000
C -3.7860230000 -3.2086950000 0.8541720000
C -2.6238600000 -3.9012930000 1.2237960000
C -1.3772960000 -3.3364040000 0.9432160000
N -1.2328610000 -2.1358700000 0.3347230000

C 1.2027660000 1.5977860000 -0.3318120000
C 1.5771190000 3.0874310000 -0.2687210000
C 2.0411260000 0.8570700000 -1.3866440000
C 1.4473470000 0.8962550000 1.0327290000
N 1.1184090000 -0.4253320000 1.1286250000
C 1.2860800000 -1.0671130000 2.3110180000
C 1.8128250000 -0.4433150000 3.4401910000
C 2.1759030000 0.9051740000 3.3499010000
C 1.9836790000 1.5765350000 2.1367720000
C 3.0084560000 1.4956610000 -2.1771270000
C 3.7407630000 0.7623130000 -3.1181730000
C 3.4843440000 -0.6071860000 -3.2473370000
C 2.5144210000 -1.1849930000 -2.4303860000
N 1.8006080000 -0.4764370000 -1.5126390000
H -3.2731420000 3.0420650000 -1.1592980000
H -4.7764590000 -3.6303230000 1.0473900000
H -2.6707600000 -4.8757900000 1.7160910000
H -0.4621090000 -3.8712430000 1.2078690000
H 0.9790160000 3.6064470000 0.4952870000
H 2.6414900000 3.2159840000 -0.0208490000
H 1.3892420000 3.5726500000 -1.2389650000
H 0.9761020000 -2.1144020000 2.3436670000
H 1.9300090000 -1.0124900000 4.3664030000
H 2.5974760000 1.4336630000 4.2101790000
H 2.2541600000 2.6299580000 2.0559040000
H 3.1923810000 2.5645270000 -2.0620330000
H 4.4952160000 1.2571450000 -3.7371520000
H 4.0221650000 -1.2308980000 -3.9667150000
H 2.2838070000 -2.2516190000 -2.5147350000
Fe 0.3926610000 -1.3226100000 -0.4454510000
H -0.8333400000 3.5225360000 -0.9477020000
N 1.5915010000 -2.9308940000 -0.1704920000
H 1.4552400000 -3.5640590000 -0.9794200000
H 1.4311660000 -3.4992860000 0.6701150000
N -0.2989200000 -2.1300320000 -2.1934380000
H -1.3101790000 -1.9466580000 -2.3139330000
N -0.0044360000 -3.5345430000 -2.4131440000
H 0.1473620000 -1.6185990000 -2.9660150000
H 2.5890590000 -2.6844270000 -0.1375390000
H -4.5391010000 -1.3867940000 -0.0521210000
H -4.1104260000 0.7191150000 -0.6938030000
H -0.2897230000 -3.7787080000 -3.3709880000
H -0.6362040000 -4.0640930000 -1.7991960000

[(bpyPy$_2$Me)Fe(NH$_3$)(N$_2$H$_4$)]$^{2+}$, multiplicity = 3
C -2.5712720000 2.2311610000 -0.8495330000

C -3.0551430000 0.9422950000 -0.6183810000
C -2.1353190000 -0.0843620000 -0.3638540000
N -0.7837850000 0.1530830000 -0.3917340000
C -0.3069380000 1.4207740000 -0.5061150000
C -1.1925780000 2.4787270000 -0.7557830000
C -3.7723720000 -1.9391780000 0.2178720000
C -2.4670140000 -1.4500610000 0.0384540000
C -3.9570200000 -3.2376290000 0.6970290000
C -2.8276310000 -4.0188290000 0.9918100000
C -1.5580460000 -3.4819360000 0.7756640000
N -1.3653430000 -2.2281880000 0.3000650000
C 1.2079730000 1.6239970000 -0.2734060000
C 1.5480950000 3.1257180000 -0.2982500000
C 2.0289690000 0.8647090000 -1.3416670000
C 1.5571610000 1.0129210000 1.1149900000
N 1.3006570000 -0.3064150000 1.2829550000
C 1.5792950000 -0.9021990000 2.4638490000
C 2.1304480000 -0.2091950000 3.5420190000
C 2.4060170000 1.1540450000 3.3813490000
C 2.1178320000 1.7702310000 2.1569930000
C 3.0161830000 1.4995800000 -2.1147870000
C 3.7461590000 0.7627410000 -3.0540450000
C 3.4766760000 -0.6018560000 -3.2038930000
C 2.4862100000 -1.1695870000 -2.4035350000
N 1.7780810000 -0.4584260000 -1.4938750000
H -3.2613050000 3.0514810000 -1.0664880000
H -4.9658300000 -3.6337940000 0.8450830000
H -2.9223880000 -5.0367720000 1.3791980000
H -0.6638980000 -4.0741550000 0.9879130000
H 0.9633100000 3.6681230000 0.4599910000
H 2.6151700000 3.2885730000 -0.0867750000
H 1.3251960000 3.5595620000 -1.2848370000
H 1.3453370000 -1.9693700000 2.5404670000
H 2.3363100000 -0.7322730000 4.4799060000
H 2.8422200000 1.7377850000 4.1978390000
H 2.3332240000 2.8312240000 2.0249900000
H 3.2200550000 2.5633570000 -1.9914360000
H 4.5133930000 1.2543570000 -3.6600480000
H 4.0146300000 -1.2221780000 -3.9257730000
H 2.2383510000 -2.2314130000 -2.4991460000
Fe 0.3542790000 -1.3706890000 -0.2665630000
H -0.8204110000 3.4965620000 -0.8747360000
N 1.5049420000 -3.0173240000 -0.1549970000
H 1.3031600000 -3.5760850000 -1.0131690000
H 1.3447640000 -3.6417900000 0.6459360000
N -0.3911300000 -2.3049290000 -2.4043630000

H -1.3917340000 -2.1969740000 -2.6312710000
N 0.0232850000 -3.6874690000 -2.5236300000
H 0.1057810000 -1.7807910000 -3.1332710000
H 2.5137850000 -2.8197630000 -0.1463560000
H -4.6313770000 -1.3027420000 -0.0085130000
H -4.1280970000 0.7363070000 -0.6214140000
H -0.1510470000 -4.0259830000 -3.4806430000
H -0.6153990000 -4.2336520000 -1.9317550000

[(bpyPy$_2$Me)Fe(NH$_3$)(N$_2$H$_4$)]$^{2+}$, multiplicity = 5
C -2.5819470000 2.2386670000 -0.8673160000
C -3.0693090000 0.9558290000 -0.6081790000
C -2.1474640000 -0.0699330000 -0.3417270000
N -0.8088790000 0.1701430000 -0.3713090000
C -0.3269520000 1.4230430000 -0.5202120000
C -1.2034190000 2.4868780000 -0.7913920000
C -3.8604330000 -1.8630410000 0.2127120000
C -2.5266230000 -1.4409890000 0.0666120000
C -4.1261150000 -3.1542310000 0.6774160000
C -3.0512170000 -3.9999590000 0.9883710000
C -1.7512080000 -3.5216620000 0.8064900000
N -1.4857350000 -2.2770440000 0.3554630000
C 1.1983720000 1.6263530000 -0.2908030000
C 1.5196040000 3.1337480000 -0.2888440000
C 2.0273340000 0.9103600000 -1.3882340000
C 1.5667800000 1.0000010000 1.0888120000
N 1.3861470000 -0.3348450000 1.2487410000
C 1.6957780000 -0.9214560000 2.4256860000
C 2.2023560000 -0.2103110000 3.5140120000
C 2.3924720000 1.1679190000 3.3667560000
C 2.0721170000 1.7762260000 2.1462650000
C 2.9701040000 1.5925140000 -2.1783340000
C 3.7202390000 0.8883190000 -3.1282890000
C 3.5186060000 -0.4881990000 -3.2758890000
C 2.5609930000 -1.0998360000 -2.4655490000
N 1.8351260000 -0.4192890000 -1.5499940000
H -3.2727320000 3.0560610000 -1.0936500000
H -5.1589520000 -3.4937980000 0.7993370000
H -3.2104580000 -5.0146870000 1.3621600000
H -0.8879770000 -4.1562580000 1.0310080000
H 0.9252180000 3.6582040000 0.4738160000
H 2.5844370000 3.3078220000 -0.0737960000
H 1.2915060000 3.5819270000 -1.2678520000
H 1.5253770000 -2.0019580000 2.4897190000
H 2.4400010000 -0.7299210000 4.4462820000
H 2.7883700000 1.7707180000 4.1899150000

H 2.2232970000 2.8499130000 2.0305490000
H 3.1298240000 2.6644410000 -2.0594750000
H 4.4553370000 1.4171260000 -3.7431950000
H 4.0818660000 -1.0807480000 -4.0019940000
H 2.3523510000 -2.1728490000 -2.5528160000
Fe 0.4356390000 -1.5296630000 -0.2829110000
H -0.8324730000 3.5012390000 -0.9384000000
N 1.6528660000 -3.2930540000 -0.0127230000
H 1.5604010000 -3.8277970000 -0.8944180000
H 1.4552520000 -3.9514370000 0.7517580000
N -0.2934890000 -2.3494780000 -2.2995610000
H -1.3086030000 -2.2749180000 -2.4738960000
N 0.1795150000 -3.6992450000 -2.5499660000
H 0.1378580000 -1.7496330000 -3.0127190000
H 2.6492460000 -3.0584770000 0.0846210000
H -4.6840450000 -1.1869490000 -0.0282010000
H -4.1447320000 0.7634940000 -0.6007900000
H -0.0806740000 -3.9727370000 -3.5081250000
H -0.3790740000 -4.3152390000 -1.9456070000

[(bpyPy$_2$Me)Fe(η^2-N$_2$H$_4$)]$^{2+}$, multiplicity = 1
C -2.6032110000 2.4256830000 -0.9365670000
C -3.1273900000 1.1389800000 -0.7644410000
C -2.2365520000 0.0745180000 -0.5796810000
N -0.8841760000 0.2730210000 -0.6621170000
C -0.3734000000 1.5243730000 -0.6500170000
C -1.2192780000 2.6303800000 -0.8189780000
C -3.8547750000 -1.7642010000 0.1249580000
C -2.5618790000 -1.2757110000 -0.1119160000
C -4.0153150000 -3.0127850000 0.7353950000
C -2.8737180000 -3.7344660000 1.1110170000
C -1.6118100000 -3.2043230000 0.8262430000
N -1.4438250000 -2.0132640000 0.2063350000
C 1.1340540000 1.5948170000 -0.3448110000
C 1.5693500000 3.0587770000 -0.1672330000
C 1.9059600000 0.9083120000 -1.4836150000
C 1.4061110000 0.7720130000 0.9449820000
N 1.0541110000 -0.5462160000 0.9356220000
C 1.3095230000 -1.3180620000 2.0211610000
C 1.9218520000 -0.8180820000 3.1680940000
C 2.2805970000 0.5351430000 3.1984110000
C 2.0205030000 1.3308250000 2.0764990000
C 2.8682180000 1.5911080000 -2.2432100000
C 3.5624210000 0.9313460000 -3.2615390000
C 3.2739150000 -0.4170000000 -3.4902040000
C 2.3067170000 -1.0353660000 -2.7016520000

N 1.6157040000 -0.4052360000 -1.7150510000
H -3.2715150000 3.2764970000 -1.0968520000
H -5.0166060000 -3.4097660000 0.9257520000
H -2.9473830000 -4.7024680000 1.6135890000
H -0.7051680000 -3.7510400000 1.1038190000
H 1.0059240000 3.5286660000 0.6534650000
H 2.6427310000 3.1279620000 0.0642720000
H 1.3782350000 3.6327470000 -1.0866140000
H 1.0098200000 -2.3666760000 1.9480010000
H 2.1076510000 -1.4836400000 4.0153640000
H 2.7597400000 0.9701970000 4.0806280000
H 2.2994790000 2.3850760000 2.0869280000
H 3.0778090000 2.6416660000 -2.0401780000
H 4.3119870000 1.4611920000 -3.8566020000
H 3.7830250000 -0.9974520000 -4.2641490000
H 2.0946130000 -2.0899760000 -2.8878160000
Fe 0.1855120000 -1.2727160000 -0.6272230000
H -0.8138000000 3.6430400000 -0.8454590000
N -0.1763700000 -2.5830510000 -2.0687110000
H -1.0278420000 -3.1592010000 -2.1038070000
N 0.7755820000 -3.1057860000 -1.1160200000
H 0.2102290000 -2.5261080000 -3.0211370000
H -4.7240960000 -1.1650970000 -0.1577710000
H -4.2069650000 0.9711520000 -0.7368650000
H 1.6788060000 -3.3364830000 -1.5522330000
H 0.4244720000 -3.9646270000 -0.6725540000

[(bpyPy$_2$Me)Fe(η^2-N$_2$H$_4$)]$^{2+}$, multiplicity = 3 (N$_2$H$_4$ becomes η^1)
C -2.5596350000 2.6162900000 -0.4511670000
C -3.1367980000 1.3449530000 -0.4503820000
C -2.2967180000 0.2249830000 -0.3991480000
N -0.9338270000 0.3607690000 -0.3776680000
C -0.3638640000 1.5906890000 -0.3416820000
C -1.1649290000 2.7411720000 -0.3805410000
C -4.0687780000 -1.5895320000 -0.2504110000
C -2.7317180000 -1.1658710000 -0.3025400000
C -4.3519250000 -2.9450540000 -0.0682810000
C -3.2854290000 -3.8471990000 0.0709060000
C -1.9788320000 -3.3675230000 -0.0057210000
N -1.6898220000 -2.0570340000 -0.2078840000
C 1.1751790000 1.6273540000 -0.2522360000
C 1.6751850000 3.0815150000 -0.1795900000
C 1.7286440000 0.9251590000 -1.5167770000
C 1.5948290000 0.8472120000 1.0234280000
N 1.1549760000 -0.4304950000 1.1445880000
C 1.4466940000 -1.1474010000 2.2554360000

C 2.2048610000 -0.6262550000 3.3028040000
C 2.6864340000 0.6826100000 3.1831090000
C 2.3783440000 1.4241510000 2.0359310000
C 2.6196890000 1.5566430000 -2.3979510000
C 3.0414810000 0.8908930000 -3.5556000000
C 2.5692050000 -0.4007840000 -3.8107420000
C 1.7029690000 -0.9860640000 -2.8874630000
N 1.2959170000 -0.3371760000 -1.7684580000
H -3.1886520000 3.5098980000 -0.4926130000
H -5.3881260000 -3.2922150000 -0.0239940000
H -3.4553710000 -4.9143600000 0.2358090000
H -1.1350920000 -4.0527350000 0.1063490000
H 1.2606480000 3.5895410000 0.7041540000
H 2.7726440000 3.1146210000 -0.1108430000
H 1.3709590000 3.6417530000 -1.0764430000
H 1.0498600000 -2.1671020000 2.2996700000
H 2.4103670000 -1.2389880000 4.1845330000
H 3.2950580000 1.1298590000 3.9749560000
H 2.7496710000 2.4448880000 1.9398260000
H 2.9867090000 2.5623150000 -2.1916810000
H 3.7328370000 1.3829750000 -4.2466580000
H 2.8668000000 -0.9579610000 -4.7031620000
H 1.3320100000 -2.0122340000 -3.0018980000
Fe 0.1051230000 -1.2516060000 -0.4022010000
H -0.7115440000 3.7324590000 -0.3569150000
N 0.9049120000 -3.7447820000 -1.6949400000
H -0.0798020000 -4.0342440000 -1.6790630000
N 1.1471220000 -2.9686490000 -0.4932190000
H 1.4565250000 -4.6113370000 -1.6349320000
H -4.8764690000 -0.8594730000 -0.3421750000
H -4.2217630000 1.2210450000 -0.4788470000
H 2.1466580000 -2.7223890000 -0.5102050000
H 1.0363600000 -3.5465940000 0.3580470000

[(bpyPy$_2$Me)Fe(η^2-N$_2$H$_4$)]$^{2+}$, multiplicity = 5 (N$_2$H$_4$ becomes η^1)
C -2.5765780000 2.6266260000 -0.4069460000
C -3.1518020000 1.3532670000 -0.3886770000
C -2.3025170000 0.2379480000 -0.3297150000
N -0.9544830000 0.3866960000 -0.3016940000
C -0.3838380000 1.6077310000 -0.3029860000
C -1.1827760000 2.7625400000 -0.3565830000
C -4.1245000000 -1.5274930000 -0.2360700000
C -2.7682280000 -1.1642260000 -0.2672100000
C -4.4735580000 -2.8779690000 -0.1365400000
C -3.4570970000 -3.8395920000 -0.0639930000
C -2.1287810000 -3.4103470000 -0.1064440000

N -1.7837500000 -2.1087820000 -0.2132400000
C 1.1682790000 1.6505290000 -0.2395530000
C 1.6467040000 3.1146080000 -0.1948100000
C 1.7294770000 0.9482010000 -1.5084390000
C 1.6338400000 0.9025520000 1.0440770000
N 1.3196480000 -0.4130680000 1.1728090000
C 1.6841950000 -1.1007340000 2.2795030000
C 2.3841650000 -0.5092590000 3.3302600000
C 2.7238050000 0.8428770000 3.2141080000
C 2.3477350000 1.5510310000 2.0655600000
C 2.5366610000 1.6228020000 -2.4385940000
C 3.0002770000 0.9498100000 -3.5766390000
C 2.6557200000 -0.3918280000 -3.7689280000
C 1.8582150000 -1.0130520000 -2.8071570000
N 1.4070800000 -0.3548530000 -1.7125920000
H -3.2109300000 3.5164970000 -0.4541230000
H -5.5266260000 -3.1730700000 -0.1104300000
H -3.6796450000 -4.9061940000 0.0237370000
H -1.3119920000 -4.1352800000 -0.0501120000
H 1.2335360000 3.6313080000 0.6842510000
H 2.7444640000 3.1656990000 -0.1421890000
H 1.3199580000 3.6573580000 -1.0941250000
H 1.3984290000 -2.1575060000 2.3138110000
H 2.6562380000 -1.1008790000 4.2082860000
H 3.2793930000 1.3505820000 4.0085970000
H 2.6140670000 2.6043630000 1.9780600000
H 2.8091820000 2.6672830000 -2.2876880000
H 3.6293860000 1.4764810000 -4.3009900000
H 2.9987760000 -0.9566210000 -4.6399820000
H 1.5741600000 -2.0721660000 -2.8790320000
Fe 0.2139010000 -1.3658240000 -0.3137820000
H -0.7378260000 3.7578180000 -0.3592410000
N 0.9818440000 -3.9534090000 -1.7501540000
H -0.0257070000 -4.0932590000 -1.8896410000
N 1.1494280000 -3.3085690000 -0.4597670000
H 1.3897450000 -4.8967570000 -1.7020440000
H -4.9014280000 -0.7612870000 -0.2834930000
H -4.2370720000 1.2347460000 -0.4166160000
H 2.1533180000 -3.0969330000 -0.3744540000
H 0.9570860000 -3.9617010000 0.3171290000

[(bpyPy$_2$Me)Fe(NH$_3$)(NH$_3$)]$^{2+}$, multiplicity = 1
C -2.5605910000 2.2304990000 -0.9564740000
C -3.0243190000 0.9305810000 -0.7271440000
C -2.0832920000 -0.0853100000 -0.5077570000
N -0.7433390000 0.1745760000 -0.6010550000

C -0.2882560000 1.4476180000 -0.6506570000
C -1.1856630000 2.5036500000 -0.8619830000
C -3.6281480000 -1.9728010000 0.2220590000
C -2.3504910000 -1.4412330000 -0.0119890000
C -3.7489310000 -3.2313500000 0.8187950000
C -2.5820980000 -3.9258120000 1.1686050000
C -1.3391320000 -3.3514810000 0.8899890000
N -1.2057150000 -2.1390110000 0.3050230000
C 1.2146090000 1.6095200000 -0.3341580000
C 1.5829600000 3.1002130000 -0.2599530000
C 2.0590820000 0.8790610000 -1.3905290000
C 1.4551340000 0.8999370000 1.0272220000
N 1.1251670000 -0.4226930000 1.1164660000
C 1.2672930000 -1.0598360000 2.3045790000
C 1.7784770000 -0.4375240000 3.4416910000
C 2.1519790000 0.9080970000 3.3546970000
C 1.9788360000 1.5785350000 2.1382620000
C 3.0296610000 1.5279520000 -2.1687870000
C 3.7764780000 0.8045970000 -3.1060080000
C 3.5320400000 -0.5662340000 -3.2413560000
C 2.5561310000 -1.1522360000 -2.4375050000
N 1.8252150000 -0.4547180000 -1.5258500000
H -3.2676520000 3.0426550000 -1.1480380000
H -4.7364240000 -3.6603230000 1.0110820000
H -2.6224710000 -4.9089670000 1.6440060000
H -0.4195110000 -3.8877750000 1.1364890000
H 0.9800640000 3.6119840000 0.5051220000
H 2.6458700000 3.2316970000 -0.0076150000
H 1.3962150000 3.5906420000 -1.2277830000
H 0.9454570000 -2.1040180000 2.3408990000
H 1.8745750000 -1.0054940000 4.3710510000
H 2.5634290000 1.4359050000 4.2202300000
H 2.2523700000 2.6313930000 2.0607840000
H 3.2059310000 2.5972040000 -2.0458950000
H 4.5338760000 1.3072230000 -3.7149800000
H 4.0835870000 -1.1849920000 -3.9546090000
H 2.3423190000 -2.2204590000 -2.5262350000
Fe 0.4112640000 -1.3127480000 -0.4728970000
H -0.8288220000 3.5313600000 -0.9422450000
N 1.5938680000 -2.9432600000 -0.1827150000
H 1.3335010000 -3.7789830000 -0.7233570000
H 1.6287350000 -3.2633740000 0.7940230000
N -0.2921230000 -2.1139980000 -2.2082680000
H -1.2854990000 -1.8878050000 -2.3613920000
H -0.2427590000 -3.1406630000 -2.2664040000
H 0.1867800000 -1.7606280000 -3.0467610000

H 2.5798910000 -2.7637880000 -0.4178540000
H -4.5158600000 -1.3990850000 -0.0555210000
H -4.0951250000 0.7151480000 -0.6875390000

[(bpyPy$_2$Me)Fe(NH$_3$)(NH$_3$)]$^{2+}$, multiplicity = 3
C -2.5665730000 2.2053190000 -0.8308930000
C -3.0405530000 0.9112750000 -0.6103240000
C -2.1113650000 -0.1131910000 -0.3810760000
N -0.7621890000 0.1323050000 -0.4247150000
C -0.2933920000 1.4040580000 -0.5250320000
C -1.1882940000 2.4599400000 -0.7492390000
C -3.7318990000 -1.9930870000 0.1669680000
C -2.4310750000 -1.4872500000 0.0021660000
C -3.9047040000 -3.3053860000 0.6116540000
C -2.7682570000 -4.0848450000 0.8822770000
C -1.5037450000 -3.5309580000 0.6825080000
N -1.3221930000 -2.2607400000 0.2491540000
C 1.2207390000 1.6179420000 -0.2899590000
C 1.5515450000 3.1214790000 -0.3247460000
C 2.0579960000 0.8556710000 -1.3419770000
C 1.5577290000 1.0204220000 1.1074960000
N 1.2913410000 -0.2949240000 1.2881550000
C 1.5425340000 -0.8702000000 2.4842200000
C 2.0844460000 -0.1663160000 3.5604080000
C 2.3772720000 1.1909070000 3.3824130000
C 2.1098140000 1.7902200000 2.1452360000
C 3.0352350000 1.4941910000 -2.1248570000
C 3.7809000000 0.7541070000 -3.0490930000
C 3.5357930000 -0.6175170000 -3.1761590000
C 2.5515940000 -1.1873190000 -2.3700510000
N 1.8320210000 -0.4742940000 -1.4719610000
H -3.2637300000 3.0244290000 -1.0288090000
H -4.9097430000 -3.7151990000 0.7474590000
H -2.8536420000 -5.1155160000 1.2367950000
H -0.6055280000 -4.1247300000 0.8688850000
H 0.9646280000 3.6654640000 0.4305510000
H 2.6178740000 3.2919210000 -0.1153270000
H 1.3238940000 3.5473340000 -1.3138200000
H 1.2915620000 -1.9317830000 2.5819560000
H 2.2684690000 -0.6762660000 4.5099970000
H 2.8074400000 1.7834120000 4.1957990000
H 2.3335540000 2.8477950000 2.0002790000
H 3.2185540000 2.5637660000 -2.0212590000
H 4.5403090000 1.2489120000 -3.6623480000
H 4.0864240000 -1.2404320000 -3.8861500000
H 2.3151010000 -2.2515960000 -2.4503720000

Fe 0.3823190000 -1.3917140000 -0.3140810000
H -0.8237890000 3.4818330000 -0.8564450000
N 1.5479250000 -3.0334640000 -0.0762520000
H 1.3168750000 -3.8047180000 -0.7168920000
H 1.4895000000 -3.4437640000 0.8665300000
N -0.3761560000 -2.1779020000 -2.4599190000
H -1.4035020000 -2.1821780000 -2.4975740000
H -0.1003600000 -3.1331570000 -2.7218550000
H -0.0845040000 -1.5835550000 -3.2458620000
H 2.5503190000 -2.8453790000 -0.2119970000
H -4.5963880000 -1.3600500000 -0.0474960000
H -4.1122600000 0.6992150000 -0.6017360000

[(bpyPy$_2$Me)Fe(NH$_3$)(NH$_3$)]$^{2+}$, multiplicity = 5
C -2.5715020000 2.2063130000 -0.8765320000
C -3.0462050000 0.9181580000 -0.6210170000
C -2.1135290000 -0.1002490000 -0.3634260000
N -0.7782320000 0.1535790000 -0.3963280000
C -0.3085500000 1.4111740000 -0.5386770000
C -1.1955250000 2.4681550000 -0.8031660000
C -3.8073840000 -1.9192760000 0.1637910000
C -2.4777020000 -1.4794820000 0.0322250000
C -4.0596670000 -3.2223030000 0.6027760000
C -2.9755840000 -4.0598730000 0.9035130000
C -1.6804090000 -3.5617730000 0.7392510000
N -1.4278980000 -2.3059250000 0.3142300000
C 1.2136040000 1.6278290000 -0.3041290000
C 1.5192800000 3.1385850000 -0.2891210000
C 2.0588570000 0.9299960000 -1.3998280000
C 1.5779300000 0.9941500000 1.0740550000
N 1.3971610000 -0.3421540000 1.2300930000
C 1.6911310000 -0.9234150000 2.4138560000
C 2.1851100000 -0.2116130000 3.5075240000
C 2.3802830000 1.1657560000 3.3609050000
C 2.0728690000 1.7712850000 2.1360820000
C 2.9855310000 1.6315350000 -2.1920430000
C 3.7591640000 0.9400360000 -3.1321150000
C 3.5971370000 -0.4430710000 -3.2681520000
C 2.6482490000 -1.0717450000 -2.4613840000
N 1.8999910000 -0.4041940000 -1.5561500000
H -3.2711020000 3.0177640000 -1.0977180000
H -5.0889310000 -3.5773430000 0.7101680000
H -3.1240230000 -5.0845390000 1.2550970000
H -0.8100430000 -4.1904080000 0.9528650000
H 0.9174640000 3.6501860000 0.4770580000
H 2.5820390000 3.3214000000 -0.0714520000

H 1.2885680000 3.5915900000 -1.2649500000
H 1.5169270000 -2.0019340000 2.4844770000
H 2.4071120000 -0.7311630000 4.4436580000
H 2.7669000000 1.7699800000 4.1874570000
H 2.2227160000 2.8449150000 2.0202650000
H 3.1140120000 2.7085740000 -2.0830810000
H 4.4823870000 1.4828520000 -3.7487710000
H 4.1827080000 -1.0262700000 -3.9839730000
H 2.4707040000 -2.1497890000 -2.5392450000
Fe 0.4878270000 -1.5418700000 -0.3461820000
H -0.8342210000 3.4868870000 -0.9455430000
N 1.6672160000 -3.3234890000 0.0366680000
H 1.4604420000 -4.1079410000 -0.5955050000
H 1.6036710000 -3.7207190000 0.9836180000
N -0.2979630000 -2.2658960000 -2.3391490000
H -1.3215760000 -2.1908300000 -2.4038780000
H -0.0921220000 -3.2509190000 -2.5523630000
H 0.0585790000 -1.7346160000 -3.1434140000
H 2.6684760000 -3.1253440000 -0.0950730000
H -4.6374810000 -1.2487350000 -0.0703160000
H -4.1193030000 0.7151220000 -0.6103440000

[(bpyPy$_2$Me)Fe(NH$_2$)(NH$_3$)]$^{2+}$, multiplicity = 2
C -2.5866610000 2.2410720000 -0.9393080000
C -3.0604590000 0.9461500000 -0.6999430000
C -2.1233790000 -0.0712290000 -0.4763760000
N -0.7886810000 0.1869430000 -0.5573040000
C -0.3222320000 1.4472890000 -0.6367280000
C -1.2115570000 2.5094810000 -0.8601030000
C -3.6793800000 -1.9571610000 0.2417580000
C -2.4012080000 -1.4342840000 -0.0010500000
C -3.7990520000 -3.2293930000 0.8112560000
C -2.6344620000 -3.9416990000 1.1273510000
C -1.3890910000 -3.3738320000 0.8417460000
N -1.2663880000 -2.1502710000 0.2837550000
C 1.1826540000 1.6026970000 -0.3320610000
C 1.5568070000 3.0923720000 -0.2615780000
C 2.0304920000 0.8664140000 -1.3852610000
C 1.4383790000 0.8906990000 1.0283630000
N 1.1356470000 -0.4348410000 1.1173860000
C 1.3357740000 -1.0960630000 2.2819680000
C 1.8578660000 -0.4721970000 3.4143640000
C 2.1838930000 0.8856980000 3.3382730000
C 1.9700840000 1.5691590000 2.1350290000
C 2.9868990000 1.5183350000 -2.1797990000
C 3.7668680000 0.7808730000 -3.0769890000

C 3.5864940000 -0.6051650000 -3.1478700000
C 2.6209400000 -1.1935260000 -2.3337870000
N 1.8450550000 -0.4737190000 -1.4836710000
H -3.2903890000 3.0555960000 -1.1333100000
H -4.7870760000 -3.6534400000 1.0114220000
H -2.6779790000 -4.9327350000 1.5857580000
H -0.4535790000 -3.8979090000 1.0538360000
H 0.9604600000 3.6057800000 0.5074170000
H 2.6218930000 3.2190150000 -0.0165730000
H 1.3652020000 3.5834330000 -1.2279080000
H 1.0709740000 -2.1563260000 2.2781150000
H 2.0035640000 -1.0503940000 4.3308000000
H 2.5997170000 1.4134970000 4.2017880000
H 2.2210610000 2.6279940000 2.0646910000
H 3.1275080000 2.5967020000 -2.0981130000
H 4.5112240000 1.2852690000 -3.7006490000
H 4.1828820000 -1.2321920000 -3.8162530000
H 2.4552400000 -2.2740980000 -2.3308700000
Fe 0.4003340000 -1.3606740000 -0.4579400000
H -0.8496150000 3.5334000000 -0.9584970000
N 1.4033200000 -2.8583810000 -0.1596780000
H 1.1872010000 -3.7993390000 -0.5086290000
H 2.3645020000 -2.8353040000 0.1989430000
N -0.3064670000 -2.1257460000 -2.1981600000
H -1.1755260000 -1.6773560000 -2.5190240000
H -0.5158670000 -3.1300910000 -2.1325900000
H 0.3523700000 -2.0265350000 -2.9816170000
H -4.5667990000 -1.3694870000 -0.0050720000
H -4.1323920000 0.7382690000 -0.6607490000

[(bpyPy$_2$Me)Fe(NH$_2$)(NH$_3$)]$^{2+}$, multiplicity = 4
C -2.5608920000 2.1769040000 -0.9764550000
C -3.0538030000 0.9007430000 -0.6905690000
C -2.1418430000 -0.1203830000 -0.3962420000
N -0.7964660000 0.1147630000 -0.4256000000
C -0.3115440000 1.3687390000 -0.5720720000
C -1.1866020000 2.4241590000 -0.8822760000
C -3.8460600000 -1.9421020000 0.1423640000
C -2.5240650000 -1.4783290000 0.0485330000
C -4.0743870000 -3.2324940000 0.6367610000
C -2.9844950000 -4.0255830000 1.0209980000
C -1.6933160000 -3.5017030000 0.8848590000
N -1.4750680000 -2.2606540000 0.4160000000
C 1.1982740000 1.5896850000 -0.2994130000
C 1.4971260000 3.0995050000 -0.2302470000
C 2.0566000000 0.9263160000 -1.4038210000

C 1.5506790000 0.9084450000 1.0569990000
N 1.2986230000 -0.4211470000 1.2015830000
C 1.5781080000 -1.0510730000 2.3662670000
C 2.1344320000 -0.3852070000 3.4579490000
C 2.4182600000 0.9771670000 3.3257420000
C 2.1251060000 1.6248090000 2.1183810000
C 2.9831870000 1.6381980000 -2.1846840000
C 3.7628490000 0.9472750000 -3.1206520000
C 3.6154690000 -0.4390170000 -3.2450700000
C 2.6734430000 -1.0763460000 -2.4356550000
N 1.9031800000 -0.4042370000 -1.5555370000
H -3.2475370000 2.9901020000 -1.2284110000
H -5.0966750000 -3.6137150000 0.7182470000
H -3.1247650000 -5.0363850000 1.4135990000
H -0.7998940000 -4.0792890000 1.1448500000
H 0.8906120000 3.5825240000 0.5508760000
H 2.5593520000 3.2753090000 -0.0055160000
H 1.2726450000 3.5824690000 -1.1927710000
H 1.3424480000 -2.1187650000 2.4043990000
H 2.3399530000 -0.9329870000 4.3812940000
H 2.8634900000 1.5403270000 4.1515540000
H 2.3461510000 2.6870770000 2.0143190000
H 3.1067230000 2.7156090000 -2.0698410000
H 4.4861250000 1.4909420000 -3.7364100000
H 4.2163900000 -1.0211820000 -3.9490680000
H 2.5324340000 -2.1615170000 -2.4745670000
Fe 0.4178050000 -1.4587330000 -0.2914660000
H -0.8080790000 3.4343000000 -1.0383610000
N 1.4345920000 -2.9436960000 -0.0205750000
H 1.4191700000 -3.7619780000 -0.6393250000
H 2.3145700000 -2.9251000000 0.5076220000
N -0.2731640000 -2.2850580000 -2.1120950000
H -1.0933430000 -1.7929410000 -2.4895020000
H -0.5518710000 -3.2696940000 -2.0130100000
H 0.4256300000 -2.2688430000 -2.8648860000
H -4.6840300000 -1.3113760000 -0.1637270000
H -4.1284630000 0.7069190000 -0.6788060000

[(bpyPy$_2$Me)Fe(NH$_2$)(NH$_3$)]$^{2+}$, multiplicity = 6
C -2.5632960000 2.1674540000 -0.9918460000
C -3.0512850000 0.8899760000 -0.6981140000
C -2.1278490000 -0.1141810000 -0.3714000000
N -0.7964970000 0.1426150000 -0.3682480000
C -0.3166620000 1.3852400000 -0.5522580000
C -1.1914110000 2.4329100000 -0.8929520000
C -3.8261340000 -1.9063300000 0.2552620000

C -2.5009950000 -1.4849400000 0.0629190000
C -4.0658730000 -3.1973330000 0.7423780000
C -2.9812160000 -4.0365700000 1.0264750000
C -1.6872870000 -3.5570470000 0.7955100000
N -1.4566750000 -2.3160990000 0.3261340000
C 1.1994180000 1.5995600000 -0.2848220000
C 1.5033410000 3.1099740000 -0.2479930000
C 2.0549380000 0.9083880000 -1.3784860000
C 1.5493420000 0.9477180000 1.0858390000
N 1.3633320000 -0.3884330000 1.2252520000
C 1.6490110000 -1.0029490000 2.3931720000
C 2.1432810000 -0.3109440000 3.5003730000
C 2.3453720000 1.0667630000 3.3763460000
C 2.0473370000 1.7001880000 2.1619000000
C 2.9701560000 1.6199670000 -2.1740780000
C 3.7647050000 0.9328630000 -3.1001710000
C 3.6424190000 -0.4566760000 -3.2090820000
C 2.7106110000 -1.0995630000 -2.3934970000
N 1.9291540000 -0.4313200000 -1.5157870000
H -3.2549910000 2.9691920000 -1.2663370000
H -5.0925630000 -3.5398520000 0.9023760000
H -3.1260670000 -5.0476280000 1.4154840000
H -0.8026820000 -4.1727610000 0.9857530000
H 0.8882570000 3.6106810000 0.5147140000
H 2.5629640000 3.2901390000 -0.0135990000
H 1.2865910000 3.5753090000 -1.2211330000
H 1.4728720000 -2.0835480000 2.4253130000
H 2.3633620000 -0.8463430000 4.4278750000
H 2.7333070000 1.6533570000 4.2148920000
H 2.2073570000 2.7745260000 2.0669910000
H 3.0759340000 2.7005840000 -2.0738130000
H 4.4800530000 1.4836100000 -3.7190850000
H 4.2544230000 -1.0381120000 -3.9041690000
H 2.5802050000 -2.1865590000 -2.4186810000
Fe 0.4907530000 -1.6062340000 -0.3587940000
H -0.8222850000 3.4427310000 -1.0718580000
N 1.5320150000 -3.1738610000 -0.0729930000
H 1.3049880000 -4.1190450000 -0.4065540000
H 2.4148690000 -3.2360040000 0.4487550000
N -0.3303210000 -2.1936330000 -2.3324250000
H -1.0982830000 -1.5933430000 -2.6597360000
H -0.7043010000 -3.1509740000 -2.3147500000
H 0.3685780000 -2.1815270000 -3.0858050000
H -4.6609010000 -1.2359360000 0.0386420000
H -4.1243080000 0.6867520000 -0.7173320000

[(bpyPy$_2$Me)Fe(NH$_3$)(NH$_2$)]$^{2+}$, multiplicity = 2
C -2.5814980000 2.2060830000 -0.8621380000
C -3.0507210000 0.9114080000 -0.6133070000
C -2.1109740000 -0.1078200000 -0.4099400000
N -0.7809720000 0.1567660000 -0.5162310000
C -0.3096100000 1.4144360000 -0.6059720000
C -1.2053890000 2.4749750000 -0.8120330000
C -3.6599670000 -1.9994760000 0.2887560000
C -2.3804620000 -1.4744320000 0.0570630000
C -3.7849200000 -3.2780730000 0.8417110000
C -2.6222730000 -3.9963810000 1.1501030000
C -1.3761790000 -3.4234320000 0.8778980000
N -1.2432900000 -2.1910340000 0.3436350000
C 1.2015030000 1.5747590000 -0.3284180000
C 1.5762860000 3.0653770000 -0.2910440000
C 2.0317370000 0.8170770000 -1.3810450000
C 1.4611930000 0.8944100000 1.0446620000
N 1.0995380000 -0.4109440000 1.1725980000
C 1.2394120000 -1.0288920000 2.3675600000
C 1.7884540000 -0.3956660000 3.4818880000
C 2.1988740000 0.9349510000 3.3548860000
C 2.0234620000 1.5856310000 2.1275310000
C 3.0001810000 1.4501010000 -2.1746170000
C 3.7439140000 0.7054590000 -3.0972950000
C 3.5001490000 -0.6671800000 -3.2072930000
C 2.5229160000 -1.2373830000 -2.3930200000
N 1.8019550000 -0.5170390000 -1.4954570000
H -3.2890290000 3.0205150000 -1.0421770000
H -4.7741700000 -3.7046780000 1.0296990000
H -2.6663210000 -4.9965460000 1.5877850000
H -0.4589020000 -3.9766280000 1.0903210000
H 0.9903980000 3.5920880000 0.4769150000
H 2.6442790000 3.1968210000 -0.0618650000
H 1.3724360000 3.5378510000 -1.2642010000
H 0.8870400000 -2.0618370000 2.4336350000
H 1.8828900000 -0.9432720000 4.4232850000
H 2.6395810000 1.4702280000 4.2011890000
H 2.3234110000 2.6285300000 2.0218600000
H 3.1773430000 2.5213030000 -2.0748350000
H 4.5005350000 1.1961530000 -3.7169620000
H 4.0505830000 -1.2982050000 -3.9103570000
H 2.2876420000 -2.3023590000 -2.4640920000
Fe 0.3748430000 -1.3769330000 -0.4458040000
H -0.8445770000 3.4982680000 -0.9196940000
N 1.6034550000 -2.9434660000 -0.0440470000
H 1.3813060000 -3.7345280000 -0.6607610000

H 1.5671050000 -3.3104720000 0.9154240000
N -0.2345790000 -2.0924510000 -2.0220480000
H 0.0938490000 -1.7567580000 -2.9346900000
H -1.1635580000 -2.5165560000 -2.1277170000
H -4.5454980000 -1.4095770000 0.0406690000
H -4.1217670000 0.7041560000 -0.5529750000
H 2.5957150000 -2.7210270000 -0.2008960000

[(bpyPy$_2$Me)Fe(NH$_3$)(NH$_2$)]$^{2+}$, multiplicity = 4
C -2.5749440000 2.2152240000 -0.9192620000
C -3.0598310000 0.9353710000 -0.6237580000
C -2.1279550000 -0.0804940000 -0.3615070000
N -0.8049290000 0.1796310000 -0.4267610000
C -0.3203010000 1.4177900000 -0.5901260000
C -1.1976500000 2.4789440000 -0.8719800000
C -3.7480960000 -1.9175690000 0.3248200000
C -2.4425590000 -1.4526770000 0.1014410000
C -3.9373710000 -3.2081880000 0.8314760000
C -2.8160960000 -4.0025620000 1.1022040000
C -1.5439320000 -3.4799230000 0.8430830000
N -1.3571800000 -2.2362720000 0.3617800000
C 1.2008030000 1.5714070000 -0.3241000000
C 1.5617090000 3.0670950000 -0.2633540000
C 2.0301790000 0.8588500000 -1.4176670000
C 1.4864640000 0.8774070000 1.0398560000
N 1.1827620000 -0.4440680000 1.1749620000
C 1.3435190000 -1.0528930000 2.3720840000
C 1.8517700000 -0.3942390000 3.4910310000
C 2.2038610000 0.9519560000 3.3607800000
C 2.0105270000 1.5900770000 2.1292940000
C 2.9389550000 1.5452560000 -2.2391900000
C 3.6994900000 0.8375910000 -3.1780180000
C 3.5373730000 -0.5476150000 -3.2864590000
C 2.6010250000 -1.1674130000 -2.4600660000
N 1.8704140000 -0.4803780000 -1.5507570000
H -3.2748050000 3.0250080000 -1.1458820000
H -4.9479240000 -3.5865160000 1.0114450000
H -2.9138030000 -5.0157100000 1.5011840000
H -0.6470810000 -4.0799490000 1.0220970000
H 0.9707840000 3.5752260000 0.5136330000
H 2.6297680000 3.2081470000 -0.0398960000
H 1.3462490000 3.5531000000 -1.2266360000
H 1.0463700000 -2.1027070000 2.4298400000
H 1.9636250000 -0.9351230000 4.4342380000
H 2.6154650000 1.5102050000 4.2070210000
H 2.2669630000 2.6446050000 2.0270850000

H 3.0620900000 2.6249360000 -2.1520400000
H 4.4121380000 1.3701840000 -3.8152180000
H 4.1132290000 -1.1433650000 -3.9994900000
H 2.4083390000 -2.2425860000 -2.5216510000
Fe 0.4835820000 -1.4949610000 -0.4227410000
H -0.8307770000 3.4928070000 -1.0378980000
N 1.7922760000 -3.1532340000 0.1209950000
H 1.7333250000 -3.8621370000 -0.6199790000
H 1.6242100000 -3.6568610000 1.0008510000
N -0.1037420000 -2.2798830000 -1.9677340000
H 0.0897030000 -1.8382650000 -2.8750330000
H -1.0087940000 -2.7611240000 -2.0132400000
H -4.6058650000 -1.2761160000 0.1091400000
H -4.1345980000 0.7439130000 -0.5832460000
H 2.7766890000 -2.8584840000 0.1644980000

[(bpyPy$_2$Me)Fe(NH$_3$)(NH$_2$)]$^{2+}$, multiplicity = 6
C -2.5751695026 2.1727958726 -0.9295395171
C -3.0615640728 0.8987442183 -0.6202083321
C -2.1359164992 -0.1106654020 -0.3163891703
N -0.8046592568 0.1408547671 -0.3442386318
C -0.3218313873 1.3811651786 -0.5370572059
C -1.2002710230 2.4312456921 -0.8617081414
C -3.8303073578 -1.9103913103 0.2766925453
C -2.5035948080 -1.4781599589 0.1224085996
C -4.0779561074 -3.2023672486 0.7555195776
C -2.9958705735 -4.0328286528 1.0711113210
C -1.6996215351 -3.5408108582 0.8822496946
N -1.4582961942 -2.2986971931 0.4223910234
C 1.1993151418 1.5960423158 -0.2925861610
C 1.5003661858 3.1073016305 -0.2613830559
C 2.0444138299 0.9093139538 -1.3924084518
C 1.5593118428 0.9435715342 1.0748865678
N 1.3830095488 -0.3949253637 1.2111758486
C 1.6551973822 -0.9878264863 2.3925125208
C 2.1323795999 -0.2879812656 3.5023003518
C 2.3348004328 1.0883777760 3.3714096743
C 2.0436942344 1.7081408825 2.1491852592
C 2.9838071585 1.6110697534 -2.1675595550
C 3.7536336443 0.9245771445 -3.1151034072
C 3.5736407459 -0.4532443158 -3.2758862428
C 2.6150437151 -1.0863444041 -2.4839827050
N 1.8735537817 -0.4205968176 -1.5702589709
H -3.2690749409 2.9773567655 -1.1898442564
H -5.1066769520 -3.5525584372 0.8822496123
H -3.1426277420 -5.0458248667 1.4541162465

H -0.8278274110 -4.1629351778 1.1056805892
H 0.8856436764 3.6107199616 0.4995920703
H 2.5595492701 3.2909637244 -0.0281630243
H 1.2818490821 3.5672205380 -1.2369211570
H 1.4778487437 -2.0652871910 2.4539167066
H 2.3382394990 -0.8177637019 4.4362549245
H 2.7123029960 1.6829548969 4.2089662091
H 2.1962292082 2.7827702291 2.0465356059
H 3.1255473431 2.6841784966 -2.0371807391
H 4.4871655241 1.4685468535 -3.7184235766
H 4.1530117401 -1.0318383001 -4.0004938881
H 2.4112832547 -2.1576900480 -2.5822595037
Fe 0.4457123925 -1.6071061491 -0.4149627384
H -0.8305545359 3.4391332478 -1.0499385229
N 1.6266342585 -3.3362101446 0.1533965932
H 1.4180436029 -4.1193578638 -0.4792077232
H 1.5622239939 -3.7212797572 1.1044434172
N -0.1456260359 -2.3178302108 -2.1073372628
H 0.0186494639 -1.9247140751 -3.0422326327
H -0.7372504561 -3.1519051792 -2.2173083241
H -4.6622128834 -1.2470183763 0.0297912067
H -4.1360033263 0.7022864025 -0.6093353794
H 2.6262343077 -3.1317550798 0.0162811114

[(bpyPy$_2$Me)Fe(MeCN)(NH$_3$)]$^{3+}$, multiplicity = 2
C -2.5752200000 2.1884830000 -0.9954320000
C -3.0279790000 0.8939750000 -0.7222740000
C -2.0773860000 -0.1008500000 -0.4668970000
N -0.7450320000 0.1823460000 -0.5532910000
C -0.2949970000 1.4496970000 -0.6602260000
C -1.2061550000 2.4835500000 -0.9165180000
C -3.5954380000 -1.9989320000 0.2898250000
C -2.3316060000 -1.4534700000 0.0328170000
C -3.6814860000 -3.2734270000 0.8602520000
C -2.5027230000 -3.9706330000 1.1561570000
C -1.2701180000 -3.3862680000 0.8535050000
N -1.1835430000 -2.1534770000 0.3091460000
C 1.1998170000 1.6526520000 -0.3447630000
C 1.5381250000 3.1510320000 -0.2942320000
C 2.0695060000 0.9152720000 -1.3763110000
C 1.4466540000 0.9720340000 1.0289840000
N 1.1519370000 -0.3510060000 1.1315870000
C 1.3265020000 -1.0091980000 2.3012640000
C 1.8180700000 -0.3680350000 3.4371480000
C 2.1409290000 0.9894050000 3.3507280000
C 1.9521350000 1.6628990000 2.1372590000

C 3.0409690000 1.5641920000 -2.1495350000
C 3.8235780000 0.8262810000 -3.0447990000
C 3.6213470000 -0.5540730000 -3.1483430000
C 2.6393510000 -1.1435870000 -2.3573930000
N 1.8798790000 -0.4237230000 -1.4925910000
H -3.2916890000 2.9846900000 -1.2156680000
H -4.6590700000 -3.7158460000 1.0711510000
H -2.5233390000 -4.9647980000 1.6094110000
H -0.3335590000 -3.9120480000 1.0482900000
H 0.9157830000 3.6605060000 0.4566980000
H 2.5953750000 3.3027860000 -0.0317800000
H 1.3546730000 3.6196010000 -1.2726660000
H 1.0633950000 -2.0694380000 2.3197640000
H 1.9421490000 -0.9362300000 4.3622890000
H 2.5356020000 1.5274590000 4.2175090000
H 2.1980290000 2.7222890000 2.0596320000
H 3.1889470000 2.6401850000 -2.0568300000
H 4.5819860000 1.3292730000 -3.6518770000
H 4.2075870000 -1.1762000000 -3.8291310000
H 2.4472780000 -2.2167830000 -2.4125990000
Fe 0.4425640000 -1.3108620000 -0.4394630000
H -0.8603850000 3.5104700000 -1.0392620000
N 1.5818950000 -2.8424020000 -0.1667190000
N -0.2306230000 -2.0848560000 -2.1838530000
H -1.2566370000 -2.1241350000 -2.2547460000
H 0.1013940000 -3.0480870000 -2.3257180000
H 0.0839150000 -1.5380510000 -2.9964010000
H -4.4964430000 -1.4287700000 0.0524950000
H -4.0953180000 0.6665370000 -0.6811910000
C 2.2968210000 -3.7429520000 0.0213640000
C 3.1854390000 -4.8625520000 0.2515740000
H 3.2041990000 -5.0897370000 1.3309850000
H 4.2003000000 -4.5959910000 -0.0881480000
H 2.8192410000 -5.7395120000 -0.3077100000

[(bpyPy$_2$Me)Fe(MeCN)(NH$_3$)]$^{3+}$, multiplicity = 4
C -2.5652790000 2.1266200000 -1.0758820000
C -3.0267520000 0.8460270000 -0.7538270000
C -2.0902080000 -0.1388000000 -0.4188830000
N -0.7599790000 0.1530280000 -0.4473190000
C -0.2985850000 1.4100250000 -0.6266620000
C -1.2002910000 2.4256650000 -0.9795160000
C -3.7227240000 -1.9788100000 0.2363800000
C -2.4173960000 -1.4926800000 0.0780450000
C -3.9056340000 -3.2574960000 0.7801440000
C -2.7868990000 -4.0137560000 1.1502840000

C -1.5121160000 -3.4703060000 0.9503350000
N -1.3370730000 -2.2413560000 0.4316860000
C 1.2008780000 1.6592380000 -0.3317980000
C 1.4708110000 3.1733690000 -0.2608290000
C 2.0924430000 1.0013080000 -1.4130670000
C 1.5232140000 0.9840960000 1.0301160000
N 1.2811890000 -0.3491980000 1.1732550000
C 1.5248070000 -0.9895510000 2.3426540000
C 2.0379550000 -0.3165610000 3.4486350000
C 2.3164020000 1.0475660000 3.3242120000
C 2.0582310000 1.6978530000 2.1097020000
C 2.9853190000 1.7253760000 -2.2149810000
C 3.7981320000 1.0405160000 -3.1284300000
C 3.7116780000 -0.3530450000 -3.2175420000
C 2.7924260000 -1.0104500000 -2.4005370000
N 2.0007550000 -0.3428940000 -1.5326520000
H -3.2751470000 2.9091980000 -1.3580650000
H -4.9159300000 -3.6553690000 0.9121640000
H -2.8884920000 -5.0124120000 1.5828600000
H -0.6092160000 -4.0315970000 1.2088330000
H 0.8406080000 3.6432220000 0.5091430000
H 2.5263610000 3.3673560000 -0.0205070000
H 1.2504160000 3.6483940000 -1.2279240000
H 1.2960340000 -2.0569250000 2.3795240000
H 2.2159500000 -0.8647350000 4.3769250000
H 2.7310700000 1.6121570000 4.1644450000
H 2.2728700000 2.7619540000 2.0119150000
H 3.0573430000 2.8103020000 -2.1340780000
H 4.4985290000 1.5977940000 -3.7577060000
H 4.3383740000 -0.9281840000 -3.9038750000
H 2.6891730000 -2.0992140000 -2.4331770000
Fe 0.5245800000 -1.3504280000 -0.3336980000
H -0.8498190000 3.4413060000 -1.1641310000
N 1.6055050000 -2.9639880000 -0.0023580000
N -0.1009330000 -2.1346350000 -2.1081150000
H -1.0090850000 -2.6098120000 -2.0209790000
H 0.5441660000 -2.8421820000 -2.4843460000
H -0.2132240000 -1.4142900000 -2.8344290000
H -4.5837820000 -1.3728520000 -0.0541450000
H -4.0956690000 0.6234920000 -0.7438170000
C 2.2752690000 -3.9094520000 0.1254800000
C 3.1070320000 -5.0813190000 0.2868900000
H 3.1925590000 -5.3173900000 1.3610170000
H 4.1079370000 -4.8673020000 -0.1255290000
H 2.6528430000 -5.9291880000 -0.2523700000

[(bpyPy$_2$Me)Fe(MeCN)(NH$_3$)]$^{3+}$, multiplicity = 6
C -2.5959630000 2.1666360000 -0.9796670000
C -3.0549660000 0.8780640000 -0.6868670000
C -2.1100880000 -0.1080370000 -0.3783730000
N -0.7824690000 0.1847340000 -0.3981580000
C -0.3235220000 1.4410190000 -0.5733580000
C -1.2288610000 2.4643400000 -0.8957020000
C -3.7321670000 -1.9605360000 0.2550180000
C -2.4298460000 -1.4840880000 0.0567290000
C -3.9146180000 -3.2645000000 0.7348990000
C -2.7948710000 -4.0601600000 1.0056110000
C -1.5219050000 -3.5308880000 0.7721100000
N -1.3468270000 -2.2749680000 0.3121530000
C 1.1849260000 1.6863570000 -0.3108170000
C 1.4644770000 3.2008020000 -0.2902840000
C 2.0539440000 0.9929590000 -1.3877350000
C 1.5431610000 1.0493350000 1.0633460000
N 1.3701730000 -0.2899390000 1.2106210000
C 1.6576630000 -0.9018150000 2.3823490000
C 2.1436010000 -0.1974700000 3.4836710000
C 2.3364010000 1.1805530000 3.3516450000
C 2.0337670000 1.8080640000 2.1341700000
C 2.9872980000 1.6902110000 -2.1685760000
C 3.7946460000 0.9907310000 -3.0749660000
C 3.6633690000 -0.3976320000 -3.1846230000
C 2.7052030000 -1.0315320000 -2.3960030000
N 1.9207480000 -0.3483560000 -1.5292640000
H -3.3085290000 2.9551800000 -1.2377660000
H -4.9251400000 -3.6504510000 0.8967910000
H -2.8936350000 -5.0793100000 1.3876830000
H -0.6199940000 -4.1211910000 0.9540950000
H 0.8397870000 3.6979630000 0.4668810000
H 2.5205020000 3.3980060000 -0.0552650000
H 1.2423840000 3.6484900000 -1.2702020000
H 1.4928330000 -1.9822830000 2.4291020000
H 2.3647610000 -0.7278190000 4.4132550000
H 2.7200220000 1.7739570000 4.1870010000
H 2.1820730000 2.8832090000 2.0331860000
H 3.0963310000 2.7706210000 -2.0734450000
H 4.5235470000 1.5330650000 -3.6846410000
H 4.2802240000 -0.9860600000 -3.8684500000
H 2.5567360000 -2.1140340000 -2.4534120000
Fe 0.5143880000 -1.4522870000 -0.3579720000
H -0.8848320000 3.4843290000 -1.0672790000
N 1.6356250000 -3.1278410000 0.0690210000
N -0.1563390000 -2.1692850000 -2.3144570000

H -1.1739200000 -2.3175210000 -2.3450330000
H 0.2589980000 -3.0771340000 -2.5658290000
H 0.0570000000 -1.5259650000 -3.0881230000
H -4.5938720000 -1.3229370000 0.0462180000
H -4.1232040000 0.6522640000 -0.6883220000
C 2.3293490000 -4.0555630000 0.2101240000
C 3.1886610000 -5.2016340000 0.3873350000
H 3.2745530000 -5.4226590000 1.4648930000
H 4.1842150000 -4.9715180000 -0.0291500000
H 2.7508290000 -6.0657960000 -0.1406960000

[(bpyPy$_2$Me)Fe(NH$_3$)(NHNH$_2$)]$^{2+}$, multiplicity = 2
C -2.5496380000 2.1879910000 -1.0197640000
C -3.0083550000 0.8844470000 -0.7958490000
C -2.0641170000 -0.1218330000 -0.5501080000
N -0.7286550000 0.1558850000 -0.6089910000
C -0.2793910000 1.4270080000 -0.6612180000
C -1.1805060000 2.4759000000 -0.8983000000
C -3.6107860000 -2.0053310000 0.1794100000
C -2.3312090000 -1.4734320000 -0.0410100000
C -3.7405250000 -3.2464570000 0.8112220000
C -2.5813510000 -3.9217100000 1.2171330000
C -1.3343150000 -3.3477250000 0.9502350000
N -1.1938310000 -2.1579740000 0.3239560000
C 1.2196960000 1.5988920000 -0.3318300000
C 1.5783200000 3.0921770000 -0.2614460000
C 2.0732940000 0.8686850000 -1.3825780000
C 1.4600810000 0.8946490000 1.0322440000
N 1.1424450000 -0.4294090000 1.1226090000
C 1.2991550000 -1.0688270000 2.3066350000
C 1.8060440000 -0.4423680000 3.4437680000
C 2.1599140000 0.9084250000 3.3577890000
C 1.9773980000 1.5790080000 2.1424750000
C 3.0502220000 1.5198240000 -2.1516750000
C 3.8014000000 0.7978220000 -3.0860120000
C 3.5526820000 -0.5712440000 -3.2324700000
C 2.5689670000 -1.1598780000 -2.4399950000
N 1.8411470000 -0.4633860000 -1.5261100000
H -3.2601650000 2.9923390000 -1.2308240000
H -4.7307230000 -3.6751910000 0.9896780000
H -2.6284790000 -4.8886140000 1.7240240000
H -0.4179360000 -3.8688490000 1.2398190000
H 0.9655510000 3.6027060000 0.4966740000
H 2.6383540000 3.2316640000 -0.0017560000
H 1.3956090000 3.5770380000 -1.2327750000
H 0.9944210000 -2.1178870000 2.3384790000

H 1.9142880000 -1.0105830000 4.3715980000
H 2.5659190000 1.4403650000 4.2234090000
H 2.2390760000 2.6349230000 2.0659590000
H 3.2270890000 2.5882140000 -2.0230900000
H 4.5652080000 1.3010470000 -3.6865390000
H 4.1062400000 -1.1861410000 -3.9475040000
H 2.3402880000 -2.2235220000 -2.5390950000
Fe 0.4287240000 -1.3398260000 -0.4758980000
H -0.8304120000 3.5057940000 -0.9792350000
N 1.6302770000 -2.9514850000 -0.1790830000
H 1.4726290000 -3.6878540000 -0.8826940000
H 1.5411870000 -3.4239260000 0.7295640000
N -0.1879550000 -2.0947890000 -2.1219910000
N -0.4392110000 -3.4039800000 -2.3632170000
H -0.0550330000 -1.6020560000 -3.0141340000
H 2.6282840000 -2.7096300000 -0.2438150000
H -4.4951820000 -1.4456760000 -0.1349240000
H -4.0780700000 0.6610390000 -0.7822150000
H -0.8600010000 -3.6149960000 -3.2736490000
H -0.8992090000 -3.8921550000 -1.5880770000

[(bpyPy$_2$Me)Fe(NH$_3$)(NHNH$_2$)]$^{2+}$, multiplicity = 4
C -2.5264280000 2.1720960000 -1.0319420000
C -3.0142800000 0.8955150000 -0.7316900000
C -2.0951900000 -0.1174970000 -0.4232080000
N -0.7600420000 0.1343920000 -0.4441010000
C -0.2787540000 1.3838280000 -0.6034250000
C -1.1538490000 2.4333350000 -0.9355950000
C -3.7893350000 -1.9502020000 0.0666630000
C -2.4670770000 -1.4749170000 0.0442870000
C -4.0478530000 -3.2211900000 0.5937940000
C -2.9809050000 -3.9807580000 1.0904400000
C -1.6890590000 -3.4411170000 1.0245760000
N -1.4327070000 -2.2238420000 0.5131810000
C 1.2329750000 1.5921230000 -0.3201190000
C 1.5334640000 3.1008390000 -0.2292750000
C 2.0920560000 0.9447320000 -1.4357060000
C 1.5578710000 0.8916540000 1.0299240000
N 1.2706940000 -0.4349550000 1.1628920000
C 1.4931950000 -1.0540600000 2.3478830000
C 2.0379610000 -0.4018300000 3.4518210000
C 2.3658160000 0.9515460000 3.3237050000
C 2.1174920000 1.5979170000 2.1073460000
C 3.0079130000 1.6740420000 -2.2137440000
C 3.7636050000 1.0080720000 -3.1876760000
C 3.5874610000 -0.3684570000 -3.3695670000

C 2.6501680000 -1.0222610000 -2.5672230000
N 1.9282500000 -0.3802840000 -1.6251790000
H -3.2181910000 2.9765460000 -1.2983080000
H -5.0702450000 -3.6104600000 0.6157150000
H -3.1364260000 -4.9744280000 1.5187670000
H -0.8300360000 -4.0071120000 1.4024800000
H 0.9200340000 3.5745440000 0.5519660000
H 2.5935000000 3.2760940000 0.0060600000
H 1.3149000000 3.5963060000 -1.1870490000
H 1.2122780000 -2.1090010000 2.4060710000
H 2.1971720000 -0.9515380000 4.3832630000
H 2.8030260000 1.5062180000 4.1594250000
H 2.3619360000 2.6552640000 2.0056230000
H 3.1410330000 2.7469750000 -2.0698760000
H 4.4819850000 1.5660630000 -3.7966050000
H 4.1562970000 -0.9285290000 -4.1170100000
H 2.4604980000 -2.0951190000 -2.6786440000
Fe 0.5031360000 -1.4444210000 -0.3592320000
H -0.7808370000 3.4427340000 -1.1101270000
N 1.7307960000 -3.0762850000 -0.0747630000
H 1.6094890000 -3.7431760000 -0.8533460000
H 1.5557670000 -3.6171530000 0.7827930000
N -0.1485560000 -2.2681520000 -1.9392050000
N -0.2261200000 -3.6173340000 -2.1651760000
H -0.0432890000 -1.7819140000 -2.8389680000
H 2.7293620000 -2.8312370000 -0.0383930000
H -4.6070000000 -1.3392660000 -0.3233100000
H -4.0892680000 0.7008760000 -0.7178760000
H -0.5816120000 -3.8653360000 -3.0947310000
H -0.7442200000 -4.1107750000 -1.4287970000

[(bpyPy$_2$Me)Fe(NH$_3$)(NHNH$_2$)]$^{2+}$, multiplicity = 6
C -2.5552740000 2.1671830000 -0.9621470000
C -3.0265410000 0.8809750000 -0.6847880000
C -2.0915730000 -0.1236540000 -0.3894580000
N -0.7598510000 0.1395250000 -0.3999700000
C -0.2952440000 1.3942720000 -0.5622050000
C -1.1836460000 2.4397500000 -0.8714430000
C -3.7826740000 -1.9410910000 0.1497490000
C -2.4546310000 -1.4974860000 0.0292880000
C -4.0357330000 -3.2356970000 0.6161490000
C -2.9548850000 -4.0591860000 0.9568370000
C -1.6586760000 -3.5553260000 0.8042810000
N -1.4078180000 -2.3101830000 0.3510030000
C 1.2215810000 1.6276220000 -0.3062340000
C 1.5093870000 3.1417560000 -0.2873780000

C 2.0835530000 0.9389060000 -1.3934040000
C 1.5799740000 0.9953710000 1.0729900000
N 1.4323290000 -0.3456600000 1.2181310000
C 1.7253270000 -0.9270490000 2.4014280000
C 2.1859360000 -0.2102360000 3.5067440000
C 2.3473090000 1.1721220000 3.3710090000
C 2.0411610000 1.7779750000 2.1458020000
C 3.0343420000 1.6420640000 -2.1545580000
C 3.8158440000 0.9569220000 -3.0933610000
C 3.6360900000 -0.4205450000 -3.2590360000
C 2.6663190000 -1.0528140000 -2.4795130000
N 1.9125630000 -0.3905310000 -1.5741580000
H -3.2562140000 2.9683420000 -1.2141550000
H -5.0649840000 -3.5933160000 0.7151350000
H -3.1036360000 -5.0747670000 1.3325220000
H -0.7891730000 -4.1695530000 1.0585200000
H 0.8848140000 3.6481790000 0.4634840000
H 2.5647870000 3.3375390000 -0.0463450000
H 1.2948820000 3.5906280000 -1.2691570000
H 1.5794250000 -2.0104500000 2.4628330000
H 2.4110670000 -0.7299660000 4.4420580000
H 2.7079170000 1.7802550000 4.2063440000
H 2.1665950000 2.8558180000 2.0385280000
H 3.1753370000 2.7149590000 -2.0213590000
H 4.5579110000 1.5011850000 -3.6860270000
H 4.2246140000 -0.9981000000 -3.9772090000
H 2.4667600000 -2.1248020000 -2.5812360000
Fe 0.5191620000 -1.5668340000 -0.3568110000
H -0.8253190000 3.4562700000 -1.0340180000
N 1.6819680000 -3.3565960000 0.0745070000
H 1.5086930000 -4.1013290000 -0.6142540000
H 1.5940240000 -3.8098180000 0.9937100000
N -0.1061910000 -2.3116700000 -2.2060950000
N -0.5044880000 -3.5632680000 -2.5375830000
H -0.0030510000 -1.7639880000 -3.0702470000
H 2.6837380000 -3.1362170000 -0.0116640000
H -4.6126740000 -1.2818710000 -0.1142900000
H -4.0985210000 0.6707920000 -0.6887160000
H -1.0192110000 -3.6659050000 -3.4182080000
H -0.9245440000 -4.0913940000 -1.7672130000

[(bpyPy$_2$Me)Fe(NHNH$_2$)(NH$_3$)]$^{2+}$, multiplicity = 2
C -2.5622260000 2.2256970000 -0.9490980000
C -3.0164990000 0.9215810000 -0.7258320000
C -2.0673650000 -0.0878320000 -0.5115780000
N -0.7309750000 0.1838220000 -0.6036510000

C -0.2853410000 1.4579620000 -0.6533860000
C -1.1894560000 2.5098450000 -0.8573410000
C -3.5946040000 -1.9844080000 0.2387660000
C -2.3239230000 -1.4474970000 -0.0184720000
C -3.6967510000 -3.2417480000 0.8423330000
C -2.5206110000 -3.9270460000 1.1788540000
C -1.2849600000 -3.3480500000 0.8764270000
N -1.1737860000 -2.1404060000 0.2793400000
C 1.2179210000 1.6250530000 -0.3456890000
C 1.5794180000 3.1168630000 -0.2582810000
C 2.0585080000 0.9103650000 -1.4174260000
C 1.4709000000 0.9029320000 1.0087380000
N 1.1752270000 -0.4280070000 1.0813400000
C 1.3489590000 -1.0898330000 2.2518500000
C 1.8381440000 -0.4679290000 3.3994690000
C 2.1634370000 0.8915720000 3.3363590000
C 1.9743180000 1.5782570000 2.1310010000
C 2.9997540000 1.5781960000 -2.2157230000
C 3.7481920000 0.8650320000 -3.1590900000
C 3.5431660000 -0.5142430000 -3.2766240000
C 2.5952860000 -1.1209660000 -2.4551060000
N 1.8560780000 -0.4280660000 -1.5472540000
H -3.2763100000 3.0332560000 -1.1343580000
H -4.6785840000 -3.6754570000 1.0531730000
H -2.5486400000 -4.9061190000 1.6647180000
H -0.3490410000 -3.8632540000 1.1094510000
H 0.9776270000 3.6174610000 0.5154060000
H 2.6434950000 3.2507290000 -0.0115640000
H 1.3837350000 3.6162210000 -1.2195830000
H 1.0860270000 -2.1501280000 2.2451210000
H 1.9589640000 -1.0480600000 4.3182760000
H 2.5555070000 1.4180040000 4.2118130000
H 2.2177550000 2.6396380000 2.0713900000
H 3.1506940000 2.6526970000 -2.1059960000
H 4.4807410000 1.3820930000 -3.7861240000
H 4.1061000000 -1.1227550000 -3.9896000000
H 2.4092200000 -2.1972900000 -2.5033700000
Fe 0.4460430000 -1.3158680000 -0.5046280000
H -0.8406720000 3.5407950000 -0.9329080000
N 1.5114070000 -2.8759040000 -0.2944060000
H 1.1821890000 -3.8277210000 -0.4977500000
N -0.2911110000 -2.0701450000 -2.2476690000
H -1.2654410000 -1.7902160000 -2.4276510000
H -0.2892330000 -3.0976500000 -2.2940050000
H 0.2328520000 -1.7544420000 -3.0741420000
N 2.7663320000 -2.9448440000 0.2185500000

H -4.4907320000 -1.4159230000 -0.0225540000
H -4.0855110000 0.6987680000 -0.6860630000
H 3.3212070000 -3.7603270000 -0.0595280000
H 3.2824010000 -2.0621020000 0.1734480000

[(bpyPy$_2$Me)Fe(NHNH$_2$)(NH$_3$)]$^{2+}$, multiplicity = 4
C -2.5639220000 2.1565130000 -0.8642230000
C -3.0063490000 0.8566760000 -0.6062010000
C -2.0505400000 -0.1427210000 -0.3805060000
N -0.7125590000 0.1343180000 -0.4571080000
C -0.2718360000 1.4096560000 -0.5807530000
C -1.1926330000 2.4441850000 -0.8125870000
C -3.6332940000 -2.0311230000 0.2588590000
C -2.3432420000 -1.5195710000 0.0419920000
C -3.7762730000 -3.3309700000 0.7537300000
C -2.6273330000 -4.0884250000 1.0261000000
C -1.3737370000 -3.5287690000 0.7674170000
N -1.2286560000 -2.2781130000 0.2793080000
C 1.2397220000 1.6580820000 -0.3499740000
C 1.5212600000 3.1721270000 -0.3317780000
C 2.0933290000 0.9668500000 -1.4382100000
C 1.5974910000 1.0220210000 1.0280050000
N 1.3735670000 -0.3072940000 1.1834340000
C 1.6077590000 -0.8925160000 2.3792160000
C 2.1039440000 -0.1890260000 3.4777670000
C 2.3715470000 1.1753310000 3.3230530000
C 2.1132660000 1.7852010000 2.0889940000
C 3.0327570000 1.6643430000 -2.2176600000
C 3.7982550000 0.9698850000 -3.1617410000
C 3.6196160000 -0.4110900000 -3.3026170000
C 2.6725580000 -1.0389930000 -2.4935250000
N 1.9246140000 -0.3652210000 -1.5923420000
H -3.2835560000 2.9556120000 -1.0637110000
H -4.7732750000 -3.7452300000 0.9302660000
H -2.6937550000 -5.1039090000 1.4256970000
H -0.4537010000 -4.0900330000 0.9542510000
H 0.9172200000 3.6723770000 0.4402140000
H 2.5823520000 3.3687940000 -0.1188870000
H 1.2806170000 3.6231050000 -1.3063680000
H 1.3961110000 -1.9651940000 2.4435030000
H 2.2763000000 -0.7077880000 4.4247680000
H 2.7719460000 1.7670790000 4.1520230000
H 2.3125550000 2.8501310000 1.9654490000
H 3.1734560000 2.7387060000 -2.0960120000
H 4.5284730000 1.5068330000 -3.7752760000
H 4.1991910000 -0.9967790000 -4.0215320000

H 2.4962580000 -2.1175660000 -2.5452500000
Fe 0.4814360000 -1.3997230000 -0.4195650000
H -0.8528860000 3.4717800000 -0.9437170000
N 1.4944720000 -2.9873000000 -0.4513790000
H 1.0774400000 -3.7981900000 -0.9275030000
N -0.3354740000 -2.0309360000 -2.4843840000
H -1.3504360000 -2.1948010000 -2.4913580000
H 0.0745830000 -2.8818250000 -2.8906140000
H -0.1759370000 -1.2923540000 -3.1809820000
N 2.2638600000 -3.4380540000 0.5797660000
H -4.5125530000 -1.4167480000 0.0510490000
H -4.0731290000 0.6248530000 -0.5672800000
H 2.5950680000 -4.4025620000 0.4810110000
H 3.0138820000 -2.7890320000 0.8365400000

[(bpyPy$_2$Me)Fe(NHNH$_2$)(NH$_3$)]$^{2+}$, multiplicity = 6
C -2.5581420000 2.1780390000 -0.9619830000
C -3.0290380000 0.8925020000 -0.6793410000
C -2.0931010000 -0.1070110000 -0.3697740000
N -0.7628600000 0.1630350000 -0.3773820000
C -0.2989670000 1.4144300000 -0.5518860000
C -1.1873990000 2.4565310000 -0.8700810000
C -3.7786080000 -1.9092300000 0.2546080000
C -2.4535710000 -1.4844250000 0.0582790000
C -4.0169830000 -3.2031150000 0.7325630000
C -2.9299510000 -4.0436230000 1.0068230000
C -1.6384950000 -3.5599890000 0.7722190000
N -1.4060170000 -2.3176590000 0.3081700000
C 1.2213360000 1.6392230000 -0.3034910000
C 1.5115170000 3.1526840000 -0.2617180000
C 2.0635280000 0.9673360000 -1.4202120000
C 1.5861040000 0.9878930000 1.0647070000
N 1.4530600000 -0.3569530000 1.1908910000
C 1.7410380000 -0.9635250000 2.3626050000
C 2.1838960000 -0.2590150000 3.4841140000
C 2.3315340000 1.1267000000 3.3718810000
C 2.0306720000 1.7541490000 2.1550480000
C 2.9405440000 1.7016460000 -2.2386800000
C 3.7090930000 1.0378230000 -3.2028920000
C 3.5964080000 -0.3508550000 -3.3306520000
C 2.7028010000 -1.0154990000 -2.4895730000
N 1.9506070000 -0.3726840000 -1.5695370000
H -3.2606420000 2.9752650000 -1.2222630000
H -5.0430940000 -3.5476530000 0.8924050000
H -3.0725930000 -5.0585730000 1.3874960000
H -0.7562540000 -4.1826110000 0.9552590000

H 0.8972530000 3.6444610000 0.5075780000
H 2.5714350000 3.3414830000 -0.0339740000
H 1.2815890000 3.6206620000 -1.2303490000
H 1.6165060000 -2.0512550000 2.3866620000
H 2.4068730000 -0.7906000000 4.4131780000
H 2.6784850000 1.7240320000 4.2208480000
H 2.1444130000 2.8351070000 2.0703120000
H 3.0355910000 2.7824530000 -2.1317950000
H 4.3941090000 1.6059850000 -3.8400560000
H 4.1850480000 -0.9129640000 -4.0608770000
H 2.5749670000 -2.1025560000 -2.5357480000
Fe 0.5147480000 -1.5407750000 -0.3908030000
H -0.8311440000 3.4731480000 -1.0390270000
N 1.6994360000 -3.1615510000 -0.2246300000
H 1.3515410000 -4.1049350000 -0.4387920000
N -0.3129890000 -2.2075040000 -2.3629880000
H -1.2787790000 -1.9007950000 -2.5380590000
H -0.3291850000 -3.2307410000 -2.4636320000
H 0.2289650000 -1.8611660000 -3.1640020000
N 2.9245650000 -3.2850150000 0.3627900000
H -4.6150900000 -1.2377440000 0.0482790000
H -4.1002660000 0.6799740000 -0.6924290000
H 3.4727720000 -4.1016190000 0.0722140000
H 3.4725660000 -2.4203180000 0.3370670000

[(bpyPy$_2$Me)Fe(MeCN)(NH$_2$)]$^{2+}$, multiplicity = 2
C -2.5765020000 2.2143490000 -0.9239790000
C -3.0272850000 0.9114830000 -0.6848210000
C -2.0747130000 -0.0931660000 -0.4723320000
N -0.7465140000 0.1920660000 -0.5625180000
C -0.2958820000 1.4578790000 -0.6403340000
C -1.2063690000 2.5047410000 -0.8539930000
C -3.6005400000 -2.0093520000 0.2209930000
C -2.3296420000 -1.4630680000 -0.0070510000
C -3.7031990000 -3.2882290000 0.7789080000
C -2.5294630000 -3.9841920000 1.0964710000
C -1.2914360000 -3.3920280000 0.8267720000
N -1.1841750000 -2.1596540000 0.2871930000
C 1.2062370000 1.6416090000 -0.3426020000
C 1.5566080000 3.1375310000 -0.2868280000
C 2.0616200000 0.9063290000 -1.3913180000
C 1.4633520000 0.9509200000 1.0271770000
N 1.1349990000 -0.3643280000 1.1359600000
C 1.3071990000 -1.0076150000 2.3131890000
C 1.8372850000 -0.3767980000 3.4383580000
C 2.1983040000 0.9705930000 3.3382310000

C 2.0041610000 1.6390160000 2.1230250000
C 3.0270990000 1.5600930000 -2.1718940000
C 3.8012470000 0.8286430000 -3.0796980000
C 3.5955360000 -0.5507650000 -3.1842410000
C 2.6184590000 -1.1417750000 -2.3848040000
N 1.8623420000 -0.4308860000 -1.5107760000
H -3.2950480000 3.0175670000 -1.1107340000
H -4.6854960000 -3.7323070000 0.9638860000
H -2.5591800000 -4.9828550000 1.5401880000
H -0.3574310000 -3.9176230000 1.0376050000
H 0.9525730000 3.6478360000 0.4786860000
H 2.6195350000 3.2833260000 -0.0435810000
H 1.3571660000 3.6151170000 -1.2582350000
H 1.0079840000 -2.0582050000 2.3424880000
H 1.9579020000 -0.9399360000 4.3674760000
H 2.6213400000 1.5040210000 4.1947840000
H 2.2744800000 2.6918500000 2.0358860000
H 3.1784360000 2.6355730000 -2.0751150000
H 4.5545360000 1.3341120000 -3.6914380000
H 4.1765070000 -1.1709880000 -3.8720070000
H 2.4157260000 -2.2138390000 -2.4371040000
Fe 0.4301380000 -1.3244030000 -0.4859370000
H -0.8600670000 3.5343360000 -0.9512070000
N 1.5928580000 -2.8115780000 -0.1073600000
N -0.1713130000 -2.0192930000 -2.0757130000
H -1.0336820000 -2.5639780000 -2.1900920000
H 0.2025620000 -1.7475660000 -2.9919590000
H -4.4960880000 -1.4366110000 -0.0317930000
H -4.0952360000 0.6863730000 -0.6384280000
C 2.3266920000 -3.6913760000 0.1045080000
C 3.2375390000 -4.7935490000 0.3632680000
H 3.2654340000 -5.0016800000 1.4457980000
H 4.2486520000 -4.5254470000 0.0142850000
H 2.8879620000 -5.6907040000 -0.1742790000

[(bpyPy$_2$Me)Fe(MeCN)(NH$_2$)]$^{2+}$, multiplicity = 4
C -2.5867440000 2.2428960000 -0.9736560000
C -3.0517180000 0.9541650000 -0.6832550000
C -2.1025730000 -0.0434520000 -0.4124210000
N -0.7855650000 0.2437310000 -0.4650600000
C -0.3206840000 1.4886340000 -0.6254850000
C -1.2148100000 2.5334470000 -0.9147810000
C -3.6762830000 -1.9204380000 0.2785700000
C -2.3846660000 -1.4228490000 0.0473040000
C -3.8292830000 -3.2139560000 0.7905500000
C -2.6867830000 -3.9780380000 1.0594120000

C -1.4288460000 -3.4269570000 0.7909040000
N -1.2784530000 -2.1806650000 0.3025850000
C 1.1951350000 1.6597880000 -0.3419180000
C 1.5403780000 3.1590220000 -0.2865290000
C 2.0532900000 0.9441840000 -1.4115540000
C 1.4704590000 0.9742670000 1.0292470000
N 1.2110180000 -0.3570950000 1.1512220000
C 1.3904550000 -0.9763380000 2.3401420000
C 1.8581170000 -0.3066400000 3.4707640000
C 2.1502920000 1.0556030000 3.3594070000
C 1.9503070000 1.6981570000 2.1308670000
C 2.9714800000 1.6316190000 -2.2211020000
C 3.7714920000 0.9224950000 -3.1254800000
C 3.6409570000 -0.4677720000 -3.2122570000
C 2.6921970000 -1.0918930000 -2.4044290000
N 1.9217980000 -0.4009810000 -1.5306370000
H -3.2996580000 3.0393440000 -1.2067990000
H -4.8290910000 -3.6167940000 0.9772040000
H -2.7572040000 -4.9911500000 1.4642390000
H -0.5115880000 -3.9968150000 0.9652380000
H 0.9299320000 3.6667580000 0.4755050000
H 2.6025550000 3.3132220000 -0.0445780000
H 1.3365250000 3.6360640000 -1.2570510000
H 1.1529240000 -2.0427150000 2.3718820000
H 1.9876600000 -0.8520380000 4.4091800000
H 2.5259630000 1.6219610000 4.2169470000
H 2.1681330000 2.7624890000 2.0405550000
H 3.0723260000 2.7146980000 -2.1491940000
H 4.4916240000 1.4577080000 -3.7519200000
H 4.2509770000 -1.0641520000 -3.8956650000
H 2.5198580000 -2.1712290000 -2.4463300000
Fe 0.5299200000 -1.4051550000 -0.4577380000
H -0.8657620000 3.5541500000 -1.0775740000
N 1.7293690000 -3.0723950000 0.1497200000
N -0.0335300000 -2.1737980000 -2.0218030000
H -0.9022530000 -2.7154610000 -2.0847070000
H 0.1646730000 -1.7327470000 -2.9278700000
H -4.5509490000 -1.3009650000 0.0665170000
H -4.1229470000 0.7417780000 -0.6544210000
C 2.4771270000 -3.9638910000 0.2223490000
C 3.4050760000 -5.0772900000 0.3128030000
H 3.5599540000 -5.3418160000 1.3718830000
H 4.3683450000 -4.7853360000 -0.1378560000
H 2.9922810000 -5.9437930000 -0.2299620000

[(bpyPy$_2$Me)Fe(MeCN)(NH$_2$)]$^{2+}$, multiplicity = 6

C -2.5906420000 2.1900580000 -0.9586400000
C -3.0497220000 0.9026020000 -0.6629910000
C -2.1030000000 -0.0876860000 -0.3638940000
N -0.7774470000 0.1945180000 -0.3841120000
C -0.3212330000 1.4465420000 -0.5639920000
C -1.2224410000 2.4790960000 -0.8826080000
C -3.7521210000 -1.9401170000 0.2025530000
C -2.4379520000 -1.4676820000 0.0618210000
C -3.9636580000 -3.2433390000 0.6690660000
C -2.8595830000 -4.0438550000 0.9872220000
C -1.5767650000 -3.5128620000 0.8127000000
N -1.3719150000 -2.2598960000 0.3640950000
C 1.1928510000 1.6918780000 -0.3119400000
C 1.4643520000 3.2084490000 -0.2740650000
C 2.0596180000 1.0244840000 -1.4077890000
C 1.5610830000 1.0420130000 1.0557780000
N 1.4222140000 -0.3015020000 1.1817330000
C 1.7182730000 -0.9029000000 2.3531750000
C 2.1754970000 -0.1988340000 3.4689850000
C 2.3322620000 1.1850200000 3.3528170000
C 2.0224210000 1.8099220000 2.1373430000
C 2.9788980000 1.7482320000 -2.1862430000
C 3.7798180000 1.0757490000 -3.1177970000
C 3.6534830000 -0.3103950000 -3.2575980000
C 2.7096280000 -0.9660360000 -2.4666750000
N 1.9339580000 -0.3120640000 -1.5735010000
H -3.3016970000 2.9809880000 -1.2146250000
H -4.9823460000 -3.6255970000 0.7834840000
H -2.9797280000 -5.0642750000 1.3606090000
H -0.6834260000 -4.1046150000 1.0343730000
H 0.8373320000 3.6959100000 0.4876900000
H 2.5193380000 3.4109080000 -0.0370610000
H 1.2396920000 3.6677960000 -1.2482050000
H 1.5831820000 -1.9881950000 2.3899950000
H 2.4022880000 -0.7311640000 4.3966010000
H 2.6920280000 1.7822270000 4.1964000000
H 2.1424000000 2.8895750000 2.0462170000
H 3.0817030000 2.8274720000 -2.0715130000
H 4.4983460000 1.6364790000 -3.7236810000
H 4.2632440000 -0.8779420000 -3.9656240000
H 2.5506690000 -2.0464670000 -2.5444080000
Fe 0.5145860000 -1.5121740000 -0.4407300000
H -0.8746390000 3.4971380000 -1.0593150000
N 1.6674490000 -3.1783270000 0.1673340000
N -0.0484320000 -2.2365590000 -2.1400950000
H -0.7135310000 -3.0143920000 -2.2405550000

H 0.1966130000 -1.9072680000 -3.0820590000
H -4.6018260000 -1.2999630000 -0.0451050000
H -4.1192090000 0.6813450000 -0.6586400000
C 2.3698880000 -4.0998380000 0.2944780000
C 3.2424690000 -5.2476460000 0.4517300000
H 3.3365630000 -5.4924820000 1.5226840000
H 4.2361700000 -5.0053700000 0.0391250000
H 2.8162080000 -6.1073930000 -0.0915820000

[(bpyPy$_2$Me)Fe(NH$_2$)(NH$_2$)]$^{2+}$, multiplicity = 3
C -2.5791080000 2.2326740000 -0.9067130000
C -3.0495650000 0.9367380000 -0.6626990000
C -2.1102590000 -0.0808380000 -0.4543720000
N -0.7811760000 0.1871580000 -0.5469830000
C -0.3120270000 1.4424360000 -0.6287040000
C -1.2048010000 2.5044720000 -0.8444330000
C -3.6592740000 -1.9726580000 0.2642710000
C -2.3842220000 -1.4481030000 0.0139400000
C -3.7732700000 -3.2535580000 0.8177440000
C -2.6088670000 -3.9748660000 1.1092140000
C -1.3644470000 -3.4048050000 0.8192810000
N -1.2532220000 -2.1709360000 0.2874280000
C 1.1954110000 1.5970410000 -0.3313080000
C 1.5691740000 3.0870850000 -0.2628130000
C 2.0308280000 0.8621800000 -1.3954620000
C 1.4467440000 0.8896620000 1.0327250000
N 1.1173080000 -0.4261270000 1.1354070000
C 1.2724920000 -1.0735480000 2.3123750000
C 1.7911150000 -0.4472830000 3.4457640000
C 2.1576210000 0.8982700000 3.3518060000
C 1.9788300000 1.5712820000 2.1363470000
C 3.0028750000 1.5127220000 -2.1721880000
C 3.7606430000 0.7832770000 -3.0941360000
C 3.5352480000 -0.5918580000 -3.2197080000
C 2.5552060000 -1.1814330000 -2.4245300000
N 1.8155360000 -0.4690120000 -1.5379780000
H -3.2866130000 3.0461580000 -1.0910400000
H -4.7600910000 -3.6789500000 1.0208630000
H -2.6499520000 -4.9743120000 1.5489280000
H -0.4248700000 -3.9332480000 1.0016300000
H 0.9723090000 3.5999400000 0.5060070000
H 2.6337920000 3.2145070000 -0.0170470000
H 1.3774090000 3.5763170000 -1.2299330000
H 0.9716480000 -2.1245360000 2.3299330000
H 1.9002210000 -1.0128220000 4.3748820000
H 2.5736060000 1.4283420000 4.2138270000

H 2.2547380000 2.6230850000 2.0573750000
H 3.1733990000 2.5833000000 -2.0562650000
H 4.5206500000 1.2870450000 -3.6990350000
H 4.1068170000 -1.2101080000 -3.9170790000
H 2.3395650000 -2.2504650000 -2.4791130000
Fe 0.4051680000 -1.3912480000 -0.4887520000
H -0.8447100000 3.5285570000 -0.9468920000
N 1.4663140000 -2.8256860000 -0.0906540000
H 1.5040800000 -3.6638040000 -0.6795310000
H 2.3096720000 -2.7456660000 0.4894330000
N -0.2086520000 -2.1162880000 -2.0525070000
H 0.0373620000 -1.7582750000 -2.9823900000
H -0.9260070000 -2.8471920000 -2.1187870000
H -4.5492590000 -1.3830900000 0.0323490000
H -4.1207520000 0.7286160000 -0.6101900000

[(bpyPy$_2$Me)Fe(NH$_2$)(NH$_2$)]$^{2+}$, multiplicity = 1
C -2.5664860000 2.1928300000 -0.8183330000
C -3.0302110000 0.9036940000 -0.5347420000
C -2.0868690000 -0.1189150000 -0.3644780000
N -0.7646350000 0.1466710000 -0.5028520000
C -0.2903600000 1.3965290000 -0.6401520000
C -1.1891680000 2.4564800000 -0.8361760000
C -3.6363420000 -2.0072030000 0.3250190000
C -2.3572830000 -1.5042380000 0.0470500000
C -3.7702180000 -3.3208220000 0.7852600000
C -2.6175740000 -4.0979920000 0.9495700000
C -1.3730370000 -3.5416320000 0.6385490000
N -1.2322280000 -2.2732960000 0.2039560000
C 1.2244490000 1.5590440000 -0.3877290000
C 1.6004710000 3.0493670000 -0.3569770000
C 2.0723170000 0.7926800000 -1.4227590000
C 1.4611030000 0.8856920000 0.9898780000
N 1.0791880000 -0.4095500000 1.1160030000
C 1.1791600000 -1.0321650000 2.3117530000
C 1.6912740000 -0.3922730000 3.4404010000
C 2.1268590000 0.9307400000 3.3190140000
C 2.0062500000 1.5755170000 2.0824100000
C 3.0480200000 1.4198130000 -2.2118640000
C 3.8268690000 0.6605550000 -3.0934650000
C 3.6185750000 -0.7203170000 -3.1688740000
C 2.6300630000 -1.2881190000 -2.3661910000
N 1.8764380000 -0.5470090000 -1.5154660000
H -3.2781840000 3.0073400000 -0.9803770000
H -4.7593400000 -3.7292040000 1.0104090000
H -2.6669860000 -5.1295310000 1.3063020000

H -0.4674940000 -4.1435850000 0.7376360000
H 1.0120310000 3.5801860000 0.4060140000
H 2.6675900000 3.1798360000 -0.1233880000
H 1.4009310000 3.5165730000 -1.3335160000
H 0.8450010000 -2.0706180000 2.3515500000
H 1.7498740000 -0.9357170000 4.3871800000
H 2.5491650000 1.4640110000 4.1758480000
H 2.3288400000 2.6116000000 1.9758740000
H 3.2055120000 2.4962690000 -2.1392900000
H 4.5885650000 1.1490500000 -3.7087290000
H 4.2044490000 -1.3578180000 -3.8364250000
H 2.4123590000 -2.3598470000 -2.3849780000
Fe 0.4169210000 -1.4345620000 -0.5512190000
H -0.8281510000 3.4749500000 -0.9822380000
N 1.5260840000 -2.7445890000 -0.0479770000
H 1.2461280000 -3.5521530000 0.5193690000
H 2.5267480000 -2.5582000000 0.0921360000
N -0.2621560000 -1.8381460000 -2.1557200000
H -1.2330640000 -2.1394890000 -2.3002040000
H 0.1360120000 -1.4612550000 -3.0232590000
H -4.5148840000 -1.3730260000 0.1859440000
H -4.0989460000 0.7001550000 -0.4376240000

[(bpyPy$_2$Me)Fe(NH$_2$)(NH$_2$)]$^{2+}$, multiplicity = 5
C -2.5489870000 2.1628630000 -0.9993200000
C -3.0382900000 0.8892360000 -0.6925810000
C -2.1223310000 -0.1259330000 -0.3879190000
N -0.7852740000 0.1239680000 -0.4254750000
C -0.2994090000 1.3701080000 -0.5893930000
C -1.1758700000 2.4203370000 -0.9127730000
C -3.8179200000 -1.9471460000 0.1647900000
C -2.4976970000 -1.4778160000 0.0857720000
C -4.0497350000 -3.2239440000 0.6931760000
C -2.9649120000 -3.9970060000 1.1267030000
C -1.6739260000 -3.4677260000 1.0042140000
N -1.4529290000 -2.2404110000 0.5029540000
C 1.2101850000 1.5863590000 -0.3076220000
C 1.5068670000 3.0944370000 -0.2076520000
C 2.0691370000 0.9425480000 -1.4220740000
C 1.5399670000 0.8773640000 1.0367610000
N 1.2574390000 -0.4478310000 1.1687860000
C 1.4830080000 -1.0885400000 2.3396750000
C 2.0303410000 -0.4423650000 3.4467590000
C 2.3576440000 0.9106630000 3.3256700000
C 2.1075120000 1.5709540000 2.1160610000
C 2.9906010000 1.6675470000 -2.1959170000

C 3.7528150000 0.9933460000 -3.1587210000
C 3.5868810000 -0.3868510000 -3.3225250000
C 2.6526610000 -1.0400380000 -2.5160640000
N 1.9112290000 -0.3832440000 -1.5999480000
H -3.2401510000 2.9692550000 -1.2604630000
H -5.0711280000 -3.6101160000 0.7616420000
H -3.1070440000 -4.9964000000 1.5456920000
H -0.7874980000 -4.0357470000 1.3043120000
H 0.8938640000 3.5621380000 0.5773590000
H 2.5673190000 3.2672950000 0.0268770000
H 1.2877110000 3.5938230000 -1.1630300000
H 1.2110450000 -2.1474030000 2.3756640000
H 2.1936320000 -0.9988060000 4.3731980000
H 2.7988100000 1.4579970000 4.1640890000
H 2.3560940000 2.6279300000 2.0225620000
H 3.1226440000 2.7410720000 -2.0555650000
H 4.4738830000 1.5469180000 -3.7683270000
H 4.1681090000 -0.9537460000 -4.0550220000
H 2.4849000000 -2.1190380000 -2.5922790000
Fe 0.4360150000 -1.5042190000 -0.3666030000
H -0.8004210000 3.4288950000 -1.0847320000
N 1.5244440000 -2.9354710000 -0.0144550000
H 1.6055730000 -3.7417390000 -0.6403440000
H 2.3524580000 -2.8564010000 0.5876060000
N -0.1917640000 -2.2312640000 -1.9429090000
H 0.1499290000 -1.9771940000 -2.8764010000
H -0.7674970000 -3.0806550000 -1.9798430000
H -4.6523530000 -1.3329930000 -0.1814320000
H -4.1129450000 0.6951440000 -0.6706440000

[(bpyPy$_2$Me)Fe(NH)(NH$_3$)]$^{2+}$, multiplicity = 3
C -2.5865660000 2.2469210000 -0.8995420000
C -3.0541710000 0.9510590000 -0.6527740000
C -2.1116290000 -0.0673940000 -0.4544460000
N -0.7821740000 0.1981150000 -0.5663570000
C -0.3176970000 1.4562660000 -0.6471530000
C -1.2107730000 2.5193430000 -0.8483770000
C -3.6569860000 -1.9608530000 0.2775790000
C -2.3830390000 -1.4352800000 0.0191860000
C -3.7660780000 -3.2433920000 0.8272820000
C -2.5988210000 -3.9688200000 1.1006440000
C -1.3578510000 -3.3981610000 0.8009930000
N -1.2495760000 -2.1597200000 0.2772550000
C 1.1893250000 1.6024640000 -0.3463730000
C 1.5711830000 3.0900690000 -0.2752100000
C 2.0346990000 0.8610150000 -1.3990330000

C 1.4284650000 0.8908530000 1.0187090000
N 1.1034620000 -0.4279400000 1.1199440000
C 1.2719240000 -1.0821030000 2.2920120000
C 1.7850390000 -0.4551750000 3.4267550000
C 2.1392420000 0.8946280000 3.3398360000
C 1.9564920000 1.5696190000 2.1269850000
C 2.9960520000 1.5104240000 -2.1900630000
C 3.7793860000 0.7715530000 -3.0830210000
C 3.5967530000 -0.6138670000 -3.1579130000
C 2.6245390000 -1.2011790000 -2.3511620000
N 1.8485420000 -0.4785510000 -1.5041390000
H -3.2960950000 3.0607460000 -1.0745550000
H -4.7510560000 -3.6687680000 1.0393030000
H -2.6375650000 -4.9718540000 1.5324960000
H -0.4146260000 -3.9289490000 0.9605580000
H 0.9764110000 3.6051460000 0.4937420000
H 2.6367110000 3.2121830000 -0.0299630000
H 1.3799560000 3.5811270000 -1.2416090000
H 0.9895630000 -2.1376630000 2.2981970000
H 1.9040380000 -1.0259610000 4.3514990000
H 2.5524890000 1.4239160000 4.2036150000
H 2.2270430000 2.6230350000 2.0500470000
H 3.1394740000 2.5882310000 -2.1068850000
H 4.5292650000 1.2751770000 -3.7006150000
H 4.1963420000 -1.2409490000 -3.8232750000
H 2.4508530000 -2.2810290000 -2.3530630000
Fe 0.4165210000 -1.3793910000 -0.4797790000
H -0.8520090000 3.5442750000 -0.9482810000
N 1.4143690000 -2.7644200000 -0.1769490000
H 2.3329490000 -2.9275020000 0.2668180000
N -0.3116590000 -2.0946750000 -2.2324470000
H -1.2205630000 -1.6966010000 -2.5043740000
H -0.4390980000 -3.1130320000 -2.1808520000
H 0.3142730000 -1.9204610000 -3.0289600000
H -4.5491000000 -1.3707620000 0.0552150000
H -4.1248150000 0.7437340000 -0.5867010000

[(bpyPy$_2$Me)Fe(NH)(NH$_3$)]$^{2+}$, multiplicity = 1
C -2.5980530000 2.2382830000 -0.8837030000
C -3.0712430000 0.9490750000 -0.6114400000
C -2.1294680000 -0.0684800000 -0.4044030000
N -0.8034580000 0.1932800000 -0.5153670000
C -0.3310090000 1.4440940000 -0.6379090000
C -1.2203160000 2.5068800000 -0.8583630000
C -3.6731890000 -1.9618600000 0.3201280000
C -2.3984710000 -1.4440200000 0.0495570000

C -3.7870990000 -3.2577040000 0.8366220000
C -2.6226800000 -4.0034340000 1.0614940000
C -1.3819790000 -3.4385630000 0.7478710000
N -1.2686510000 -2.1867030000 0.2613440000
C 1.1821750000 1.5921640000 -0.3581800000
C 1.5619470000 3.0816430000 -0.3073740000
C 2.0405330000 0.8364090000 -1.3927750000
C 1.4349620000 0.8970900000 1.0090690000
N 1.1304390000 -0.4253960000 1.1126110000
C 1.3149180000 -1.0746940000 2.2873610000
C 1.8234980000 -0.4365000000 3.4173960000
C 2.1527990000 0.9193600000 3.3273130000
C 1.9547740000 1.5877800000 2.1132890000
C 2.9986060000 1.4810640000 -2.1905070000
C 3.8061830000 0.7342910000 -3.0554000000
C 3.6506960000 -0.6555260000 -3.0966410000
C 2.6781740000 -1.2388940000 -2.2876650000
N 1.8802320000 -0.5105260000 -1.4645020000
H -3.3056780000 3.0519900000 -1.0672780000
H -4.7723720000 -3.6764970000 1.0602900000
H -2.6635910000 -5.0169690000 1.4682360000
H -0.4376030000 -3.9806900000 0.8603500000
H 0.9666250000 3.6055970000 0.4551190000
H 2.6274350000 3.2093690000 -0.0647400000
H 1.3683760000 3.5602910000 -1.2795310000
H 1.0442220000 -2.1338850000 2.3009180000
H 1.9582700000 -1.0042400000 4.3418290000
H 2.5591080000 1.4574640000 4.1888620000
H 2.2053520000 2.6458430000 2.0318360000
H 3.1202740000 2.5633470000 -2.1360130000
H 4.5527090000 1.2361820000 -3.6783520000
H 4.2685700000 -1.2883920000 -3.7392710000
H 2.5184430000 -2.3214410000 -2.2862600000
Fe 0.4293030000 -1.3901060000 -0.4699790000
H -0.8602990000 3.5273430000 -0.9929850000
N 1.2909790000 -2.8207760000 -0.1097560000
H 2.3076000000 -2.6235140000 0.0613720000
N -0.3129240000 -2.0364620000 -2.2405220000
H -1.1151030000 -1.4846510000 -2.5717700000
H -0.6315500000 -3.0098810000 -2.1657110000
H 0.3761020000 -2.0166940000 -3.0039550000
H -4.5623430000 -1.3549210000 0.1340020000
H -4.1428170000 0.7480280000 -0.5417200000

[(bpyPy$_2$Me)Fe(NH)(NH$_3$)]$^{2+}$, multiplicity = 5
C -2.5930951701 2.2388102740 -0.9773191524

C -3.0677731407 0.9530798313 -0.6822881912
C -2.1227450836 -0.0406559036 -0.3838112707
N -0.8040995458 0.2377912160 -0.4146641419
C -0.3377154715 1.4755608051 -0.5970483039
C -1.2193767911 2.5241466153 -0.9095010533
C -3.6871798171 -1.9079161949 0.3641042371
C -2.4043089947 -1.4202573574 0.0767687082
C -3.8295888488 -3.2048053805 0.8725372179
C -2.6873252078 -3.9888881655 1.0786624377
C -1.4376045345 -3.4545594845 0.7509950529
N -1.2994528175 -2.2027664591 0.2684675855
C 1.1816764393 1.6238700173 -0.3151283269
C 1.5593289376 3.1146542184 -0.2660565566
C 2.0149655886 0.8801112875 -1.3846266202
C 1.4580807635 0.9332102262 1.0499534062
N 1.2877731739 -0.4125087928 1.1319741920
C 1.5255600002 -1.0738383092 2.2844253691
C 1.9330546914 -0.4124000391 3.4439957586
C 2.1122521078 0.9732740422 3.3864084333
C 1.8787454890 1.6489660588 2.1804599048
C 2.9155259829 1.5514746860 -2.2277245679
C 3.7221903654 0.8286279490 -3.1142311073
C 3.6366155382 -0.5678685300 -3.1322131985
C 2.7202050628 -1.1837972132 -2.2827360090
N 1.9150242683 -0.4736183412 -1.4550657102
H -3.2997339207 3.0355896964 -1.2273839000
H -4.8241254846 -3.5956243215 1.1064341165
H -2.7530048758 -5.0046663534 1.4757349012
H -0.5108129966 -4.0259505075 0.8555187786
H 0.9583104544 3.6365242336 0.4934435523
H 2.6242671413 3.2458570512 -0.0210670739
H 1.3636316695 3.5955449190 -1.2362832577
H 1.3929676338 -2.1598944406 2.2450991661
H 2.1169075140 -0.9815150905 4.3591602939
H 2.4406719822 1.5318162269 4.2681870624
H 2.0274566149 2.7284471878 2.1294070602
H 2.9962110982 2.6382315506 -2.1885939304
H 4.4225607888 1.3567673078 -3.7686647103
H 4.2665304314 -1.1794529014 -3.7836943350
H 2.6082970167 -2.2714142799 -2.2299891341
Fe 0.5016690633 -1.4738120049 -0.4513344025
H -0.8640986809 3.5410789059 -1.0817572610
N 1.4543920528 -3.0214115593 -0.1788123534
H 1.9594999684 -3.8725628600 0.1192186503
N -0.2570334438 -2.0619226160 -2.2754336082
H -0.9602226754 -1.4187596753 -2.6627960746

H -0.6955192786 -2.9871642757 -2.1960562468
H 0.4770127714 -2.1569777517 -2.9887719650
H -4.5631640074 -1.2752736239 0.2022575796
H -4.1399908229 0.7422941264 -0.6753620013

[(bpyPy$_2$Me)Fe(NH$_3$)(NH)]$^{2+}$, multiplicity = 3
C -2.5396260000 2.1898430000 -0.9808880000
C -3.0121980000 0.8945440000 -0.7409470000
C -2.0750150000 -0.1206580000 -0.5085400000
N -0.7442430000 0.1469790000 -0.5902160000
C -0.2735420000 1.4069910000 -0.6521990000
C -1.1672220000 2.4644260000 -0.8832480000
C -3.6371290000 -1.9783890000 0.2485790000
C -2.3540910000 -1.4706920000 0.0034720000
C -3.7733670000 -3.2232710000 0.8732080000
C -2.6201240000 -3.9238280000 1.2449910000
C -1.3684560000 -3.3706890000 0.9537600000
N -1.2285430000 -2.1780640000 0.3445380000
C 1.2262500000 1.5767900000 -0.3126720000
C 1.5831220000 3.0709110000 -0.2422960000
C 2.0902910000 0.8481690000 -1.3592940000
C 1.4490350000 0.8814400000 1.0601980000
N 1.1200270000 -0.4343710000 1.1580440000
C 1.2575870000 -1.0761920000 2.3398320000
C 1.7527760000 -0.4475640000 3.4822220000
C 2.1175340000 0.8990000000 3.3916650000
C 1.9601730000 1.5678570000 2.1712330000
C 3.0841980000 1.5022820000 -2.1045650000
C 3.8167370000 0.7927800000 -3.0622550000
C 3.5254500000 -0.5594850000 -3.2704410000
C 2.5280340000 -1.1508960000 -2.4981730000
N 1.8423610000 -0.4715480000 -1.5470960000
H -3.2440170000 3.0015890000 -1.1836720000
H -4.7669550000 -3.6352820000 1.0706820000
H -2.6732170000 -4.8938350000 1.7449530000
H -0.4565070000 -3.9133250000 1.2134490000
H 0.9620210000 3.5819260000 0.5084090000
H 2.6397020000 3.2095820000 0.0303780000
H 1.4125460000 3.5532310000 -1.2168440000
H 0.9570060000 -2.1272820000 2.3672030000
H 1.8456860000 -1.0108890000 4.4144380000
H 2.5160560000 1.4320650000 4.2600350000
H 2.2351720000 2.6200860000 2.0939510000
H 3.2853220000 2.5613600000 -1.9428540000
H 4.5941610000 1.2977290000 -3.6433950000
H 4.0512450000 -1.1560620000 -4.0206960000

H 2.2368880000 -2.1924570000 -2.6533940000
Fe 0.4105400000 -1.3929590000 -0.5085760000
H -0.8083910000 3.4902080000 -0.9729750000
N 1.6902740000 -2.9126160000 -0.1210920000
H 2.5114050000 -2.5954320000 0.4102220000
N -0.1613440000 -2.1984370000 -1.9466760000
H -0.4498750000 -3.1727910000 -2.1410500000
H -4.5181500000 -1.4009830000 -0.0413080000
H -4.0839560000 0.6855490000 -0.7045300000
H 1.2955670000 -3.6984520000 0.4104930000
H 2.0566400000 -3.3407320000 -0.9801060000

[(bpyPy$_2$Me)Fe(NH$_3$)(NH)]$^{2+}$, multiplicity = 1
C -2.5545170000 2.1810540000 -0.8727090000
C -3.0225240000 0.8863680000 -0.6268440000
C -2.0820850000 -0.1347450000 -0.4395700000
N -0.7517290000 0.1304610000 -0.5542460000
C -0.2763400000 1.3900410000 -0.6375870000
C -1.1780930000 2.4479380000 -0.8307000000
C -3.6266020000 -2.0202510000 0.2853790000
C -2.3513800000 -1.5057650000 0.0108590000
C -3.7426830000 -3.3082070000 0.8175850000
C -2.5779720000 -4.0475370000 1.0615960000
C -1.3367340000 -3.4844710000 0.7506150000
N -1.2140290000 -2.2401020000 0.2411040000
C 1.2311660000 1.5717040000 -0.3444950000
C 1.5820000000 3.0684400000 -0.3020150000
C 2.0975860000 0.8288650000 -1.3788590000
C 1.4683480000 0.9007700000 1.0378080000
N 1.1110570000 -0.4025440000 1.1564510000
C 1.2094160000 -1.0143520000 2.3558990000
C 1.7169980000 -0.3755860000 3.4878010000
C 2.1302560000 0.9546440000 3.3679430000
C 1.9940950000 1.6013790000 2.1331060000
C 3.0945200000 1.4731760000 -2.1284430000
C 3.8636720000 0.7398410000 -3.0392590000
C 3.6126850000 -0.6274370000 -3.1916770000
C 2.6008820000 -1.2061730000 -2.4264880000
N 1.8722920000 -0.4986050000 -1.5311330000
H -3.2621160000 2.9973010000 -1.0435500000
H -4.7283940000 -3.7266880000 1.0390820000
H -2.6172640000 -5.0566580000 1.4785010000
H -0.4181680000 -4.0534320000 0.9094550000
H 0.9745170000 3.5878570000 0.4538450000
H 2.6426420000 3.2135910000 -0.0495160000
H 1.3930380000 3.5370290000 -1.2800240000

H 0.8566020000 -2.0482500000 2.4158060000
H 1.7783980000 -0.9174960000 4.4352660000
H 2.5418560000 1.4940640000 4.2261980000
H 2.2946170000 2.6447410000 2.0333500000
H 3.2735540000 2.5414310000 -2.0047140000
H 4.6444100000 1.2376880000 -3.6222660000
H 4.1793430000 -1.2445250000 -3.8942040000
H 2.3319460000 -2.2587000000 -2.5427250000
Fe 0.3927440000 -1.4159150000 -0.5528110000
H -0.8189240000 3.4722580000 -0.9329690000
N 1.6661440000 -2.8973240000 -0.0419790000
H 2.6420610000 -2.6008590000 -0.1753150000
N -0.0540660000 -2.0556460000 -2.0722480000
H -1.0256370000 -2.4484330000 -2.0708060000
H -4.5147400000 -1.4153010000 0.0886370000
H -4.0927120000 0.6772430000 -0.5606380000
H 1.6075640000 -3.2015170000 0.9379860000
H 1.5401370000 -3.7432100000 -0.6105240000

[(bpyPy$_2$Me)Fe(NH$_3$)(NH)]$^{2+}$, multiplicity = 5
C -2.5125240000 2.1726860000 -1.0370240000
C -2.9992830000 0.8917110000 -0.7535490000
C -2.0734210000 -0.1180140000 -0.4517050000
N -0.7462850000 0.1407700000 -0.4784600000
C -0.2656360000 1.3880980000 -0.6137190000
C -1.1410170000 2.4417030000 -0.9284780000
C -3.7384530000 -1.9254880000 0.2046410000
C -2.4199090000 -1.4703420000 0.0452460000
C -3.9619110000 -3.1830400000 0.7771930000
C -2.8641800000 -3.9520650000 1.1817540000
C -1.5768520000 -3.4412600000 0.9785420000
N -1.3600860000 -2.2337640000 0.4278350000
C 1.2421640000 1.5807360000 -0.2961860000
C 1.5614860000 3.0837770000 -0.1984590000
C 2.0992260000 0.9195650000 -1.3991500000
C 1.5181470000 0.8700360000 1.0604150000
N 1.2392460000 -0.4574320000 1.1733120000
C 1.3973390000 -1.0842240000 2.3618000000
C 1.8722350000 -0.4329860000 3.4992090000
C 2.1991290000 0.9215700000 3.3931610000
C 2.0153960000 1.5743670000 2.1681730000
C 3.0354770000 1.6285920000 -2.1689170000
C 3.7545950000 0.9585390000 -3.1671480000
C 3.5159420000 -0.4022030000 -3.3900060000
C 2.5675010000 -1.0440440000 -2.5934960000
N 1.8956080000 -0.3976880000 -1.6157660000

H -3.2065410000 2.9779300000 -1.2948130000
H -4.9827470000 -3.5542180000 0.9073760000
H -2.9908060000 -4.9353100000 1.6416300000
H -0.6953480000 -4.0228510000 1.2647900000
H 0.9356400000 3.5653730000 0.5676690000
H 2.6179480000 3.2439420000 0.0622960000
H 1.3694280000 3.5807120000 -1.1611550000
H 1.1273730000 -2.1431980000 2.3987640000
H 1.9813120000 -0.9856190000 4.4359860000
H 2.5862480000 1.4749210000 4.2539530000
H 2.2574650000 2.6338640000 2.0856490000
H 3.2076290000 2.6920100000 -2.0004680000
H 4.4877480000 1.5040390000 -3.7693500000
H 4.0437810000 -0.9612620000 -4.1672360000
H 2.3101160000 -2.0978520000 -2.7363040000
Fe 0.5365150000 -1.5331530000 -0.4403800000
H -0.7725180000 3.4570420000 -1.0768500000
N 1.8506850000 -3.1061960000 0.0445700000
H 2.7192700000 -2.7798730000 0.4883350000
N -0.0215190000 -2.4146080000 -1.8135620000
H -0.4533830000 -3.3487280000 -1.9134360000
H -4.5802170000 -1.3045590000 -0.1103090000
H -4.0736250000 0.6940330000 -0.7455070000
H 1.4614820000 -3.8240500000 0.6695940000
H 2.1279660000 -3.6138350000 -0.8045110000

[(bpyPy$_2$Me)Fe(NH$_2$)(NH$_3$)]$^{3+}$, multiplicity = 3
C -2.5750700000 2.2362470000 -0.9707640000
C -3.0472160000 0.9405690000 -0.7237130000
C -2.1098880000 -0.0704970000 -0.4884120000
N -0.7777330000 0.1995890000 -0.5692140000
C -0.3118500000 1.4573580000 -0.6497320000
C -1.2035330000 2.5138960000 -0.8860840000
C -3.6565990000 -1.9516170000 0.2563520000
C -2.3838920000 -1.4280820000 0.0053510000
C -3.7695230000 -3.2169910000 0.8461260000
C -2.6071290000 -3.9258780000 1.1739680000
C -1.3623230000 -3.3670920000 0.8731610000
N -1.2531550000 -2.1476860000 0.3024820000
C 1.1873530000 1.6092510000 -0.3288790000
C 1.5677650000 3.0960940000 -0.2445810000
C 2.0202160000 0.8779530000 -1.3947690000
C 1.4313960000 0.8863740000 1.0279070000
N 1.1333830000 -0.4419880000 1.1181350000
C 1.3157690000 -1.1227970000 2.2745670000
C 1.8128440000 -0.5023530000 3.4184340000

C 2.1374650000 0.8555610000 3.3485900000
C 1.9459630000 1.5513220000 2.1454420000
C 2.9712070000 1.5276170000 -2.1925850000
C 3.7455230000 0.7891200000 -3.0944240000
C 3.5705970000 -0.5972840000 -3.1674630000
C 2.6088480000 -1.1892180000 -2.3547940000
N 1.8349980000 -0.4620590000 -1.5080700000
H -3.2824350000 3.0458310000 -1.1709210000
H -4.7570780000 -3.6399100000 1.0506560000
H -2.6487270000 -4.9089640000 1.6493760000
H -0.4323870000 -3.8976820000 1.0913000000
H 0.9674310000 3.6033480000 0.5254260000
H 2.6323590000 3.2141420000 0.0056000000
H 1.3813000000 3.5927990000 -1.2084300000
H 1.0607120000 -2.1854340000 2.2637190000
H 1.9440360000 -1.0845210000 4.3336830000
H 2.5401100000 1.3796150000 4.2203160000
H 2.1988600000 2.6101480000 2.0882410000
H 3.1160170000 2.6047030000 -2.1066370000
H 4.4884440000 1.2941490000 -3.7186140000
H 4.1671520000 -1.2232150000 -3.8356750000
H 2.4497220000 -2.2708390000 -2.3625740000
Fe 0.4073000000 -1.3524270000 -0.4601050000
H -0.8442530000 3.5389240000 -0.9840000000
N 1.4189240000 -2.8596560000 -0.2069750000
H 1.1783930000 -3.8001080000 -0.5482760000
H 2.3610330000 -2.8543200000 0.2067300000
N -0.2974570000 -2.1188030000 -2.1901170000
H -1.0959930000 -1.5798640000 -2.5538760000
H -0.6108860000 -3.0947210000 -2.1030400000
H 0.4039840000 -2.1065580000 -2.9422800000
H -4.5466210000 -1.3720580000 0.0012380000
H -4.1182880000 0.7307670000 -0.6852390000

[(bpyPy$_2$Me)Fe(NH$_2$)(NH$_3$)]$^{3+}$, multiplicity = 1
C -2.5600290000 2.1972380000 -0.9935870000
C -3.0362370000 0.9061110000 -0.7356780000
C -2.1027030000 -0.0994490000 -0.4671150000
N -0.7670780000 0.1696240000 -0.5208680000
C -0.2971490000 1.4278010000 -0.6250110000
C -1.1881870000 2.4750750000 -0.8956290000
C -3.6551700000 -1.9685480000 0.2883710000
C -2.3806360000 -1.4531960000 0.0185340000
C -3.7713100000 -3.2305230000 0.8810000000
C -2.6071900000 -3.9419450000 1.1946420000
C -1.3653430000 -3.3856350000 0.8741190000

N -1.2482550000 -2.1743570000 0.2941920000
C 1.1997250000 1.6079930000 -0.3150080000
C 1.5545830000 3.1071690000 -0.2494010000
C 2.0491500000 0.8657390000 -1.3616650000
C 1.4513150000 0.8946160000 1.0420220000
N 1.1141920000 -0.4153230000 1.1418270000
C 1.2334180000 -1.0739800000 2.3197120000
C 1.7390440000 -0.4527470000 3.4605820000
C 2.1349230000 0.8839300000 3.3711170000
C 1.9868980000 1.5567050000 2.1532560000
C 3.0117110000 1.5069470000 -2.1547360000
C 3.7739460000 0.7633400000 -3.0616500000
C 3.5696730000 -0.6184970000 -3.1506380000
C 2.6001960000 -1.2000750000 -2.3390530000
N 1.8533010000 -0.4712490000 -1.4696490000
H -3.2635060000 3.0035860000 -1.2191220000
H -4.7578520000 -3.6445350000 1.1068240000
H -2.6430080000 -4.9179060000 1.6840990000
H -0.4362150000 -3.9056010000 1.1050700000
H 0.9425750000 3.6098810000 0.5135980000
H 2.6158200000 3.2430630000 0.0031670000
H 1.3621390000 3.5874780000 -1.2203640000
H 0.9103480000 -2.1168440000 2.3404830000
H 1.8236750000 -1.0232270000 4.3890260000
H 2.5496590000 1.4080810000 4.2370250000
H 2.2861430000 2.5976220000 2.0735640000
H 3.1664520000 2.5829410000 -2.0673130000
H 4.5237600000 1.2608320000 -3.6835590000
H 4.1513320000 -1.2495450000 -3.8275450000
H 2.4182700000 -2.2779010000 -2.3648890000
Fe 0.4160580000 -1.3763490000 -0.4412920000
H -0.8251510000 3.4960500000 -1.0146880000
N 1.3860630000 -2.7772420000 -0.0961120000
H 1.0525940000 -3.7568440000 -0.0700990000
H 2.3892230000 -2.7683700000 0.1635500000
N -0.3283900000 -2.0596650000 -2.1855260000
H -1.1166380000 -1.4938540000 -2.5307690000
H -0.6603870000 -3.0311370000 -2.1239450000
H 0.3733420000 -2.0449610000 -2.9369180000
H -4.5434210000 -1.3793130000 0.0504570000
H -4.1075320000 0.6940420000 -0.7193130000

[(bpyPy$_2$Me)Fe(NH$_2$)(NH$_3$)]$^{3+}$, multiplicity = 5
C -2.5729800000 2.1755620000 -0.9182010000
C -3.0535180000 0.8895900000 -0.6485670000
C -2.1295070000 -0.1266100000 -0.3899420000

N -0.7875490000 0.1393480000 -0.4535670000
C -0.3047190000 1.3939410000 -0.5827270000
C -1.1993250000 2.4417590000 -0.8473420000
C -3.7466830000 -1.9802380000 0.2595120000
C -2.4538490000 -1.4920460000 0.0425270000
C -3.9064550000 -3.2793870000 0.7609440000
C -2.7745640000 -4.0579510000 1.0347050000
C -1.5083530000 -3.5254450000 0.7775840000
N -1.3572300000 -2.2738570000 0.2951260000
C 1.2013400000 1.6028680000 -0.3110400000
C 1.5281340000 3.1062570000 -0.2957490000
C 2.0465980000 0.8657790000 -1.3721200000
C 1.5164190000 0.9592580000 1.0709690000
N 1.2224050000 -0.3543800000 1.2326220000
C 1.4460230000 -0.9835980000 2.4074630000
C 2.0015260000 -0.3160970000 3.4992540000
C 2.3288450000 1.0352220000 3.3514740000
C 2.0832140000 1.6795320000 2.1297090000
C 3.0175030000 1.5209050000 -2.1442800000
C 3.8037560000 0.7873720000 -3.0396650000
C 3.6155350000 -0.5950950000 -3.1390460000
C 2.6327600000 -1.1882300000 -2.3501590000
N 1.8578420000 -0.4693970000 -1.5026040000
H -3.2731480000 2.9861650000 -1.1382870000
H -4.9101960000 -3.6761030000 0.9374720000
H -2.8587790000 -5.0715780000 1.4343670000
H -0.5943730000 -4.0997390000 0.9525670000
H 0.9267900000 3.6224050000 0.4675060000
H 2.5913470000 3.2683220000 -0.0667730000
H 1.3148990000 3.5584770000 -1.2755760000
H 1.1686250000 -2.0406240000 2.4675990000
H 2.1679130000 -0.8537880000 4.4360090000
H 2.7705180000 1.5958950000 4.1806690000
H 2.3340910000 2.7342570000 2.0146200000
H 3.1696580000 2.5956320000 -2.0450130000
H 4.5622190000 1.2950810000 -3.6428070000
H 4.2138530000 -1.2151450000 -3.8114300000
H 2.4552240000 -2.2656590000 -2.3919710000
Fe 0.3723990000 -1.4366510000 -0.3758730000
H -0.8345600000 3.4602110000 -0.9803280000
N 1.3974890000 -2.9240840000 -0.1459380000
H 1.3575550000 -3.7439020000 -0.7672640000
H 2.1714240000 -2.9962710000 0.5295180000
N -0.3829140000 -2.0880200000 -2.3584160000
H -1.1547500000 -1.4940010000 -2.6902480000
H -0.7461460000 -3.0504580000 -2.3407670000

H 0.3229740000 -2.0619840000 -3.1048310000
H -4.6165910000 -1.3546720000 0.0478300000
H -4.1256250000 0.6839210000 -0.6229590000

[(bpyPy$_2$Me)Fe(N)(NH$_3$)]$^{2+}$, multiplicity = 2
C -2.6071360000 2.2491750000 -0.8674970000
C -3.0690000000 0.9536270000 -0.6046050000
C -2.1167530000 -0.0589300000 -0.4161430000
N -0.7969130000 0.2154510000 -0.5397050000
C -0.3352590000 1.4680730000 -0.6520380000
C -1.2315680000 2.5297310000 -0.8503920000
C -3.6463400000 -1.9600610000 0.3133500000
C -2.3737460000 -1.4384450000 0.0413150000
C -3.7588270000 -3.2532530000 0.8367570000
C -2.5941460000 -3.9938380000 1.0735590000
C -1.3542320000 -3.4263820000 0.7623180000
N -1.2428440000 -2.1788440000 0.2628070000
C 1.1789030000 1.6074450000 -0.3747010000
C 1.5652280000 3.0950590000 -0.3149670000
C 2.0285490000 0.8573490000 -1.4223980000
C 1.4268460000 0.9050130000 0.9931110000
N 1.1210100000 -0.4171730000 1.1053990000
C 1.3023600000 -1.0673540000 2.2786370000
C 1.8057310000 -0.4263010000 3.4093860000
C 2.1346220000 0.9291220000 3.3160520000
C 1.9417740000 1.5955020000 2.0998420000
C 2.9541760000 1.5152400000 -2.2477540000
C 3.7660130000 0.7771270000 -3.1160640000
C 3.6549420000 -0.6172710000 -3.1297890000
C 2.7115600000 -1.2152110000 -2.2972910000
N 1.9033680000 -0.4931030000 -1.4826850000
H -3.3232720000 3.0590650000 -1.0345590000
H -4.7443500000 -3.6737270000 1.0567140000
H -2.6329800000 -5.0054340000 1.4861480000
H -0.4140270000 -3.9705300000 0.8960940000
H 0.9769200000 3.6142520000 0.4565750000
H 2.6335410000 3.2179570000 -0.0824610000
H 1.3619080000 3.5809730000 -1.2812710000
H 1.0395360000 -2.1279380000 2.2905990000
H 1.9375540000 -0.9924670000 4.3349960000
H 2.5378660000 1.4699700000 4.1773210000
H 2.1909760000 2.6538220000 2.0188070000
H 3.0482590000 2.6007690000 -2.2121220000
H 4.4852340000 1.2899830000 -3.7616210000
H 4.2837440000 -1.2418870000 -3.7695880000
H 2.5883610000 -2.3014700000 -2.2560860000

Fe 0.4636820000 -1.4162630000 -0.4866660000
H -0.8807390000 3.5554050000 -0.9719560000
N 1.3281760000 -2.7375360000 -0.1999760000
N -0.2834020000 -1.9953650000 -2.2638940000
H -0.9545850000 -1.3141590000 -2.6418530000
H -0.7705370000 -2.8980350000 -2.2049180000
H 0.4438150000 -2.1068930000 -2.9822260000
H -4.5369440000 -1.3567990000 0.1222290000
H -4.1386560000 0.7469910000 -0.5251080000

[(bpyPy$_2$Me)Fe(N)(NH$_3$)]$^{2+}$, multiplicity = 4
C -2.6148920000 2.2853280000 -0.8877650000
C -3.0828070000 0.9893210000 -0.6353870000
C -2.1355290000 -0.0256510000 -0.4418580000
N -0.8109360000 0.2406500000 -0.5528240000
C -0.3473990000 1.4936670000 -0.6486710000
C -1.2387380000 2.5592600000 -0.8522270000
C -3.6682440000 -1.9316960000 0.2870090000
C -2.3990470000 -1.4019820000 0.0207310000
C -3.7718530000 -3.2225590000 0.8198800000
C -2.6063550000 -3.9604430000 1.0687400000
C -1.3687310000 -3.3927050000 0.7559420000
N -1.2690580000 -2.1432050000 0.2553580000
C 1.1664770000 1.6308000000 -0.3603720000
C 1.5605630000 3.1158040000 -0.2990230000
C 2.0067090000 0.8765640000 -1.4113460000
C 1.4200800000 0.9248610000 1.0049070000
N 1.1727020000 -0.4116170000 1.0891750000
C 1.4075750000 -1.0954780000 2.2313260000
C 1.8789220000 -0.4612090000 3.3805210000
C 2.1341530000 0.9123670000 3.3233590000
C 1.9106250000 1.6066230000 2.1257420000
C 2.9417790000 1.5204680000 -2.2347030000
C 3.7488140000 0.7683140000 -3.0969030000
C 3.6269590000 -0.6255840000 -3.1057220000
C 2.6753150000 -1.2123920000 -2.2751290000
N 1.8695590000 -0.4739780000 -1.4728020000
H -3.3260510000 3.0983650000 -1.0598850000
H -4.7563670000 -3.6477670000 1.0356260000
H -2.6461230000 -4.9703140000 1.4848550000
H -0.4226760000 -3.9302180000 0.8823120000
H 0.9705320000 3.6380560000 0.4691140000
H 2.6281660000 3.2314600000 -0.0590730000
H 1.3657510000 3.6034860000 -1.2662110000
H 1.2215470000 -2.1728650000 2.1927430000
H 2.0510080000 -1.0444990000 4.2886220000

H 2.5158040000 1.4468120000 4.1984440000
H 2.1215070000 2.6750670000 2.0726660000
H 3.0493060000 2.6048960000 -2.2012010000
H 4.4762020000 1.2713050000 -3.7411340000
H 4.2544150000 -1.2574140000 -3.7395650000
H 2.5356150000 -2.2967820000 -2.2203410000
Fe 0.4151040000 -1.3634960000 -0.4673740000
H -0.8821030000 3.5841670000 -0.9636040000
N 1.3604800000 -2.8354280000 -0.2475220000
N -0.2617880000 -2.0994780000 -2.2266130000
H -1.1169580000 -1.6361260000 -2.5627610000
H -0.4634360000 -3.1043590000 -2.1512930000
H 0.4285290000 -2.0037660000 -2.9816870000
H -4.5630370000 -1.3382980000 0.0852790000
H -4.1536700000 0.7841080000 -0.5676740000

[(bpyPy$_2$Me)Fe(NH$_3$)(N)]$^{2+}$, multiplicity = 2
C -2.5642120000 2.2289620000 -0.8426820000
C -3.0420920000 0.9360100000 -0.6048370000
C -2.1106790000 -0.0946610000 -0.4288300000
N -0.7787040000 0.1619830000 -0.5505020000
C -0.2928040000 1.4164540000 -0.6266510000
C -1.1865560000 2.4846470000 -0.8047630000
C -3.6849330000 -1.9637010000 0.2759090000
C -2.4004860000 -1.4638680000 0.0237050000
C -3.8233320000 -3.2512580000 0.8071240000
C -2.6733260000 -4.0016330000 1.0784210000
C -1.4199420000 -3.4504540000 0.7887590000
N -1.2825990000 -2.2133850000 0.2767440000
C 1.2188620000 1.5841170000 -0.3539250000
C 1.5840810000 3.0782320000 -0.3209660000
C 2.0536690000 0.8353270000 -1.4089920000
C 1.4801950000 0.9157990000 1.0286560000
N 1.1153700000 -0.3822630000 1.1646490000
C 1.2443280000 -0.9900760000 2.3621960000
C 1.7831530000 -0.3487040000 3.4789920000
C 2.2005700000 0.9783110000 3.3405240000
C 2.0399540000 1.6195450000 2.1051380000
C 3.0432090000 1.4737380000 -2.1740580000
C 3.7834780000 0.7429960000 -3.1091900000
C 3.5134650000 -0.6196170000 -3.2721070000
C 2.5129470000 -1.1949410000 -2.4918250000
N 1.8104040000 -0.4879030000 -1.5730610000
H -3.2664140000 3.0518630000 -1.0036930000
H -4.8180430000 -3.6599750000 1.0065000000
H -2.7313830000 -5.0088920000 1.4987320000

H -0.5080550000 -4.0262780000 0.9648820000
H 0.9946200000 3.6028090000 0.4459670000
H 2.6502490000 3.2150900000 -0.0880600000
H 1.3811330000 3.5462140000 -1.2961940000
H 0.8928590000 -2.0243110000 2.4351730000
H 1.8657060000 -0.8852230000 4.4277910000
H 2.6366880000 1.5205470000 4.1849730000
H 2.3469110000 2.6598330000 1.9930130000
H 3.2378380000 2.5382620000 -2.0436250000
H 4.5561820000 1.2387130000 -3.7044090000
H 4.0555980000 -1.2352080000 -3.9945930000
H 2.2394960000 -2.2466730000 -2.6080520000
Fe 0.3450420000 -1.4115640000 -0.5815380000
H -0.8195020000 3.5070640000 -0.8982600000
N 1.6020970000 -2.8987290000 -0.0884220000
H 1.4578630000 -3.7514290000 -0.6423240000
H 1.5375640000 -3.1848910000 0.8968740000
N -0.1675210000 -2.0361960000 -1.9733660000
H 2.5831050000 -2.6211640000 -0.2270840000
H -4.5642680000 -1.3520350000 0.0611380000
H -4.1137720000 0.7370230000 -0.5352650000

[(bpyPy$_2$Me)Fe(NH$_3$)(N)]$^{2+}$, multiplicity = 4
C -2.5306310000 2.2084930000 -0.8929070000
C -3.0039710000 0.9092510000 -0.6879970000
C -2.0718670000 -0.1097690000 -0.4571700000
N -0.7333210000 0.1512720000 -0.4899630000
C -0.2665190000 1.4156910000 -0.5554370000
C -1.1587600000 2.4744930000 -0.7848620000
C -3.6584370000 -2.0139780000 0.1238860000
C -2.3723640000 -1.4804870000 -0.0373860000
C -3.8003300000 -3.3138200000 0.6189580000
C -2.6515240000 -4.0500360000 0.9409290000
C -1.3962380000 -3.4740540000 0.7363240000
N -1.2562270000 -2.2149530000 0.2680450000
C 1.2394990000 1.5994410000 -0.2695590000
C 1.6037230000 3.0939030000 -0.2573890000
C 2.0494850000 0.8433140000 -1.3363720000
C 1.5123480000 0.9502590000 1.1175290000
N 1.1881350000 -0.3587390000 1.2639410000
C 1.3453470000 -0.9618040000 2.4634110000
C 1.8624890000 -0.2961660000 3.5747430000
C 2.2320040000 1.0446380000 3.4295800000
C 2.0495860000 1.6744730000 2.1915850000
C 3.0277010000 1.4662760000 -2.1247150000
C 3.7179310000 0.7269110000 -3.0923860000

C 3.4108980000 -0.6271180000 -3.2640710000
C 2.4296000000 -1.1919190000 -2.4533460000
N 1.7765040000 -0.4757740000 -1.5033570000
H -3.2311100000 3.0246940000 -1.0906030000
H -4.7958700000 -3.7471030000 0.7503230000
H -2.7145140000 -5.0668010000 1.3368200000
H -0.4837390000 -4.0334540000 0.9515370000
H 1.0122850000 3.6289380000 0.5007270000
H 2.6696660000 3.2347140000 -0.0251810000
H 1.4022660000 3.5486780000 -1.2389940000
H 1.0380160000 -2.0093770000 2.5347030000
H 1.9701310000 -0.8268100000 4.5242270000
H 2.6532170000 1.6043640000 4.2700970000
H 2.3253450000 2.7227850000 2.0742110000
H 3.2530250000 2.5241520000 -1.9892090000
H 4.4822170000 1.2113710000 -3.7075220000
H 3.9134720000 -1.2440580000 -4.0132980000
H 2.1288530000 -2.2373710000 -2.5608740000
Fe 0.4315840000 -1.3871970000 -0.3567750000
H -0.7947830000 3.4988020000 -0.8693140000
N 1.6672700000 -2.9420320000 -0.0010600000
H 2.6526100000 -2.6754600000 -0.1326070000
N -0.0816540000 -2.2467590000 -1.8904340000
H -4.5350370000 -1.4151450000 -0.1335820000
H -4.0748990000 0.6945140000 -0.6842690000
H 1.6215250000 -3.3093650000 0.9600240000
H 1.4927740000 -3.7409330000 -0.6239530000

[(bpyPy$_2$Me)Fe(NH)(NH$_2$)]$^{2+}$, multiplicity = 4
C -2.5919440000 2.2288220000 -0.9356270000
C -3.0658410000 0.9388490000 -0.6692960000
C -2.1288180000 -0.0801260000 -0.4545380000
N -0.7988540000 0.1789750000 -0.5730700000
C -0.3267860000 1.4338590000 -0.6612220000
C -1.2163030000 2.4971760000 -0.8807080000
C -3.6835930000 -1.9462760000 0.3253920000
C -2.4082940000 -1.4334300000 0.0561700000
C -3.7979470000 -3.2144270000 0.9091490000
C -2.6361870000 -3.9356680000 1.2091110000
C -1.3911620000 -3.3771510000 0.8973350000
N -1.2843310000 -2.1568660000 0.3425300000
C 1.1774340000 1.5878710000 -0.3438020000
C 1.5527850000 3.0772850000 -0.2738750000
C 2.0310210000 0.8473640000 -1.3885720000
C 1.4147700000 0.8818080000 1.0238580000
N 1.1072010000 -0.4393370000 1.1216790000

C 1.2894940000 -1.0997890000 2.2869220000
C 1.7940290000 -0.4712080000 3.4248830000
C 2.1274950000 0.8839910000 3.3425720000
C 1.9363400000 1.5634320000 2.1326440000
C 2.9951060000 1.4964990000 -2.1771260000
C 3.7664650000 0.7580090000 -3.0796400000
C 3.5619890000 -0.6230780000 -3.1770320000
C 2.5850260000 -1.2102710000 -2.3771110000
N 1.8385460000 -0.4873290000 -1.5068030000
H -3.2977790000 3.0427220000 -1.1245440000
H -4.7856210000 -3.6313980000 1.1260610000
H -2.6797510000 -4.9261700000 1.6694380000
H -0.4522930000 -3.9110220000 1.0718170000
H 0.9486270000 3.5924770000 0.4880830000
H 2.6155580000 3.2029770000 -0.0191020000
H 1.3707880000 3.5641400000 -1.2438920000
H 1.0269970000 -2.1608460000 2.2871300000
H 1.9235160000 -1.0440670000 4.3466810000
H 2.5339140000 1.4154440000 4.2083040000
H 2.1939560000 2.6203730000 2.0606430000
H 3.1461790000 2.5724600000 -2.0870410000
H 4.5190160000 1.2595250000 -3.6955140000
H 4.1428650000 -1.2461560000 -3.8620690000
H 2.3750350000 -2.2813050000 -2.4155160000
Fe 0.3833060000 -1.4108340000 -0.4955710000
H -0.8544650000 3.5203240000 -0.9888360000
N 1.3725770000 -2.8022660000 -0.1754280000
H 2.3247480000 -3.0280780000 0.1555970000
N -0.2611060000 -2.0465650000 -2.0938740000
H -0.7331970000 -1.4660410000 -2.7971720000
H -0.1337480000 -3.0149300000 -2.4055100000
H -4.5736040000 -1.3603700000 0.0842130000
H -4.1373600000 0.7382910000 -0.5998530000

[(bpyPy$_2$Me)Fe(NH)(NH$_2$)]$^{2+}$, multiplicity = 2
C -2.5864650000 2.2049550000 -0.8193430000
C -3.0487510000 0.9137370000 -0.5403760000
C -2.1055790000 -0.1078840000 -0.3698480000
N -0.7823450000 0.1610990000 -0.5154340000
C -0.3110440000 1.4115800000 -0.6394430000
C -1.2101180000 2.4726480000 -0.8295050000
C -3.6371630000 -2.0044960000 0.3765200000
C -2.3706570000 -1.4859040000 0.0738270000
C -3.7359690000 -3.3078130000 0.8774300000
C -2.5682410000 -4.0595260000 1.0612890000
C -1.3345040000 -3.4926410000 0.7252490000

N -1.2401710000 -2.2354000000 0.2501820000
C 1.2026350000 1.5670820000 -0.3780410000
C 1.5840130000 3.0559470000 -0.3369200000
C 2.0387060000 0.8077940000 -1.4249050000
C 1.4352790000 0.8846820000 0.9992510000
N 1.0592150000 -0.4140240000 1.1292500000
C 1.1509730000 -1.0345370000 2.3274990000
C 1.6526020000 -0.3903220000 3.4582850000
C 2.0824340000 0.9342710000 3.3357010000
C 1.9671890000 1.5764290000 2.0967370000
C 3.0056400000 1.4388570000 -2.2227540000
C 3.7751220000 0.6827770000 -3.1136760000
C 3.5700610000 -0.6992540000 -3.1897470000
C 2.5902920000 -1.2716680000 -2.3819270000
N 1.8411360000 -0.5292960000 -1.5279690000
H -3.2998650000 3.0186340000 -0.9779510000
H -4.7153820000 -3.7291880000 1.1212340000
H -2.6007100000 -5.0795320000 1.4529470000
H -0.3920980000 -4.0400910000 0.8230850000
H 0.9963410000 3.5833300000 0.4294070000
H 2.6517600000 3.1812580000 -0.1037100000
H 1.3846710000 3.5289600000 -1.3103910000
H 0.8183180000 -2.0749040000 2.3655080000
H 1.7061450000 -0.9309360000 4.4067210000
H 2.4961180000 1.4724110000 4.1937510000
H 2.2844380000 2.6144010000 1.9923860000
H 3.1622370000 2.5151850000 -2.1491250000
H 4.5303680000 1.1728820000 -3.7353120000
H 4.1541540000 -1.3341420000 -3.8609070000
H 2.3769510000 -2.3436530000 -2.3977790000
Fe 0.4106810000 -1.4346240000 -0.5245350000
H -0.8505920000 3.4937860000 -0.9617860000
N 1.4607610000 -2.6924620000 -0.0243450000
H 2.3633930000 -2.5920210000 0.4773750000
N -0.2770660000 -1.9196490000 -2.1325450000
H 0.0166770000 -1.4383350000 -2.9907720000
H -1.2380130000 -2.2680340000 -2.2335960000
H -4.5307390000 -1.3939320000 0.2274540000
H -4.1170420000 0.7092350000 -0.4405700000

[(bpyPy$_2$Me)Fe(NH)(NH$_3$)]$^{3+}$, multiplicity = 2
C -2.5712280000 2.2178060000 -0.9244260000
C -3.0404620000 0.9284080000 -0.6477880000
C -2.1012650000 -0.0852620000 -0.4272160000
N -0.7705480000 0.1827520000 -0.5421920000
C -0.3008830000 1.4384110000 -0.6547530000

C -1.1957630000 2.4919110000 -0.8845300000
C -3.6404530000 -1.9649730000 0.3409270000
C -2.3720780000 -1.4467620000 0.0496240000
C -3.7418760000 -3.2539960000 0.8773340000
C -2.5754500000 -3.9942470000 1.1044650000
C -1.3371510000 -3.4344950000 0.7740110000
N -1.2433500000 -2.1872140000 0.2691490000
C 1.2024080000 1.6004320000 -0.3559550000
C 1.5760260000 3.0896330000 -0.2897540000
C 2.0512150000 0.8559290000 -1.3993340000
C 1.4395390000 0.8939320000 1.0069640000
N 1.0901310000 -0.4136590000 1.1217190000
C 1.2095750000 -1.0691570000 2.3009040000
C 1.7191110000 -0.4396080000 3.4351800000
C 2.1123280000 0.8976740000 3.3382280000
C 1.9656540000 1.5675760000 2.1175620000
C 3.0240870000 1.4969890000 -2.1807580000
C 3.8024400000 0.7539990000 -3.0734640000
C 3.6037640000 -0.6283190000 -3.1627700000
C 2.6207620000 -1.2121900000 -2.3696260000
N 1.8564830000 -0.4799050000 -1.5176300000
H -3.2806960000 3.0277400000 -1.1153540000
H -4.7232360000 -3.6725840000 1.1163780000
H -2.6075080000 -5.0004060000 1.5289180000
H -0.4009170000 -3.9833090000 0.9076010000
H 0.9733160000 3.6033420000 0.4735390000
H 2.6392690000 3.2151110000 -0.0383990000
H 1.3896230000 3.5731950000 -1.2604150000
H 0.8875760000 -2.1126150000 2.3252160000
H 1.8076020000 -1.0057220000 4.3658790000
H 2.5260010000 1.4244310000 4.2029140000
H 2.2539230000 2.6156760000 2.0349680000
H 3.1764320000 2.5726760000 -2.0894920000
H 4.5621340000 1.2526650000 -3.6823840000
H 4.1991890000 -1.2590480000 -3.8278560000
H 2.4350880000 -2.2893450000 -2.4051090000
Fe 0.4349780000 -1.3973700000 -0.4846550000
H -0.8364190000 3.5133510000 -1.0118580000
N 1.3753370000 -2.6806310000 -0.1166570000
H 2.3493850000 -2.9071240000 0.1738350000
N -0.3375670000 -2.0178310000 -2.2341420000
H -1.1797250000 -1.4962890000 -2.5132370000
H -0.5971940000 -3.0119080000 -2.1834890000
H 0.3275570000 -1.9216700000 -3.0134780000
H -4.5331570000 -1.3640010000 0.1543140000
H -4.1105950000 0.7214480000 -0.5781100000

[(bpyPy$_2$Me)Fe(NH)(NH$_3$)]$^{3+}$, multiplicity = 4
C -2.5929170000 2.2451530000 -0.9354480000
C -3.0619770000 0.9526910000 -0.6685440000
C -2.1216000000 -0.0597400000 -0.4482420000
N -0.7909410000 0.2088430000 -0.5506700000
C -0.3246110000 1.4637540000 -0.6516240000
C -1.2192660000 2.5195620000 -0.8832730000
C -3.6569570000 -1.9546550000 0.2937580000
C -2.3913700000 -1.4214080000 0.0300680000
C -3.7530760000 -3.2405040000 0.8417350000
C -2.5844050000 -3.9679150000 1.1084160000
C -1.3475000000 -3.3998640000 0.7997490000
N -1.2568460000 -2.1529450000 0.2846040000
C 1.1776710000 1.6209450000 -0.3439570000
C 1.5588170000 3.1081840000 -0.2807380000
C 2.0178410000 0.8714620000 -1.3917500000
C 1.4219550000 0.9150030000 1.0197140000
N 1.1329430000 -0.4127540000 1.1191730000
C 1.3300890000 -1.0917900000 2.2744410000
C 1.8233840000 -0.4598770000 3.4137300000
C 2.1362410000 0.9002770000 3.3377550000
C 1.9365270000 1.5886710000 2.1325170000
C 2.9806480000 1.5058550000 -2.1875150000
C 3.7704900000 0.7514620000 -3.0626920000
C 3.5981800000 -0.6362750000 -3.1137910000
C 2.6249020000 -1.2155790000 -2.3054620000
N 1.8404470000 -0.4716530000 -1.4831720000
H -3.3021360000 3.0546940000 -1.1286400000
H -4.7353850000 -3.6704470000 1.0559960000
H -2.6191290000 -4.9715600000 1.5379250000
H -0.4075030000 -3.9368060000 0.9530270000
H 0.9590770000 3.6265990000 0.4817570000
H 2.6231380000 3.2284530000 -0.0306300000
H 1.3730010000 3.5914460000 -1.2516490000
H 1.0844140000 -2.1566360000 2.2711110000
H 1.9653830000 -1.0387490000 4.3295860000
H 2.5394880000 1.4300240000 4.2056640000
H 2.1840920000 2.6483950000 2.0668480000
H 3.1219680000 2.5848480000 -2.1187050000
H 4.5219160000 1.2469320000 -3.6845250000
H 4.2041720000 -1.2734630000 -3.7628900000
H 2.4554850000 -2.2958290000 -2.3050280000
Fe 0.3914290000 -1.3530260000 -0.4459780000
H -0.8588970000 3.5417510000 -1.0019950000
N 1.3922250000 -2.7875190000 -0.2000910000

H 2.2779590000 -3.2133830000 0.1190460000
N -0.3095100000 -2.0449910000 -2.2145710000
H -1.1055230000 -1.4989100000 -2.5725060000
H -0.6114260000 -3.0248680000 -2.1358590000
H 0.4065770000 -2.0218470000 -2.9528260000
H -4.5538340000 -1.3702650000 0.0774810000
H -4.1322390000 0.7437010000 -0.6065320000

[(bpyPy$_2$Me)Fe(NH$_2$)(NH$_2$)]$^{3+}$, multiplicity = 4
C -2.5651280000 2.2335530000 -0.9511030000
C -3.0440630000 0.9440540000 -0.6874630000
C -2.1113290000 -0.0741810000 -0.4618350000
N -0.7804160000 0.1908020000 -0.5525520000
C -0.3010000000 1.4399560000 -0.6519850000
C -1.1905060000 2.5000320000 -0.8903980000
C -3.6554290000 -1.9619730000 0.2697230000
C -2.3865350000 -1.4313330000 0.0180820000
C -3.7605480000 -3.2408710000 0.8308580000
C -2.5955510000 -3.9620640000 1.1307550000
C -1.3535530000 -3.3976450000 0.8371850000
N -1.2531910000 -2.1609080000 0.2996840000
C 1.2025800000 1.5933220000 -0.3439920000
C 1.5865670000 3.0798940000 -0.2822090000
C 2.0382410000 0.8414180000 -1.3931760000
C 1.4436360000 0.8885710000 1.0202410000
N 1.1268210000 -0.4317570000 1.1216650000
C 1.2863510000 -1.0995050000 2.2890570000
C 1.7909480000 -0.4726970000 3.4266850000
C 2.1455050000 0.8762430000 3.3410280000
C 1.9681890000 1.5597700000 2.1299170000
C 3.0127720000 1.4706160000 -2.1794110000
C 3.7817690000 0.7167560000 -3.0731660000
C 3.5715370000 -0.6638470000 -3.1578000000
C 2.5898900000 -1.2392580000 -2.3564510000
N 1.8375450000 -0.4960070000 -1.5044210000
H -3.2679050000 3.0473560000 -1.1496520000
H -4.7459320000 -3.6699800000 1.0321160000
H -2.6364690000 -4.9589610000 1.5751030000
H -0.4195220000 -3.9334020000 1.0243470000
H 0.9875300000 3.5999950000 0.4797040000
H 2.6507070000 3.1979240000 -0.0306700000
H 1.4037340000 3.5628740000 -1.2538200000
H 0.9971760000 -2.1535600000 2.3060800000
H 1.9030830000 -1.0461720000 4.3500590000
H 2.5568570000 1.4021390000 4.2074120000
H 2.2388580000 2.6133520000 2.0583950000

H 3.1762580000 2.5449760000 -2.0912400000
H 4.5417600000 1.2077690000 -3.6880300000
H 4.1534400000 -1.2995430000 -3.8300360000
H 2.3824020000 -2.3104430000 -2.3913560000
Fe 0.3818730000 -1.3811050000 -0.4630510000
H -0.8235760000 3.5199950000 -1.0077450000
N 1.4570180000 -2.8580050000 -0.1571200000
H 1.4052930000 -3.7313660000 -0.6980010000
H 2.2612890000 -2.8647490000 0.4867180000
N -0.2172930000 -2.0416540000 -2.0852080000
H -0.8674670000 -2.8338130000 -2.1770260000
H -0.0062370000 -1.6103970000 -2.9948830000
H -4.5483600000 -1.3793740000 0.0333010000
H -4.1159860000 0.7415120000 -0.6321940000

[(bpyPy$_2$Me)Fe(NH$_2$)(NH$_2$)]$^{3+}$, multiplicity = 2
C -2.5498790000 2.2118680000 -0.9257390000
C -3.0282910000 0.9227650000 -0.6644420000
C -2.0970270000 -0.0967110000 -0.4410090000
N -0.7655800000 0.1700770000 -0.5331790000
C -0.2818320000 1.4215370000 -0.6414390000
C -1.1737080000 2.4777090000 -0.8744040000
C -3.6473360000 -1.9713940000 0.2981680000
C -2.3736380000 -1.4600170000 0.0195170000
C -3.7616890000 -3.2548950000 0.8440660000
C -2.5994180000 -3.9899250000 1.1043380000
C -1.3552510000 -3.4364340000 0.7835410000
N -1.2444730000 -2.2006980000 0.2549240000
C 1.2237940000 1.5864970000 -0.3558940000
C 1.5944500000 3.0762760000 -0.2859440000
C 2.0582660000 0.8514200000 -1.4173910000
C 1.4718580000 0.8736280000 1.0005930000
N 1.1062650000 -0.4312280000 1.1016670000
C 1.2026420000 -1.0812350000 2.2853740000
C 1.7202920000 -0.4653810000 3.4238600000
C 2.1436370000 0.8631010000 3.3291350000
C 2.0101240000 1.5385520000 2.1092250000
C 3.0446740000 1.4874480000 -2.1847670000
C 3.8059330000 0.7438670000 -3.0926030000
C 3.5749890000 -0.6313340000 -3.2117480000
C 2.5793940000 -1.2098370000 -2.4297120000
N 1.8352230000 -0.4767490000 -1.5612820000
H -3.2530200000 3.0269680000 -1.1180800000
H -4.7475300000 -3.6697780000 1.0706220000
H -2.6374150000 -4.9872390000 1.5484680000
H -0.4325250000 -3.9939700000 0.9616140000

H 0.9972450000 3.5854250000 0.4847500000
H 2.6591950000 3.2006850000 -0.0403470000
H 1.4033870000 3.5646720000 -1.2532850000
H 0.8538720000 -2.1167070000 2.3147900000
H 1.7850480000 -1.0300940000 4.3572890000
H 2.5647130000 1.3803670000 4.1960530000
H 2.3187580000 2.5810220000 2.0295650000
H 3.2211970000 2.5571960000 -2.0717200000
H 4.5765020000 1.2372930000 -3.6920880000
H 4.1543240000 -1.2598460000 -3.8929580000
H 2.3650960000 -2.2807400000 -2.4816360000
Fe 0.4097390000 -1.3899000000 -0.5387250000
H -0.8066660000 3.4969620000 -0.9966260000
N 1.4669290000 -2.7673260000 -0.0743320000
H 1.2832920000 -3.7510900000 -0.3225120000
H 2.3103580000 -2.6752740000 0.5113220000
N -0.2198610000 -2.0496860000 -2.0866110000
H -0.9533000000 -2.7698030000 -2.1769200000
H 0.0554430000 -1.6903170000 -3.0142380000
H -4.5346560000 -1.3674900000 0.0959480000
H -4.0999140000 0.7180730000 -0.6130730000

MeCN, multiplicity = 1
C -7.9305190000 -10.7267220000 1.0655210000
C -6.4737070000 -10.6286630000 1.1098320000
H -8.2821500000 -11.4458010000 1.8240930000
H -8.2537290000 -11.0687220000 0.0681850000
H -8.3795340000 -9.7405370000 1.2700280000
N -5.3082150000 -10.5499520000 1.1453180000

NH_3, multiplicity = 1
N -3.4062600000 2.0314360000 -0.0471600000
H -2.3807850000 1.9549480000 0.0223060000
H -3.6991510000 2.1535560000 0.9330710000
H -3.6990690000 1.0670120000 -0.2609860000

N_2H_4, multiplicity = 1
N -5.65593157558449 -0.68732489801612 0.06171968010262
N -5.58810331553809 0.79856577094464 -0.06171888099823
H -5.08293721478638 1.08382092202259 0.79073703827746
H -6.54838235021633 1.09907279415619 0.16372799703163
H -4.69565325326846 -0.98783209975199 -0.16372998040384
H -6.16110020380625 -0.97258000455531 -0.79073473880964

Ferrocene, multiplicity = 1
C 1.1627240000 0.3769360000 -1.6333370000

C 0.7167690000 -0.9903940000 -1.6334520000
C -0.7212130000 -0.9887400000 -1.6324780000
C -1.1639780000 0.3796340000 -1.6318610000
C 0.0003550000 1.2231080000 -1.6325230000
H 2.2018030000 0.7129070000 -1.6174890000
H 1.3578040000 -1.8747880000 -1.6190580000
H -1.3642490000 -1.8716700000 -1.6173630000
H -2.2022550000 0.7180140000 -1.6147190000
H 0.0016210000 2.3155870000 -1.6151990000
Fe 0.0000100000 -0.0004580000 0.0003460000
C -0.7168910000 -0.9906570000 1.6335370000
C -1.1627810000 0.3767810000 1.6335310000
C -0.0002810000 1.2228930000 1.6328970000
C 1.1640490000 0.3792990000 1.6321590000
C 0.7211570000 -0.9890990000 1.6326470000
H -1.3580070000 -1.8749910000 1.6189140000
H -2.2018330000 0.7128450000 1.6177600000
H -0.0014710000 2.3153770000 1.6157350000
H 2.2023510000 0.7176150000 1.6152970000
H 1.3641030000 -1.8720960000 1.6174310000

Ferrocenium, multiplicity = 2
C 1.0034420000 0.7144730000 -1.7331470000
C 1.0035960000 -0.7133810000 -1.7318490000
C -0.3564340000 -1.1611110000 -1.6909750000
C -1.2040500000 0.0005970000 -1.6691700000
C -0.3563670000 1.1620220000 -1.6928500000
H 1.8888220000 1.3527350000 -1.7038460000
H 1.8891410000 -1.3513810000 -1.7022350000
H -0.6866650000 -2.2006720000 -1.6539200000
H -2.2949760000 0.0008010000 -1.6290140000
H -0.6864970000 2.2016360000 -1.6560550000
Fe -0.0000040000 -0.0000010000 -0.0000120000
C -1.0034430000 -0.7144700000 1.7331380000
C -1.0035920000 0.7133860000 1.7318380000
C 0.3564410000 1.1611120000 1.6909570000
C 1.2040500000 -0.0006030000 1.6691450000
C 0.3563630000 -1.1620260000 1.6928340000
H -1.8888300000 -1.3527250000 1.7039000000
H -1.8891400000 1.3513880000 1.7022790000
H 0.6866770000 2.2006740000 1.6539250000
H 2.2949790000 -0.0008130000 1.6289990000
H 0.6864890000 -2.2016420000 1.6560600000

TEMPO, multiplicity = 2
O -1.2492590000 -0.2906870000 0.4243790000

N -2.4129740000 -0.5340430000 -0.0687860000
C -3.4514420000 0.5490390000 0.1228870000
C -4.6960800000 0.2509660000 -0.7421770000
H -5.5014500000 0.9355480000 -0.4207760000
H -4.4638250000 0.5014720000 -1.7949570000
C -5.1476780000 -1.2107660000 -0.6758460000
H -5.4361800000 -1.4866460000 0.3554200000
H -6.0455870000 -1.3534200000 -1.3025480000
C -4.0144930000 -2.1081980000 -1.1806130000
H -3.7869970000 -1.8351070000 -2.2285590000
H -4.3164130000 -3.1712540000 -1.1859230000
C -2.7198870000 -1.9890100000 -0.3460300000
C -3.8038920000 0.6307340000 1.6263430000
H -2.8760220000 0.7150000000 2.2158510000
H -4.3596980000 -0.2576200000 1.9695330000
H -4.4287020000 1.5213850000 1.8144360000
C -2.8078220000 1.8741840000 -0.3275270000
H -2.5005240000 1.8157310000 -1.3861620000
H -1.9229070000 2.1052830000 0.2851840000
H -3.5423850000 2.6909560000 -0.2199830000
C -2.8390140000 -2.7330520000 1.0051460000
H -1.9496110000 -2.5175820000 1.6208750000
H -2.8942580000 -3.8211660000 0.8270550000
H -3.7387810000 -2.4294760000 1.5664850000
C -1.5302660000 -2.5558200000 -1.1433170000
H -0.6015970000 -2.4934790000 -0.5549750000
H -1.3917840000 -1.9954650000 -2.0842510000
H -1.7274370000 -3.6127590000 -1.3915770000

TEMPOH, multiplicity = 1

O 1.7239200000 0.5195110000 0.6071560000
N 0.5534440000 0.3613860000 -0.2439160000
C -0.4595910000 1.3790490000 0.1817410000
C -1.7239750000 1.1449220000 -0.6810960000
H -2.5119790000 1.8386490000 -0.3351500000
H -1.4870780000 1.4192890000 -1.7271180000
C -2.2101380000 -0.3080670000 -0.6503750000
H -2.5384080000 -0.5847590000 0.3688100000
H -3.0925410000 -0.4249890000 -1.3052220000
C -1.0831280000 -1.2344750000 -1.1182140000
H -0.8361020000 -0.9931040000 -2.1697860000
H -1.3998570000 -2.2935460000 -1.0955690000
C 0.2054860000 -1.0948060000 -0.2712530000
C -0.7963730000 1.3664520000 1.6928030000
H 0.1334780000 1.3495940000 2.2837190000

H -1.4123610000 0.5014020000 1.9846770000
H -1.3576380000 2.2812190000 1.9552670000
C 0.1382480000 2.7576460000 -0.1734590000
H 0.4358270000 2.7807910000 -1.2365620000
H 1.0277660000 2.9682800000 0.4435080000
H -0.6054260000 3.5545730000 0.0045100000
C 0.0393240000 -1.7467730000 1.1238350000
H 0.8885640000 -1.4675830000 1.7693970000
H 0.0283560000 -2.8466450000 1.0207360000
H -0.8953500000 -1.4484380000 1.6253240000
C 1.3640760000 -1.8028180000 -1.0063710000
H 2.2919150000 -1.7559690000 -0.4116310000
H 1.5480220000 -1.3194310000 -1.9820880000
H 1.1147770000 -2.8646390000 -1.1788790000
H 2.4087420000 0.8122760000 -0.0237950000

C.16 References

[1] Canary, J. W.; Wang, Y.; Roy, R. Tris[(2-pyridyl)methyl]amine (TPA) and (+)-bis[(2-pyridyl)methyl]-1-(2-pyridyl)-ethylamine (α-METPA). *Inorg. Synth.* **1998**, *32*, 70–75.

[2] Diebold, A.; Hagen, K. S. Iron(II) Polyamine Chemistry: Variation of Spin State and Coordination Number in Solid State and Solution with Iron(II) Tris(2-pyridylmethyl)amine Complexes. *Inorg. Chem.* **1998**, *37*, 215–223.

[3] Khnayzer, R. S.; Thoi, V. S.; Nippe, M.; King, A. E.; Jurss, J. W.; El Roz, K. A.; Long, J. R.; Chang, C. J.; Castellano, F. N. Towards a Comprehensive Understanding of Visible-Light Photogeneration of Hydrogen from Water Using Cobalt(II) Polypyridyl Catalysts. *Energy Environ. Sci.* **2014**, *7*, 1477–1488.

[4] Chen, L.; Su, X.-J.; Jurss, J. W. Selective Alkane C–H Bond Oxidation Catalyzed by a Non-Heme Iron Complex Featuring a Robust Tetradentate Ligand. *Organometallics* **2018**, *37*, 4535–4539.

[5] Sheldrick, G. SHELXT - Integrated Space-Group and Crystal-Structure Determination. *Acta Crystallogr., Sect. C: Struct.* **2015**, *71*, 3–8.

[6] Dolomanov, O. V.; Bourhis, L. J.; Gildea, R. J.; Howard, J. A. K.; Puschmann, H. OLEX2: a Complete Structure Solution, Refinement and Analysis Program. *J. Appl. Crystallogr.* **2009**, *42*, 339–341.

[7] Macpherson, J. V. A Practical Guide to Using Boron Doped Diamond in Electrochemical Research. *Phys. Chem. Chem. Phys.* **2015**, *17*, 2935–2949.

[8] Lindley, B. M.; Appel, A. M.; Krogh-Jespersen, K.; Mayer, J. M.; Miller, A. J. M. Evaluating the Thermodynamics of Electrocatalytic N_2 Reduction in Acetonitrile. *ACS Energy Lett.* **2016,** *1*, 698–704.

[9] Zott, M. D.; Garrido-Barros, P.; Peters, J. C. Electrocatalytic Ammonia Oxidation Mediated by a Polypyridyl Iron Catalyst. *ACS Catal.* **2019,** *9*, 10101–10108.

[10] Neese, F. Software Update: the ORCA Program System, Version 4.0. *WIREs Comput. Mol. Sci.* **2018**, *8*, e1327.

[11] Warren, J. J.; Tronic, T. A.; Mayer, J. M. Thermochemistry of Proton-Coupled Electron Transfer Reagents and its Implications. *Chem. Rev.* **2010**, *110*, 6961–7001.

Appendix D

Supplementary Information for Chapter 5

.

D.1 General procedures

General Considerations: All manipulations of inorganic complexes were carried out using standard Schlenk or glovebox techniques under an N_2 or Ar atmosphere. Unless otherwise noted, solvents were deoxygenated and dried by thoroughly sparging with N_2 gas followed by passage through an activated alumina column in a solvent purification system (SG Water, USA LLC). For electrochemical measurements under an Ar atmosphere, solvents were further degassed and then stored under Ar. All solvents were stored over activated 3 or 4 Å molecular sieves prior to use. Anhydrous ammonia gas was dried by passage through a calcium oxide drying tube. All reagents were purchased from commercial vendors and used without further purification unless otherwise stated. Tris(2-pyridylmethyl)amine (TPA),[1] tris(2-pyridylmethylamine) iron(II) triflate bis-acetonitrile ([(TPA)Fe(MeCN)$_2$]OTf$_2$),[2] 6-(1,1-di(pyridin-2-yl)ethyl)-2,2'-bipyridine (BPM),[3] 6-(1,1-di(pyridin-2-yl)ethyl)-2,2'-bipyridine iron(II) triflate bis-acetonitrile ([(BPM)Fe(MeCN)$_2$]OTf$_2$),[4] bis(4-(dimethylamino)pyridin-2-yl)methanone,[5] tris(4-(dimethylamino)-2-picolyl)amine (TPA^{NMe2}),[6] tris(4-methoxy-2-picolyl)amine (TPA^{OMe}),[6] 4-(trifluoromethyl)pyridine-2-carboxaldehyde,[7] 4-(trifluoromethyl)-2-ethylpyridine,[8] bis(4-(dimethylamino)pyridin-2-yl)methanone,[9] and methylenetriphenylphosphorane[10] were synthesized according to literature procedures.

Electrochemistry: Voltammetry experiments were carried out with a Biologic VSP-300 or CH Instruments 600B potentiostat using a one-compartment three-electrode cell, and coulometry experiments were carried out with a Biologic VSP-300 potentiostat using a one-compartment three-electrode cell with a septum capped 14/20 joint for headspace analysis.

For voltammetry, a boron-doped diamond (BDD) working electrode (3 mm diameter), a Pt wire counter electrode, and an Ag/AgOTf reference electrode (5 mM AgOTf and 0.1 M $TBAPF_6$ in MeCN) were employed. For controlled potential coulometry (CPC), the same reference electrode was used, but a BDD plate (geometric area: 4 cm^2) and a Pt mesh were used as working and counter electrodes, respectively. All redox potentials in the present work are reported versus the Fc/Fc^+ couple, measured before each experiment to be approximately +0.12 V versus the Ag/AgOTf reference electrode.

Cyclic voltammograms (CVs) were collected at 100 $mV \cdot s^{-1}$ unless otherwise specified. $E_{1/2}$ values for the reversible waves were obtained from the half potential between the oxidative and reductive peaks. CV measurements were performed applying IR compensation, compensating 85% of the resistance measured at one high frequency value (100 kHz).

Gas Chromatography: Gas chromatography was performed in the Caltech Environmental Analysis Center using HP 5890 Series II instruments. Gas quantification was performed with a molecular sieve column attached to a thermal conductivity detector using argon as the carrier gas. Standard curves were generated by direct injection of hydrogen or nitrogen gas. Quantification of background nitrogen was determined using the background oxygen signal. Isotopic measurements were performed with a separate HP 5890 Series II instrument equipped with a GasPro column using helium as the carrier gas.

NMR: NMR spectroscopy was performed using Varian and Bruker 400 MHz NMR spectrometers equipped with broadband auto-tune probes. ^1H NMR chemical shifts are reported in ppm relative to tetramethylsilane, using residual solvent resonances as internal standards.

UV-Vis: Spectra were collected using a Cary 60 instrument with Cary WinUV software.

X-ray Crystallography: XRD studies were carried out at the Caltech Beckman Institute Crystallography Facility on a Bruker D8 Venture diffractometer (Cu Kα radiation). The crystals were mounted on a glass fiber under Paratone N oil. Structures were solved using direct methods with SHELXS or SHELXT and refined against F^2 on all data by full-matrix least squares with SHELXL.[11] All of the solutions were performed in the Olex2 program.[12]

D.2 Synthetic procedures

TPA derivatives

TPA^{CF3} (tris(4-(trifluoromethyl)-2-picolyl)amine)

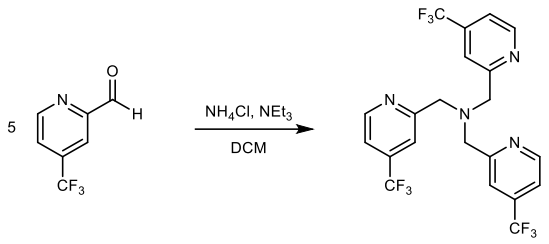

Ammonium chloride (15 mg, 1 eq), 4-(trifluoromethyl)-pyridine-2-carbaldehyde (250 mg, 5 eq), and triethylamine (44 µL, 1.1 eq) were combined in dichloromethane (5 mL). Sodium triacetoxyborohydride (270 mg, 4.5 eq) was added as a solid, and the mixture was stirred at room temperature for 48 h. A saturated aqueous solution of sodium carbonate was added, and the organic phase was separated. The aqueous phase was extracted twice with dichloromethane, dried over sodium sulfate, filtered, and concentrated under reduced pressure. The remaining oil was dissolved in ethyl acetate and added to a silica plug. The silica plug was eluted with ethyl acetate until the eluent was colorless, then the product was eluted with methanol, dried over sodium sulfate, and concentrated under reduced pressure to yield a yellow oil (48 mg, 34% yield).

^{1}H NMR ($CDCl_3$, 400 MHz): δ (ppm) = 8.71 (d, *J* = 5.1 Hz, 3H), 7.72 (d, *J* = 1.8 Hz, 3H), 7.36 (dd, *J* = 5.1, 1.7 Hz, 3H), 4.07 (s, 6H).

^{13}C{^{1}H} NMR ($CDCl_3$, 101 MHz): δ (ppm) = 160.55 (s), 150.19 (s), 138.85 (q, *J* = 34.1 Hz), 122.74 (q, *J* = 273.3 Hz), 118.82 (q, *J* = 3.6 Hz), 117.87 (q, *J* = 3.8 Hz), 60.55 (s).

^{19}F{^{1}H} NMR ($CDCl_3$, 376 MHz): δ (ppm) = −65.1 (s).

MS (ESI, UHPLC-MS (CH_3CO_2H), *m/z*): calculated for $C_{21}H_{15}F_9N_4$ + H, $[M+H]^+$: 495.1, found: 495.1.

General note about the synthesis of iron compounds: For the preparation of the following iron complexes, only the crystalline yield for the first crop of crystals is reported. Higher yields can be obtained if the supernatant is concentrated and recrystallized.

$[(TPA^{NMe2})Fe(MeCN)_2]OTf_2$

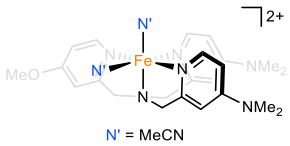

White solids TPA^{NMe2} (tris(4-(dimethylamino)-2-picolyl)amine) (30 mg, 1 eq) and $FeOTf_2 \cdot 2$ MeCN (31 mg, 1 eq) were each dissolved in 0.4 mL acetonitrile. The solution of $FeOTf_2$ was added to the solution of TPA^{NMe2}, instantly producing a pale orange-brown solution. The solution was filtered through Celite, and diethyl ether (2 mL) was layered on top of the filtrate. This mixture was placed in a freezer (−30 °C) until a purple-gray (this compound changes color with varying temperature) precipitate appeared. The precipitate was isolated by decanting the supernatant and drying under vacuum (50.7 mg, 83% yield).

^{1}H NMR (25 °C, CD_3CN, 400.15 MHz): δ (ppm) = 94.92 (s), 93.33 (s), 43.73 (s), 35.32 (s), 15.88 (s).

$^{19}F\{^{1}H\}$ NMR (25 °C, CD_3CN, 376 MHz): δ (ppm) = −77.1.

UV-vis (MeCN): nm [$cm^{-1}M^{-1}$]): 225 [20000], 283 [40000], 342 [3900].

MS (ESI, direct injection in MeCN, *m/z*): calculated for $C_{25}H_{33}N_7O_3F_3SFe$, $[M]^+$: 624.2, found: 624.3.

Electrochemistry: $E_{1/2}$ = 0.21 V vs Fc/Fc^+ (MeCN, 0.1 M $TBAPF_6$, BDD disk electrode).

[(TPA^{OMe})Fe(MeCN)$_2$]OTf$_2$

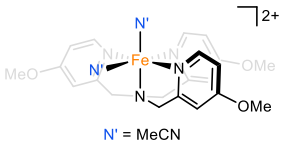

White solids TPA^{OMe} (tris(4-methoxy-2-picolyl)amine) (25 mg, 1 eq) and $FeOTf_2 \cdot 2$ MeCN (29 mg, 1 eq) were each dissolved in 0.25 mL acetonitrile. The solution of $FeOTf_2$ was added to the solution of TPA^{OMe}, instantly producing a purple-red solution. The solution was filtered through Celite, and diethyl ether (2 mL) was layered on top of the filtrate. This mixture was placed in a freezer (−30 °C) until dark purple needle-shaped crystals appeared. The precipitate was isolated by decanting the supernatant and drying under vacuum (34.7 mg, 64% yield).

^{1}H NMR (25 °C, CD_3CN, 400.15 MHz): δ (ppm) = 38.51 (s), 30.31 (s), 22.62 (s), 20.02 (s), 4.63 (s).

$^{19}F\{^1H\}$ NMR (25 °C, CD_3CN, 376 MHz): δ (ppm) = −78.1.

UV-vis (MeCN): nm [$cm^{-1}M^{-1}$]): 235 [24000], 339 [5100], 375 [4700].

MS (ESI, direct injection in MeCN, *m/z*): calculated for $C_{22}H_{24}N_4O_6F_3SFe$, $[M]^+$: 585.1, found: 585.2.

Electrochemistry: $E_{1/2}$ = 0.55 V vs Fc/Fc^+ (MeCN, 0.1 M $TBAPF_6$, BDD disk electrode).

[(TPA^{CF3})Fe(MeCN)$_2$]OTf$_2$

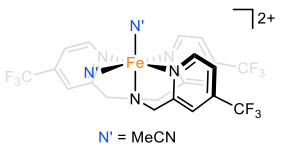

Yellow oil TPA^{CF3} (tris(4-(trifluoromethyl)-2-picolyl)amine) (72 mg, 1 eq) and white solid $FeOTf_2 \cdot 2$ MeCN (63 mg, 1 eq) were each dissolved in 0.5 mL acetonitrile. The solution of $FeOTf_2$ was added to the solution of TPA^{CF3}, instantly producing a purple-red solution. The solution was filtered through Celite, and diethyl ether (2 mL) was layered on top of the filtrate. This mixture was placed in a freezer (−30 °C) until dark red-brown crystals appeared. The precipitate was isolated by decanting the supernatant and drying under vacuum (47.5 mg, 35% yield).

^{1}H NMR (25 °C, CD_3CN, 400.15 MHz): δ (ppm) = 11.07 (s), 8.43 (s), 5.86 (s), 3.66 (s).

$^{19}F\{^1H\}$ NMR (25 °C, CD_3CN, 376 MHz): δ (ppm) = −65.9 (s), −78.9 (s).

UV-vis (MeCN): nm [$cm^{-1}M^{-1}$]): 225 [9900], 262 [13000], 388 [6600], 428 [8900].

MS (ESI, direct injection in MeCN, *m/z*): calculated for $C_{22}H_{15}N_4O_3F_{12}SFe$, $[M]^+$: 699.0, found: 699.0.

Electrochemistry: $E_{p/2}$ = 1.09 V (irreversible) vs Fc/Fc^+ (MeCN, 0.1 M $TBAPF_6$, BDD disk electrode).

BPM – dipyridyl substitution

2,2'-(ethene-1,1-diyl)bis(4-(dimethylamino)pyridine)

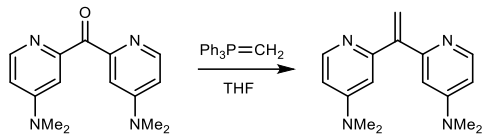

Note: This compound was prepared with modifications to the literature procedure for 2,2'-(ethene-1,1-diyl)dipyridine.[13] Notably, poor performance was observed when methylenetriphenylphosphorane was generated *in situ*, presumably due to residual potassium salts (i.e., KBr).

Bis(4-dimethylaminopyridin-2-yl)methanone (406 mg, 1.5 mmol, 1 eq) was suspended in anhydrous tetrahydrofuran (15 mL, 0.1 M) in a glovebox and cooled to −30 °C, after which isolated methylenetriphenylphosphorane (435 mg, 1.58 mmol, 1.05 eq) was added in one portion. This mixture was warmed to room temperature and allowed to react for at least 4 h (reaction times up to overnight have no deleterious impact). Outside of the glovebox, the reaction was quenched with minimal water and concentrated to yield a viscous orange-red oil. The oil was purified by silica gel column chromatography by loading with dichloromethane, eluting the triphenylphosphine oxide with 3:1 ethyl acetate:acetone plus 1% triethylamine, then eluting the product with acetone plus 1% triethylamine to afford a white crystalline solid (346 mg, 86% yield).

R_f = 0.3 (acetone plus 1% triethylamine; TLC plates treated with triethylamine).

^{1}H NMR ($CDCl_3$, 400 MHz): δ (ppm) = 8.29 (d, *J* = 5.9 Hz, 2H), 6.67 (d, *J* = 2.7 Hz, 2H), 6.46 (dd, *J* = 5.9, 2.6 Hz, 2H), 5.94 (s, 2H), 3.00 (s, 12H).

^{13}C{^{1}H} NMR ($CDCl_3$, 101 MHz): δ (ppm) = 158.66 (s), 154.77 (s), 150.57 (s), 149.32 (s), 118.66 (s), 106.38 (s), 105.47 (s), 39.18 (s).

HRMS (ESI, TOF (CH_3CO_2H), *m/z*): calculated for $C_{16}H_{20}N_4$ + H, $[M+H]^+$: 269.1761, found: 269.1763.

2,2'-(ethane-1,1-diyl)bis(4-(dimethylamino)pyridine)

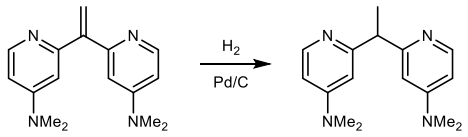

2,2'-(ethene-1,1-diyl)bis(4-(dimethylamino)pyridine) (268 mg, 1 mmol, 1 eq), Pd/C (43 mg, 5% by mass Pd, 0.02 eq), and activated carbon (134 mg, 0.5 mass eq) were suspended in methanol (10 mL, 0.1 M). The headspace of this mixture was purged with nitrogen and then hydrogen. A hydrogen atmosphere was maintained using a balloon, and the mixture was allowed to react for 12 h. The suspension was allowed to settle, and the solution was filtered through Celite. The remaining solids were washed with methanol, and the supernatant was filtered through Celite. The combined solution was concentrated, dissolved in dichloromethane, dried over sodium sulfate, and concentrated again to afford an off-white

crystalline solid after gentle heating under vacuum. (247 mg, 91% yield). This material was used without further purification.

^{1}H NMR ($CDCl_3$, 400 MHz): δ (ppm) = 8.19 (d, *J* = 6.0 Hz, 2H), 6.58 (d, *J* = 2.6 Hz, 2H), 6.34 (dd, *J* = 6.0, 2.6 Hz, 2H), 4.21 (q, *J* = 7.2 Hz, 1H), 2.95 (s, 12H), 1.71 (d, *J* = 7.2 Hz, 3H).

^{13}C{^{1}H} NMR ($CDCl_3$, 101 MHz): δ (ppm) = 164.30 (s), 154.84 (s), 149.03 (s), 105.02 (s), 104.81 (s), 50.39 (s), 39.13 (s), 19.94 (s).

MS (ESI, UHPLC-MS (CH_3CO_2H), *m/z*): calculated for $C_{16}H_{22}N_4$ + H, $[M+H]^+$: 271.2, found: 271.2.

HRMS (ESI, TOF (CH_3CO_2H), *m/z*): calculated for $C_{16}H_{22}N_4$ + H, $[M+H]^+$: 271.1917, found: 271.1919.

BPM^{NMe2} (6-(1,1-bis(4-(dimethylamino)pyridin-2-yl)ethyl)-2,2'-bipyridine)

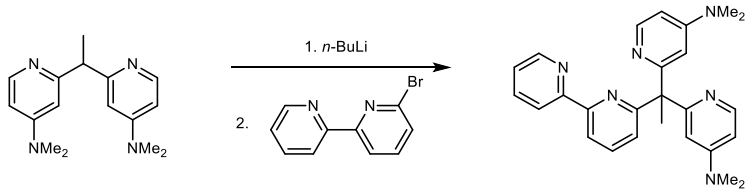

This compound was prepared by analogy to the parent ligand.[3] In a Schlenk tube under nitrogen, 2,2'-(ethane-1,1-diyl)bis(4-(dimethylamino)pyridine (135 mg, 0.5 mmol, 1 eq) was

dissolved in 2 mL dry tetrahydrofuran and cooled in a dry ice/acetone bath. A 1.6 M *n*-BuLi solution in hexanes (0.31 mL, 0.5 mmol, 1 eq) was added dropwise via syringe, and the solution turned yellow-orange. The mixture was stirred for 45 additional minutes, then 6-bromo-2,2'-bipyridine (118 mg, 0.5 mmol, 1 eq) was added as a solution in 0.5 mL tetrahydrofuran. The solution was warmed to room temperature and stirred for 16 h, after which time the reaction was quenched with water. The solution was concentrated, transferred to a separatory funnel, and extracted with dichloromethane. The combined organic fractions were concentrated and purified via column chromatography on neutral alumina using methanol:dichloromethane (1:49) to afford a waxy colorless solid. (163 mg, 77% yield).

R_f = 0.2 (methanol; TLC plates treated with methanol).

^{1}H NMR ($CDCl_3$, 400 MHz): δ (ppm) = 8.56 (ddd, *J* = 4.8, 1.9, 0.9 Hz, 1H), 8.31 (dt, *J* = 8.1, 1.1 Hz, 1H), 8.19 (dd, *J* = 5.8, 0.6 Hz, 2H), 8.15 (dd, *J* = 7.8, 0.9 Hz, 1H), 7.65 (td, *J* = 7.7, 1.8 Hz, 1H), 7.60 (t, *J* = 7.8 Hz, 1H), 7.17 (ddd, *J* = 7.5, 4.8, 1.3 Hz, 1H), 7.11 (dd, *J* = 7.9, 0.9 Hz, 1H), 6.31 – 6.25 (m, 4H), 2.79 (s, 12H), 2.33 (s, 3H).

^{13}C{^{1}H} NMR ($CDCl_3$, 101 MHz): δ (ppm) = 166.41 (s), 165.44 (s), 156.89 (s), 154.50 (s), 154.27 (s), 148.86 (s), 148.79 (s), 136.66 (s), 136.48 (s), 124.42 (s), 123.30 (s), 121.47 (s), 117.99 (s), 106.72 (s), 104.38 (s), 60.37 (s), 39.04 (s), 27.16 (s).

MS (ESI, UHPLC-MS (CH_3CO_2H), *m/z*): calculated for $C_{26}H_{28}N_6$ + H, $[M+H]^+$: 425.3, found: 425.3.

HRMS (ESI, TOF (CH_3CO_2H), *m/z*): calculated for $C_{26}H_{28}N_6$ + H, $[M+H]^+$: 425.2448, found: 425.2448.

bis(4-methoxypyridin-2-yl)methanone

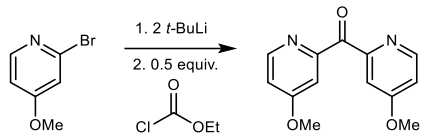

This compound was prepared by analogy to the known analogue, bis(4-(dimethylamino)pyridin-2-yl)methanone.[5] In a 100 mL flask under nitrogen, 2-bromo-4-methoxypyridine (0.7 g, 3.7 mmol, 1 eq) was dissolved in 30 mL dry diethyl ether and cooled in a dry ice/acetone bath. A 1.7 M *t*-BuLi solution in pentane (4.4 mL, 7.4 mmol, 2 eq) was added dropwise via syringe, and the solution slowly turned red-orange. The mixture was stirred for 5 additional minutes before neat ethyl chloroformate (0.18 mL, 1.8 mmol, 0.5 eq) was added all at once via syringe, after which the solution darkened. The solution was stirred 30 additional minutes in the dry ice/acetone bath, warmed to approximately 0 °C, and then quenched with water. The mixture was transferred to a separatory funnel and extracted with additional diethyl ether. The combined organic fractions were dried over sodium sulfate and concentrated under reduced pressure. The crude material was eluted through a plug of silica using acetone and then purified by silica gel column chromatography (3:1 ethyl acetate:acetone plus 1% triethylamine; R_f = 0.3) to yield an off-white solid (0.267 g, 59% yield). This material can be crystallized from cold 1:3 acetone:diethyl ether.

^{1}H NMR ($CDCl_3$, 400 MHz): δ (ppm) = 8.56 (dd, *J* = 5.7, 0.5 Hz, 2H), 7.61 (dd, *J* = 2.6, 0.5 Hz, 2H), 6.99 (dd, *J* = 5.7, 2.6 Hz, 2H), 3.93 (s, 6H).

^{13}C{^{1}H} NMR ($CDCl_3$, 101 MHz): δ (ppm) = 193.11 (s), 166.28 (s), 156.11 (s), 150.42 (s), 112.73 (s), 110.93 (s), 55.53 (s).

MS (ESI, UHPLC-MS (CH_3CO_2H), *m/z*): calculated for $C_{13}H_{12}N_2O_3$ + H, $[M+H]^+$: 245.1, found: 245.1.

HRMS (ESI, TOF (CH_3CO_2H), *m/z*): calculated for $C_{13}H_{12}N_2O_3$ + H, $[M+H]^+$: 245.0921, found: 245.0927.

2,2'-(ethene-1,1-diyl)bis(4-(methoxypyridine)

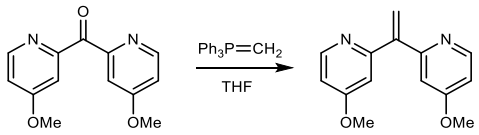

Note: This compound was prepared with modifications to the literature procedure for 2,2'-(ethene-1,1-diyl)dipyridine.[13] Notably, poor performance was observed when methylenetriphenylphosphorane was generated *in-situ*, presumably due to residual potassium salts (i.e., KBr).

Bis(4-methoxypyridin-2-yl)methanone (366 mg, 1.5 mmol, 1 eq) was dissolved in anhydrous tetrahydrofuran (15 mL, 0.1 M) in a glovebox and cooled to −30 °C, after which isolated methylenetriphenylphosphorane (435 mg, 1.58 mmol, 1.05 eq) was added in one portion.

This mixture was warmed to room temperature and allowed to react for at least 4 h (reaction times up to overnight have no deleterious impact). Outside of the glovebox, the reaction was quenched with minimal water and concentrated to yield a viscous orange-red oil. The oil was purified by silica gel column chromatography by loading with dichloromethane, eluting the triphenylphosphine oxide with 4:1 ethyl acetate:acetone plus 1% triethylamine, then eluting the product with 3:1 ethyl acetate:acetone plus 1% triethylamine to afford an off-white crystalline solid (269 mg, 74% yield).

R_f = 0.3 (4:1 ethyl acetate:acetone plus 1% triethylamine; TLC plates treated with triethylamine).

^{1}H NMR ($CDCl_3$, 400 MHz): δ (ppm) = 8.49 (d, *J* = 5.7 Hz, 2H), 6.95 (d, *J* = 2.4 Hz, 2H), 6.79 (dd, *J* = 5.7, 2.5 Hz, 2H), 6.04 (s, 2H), 3.86 (s, 6H).

^{13}C{^{1}H} NMR ($CDCl_3$, 101 MHz): δ (ppm) = 166.05 (s), 159.50 (s), 150.57 (s), 148.72 (s), 120.38 (s), 109.55 (s), 108.54 (s), 55.14 (s).

HRMS (ESI, TOF (CH_3CO_2H), *m/z*): calculated for $C_{14}H_{14}N_2O_2$ + H, $[M+H]^+$: 243.1128, found: 243.1133.

2,2'-(ethane-1,1-diyl)bis(4-methoxypyridine)

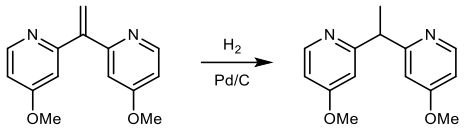

2,2'-(ethene-1,1-diyl)bis(4-methoxypyridine) (242 mg, 1 mmol, 1 eq), Pd/C (43 mg, 5% by mass Pd, 0.02 eq), and activated carbon (121 mg, 0.5 mass eq) were suspended in methanol (10 mL, 0.1 M). The headspace of this mixture was purged with nitrogen and then hydrogen. A hydrogen atmosphere was maintained using a balloon, and the mixture was allowed to react for 12 h. The suspension was allowed to settle, and the solution was filtered through Celite. The remaining solids were washed with methanol, and the supernatant was filtered through Celite. The combined solution was concentrated and purified by column chromatography to afford a white solid (127 mg, 52% yield).

Chromatography: Silica was slurry-packed with 1:19 methanol:dichloromethane then equilibrated with 1:49 methanol:dichloromethane. A gradient of 1:49 to 1:19 methanol:dichloromethane was used to elute the product, as well as a dimeric product characterized below.

R_f = 0.3 (1:19 methanol:dichloromethane).

^{1}H NMR ($CDCl_3$, 400 MHz): δ (ppm) = 8.36 (d, *J* = 5.8 Hz, 2H), 6.81 (d, *J* = 2.5 Hz, 2H), 6.64 (dd, *J* = 5.7, 2.5 Hz, 2H), 4.34 (q, *J* = 7.2 Hz, 1H), 3.79 (s, 6H), 1.71 (d, *J* = 7.2 Hz, 3H).

$^{13}C\{^{1}H\}$ NMR ($CDCl_3$, 101 MHz): δ (ppm) = 166.09 (s), 165.52 (s), 150.34 (s), 108.26 (s), 107.90 (s), 55.03 (s), 49.99 (s), 19.67 (s).

MS (ESI, UHPLC-MS (CH_3CO_2H), *m/z*): calculated for $C_{14}H_{16}N_2O_2$ + H, $[M+H]^+$: 245.1, found: 245.1.

HRMS (ESI, TOF (CH_3CO_2H), *m/z*): calculated for $C_{14}H_{16}N_2O_2$ + H, $[M+H]^+$: 245.1285, found: 245.1287.

Byproduct from synthesis of 2,2'-(ethane-1,1-diyl)bis(4-methoxypyridine):

2,2',2'',2'''- 2,2',2'',2'''-(butane-1,1,3,3-tetrayl)tetrakis(4-methoxypyridine)

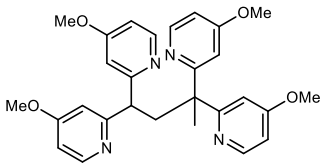

Isolated from the above reaction as a pale oil (75.6 mg, 31% yield).

R_f = 0.1 (1:19 methanol:dichloromethane).

^{1}H NMR ($CDCl_3$, 400 MHz): δ (ppm) = 8.31 (dd, *J* = 5.6, 0.9 Hz, 2H), 8.27 (dd, *J* = 5.7, 0.9 Hz, 2H), 6.78 (d, *J* = 2.5 Hz, 2H), 6.70 (d, *J* = 2.2 Hz, 2H), 6.55 (dd, *J* = 2.5, 1.1 Hz, 2H), 6.53 (dd, *J* = 2.4, 1.1 Hz, 2H), 4.27 (t, *J* = 6.0 Hz, 1H), 3.77 (s, 6H), 3.74 (s, 6H), 3.40 (d, *J* = 5.8 Hz, 2H), 1.72 (s, 3H).

$^{13}C\{^{1}H\}$ NMR ($CDCl_3$, 101 MHz): δ (ppm) = 168.19 (s), 165.72 (s), 165.58 (s), 165.11 (s), 149.76 (s), 149.64 (s), 108.52 (s), 108.12 (s), 107.20 (s), 54.96 (s), 54.87 (s), 52.99 (s), 51.92 (s), 44.21 (s), 25.63 (s).

HRMS (ESI, TOF (CH_3CO_2H), *m/z*): calculated for $C_{28}H_{30}N_4O_4$ + H, $[M+H]^+$: 487.2340, found: 487.2361.

BPM^{OMe} (6-(1,1-bis(4-methoxypyridin-2-yl)ethyl)-2,2'-bipyridine)

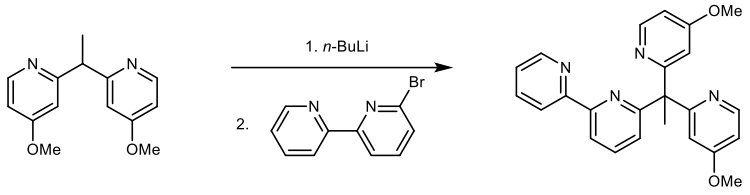

This compound was prepared by analogy to the parent ligand.[3] In a Schlenk tube under nitrogen, 2,2'-(ethane-1,1-diyl)bis(4-methoxypyridine (122 mg, 0.5 mmol, 1 eq) was dissolved in 2 mL dry tetrahydrofuran and cooled in a dry ice/acetone bath. A 1.6 M *n*-BuLi solution in hexanes (0.31 mL, 0.5 mmol, 1 eq) was added dropwise via syringe, and the solution turned yellow-orange. The mixture was stirred for 45 additional minutes, then 6-bromo-2,2'-bipyridine (118 mg, 0.5 mmol, 1 eq) was added as a solution in 0.5 mL tetrahydrofuran. The solution was warmed to room temperature and stirred for 24 h, after which time the reaction was quenched with water. The solution was concentrated, transferred to a separatory funnel, and extracted with dichloromethane. The combined organic fractions were concentrated and purified via column chromatography to afford a white solid (166 mg, 83% yield).

Chromatography: Silica was slurry-packed with 1:49 methanol:dichloromethane then equilibrated with 1:99 methanol:dichloromethane. A gradient of 1:99 to 1:19 methanol:dichloromethane was used to elute the product.

R_f = 0.3 (1:9 methanol:dichloromethane).

^{1}H NMR ($CDCl_3$, 400 MHz): δ (ppm) = 8.56 (ddd, *J* = 4.9, 1.9, 1.0 Hz, 1H), 8.38 (dd, *J* = 5.6, 0.8 Hz, 2H), 8.20 (ddt, *J* = 8.8, 7.7, 1.1 Hz, 2H), 7.64 (td, *J* = 7.8, 0.9 Hz, 2H), 7.19 – 7.15 (m, 1H), 7.09 (dd, *J* = 7.8, 1.0 Hz, 1H), 6.60 (ddd, *J* = 5.6, 2.4, 0.9 Hz, 2H), 6.56 (dd, *J* = 2.4, 0.8 Hz, 2H), 3.66 (d, *J* = 0.9 Hz, 6H), 2.32 (d, *J* = 1.0 Hz, 3H).

^{13}C{^{1}H} NMR ($CDCl_3$, 101 MHz): δ (ppm) = 167.66 (s), 165.72 (s), 164.37 (s), 156.55 (s), 154.55 (s), 150.12 (s), 148.88 (s), 136.87 (s), 136.71 (s), 123.94 (s), 123.46 (s), 121.30 (s), 118.37 (s), 110.37 (s), 106.96 (s), 60.23 (s), 54.96 (s), 27.10 (s).

MS (ESI, UHPLC-MS (CH_3CO_2H), *m/z*): calculated for $C_{24}H_{22}N_4O_2$ + H, $[M+H]^+$: 399.2, found: 399.1.

HRMS (ESI, TOF (CH_3CO_2H), *m/z*): calculated for $C_{24}H_{22}N_4O_2$ + H, $[M+H]^+$: 399.1816, found: 399.1821.

2,2'-(ethane-1,1-diyl)bis(4-(trifluoromethyl)pyridine)

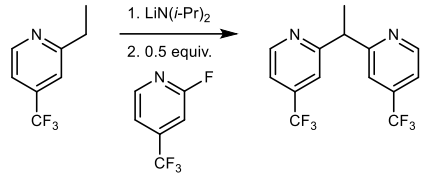

This compound was prepared by analogy to the procedure reported for the parent dipyridylethane.[14] In a Schlenk tube under nitrogen, 2-ethyl-4-(trifluoromethyl)pyridine (876 mg, 2 eq) was dissolved in THF (7 mL) and cooled to −78 °C while stirring. A 2.0 M solution of lithium diisopropylamide in THF/heptane/ethylbenzene (2.5 mL, 2 eq) was added dropwise via syringe, and the solution turned dark purple. The solution was warmed to room temperature for 5 minutes then cooled to −78 °C prior to dropwise addition of a cooled solution of 2-fluoro-4-(trifluoromethyl)pyridine (413 mg, 1 eq) in THF (3 mL). The reaction was warmed to room temperature after which it was stirred for 30 minutes then quenched with water. The mixture was concentrated, diluted in water, and extracted with dichloromethane. The organic extract was dried over sodium sulfate, concentrated, subjected to a silica plug with 1:4 ethyl acetate:hexane, and concentrated to a yellow oil that was used without further purification (0.15 g, 19% yield).

R_f = 0.3 (1:9 ethyl acetate:hexane).

^{1}H NMR ($CDCl_3$, 400 MHz): δ (ppm) = 8.73 (dt, *J* = 5.1, 0.8 Hz, 2H), 7.57 – 7.54 (m, 2H), 7.37 (ddd, *J* = 5.1, 1.7, 0.8 Hz, 2H), 4.61 (q, *J* = 7.2 Hz, 1H), 1.80 (d, *J* = 7.2 Hz, 3H).

$^{13}C\{^{1}H\}$ NMR ($CDCl_3$, 101 MHz): 164.46 (s), 150.34 (s), 138.89 (q, J = 33.9 Hz), 122.80 (q, J = 273.3 Hz), 118.10 (q, J = 3.6 Hz), 117.49 (q, J = 3.5 Hz), 49.90 (s), 19.79 (s).

$^{19}F\{^{1}H\}$ NMR ($CDCl_3$, 376 MHz): δ (ppm) = −64.8 (s).

MS (ESI, UHPLC-MS (CH_3CO_2H), *m/z*): calculated for $C_{14}H_{10}N_2F_6$ + H, $[M+H]^+$: 321.1, found: 321.1.

BPM^{CF3} (6-(1,1-bis(4-(trifluoromethyl)pyridin-2-yl)ethyl)-2,2'-bipyridine)

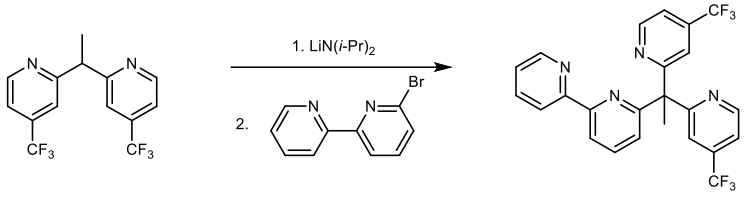

This compound was prepared by analogy to the parent ligand.[3] In a Schlenk tube under nitrogen, 2,2'-(ethane-1,1-diyl)bis(4-trifluoromethyl)pyridine (0.1 g, 1 eq) was dissolved in 3 mL tetrahydrofuran and cooled in a dry ice/acetone bath. A 2.0 M lithium diisopropylamide solution in THF/heptane/ethylbenzene (0.16 mL, 1.05 eq) was added dropwise via syringe, and the solution turned red. The mixture was stirred for 5 additional minutes then warmed to room temperature. The solution was returned to the dry ice/acetone bath before 6-bromo-2,2'-bipyridine (0.073 g, 1 eq) was added as a solid. The solution was warmed to room temperature then heated to 70 °C for 1.5 d, after which time the reaction was cooled to room temperature and quenched with water. The solution was concentrated, transferred to a separatory funnel, and extracted with dichloromethane. The combined organic fractions were dried over sodium sulfate, concentrated, and purified via silica gel column chromatography using 1:4 ethyl acetate:hexane to afford a viscous yellow oil (0.075 g, 51% yield).

R_f = 0.2 (1:4 ethyl acetate:hexane).

^{1}H NMR ($CDCl_3$, 400 MHz): δ (ppm) = 8.68 (dt, *J* = 5.1, 0.8 Hz, 2H), 8.57 (ddd, *J* = 4.8, 1.8, 0.9 Hz, 1H), 8.26 (dd, *J* = 7.9, 0.9 Hz, 1H), 7.98 (dt, *J* = 8.1, 1.1 Hz, 1H), 7.73 (t, *J* = 7.9

Hz, 1H), 7.62 (td, *J* = 7.7, 1.8 Hz, 1H), 7.41 (dt, *J* = 1.6, 0.8 Hz, 2H), 7.32 (ddd, *J* = 5.1, 1.7, 0.8 Hz, 2H), 7.23 – 7.15 (m, 2H), 2.33 (s, 3H).

$^{13}C\{^{1}H\}$ NMR ($CDCl_3$, 101 MHz): δ (ppm) = 167.10 (s), 162.96 (s), 155.88 (s), 154.91 (s), 149.53 (s), 148.97 (s), 138.11 (q, *J* = 33.7 Hz), 137.60 (s), 136.83 (s), 123.78 (s), 123.09 (s), 122.92 (q, *J* = 273.6 Hz), 121.08 (s), 119.57 (q, *J* = 3.8 Hz), 118.96 (s), 117.13 (q, *J* = 3.6 Hz), 60.54 (s), 27.10 (s).

$^{19}F\{^{1}H\}$ NMR ($CDCl_3$, 376 MHz): δ (ppm) = −64.7 (s).

MS (ESI, UHPLC-MS (CH_3CO_2H), *m/z*): calculated for $C_{24}H_{16}N_4F_6$ + H, $[M+H]^+$: 475.1, found: 475.1.

[(BPM^{NMe2})Fe(MeCN)$_2$]OTf$_2$

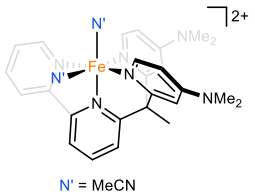

White solids BPM^{NMe2} (6-(1,1-bis(4-(dimethylamino)pyridin-2-yl)ethyl)-2,2'-bipyridine) (30 mg, 1 eq) and FeOTf$_2$ · 2 MeCN (31 mg, 1 eq) were each dissolved in 0.5 mL acetonitrile. The solution of FeOTf$_2$ was added to the solution of BPM^{NMe2}, instantly producing a purple solution. The solution was filtered through a glass microfilter, and diethyl ether (2 mL) was layered on top of the filtrate. This mixture was placed in a freezer (−30 °C) until a purple precipitate appeared. The precipitate was isolated by decanting the supernatant and drying under vacuum (50.7 mg, 83% yield).

^{1}H NMR (25 °C, CD$_3$CN, 400.15 MHz): δ (ppm) = 9.55 (d, *J* = 5.5 Hz, 1H), 8.49 (d, *J* = 6.8 Hz, 2H), 8.39 (d, *J* = 8.0 Hz, 1H), 8.27 (d, *J* = 7.9 Hz, 1H), 8.17 (td, *J* = 7.9, 0.9 Hz, 1H), 8.13 (t, *J* = 7.9 Hz, 1H), 7.94 (d, *J* = 8.0 Hz, 1H), 7.74 (t, *J* = 6.5 Hz, 1H), 7.04 (d, *J* = 2.7 Hz, 2H), 6.60 (dd, *J* = 6.9, 2.7 Hz, 2H), 3.07 (d, *J* = 1.0 Hz, 12H), 2.70 (s, 3H).

^{19}F{^{1}H} NMR (25 °C, CD$_3$CN, 376 MHz): δ (ppm) = −79.3.

UV-vis (MeCN): nm [cm^{-1}M^{-1}]): 331 [12000], 393 [4400], 498 [2800], 528 [3200].

MS (ESI, direct injection in MeCN, *m/z*): calculated for $C_{27}H_{28}N_6O_3F_3SFe$, $[M]^+$: 629.1, found: 629.2.

Electrochemistry: $E_{1/2}$ = 0.45 V vs Fc/Fc^+ (MeCN, 0.1 M $TBAPF_6$, BDD disk electrode).

[(BPM^{OMe})Fe(MeCN)$_2$]OTf$_2$

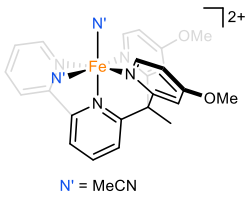

White solids BPM^{OMe} (6-(1,1-bis(4-methoxypyridin-2-yl)ethyl)-2,2'-bipyridine) (26 mg, 1 eq) and $FeOTf_2 \cdot 2$ MeCN (28.5 mg, 1 eq) were each dissolved in 0.3 mL acetonitrile. The solution of $FeOTf_2$ was added to the solution of BPM^{OMe}, instantly producing a purple solution. The solution was filtered through a glass microfilter, and diethyl ether (1.5 mL) was layered on top of the filtrate. This mixture was placed in a freezer (−30 °C) until a purple precipitate appeared. The precipitate was isolated by decanting the supernatant and drying under vacuum (50.2 mg, 92% yield).

^{1}H NMR (25 °C, CD_3CN, 400.15 MHz): δ (ppm) = 9.57 (d, *J* = 5.5 Hz, 1H), 8.94 (d, *J* = 6.5 Hz, 2H), 8.40 (d, *J* = 8.0 Hz, 1H), 8.28 (d, *J* = 7.9 Hz, 1H), 8.18 (dt, *J* = 13.5, 7.9 Hz, 2H), 7.99 (d, *J* = 7.9 Hz, 1H), 7.77 (t, *J* = 6.6 Hz, 1H), 7.46 (d, *J* = 2.6 Hz, 2H), 7.00 (dd, *J* = 6.7, 2.6 Hz, 2H), 3.93 (s, 6H), 2.74 (s, 3H).

^{19}F{^{1}H} NMR (25 °C, CD_3CN, 376 MHz): δ (ppm) = −79.3.

UV-vis (MeCN): nm [$cm^{-1}M^{-1}$]): 305 [24000], 338 [5500], 387 [3500], 496 [2900].

MS (ESI, direct injection in MeCN, *m/z*): calculated for $C_{25}H_{22}N_4O_5F_3SFe$, $[M]^+$: 603.1, found: 603.2.

Electrochemistry: $E_{1/2}$ = 0.69 V vs Fc/Fc^+ (MeCN, 0.1 M $TBAPF_6$, BDD disk electrode).

[(BPM^{CF3})Fe(MeCN)$_2$]OTf$_2$

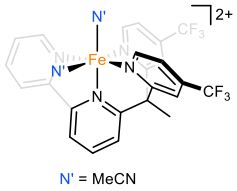

Yellow oil BPM^{CF3} (6-(1,1-bis(4-(trifluoromethyl)pyridin-2-yl)ethyl)-2,2'-bipyridine) (87.8 mg, 1 eq) and white solid $FeOTf_2 \cdot 2$ MeCN (80.6 mg, 1 eq) were each dissolved in 0.3 mL acetonitrile. The solution of $FeOTf_2$ was added to the solution of BPM^{CF3}, instantly producing an orange solution. The solution was filtered through a glass microfilter, and diethyl ether (1.5 mL) was layered on top of the filtrate. This mixture was placed in a freezer (−30 °C) until an orange-red precipitate appeared. The precipitate was isolated by decanting the supernatant and drying under vacuum (163.8 mg, 97% yield).

^{1}H NMR (25 °C, CD_3CN, 400.15 MHz): δ (ppm) = 9.57 (d, *J* = 5.6 Hz, 1H), 9.53 (d, *J* = 6.0 Hz, 2H), 8.42 (d, *J* = 7.9 Hz, 1H), 8.26 (dt, *J* = 15.7, 7.9 Hz, 3H), 8.15 (s, 2H), 8.04 (d, *J* = 7.8 Hz, 1H), 7.83 (t, *J* = 6.6 Hz, 1H), 7.68 (d, *J* = 5.9 Hz, 2H), 2.91 (s, 3H).

^{19}F{^{1}H} NMR (25 °C, CD_3CN, 376 MHz): δ (ppm) = −65.3, −79.3.

UV-vis (MeCN): nm [$cm^{-1}M^{-1}$]): 259 [16000], 301 [19000], 361 [4100], 425 [6000], 463 [5000].

MS (ESI, direct injection in MeCN, *m/z*): calculated for $C_{25}H_{16}N_4O_3F_9SFe$: 679.0, found: 679.2.

Electrochemistry: $E_{p/2}$ = 0.96 V (irreversible) vs Fc/Fc^+ (MeCN, 0.1 M $TBAPF_6$, BDD disk electrode).

D3. Additional voltammetry data related to *E*°

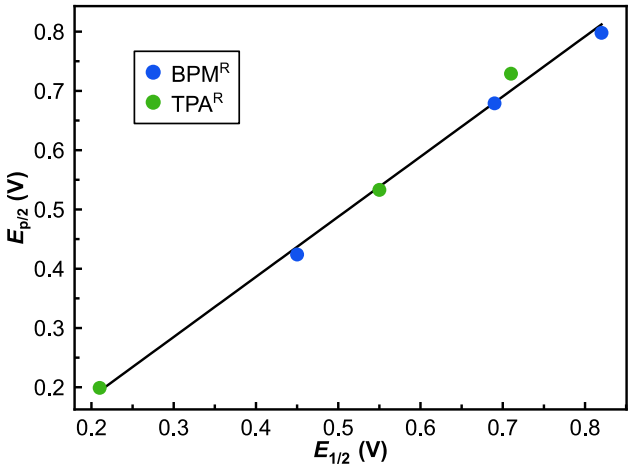

Figure D1. Correlation between half-wave ($E_{1/2}$) and half-peak ($E_{p/2}$) potentials for both $[(TPA^{R})Fe(MeCN)_2]^{2+}$ and $[(BPM^{R})Fe(MeCN)_2]^{2+}$ for R = NMe_2, OMe, H. Potentials are reported versus Fc/Fc^{+}.

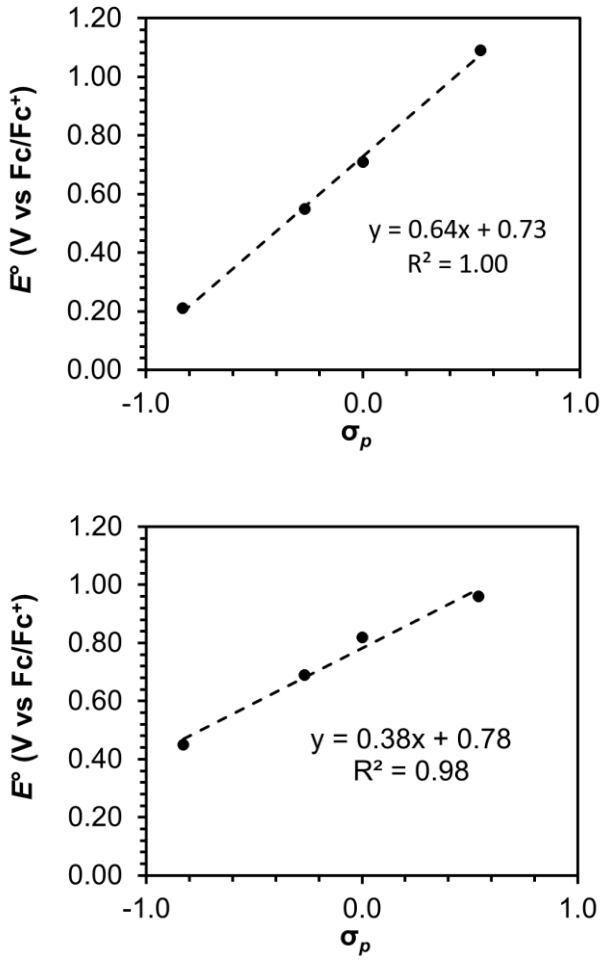

Figure D2. Electrochemical data for $[(TPA^{R})Fe(MeCN)_2]^{2+}$ (left) and $[(BPM^{R})Fe(MeCN)_2]^{2+}$ (right) analyzed using a Hammett parameter. $E°$ represents $E_{1/2}$ or $E_{p/2}$ and is plotted as a function of Hammett σ_p. From left to right, R = NMe_2, OMe, H, CF_3.

D4. Additional voltammetry data for R = CF_3

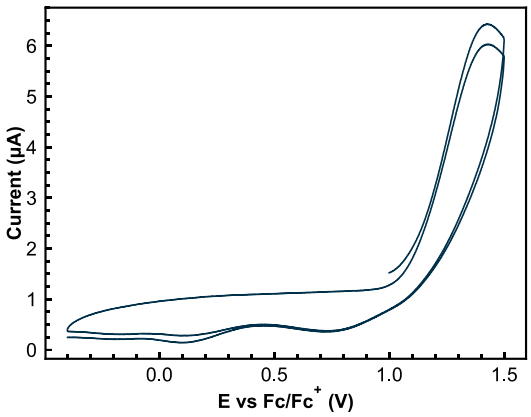

Figure D3. Cyclic voltammetry (2 scans at 100 mV/s) of $[(TPA^{CF3})Fe(MeCN)_2]^{2+}$ in acetonitrile using 0.1 M tetrabutylammonium hexafluorophosphate as supporting electrolyte.

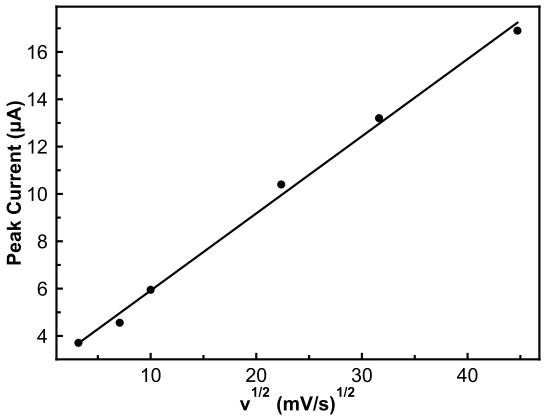

Figure D4. Randles–Ševčík plot from cyclic voltammograms of $[(TPA^{CF3})Fe(MeCN)_2]^{2+}$ in acetonitrile using 0.1 M tetrabutylammonium hexafluorophosphate as supporting electrolyte. The linear behavior is indicative of a freely diffusing, non-catalytic electroactive species, which, when combined with similar peak currents between scans, corroborates assignment of this redox feature as reversible.

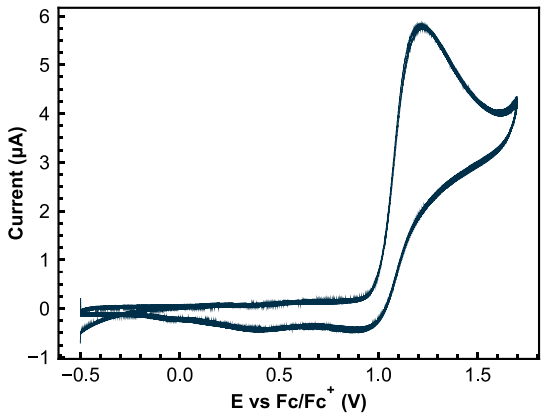

Figure D5. Cyclic voltammetry (2 scans at 100 mV/s) of $[(BPM^{CF3})Fe(MeCN)_2]^{2+}$ in acetonitrile using 0.1 M tetrabutylammonium hexafluorophosphate as supporting electrolyte.

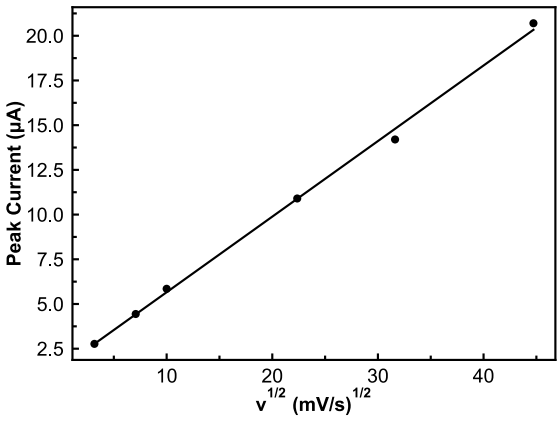

Figure D6. Randles–Ševčík plot from cyclic voltammograms of $[(BPM^{CF3})Fe(MeCN)_2]^{2+}$ in acetonitrile using 0.1 M tetrabutylammonium hexafluorophosphate as supporting electrolyte. The linear behavior is indicative of a freely diffusing, non-catalytic electroactive species, which, when combined with similar peak currents between scans, corroborates assignment of this redox feature as reversible.

D5. E_1 voltammetry

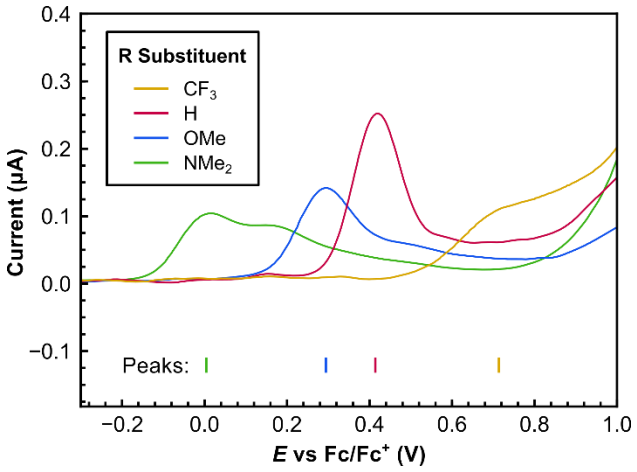

Figure D7. Differential pulse voltammetry of $[(TPA^{R})Fe(MeCN)_2]^{2+}$ in acetonitrile with 50 equiv. NH_3 using 0.05 M ammonium triflate as supporting electrolyte with BDD WE. Peak locations (indicated by vertical bars in plot) were picked using the peak picking function in EC-Lab.

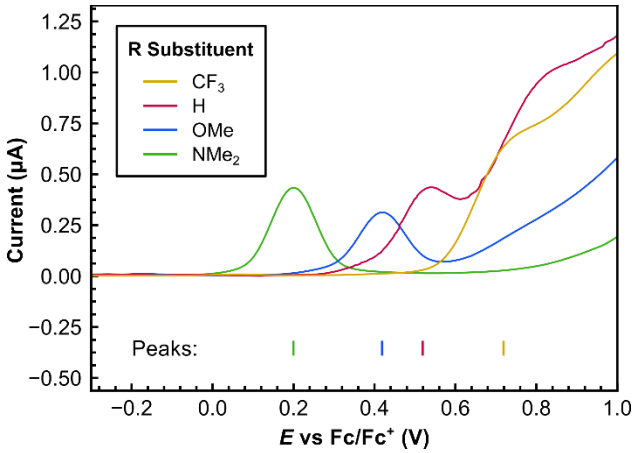

Figure D8. Differential pulse voltammetry of $[(BPM^{R})Fe(MeCN)_2]^{2+}$ in acetonitrile with 50 equiv. NH_3 using 0.05 M ammonium triflate as supporting electrolyte with BDD WE. Peak locations (indicated by vertical bars in plot) were picked using the peak picking function in EC-Lab.

D6. Catalytic controlled potential coulometry experiments

The data in the main text related to catalytic activity versus $E°$ was obtained coulometrically. While such data is typically obtained from an assessment of catalytic current via voltammetric methods, the low faradaic efficiencies observed with some of the catalysts under our catalytic conditions make such analyses unadvisable. Lowered faradaic efficiencies are observed with more electron-donating R-substituents that also result in lower overall activity. This is partially due to the catalytic conditions required for uniform comparison of the systems, i.e., low overall ammonia concentration to prevent ligand demetallation for CF_3-substituted catalysts. Since the catalytic rate is dependent on ammonia concentration, using only 50 equiv. NH_3 results in lower rates and facilitates unproductive, reversible redox processes with early intermediates, for example $Fe^{II}–NH_3 \rightleftharpoons Fe^{III}–NH_2$, thus lowering the faradaic efficiency for N_2.

Coulometric analysis of turnover frequency can accurately reflect the intrinsic turnover frequency, provided that catalyst decomposition is negligible or equivalent between systems. Employing a high catalyst concentration (0.4 mM) as compared to the optimal concentration (0.05 mM) and a relatively short reaction time (8 h vs 48 h) both serve to mitigate effects related to catalyst loss.

Procedures for controlled potential coulometry (CPC)

Preparation of the BDD electrode: A 10 cm^2 boron-doped diamond (BDD) plate electrode (IKA) was physically attached to standard electrical wire, and the connection was covered

with Teflon tape. The surface area of the electrode submerged in solution was approximately 4 cm^2.

BDD has a surface that exists in various states of reduction (H-terminated) and oxidation (O-terminated).[15] In order to remove attached nitrogen and iron generated during controlled potential coulometry experiments and to ensure a reliable electrode surface prior to CPC measurements, the BDD plate electrode was oxidatively treated prior to use. First, the electrode was soaked in dilute nitric acid (~2 M) for 5 minutes. Then, a potential of 3.0 V vs Ag/AgCl was applied to the BDD electrode in a 0.5 M H_2SO_4 solution for 10 minutes. The electrode was then thoroughly rinsed with water prior to use.

Preparation of the platinum counter electrode: In order to ensure a highly active Pt surface for HER prior to CPC experiments, the Pt mesh counter electrode was soaked in concentrated hydrochloric acid for at least 5 minutes prior to usage.

Preparation of the custom Ag/AgOTf reference electrode: To ensure reliable potential measurements, the custom Ag/AgOTf reference electrode was prepared prior to each CPC experiment then a CV of ferrocene was measured. In a glass tube fitted with a Vycor porous glass frit attached by Teflon heatshrink tubing, an acetonitrile solution containing 5 mM AgOTf and 0.1 M $TBAPF_6$ or 0.05 M NH_4OTf was added. A silver wire was placed inside and the electrode was sealed.

Preparation of ammonia solutions: Saturated 2 M solutions[16] in acetonitrile were prepared by bubbling anhydrous ammonia through acetonitrile in a Schlenk tube under an

argon/ammonia atmosphere. More dilute stock solutions were immediately prepared from this saturated solution.

CPC: Inside an argon glovebox, a gas-tight electrochemical cell equipped with a 24/40 cap containing three tungsten rods for electrical contacts and a 14/20 joint carefully sealed with a Suba-Seal septum was prepared. A BDD plate electrode (A = 4 cm^2), high surface area platinum mesh electrode, and custom Ag/AgOTf reference electrode were connected to the 24/40 cap. All chemical reagents were then rapidly added to the cell to prevent evaporation of ammonia, then the cell was sealed with the 24/40 cap. Prior to each CPC experiment, a ZIR and CV were taken. No IR compensation was applied for CPC measurements. The CPC experiment was conducted for 8–48 h, then the cell was removed from the glovebox for analysis by gas chromatography. For headspace analysis, 100 μL of the headspace was injected into a GC-TCD for quantification using a lockable Hamilton syringe with a 26S gauge needle.

Table D1. Results of catalytic CPC experiments performed at 0.85 V vs Fc/Fc^+ for 8 h for examining the E_2 LFER with 0.4 mM [Fe] and 20 mM NH_3 (50 equivalents) in 10 mL acetonitrile total. Low ammonia concentrations were used to prevent demetallation.

Entry	Fe Source	Eq. N_2	Charge (C)	FE N_2 (%)	FE H_2 (%)
1	$[(TPA^{NMe2})Fe(MeCN)_2]OTf_2$	0.73	3.9	44	16
2	$[(TPA^{NMe2})Fe(MeCN)_2]OTf_2$	0.51	8.2	14	14
3	$[(TPA^{OMe})Fe(MeCN)_2]OTf_2$	1.5	24.8	14	16
4	$[(TPA^{OMe})Fe(MeCN)_2]OTf_2$	1.4	25	13	18
5	$[(TPA^{H})Fe(MeCN)_2]OTf_2$	3.3	18.3	42	44
6	$[(TPA^{H})Fe(MeCN)_2]OTf_2$	2.9	15.6	44	42
7	$[(TPA^{CF3})Fe(MeCN)_2]OTf_2$	4.0	14.4	65	56
8	$[(TPA^{CF3})Fe(MeCN)_2]OTf_2$	3.7	19.7	43	51
9	$[(BPM^{NMe2})Fe(MeCN)_2]OTf_2$	6.0	22.2	63	55
10	$[(BPM^{NMe2})Fe(MeCN)_2]OTf_2$	6.3	24.1	61	55
11	$[(BPM^{OMe})Fe(MeCN)_2]OTf_2$	12.8	34.4	87	75
12	$[(BPM^{OMe})Fe(MeCN)_2]OTf_2$	12.7	39.1	76	68
13	$[(BPM^{H})Fe(MeCN)_2]OTf_2$	14.4	41.0	82	73
14	$[(BPM^{H})Fe(MeCN)_2]OTf_2$	12.6	39.2	75	67
15	$[(BPM^{CF3})Fe(MeCN)_2]OTf_2$	7.4	18.5	94	82
16	$[(BPM^{CF3})Fe(MeCN)_2]OTf_2$	9.4	24.3	90	84

Table D2. Results of catalytic CPC experiments performed at 0.85 V vs Fc/Fc^+ for 48 h with 0.05 mM [Fe] and 100 mM NH_3 (2000 equivalents) in 10 mL acetonitrile total. Reload experiments are listed as x.1 and x.2 for the first and second experiment, respectively. The reload was stopped after 24 h when current ceased. LOQ indicates that too little gas was produced to exceed the limit of quantification.

Entry	Fe Source	Eq. N_2	Charge (C)	FE N_2 (%)	FE H_2 (%)
1	$[(BPM^{OMe})Fe(MeCN)_2]OTf_2$	383	108.9	102	83
1.1	$[(BPM^{OMe})Fe(MeCN)_2]OTf_2$	52	17.8	85	75
2	$[(BPM^{OMe})Fe(MeCN)_2]OTf_2$	381	113.9	98	86
3	$[(BPM^{OMe})Fe(MeCN)_2]OTf_2$	rinse test	113.7	rinse test	rinse test
3 – rinse test	$[(BPM^{OMe})Fe(MeCN)_2]OTf_2$	LOQ	1.5	LOQ	LOQ

Rinse test procedure: After performing 48 h of CPC (entry 3), the electrochemical cell was purged and opened inside of the glovebox to prevent exposure of the working electrode to ambient conditions. The working electrode was thoroughly rinsed with acetonitrile. Then, fresh acetonitrile containing 0.05 M NH_4OTf and 100 mM NH_3 (2000 equivalents) was added to the electrochemical cell, and the cell was resubjected to a potential of 0.85 V vs Fc/Fc^+ for 48 h (entry 3 – rinse test).

D7. CV of $[(BPM^{OMe})Fe(N')_2]^{2+}$ under catalytic conditions

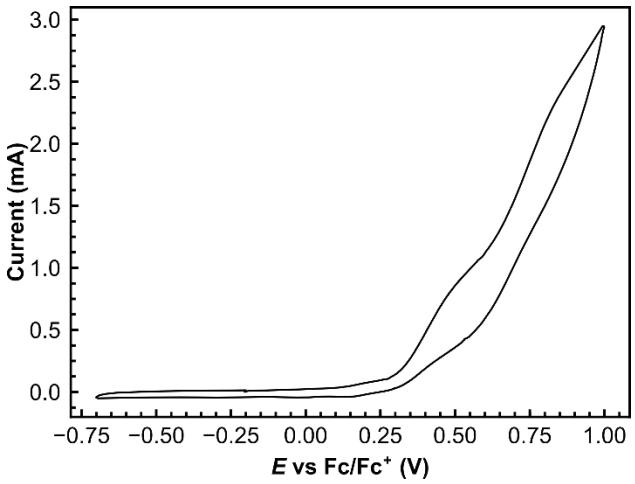

Figure D7. Cyclic voltammogram of 0.05 mM $[(BPM^{OMe})Fe(N')_2]^{2+}$ in acetonitrile containing 0.05 M ammonium triflate electrolyte and 2000 equiv. NH_3 (0.1 M). A BDD plate working electrode, platinum mesh counter electrode, and Ag/AgOTf reference electrode were used.

D8. NMR spectra of iron complexes used for Evans method

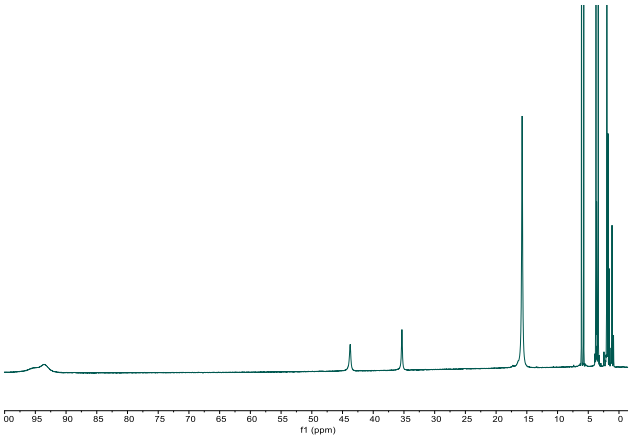

Figure D8. ^{1}H NMR spectrum of [(TPA^{NMe2})Fe(MeCN)$_2$]OTf$_2$ in CD_3CN at 25 °C.

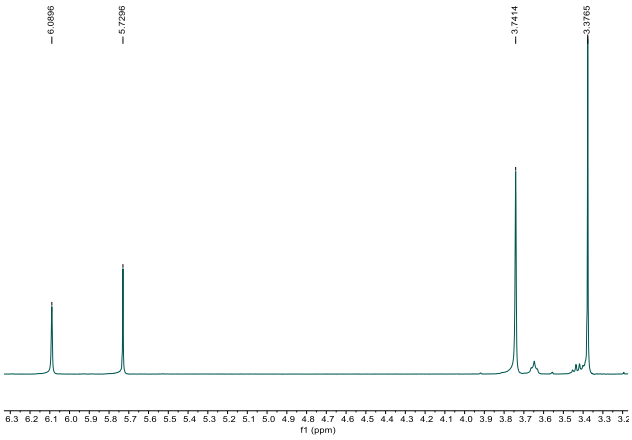

Figure D9. Trimethoxybenzene signals used for Evan's method for [(TPA^{NMe2})Fe(MeCN)$_2$]OTf$_2$ in CD_3CN at 25 °C. [Fe] = 0.011 M, Δf = 145 Hz, f = 400.15 MHz, μ_B = 4.4.

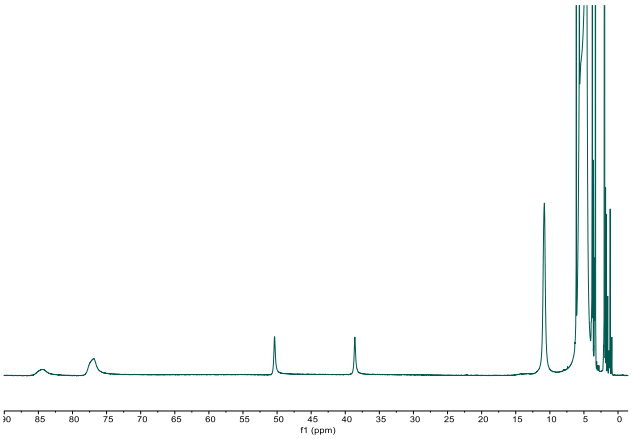

Figure D10. ^{1}H NMR spectrum of [(TPA^{NMe2})Fe(L)$_2$]OTf$_2$ (L = MeCN, NH$_3$), formed by mixing [(TPA^{NMe2})Fe(MeCN)$_2$]OTf$_2$ with 75 equivalents of NH$_3$ in CD$_3$CN at 25 °C.

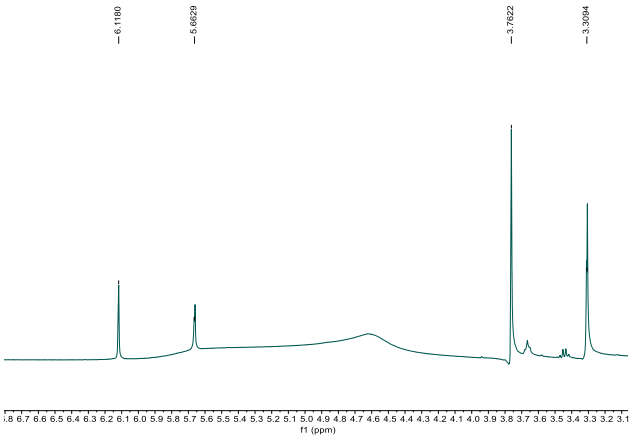

Figure D11. Trimethoxybenzene signals used for Evan's method for [(TPA^{NMe2})Fe(L)$_2$]OTf$_2$ (L = MeCN, NH$_3$), formed by mixing [(TPA^{NMe2})Fe(MeCN)$_2$]OTf$_2$ with 75 equivalents of NH$_3$ in CD$_3$CN at 25 °C. [Fe] = 0.011 M, Δf = 182 Hz, f = 400.15 MHz, μ_B = 4.9.

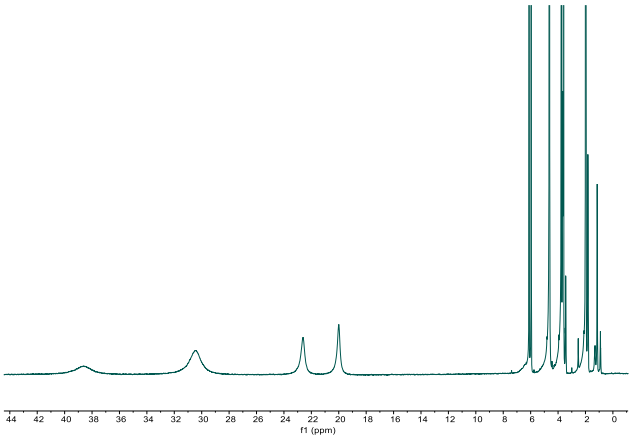

Figure D12. ^{1}H NMR spectrum of [(TPA^{OMe})Fe(MeCN)$_2$]OTf$_2$ in CD_3CN at 25 °C.

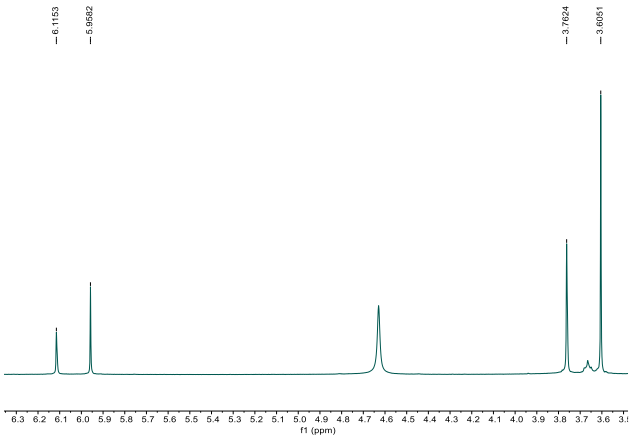

Figure D13. Trimethoxybenzene signals used for Evan's method for [(TPA^{OMe})Fe(MeCN)$_2$]OTf$_2$ in CD_3CN at 25 °C. [Fe] = 0.011 M, Δf = 62.9 Hz, f = 400.15 MHz, μ_B = 2.9.

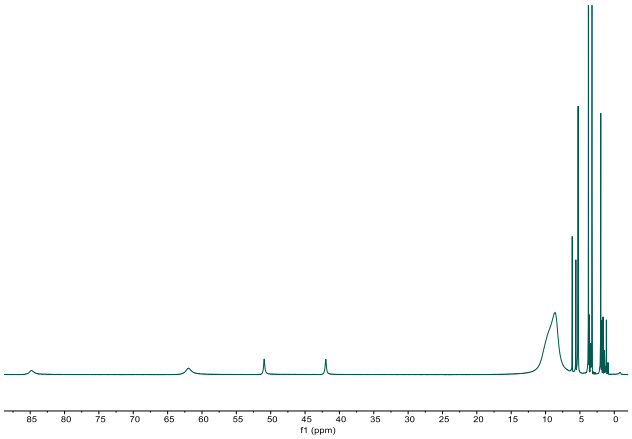

Figure D14. ^{1}H NMR spectrum of [(TPA^{OMe})Fe(L)$_2$]OTf$_2$ (L = MeCN, NH$_3$), formed by mixing [(TPA^{OMe})Fe(MeCN)$_2$]OTf$_2$ with 75 equivalents of NH$_3$ in CD$_3$CN at 25 °C.

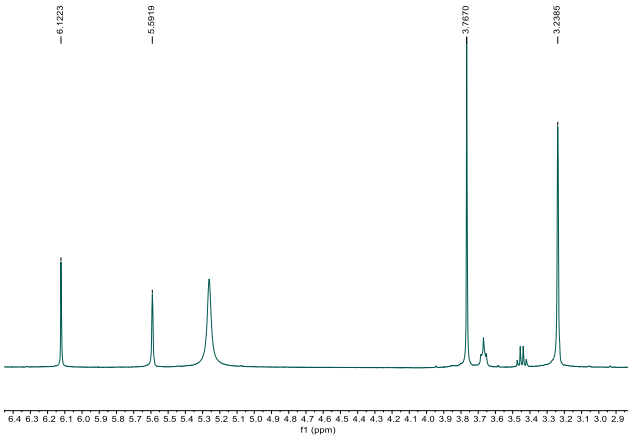

Figure D15. Trimethoxybenzene signals used for Evan's method for [(TPA^{OMe})Fe(L)$_2$]OTf$_2$ (L = MeCN, NH$_3$), formed by mixing [(TPA^{OMe})Fe(MeCN)$_2$]OTf$_2$ with 75 equivalents of NH$_3$ in CD$_3$CN at 25 °C. [Fe] = 0.011 M, $\Delta f = 212$ Hz, f = 400.15 MHz, $\mu_B = 5.4$.

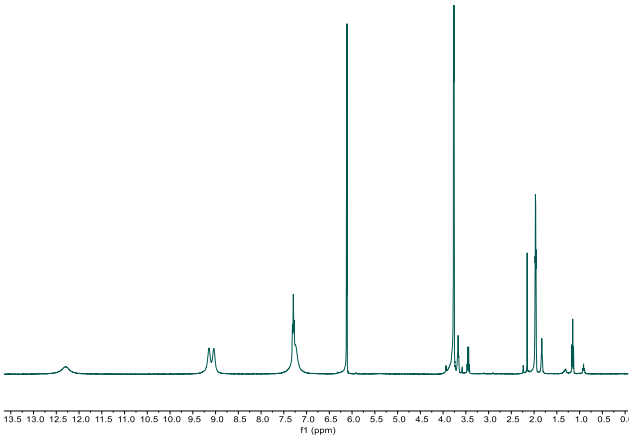

Figure D16. ^{1}H NMR spectrum of [(TPA)Fe(MeCN)$_2$]OTf$_2$ in CD_3CN at 25 °C.

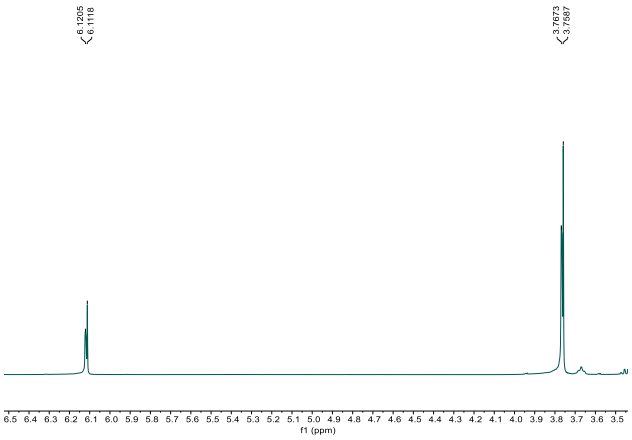

Figure D17. Trimethoxybenzene signals used for Evan's method for [(TPA)Fe(MeCN)$_2$]OTf$_2$ in CD_3CN at 25 °C. [Fe] = 0.011 M, $\Delta f = 3.46$ Hz, $f = 400.15$ MHz, $\mu_B = 0.68$.

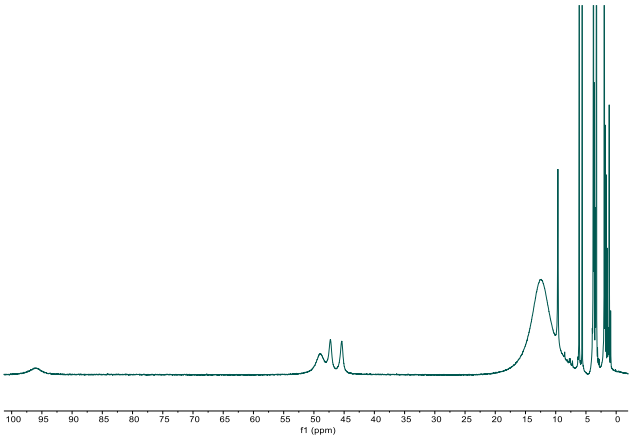

Figure D18. ^{1}H NMR spectrum of $[(TPA)Fe(L)_2]OTf_2$ (L = MeCN, NH_3), formed by mixing $[(TPA)Fe(MeCN)_2]OTf_2$ with 75 equivalents of NH_3 in CD_3CN at 25 °C.

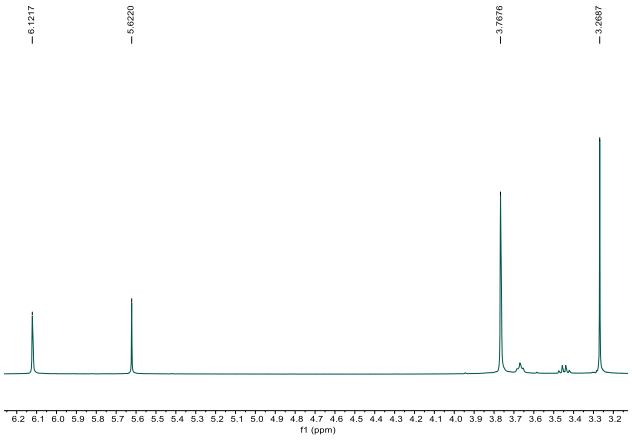

Figure D19. Trimethoxybenzene signals used for Evan's method for $[(TPA)Fe(L)_2]OTf_2$ (L = MeCN, NH_3), formed by mixing $[(TPA)Fe(MeCN)_2]OTf_2$ with 75 equivalents of NH_3 in CD_3CN at 25 °C. [Fe] = 0.011 M, Δf = 200 Hz, f = 400.15 MHz, μ_B = 5.2.

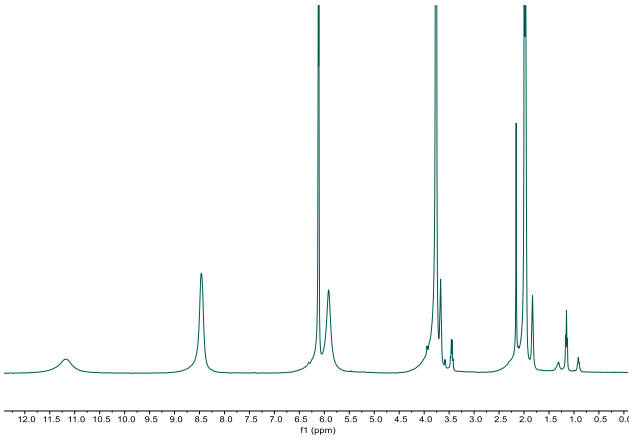

Figure D20. ^{1}H NMR spectrum of [(TPA^{CF3})Fe(MeCN)$_2$]OTf$_2$ in CD_3CN at 25 °C.

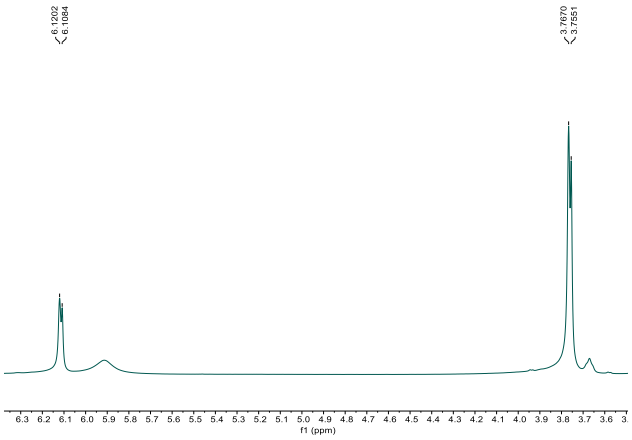

Figure D21. Trimethoxybenzene signals used for Evan's method for [(TPA^{CF3})Fe(MeCN)$_2$]OTf$_2$ in CD_3CN at 25 °C. [Fe] = 0.011 M, Δf = 4.74 Hz, f = 400.15 MHz, μ_B = 0.78.

Note: At the total NH_3/[Fe] concentrations required for NMR experiments, the TPA^{CF3} ligand dissociates, thus NMR data for [(TPA^{CF3})Fe(L)$_2$]OTf$_2$ is unavailable.

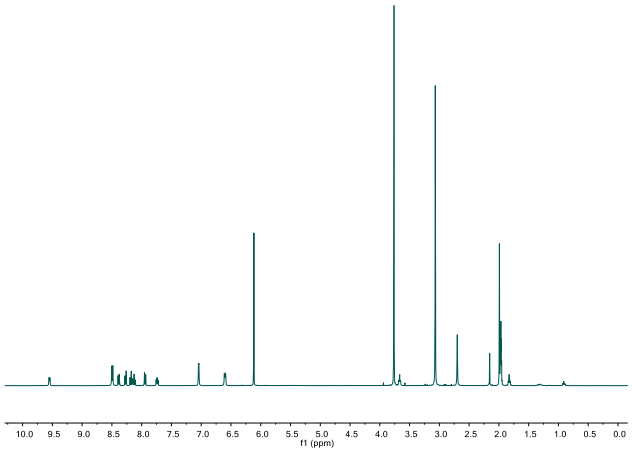

Figure D22. ^{1}H NMR spectrum of [(BPM^{NMe2})Fe(MeCN)$_2$]OTf$_2$ in CD_3CN at 25 °C.

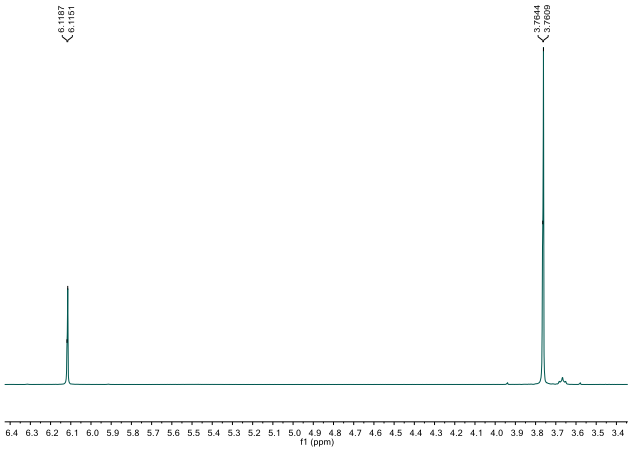

Figure D23. Trimethoxybenzene signals used for Evan's method for [(BPM^{NMe2})Fe(MeCN)$_2$]OTf$_2$ in CD_3CN at 25 °C. [Fe] = 0.011 M, $\Delta f = 1.4$ Hz, $f = 400.15$ MHz, $\mu_B = 0.43$.

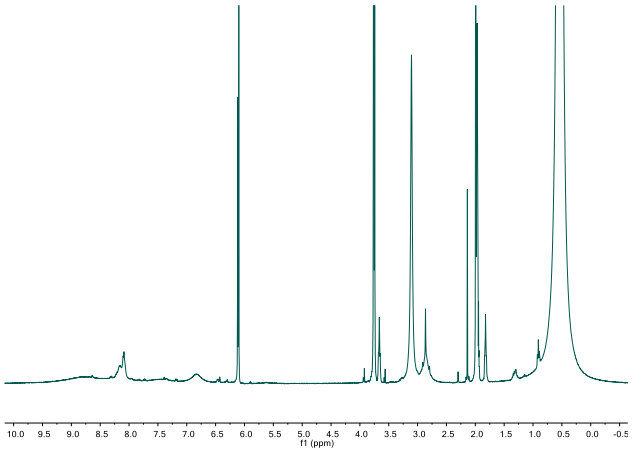

Figure D24. ^{1}H NMR spectrum of [(BPM^{NMe2})Fe(L)$_2$]OTf$_2$ (L = MeCN, NH$_3$), formed by mixing [(BPM^{NMe2})Fe(MeCN)$_2$]OTf$_2$ with 75 equivalents of NH$_3$ in CD$_3$CN at 25 °C.

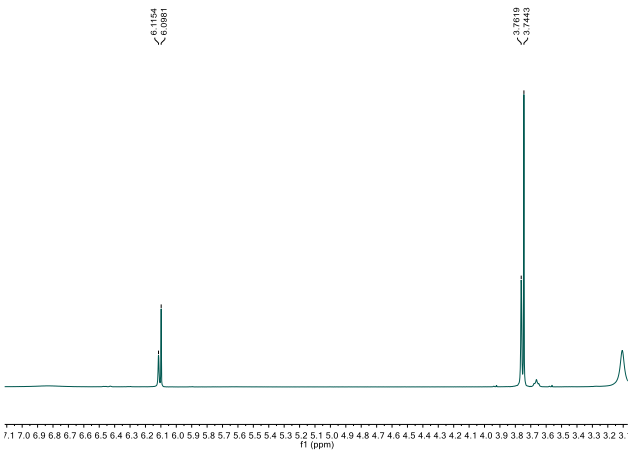

Figure D25. Trimethoxybenzene signals used for Evan's method for [(BPM^{NMe2})Fe(L)$_2$]OTf$_2$ (L = MeCN, NH$_3$), formed by mixing [(BPM^{NMe2})Fe(MeCN)$_2$]OTf$_2$ with 75 equivalents of NH$_3$ in CD$_3$CN at 25 °C. [Fe] = 0.011 M, $\Delta f = 7.0$ Hz, $f = 400.15$ MHz, $\mu_B = 0.96$.

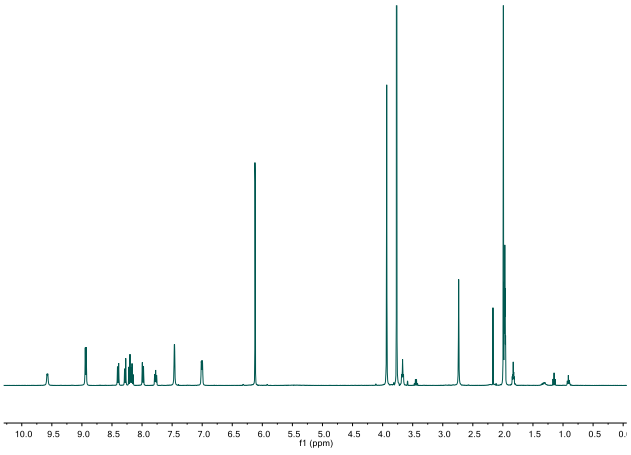

Figure D26. ^{1}H NMR spectrum of [(BPM^{OMe})Fe(MeCN)$_2$]OTf$_2$ in CD_3CN at 25 °C.

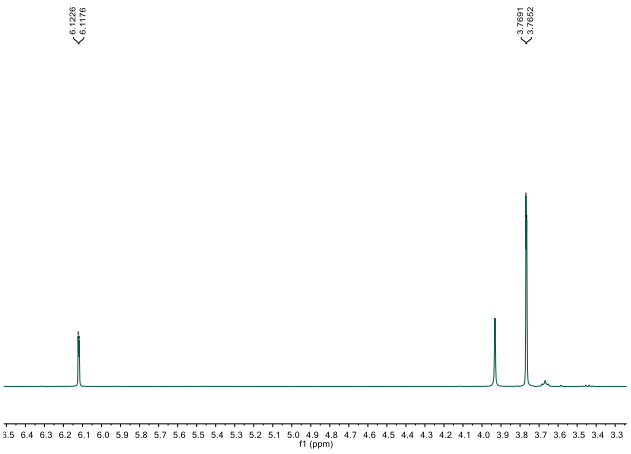

Figure D27. Trimethoxybenzene signals used for Evan's method for [(BPM^{OMe})Fe(MeCN)$_2$]OTf$_2$ in CD_3CN at 25 °C. [Fe] = 0.011 M, Δf = 1.8 Hz, f = 400.15 MHz, μ_B = 0.48.

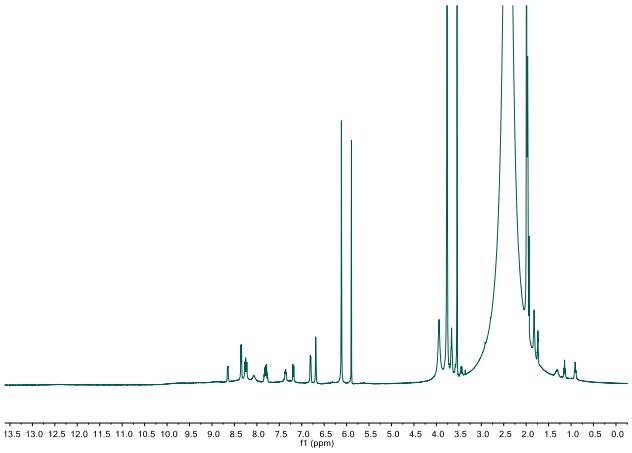

Figure D28. ^{1}H NMR spectrum of [(BPM^{OMe})Fe(L)$_2$]OTf$_2$ (L = MeCN, NH$_3$), formed by mixing [(BPM^{OMe})Fe(MeCN)$_2$]OTf$_2$ with 75 equivalents of NH$_3$ in CD$_3$CN at 25 °C.

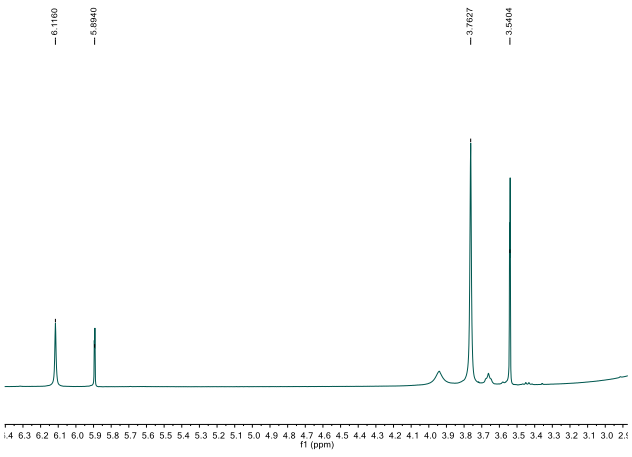

Figure D29. Trimethoxybenzene signals used for Evan's method for [(BPM^{OMe})Fe(L)$_2$]OTf$_2$ (L = MeCN, NH$_3$), formed by mixing [(BPM^{OMe})Fe(MeCN)$_2$]OTf$_2$ with 75 equivalents of NH$_3$ in CD$_3$CN at 25 °C. [Fe] = 0.011 M, Δf = 88.9 Hz, f = 400.15 MHz, μ_B = 3.4.

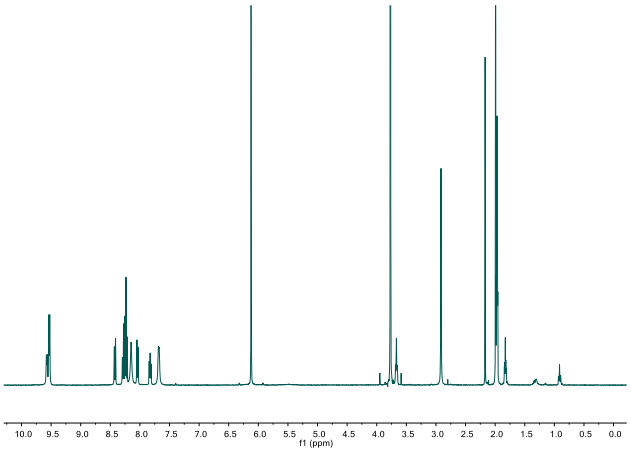

Figure D30. ^{1}H NMR spectrum of [(BPM^{CF3})Fe(MeCN)$_2$]OTf$_2$ in CD_3CN at 25 °C.

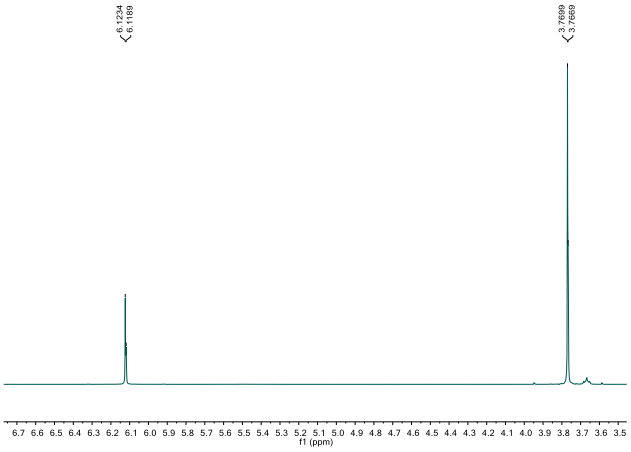

Figure D31. Trimethoxybenzene signals used for Evan's method for [(BPM^{CF3})Fe(MeCN)$_2$]OTf$_2$ in CD_3CN at 25 °C. [Fe] = 0.011 M, Δf = 1.5 Hz, f = 400.15 MHz, μ_B = 0.45.

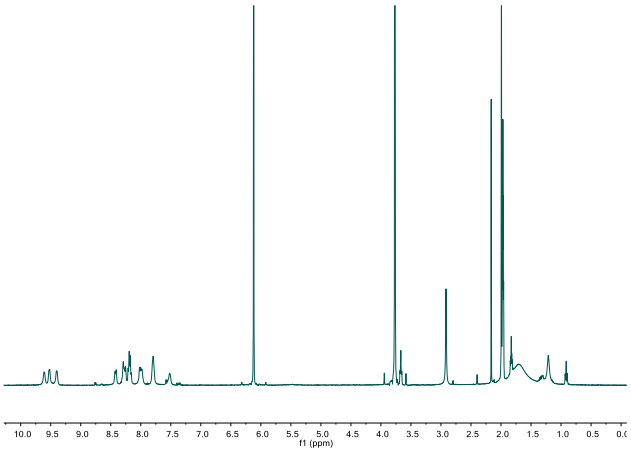

Figure D32. ^{1}H NMR spectrum of [(BPM^{CF3})Fe(L)$_2$]OTf$_2$ (L = MeCN, NH$_3$), formed by mixing [(BPM^{CF3})Fe(MeCN)$_2$]OTf$_2$ with 5 equivalents of NH$_3$ in CD$_3$CN at 25 °C. Demetallation occurs with 75 equivalents.

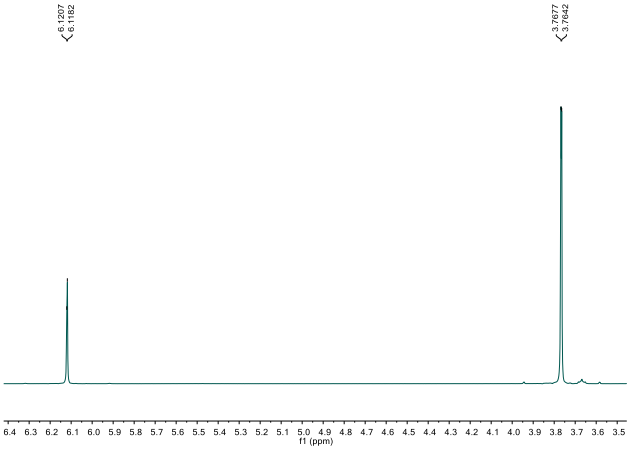

Figure D33. Trimethoxybenzene signals used for Evan's method for [(BPM^{CF3})Fe(L)$_2$]OTf$_2$ (L = MeCN, NH$_3$), formed by mixing [(BPM^{CF3})Fe(MeCN)$_2$]OTf$_2$ with 5 equivalents of NH$_3$ in CD$_3$CN at 25 °C. Demetallation occurs with 75 equivalents. [Fe] = 0.011 M, Δf = 1.2 Hz, f = 400.15 MHz, μ_B = 0.40.

D9. UV-vis titration data for stability against demetallation

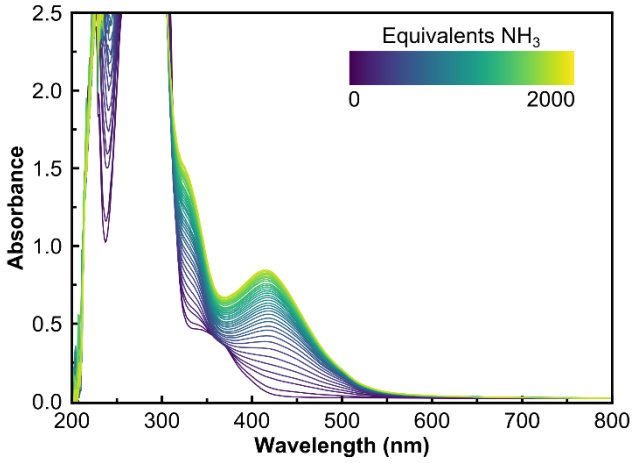

Figure D34. UV-vis spectra of acetonitrile solution containing 0.12 mM $[(TPA^{NMe2})Fe(MeCN)_2]OTf_2$ and varying equivalents NH_3 in a 1 cm cuvette.

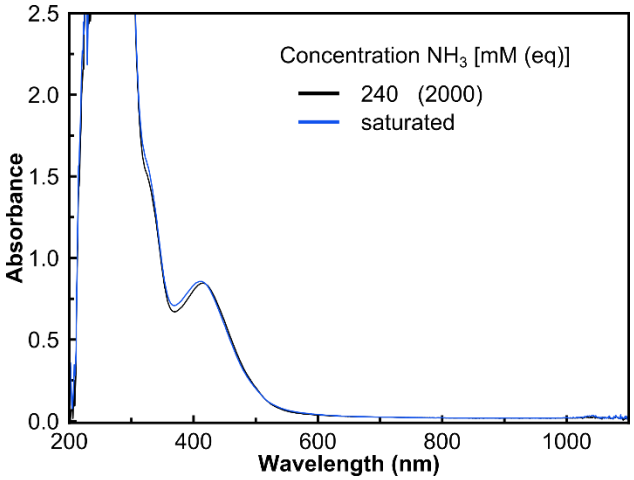

Figure D35. Selected UV-vis spectra used for determining the onset of demetallation for acetonitrile solution containing 0.12 mM $[(TPA^{NMe2})Fe(MeCN)_2]OTf_2$ and varying equivalents NH_3 in a 1 cm cuvette.

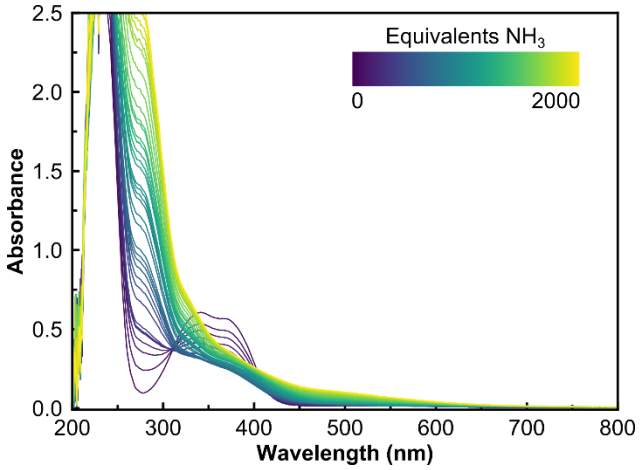

Figure D36. UV-vis spectra of acetonitrile solution containing 0.12 mM $[(TPA^{OMe})Fe(MeCN)_2]OTf_2$ and varying equivalents NH_3 in a 1 cm cuvette.

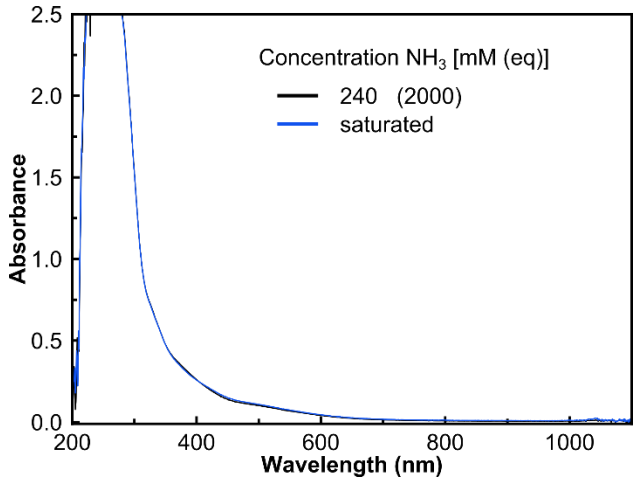

Figure D37. Selected UV-vis spectra used for determining the onset of demetallation for acetonitrile solution containing 0.12 mM $[(TPA^{OMe})Fe(MeCN)_2]OTf_2$ and varying equivalents NH_3 in a 1 cm cuvette.

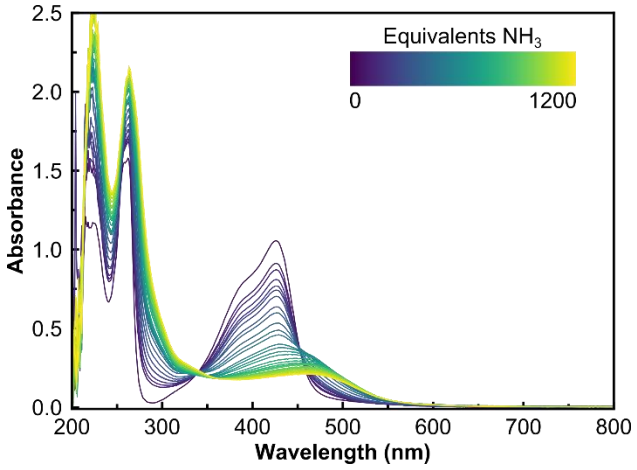

Figure D38. UV-vis spectra of acetonitrile solution containing 0.12 mM $[(TPA^{CF3})Fe(MeCN)_2]OTf_2$ and varying equivalents NH_3 in a 1 cm cuvette.

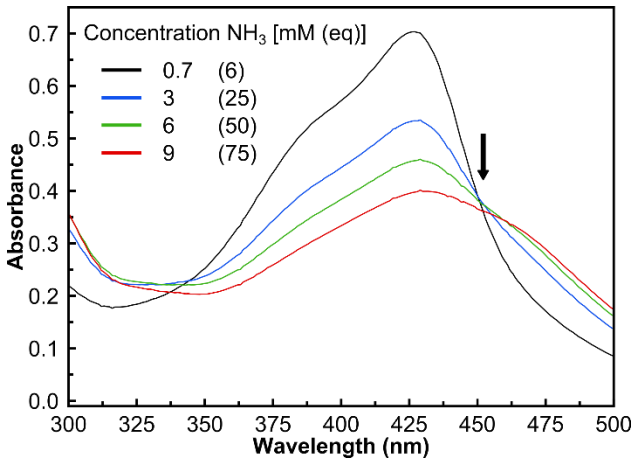

Figure D39. Selected UV-vis spectra used for determining the onset of demetallation for acetonitrile solution containing 0.12 mM $[(TPA^{CF3})Fe(MeCN)_2]OTf_2$ and varying equivalents NH_3 in a 1 cm cuvette.

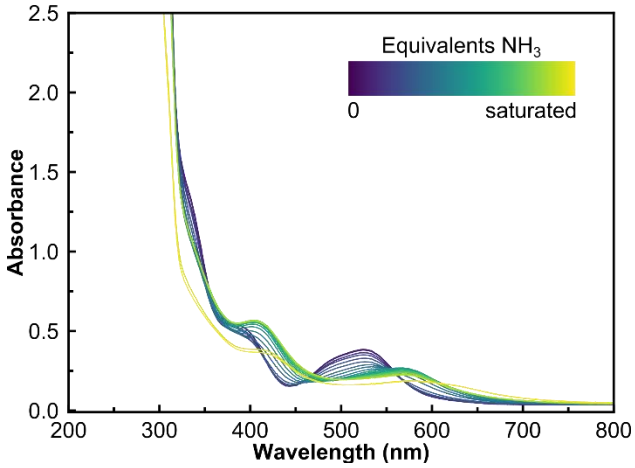

Figure D40. UV-vis spectra of acetonitrile solution containing 0.12 mM $[(BPM^{NMe2})Fe(MeCN)_2]OTf_2$ and varying equivalents NH_3 in a 1 cm cuvette.

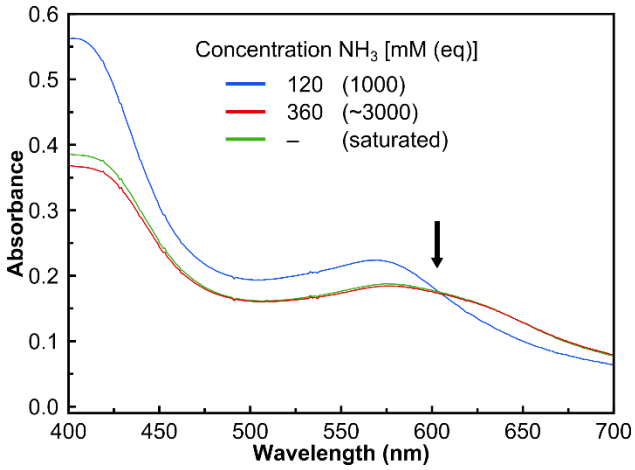

Figure D41. Selected UV-vis spectra used for determining the onset of demetallation for acetonitrile solution containing 0.12 mM $[(BPM^{NMe2})Fe(MeCN)_2]OTf_2$ and varying equivalents NH_3 in a 1 cm cuvette.

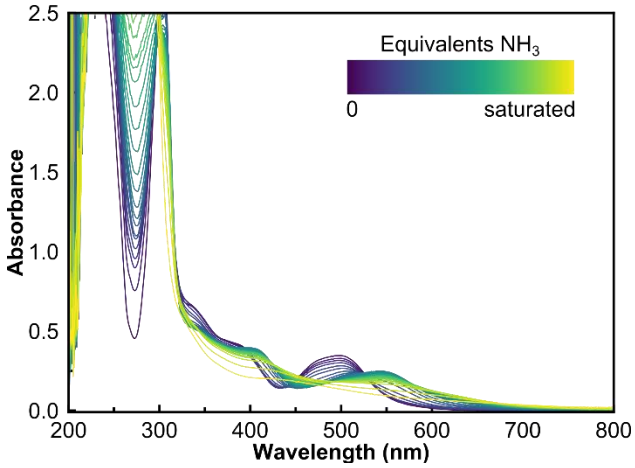

Figure D42. UV-vis spectra of acetonitrile solution containing 0.12 mM $[(BPM^{OMe})Fe(MeCN)_2]OTf_2$ and varying equivalents NH_3 in a 1 cm cuvette.

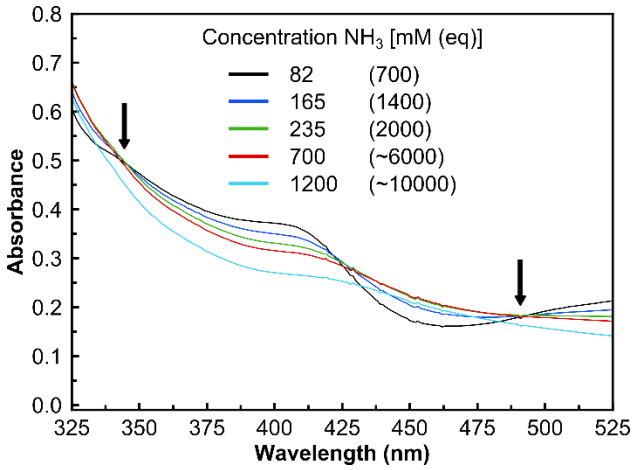

Figure D43. Selected UV-vis spectra used for determining the onset of demetallation for acetonitrile solution containing 0.12 mM $[(BPM^{OMe})Fe(MeCN)_2]OTf_2$ and varying equivalents NH_3 in a 1 cm cuvette.

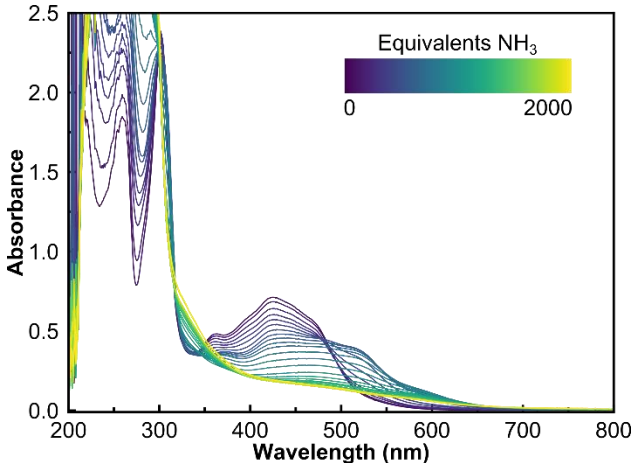

Figure D44. UV-vis spectra of acetonitrile solution containing 0.12 mM $[(BPM^{CF3})Fe(MeCN)_2]OTf_2$ and varying equivalents NH_3 in a 1 cm cuvette.

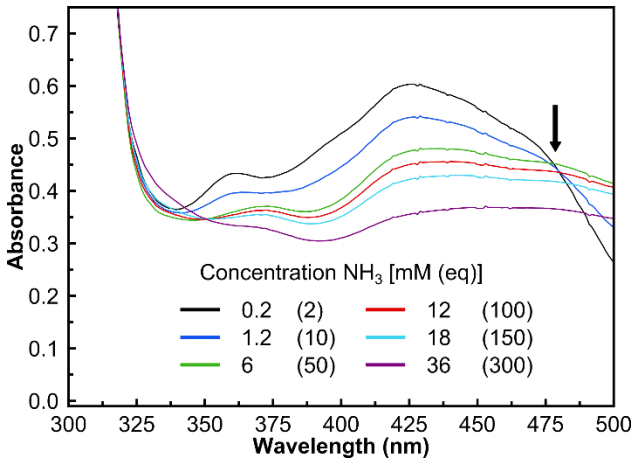

Figure D45. Selected UV-vis spectra used for determining the onset of demetallation for acetonitrile solution containing 0.12 mM $[(BPM^{CF3})Fe(MeCN)_2]OTf_2$ and varying equivalents NH_3 in a 1 cm cuvette.

D10. Mass spectrometry

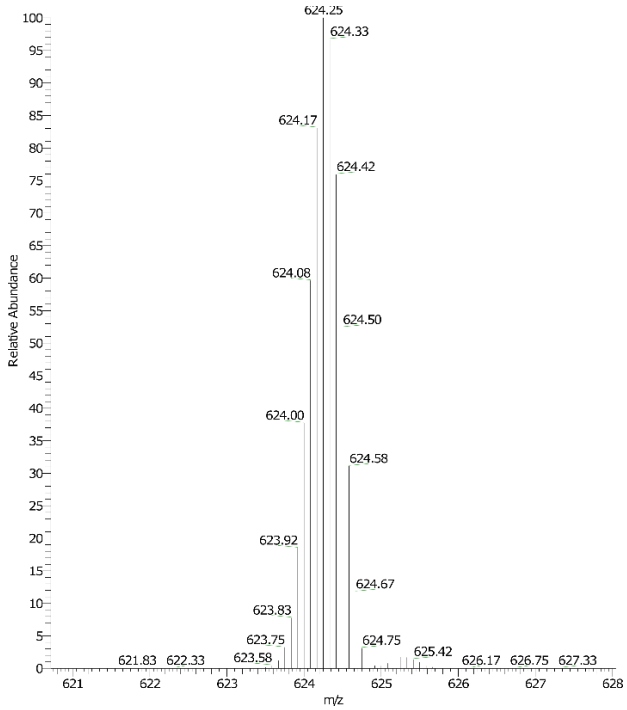

Figure D47. ESI mass spectrum of $[(TPA^{NMe2})Fe(MeCN)_2]OTf_2$ in acetonitrile.

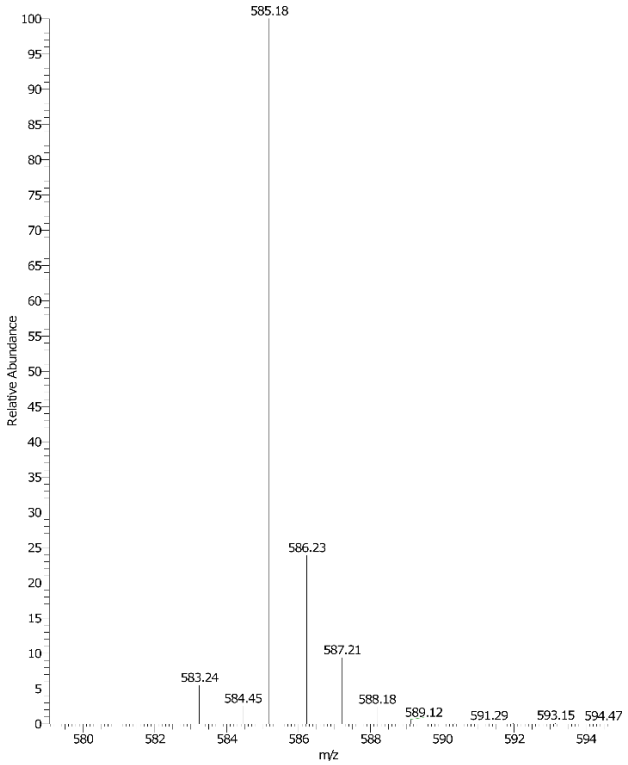

Figure D48. ESI mass spectrum of $[(TPA^{OMe})Fe(MeCN)_2]OTf_2$ in acetonitrile.

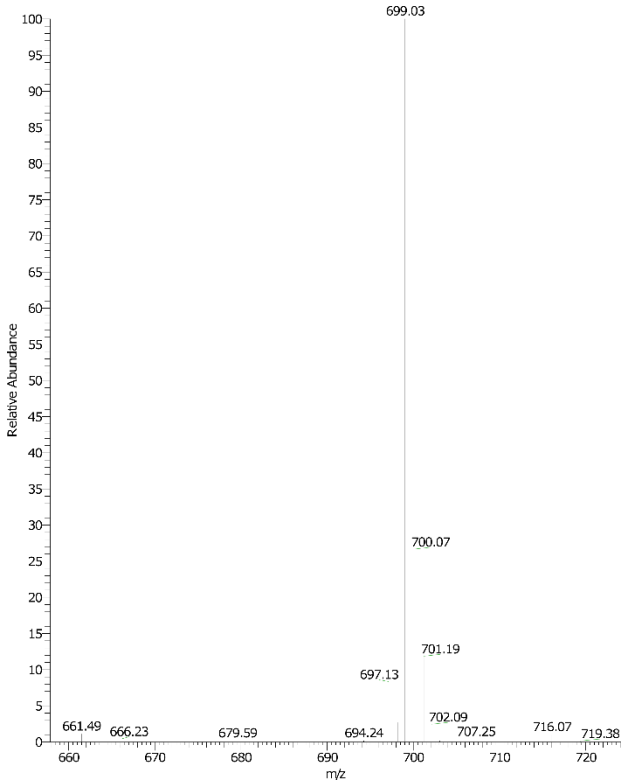

Figure D49. ESI mass spectrum of $[(TPA^{CF3})Fe(MeCN)_2]OTf_2$ in acetonitrile.

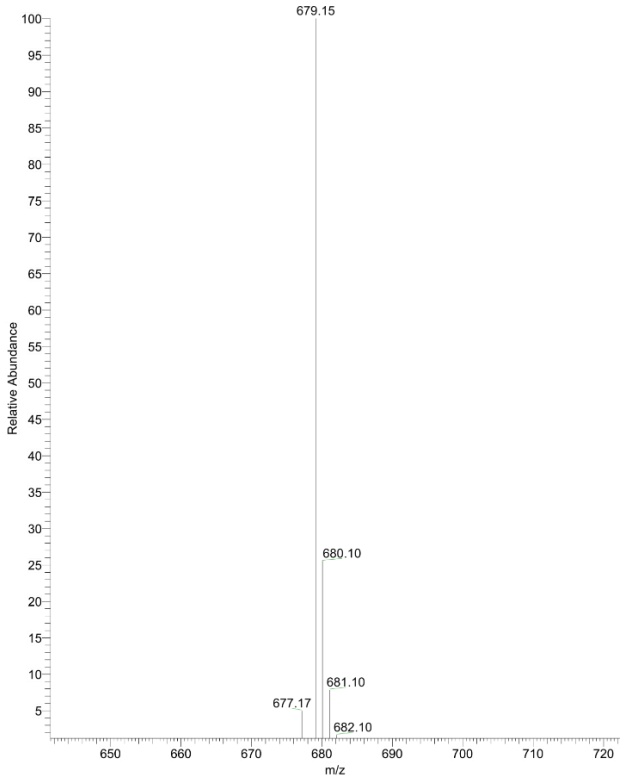

Figure D50. ESI mass spectrum of $[(BPM^{CF3})Fe(MeCN)_2]OTf_2$ in acetonitrile.

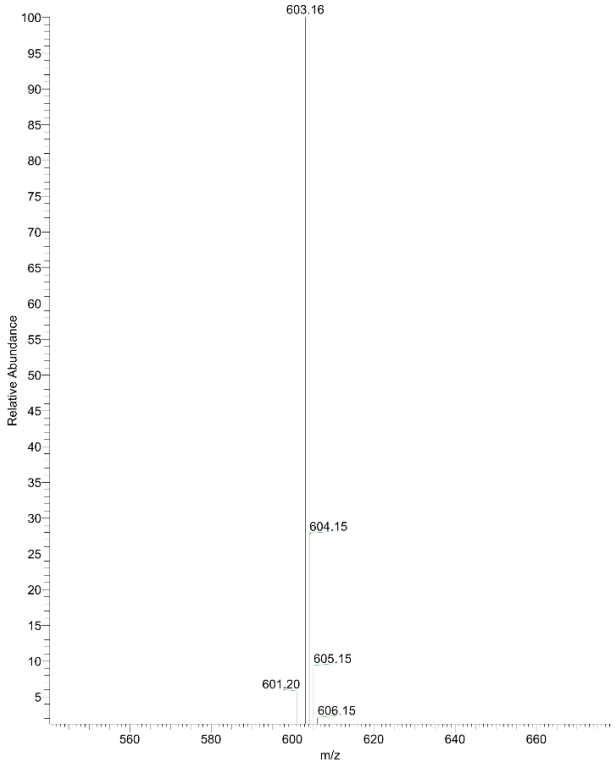

Figure D51. ESI mass spectrum of $[(BPM^{OMe})Fe(MeCN)_2]OTf_2$ in acetonitrile.

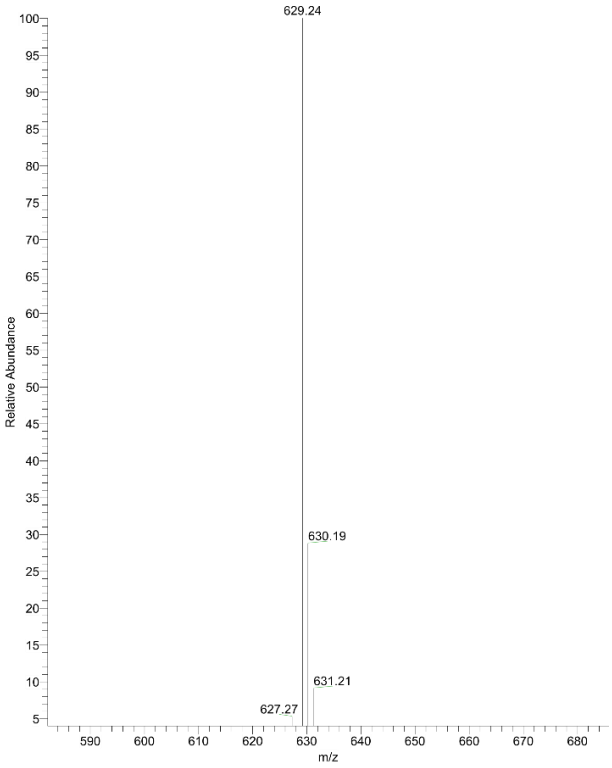

Figure D52. ESI mass spectrum of $[(BPM^{NMe2})Fe(MeCN)_2]OTf_2$ in acetonitrile.

D11. NMR spectra

TPA^{CF3} (tris(4-(trifluoromethyl)-2-picolyl)amine)

^{1}H NMR:

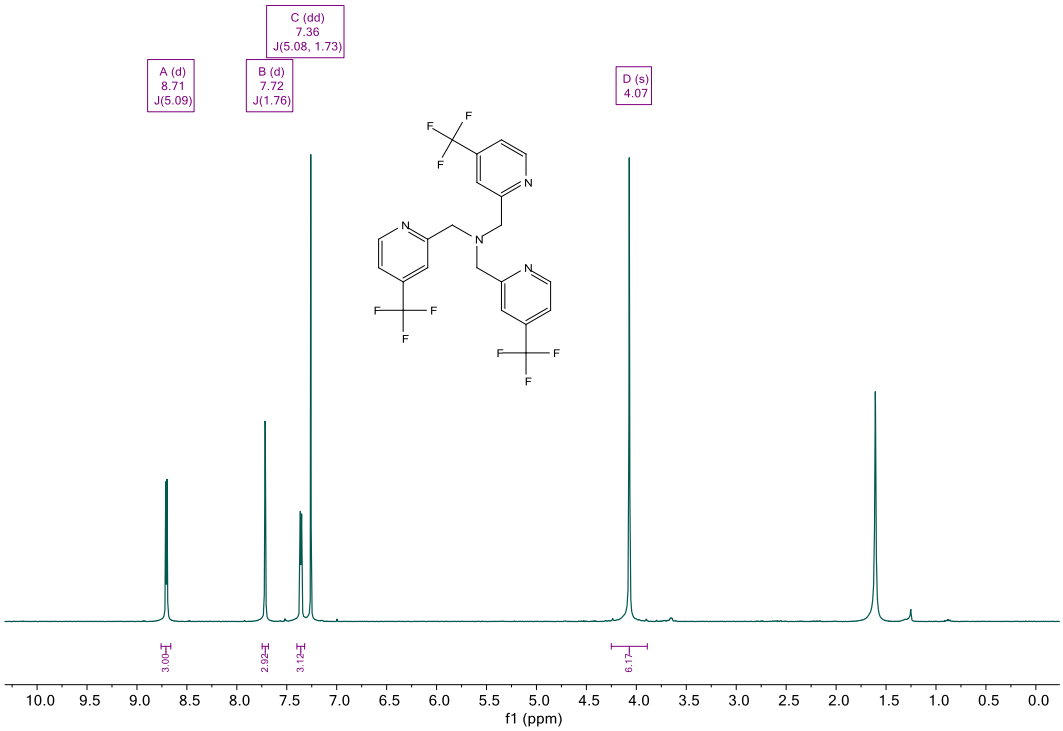

^{13}C{^{1}H} NMR:

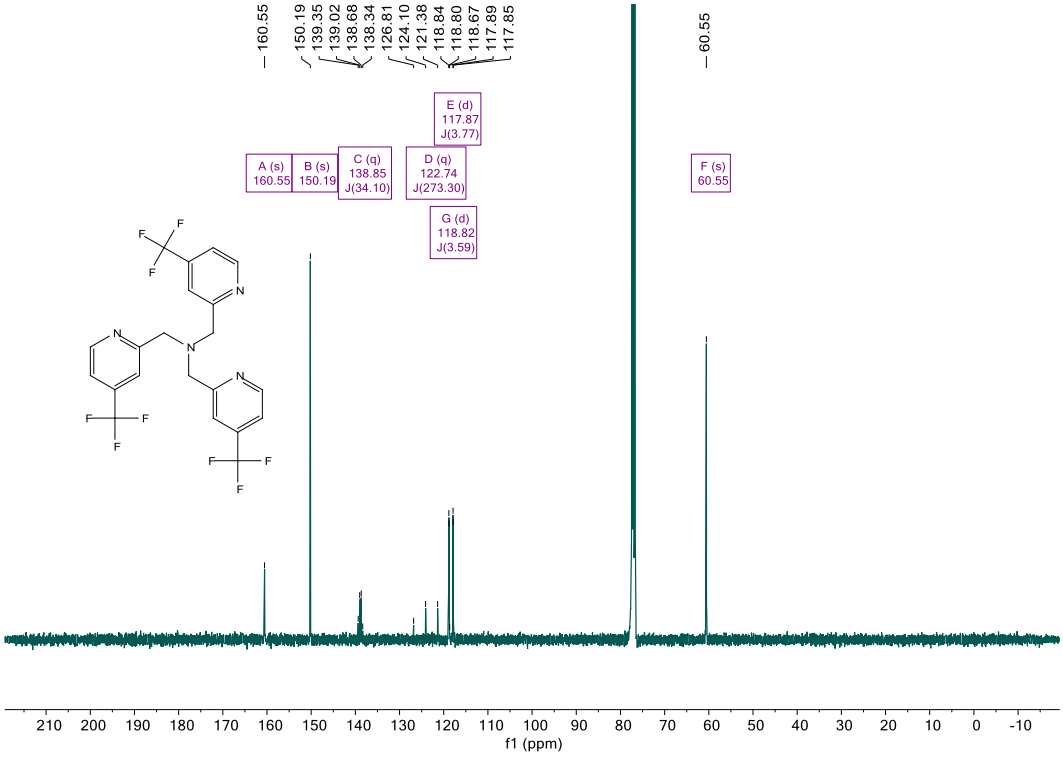

2,2'-(ethene-1,1-diyl)bis(4-(dimethylamino)pyridine)

^{1}H NMR:

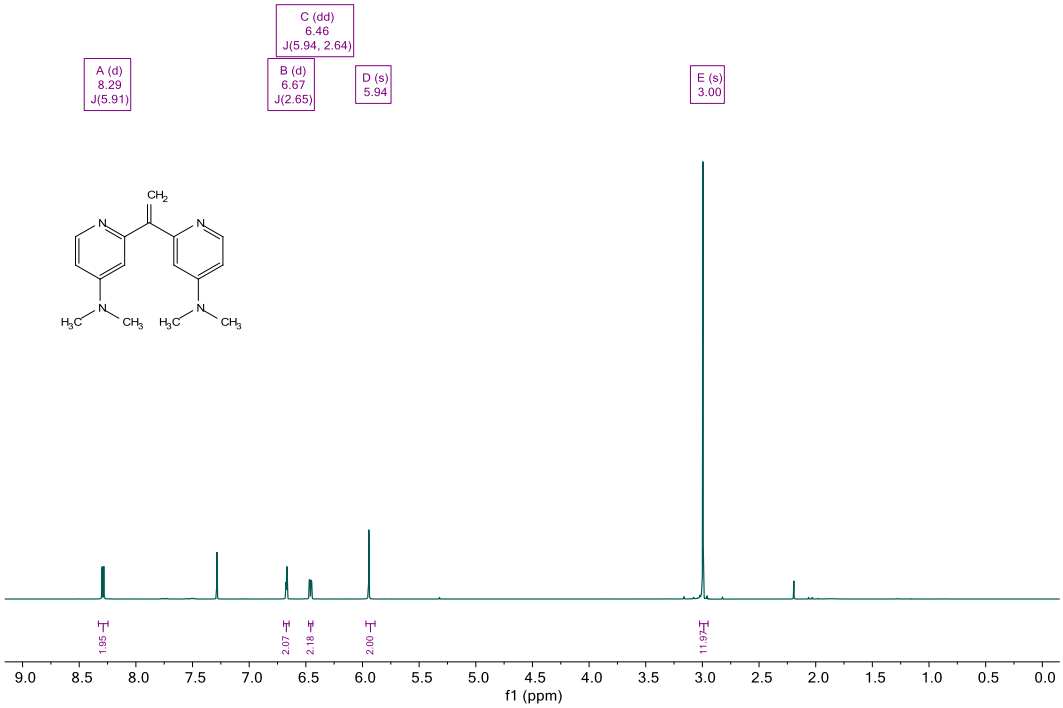

^{13}C{^{1}H} NMR:

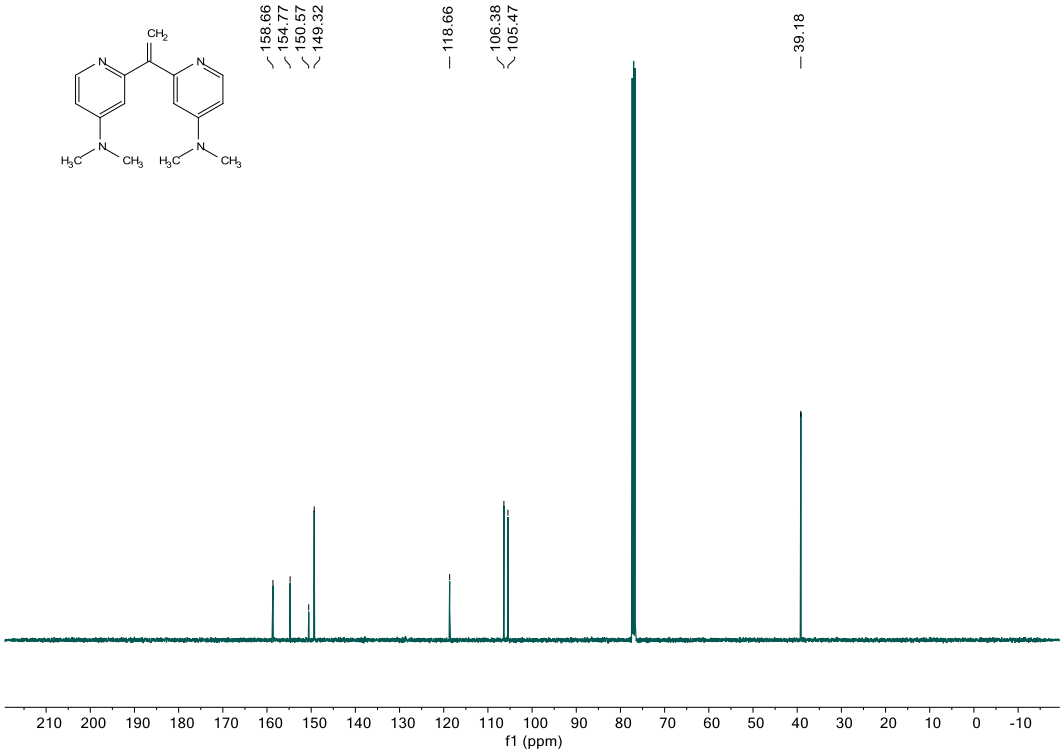

2,2'-(ethane-1,1-diyl)bis(4-(dimethylamino)pyridine)

^{1}H NMR:

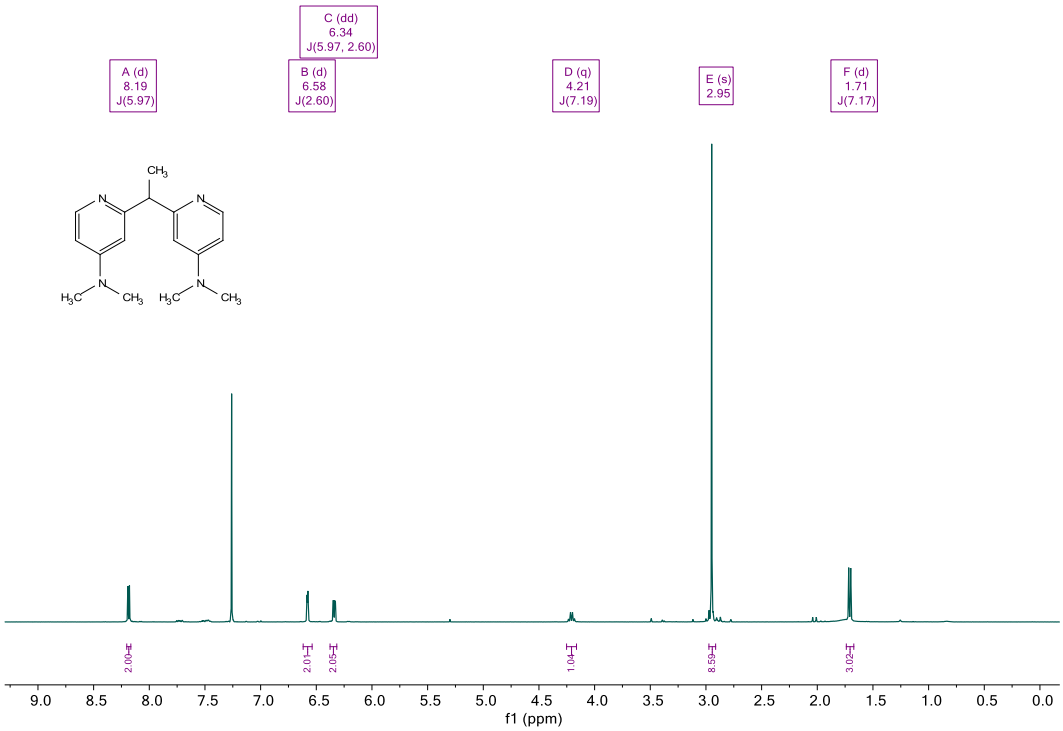

^{13}C{^{1}H} NMR:

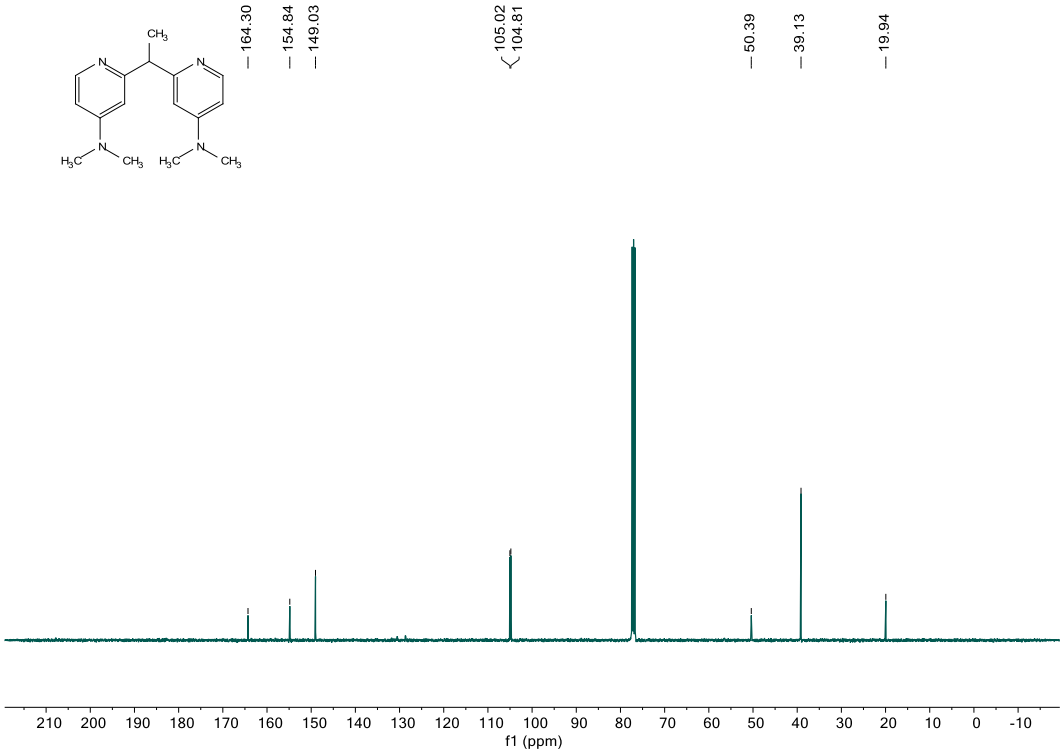

BPM^{NMe2} (6-(1,1-bis(4-(dimethylamino)pyridin-2-yl)ethyl)-2,2'-bipyridine)

^{1}H NMR:

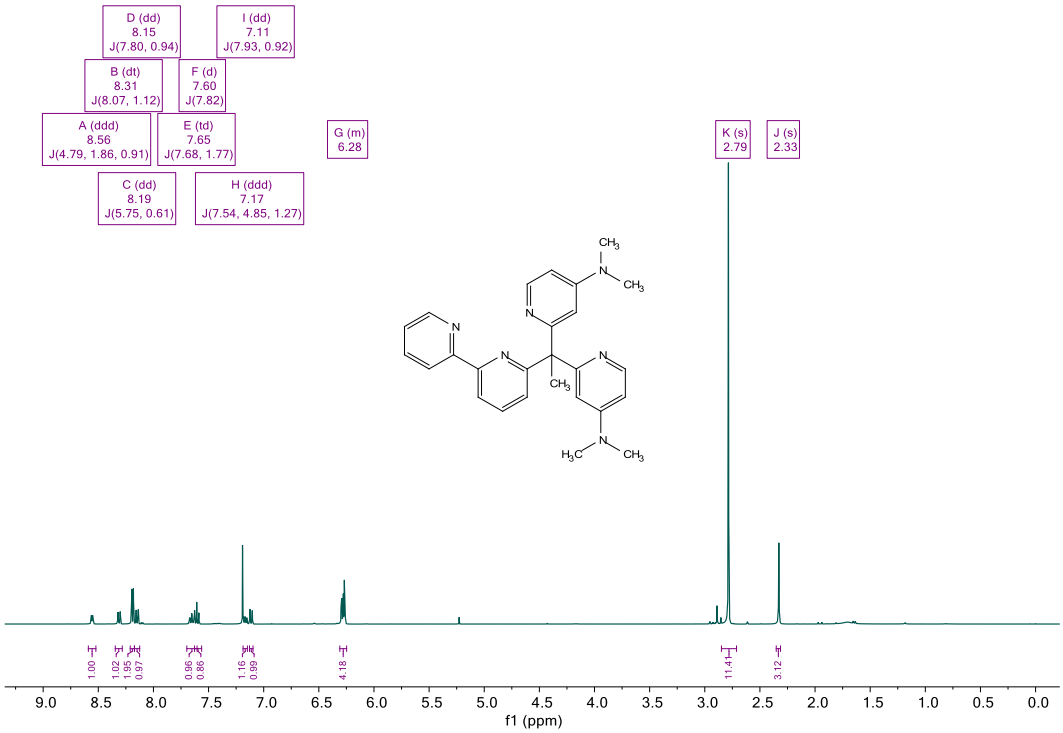

^{13}C{^{1}H} NMR:

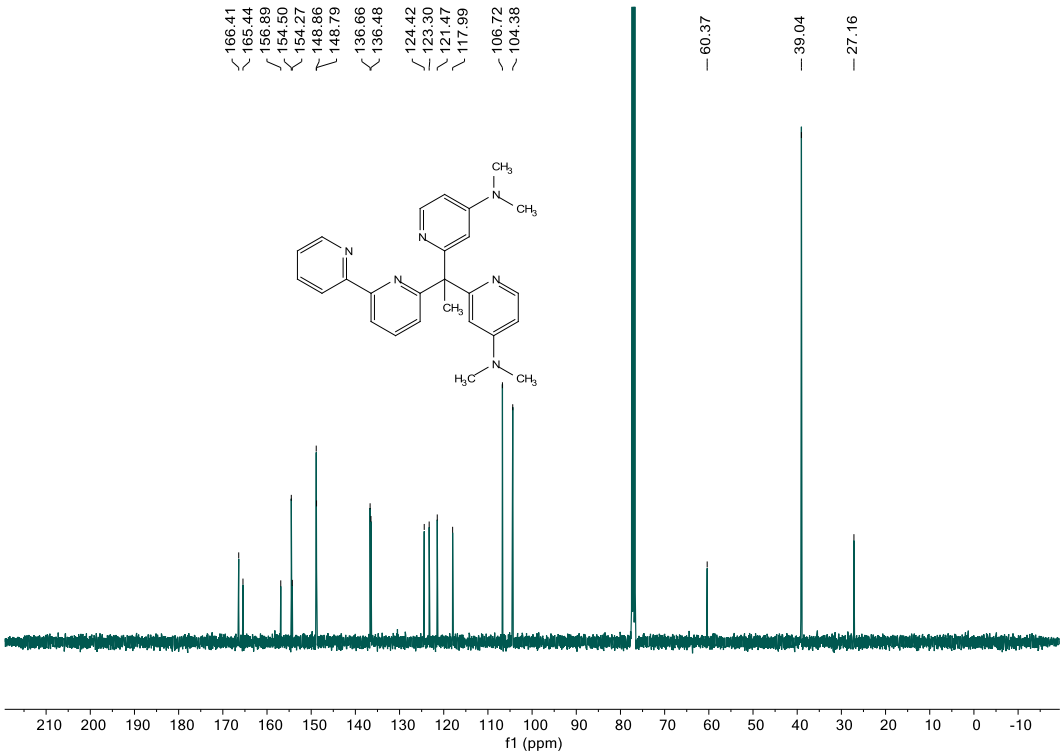

bis(4-methoxypyridin-2-yl)methanone

^{1}H NMR:

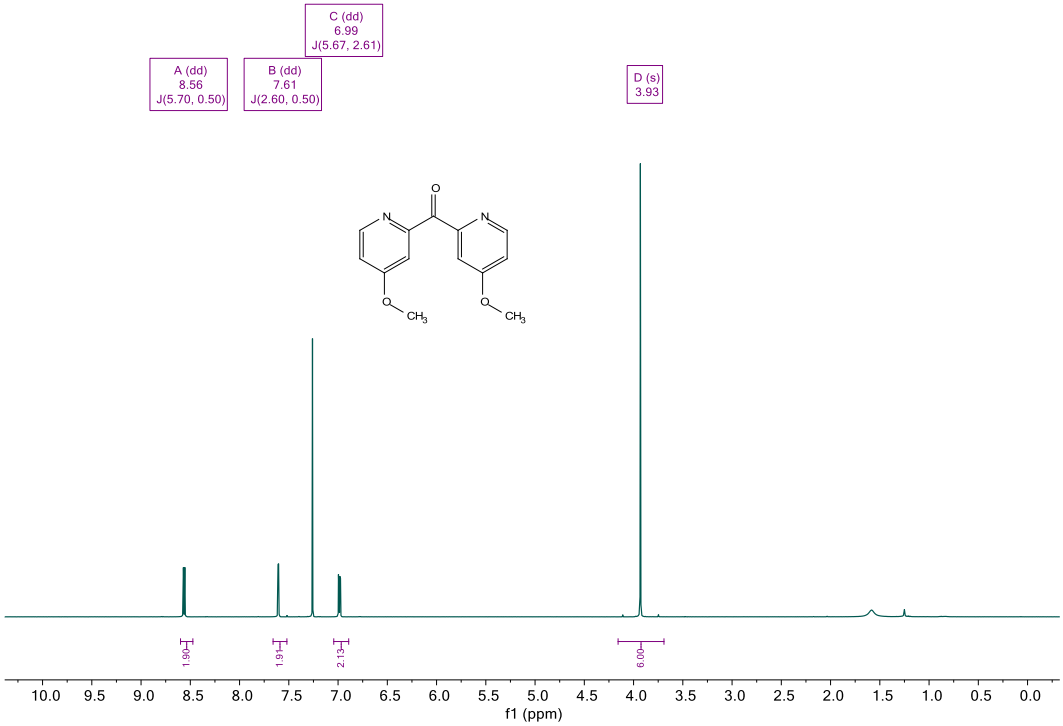

^{13}C{^{1}H} NMR:

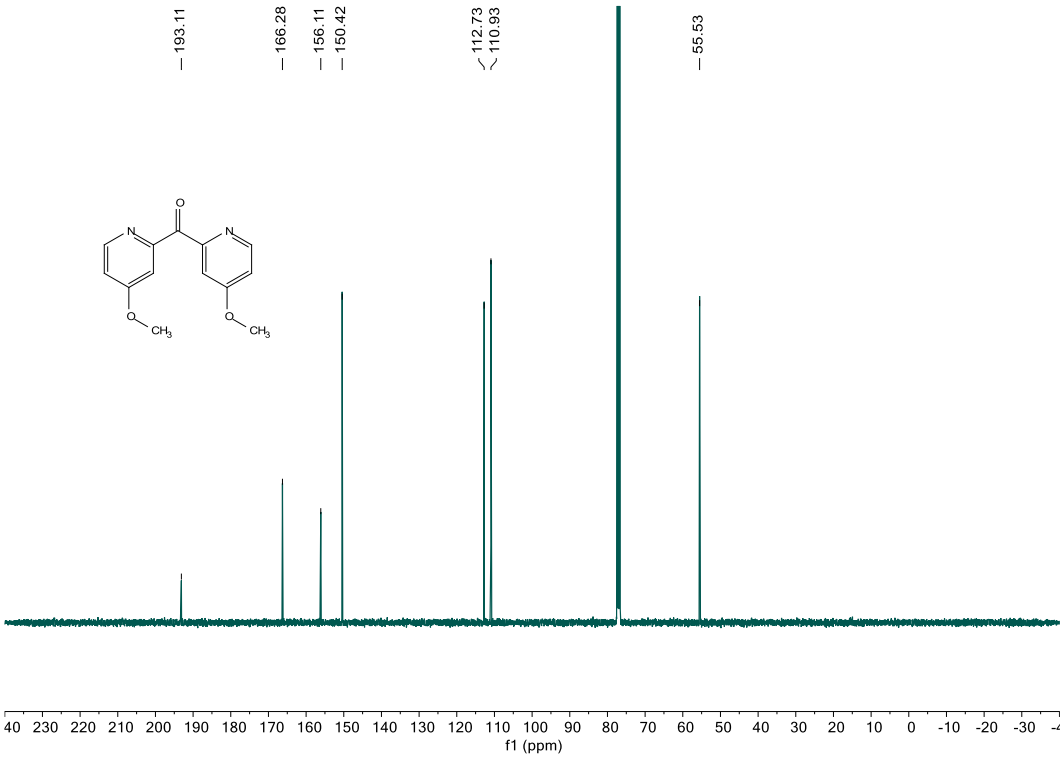

2,2'-(ethene-1,1-diyl)bis(4-(methoxypyridine)

^{1}H NMR:

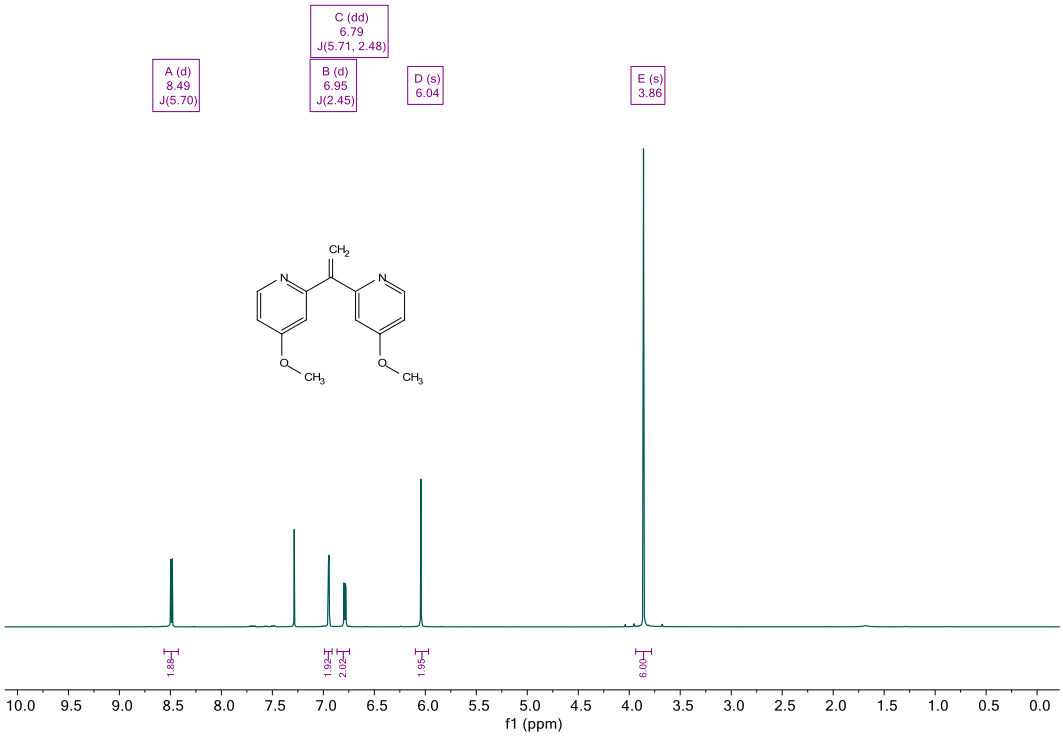

^{13}C{^{1}H} NMR:

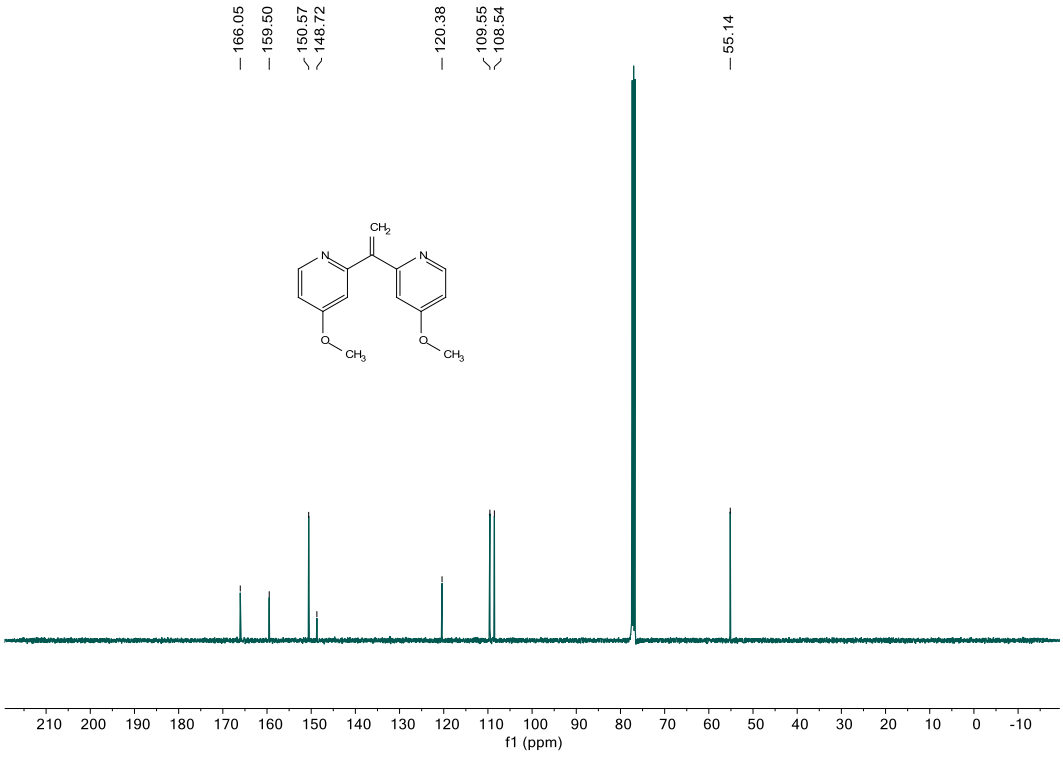

2,2'-(ethane-1,1-diyl)bis(4-methoxypyridine)

^{1}H NMR:

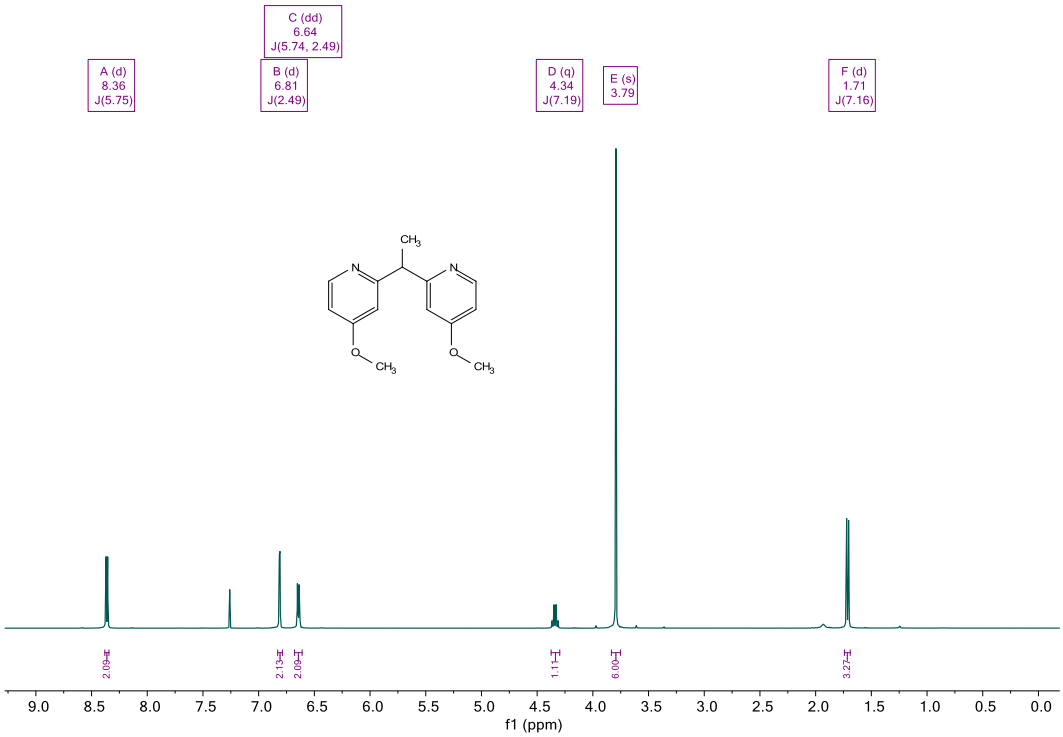

^{13}C{^{1}H} NMR:

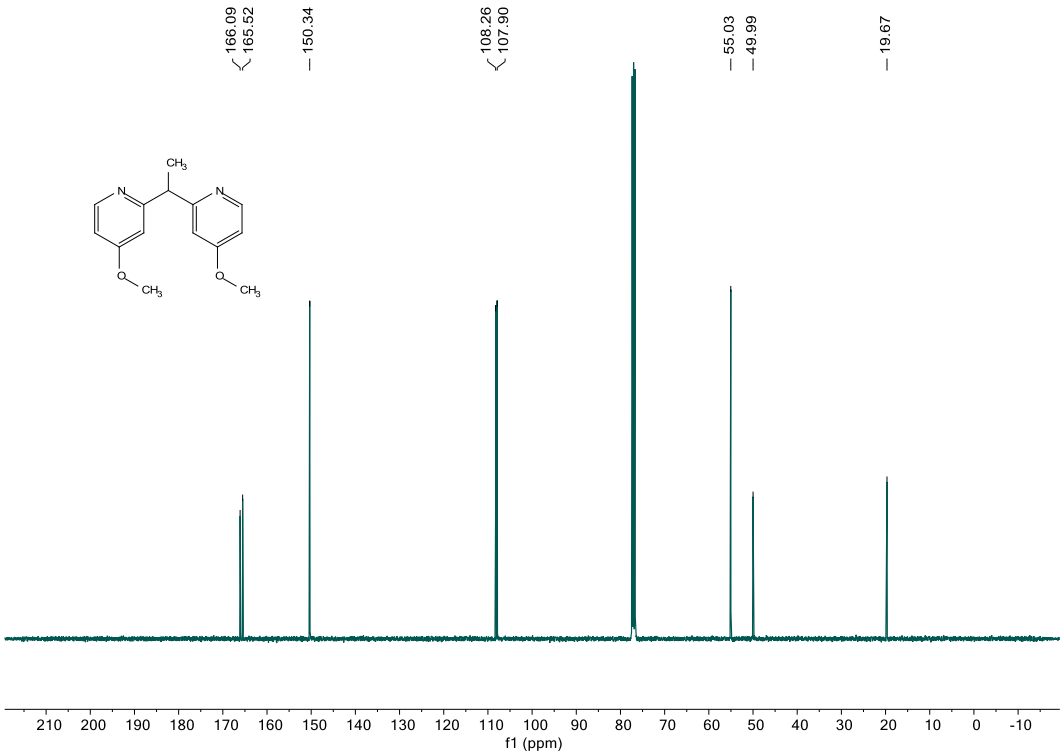

2,2',2'',2'''- 2,2',2'',2'''-(butane-1,1,3,3-tetrayl)tetrakis(4-methoxypyridine)

^{1}H NMR:

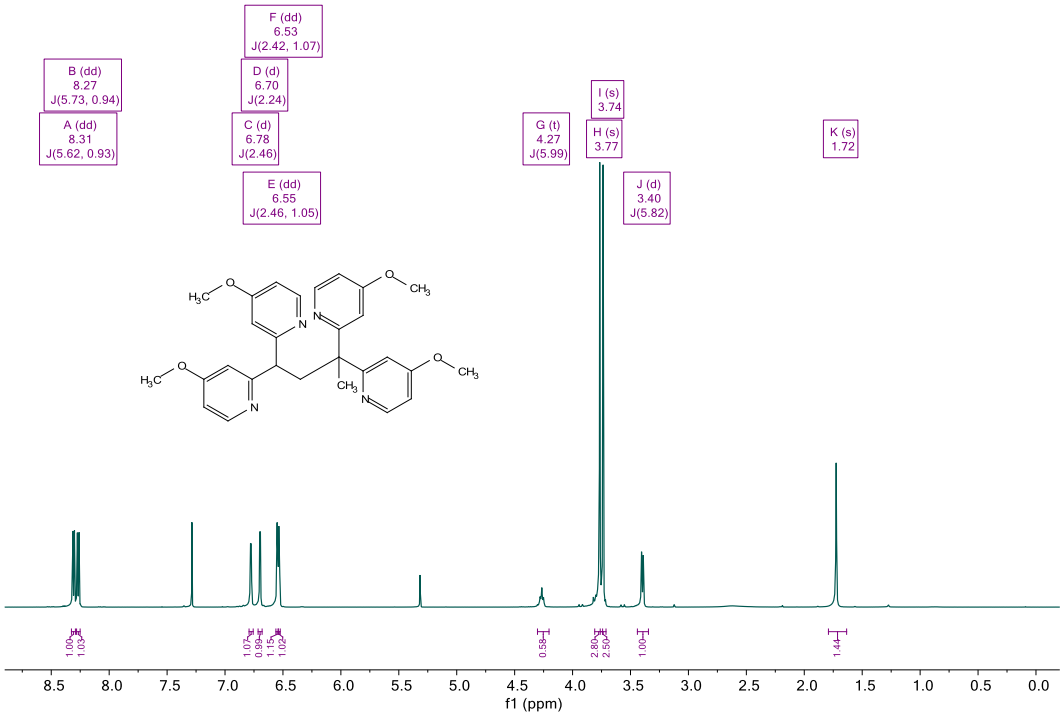

^{13}C{^{1}H} NMR:

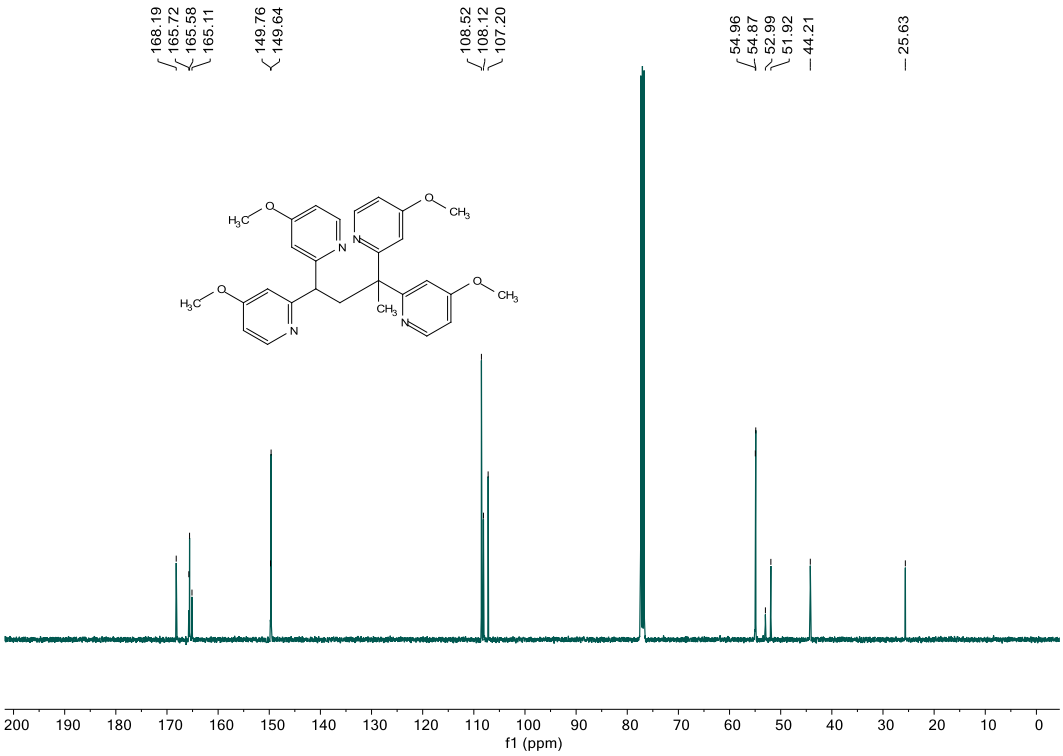

BPM^{OMe} (6-(1,1-bis(4-methoxypyridin-2-yl)ethyl)-2,2'-bipyridine)

^{1}H NMR:

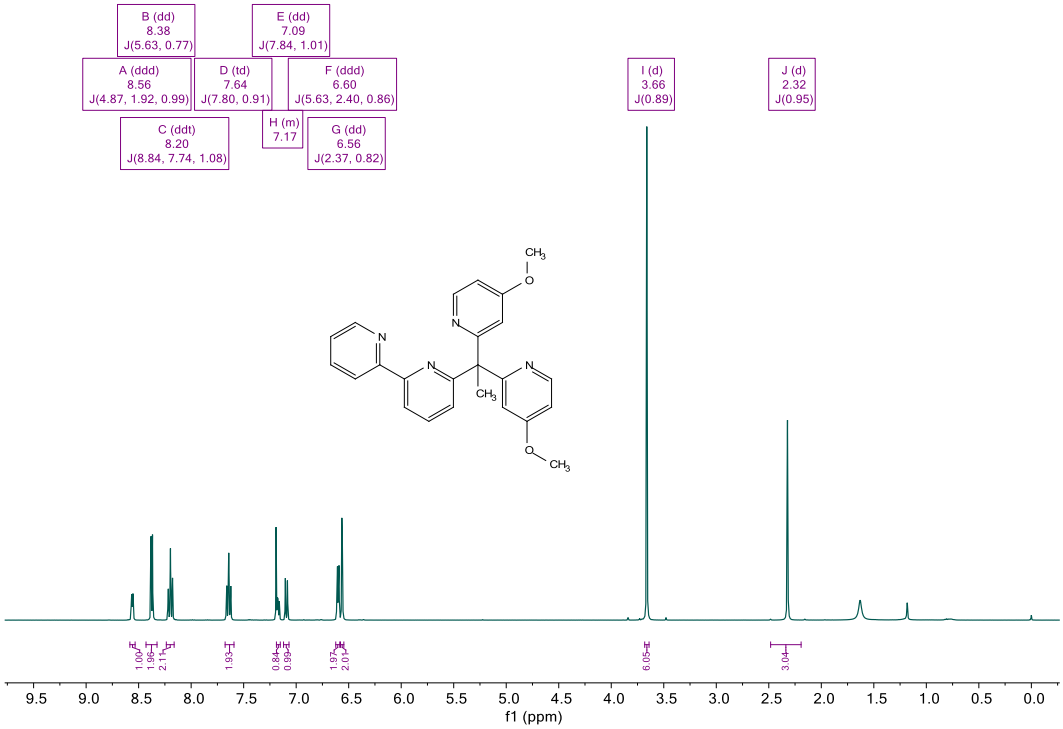

^{13}C{^{1}H} NMR:

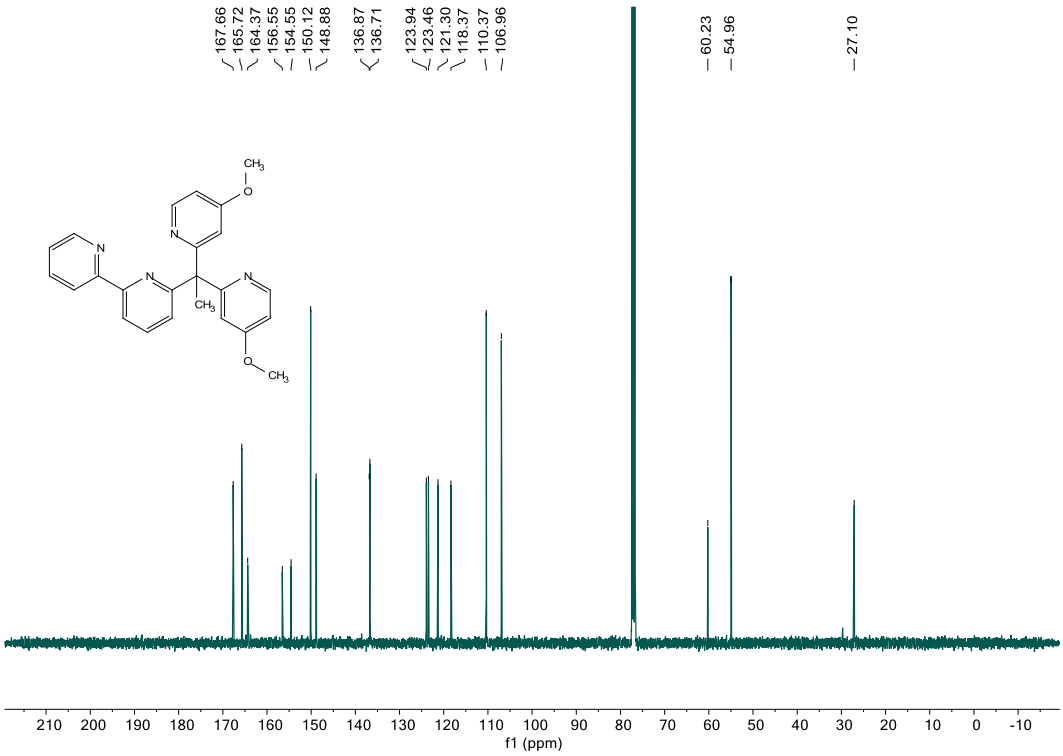

2,2'-(ethane-1,1-diyl)bis(4-(trifluoromethyl)pyridine)

^{1}H NMR:

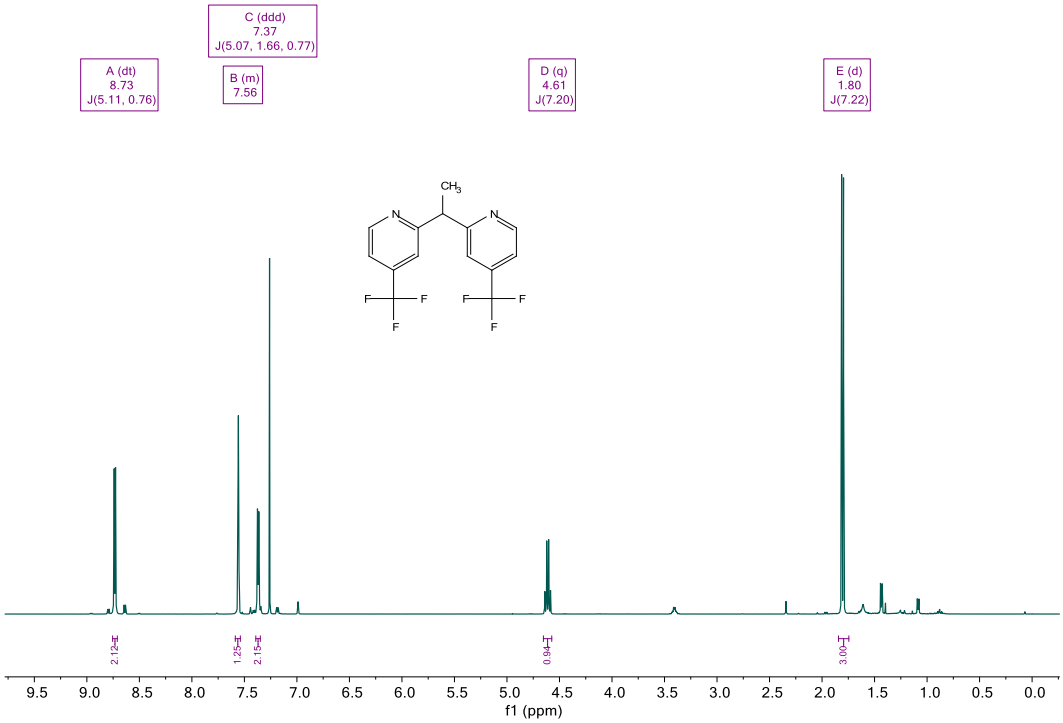

^{13}C{^{1}H} NMR:

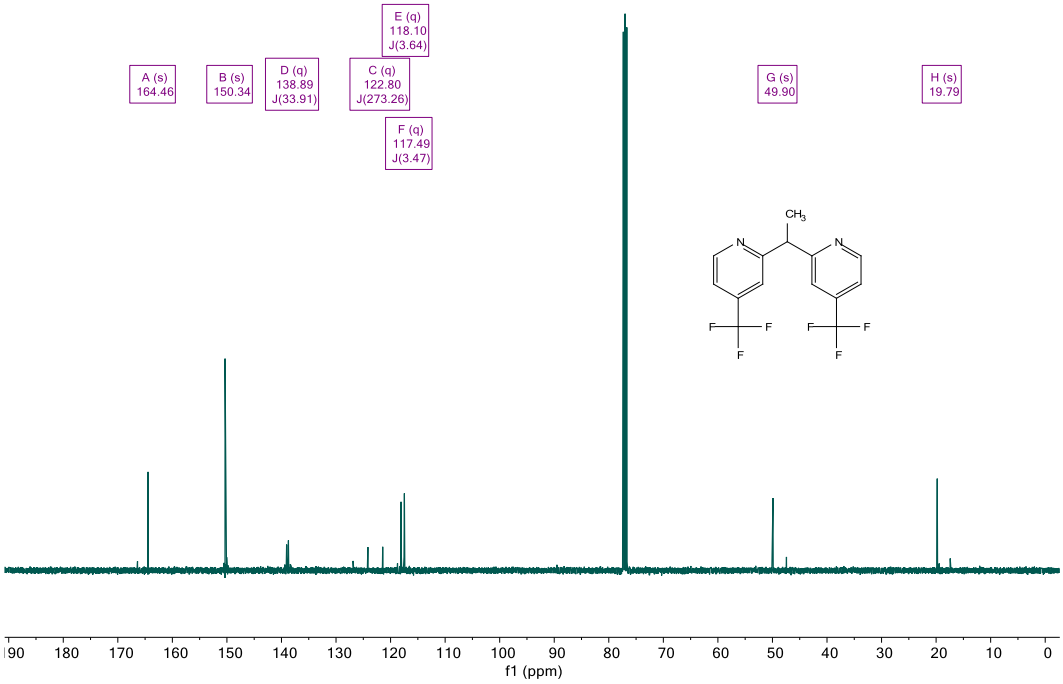

BPM^{CF3} (6-(1,1-bis(4-(trifluoromethyl)pyridin-2-yl)ethyl)-2,2'-bipyridine)

^{1}H NMR:

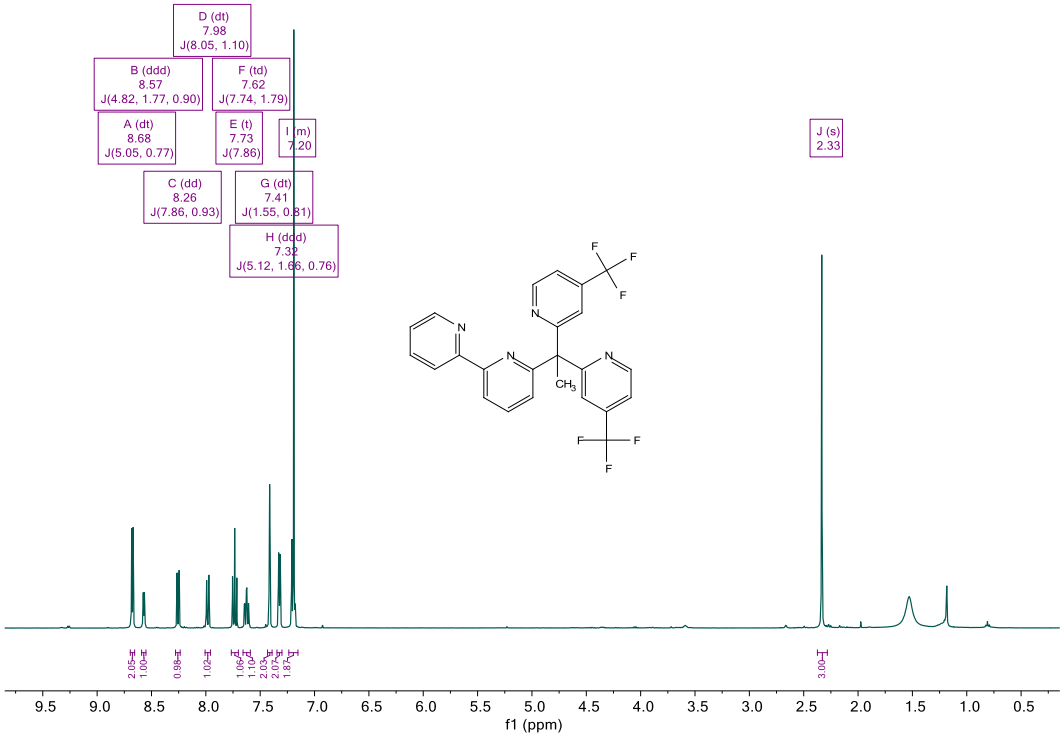

^{13}C{^{1}H} NMR:

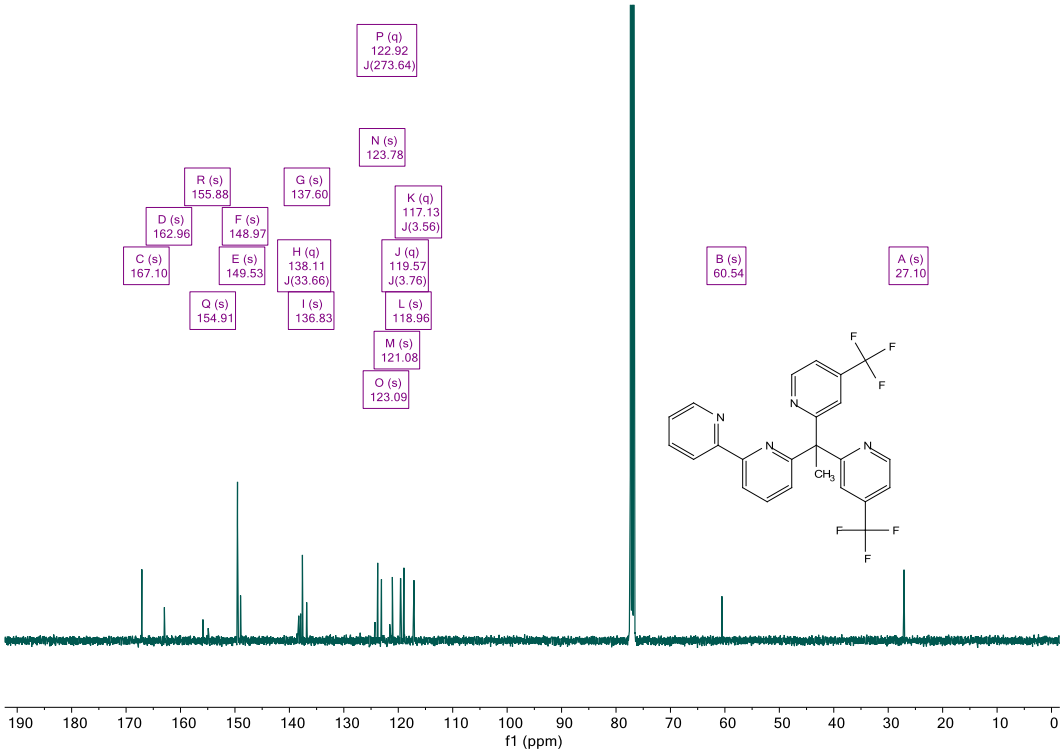

D.12 References

[1] Canary, J. W.; Wang, Y.; Roy, R. Tris[(2-pyridyl)methyl]amine (TPA) and (+)-bis[(2-pyridyl)methyl]-1-(2-pyridyl)-ethylamine (α-METPA). *Inorg. Synth.* **1998**, *32*, 70–75.

[2] Diebold, A.; Hagen, K. S. Iron(II) Polyamine Chemistry: Variation of Spin State and Coordination Number in Solid State and Solution with Iron(II) Tris(2-pyridylmethyl)amine Complexes. *Inorg. Chem.* **1998**, *37*, 215–223.

[3] Khnayzer, R. S.; Thoi, V. S.; Nippe, M.; King, A. E.; Jurss, J. W.; El Roz, K. A.; Long, J. R.; Chang, C. J.; Castellano, F. N. Towards a Comprehensive Understanding of Visible-Light Photogeneration of Hydrogen from Water Using Cobalt(II) Polypyridyl Catalysts. *Energy Environ. Sci.* **2014**, *7*, 1477–1488.

[4] Chen, L.; Su, X.-J.; Jurss, J. W. Selective Alkane C–H Bond Oxidation Catalyzed by a Non-Heme Iron Complex Featuring a Robust Tetradentate Ligand. *Organometallics* **2018**, *37*, 4535–4539.

[5] Miller, S. L.; Chotana, G. A.; Fritz, J. A.; Chattopadhyay, B.; Maleczka, R. E., Jr.; Smith, M. R., III. C–H Borylation Catalysts that Distinguish Between Similarly Sized Substituents Like Fluorine and Hydrogen. *Org. Lett.* **2019**, *21*, 6388–6392.

[6] Zhang, C. X.; Kaderli, S.; Costas, M.; Kim, E.; Neuhold, Y.; Karlin, K. D.; Zuberbühler, A. D. Copper(I)–Dioxygen Reactivity of $[(L)Cu^{I}]^{+}$ (L = Tris(2-Pyridylmethyl)amine): Kinetic/Thermodynamic and Spectroscopic Studies Concerning the Formation of $Cu–O_2$ and $Cu_2–O_2$ Adducts as a Function of Solvent Medium and 4-Pyridyl Ligand Substituent Variations. *Inorg. Chem.* **2003**, *42*, 1807–1824.

[7] Koide, K.; Bein, K.; Bressin, R.; Burrows, J.; Gambino, A.; Leikauf, G.; Pham, D. Analogs of 2-Pralidoxime as Antidotes Against Organophosphorus Nerve Agents. WO2020027905A2, February 6, 2020.

[8] Nippe, M.; Khnayzer, R. S.; Panetier, J. A.; Zee, D. Z.; Olaiya, B. S.; Head-Gordon, M.; Chang, C. J.; Castellano, F. N.; Long, J. R. Catalytic Proton Reduction with Transition Metal Complexes of the Redox-Active Ligand Bpy2PYMe. *Chem. Sci.* **2013**, *4*, 3934–3945.

[9] Miller, S. L.; Chotana, G. A.; Fritz, J. A.; Chattopadhyay, B.; Maleczka, R. E.; Smith, M. R. C–H Borylation Catalysts That Distinguish Between Similarly Sized Substituents Like Fluorine and Hydrogen. *Org. Lett.* **2019**, *21*, 6388–6392.

[10] Mu, X.; Axtell, J. C.; Bernier, N. A.; Kirlikovali, K. O.; Jung, D.; Umanzor, A.; Qian, K.; Chen, X.; Bay, K. L.; Kirollos, M.; Rheingold, A. L.; Houk, K. N.; Spokoyny, A. M. Sterically Unprotected Nucleophilic Boron Cluster Reagents. *Chem* **2019**, *5*, 2461–2469.

[11] Sheldrick, G. SHELXT - Integrated Space-Group and Crystal-Structure Determination. *Acta Crystallogr., Sect. C: Struct.* **2015**, *71*, 3–8.

[12] Dolomanov, O. V.; Bourhis, L. J.; Gildea, R. J.; Howard, J. A. K.; Puschmann, H. OLEX2: a Complete Structure Solution, Refinement and Analysis Program. *J. Appl. Crystallogr.* **2009**, *42*, 339–341.

[13] Subramanyam, C. An Unusual Dependency of Counterion During Wittig Methylenation of Bis-Heteroaryl Ketones. *Tetrahedron Lett.* **1995**, *36*, 9249–9252.

[14] Bechlars, B.; D'Alessandro, D. M.; Jenkins, D. M.; Iavarone, A. T.; Glover, S. D.; Kubiak, C. P.; Long, J. R. High-Spin Ground States via Electron Delocalization in Mixed-Valence Imidazolate-Bridged Divanadium Complexes. *Nat. Chem.* **2010**, *2*, 362–368.

[15] Macpherson, J. V. A Practical Guide to Using Boron Doped Diamond in Electrochemical Research. *Phys. Chem. Chem. Phys.* **2015**, *17*, 2935–2949.

[16] Lindley, B. M.; Appel, A. M.; Krogh-Jespersen, K.; Mayer, J. M.; Miller, A. J. M. Evaluating the Thermodynamics of Electrocatalytic N_2 Reduction in Acetonitrile. *ACS Energy Lett.* **2016,** *1*, 698–704.